Hydrogen Evolution And Transport In Semiconductors

Daniel James Pyke

Australian National University

A thesis submitted for the degree of
Doctor of Philosophy of
The Australian National University.

October 2013

Research School of Physics and Engineering
Australian National University

Declaration

This is to certify that

1. this thesis comprises only my original work towards the PhD except where indicated,
2. due acknowledgement has been made in the text of all other material used, and
3. the thesis is less than 100,000 words in length, exclusive of tables, maps, bibliographic listings or appendices.

I authorise the Director or other authority of the Research School of Physics and Engineering to make or have made a copy of this report for supply to any person judged to have an acceptable reason for access to the information, i.e. for research, study or instruction.

Signature. . . . . .

Daniel James Pyke

Acknowledgments

EVERYBODY always features heartfelt, teary-eyed and hand-wringing sentiments in their acknowledgements for their PhD. And yes, while I accept the tenure of this doctorate was rather long, a significant fraction of my scholarly life no less, it is just another project or degree. When you look at the number of people either achieving their PhD, or writing their thesis, it doesn't look so significant. And to go on about how wonderful your parents were, or the tutors who valiantly encouraged you through undergrad, or your favourite pet cat/dog/tiger quoll, seems a little hyperbolic for what is a glorified technical report. No-one really cares.

While it is unquestionable that many people deserve thanks and acknowledgement for the help and support they provided to me over the course of this PhD, is this really the best forum for that? I mean, considering the number of people who'll actually read my PhD, it's unlikely that those worthies'll ever see themselves in the front matter here. Or even know what colour leather in which it's bound. Surely some sort of letter, chocolate box, flowers or even just general announcement would be more efficient, making it clear to all and sundry my appreciation? I guess one counter argument is the permanence of this thank-you, even if stored away in a dusty archive, not even studied by top men.

Look, there is always the need for acknowledgements, I can hardly deny that. There are a rather large body of people without which this PhD would not have been possible nor taken the shape it did. However I don't think it's too cynical to want to stick to the facts. Or as close to them as I can, before succumbing to the same peer-pressure that has everyone's acknowledgements basically look the same.

My supervisors Professor Rob Elliman and Associate Professor Jeff McCallum obviously deserve the first shout out, as it'd be rather difficult to pursue a PhD without their ok, and I'd be rather odd as a student without any academic hierarchy. In fact, if it weren't for Jeff, I'd not even be in this field, thanks to a supervisory quality-and-not-topic-based selection that goes back to Honours. And I wouldn't have been in Canberra if Rob hadn't taken a chance on someone he'd never met. Despite not being the most interactive student, and certainly a long way from being the best, I don't think there was ever a chance of them throwing me out for being πολύ-τροπος as each topic jumped to a new one prior to wrapping up the first . . . which I reckon may have been a majority trait amongst the

group of us anyway. In any event, I'd like to think it was more than just because of the money. Hopefully.

A number of the immediate members of "Rob's group" too played significant bit-parts in my PhD production. Kidane Belay particularly as an advisor as well as a bang-up sample implanter superhero was essential to keeping my project going around certain temporal pinch-points. Or lending me his lawnmower on such a regular basis I think I should've been making repayments. My fellow PhD student-cum-postdoc Taehyun Kim too proved a willing set of hands when my time plus optical profiling data requirements couldn't coincide, and lent a receptive ear to my out-loud thought processes.

The technical staff too need to be given their dues, as I certainly couldn't have fixed the low energy implanter or PIPS whenever things went pear shaped. For that, in the non-judgemental reverse alphabetical order, my undisguised thanks goes out to David Weisser, Craig Saint, Wasantha Ramasundara, David Llewellyn, Tom Kitchen, Bernie King, David Kelly, Dane Kelly, Steven Huynh, and David Anderson within the RSPE at ANU.

There are of course technical staff elsewhere that provided much more than adequate assistance. At University of Melbourne, Paul Spizziri was essential in keeping the Raman system on the up, and I'm naturally indebted to him continuing to let me play with it despite running away to a different university. Armand Atanacio was a good sort and didn't mind me hovering over his shoulder as he operated the SIMS at ANSTO.

To my colleagues (yep, that's right) in the IT department of RSPE, Julie Dalco, James Irwin and Martin Conway, without whom I think the EME computers would have collapsed in a ditch, the ditch flooded with water, the water set on fire and the fire hurled into the sun. Plus for letting me into that world of "have you tried turning it on and off again?" for most of my PhD . . . or just smiling and humouring me as I tried (and generally failed) to fix problems that they'd have pushed off a cliff or under a rug long before. That said, I really did enjoy that trouble shooting and assistance work, and I hope I helped more than hindered the department with my eagerness. And Sean Crosby, then of the IT folk clan at School of Physics in the University of Melbourne, for being able to provide both tech AND support for me as I did that whole writing up thing south of the Murray, he I owe more than a bit of appreciation.

And administrative folk – they who without which this great bureaucratic windmill (as in you always end up in the same place, and if you want to get any work done, you've got to go round and round a rather large number of times . . . ok, maybe too laboured an analogy?) would crunch to a halt – to Scott Yates, Liudmila Mangos, Cilla Gloger and Trish Gigliuto: thanks must go for always being helpful under the most trying of circumstances, and putting up with irritating PhD students who are too lazy to discover what they're meant to do by looking at the right website, or listening at the group meeting, plus finding a spot for a student to work who's not even supposed to be at your uni, but

mainly because I've always been told to keep on their good side or they'll turn on you like a savage honey badger.

Countless fellow PhD students and postdocs, too . . . actually, rather countable. In fact, listable. Ok, let's start again – I had a great group of friends at ANU for all that "the implanter's down again", spare-time-filling social calendar. I do feel awkward about listing them in any particular order, though. I mean, again, do I want to play favourites? Actually, this is my thesis, let's just play a straight bat shall we? Bianca Haberl, for aiding my European trip plans, Si material knowledge or just listening to my martyred sigh as I complained about things I'd caused unto myself, not to mention letting me live with you when my previous housemate decided he didn't need a married man in the house, eternal thanks. Ian McKerracher, Hannah Joyce, Sarah Wittig, Greg Jolley, Jordan Kang, Patrick Parkinson, Leandro Araujo, Raquel Giulian, Martin Conway (again), Michelle Day, Thomas Bierschenk, Haroldo Hattori, Hoe Tan, Taehyun Kim (again!), Supakit Chanvanichborikarn, Sarita Deshmukh, Dinesh Venkatachalam, Keng Chan, Jenny Jiang, Matias Rodriguez, Aruni Fonseka, Fouad Karouta, Simon Ruffell, Dave Sprouster, David Oliver, Alexey Glushenkov, Elena Nobleza, Anwaar Malik, Peter Kuffner, Boshra Afra, Danyu Liu, Kerstin Wagner, Elizabeth Goldschmidt, Daniel Recht, Claudia Schnohr, Avi Shalav, Suriati Paiman, Jennifer Zhu, Khu Vu, Sothia Toch, Adeline Mouzard, Matt Zuparic (well, he *was* at ANU for a bit) and Zohair Hussain – all of them contributed something positive (magnitudes, scales and involvement may vary by orders) towards my PhD and time in Canberra in general. And for University of Melbourne, Nik Stavrias, Laurence Deam, Tom Milburn, Samantha Lichter, Nina Eikenberg, Jessica van Donkelaar, Victor Peronicic, Mark Kowarsky, Babs Fairchild, Paul Fraser, Sean Crosby (AGAIN!), Trish Gigliuto (ditto), Byron Villis, Brett Johnson, Herianto Lim, Rachel Gore, Kin Kiong Lee, Daniel Wells, Katharina Koenig, Jinghua Fang, Michelle Livett, Jude Prezens and Colin Entwisle, who made the return run to Melbourne in the early days, and my rather permanent "Temporarily based at" visit later on, into events full of fun, while being productive, educational and economically viable.

Following the hiccough of my "cyclist versus truck" incident last year, I feel too that some thanks should go to the various medical and rehabilitation experts who patched me up and got me back on my feet. However this may stray into irrelevance to the matter at hand, so my vague hand-wavey thanks is the best I can offer here to the staff at Royal Melbourne Hospital and Epworth Rehabilitation Hospital Camberwell. For their direct involvement in things PhD-related, I must at least explicitly mention my neuropsychologists Michelle Morandin and Bronwyn Coward at Epworth, and the pragmatic yet optimistic counsellor Carmel Stafford. All three of these wonderful women gave me some more of the tools that allowed me to get back on this beast's back following the accident.

. . . is this getting too long?

I could list friends, family and so on to this mix, but remember from the beginning, we're here having this one-way conversation because of the *Doctor of Philosophy* part of this data-printed-on-dead-tree glorified flower press. So my love and thanks to them, self evident as it is, doesn't need publishing in this text.

But quite frankly, for putting up with more than her fair share of "my partner's living in another state", "it's only two years past standard completion time", "most people at ANU take longer to finish", "really, I'm unlikely to get a job after this anyway", and so on, to Dr Waven Zhang Pyke I owe the greatest debt of gratitude. Even despite that whole "boyfriends that move to Canberra get dumped" stuff at the beginning, I'm always amazed at the patience demonstrated by someone who espouses to have very little. Maybe now I've gotten back to Ithaki, my love, all this will prove worthwhile.

Abstract

Silicon-on-insulator (SOI) structures are used for the fabrication of integrated electronic circuits, photonic devices and structures, and micro-electro-mechanical systems (MEMS). The most common fabrication method for SOI is a hydrogen-induced cleavage technique in which ion-implanted hydrogen is employed to initiate and propagate cracks in a plane parallel to the silicon surface. Considerable research effort has been devoted to understanding this cleavage technique in (100) silicon but several fundamental issues remain unclear, including the role of stress on hydrogen platelet alignment, and the details of the bond-breaking processes associated with crack propagation (i.e. stress induced or hydrogen-mediated). In addition, there is keen interest in extending the technique to other silicon orientations (i.e., (110) and (111)) and semiconductor materials (e.g. Ge, SiGe).

Initially, the intrinsic behaviour of hydrogen ion-implanted into Ge and Si was examined by ion beam analysis, optical profilometry and microscopy, to establish the influence of lattice damage and hydrogen evolution. In particular, hydrogen-induced blistering and crater formation under thermal annealing from T=300-650°C was studied to determine the activation energies in Ge and Si in several crystalline orientations. Secondly, the same techniques were employed as the influence of compositional and extrinsic applied stresses upon hydrogen's evolution within Si was studied, with the former exploring recrystallised amorphous Si layers, SiGe composites and delta-doped Si layers, and the latter by mechanical stress application onto Si(100) by uniquely developed solutions. TEM was used to study the defect evolution related to the hydrogen and ion-implantation damage under anneals applied to samples under stress, in addition to samples produced in different strain conditions.

Blistering rate and areal density followed logistic sigmoidal functions in all materials. Constant activation energies were measured for all Si samples under selected implantation

conditions, but multiple activation energies were found in each Ge sample when the conditions were varied. Si(100) and Si(111) both blistered readily for all temperatures, Si(110) required higher H fluence and Ge showed inconsistent behaviour at different implantation conditions. Blister crater depth and roughness may be closer linked to local H concentration rather than total implantation fluence. High level doping of Si does not significantly change the dynamics of H blister formation, with potentially exploitable benefits for SOI production.

Stress induced by ion implantation in Si and Ge is measurable and tensile, though relaxes somewhat with thermal annealing, in the order of $<$1 MPa. Both 50 and 375 μm thick Si wafers behave similarly when implanted with H. Tensile stress applied to H-implanted thick Si(100) influenced hydrogen defect alignment within the lattice, shifting complexes to {011} and {100} planes following annealing. In ULTRATHIN® Si, application of tensile stress may relatively diminish and compressive stress enhance diffusion of H, although *any* applied stress during implantation decreases H concentration. Tensile stress applied during thermal annealing may increase RBS dechannelling yields of the Si crystal, while compressive stress decreases direct scattering yields. Applied stresses above σ=400 MPa cause the height of hydrogen surface blisters to decrease and density to increase. Blisters formed during annealing are not permanently decorated with nor contain hydrogen, whether under applied stress or not. Orientations of detectable defects are not strongly affected by application of stress, however concentrations decrease at high stress. The location of the ion-cut inducing defect does not appear to correspond to long term measurements of H or implantation damage, and may be even shallower, but this cannot be unambiguously confirmed.

Contents

List of Figures

List of Tables

οὐ γὰρ ἐγώ γέ τί φημι τέλος χαριέστερον εἶναι
ἢ ὅτ᾽ ἐυφροσύνη μὲν ἔχῃ κάτα δῆμον ἅπαντα,
δαιτυμόνες δ᾽ ἀνὰ δώματ᾽ ἀκουάζωνται ἀοιδοῦ
ἥμενοι ἐξείης, παρὰ δὲ πλήθωσι τράπεζαι
σίτου καὶ κρειῶν, μέθυ δ᾽ ἐκ κρητῆρος ἀφύσσων
οἰνοχόος φορέῃσι καὶ ἐγχείῃ δεπάεσσι·
τοῦτό τί μοι κάλλιστον ἐνὶ φρεσὶν εἴδεται εἶναι.
σοὶ δ᾽ ἐμὰ κήδεα θυμὸς ἐπετράπετο στονόεντα
εἴρεσθ᾽, ὄφρ᾽ ἔτι μᾶλλον ὀδυρόμενος στεναχίζω·
τί πρῶτόν τοι ἔπειτα, τί δ᾽ ὑστάτιον καταλέξω·
κήδε᾽ ἐπεί μοι πολλὰ δόσαν θεοὶ Οὐρανίωνες.

...

εἰ δ᾽ ἄγε τοι καὶ νόστον ἐμὸν πολυκηδέ᾽ ἐνίσπω,
ὅν μοι Ζεὺς ἐφέηκεν ἀπὸ Τροίηθεν ἰόντι.

- Homer, Odyssey, Book IX.5-15,37-38

Chapter 1

Introduction

SILICON-on-insulator materials (SOI), or to be more general semiconductor-on-insulators [1], are increasingly becoming the material of choice for a host of applications, such as personal computer processors [2], entertainment devices [3], sensor and detector applications [4], high performance RF devices [5] and silicon photonics [6], amongst others [7–10]. Formerly most SOI was manufactured via implantation of oxygen ions, using ion beam acceleration and high temperature annealing [11], or expensive bonding and polish/etchback processes [12]. However, the high rate of defect production within the material and manufacturing cost of these methods lead to the development of the ion-cut or SmartCut™ technique [13]. This method employs the implantation of a specific fluence of hydrogen ions into an oxidised semiconductor wafer, which are ultimately used to rupture the lattice at their implant site, via their thermal transformation into larger complexes such as cavities and hydrogen gas bubbles [7, 14, 15]. The precise location at which this fracture takes place was initially assumed to lie at the peak in the implanted hydrogen profile [16–20]. Others posited that the break would occur at the peak in the ion implantation damage profile [21–23], or at intermediate depths [24, 25]. However, recent evidence increasingly points to the breakage forming at the peak in the material's strain profile, a consequence of the local hydrogen concentration and its implantation damage [26, 27]. Speculation has ensued that this strain profile could be tailored to improve the ion-cut process by localising the hydrogen profile, requiring lower fluence [28]. Strain modification is increasingly used in integrated circuits [29], light emitting diodes (LEDs) [30, 31], quantum dots [32, 33], high-speed transistors [34], multijunction solar cells [35, 36], metal-

oxide-semiconductor field effect transistors (MOSFETS) [37] and micro-electromechanical devices (MEMs) [15]. Modification of the materials to include different strain fields, or altering the strain field within an existing hydrogen-implanted semiconductor, may lead to improvements in the process. Simultaneously, a better understanding of the behaviour of hydrogen within semiconductors under a range of strain or stressed environments would improve our understanding of the hydrogen-semiconductor system as a whole, for other potential applications.

Synopsis of the Thesis

To ascertain the behaviour of hydrogen in strained semiconductors, this investigation explored ion-implanted hydrogen in silicon and germanium. As the crystallographic orientation is also of interest, Si wafers in (100), (110) and (111) were contrasted. In order to allow mechanical application of strain upon hydrogen within silicon, ULTRATHIN® Si (100) wafers (∼50 μm thick) were employed, and a mechanism for straining the wafers – both under compression and tension – during implantation and or annealing was developed.

The key principle of this thesis is that the application of external strain fields can be controlled to alter the trapping or diffusion of hydrogen within semiconductors, allowing manipulation of the hydrogen profile to improve upon the ion-cut process.

An overview of the ion-cut system, and the influences of strain in semiconductors, particularly on hydrogen, are presented in Chapter 2. Techniques used to quantify the evolution of hydrogen in each system, via ion beam, optical interferometry, electron microscopy, x-ray diffraction and others, are elaborated upon in Chapter 3. (Simulations to determine the potential for mechanically applied stresses to semiconductors, and the evolution of implanted hydrogen profiles under annealing, are presented in Chapter A.)

The basic behaviour of hydrogen in silicon and germanium under various fluence and annealing conditions is first outlaid in Chapter 4, including the influences of and behaviour along different crystal directions. The blistering and cratering behaviour of hydrogen annealed in Si and Ge when no external confinement is applied are presented in Chapter 4, suggesting the direct relationship between implant fluence and energy and the blister dimensions, along with ultimate crater surface roughness. Determined via electron mi-

croscopy, ion beam analysis and optical techniques, the influences of stress in mechanically strained semiconductors on ion implanted hydrogen is expanded upon in Chapter 5.

Chapter 6 contains summaries of the results and analysis presented in Chapters 4, and 5, along with conclusions and further potential avenues of investigation.

The thesis, or hypothetical proposition, of this investigation was that stress can be applied to semiconductor systems to modify the behaviour of hydrogen's transport and trapping. While strictly this thesis was confirmed, and its results revealing scientifically, the magnitude of the effects upon hydrogen would perhaps fail to prove beneficial commercially.

Chapter 2

Literature Review

An overarching review of the relevant themes of this thesis is given by presenting a focused history of previous work in key areas. What are the questions and pertinent issues that exist in this specific field that we seek to address? In consideration of the relevance, import and interest of this investigation, it is worth remembering the argument of John Henry Newman *et al.* [38] that all knowledge is for knowledge's sake.

The original impetus for this project was the development of the wafer slicing technique SmartCut™ [13]. The use of this particular method of fabricating silicon on insulator (SOI) has become increasing prevalent [28]. The origins of this technique are reviewed in Section 2.1. Reliant for the most part upon the interactions between the hydrogen ions implanted to produce the SmartCut™ effect, a broader examination of the interactions of hydrogen in semiconductors is presented in Section 2.2. Strain and stress are used in this thesis in an attempt to enhance the trapping or mitigating the diffusion of hydrogen within the semiconductor. As such, this key factor is explored in Section 2.3, describing the nature of intrinsic and extrinsic stresses applied within and upon semiconductors, and its influence on dopants.

2.1 SmartCut and its origins

SmartCut™, or "Smart-Cut" as Bruel first described it [13], was developed at CEA-Leti in Grenoble under the code name "IMPROVE" (IMplantation of PROton Voids Engineering)

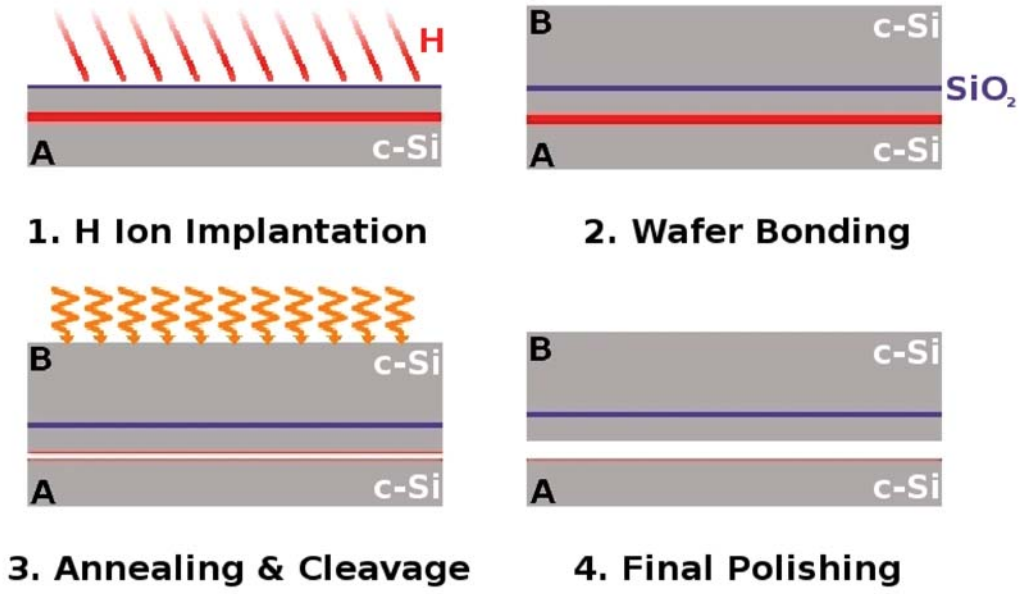

Figure 2.1: Flowchart representing the basic SmartCut™ process, adapted from Fig. 1 as shown in [13].

in 1994. The basic form of the technique was initially described by Bruel as follows: Hydrogen ions are ion implanted into an oxide-capped silicon wafer at fluences between 3.5-10$\times 10^{16}$cm^{-2} (1). This wafer, labelled "A" is then bonded by its implanted surface to the polished surface of another silicon wafer, labelled "B", by means of hydrophilic bonding [39] (2). The combined wafer system is then exposed to a two tier annealing regimen – firstly at T=400-600°C to split the wafer along hydrogen implantation region, causing a thin layer of crystalline material from wafer "A" to remain attached to wafer "B", and secondly at T$\geqslant$1000°C to strengthen the chemical bonding between the original A-B wafer interface (3). The remaining composite wafer (B wafer + A sliver) is then polished to remove surface micro-roughness, prior to use in device fabrication, etc., while the remainder of the "A" wafer can also be polished and used again for the same process (4). This process is shown schematically in Fig. 2.1, and in addition to its trademarked name, is generically known as wafer delamination, ion-cut or hydrogen slicing.

SmartCut™ evolved from work studying the behaviour of ion implantation of hydrogen in semiconductors [40–45], in concert with results of hydrogen/proton damage to metals in high temperature environments such as nuclear fission and fusion reactors [46–48].

The generic use of a layer lift-off after ion beam bombardment of surrounding material

has also been fashioned for fabrication of micro- and nanometre scale devices, in media from silicon [49, 50] to diamond [51, 52].

SmartCut™ as a process has made significant improvements by insightful selection of conditions and a largely evolutionary analysis. As such, advanced substrates are now fabricated on mass industrial scale for use in microelectronics [7, 8].

Despite the en masse production via SmartCut™, the precise details are not fully understood. Such a lack of understanding prevents directed improvement and modification of the process, relying instead on evolutionary progress. In order to clarify the rôle of each constituent, it becomes useful to factorise the SmartCut™ process into its key elements. Significant research has focused on the substrate type and structure [15, 21, 53–56], wafer bonding [16,57], hydrogen species, concentration and energy [18,58–63], introduction mechanism and diffusion dynamics [64–68], defects (including voids, cavities and blisters) formation and evolution (including activation energies) [19, 20, 22, 69–72], wafer exfoliation and cracking [73–78], and contributions by stress and strain [79–81], additional dopants [82–88] and thermal and environmental conditions required to initiate the process, in addition to resultant roughness [19, 77, 89–96] and residual elemental composition of fabricated structures [9,97,98]. Few of these investigations focused exclusively on one aspect, possibly due to difficulties in isolating elements of the system or process, but a picture of the process as a whole has been significantly developed. Feng *et al.* [14], Xu *et al.* [99], Gu *et al.* [78] and Cerofolini *et al.* [100], amongst others, have all developed theoretical models to explain the behaviour of hydrogen within semiconductors, and the evolution of defects and cavities via hydrogen used in ion-cut material.

Recent work by David *et al.* [101] and Moras *et al.* [102] have suggested that the macro-scale cracking used by the SmartCut™ process is not pressure driven, due to its high regularity and nanoscale smoothness of the resultant surfaces. Rather, both works suggest it proceeds from stress-corrosion cracking, using the hydrogen as a method of lowering the energy requirements of bond breaking.

Work by Nickel *et al.* [103] suggests that the relationship between the hydrogen, the defects which its implantation precipitates and the strain those defects engender is symbiotic. Hydrogen implantation is shown to move the Fermi level towards the surface, making it favourable for hydrogen-induced platelets to develop in that region. The platelets that de-

velop then increase the localised strain around them, forcing the favourable growth region deeper into the wafer.

Most early work focused on wafer splitting in (100) oriented Si wafers, with the cleavage occurring in a plane parallel with the surface. Interestingly, a number of sources have reported ion cut occurring preferentially along the (111) plane [75, 104]. However, Perez *et al.* [75] elaborate that the stress density and resultant trapping that occur in practicality seem to counter the ease of splitting in this plane, instead producing the {001} plane cracking most regularly seen. Gu *et al.* [105] also explain this discrepancy as the result of distortion of the silicon lattice due to the H implantation, which prevents both growth and natural cleavage (leading to ion-cut) via {111}-aligned platelets.

Surface blistering

When the constricting strain field produced by the handle wafer (labelled Wafer B in Fig. 2.1) is absent, the evolution of hydrogen in the silicon differs [106]. Rather than forming platelets generally restricted to the {100} planes within the material, the hydrogen is free to agglomerate through a variety of processes into "bubbles" and three dimensional cavities potentially centred around the peak in either the local strain field or the hydrogen concentration, which share similar distributions (although a slight offset exists between the strain field and implanted hydrogen profile). At lower ion implantation energies (<10keV) and/or high enough fluences ($>1.5\times10^{17}\text{cm}^{-2}$), blistering can occur during the implantation process [13] under appropriate thermal conditions (generally room temperature or higher) [28], particular wafer crystalline orientations [107] or materials [21].

Studying ion-cut type phenomena can involve reasonable levels of complexity, largely due to the activity occurring buried within a semiconductor wafer. To simplify investigating the atomistic processes of wafer slicing, Tong *et al.* [108] presented a comparison of blistering on unbonded wafers with hydrogen-induced splitting in SOI bonded wafer pairs (à la SmartCut™). Tong found that the behaviour showed some differentiation, in that the time for splitting is ten times longer than blistering. But both are sufficiently similar in activation energies to allow use of either situation to further explore the system's particulars. Thus in our study and many others, surface blistering/cratering of hydrogen-implanted semiconductors stands in proxy for the more difficult to measure complete ion-cut system.

Examining the blisters which develop on the surface of the hydrogen-implanted semi-

conductors when annealed, Huang *et al.* [90] and Coupeau *et al.* [109] demonstrated that the blisters simply "appear" once a critical energy level is reached, more like a step-function and not a gradual growth process.

The blisters' sizes also appear to be limited by the system as a whole, as Weldon *et al.* [106] reports that the hydrogen-induced defects evolving within Si(100) are dynamically linked to a perpendicular restoring force provided through strain applied by the "handle wafer" used in the SmartCut™ process. This restoring force also is presumed to aid in the propagation of the cracks between the platelets, planar within the substrate. Proceeding from this assertion, then there should be some upper limit to which a hydrogen-induced blister or platelet can extend within the plane without external influence. This conclusion may also indicate that the ultimate size a blister can grow to in any substrate without out-of-plane stress would solely depend on annealing exposure time, as further time would allow more accumulation of hydrogen.

Hong *et al.* [69] calculates the size (=radius) and height of the hydrogen-induced surface blisters depending upon a given pressure of H gas within them. Their predictions, calculated with data of blister sizes, suggests an internal pressure of P=100 MPa-1 GPa.

The ability of the hydrogen to evolve not into blisters but instead a linked array of platelets that ultimately cleaves the wafer has been particularly investigated. Feng *et al.* [14] calculated a relationship between the size the blisters can grow, R, to the hydrogen concentration's depth, h, for the circumstances where no handle wafer is present, using thin film approximations – $h/R \ll 1$. This leads to blister and crater formation (exfoliation) of the wafer for fluences half that required for SmartCut™, indicating the "handle" wafer presence has a stiffening effect upon the donor wafer, changing the energetics of the wafer slicing process. Similarly, at small depths h, rather than cause continuous planar cracking, the surface may blister and flake off, given a ratio of splitting to flaking proportional to squares of the stress intensity factor at the crack tip, hydrogen embrittlement, and inversely proportional to depth and the square of the maximal stress condition for crack propagation.

Reboh *et al.* [110, 111] demonstrate differing behaviour for samples ion implanted at different beam currents for samples implanted to depths to fulfil Feng's $h/R \ll 1$ relationship [14]. For implantations at low beam currents ($I \sim 0.25$ μA), it is possible for a stable stress corrosion-type cracking to occur. Akin to that described by Moras [101] and

David [102], corrosion cracking would appear to form through combination of pressure build up and weakening of the Si-Si bonds through the reactivity of hydrogen, further lowering energy requirements in breaking Si=H-H=Si complexes. For high beam currents ($I \sim 1.5\ \mu$A), no such stable state exists. Instead the thermal formation of gaseous hydrogen after sufficient annealing leads to large scale micro-crack formation, with the planar separation driven by out-of-plane stress constricting the evolution of the crack to linking the microcracks.

The "Elusive Hydrogen"

Düngen *et al.* [112] showed that following a SmartCut™-like exfoliation and layer transfer for H-implanted Si(100), most Raman-measurable hydrogen was present in the transferred layer, with only trace amounts in the donor wafer. Other measurements of hydrogen evolution in similar systems do not make it clear where the hydrogen goes. A certain degree of uncertainty is present when attempting to optically characterise the evolution of the hydrogen. Beyond certain thermal anneals, a significant fraction of the total hydrogen content is not observed by optical techniques, reported by Chabal and Weldon *et al.* [57, 106, 113].

Termed "elusive hydrogen" by Terreault [28], the absence of hydrogen may reveal something more telling than the necessity of complementary measurement techniques. As measurements for IR and Raman are often performed at room temperature, the sample is allowed to cool between anneals, potentially changing the form of the hydrogen present in its structure, as observed by Ma *et al.* [114]. Terreault also suggests a thermal dependence may exist for certain states of hydrogen, leading to a perceived lack of H. The interstitial, Si-bonded and multivacancy-trapped molecular hydrogen may transition to free gaseous H_2 during annealing, but fall back into alternative optically invisible forms on cooling before measurement. However this is not conclusively proven, with comparisons made across different studies to support the argument. Alternative measurement techniques sensitive to the structure of hydrogen takes would allow resolution of this mystery.

Increased efficiency via co-implantation alongside H

Co-implantation by an additional ion such as He, Ar, B, As, or P was developed in an attempt to decrease the fluence, thermal, mechanical and ultimately cost factors of the SmartCut™ process [115–120]. Particularly, some of the earliest work by Tong *et al.* [82]

used a boron co-implantation, showing the capacity to significantly reduce the blistering temperature. Increasing boron concentration appeared to aid the formation of hydrogen defect complexes via increased trapping and higher point-defect concentration produced by the additional implantation, lowering blistering (or splitting) temperatures to T$\sim$300°C. Activation of the B by a light anneal (T=250°C) also showed further decreases in hydrogen blistering's required thermal energy. (Tong co-incidentally showed that the Si layer could successfully be transferred onto lattice mismatched substrates such as quartz and sapphire.) This facilitation by boron of hydrogen diffusion and reduced energy requirements (demonstrated by increased surface blister density) was confirmed by Höchbauer *et al.* [121], who also reported that this was mediated particularly by boron at interstitial sites. Examining these claims by Tong and Höchbauer, Lee *et al.* [122] found that the number of defect or trap sites actually *decreases* with the presence of B, and explained that increase in diffusivity of hydrogen was due to a decrease in trap density, allowing greater H-related complex formations, such as platelets and blisters.

A "multi-implantation" process was investigated by Usenko [123, 124], where the Si wafer was irradiated by near-amorphisation levels of Si ions (180keV, 2×10^{15}cm^{-2}, RT) then (395keV, 1×10^{15}cm^{-2}, RT) Ar ions prior to hydrogenation by 300W RF plasma, producing a hydrogen concentration of approximately $\Phi_H \sim 10^{16}$cm^{-2}. Trapping of the hydrogen was measured on the damage caused by either the Si or Ar implantation. Usenko concluded the key factor driving the planar slicing of the Si is the pressure (and hence concentration) in the hydrogen platelets. Via this method, the pressure is increased by increasing the precursor irradiation fluences, which would prevent increasing the ion-cut process without also the ion implantation damage.

An alternative co-implantation is the use of helium, which could assist in the production of cavities prior to the H implantation, or alter the damage or defect density and local strain environment. Duo *et al.* [115, 116] performed a comparison of helium implantation before or after the hydrogen, and found little influence on the diffusion behaviour or evolution of the hydrogen profile. The strain field induced by (presumedly) the implantation decreases and shift deeper with thermal annealing, and the helium showed greater mobility, diffusing alongside the hydrogen profile, effectively combining its molecular gas volume to the defects precipitated by the hydrogen.

Qian *et al.* [58] reported on single He and H implants in addition to co-implantation of both ions in Si, all at low energies in order to exfoliate a thin silicon layer. The thermal annealing requirements for blistering was higher in the shallow implant, with suggestions that radiation defects induced by the higher energy implantations aid their blistering and exfoliation rates. The co-implanted Si showed 10%-15% larger blisters, however similar to Duo [116], the region which blistered (and ultimately exfoliated) did not change significantly. However, later work [125] showed a lower total fluence (around $\times 2.5$) was required to produce surface blistering comparable to H only implantation.

The pre-existing network of cavities (labelled cracks) and stress fields produced by implanting and annealing He in Si were used by Reboh *et al.* [126] to study the behaviour of cracking mechanisms in subsequently implanted H ions. The presence of hydrogen at the crack tip–substrate interface within Si allowed propagation of planar micro-cracks at lower temperatures than would otherwise occur. The angle between crack-type defects determined how readily they would use elastic interactions and combine to form a continuous micro-crack, or use plastic interactions and produce twinning defects and prevent the linkage. Stressed or strained interfaces around the cracks aid the propagation at lower energy anneals and hydrogen concentrations.

Work by Wang *et al.* [127] and Liu *et al.* [119,128] used co-implantation of H and He into Si(100) substrates at higher energies – 160 keV for He and 110 keV for H – both at fluences individually below the ion-cut threshold. Wang reported the lowering of total fluence inducing blistering, although the resultant surface was rougher than reported elsewhere, potentially due to two peak damage locations produced by the dual implantation. Liu [119] expanded to contrast Si wafers coated in either Si_3N_4 or SiO_2 layers, implanted under the same conditions as Wang, either solely He or the ordered combination of He-H. In the Si_3N_4 coated sample, two surface blistering (and cratering) events occurred under high temperature ($T>600°C$) annealing, from the oxide-wafer interface, and from the implanted ion profiles' peak depth. The SiO_2 samples showed no exfoliation even at $T=1100°C$, but large scale surface blister formation, of increasing dimensions with higher annealing temperature. Liu proposed that this variation between oxide and nitride layers may be due to the different strain conditions applied. As Si_3N_4 has a lower tensile strain, it may sooner suffer separation from the bulk than SiO_2, and this difference in strain may be changing

the diffusion and trapping dynamics for the He and (more significantly) H. As such, it was concluded that Si_3N_4 was unsuitable in ion-cut applications, and minimal benefits were seen for He and H co-implantation. In contrasting the roughness of the samples when implanted at different H energies (40keV, 110keV) following a constant He implant (160 keV), Liu *et al.* [128] showed that the behaviour was largely consistent with that seen in singular H implanted Si. The shallower, E=40 keV implantation produced surface blisters and craters to the approximate depth of the H profile peak, while the E=110 keV implantation seemed to induce a complete surface exfoliation, to a depth again consistent with the implantation profile peak's depth. However the total implanted fluence which allowed these samples to blister or exfoliate was again lower than that required for similar behaviour in single ion implantations.

Hydrogen's interaction with dopants

The influence of dopants in modern day device engineering has led to significant research. In particular, the role of B in its interactions with hydrogen has been heavily investigated [56, 83, 86–88, 121, 122, 129–132], as have boron-silicon interactions [131, 133–135]. The role phosphorus can play in passivating an array of defects in compound semiconductors, such as threaded dislocations, was investigated by Christensen *et al.* [136, 137] and others [138, 139]. Gosele *et al.* [140] explored how carbon could influence the diffusivity of point defects within silicon, altering the kinetics for hydrogen-related defect formation by varying vacancy and self-interstitial defect availability. How metal dopants such as Cu and Ni would affect the electronic properties by interacting with dislocations within silicon was reported by Seibt *et al.* [141]. Other work by Li *et al.* [142] investigated the influence of a range of dopants upon both the silicon structure and hydrogen evolution.

According to Li, the range of the implantation damage and hydrogen platelets increases in As- and P- doped Si, but decreases in B-doped Si. Changes in the Fermi level of the Si were used to explain the greater possibility of platelet formation in n-type Si, explained using Johnson's theory [143–147]. Discussed by Van der Walle *et al.* [148], paring is suggested as a possibility for the decreasing roughness and range of damage in p-type material. While Li *et al.* discuss completely exfoliated surfaces, akin to lift-off of the layer by ion-cut [16, 17], individual blisters or cavities are not discussed, nor is the process duration apparent from the fixed anneal temperature and interval. As the stress within the Si

crystal due to the implantation damage is a contributor to the ion-cut process [106], it is likely that the changes produced by differing dopant levels within the substrate will not only influence the roughness (via range of the damage described in Li [142]) but also the energetics of the process, changing blistering sizes and rates.

Implantation of boron into silicon prior to hydrogen implantation is shown to influence the diffusion of the hydrogen ions under subsequent evolution, with the hydrogen tending to trap at the boron profile peak if deeper, or at the silicon vacancy peak produced by the boron implantation if shallower [86]. Work by Nurmela *et al.* [87] suggests that boron dopants grown epitaxially into the silicon wafer will reduce the implantation damage (with low level annealing) compared to an equivalent implant into an intrinsic Si wafer, while complementary work [121] suggests that the substitutional boron assists the nucleation of hydrogen into bubbles to blister or crater in n-type Si substrates. Henttinen *et al.* [85] further suggests that the role of boron acceptor nucleation expedites the blistering process in the Si:H system, and shifts the blister location closer to the Si surface. Interestingly, Henttinen reports that As doping of the Si results in no significant change in the exfoliation behaviour. In all, this suggests that dopants are at worst a nuisance to preparation for the ion-cut process; at best, they may serve to engineer particular behaviour for specific microelectronic device requirements.

Alternatives to ion implantation

While the initial process of SmartCut™ involved ion implantation to introduce the protons or hydrogen into the semiconductors, there has been significant research into the use of hydrogen plasmas [149–154]. The use of plasma is not particularly new to materials modification for microelectronics, and is still undergoing refinement and development [98, 151]. A large motivation for using plasma hydrogenation rather than ion implantation was to minimise damage and defect development in the overlying Si layer, seen in work by Usenko [123], Chu [150] and Shao [153]. Düngen [98] and Usenko also indicate that lower hydrogen concentrations may be required for exfoliation when introduced by hydrogen plasma. In particular, Düngen uses a combination of ion-implantation at low hydrogen fluence to produce a low density of lattice damage and trapping sites, prior to plasma exposure, to allow the hydrogen ions from the plasma to accumulate at a specified depth. However the low temperature plasma ($T<450°C$) produced a significantly

higher concentration of hydrogen platelets along {111}, and does not appear conducive to SmartCut™ processes.

Alternative material substrates

The use of this wafer slicing technique has expanded to transfer of silicon onto other substrates (e.g. sapphire, Ge, SiC, etc.) [15, 155–159], as well as Si_xGe_{1-x} composites [160–163]. More recently, focus has shifted to the operation of this process within Ge and III-V semiconductors [9, 15, 54, 164], and fabricating composite devices by layer transfer [4, 165, 166].

Similar to other electronic production techniques, Yun *et al.* [104] has shown that the technique can be expanded to use with masks, enabling patterned layer lift-off. Yun also showed that SmartCut™ can produce composites via layer transfer in polycrystalline silicon [167], and area of great interest, for example, to solar cell research [168, 169].

Working in Ge, Hurley *et al.* [118] and Ma *et al.* [56,130] also employed co-implantation with the goal of reducing the thermal budget of the ion-cut process. The choice of elements to co-implant – He for Hurley and B for Ma – corresponds with expectation of behaviour as in Si. The behaviour too, was not dissimilar to co-implanted or singly implanted Si.

The activation energies for blistering determined by Hurley for co-implanted He and H in Ge(100) were quite similar to those reported for H-implanted Ge [21, 108, 170], though variations with temperature were only seen in Yang *et al.* [171]. The lower activation energies than seen in Si followed predictions based upon the materials' respective bond energies (Ge: 1.61 eV, Si: 1.81 eV).

Ma *et al.* [56, 130] initially implanted Ge(100) substrates with B ions prior to H, with fluences of $\Phi_H = 5 \times 10^{15}\text{cm}^{-2}$ at energies designed to superimpose with the H profile, as well as complementary Si(100) samples for comparison. The blistering temperature and hence activation energy decreased in Ge with increasing B concentration, as in Si [82, 121, 122]. The absolute temperature required to induce blisters in H-implanted Ge was reported to be higher than Si, contrary to the behaviour in solely H-implanted Si and Ge [108]. Also, Ma showed different orientation of hydrogen-related defects occurring at strict depths within the implanted Ge. The enhancement of blistering via boron co-implantation is postulated to benefit from lower trap density, as suggested for Si by Lee *et*

al. [122]. Similar to Tong, Ma also showed that Ge layers could be transferred successfully onto SiO_2/Si wafers.

Influence of local stresses

Huang *et al.* [172] investigated the use of a buried lattice-mismatched layer to act as a trap for diffusing elements, such as hydrogen, and to minimise the strain required to SmartCut™. In the context of transferring a Si layer onto a quartz substrate, a B-Ge epitaxial layer was deposited upon a Si substrate, and then Si epitaxially grown over as a surface layer. A high temperature plasma was used to introduce hydrogen ions into the material, with hopes of trapping at the Si/B-Ge interface. It is unclear if the accumulation of hydrogen at the interface was due to the trapping capacity and local strain change by the boron, or by a potentially high defect region that the fabrication method can produce. The presence of B causes a lower temperature blistering activation energy, and it is asserted this would allow blistering damage to be limited to the B-Ge region of the donor wafer.

Toyoda *et al.* [173] report significant stress and screw dislocations are formed when two non-lattice matched wafers are bonded directly, without either an oxide or buffer layer between them. This limitation could provide a benefit of preventing unwanted diffusion from one layer to another, as the dislocations act as a trap. However, as the diffusing element, such as hydrogen, would concentrate at the interface, this may not be useful for ion-cut type processes.

Overall, the indications that strain fields and localised stress can influence the evolution of hydrogen within semiconductors shows potential for improving upon not only the ion-cut technique, but the manipulation of hydrogen within numerous semiconductor fabrication processes, from traditional CMOS to advanced MEMS devices.

2.2 Hydrogen in semiconductors

More broadly than just the previously discussed SmartCut™, the behaviour of hydrogen present within materials, whether intrinsically or introduced, has been widely researched over the past seventy years, prior to exploration of potential applications.

The limits of hydrogen's solubility in silicon described by Acco *et al.* [174], its interaction

with defects within crystalline materials compiled by Myers *et al.* [175], or particularly germanium [176–178], as well as its influence on semiconductors generally as reviewed by Van der Walle *et al.* [179] and Pearton [180], and ultimately the key role it plays in the ion-cut process as assessed by Terreault [28] and Feng *et al.* [14] indicate the breadth of hydrogen's native and engineered influence. In the case of the ion-cut or "Smart-Cut" technique [16, 17, 170, 181], there are a sufficient number of sub-elements that influence the system to occupy even the most fervent researcher.

The evolution of atomic or molecular hydrogen in semiconductors under thermal annealing is of particular interest, as the additional energy provides impetus for diffusion, hydrogen gas formation and ultimately rupture of the material substrate.

In the most commonly used material, silicon, hydrogen has tremendous impact on its thermal, electronic and mechanical properties. A thorough understanding of hydrogen's precise behaviour in silicon in addition to other potential materials is thus crucial to the ability to control and improve upon the ion-cut technique.

Introduced Hydrogen

In addition to native hydrogen concentrations present within a material [182, 183] or in-diffusing from the surface [184–187], hydrogen's deliberate introduction into semiconductors serves a wide array of purposes. For example, the hydrogenation of an amorphous layer, while detrimental to the solid phase epitaxy (SPE) process [188–190], is particularly beneficial for solar cell fabrication [168, 191, 192] due to its ability to reduce the density of both dislocations and electrically active dangling bonds. Work by Nakamura *et al.* shows H acting to eliminate defects caused by oxygen and other impurities within (100) silicon [193]. Pavesi *et al.* [194] report similar theoretical work to support H in GaAs acting to passivate Si dopants, because the H has an energy lower in the GaAs matrix making it a ready donor to the Si atoms. Similar deep donor action was reported by Tavendale *et al.* [195], with the potential for decreasing recombination centres, although hydrogen's presence in metal-oxide semiconductor field-effect transistor (MOSFET) devices was seen as a potential nuisance. Johnson [144, 145] demonstrated hydrogen neutralising shallow acceptor impurities in (100) silicon, more efficiently in some cases than other bonds, such as P-H. For such neutralisation, there is the added requirement of additional positive holes in the vicinity, without which the H bond will prove electronically parasitic. Chevallier *et*

al. [43] effuse with the potential beneficial uses for hydrogenation, in III-V field-effect transistor (FET) devices, photovoltaics, MOSFETs, and optical wave guides, among others.

Even the essential influence on the structure of the semiconductor from hydrogen's presence is important. Expansion of the substrate lattice in Si(100) has been measured by Giguere *et al.* for ion implanted hydrogen fluences greater than $3 \times 10^{16}\text{cm}^{-2}$, with step heights as high as 20 nm [49].

When modifying the material by ion implantation, the range of damage that is caused extends beyond the superficial. Suggestions have been made that this internal damage induced by the ion implantation could act as a trap for additional hydrogen ions introduced by plasma, leading to supersaturation of the silicon. Such saturation is presented in work by Saad [196], discussing the exposure of various hydrogen implanted substrates to hydrogen plasmas. Keinonen *et al.* [42] discuss how most H implantation into Si cannot cause amorphous regions due to critical energy per volume requirements. Also, Keinonen asserts that the damage distribution caused by the implantation is not a reflection of the deposited energy profile.

Defect Development

The evolution of defects produced within silicon via ion implanted species has been investigated due to its paramount importance to the microelectronics industry [197]. Hydrogen concentrations resulting from almost any fluence and energy implanted into silicon can induce several kinds of defect structures. From the basic vacancies and interstitials, these can vary to significantly more complex forms, such as voids, platelets, dislocation loops, stacking faults, and {311} rod-like defects [198]. Exposed to moderate to high temperature anneals, these defects can evolve into more complex structures, such as hydrogen within platelets growing via Ostwald ripening to form larger blisters or voids [199].

Turnbull and Fisher greatly enhanced our understanding of the nucleation mechanisms involved in defect development in intrinsic crystalline systems [200, 201]. Turnbull's initial models accounted only for short-range migration of interstitials and defects to form new crystalline structures within a homogeneous phase [200]. Dealing in heterogeneous phased structures, Turnbull describes how different crystalline phases within a material

can combine to form "embryos" or new structural forms, often defective, either within a single element or in compound materials, and need sufficient free energy contained within the interface between the two states to grow the structure or cavity [201].

Williams *et al.* [202] and Wong-Leung [203] describe that open volume defects are formed by the movement of free interstitials (or other crystal components provided enough energy to diffuse or migrate freely), and their separation from the available vacancies. Depleted of interstitials which themselves form clusters of defects such as loops, the vacancies can cluster together into more stable, coarser defects. As the more stable defects are voids in the material according to Plekhanov *et al.* [204], these findings lay the groundwork for the description of the cavities found in crystalline Si. The most common defect type intrinsically present in Si(100) is reported to be self-interstitials [205]. Many of these defects are regularly seen in a variety of ion-implanted crystals like Si and Ge, and the type of defects has also shown to be controllable via fluence and implantation energy [206, 207]. Post-implantation annealing can also remove such defects, with sufficiently high temperatures showing the dissolution of types like dislocation loops [208]. In the particular scope of this project, defects formed by or in concert with hydrogen have shown a degree of thermal and concentration-based selectability.

The presence of Si vacancy-type defects in situations where SmartCut™ could be performed may indicate their necessity in the process. For example, Bech Nielson *et al.* [209] showed that the vacancies present in Si were an intrinsic part of the formation of hydrogen-related platelets. Reboredo *et al.* [210] shows a model whereby they concluded the VH_4 complex (four hydrogen atoms attached to a silicon vacancy) lead to H void extended defects (such as platelets) nucleating. Formation of this complex requires the ejection of a Si ion, increasing the local interstitial concentration in the process. The process as described by [210] is exothermic, with the resultant hydrogen complex featuring a E=–0.6 eV activation energy. These larger, more energetically favourable, defect clusters ultimately show preferential alignment along the (100) (when introduced by ion implantation) or (111) (when introduced by plasma) planes. Jones *et al.* [211] demonstrates using density of states lattice model simulations that the formation of these clusters as tetrahedral structures led to a wider valance band and a smaller difference between the highest occupied and lowest unoccupied (HOMO-LUMO) electron eigenvalues. Experimental results confirmed the or-

bital distance closing, while the widening of the valance band was underestimated; despite these shortcomings, the theory concluded that the formation of the larger clusters was energetically favourable.

In addition to this focus on Si, Comer *et al.* [212] showed similar H vacancy related defect evolution in germanium. The Ge-H bond (1.541 Å) distorts within the crystal, and the reconstructed Ge-Ge bond stretching over the new void has a longer bond of 2.79 Å (contrasted with the intrinsic 2.4 Å). VH_4 vacancies were also energetically favourable as the form of hydrogen in Ge, with a bond length of 1.526 Å, however V_2H_6 has the shortest bond length of 1.52 Å suggesting it would be the most common hydrogen-germanium complex.

Molecular Hydrogen

Hydrogen in semiconductors is not always present solely as its atomic form, but can either be already in or evolve into its molecular form. Some research has used molecular hydrogen as its ion implantation source, relying upon the high energetic environment to fracture the molecule into its atomic components (e.g. [26, 85, 123, 213]). Work by Van de Walle and Tuttle [214] show H_2 can readily dissociate and diffuse through Si, with an activation energy of only E=0.15eV for diffusion. The evolution of ion-implanted hydrogen into molecular hydrogen is of paramount interest to the Semiconductor-on-insulator (SCOI) industry, due to the assumed involvement of molecular hydrogen in the SmartCut™ process. Fukata *et al.* [215] points out that most hydrogen will not remain in the atomic form due to inherent energy instability, and will rather cluster into molecular forms. Hence a significant fraction of research on the topic of hydrogen in semiconductors actually focuses on the molecular form and its evolution [148, 216–220].

Stein *et al.* [221] examined hydrogen decorating cavities in Si with Fourier Transform Infrared (FTIR), establishing strong Si-H bonds on the {100} and {111} faceted planes, presumedly in pre-formed voids, as a more energetically favourable form than free H_2. It was not clearly established that the planar forms measured were localised in the voids, but could also have been in the Si crystal. Stein did however establish that not only was molecular hydrogen forming as a gas within the cavities, it was escaping following annealing at $T \geqslant 600°C$, as the cavity surface Si-H bonds were determined to require a dissociation energy of E=2.5±0.2 eV.

Cavities And Hydrogen

How hydrogen reacts to structural defects within silicon or other semiconductors is also a key question. Voids formed in the ion damaged region of implanted Si were directly observed by Williams *et al.* [202], showing stable formation after high temperature (>800°C) anneal. Similar voids or cavities had been identified in helium-implanted silicon and germanium, with much of the early work by Follstaedt and Myers [222], which showed the cavities were strongly surface decorated by hydrogen, and contained H_2 gas.

Positron beam annihilation studies of these type of cavities produced by hydrogen implantation in Si indicated the cavities and hydrogen filling occurred in an annealing window between T=400-600°C, with hydrogen release occurring at T>700°C [223]. In samples ion implanted at T∼600°C, the following decoration and filling with hydrogen, Schut *et al.* reported the cavities to have an internal pressure of P=1 MPa. This is in contrast to reports by Hong *et al.* [69] and Coupeau *et al.* [109], who reported pressures in high megapascal to low gigapascal range.

These cavities clearly have the capacity to reach significant gas pressures prior to rupturing, but if the hydrogen is driven out uncatastrophically, they can act as a useful sink for metals and other fast-diffusing impurities [222]. Origins of these blisters in hydrogen implanted systems were reportedly small platelet-type defects [44, 70, 175], which undergo Ostwald ripening as the smaller defects dissociate to enlarge the bigger defects. The manner in which the larger voids can join together into microscopic cracks lead to the development of crystal delamination or slicing as a fabrication technique [13, 113, 224]. With the advent in the 1990s of ion-cut wafer slicing, much of the work around hydrogen in semiconductors refocused on this fabrication technique.

2.3 Stress and strain in semiconductors

The rôle of stress and strain within semiconductors is not only one of the most widely researched fields today, it has always been at the forefront of developments [225]. The essential behaviour of strain was initially formalised theoretically by Stoney in 1909 [226]. Once interest was sparked in semiconductor materials by the electronics revolution in the middle of last century, the intrinsic strains occurring within Si and Ge were determined by

Wortman and Evans [227]. Theoretical determination of the elastic constants of these, as well as several III-V semiconductors, was performed by Brantley [228].

More recently, the potential to enhance carrier mobility, shift electronic band gaps or apply quantum confinement in devices has again increased interest in stress. Rather than intrinsic stresses, focus now is on applying stress via either compositional or extrinsic means. Compositional methods include heterostructures with mismatched lattice constants [229] (often III-V semiconductor stacks [36]), and extrinsic mechanical modification of the semiconductors includes thin films or strain apparatus [230, 231]. Thus the capacity to modify behaviour of integrated circuits [29], light emitting diodes (LEDs) [30, 31], quantum dots [32, 33], high-speed transistors [34], multijunction solar cells [35, 36], MOSFETs [37] and micro-electromechanical devices (MEMs) [15] has increased the volume of strain research. In particular reference to this thesis, the use of stress and strain to modify the ion-cut process [232–234] is of paramount interest.

Stress Induction Methods

The methods to induce strain or stress within a structure, particularly crystalline or paracrystalline semiconductors, are quite varied. They include distortion of the lattice by internal damage or defects, the incorporation or combination of materials with distinctly different lattice parameters, external application by surface-applied thin films, or mechanically distorting the lattice by torsional or bending forces. An excellent reference on strain in semiconductors is the review by Dunstan [225].

Self-ion implantation has also been shown to be disruptive and destructive, and it often used as a vehicle to amorphise crystalline material, such as silicon and germanium [235–237]. In additional to the production of defects and damage, ion implantation into a semiconductor composed of a different element (or elements) modifies the structural components, inducing stresses and strains [238–241]. Volkert [242, 243] showed a new form of stress in radiation-induced plastic flow that was present in amorphised Si, that abated in material that was crystallised by solid phase epitaxy. The key interest in this modification in this project is the change in the stress environment.

Considering the stress produced from within a crystalline structure, Chami *et al.* report that stresses produced via self-ion implantation into silicon are only expected to be present until the amorphisation threshold – or sufficient lattice damage – is reached [244]. Also,

Chami describes how the strain profile produced by the implantation corresponds to the energy deposition profile of the same ion implantation, indicating the energy dissipation provides the requirements to stress the lattice structure.

Stress within silicon, germanium or composite semiconductor is also produced by lattice mismatches resulting during SPE, described in great detail by Olson and Roth [188]. Interestingly, SPE can also produce crystalline layers from material deposited atop a different species substrate [33], where the differences in lattice constant can results in a fully strained layer. Incorporation of dopants or other desirable species into the new matrix has also been reported [231].

Stress can also be applied to a semiconductor environment externally in a number of ways. For example, the evolution of hydrogen ion implanted into crystalline silicon is influenced by the ambient pressure during the diffusion-inducing anneal, in work by Kulik *et al.* [245], with greater pressures slowing the diffusion rate. Hall [246] showed that changes in the elastic constants alter the Fermi energy of Si, suggesting that stresses applied to a semiconductor affect it not just mechanically, but also electrically.

Hydrogen And Stress

Hydrogen as an implant species has been seen to cause stress in bulk materials [247,248] in addition to influencing semiconductors on the nanometre-scale [29, 175]. Miclaus *et al.* [249] showed that overlap in the ion damage profile caused by the implantation (often associated with Si vacancies produced), and the profile of the hydrogen ions describes the profile of the stress in crystalline silicon. Bak-Misiuk *et al.* [250] reported the stress of the hydrogen implantation facilitated the "smart cutting" of a SOI wafer system, and that the loss of the hydrogen with annealing implied that the stress was relieved by its out-diffusion. Lee *et al.* [234] showed that for low energy and low mass ion implantation, the tensile stress profile created by the Si vacancy distribution can be approximated by the Si ion damage distribution (often determined by Rutherford backscattering and channelling, or simulated by software package SRIM [251]), but that the stress profile is much as described by Miclaus [249].

The evolution of vacancies allowing the formation of hydrogen complexes such as

platelets was reported to be driven by the stress gradient, diffusing towards the peak in the tensile stress profile. Aggregation of vacancies and hydrogen leads to platelet formation at this peak, leading to Lee [234] showing higher stress gradients could be beneficial: if narrower and steeper out-of-plane tensile stress profiles are present, the resultant cleavage via the ion-cut would be smoother. As witnessed under the intrinsic stresses produced during implantation, the interest then is on how this could be manipulated, and the greater interest in this project is how hydrogen can be affected by extrinsic stresses, or develops symbiotically under additional stressed environments, in particular in ion-cut type systems.

As described in Section 2.1, hydrogen plays several rôles within the SmartCut™ process. Hydrogen provides internal pressure via formation of gas pockets or voids within the substrate, its implantation produces a profile of damage that produces local changes in the strain environment of the substrate, it modifies bond energies with the substrate by complexing with the material, altering the Fermi level and (often) lowering the energy required to break the bonds. All of these factors require not only the hydrogen to enter the substrate violently, but for the hydrogen to be present at key locations to facilitate the wafer slicing process. In a number of steps, this involves the hydrogen diffusing or otherwise shifting its position within the substrate. To that end, the capacity to trap or diffuse hydrogen differently, as mentioned above, is of keen interest.

Hydrogen Plasma Introduction To SiGe And Diffusion

One potential avenue of influence may be in that diffusion is altered by stress in semiconductor materials [252–254], whether the stress is intrinsic or extrinsic in origin.

The stress present within pseudomorphic SiGe layers, either on the surface or buried within a single material substrate, whether Si or Ge, has been suggested as a trap for in-diffusing hydrogen, as work by Yamashita *et al.* [255] shows fully strained SiGe acts as an effective H diffusion barrier. Previous research by Pitera *et al.* [256] demonstrated how the presence of tensile strain produced by SiGe layers aligned hydrogen platelets to the {001} plane, as both ion implanted and plasma introduced hydrogen normally has a tendency to align along the {111} plane [103, 146]. As attempts to produce very thin layers by ion-cut using ion implantation of hydrogen can produce electronically defective material and an inherently large surface roughness, Okba *et al.* [257] investigated introduction of hydrogen via a plasma to a Si substrate containing a buried narrow compressively strained SiGe layer.

Increasing duration of plasma exposure increases the hydrogen present in the strained SiGe layer, and decreases the hydrogen (and any defects formed by it) in the overlying Si layer. The hydrogen was assumed to preferentially add to the platelets present in the strain layer from smaller defects within the Si by a nonconservative Ostwald ripening process, but this does not explain the initial bias for hydrogen to accumulate in the compressively strained region. Using stress to modify the diffusion of hydrogen Pitera *et al.* [256] reports that the solubility of hydrogen increases under tensile stress ($\sigma > 0$), while compressive stress ($\sigma < 0$) produces a decrease in solubility. Considering this, Okba [257] suggests that the stressed layer acts as a sink for vacancies produced in the hydrogenation, which in turn are more conducive to formation of hydrogen complexes.

When introduced to an intrinsic Si wafer via plasma, hydrogen does not produce the same damage profile as ion implantation. Shao *et al.* [153] showed that that prevented ion-cut to readily occur, with no preferential location at which the hydrogen could concentrate. However, in using a thin buried tensionally-strained SiGe layer present within a Si(100) substrate, Shao indicated such a preferential site now existed, and ion-cut type processes were possible, and at half the concentrations required when using ion implantation. This influence was qualified later [80], establishing that the presence of hydrogen platelets produces a higher stress shear between the SiGe layer and the surrounding Si, increasing the likelihood of microcracks formed in the layer to solely propagate within it. In later work, Shao *et al.* [160] again demonstrated trapping of hydrogen at a thin tensile SiGe layer, even when introduced by ion implantation and prior to annealing. However, it was found that if the hydrogen were ion-implanted deeper than a sufficiently thin layer, the subsequent ion damage to the SiGe and relaxation in strain caused by its decreasingly defined interfaces lessened the possibility of the thin layer acting as a ion-cut crack nucleation location.

Isaacson *et al.* [258] further confirmed much of the work by Pitera [256], and also indicated that H tends to getter or trap at Si:Ge interfaces, in part due to the localised misfit dislocations, in cases where the heterostructure is no longer fully strained (if the layer > critical thickness as defined by Matthews [259]). Isaacson suggested the use of a particularly engineered heterostructure to allow ready re-use for multiple wafer splitting applications. Unlike Shao [160], Isaacson reported trapping of hydrogen at thin SiGe layers, proportionally to the Ge (or shear strain) content, despite having ion-implanted through

(and caused lattice damage, and relaxation, to) them. This difference may be due to the SiGe layers being thicker (as the values are not given) and less susceptible to disruption by ion implantation. While the proportion of trapped hydrogen in the strained regions was between 1.3–2 times that seen in an intrinsic Si implantation, this concentration did not significantly change upon annealing of the heterostructure. The proportion of trapping at the deeper strained layers is reasoned similarly to the behaviour in Shao [80], in that the damage caused by the implantation process has had less impact deeper into the material, preserving more of the thin layers' strain. Strain values of 1.6% or higher were required to influence the evolution of the hydrogen platelets and defect structures within ion-cut type behaviour. These findings further suggest that the influence of strain (so far discussed via internal composition of the substrate) upon the distribution of hydrogen, whether still in the as-implanted or following thermal annealing state, is significant.

Hydrogen Evolution In Stressed Intrinsic Silicon

Large scale interest has also been expressed in the influence of strain on hydrogen within intrinsic semiconductors. Bech Nielson *et al.* [260] reported how externally applied stresses could shift the apparent wavenumber of Si:H related vibrational modes, indicating changes in bond structure between the H and the Si.

The formation of voids within Si(100) as a result of hydrogen evolution under different stress conditions was modelled by Swadener *et al.* [233], accounting for Si bond energies and mechanical properties. These simulations showed that for large numbers of vacancies, {111} platelets were generally more energetically favourable under zero net stress conditions, while biaxial stresses applied in the (110) plane lead to an environment more conducive to {001} platelets. Interestingly, in a low vacancy condition, low biaxial stresses in the (110) plane also promote {001} platelet growth, with similar energetics for both at high vacancy concentrations, in this case providing a better environment for very small platelet sizes. These predictions suggests a higher number of {001} platelets in the (100) biaxial stress produced by ion implantation, with larger numbers of {111} platelets in the regions were the stress is lower.

External Stress Application Methods

An unexpected development in co-implantation of He and H into Si(100) was shown in work by Reboh *et al.* [120, 261], where He platelets induced in Si led to change in

the local stress environment, and therefore different evolution for the complementary H implant. The local (presumed compressive) stress induced by over-pressurised He platelets preferentially aligned the H platelets that formed subsequent to ion implantation along the {111} family of lattice planes, while unstrained H aligned along {001}. The influence of compressive stress exhibited here is in agreement with tensile stresses influence as reported by Swadener [233], Isaacson [258] and Okba [257].

In addition to the compositional or internal influences upon intrinsic and heterostructure semiconductors described above, application of mechanical stresses from an extrinsic source have also been investigated. One such method is the use of a thin surface layer or film to influence the environment beneath it. The use of thin films deposited upon the surface of a wafer to alter the local strain field was shown by McKerracher *et al.* [230] and Moutanabbir *et al.* [262]. (Surface films themselves can experience stress due to changes in their own structure, for example surface cracks forming on a rich SiO_x layer when tensile stress evolves due to hydrogen diffusion under annealing [263].) The stress σ applied by the bulk onto a crystalline thin film can be determined by the Stoney Equation [226], given by Eq. 2.1.

$$\sigma = \frac{1}{t_f}\frac{E_s t_s^2}{6(1-\nu_s)}\left(\frac{1}{R_B} - \frac{1}{R_A}\right) \tag{2.1}$$

where the t_f is the thin film thickness, t_s is the substrate thickness, ν_s is the Poisson ratio for the substrate, R_A and R_B are the before and after radii of curvature of the wafer respectively, and E_s is Young's modulus for the relevant crystalline element's structure (e.g. crystal orientation, thermal agitation, electronic excitation) [228, 264].

Ohring [265] listed an array of stress values resultant from thin film deposition, which showed a range of both compressive and tensile strains from 10^{-2}GPa for semiconductor films through to 10^{2}GPa for metal films (see that publication's Table 12-1, page 743). Volkert [266] showed that strain was relaxed in thin film SiGe structures by dislocation nucleation produced via thermal annealing. The "handle" wafer applied in the SmartCut™ process serves a similar rôle in the evolution of hydrogen, as its presence has a stiffening effect upon the underlying donor wafer, changing the dynamic of the exfoliation process [78]. Rather than forming film-like layers, the growth of Ge upon Si(100) has been reported to

show several stress-relief structures forming, such as faceted islands and three dimensional truncated square pyramids, and any high temperature annealing leads to the degradation of the distinct facets, indicating a relaxation of the stress environment [34].

Another method to mechanically induce extrinsic stress upon semiconductor wafers was employed in work by Olson *et al.* [267] and Rudawski *et al.* [268, 269], where a special apparatus was developed to apply in-plane uniaxial and biaxial strains upon their materials. The use of Stoney's equation for thin films is not appropriate is this case, as the thermal expansion of the proposed "layers" during annealing at T$\geqslant$300°C for Si or Ge is great enough that the initial conditions no longer hold [267]. Instead, a classical beam-bending argument can be adapted to calculate the uniaxial stress σ present in a wafer under external forces, shown in Eq. 2.2, derived from work by Bernoulli and Euler in the eighteenth century [270], and elaborated upon by Filon in 1903 [271], and Timoshenko in the mid-twentieth century [272].

$$\sigma = \frac{E_{[hkl]} \cdot c}{r} \tag{2.2}$$

Equation 2.2 is a one dimensional simplification of the tensor which describes the stress in a wafer which has a Young's modulus E in the $[hkl]$ crystal axis, a thickness of $\mathbf{2}c$ and a radius of curvature r [231, 273]. This equation and its origins are discussed in further detail in Section A.1.

The application of this form of external mechanical stress and its influence on SPE in work by Rudawski *et al.* [268, 269] and Olson *et al.* [267] showed stress lead to greater defective growth. Compressive stress influences the α/c interface roughness, while the influence of tensile stress was unclear [231]. The influence of external stress on the SPE process generally was somewhat at odds with reports by Wzorek *et al.* [274], but even that work showed influence at high temperature anneals. The use of this mechanical stress apparatus has not been significantly explored outside SPE of Si, but in concert with the potential to modify platelet orientation and depth range [120, 234, 256, 258], could provide an alternative to compositional or thin film stress.

Chapter 3

Experimental Method

MATERIALS and techniques used in the experiments of this project are provided a general overview in this chapter. It has two major purposes; firstly to describe the technical processes used to fabricate the materials used in the study, and secondly to describe the operation of the major experimental techniques used to analyse them.

3.1 Sample fabrication

In each of the subsections of this study, a number of substrate types were used. These consisted of Ge and Si wafers of several crystal orientations and dopant concentrations.

For the experiments in Chapter 4, (100), (110) and (111) silicon wafers and (100) germanium wafers were sourced. The Si (100) wafers were p-type B-doped with a resistivity of 10-20 Ω cm, the Si (110) wafers p-type B-doped ρ=20-70 Ω cm, the Si (111) wafers p-type B-doped with a resistivity of 7-15 Ω cm and the Ge (100) wafers were undoped, ρ>40 Ω cm.

Also in Chapter 4, an investigation of the influence of dopant -type and -level in Si upon implanted hydrogen was undertaken. For the investigations of the influence of dopants, substrates used were p-type B doped Si(100) with ρ<0.05 Ω cm (labelled csi400), n-type P doped Si(100) with ρ=0.0011 Ω cm (labelled csi500), and n-type As doped Si(100) with ρ=0.001-0.005 Ω cm (labelled csi600). All the above wafers were polished to a thickness between 350-405 μm.

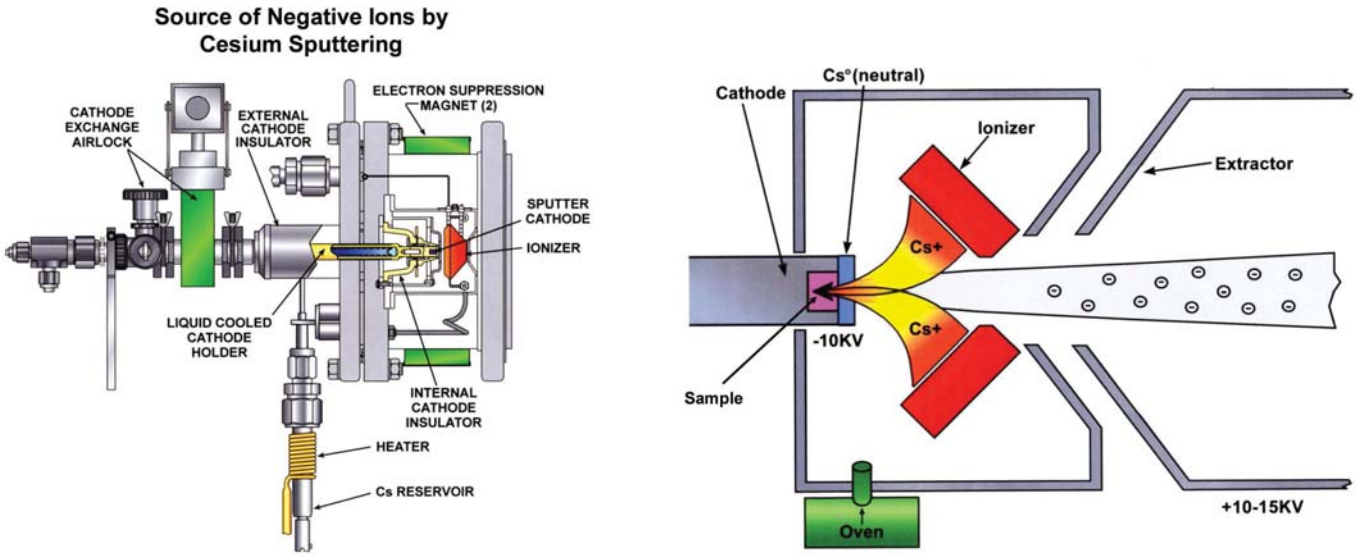

(a) (b)

Figure 3.1: (a) Schematic of the source of negatively charged ions by Cs sputtering (SNICS) in low energy implanter; (b) representation of production of negative ions in both low and high energy ion implanters.

For the investigation of the influence of stress on hydrogen behaviour explored in Chapter 5, there was an additional wafer type employed. In the study of external mechanical strain, undoped 3" ULTRATHIN® (100) silicon wafers were used, with ρ<20 Ω cm. These wafers had a nominal thickness of 50±5 μm. Some of this wafer material was also examined in Chapter 4.

3.1.1 Ion implantation

The silicon and germanium wafers were implanted with a range of regimes to study the ion-cut process and the evolution of hydrogen in this process. Almost all ion implantation in this project was performed on a custom-built low energy ion implanter, while the small number of implantation energies greater than E=150 keV were performed on a NEC 1.7 MV 5SDH-4 high energy ion implanter; both in the facilities of the Department of Electronic Materials Engineering in the Research School of Physics and Engineering at The Australian National University. A schematic of each implanter is presented in Appendix B.1.

For both implanters, the ion source is a SNICS (Source of Negative Ions from Cesium Sputtering) source whereby negative ions are produced by Cs ion sputtering of solid cath-

odes. This process and source assembly is shown schematically in Fig. 3.1. A TiH_2 solid cathode was used as the hydrogen ion source in this project. The source assembly combines differential accelerating extraction voltages capable of producing high currents of negative ions at energies of up to 150 keV. For the low energy implanter, these negative ions are then selected by a 90° magnet and scanned across the sample with a (x, y) frequency of (517,64) Hz. The shape of the scanned beam's profile in both directions is monitored with a rotating wire beam profile monitor, and displayed on a cathode ray oscilloscope (CRO). The beam is focused to a small spot size of approximately 2 mm FWHM on the sample holder and scanned over an aperture, typically 0.3 cm^2 to 4 cm^2 in area. For the high energy implanter, a high voltage accelerator is used to change the charge state of the ions by passing them through a nitrogen stripping gas. Changing to positive charge allows the ions to be further accelerated to energies between 1.7-10 MeV. The positive ion beam is then steered and scanned over the sample surface with the same spot size and frequency as described for the low energy implanter. Implantation occurred under a high vacuum environment ($\sim 10^{-7}$ Torr) and the samples were mounted onto the stage by Ta wires to ensure good thermal contact. Specific details of each particular implantation condition (such as energy and beam current) applied are provided in appropriate sections.

3.1.1.1 Intrinsic hydrogen evolution study

In order to examine the intrinsic behaviour of hydrogen-induced blistering and related phenomena in semiconductors, several key elements were investigated: hydrogen fluence, implantation energy, wafer crystallographic orientation and anneal temperature. The basic pattern to study these was a matrix of energies and fluences into each type of crystal wafer, which were described at the beginning of Section 3.1. The implantation regimes are listed in Table 3.1.

3.1.1.2 Stress affected hydrogen evolution study

In this study, following on from the work upon hydrogen blistering and evolution, samples were produced with the goal of understanding how the key parameters affect hydrogen clustering and wafer splitting. This included modifying the material by mechanically stressing the samples during the implantation, to establish what effect the external stress would

Substrate	Fluence at each implantation energy $\times 10^{16}$cm^{-2}					$T_{implant}$ °C
	20 keV	40 keV	60 keV	80 keV	500 keV	
Si(100)	1	1	1	1	1	20
	3	3	3	3	3	20
	6	6	6	6	6	20
	10	10	10	10	10	20
	15	15	15	15	15	20
Si(110)	1	1	1	1	-	20
	3	3	3	3	-	20
	6	6	6	6	-	20
	10	10	10	10	-	20
	15	15	15	15	-	20
Si(111)	-	6	-	-	-	20
Ge(100)	0.6	0.6	0.6	0.6	0.6	20
	1	1	1	1	1	20
	3	3	3	3	3	20
	6	6	6	6	6	20
	10	10	10	10	10	20
B-doped Si	-	6	-	-	-	20
P-doped Si	-	6	-	-	-	20
As-doped Si	-	6	-	-	-	20

Table 3.1: Sample implantations for intrinsic hydrogen evolution study in Chapter 4.

have on the hydrogen distribution, platelet orientation and subsequent evolution under annealing. The standard hydrogen implantation for the mechanically stressed samples was the same as that in the intrinsic behaviour study – H(40 keV, 6×10^{16} cm^{-2}, RT). These implantation conditions were selected to maximise our ability to resolve changes via ion beam analysis (IBA) techniques available to us, e.g. beam energy, detector resolution, spot size. Primarily, the conditions were set by the limitations and capabilities of measurement of the elastic recoil detection (ERD) system at ANU.

The induced stress due to ion implantation and annealing on semiconductors was investigated in three substrate types – bulk and ULTRATHIN® (375 and 50 μm respectively) Si(100) and Ge(100). The effects of external mechanical stresses were then contrasted in two sections. The influence on the implantation of H into bulk Si(100) was studied, and secondly the effects of high levels of stress upon H-implanted ULTRATHIN® Si(100) during the implantation process, subsequent annealing, or both.

The ion implantation energies and fluences used on these substrates are described again

in the appropriate chapter, and are listed below:

- ULTRATHIN® 50 μm crystalline silicon,
  1. H 3×10^{16} cm^{-2}, 45 keV, RT, unstressed
  2. H 6×10^{16} cm^{-2}, 40 keV, RT, unstressed
  3. H 6×10^{16} cm^{-2}, 40 keV, RT, compressive stresses (-354 MPa$<\sigma<$-262 MPa)
  4. H 6×10^{16}cm^{-2}, 40 keV, RT, tensile stresses (164 MPa$<\sigma<$283 MPa)
- 375 μm crystalline silicon, (100) orientated
  1. H 3×10^{16} cm^{-2}, 45 keV, RT, unstressed
  2. H 6×10^{16} cm^{-2}, 40 keV, RT, unstressed
  3. H 6×10^{16} cm^{-2}, 40 keV, RT, tensile stress ($\sigma<$156 MPa)
- 375 μm crystalline germanium, (100) orientated
  1. H 3×10^{16} cm^{-2}, 45 keV, RT, unstressed

3.2 Experimental techniques

A number of different techniques were employed over the course of this project. This section will describe the essential elements of each technique, but focus more on the specifics relevant to this particular study. The primary techniques used in this project were:

- Rutherford Backscattering Spectrometry - channelled (RBS-C)
- Elastic Recoil Detection (ERD)
- Optical profilometry (OP)
- Cross-sectional Transmission Electron Microscopy (XTEM)

In addition to these techniques, there were specific solutions tailored to this project. During the annealing study described in Section 4.6, a specialised rig needed to be produced to allow monitoring of the changes in the samples. The configuration of this camera setup is described in Section 3.3.1. In the mechanical stresses study described in Section 5.4, an in-house designed apparatus (or stress "boat") was used to stress the wafers during implantations and anneals, and its schematics and operation are described in Section 3.3.2.

3.2.1 Rutherford Backscattering Spectrometry

Rutherford backscattering spectrometry, or RBS, is a non-destructive characterisation technique that allows determination of material composition, impurity concentrations and crystalline structure [275]. Excellent comprehensive references on the underlying theory and analysis of this method are Chu, Mayer and Nicolet [276] and Feldman, Mayer and Picraux [277].

All RBS in this project was completed within the Department of Electronic Materials Engineering (EME) in the Research School of Physics and Engineering (RSPE) at the Australian National University (ANU). The measurements were performed upon a NEC 5SDH tandem pelletron (diagrams of which can be found in Appendix B.1) using irradiation beams of either E=2 MeV and 3 MeV $^4He^+$ ions, within two separate target chambers featuring different detector positions and unique goniometers. Each chamber is shown in Fig. 3.2. For the beam at E=2 MeV, measurements occurred simultaneously on two fixed detectors, one at a backwards scattering angle of ϕ=167.9° and a glancing angle of ϕ=75°, relative to the incident ion beam path, and the beam spot was approximately 1 mm diameter. Each of these scattering angles was measured in the (x, z) plane, where x is aligned with the incident beam. For the E=3 MeV measurements, one fixed and one movable detector were used, though both were used at set locations of ϕ=168.32° and ϕ=70° for RBS measurements, while the beam spot was closer to 3 mm by 3 mm in area. In the second chamber, the scattering angles ϕ were swept out in the (x, y) plane. The detectors in both chambers were biased with 50 V. During operation, to minimise contamination by hydrocarbons and other molecular species, a cold shield was placed within the scattering chamber used for E=2 MeV measurements, and cooled to cryogenic temperatures by liquid nitrogen. Specific details of individual experiments such as charge collected and beam current are provided in the relevant results sections.

In order to probe the damage caused within nominally crystalline materials, a subset of RBS measurements where the beam is aligned along one of the crystal structures' main axes was used, known as channelling [278–280]. Channelling measurements were performed by aligning the ion beam along the desired crystalline axis, to identify damage such as dislocations and interstitial atoms within the lattice, and to some small degree stress (seen in the magnitude of the dechannelled signal). The determination of the forms that disrupt the

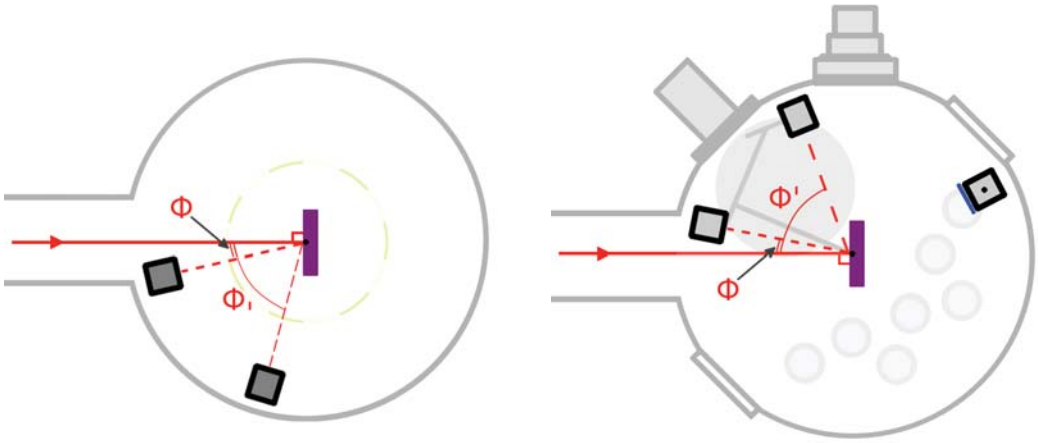

(a) (b)

Figure 3.2: RBS beam line chambers used in this project for (a) E=2 MeV and (b) E=3 MeV measurements. Key to (a): ϕ=12.10°, ϕ_I=75.0°. Key to (b): ϕ=11.68°, ϕ^I=70.0°.

"perfect" crystalline signal in the samples studied requires a calibration against the random yield χ and that of a "perfect" crystal. The resultant spectrum from a practical (rather than ideal) channelled measurement has yield due to two main factors: dechannelling of the ion beam within the crystal lattice increasing with depth, and direct scattering from defects or irregularities within the crystal. The amount of dechannelling that occurs at a given depth of the crystal is largely dependent upon the incident beam energy (and hence velocity) [281] and angle [282, 283].

Picraux *et al.* [284,285] showed that the perfection of crystalline layers grown by epitaxy or heteroepitaxial Si samples can be probed with high quantitative accuracy by channelled ion beams. The defect densities can be determined with a high degree of confidence, and this method was applied in this thesis. When measuring the scattered ion beam, Williams *et al.* [283] report how the measurements can easily be distorted by small variations in angle and position of the detectors relative to the sample surface. To ensure that the randomly aligned, non-channelled yield χ from a sample is properly detected, careful positioning of the detectors is required. For example, all random angles are not created equal, as scattered ions originating too near a channelled path or plane may cause oscillations indicating a higher yield. To counter this, during all measurements at random angles, the goniometer was rotated through 3–4° around a pole aligned with the channel in 30–50 steps to minimise

the influence of planar channelling. Williams also suggests that relative damage in the near surface region of channelled measurements can proportionally alter the relative depth scales beyond any scattering incident. As such, secondary depth values beyond the direct scattering peaks examined in each sample in this study must be dealt with cautiously.

Manual calculations allowing the determination of the two components measured in the channelled spectra – dechannelled and direct scattered yields – are given by a number of sources, including Feldmann *et al.* [277], Shao *et al.* [286, 287], and Cerofolini *et al.* [288]. The theory and equations governing the method of extracting these data are further described in [276, 277, 288–291]; alternatively, a number of software packages exist which allow the user to extract this information from the collected data via fitting simulations [292–297]. For all ion beam analysis (IBA) techniques, Szilagyi [298] reported that few of the specialised analysis software packages account for all beam energy spread effects associated with the geometry, with the exception of Data Furnace and (W)Depth [299,300].

In this project, the data was collected by in-house designed software suites, stored in binary format files which were analysed using the RUMP program [293]. Subroutines within RUMP were used to separate and extract the direct scattering and dechannelling components of the RBS-C data, determining concentrations and distributions of implantation damage and defects.

3.2.2 Elastic Recoil Detection

The ion beam analysis technique which was especially developed for this research project within EME was elastic recoil detection analysis, or ERD. An excellent reference on the topic is Tirira, Serruys and Trocellier [301]. All ERD undertaken in this project was performed upon the same NEC 5SDH tandem pelletron at the ANU as was used for the RBS measurements.

The chamber and goniometer used in this project are shown in Fig. 3.3. An in-depth operation procedure for this equipment is detailed in Appendix C. The goniometer is capable of rotating and tilting across a range of angles, defined relative to the beam line angular position of (α,β)=(0,0). Rotation occurs left and right around an axis which is normal to the plane containing the analysing beam and detectors, over an angular range of ($-90^\circ < \alpha < 155^\circ$). Tilting occurs up and down, around an axis parallel to the sample

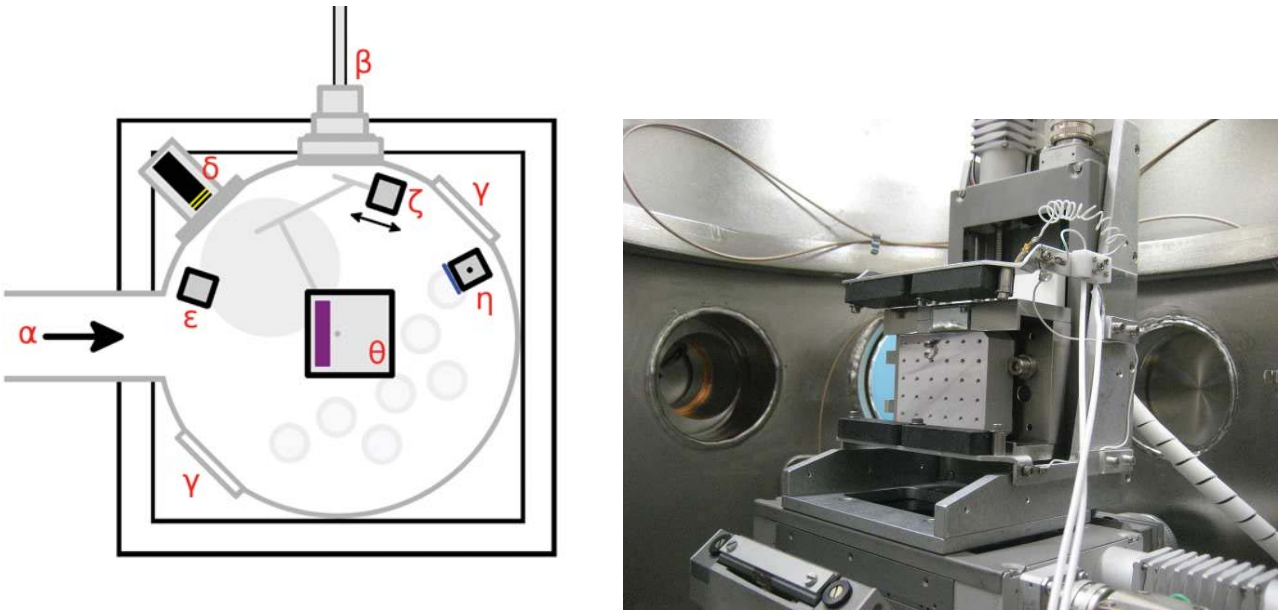

Figure 3.3: (a) Schematic diagram of ERD chamber, indicating detector positions relative to beamline and sample mount. $\boldsymbol{\alpha}$ - incoming beam, $\boldsymbol{\beta}$ - sample loadlock interchange, $\boldsymbol{\gamma}$ - chamber windows, $\boldsymbol{\delta}$ - digital video camera, $\boldsymbol{\varepsilon}$ - back angled detector, $\boldsymbol{\zeta}$ - moving detector, $\boldsymbol{\eta}$ - forward scattering detector (plus Mylar foil), $\boldsymbol{\theta}$ - Goniometer and sample mounting puck; (b) Photograph of goniometer used for ERD in this project.

mounting puck face and contained within the aforementioned plane, over (-20° < β <50°).

Two solid state detectors were fixed at scattering angles of θ=168.32° and 25° relative to the beam line, as seen in Fig. 3.3(a) labelled ε and η, and a E=3 MeV $^4He^+$ ion beam used. The forward scattering (25°) detector had a Mylar foil placed in its beam path. The Mylar foil acts to screen out the incident He ions while allowing passage of the hydrogen ions, via relative stopping powers of their different atomic masses [302]. For E=3 MeV, simulations in software package RUMP [293] and stopping powers measured by Kìss *et al.* [303], Santry *et al.* [304, 305] and Rauhala *et al.* [306, 307] were used to calculate the optimum thickness of the foil. Requirements were that the hydrogen spectra would not be sufficiently degraded, while preventing the He spectra from obscuring the H yield. From the results of RUMP simulations and the previous work listed, a 12.6 μm thick Mylar foil was selected. Each detector was biased with 50 V during operation.

In addition to this forward scattering fixed detector, and the detector positioned at a scattering angle of θ=168.32° for corresponding RBS measurements, there was also an unshielded detector mounted on a moving arm within the chamber, labelled ζ in Fig. 3.3. When performing ERD measurements, this detector was positioned at a scattering angle

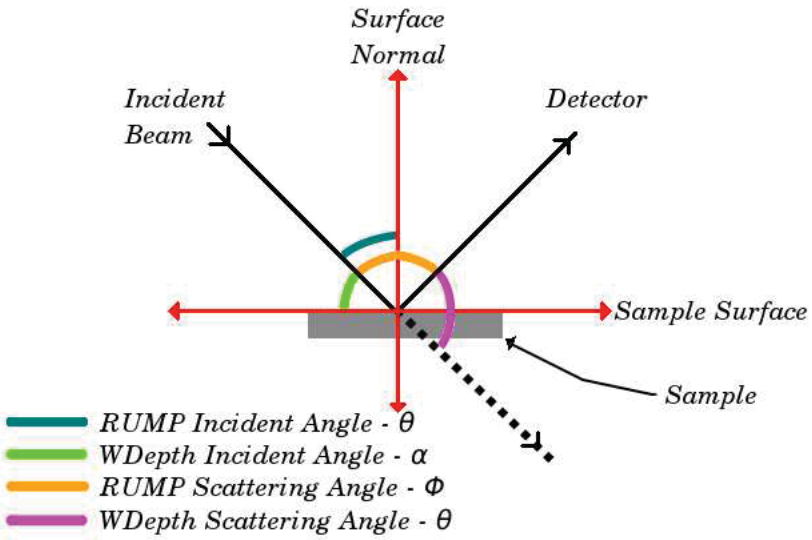

Figure 3.4: Scattering angles simulated by WDepth software [300] for ERD measurements, contrasted with RUMP [293] and relative to geometry of ERD chamber.

of θ=90°, allowing simultaneous collection of the RBS spectra from the material. Such spectra were useful to ensure comparable yield scaling between data collected on different dates and/or different mountings on the sample puck.

Any significant amount of surface roughness on the sample leads to large propagating errors in measuring compositions and depths in the ERD spectra collected [301]. Without sufficiently sophisticated deconvolution routines, this eliminates it as a useful technique for most blistered or cratered surfaces in either Chapters 4 or 5. However, as its main purpose in this project was the identification of hydrogen profiles within the bulk of the material prior to blistering, this limitation was not significant.

To establish the angular position of the forward scattering detector in the chamber for this study, the ERD system was modelled with the Szilagyi and Pazsti code "DEPTH" [299, 308] (or more specifically its MS Windows incarnation "WDepth" [300]). WDepth was used to simulate the potential incoming and exit angles of the He beam, to find the combination that yielded the optimum resolution for the materials to be studied, i.e., Si and Ge implanted with H. The angles which WDepth simulates, α and θ, equate to the incident beam relative to the sample surface, and the scattering angle from the beam (complement to RUMP's ϕ) respectively, shown in Fig. 3.4.

A typical WDepth simulation is shown in Fig. 3.5, in this particular case for hydrogen-implanted silicon, listing the dependencies considered in each sample configuration. The

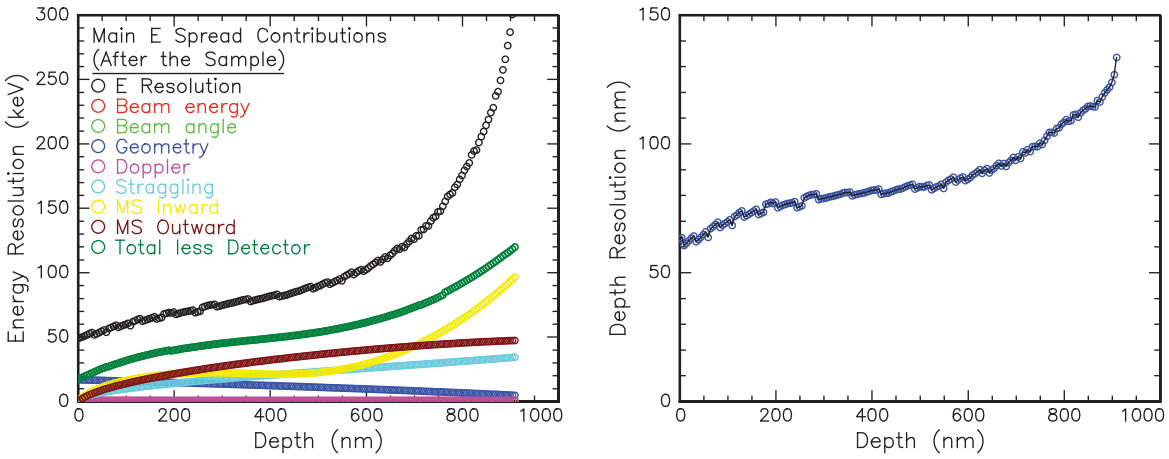

(a) (b)

Figure 3.5: WDepth simulation results for (a) energy and (b) depth resolution when measuring H(40keV,6×10^{16}cm^{-2},RT)-implanted Si(100) via 3 MeV He ERD. Parameters as follows: α=10°, θ=25°, Mylar foil 12.6 μm thick, detector FWHM 15 keV, detector aperture 1.5 mm × 12 mm, beam aperture 2.5 × 2.5 mm, sample-detector distance 14.5 mm.

chief components of interest in WDepth simulations when considering the configuration of the ERD system are the geometric contribution to the signal, the total signal resolution (both in keV, in Fig. 3.5(a)) and the local depth resolution (in nanometres, in Fig. 3.5(b)). Ideally, the geometric contribution should be kept less than or equal to the straggling or multiscattering components. As the geometry can be more readily controlled within the ERD system than many of the other contributing factors, it seems reasonable to optimise the resolution through adjustment of the angles. It is also important to consider the influence on the yield collected from the sample, to ensure sufficient signal for accurate assessment of the hydrogen distribution. The geometric configuration must thus be balanced between these two demands for what affects the x and y resolution in the data sets.

The range of incident and scattering angles for simulation were selected from those found in the literature (for example, [25, 309–314]), and accepting certain physical limitations for any forward scattering geometries (e.g. $\alpha < \theta$, $\alpha + \theta < 115°$, etc.) to consider adjacent values. The ultimate goal of this optimisation was to examine hydrogen implantations ranging up to a micron deep within either Si, Ge or composites. Thus having better resolution between 400 and 500 nm would be preferable to having higher accuracy at 900-1000 nm. Under those constraints, simulations where produced for values ranging over ($10° < \alpha < 30°$, $15° < \theta < 40°$). The depth resolution and geometric component for

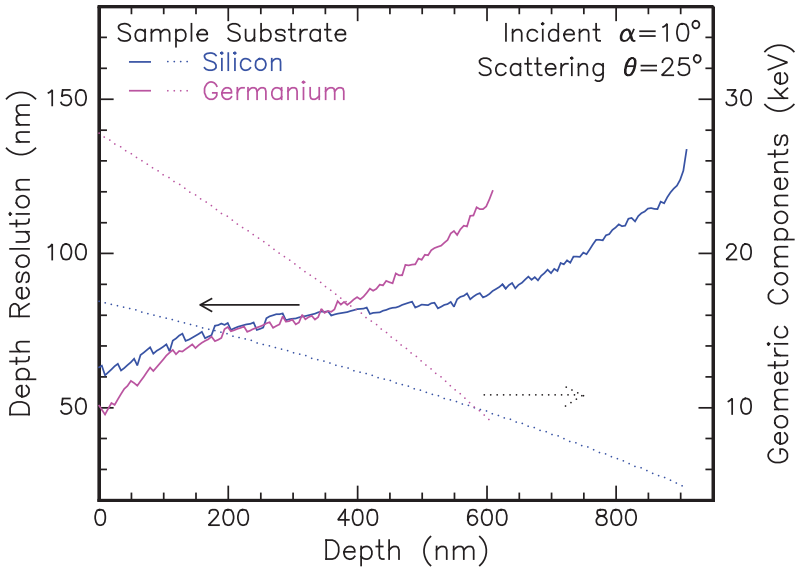

Figure 3.6: Depth Resolution and geometric component for E=3 MeV $^4He^+$ ERD measurements of H(40keV,6×10^{16}cm^{-2},RT) Si and Ge as simulated by WDepth [300] for incident angle α=10° and scattering angle θ=25°. Parameters of simulation as follows: Mylar foil 12.6 μm thick, detector FWHM 15 keV, detector aperture 1.5 mm × 12 mm, beam aperture 2.5 × 2.5 mm, sample-to-detector distance 14.5 mm.

the full range of potential incident and scattering angles for both silicon and germanium are shown in Fig. B.1 and B.2 in Appendix B.1.

The optimum parameters determined by WDepth to accommodate both Si and Ge substrates was an incident and scattering angle of $(\alpha, \theta) = (10°, 25°)$. Figure 3.6 shows the relative resolution achievable at this geometry, as well as the influence of the geometric component.

Geometric factors influencing depth and energy resolution include a beam aperture designed to limit angular spread in the detected beam. WDepth simulations for calibrating incident and scattering angles defined this aperture to have a width of 1.5 mm wide and height of 12 mm. From the silicon optimised $(\alpha, \theta) = (10°, 20°)$, WDepth then determined the optimum aperture dimensions, the specific details of which are included in Appendix B.1. From these aperture dimension simulations, the selected size for the physical slit was thus 2×12 mm.

From the optimised parameters determined for geometry and aperture size, Fig. 3.7 contrasts the WDepth simulated ERD spectrum with experimentally measured data from a H(40keV,6×10^{16}cm^{-2},RT)-implanted Si(100) sample. There is clearly excellent agreement

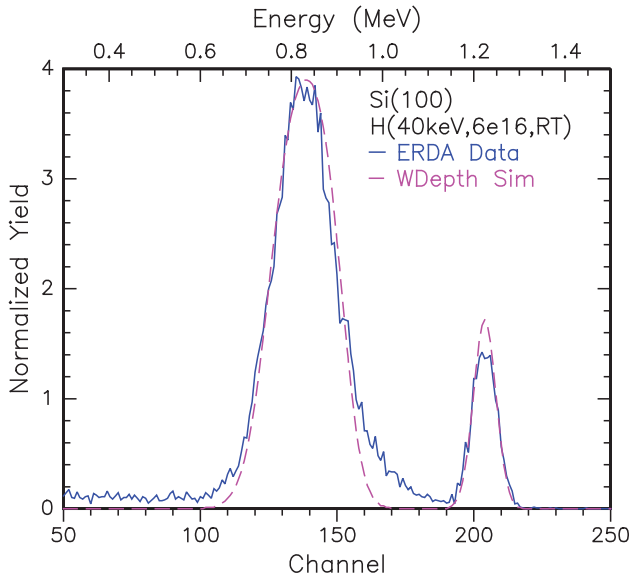

Figure 3.7: Comparison of WDepth generated simulation of a H(40keV,6×10^{16}cm^{-2},RT)-implanted Si(100) profile, and experimental data measured by 3 MeV $^4He^+$ ERD. Parameters of simulation listed in caption of Fig. 3.5, experimental parameters as defined by RUMP: IBM geometry, θ=-80°, ϕ=155°; Q=20 μC, I=17.5 nA, Mylar foil 12.6 μm thick.

between the simulation and collected spectra, giving high confidence in the calibration of this technique and its ability to quantify hydrogen concentrations.

3.2.3 Optical Profilometry

Optical profilometry or profiling is a general term used in this project to describe a specific method of using interferometry to characterise sample surfaces. Operating on the same principles as a Michelson interferometer, the optical profiler uses a mirror to produce a reference light source to contrast with the beam reflected from the sample surface.

The profiler has two modes of operation – phase-shifting interferometry (PSI) and vertical scanning interferometry (VSI). A white light source is used in both modes. In VSI mode, the light is passed through a neutral density filter, to maintain the coherence length of the light. In PSI mode, the light is passed through a narrow bandwidth filter, to produce a coherent monochromatic source of wavelength λ=550 nm. PSI mode is close to the original Michelson interferometry, as the incident light is recombined with a reference beam produced by a beam splitter upon leaving the original light source. The intensity of the measured light after it has recombined is contrasted with a number of small fixed

distance changes known to match phases of the source light. The changes are performed by moving the reference source with a Piezoelectric transducer. These phase shifts give the technique its name, and the changes in intensity indicate wavefront lengths and are used to describe the sample. Limitations exist when the wavefront cannot be adequately reconstructed, such as at sharp interfaces which exceed $\lambda_{\text{light}}/4$, indicating PSI mode can usually only be used for smoother, more regular surfaces. As PSI mode uses a narrow bandwidth of green wavelength light for its measurements, it has a total vertical range of approximately 160 nm, but has a remarkably precise vertical resolution (particularly considering its use of visible light wavelengths) of 1-3 Å.

VSI mode uses the coherence of the light rather than its phase changes to map the surface by similar interferometry. The light is focused on the sample, and then the objective is translated vertically from under to over focused. As the objective is translated, precise images are captured from the surface, recording the change in the observed interference pattern. The maximum in the overall wave packet is determined to be the focus point, and from the position of the envelop relative to the interference fringes, the distance between the objective at that peak is determined. White light is used in conjunction with a neutral density filter. The light's short coherence length allows greater precision in pin-pointing distances as interference fringes form only at a narrow depth range around the focus. As the smaller coherence length lends itself to larger changes in height, it has a sharper drop off between interference fringes, leading to less small-scale accuracy. The range of VSI is therefore much greater than PSI, at approximately 2 mm within an individual scan, while the finest vertical resolution is between 1-3 nm.

To ensure the horizontal or lateral accuracy of the profiler was sufficient for the samples in this study, an Atomic Force Microscope (located in the Department of Applied Mathematics within the RSPE, ANU) was briefly employed to examine generally representative blistered H-implanted Si(100). The roughness values determined from the peaks and troughs of the crater floor were found to be in good agreement with those obtained by the optical profiler. The value of lateral resolution is ultimately limited by the objective lens used and the detector sensitivity.

All optical profiling in this project was performed on a Bruker (née Veeco) Wyko NT9100 Profiler [315], located in the Department of Laser Physics within the Research

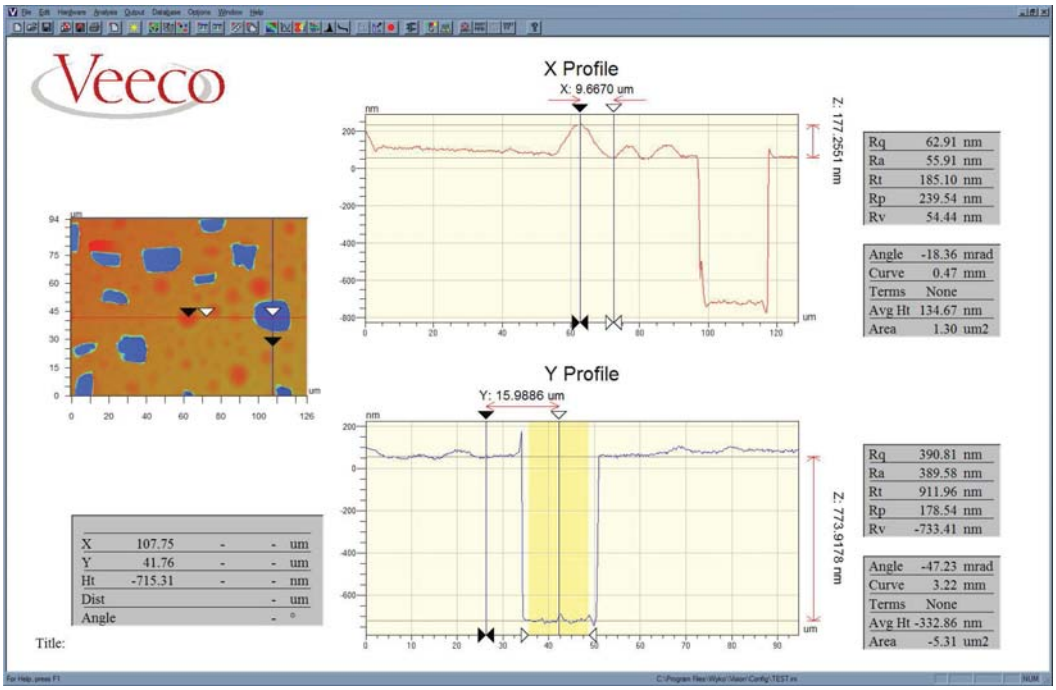

Figure 3.8: Screen shot of the Vision3D Vision for Profilers software, used to operate the optical profiler and perform measurements. Sample: H(65keV,5.35×10^{16}cm^{-2},RT)-implanted Si(100), annealed at T=550°C/30 minutes. Settings: VSI mode, ×50 lens, F.o.V. ×1.0

School of Physics and Engineering at the Australian National University. Most measurements were performed with a ×50 objective lens, and the Field Of View (FoV) of the detector set to ×2, producing a ×100 relative magnification. Fig. 3.8 shows a screen shot of the proprietary Vision3D (Vision for Profilers v4.01) software which operated the profiler, measuring hydrogen-induced blister heights and crater depths.

In addition to performing individual scans on sample surfaces, the Vision32 software used to operate the profiler was capable of a "stitching" function. Multiple scans over a user-determined length and breadth of the sample were combined to create a larger surface profile. This combination had the benefits of assisting in identifying small changes in curvature or step heights, which were not as clear in small sampling areas.

Measurements by the optical profiler largely focused on determining the dimensions of hydrogen-induced surface blisters and craters in the different semiconductor materials. The influence of swelling from ion implantation was also examined, as well as curvature changes induced by the ion implantation.

3.2.4 Cross-sectional Transmission Electron Microscopy

First developed by Ruska and Knoll in 1931 [316, 317], transmission electron microscopy (TEM) is an essential tool in the study of nanometre-scale phenomena in materials science. An excellent resource on the constituents and operation of TEM is the four volume series titled "*Transmission Electron Microscopy - A Textbook for Materials Science*" by Williams and Carter [318].

All TEM analysis in this project was performed upon a Philips CM300 administered by the Centre for Advanced Microscopy (CAM) within the Research School of Earth Sciences (RSES) at the Australian National University, as shown in Appendix B.2. The CM300 operated with a high tension voltage of 300 kV. While this accelerating voltage is not ideal in that it allows electrons to displace silicon atoms, lower energy beams provide insufficient resolution for the samples in this project. Micrographs in bright (BF) and dark field (DF) and diffraction patterns were imaged onto emulsion photographic film fed into the beam path beneath the screen from a connected canister. In addition to this negative canister, a digital CCD camera was fitted beneath the screen, allowing capture of micrographs electronically. To maximise contrast in the micrographs to allow easier identification of defect types, samples were imaged off zone axis (OZA). Operation of the TEM was performed by Mr David Llewellyn (CAM) and Dr Bianca Haberl (EME).

Samples were required to be thinned prior to TEM examination to allow electron transmission. All samples prepared in this study were cross-sections; planar samples were not produced or examined. Preparation began with samples cut in half, and the two pieces glued face-to-face with Gatan G1 Epoxy, undergoing between 10-30 minutes setting anneal at T=100°C in a small electric oven. Following bonding, two methods of sample preparation were used in the course of this project.

The first involved a series of additional pieces of silicon wafer being glued either side of the sample to build a small "stack" with the sample material of interest sandwiched in the centre. A Gatan ultrasonic cutter (Model #601) was used to cut a cylinder from this stack, centred around the sample material. This cylinder was then wet polished down using SiC sheets and a Gatan disc grinder (Model #623) on both sides until approximately 100 μm in height. (For greater supply of material, the cylinder could be initially sliced into circular sections using a diamond blade saw prior to polishing, provided the segments were large

enough to accommodate the required polishing.) A Gatan dimple grinder then polished the central region of the sample to a thickness between 0–10 μm. The polished samples were finally thinned by ion milling in a Gatan Precision Ion Polishing System (PIPS), using Ar ions accelerated under E=4–5 keV potential, angled at 3–4° relative to the sample surface.

The second alternative has the original face-to-face sample polished down to a thickness of $\sim$10 μm using the same disc grinder and SiC paper. A 3 mm Cu ring is then glued over the sample, connecting at the extremities of the "sandwich", using Araldite epoxy. Following a $\geqslant$12 hour setting period, the combined sample-and-ring is then also ion milled in the PIPS at settings as above. Some photographic record of each of these processes is shown in Appendix B.2.

All sample preparation was performed on equipment located within the Department of Electronic Materials Engineering (EME) in the Research School of Physics and Engineering (RSPE) at the Australian National University.

TEM was employed to determine the depth and range of hydrogen-related defects such as platelets or cavities present within the semiconductors, both before and after annealing, and following application of external strain.

3.3 Unique experimental solutions

Over the course of any project, there are undoubtedly specific needs that standardised techniques do not necessarily cover. Often these are less technically advanced challenges, but still require a solution particular to that work. In this project, it was no different, and several situations adapted for are described in this section.

3.3.1 Blistering monitoring and recording facility

In order to determine the activation energies of hydrogen surface blistering and cratering phenomena, a system of recording the annealing process at sufficient quality with high accuracy temperature calibration was required. This was assembled using a resistively heated hot stage with a vacuum chuck, an optical binocular microscope and a commercially available digital web camera. A photograph of the complete set-up is shown in Fig. 3.9,

Figure 3.9: Apparatus designed to observe hydrogen blisters and craters forming during the annealing process.

and a schematic of the equipment is shown in Fig. 3.10.

The resistively heated hot stage was thermally monitored by a thermocouple connected to a wire which passed up the vacuum tube aperture, to make contact with the stage immediately below where each sample was attached. Both the readout from electrical input to the stage temperature controller and the thermocouple monitor were in near perfect agreement. To confirm the accuracy of the readouts and thus the accuracy with which the temperature could be known, further calibration was undertaken by measuring the melting points of several elements. The exact read-out temperature at which the element became a liquid from a solid was noted, and plotted against the value in the literature. This experiment determined the following relationship between the actual temperature T_{actual} and the set point or thermocouple read out temperature T_{tc}, which is shown in Appendix B.3, as:

$$T_{actual} = 1.003T_{tc} - 1.108$$

where both temperatures are in degrees Celsius. Thus the temperature of the annealing surface upon the hotplate was known to an accuracy of $\sim$0.1%.

Placed above the stage was a conventional binocular microscope. This microscope

provided sufficient magnification to resolve the hydrogen blisters and craters present on the surface during and following annealing. This microscope had a maximum magnification of $\times 10$, which was used throughout the experiments. The web camera was affixed at the appropriate height and angle to approximate looking through the eyepiece, using a retort stand mounted on the surrounding laboratory table, as shown in the photograph. The second eyepiece was left unobscured, allowing the user to focus the microscope upon the differing sample surface heights.

A Microlight™ 150 optic fibre light source with poseable lamps was used to illuminate the sample, to ensure flat, equal lighting across the material. In order to minimise the influence of "heat haze" effect or irregular changes in refractive index induced by heating of the air above the stage, a small 12V DC electric fan was placed such that it forced air across the stage. This fan thus removed the heated air with a constant stream of cooler ambient air and prevented such seeing problems.

The web camera selected was a Logitech™ C510 high definition webcam, with an 8MP digital sensor and a stated capacity to record footage at 720p (720 horizontal lines within a progressively scanning video signal). This camera was primarily selected for its resolution, at 1600×1200 pixels, with the assistance of the microscope, capable of resolving the hydrogen-related features on the sample surface. An earlier test using a Microsoft™ web camera with a nominal resolution of 640×480 pixels provided insufficient resolution of the surface features. The C510 camera's twin-axis rotatable stand also proved beneficial to aligning the camera lens to the aperture of the microscope eyepiece.

The C510 webcam was connected to a desktop PC which used the proprietary software accompanying the camera to record the video stream. This use of the Logitech-issued software was necessary as the camera had an automatic brightness/intensity filter which would activate if not suppressed by software controls. This automatic filter would lead to adjustments in the recorded signal, making areal identification of the number of surface blisters by intensity quite difficult. This also prevented use of frame collection programs, as non-proprietary software had the aforementioned difficulties, and the bundled package did not feature regular interval, automated frame collections. The files produced from the video stream varied in size according to duration of collection, from tens of megabytes up to hundreds of gigabytes. Somewhat unwieldy to manipulate, regular interval frames were

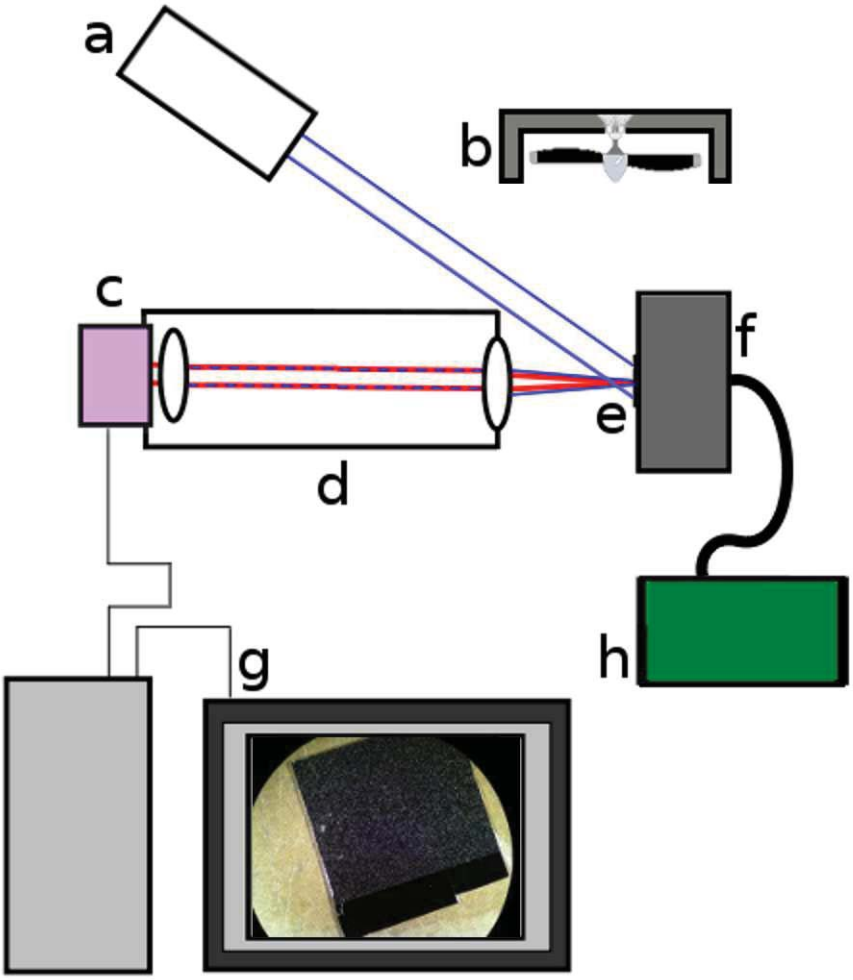

Figure 3.10: Schematic diagram of hydrogen blister/cratering monitoring equipment used in this project. Key: (a) Microlight™ 150 optic fibre light source, (b) 12 V DC electric fan, (c) Logitech™ C510 HD 8 MP webcam, (d) conventional optical microscope (×10 magnification), (e) sample, (f) resistive hot plate, (g) control & recording PC, (h) diaphragm pump.

then extracted from these files to measure instantaneous blister numbers and areal density. Each individual frame was examined using the software suite imageJ [319, 320], by fitting a background intensity and counting the blister/crater numbers by regions excluded, and roughly circular areas fit to the hydrogen-induced features.

Due to difficulties caused by misidentification (e.g. detritus on the sample surface mistaken for craters), measurement limitations (e.g. when multiple craters are in too close proximity for easy resolution, or when the threshold limit overlays them with a continuous area) and minor intensity variations (e.g. caused by refractive index changes above stage by heating the air), often the number of blisters identified was measured by an approximation based upon the intensity of the frame. The initial, un-blistered surface was used to calibrate intensity at zero blisters, and the first series of frames to include blisters were used to calibrate the intensity from the absolute number of blisters present. This number was determined by manual counting of the blisters and fitting a relationship between this number and the intensity measured, and then extrapolated for all subsequent intensity measurements. In the case of very low blistering rates, where individual blisters were readily identified in each frame, manual counting was performed.

3.3.2 Stainless steel stress apparatus

To facilitate the mechanical application of stress on semiconductor wafers, it was necessary to construct an apparatus specific to the proposed materials and conditions. The key features were to be able to apply a reproducible and controllable stress to a thin silicon wafer, for the apparatus to be able to withstand high temperature anneals, and to be mountable in the ion implanter and RBS/ERD chambers for implantation and examination of wafers under stress.

A mechanism designed to meet these conditions is shown in a line drawing three dimensional assay in Fig. 3.11. The specific schematic for this apparatus is presented in Appendix E. The apparatus or boat was machined from 430 grade Ferrite stainless steel with a low thermal expansion coefficient of 10.4×10^{-6}cm/cm/°C to allow use under high temperature conditions. While this material is limited to an upper ceiling temperature of approximately T=900°C, this was not significant as the range of anneals performed in this study was lower (T<850°C). Visible along the length of the boat are the holes for anchor-

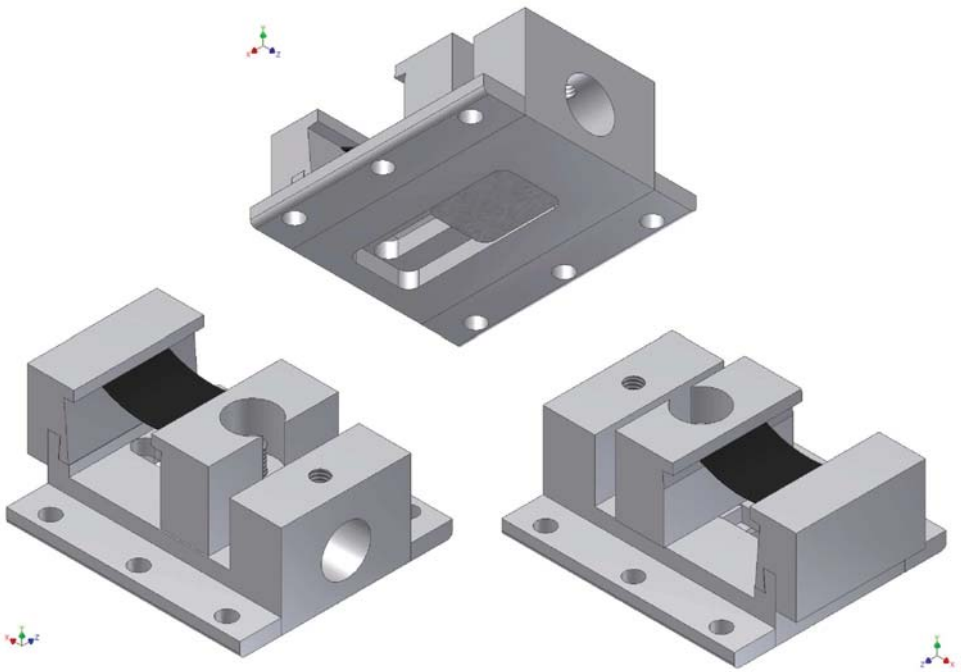

Figure 3.11: Three dimensional assay of stainless steel apparatus used to stress ULTRATHIN® silicon wafers. Design here features larger, dual location shelves, allowing compressive or tensile stresses to be applied to the external face of the wafer. Here the wafer, shown in black, is experiencing compressive stress on the outer face.

ing screws, which allow attachment to the ion implantation and ion beam analysis stages at the ANU. The shelf in the centre is slotted over a threaded shaft which is connected to a rectangular plate. This plate is slotted into the bottom of the boat, allowing it to slide the shelf back and forth, and then anchored with a threaded nut (not shown in schematic) once at a desired location.

The motion of the shelf can be finely controlled by use of a vernier driven screw fitted to the apparatus, as shown in Fig. 3.12. This allows precision and easily repeatable modifications of the displacement between the moving shelf and its affixed counterpart that forms the end of the boat (seen on the right of the schematic). In order to stress a wafer, it is placed across the two shelves, and once the displacement of the shelves is decreased below the length of the wafer, it will begin to distort within the apparatus. In the case of the ULTRATHIN® wafers examined in this work, the degree of distortion from unstressed wafers is quite visibly detectable, and the net change in projected length upon the horizontal axis is recordable from the Vernier scale.

There were two distinct variations in the apparatus' configuration, with combinations

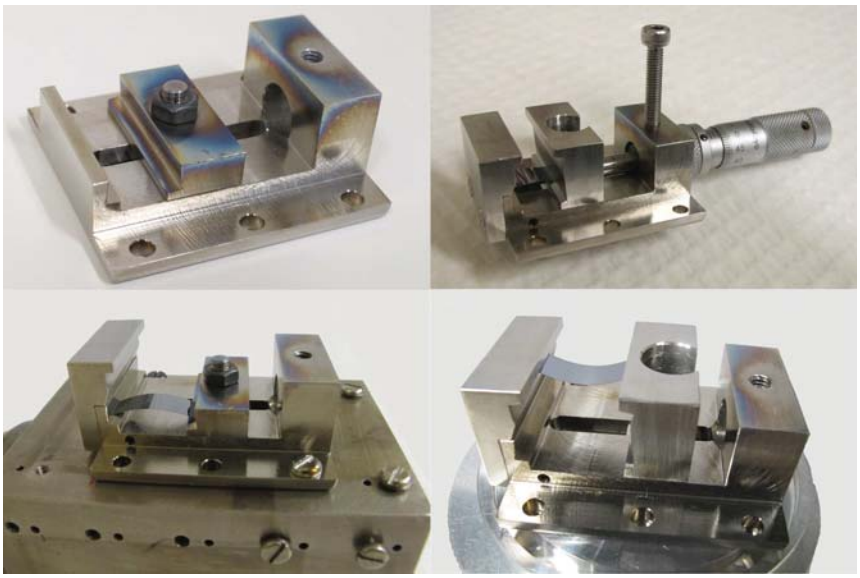

Figure 3.12: Photographs of stainless steel stress apparatus, showing (clockwise from top right) both original small single shelves; large double shelves and Vernier screw drive attached with grub screw, with sample on lower shelves producing a tensile stress for implantation; large double shelves with sample on upper shelves, producing a compressive stress for implantation; mixed single and double shelves with sample on lower shelves undergoing tensile stress, attached to ion implanter holder.

of the two states also possible. The first (shown top left of Fig. 3.12) features two low jaws or shelves, upon which the positioned wafer would be exposed to mechanical stress. However, this configuration only allows for the side of the wafer under tension to be exposed to external analysis or modification. In order to allow for an externally-facing compressive environment to be created, a second configuration was developed, with larger jaws or shelves attached to (or replacing, in the moving shelf's case) the existing apparatus. This configuration is shown in Fig. 3.11. For the majority of the experiments performed across this project, often a combination of shelves was used – the most common configuration being the small moving shelf with the larger end shelf.

The overall width of the support block and height of the shelves was tailored to both the dimensions of the quartz tubes used in the gas furnace which was to be used in stressed sample annealing, and the spacings of the screw threads upon the holders or stages of the ion beam analysis and implantation equipment. The greatest extent between the two shelves was also designed to fit similar lengths of wafers as those stressed in work by Rudawski *et al.* [321] – approximately 20 mm.

Visible in Fig. 3.12 are also the after-effects of the annealing process to which the ap-

paratus was exposed. Discolouration due to oxidation of the stainless steel surface, caused by extraction from the furnace into an oxygen atmosphere while at high temperature, shows around the top of the vernier hutch and the sliding shelf. Any additional oxygen appears to be tightly bound to the metal, not providing any source of contamination for samples annealed on the apparatus subsequent to this chemical reaction. Confirmed with IBA techniques, samples did not show any significant oxygen content, or other composites formed from Fe, C or N.

The primary motivation for changing from the large to the smaller shelves or combinations thereof was due to difficulties within the ion implantation chambers. In both the low and high energy implanters, the larger shelves would prevent full rotation of the sample holder, due to them intersecting with the wall of the copper cold shield. The use of the smaller shelf in the moving position, at certain heights of the implantation holder, allowed for a greater rotational freedom before conflict occurred.

The method by which the stress this apparatus applied to the sample wafers was determined is described in Section 5.4.2, and the theory of the physics used to fit the strained wafers is detailed in Appendix A.1.

In the event this method proves successful in modifying the evolution of the hydrogen to forms more beneficial to the ion-cut or any other process, it is a valid question as to how useful it would be to industrial scale production. With larger and larger wafers being produced and used, another viable possibility may be deposition of thin films onto the substrates to apply the same stresses. The use of SiO_xN_y films to produce stress in similar semiconductor materials has been investigated elsewhere [230], with promising results. Depending upon the degree to which contamination would play a negative role for device production, work presented by Ohring [265] shows significant stress values (in the order of gigapascals, for both tensile or compressive stress) can be achieved with evaporated or sputtered metal films upon Si.

Chapter 4

Phenomenology of hydrogen blistering in semiconductors

EXPLORING the behaviour of hydrogen in semiconductors, this chapter focuses on hydrogen induced blistering phenomena. A collection of key areas of influence and behaviour are broken down into a number of subcategories. In the first half of the chapter, hydrogen's influence within semiconductors is established, prior to external blistering. In the second half, the external manifestation of blisters on semiconductor surfaces is explored.

Opening the first half of the chapter is a discussion of the swelling induced by the implantation of hydrogen into various materials, in Section 4.3.

The bulk of the chapter, broken up into four subsections, explores both the mechanics and the kinetics of the hydrogen blistering process in semiconductors. Section 4.4 focuses on the critical hydrogen concentrations required to induce surface blistering, followed by a study of hydrogen blister dimensions with relation to material, implantation conditions and annealing in Section 4.5. The kinetics of hydrogen blistering is examined in Section 4.6, which establishes blistering appearance times and rates, temperature dependence and activation energies. Section 4.7 details the crater depths and floor roughnesses of ruptured hydrogen blisters produced in several materials and crystal orientations. Finally, Section 4.8 contrasts the behaviour established in intrinsic Si(100) with a series of heavily-doped substrates, determining what influence such dopants have on the blistering process.

4.1 Experimental materials

In Sections 4.3 and 4.4 of this investigation, substrates used included silicon wafers cut in both (100) and (110) orientations, and (100) germanium wafers. The Si (100) wafers were p-type B-doped with a resistivity of 10-20 Ω cm, the Si (110) wafers were p-type B-doped, ρ=20-70 Ω cm, and the Ge (100) wafers were undoped, ρ>40 Ω cm. All wafers were polished to a thickness between 350-405 μm. Silicon samples were ion implanted with hydrogen ions at energies from 20 keV to 500 keV, with fluences from 1×10^{16}cm^{-2} to 1.5×10^{17} cm^{-2} at each energy, nominally at room temperature. For the Ge(100) wafers, the same implantation energies were applied, but the fluence levels decreased, from 6×10^{15} cm^{-2} to 1×10^{17} cm^{-2}. To minimise channelling effects, the sample surface normal was tilted at 7° with respect to the incident ion beam.

A shift to studying behaviour of blistering and cratering at a fixed fluence occurs in Section 4.6. A "standard conditions" implantation is defined, and used throughout this research project. The "standard conditions" are an ion implantation energy of E=40 keV and hydrogen fluence of $\Phi_H = 6 \times 10^{16}$cm^{-2} while the sample is at room temperature. This implantation was performed into the aforementioned Si(100), Si(110) and Ge wafers. Additionally, p-type B-doped Si(111) wafers with a resistivity of ρ=7.5-15 Ω cm were also implanted with hydrogen ions at E=40 keV and $\Phi_H = 6 \times 10^{16}$cm^{-2} at room temperature. Ion beam current during implantation ranged from I=0.75-2.0 μA, and is unlikely to cause any localised dynamic annealing of the substrates. An expansion of this study involved a series of implantations with energies from E=25–125 keV, with either a fixed ion fluence of $\Phi_H = 5 \times 10^{16}$cm^{-2}, or one selected to maintain a constant hydrogen profile peak concentration. These expansions are detailed further within the chapter. To further explore the influence of dopants upon the blistering/cratering process, a series of commercially purchased highly *p*- or *n*-type doped wafers were also implanted with this "standard" fluence and energy of hydrogen, as described in Section 4.8.

Annealing was performed either in a conventional quartz tube gas furnace, or upon a resistively heated hot stage, at preset temperatures. At the desired annealing position within the tube, furnace temperature readings from the controller were confirmed via thermocouple probe measurement. During annealing in the furnace, samples were immersed within an Ar ambient, with a gas flow of approximately 1 cm^{3}s^{-1} within a quartz "boat"

receptacle. For the hot stage, samples were exposed under atmospheric conditions, held in direct contact with the stage by a vacuum chuck. Samples were placed either in the furnace or upon the hot stage once the required preset temperature was reached. The calibration of the actual hot stage temperature to the controller read out, as described in Section 3.3.1 and Appendix B.3, gives high confidence in temperature values. Additionally, the vacuum chuck affixing the samples guarantees excellent thermal contact, and temperatures are assumed to instantly reach equilibrium with the stage.

When the quartz tube was opened and the boat inserted, the short exposure to a room temperature environment and addition of the boat's thermal mass led to the annealing temperature temporarily decreasing. The exact rate at which the temperature would return to preset conditions varied, and known details are provided for the appropriate anneals. Generally the temperature T would decrease by ΔT $\sim$15°C, then return to equilibrium within 5 minutes, as determined by the furnace controller. Around the centre of the furnace where the samples were annealed, the variation in temperature was approximately $\pm$3°C at $\pm$5 cm, as determined by thermocouple probe. Despite a number of previous works emphasising its influence upon the annealing process [322–324], the furnace's ramp rate is not known precisely, nor the rate with which the sample reaches equilibrium with the preset temperature. Such difficulties were largely due to the inability to use the thermocouple within the furnace tube simultaneously with the quartz boat. Nor did the boat have a fitting or attachment which would allow its temperature to be monitored by some kind of contact probe. Suggestions to modify or manufacture such a boat should be considered for future work.

4.2 Experimental methods

Section 4.4 presents an examination of the samples immediately after annealing at a fixed temperature and duration, and Section 4.6 contains an examination of samples during the annealing process to establish onset specific details, and at the completion of the blistering/cratering process. In Section 4.3, the underlying swelling due to the ion implantation is explored prior to any annealing, while Section 4.8 expands upon the blistering onset work in highly doped substrates.

All these branches of the chapter involve significant use of the Wyko Optical profilometer, as described in Section 3.2.3, to measure the small changes in the wafers or to systematically quantify the blisters and craters following annealing. Blister measurement was performed manually, which required the user to select each individual blister and profile it. Measuring each of the major axes of the blister, plus its mean height above the sample surface, often took substantial duration – approximately 1 hour per ∼25 blisters. Measurement was also more difficult for irregularly shaped blisters, encouraging selection of more symmetrical blisters. These factors also affect the measurement of ruptured blister craters and their floor roughness. As such, an anthropic bias may be present in the blister dimension values. To attempt to limit the impact of human-based selection, profiling was performed on a minimum of 100 blisters per sample, starting from the approximate centre of the sample's implanted (thus blistered) area. Substantial analysis of the data collected by the video camera monitoring the blistering process, as described in Section 3.3.1, was performed using the software suite imageJ [319, 320].

The samples were characterised in the as-implanted state and post-annealing to examine the evolution of the hydrogen profile and blisters subsequently formed. Ion beam analytical (IBA) techniques were particularly useful. Rutherford backscattering spectroscopy (RBS) was used in channelled mode (RBS-C) to examine implantation-induced damage to the material post-implant and prior to annealing. Similarly, hydrogen profiles and distribution in the as-implanted state were examined with elastic recoil detection analysis (ERD). The surface blisters and craters which occurred in the material post-annealing were examined with a Wyko Optical interferometry profiler, measuring both major axial dimensions and heights/depths of the features, as well as roughness of any crater floors.

4.3 Implantation induced swelling

Swelling induced by ion implantation was measured across the interface between implanted and unimplanted material. Samples produced in this manner – by selective masking of the sample – were hydrogen implanted Ge(100), Si(100) and Si(110) wafers.

Following ion implantation, swelling was observed in all semiconductor substrates. Distinguished by the optical profiler, a discontinuity occurring on a nanometre scale was ob-

served between implanted and unimplanted regions of the material in the as-implanted state, as shown in Fig. 4.1.

Small pit-like indents are visible on the surface of the sample implanted at T=60°C. These samples were heated *in situ* by application of heated nitrogen gas stream to the side of the sample holder outside the implant chamber. Such a gas flow may have transferred a significant electrostatic charge to the surface of the holder and any attached samples. Blast defects could then have formed when the electrostatic charge was discharged into the chamber vacuum [325].

Many previous investigations into ion-induced swelling [326–329] dealt with heavy ions with fluences and energies high enough to amorphise the crystal, rather than the lower energy, low mass H ions dealt with in this study. Previous work also suggests that these step heights only occur in silicon when the fluence of the implanted ion (whether H, He, etc.) is sufficient to induce bubble formation within the bulk [327]. In this work, the fluence range drops below that required to induce ion-cut, and suggests that bubble formation is not a prerequisite of swelling within a crystal wafer structure.

The temperature of the substrate during implantation has a significant influence on the resultant swelling, as reported elsewhere [94, 330–332]. When silicon was implanted at three different temperatures – room temperature (T=20°C), T=60°C and cooled by liquid nitrogen (T=-190°C) – there was a small increase in swelling from the cooled material. Figure 4.2 shows the RBS-C spectra collected from each of these thermal regimes for a hydrogen implantation at E=40 keV over a range of hydrogen fluences. Ion induced damage increases with implantation fluence, and as the temperature decreases, the local damage caused by equivalent implantation fluences increases. The increases in direct scattering yield are not linear with increasing fluence at each temperature. Large yield increases occur in the LN2 implantations between 3 and $6\times10^{16}\text{cm}^{-2}$, and in both the T=60°C and room temperatures implantations between 1 and $3\times10^{17}\text{cm}^{-2}$. The transition in the LN2 implanted samples' yields coincides with the fluences required to induce hydrogen blistering/cratering for ion-cut techniques, however it is unclear to what the transition in the high-temperature implantations relates. Contrasting the implanted fluence and resultant direct scattering yield individually with optical profiler measurements, the swelling changes in height measured are not directly coupled to the implantation damage at all

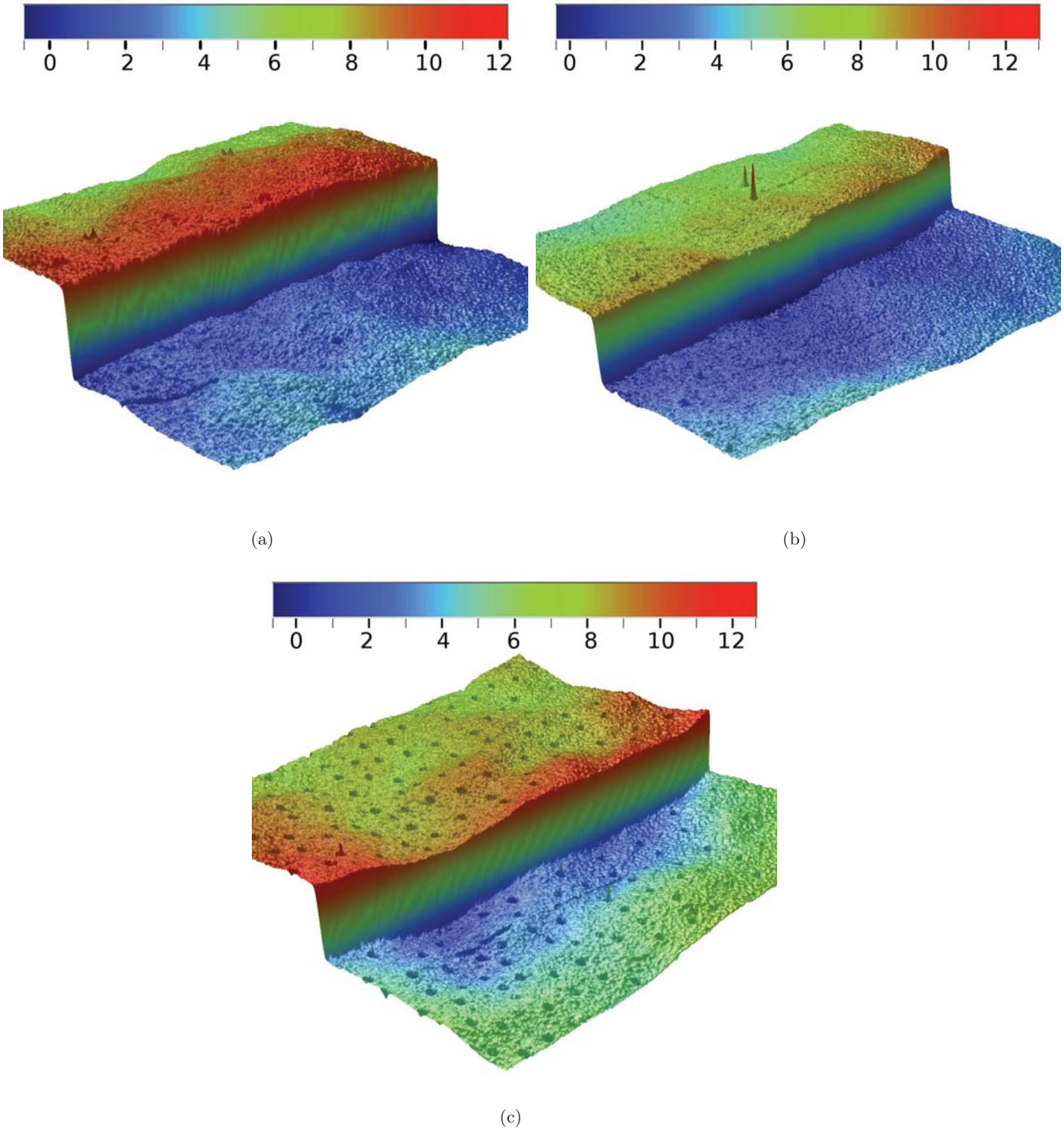

Figure 4.1: Optical profiler measurements of the interface between masked silicon (lower) and ion-implanted silicon (higher), from H(40keV,1×10^{17}cm^{-2}) performed at (a) cryogenic (i.e., T=-196°C), (b) room and (c) elevated (i.e., T=60°C) temperatures. Vertical scales as marked, in nanometres, represent relative height above the unimplanted surface. Scan area (a) 307×304 μm, (b) 190×170 μm, (c) 308×307 μm. Profile settings: (a,c) PSI Mode, magnification ×10, FoV ×1; (b) PSI Mode, magnification ×10, FoV ×2.

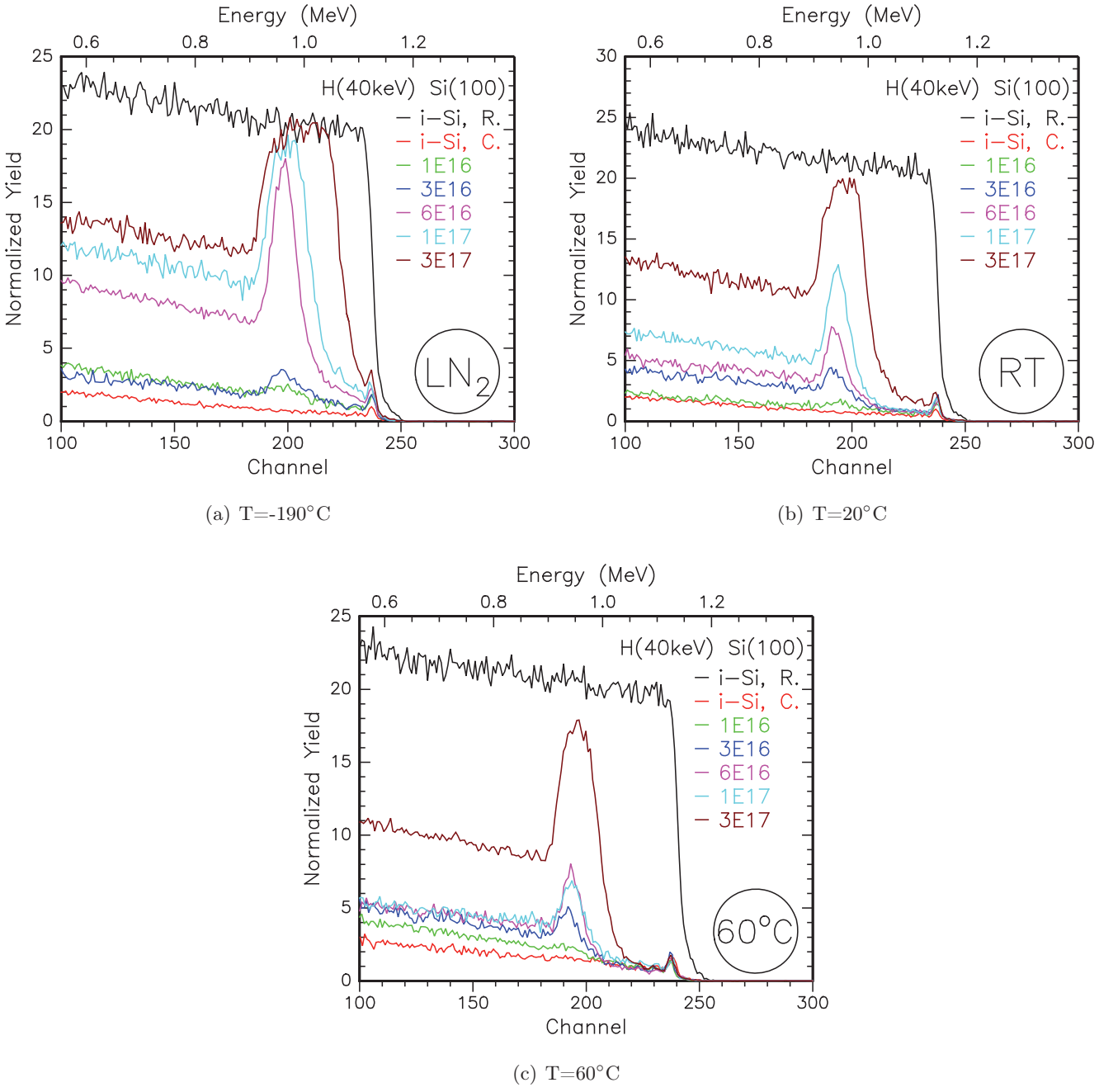

(a) T=-190°C

(b) T=20°C

(c) T=60°C

Figure 4.2: 2MeV $^4He^+$ RBS-C measurements from (a) liquid nitrogen-cooled, (b) room temperature and (c) T=60°C-heated hydrogen-implanted Si(100). Analysing beam channelled along ⟨100⟩ crystalline axis, Q=20 μC, I=30 nA, detector at a scattering angle of 168°. Also included for comparison in each spectra are measurements from intrinsic Si(100) along channelled (C.) and random (R.) incident beam angles.

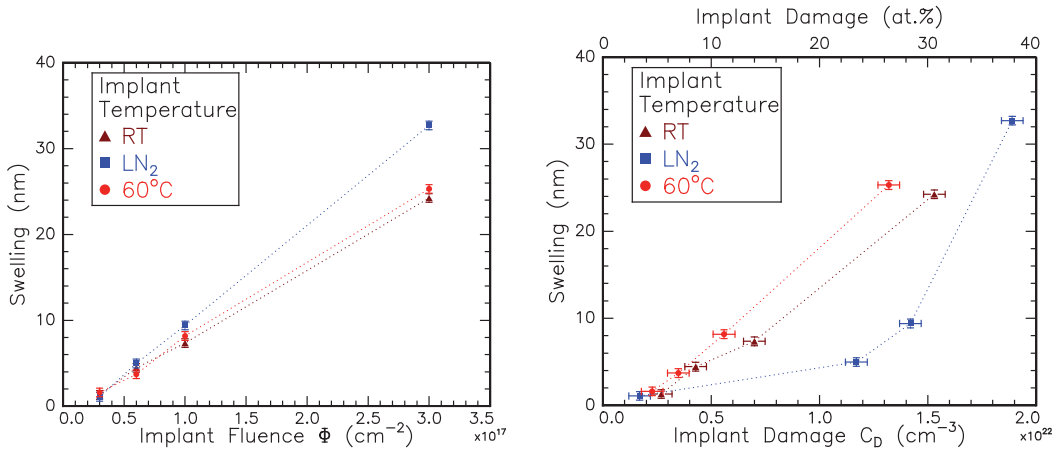

Figure 4.3: Swelling heights (nm) determined by optical profilometer contrasted with (a) implantation fluence and (b) direct scattering yield (=ion beam implantation damage) (cm^{-3} or at.%) determined by RBS-C, for E=40 keV H-implanted Si(100) at fluences between 3×10^{16}, 6×10^{16}, 1×10^{17} & $3\times10^{17}cm^{-2}$ and different temperatures as labelled.

temperatures, as shown in Fig. 4.3.

These measurements, in conjunction with data in Table 4.1, show that at low fluences, swelling is similar at all implantation temperatures. However, at $\Phi_H \geqslant 6\times10^{16}cm^{-2}$ in the cryogenically-cooled implantation, a large increase in ion damage occurs without a correspondingly large increase in swelling. While the implanted region of the nitrogen-cooled silicon swelled approximately 10-30% higher than the warmer implantations at $\Phi_H = 6 \times 10^{16}cm^{-2}$, its damage yield increased by a factor of three. This is surprising as radiation damage will generally scale with implantation fluence under the conditions of this study. However, RBS-C may not be sensitive to all significant defects that form in this system, and may grossly underestimate the concentration in the other samples. For example, if the majority of defects were large vacancy clusters with most interstitials diffused deep into the sample, the RBS-C statistics would be inaccurate.

The lack of major differences in swelling between samples implanted at room temperature and T=60°C, with some small changes visible in cryogenic implantations is generally inconsistent with the previous experimental work [326, 327]. Higher temperatures are suggested to produce greater induced swelling, via increasing mobility of the interstitial defects assumed to induce the swelling. Giri [326] expects less swelling at low temperature (i.e.,-200°C) implantations, due to decreasing interstitial mobility to the surface. In contrast,

Tamulevičius *et al.* [333] predict high temperature implantations would result in greater recombination of interstitials and vacancies, minimising swelling.

In our work, as shown in Table 4.1, we can see no significant change in swelling between the T=60°C and room temperature implantations, and quantifiably larger swelling measured in the liquid nitrogen cooled implantation. While Fig. 4.3 reveals that increasing damage does not mean an increase in sample swelling, it is unclear if this is a result of lack of sensitivity to present defect types by RBS-C.

Within each material for a set fluence, variation in implantation energy produces no appreciable change in swelling. While Table 4.1 shows that there is variation in the induced swelling between each crystal type and orientation, varying implant energy from 20 keV to 80 keV for a set material only produced changes in swelling within the measurement error. The range over which the damage is produced is less important than the total amount of damage, in agreement with previous findings [326].

Conclusion

The data shows an increasing fluence produces a greater swelling. There is also a weak correlation between decreasing implantation temperature and increasing swelling, with cryogenic implantations showing 10–30% greater swelling than room or elevated temperature implantations. No strong link exists between implantation energy and swelling, which also suggests the swelling is largely caused by the cumulative implant fluence, independent of the integrated volume within which it occurs.

RBS-C analysis shows increasing levels of ion beam damage do not necessarily produce higher swelling. However, RBS-C may not be able to accurately determine the defect concentration if their structure changes (i.e., from amorphous clusters at liquid nitrogen temperature to intermediate defect complexes at T=60°C, etc.).

For our standard condition implantation of H(40keV,6×10^{16}cm$-$2,RT), the magnitude of swelling manifested was 4.44 nm for Si(100), 3.34 nm for Si(110) and 3.08 nm for Ge(100). This is relatively small compared to the sizes and depths of hydrogen-induced blisters and craters analysed in this study, and is unlikely to significantly influence the blister profiling measurements.

Fluence	Si(100)				Ge(100)				Si(110)			
	T=20°C		T=-196°C	T=60°C	T=20°C				$T_{implant}$=20°C			
cm^{-2}	20keV	40keV			20keV	40keV	60keV	80keV	20keV	40keV	60keV	80keV
1×10^{16}	0.50	n/a	n/a	n/a	n/a	0.42	0.30	1.2	n/a	n/a	n/a	n/a
3×10^{16}	1.05	1.30	1.08	1.60	1.27	1.80	1.65	1.85	1.45	n/a	1.46	1.28
6×10^{16}	2.50	4.44	4.97	3.71	2.56	3.08	3.15	3.66	3.34	2.47	2.62	3.21
1×10^{17}	5.00	7.35	9.40	8.17	3.59	3.60	3.76	2.92	5.96	5.33	5.56	5.63
1.5×10^{17}	9.05	n/a	n/a	n/a	n/a	n/a	n/a	n/a	10.15	9.30	9.51	8.47
3×10^{17}	n/a	24.25	32.70	25.31	n/a	n/a	n/a	n/a	n/a	n/a	n/a	n/a

Table 4.1: Swelling of semiconductor surfaces, as measured by optical profilometry at a masked interface, by hydrogen ion implantation at temperatures, energies and fluences as labelled; units in nanometres. n/a=not ascertained.

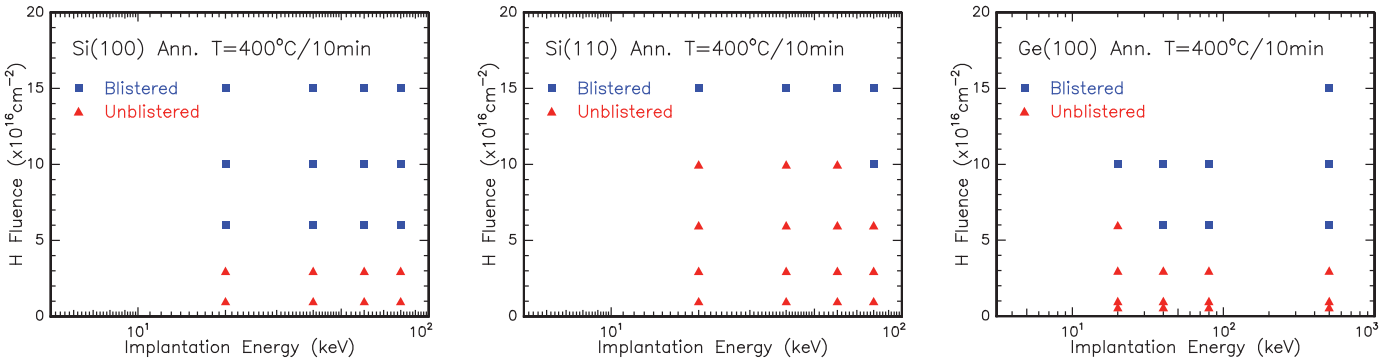

Figure 4.4: Blistering events in T=400°C/10 minutes annealed H-implanted Si(100), Si(110) & Ge(100)

4.4 Implantation conditions for blister formation

Silicon wafers in both (100) and (110) planes, and germanium (100)-oriented wafers were implanted with low to high energy hydrogen ions and then annealed for a set interval in an inert atmosphere. Hydrogen ion energies ranged in 20 keV steps from 20 keV to 80 keV, as well as a higher 500 keV energy implantation for Ge. The silicon samples were implanted with fluences $1\times10^{16}\text{cm}^{-2}$, $3\times10^{16}\text{cm}^{-2}$, $6\times10^{16}\text{cm}^{-2}$, $1\times10^{17}\text{cm}^{-2}$ and $1.5\times10^{17}\text{cm}^{-2}$ of hydrogen. After initial testing the germanium wafers were found to blister more catastrophically than the silicon (as per [21]), becoming incredibly fragile following ion implantation and annealing. Elements of this behaviour are also reported in Section 4.6.2. In order to allow examination without destruction of the samples, the fluences selected for implantation into Ge were lower, ranging from $6\times10^{15}\text{cm}^{-2}$ to $1\times10^{17}\text{cm}^{-2}$ hydrogen implantation. Sections of each implant were annealed in the argon ambient of a quartz tube gas furnace, with a gas flow rate of $\sim$1 cm^3s^{-1}, at T=400°C for 10 minutes. Within the furnace, a thermocouple probe determined the thermal gradient around the position where the samples were annealed as ΔT=1°C.cm^{-1}, giving a largely uniform annealing environment. Temperature variation recorded during the annealing process was slight, with 393$\pm$1°C <T<408$\pm$1°C. An identical series of Si(100) samples were also annealed at T=400°C for 10 minutes in a Rapid Thermal Anneal (RTA) furnace, under an Ar flow of 1.48-1.55 cm^3s^{-1}, to confirm behavioural trends. Blister occurrence and dimensions were in good agreement between the two sample sets, giving confidence in the behaviour's reproducibility.

Figure 4.4 shows the graphs of the fluences and energies of hydrogen implanted in silicon in both crystal orientations and germanium that blistered when annealed for 10 minutes. Initially we may infer from these graphs that blistering requires certain energies and fluences to occur in each material. However, such predictions are hampered by the low range of fluences and short duration of the thermal anneal. Rather, we can obtain a comparative indication of early stage evolution of blistering.

Terreault [28] uses his work and data from Aspar *et al.* [17], Beddell and Lanford [21], Höchbauer *et al.* [24], Huang *et al.* [90], Lu *et al.* [152] and Moutanabbir *et al.* [61] to infer an upper limit for the fluence which leads to blistering in Si(100), increasing with energy, and describes this limit as lying between 8×10^{16} and $1.6 \times 10^{17}\text{cm}^{-2}$ for E=40 keV. His figure (Fig. 2 in [28]) gives a specific upper limit of $1.2\times10^{17}\text{cm}^{-2}$. Replicated in Fig. 4.5, including a selection of data from other researchers, the limits suggested by Terreault are indicated by the red dotted lines and shaded region. The lower limit seems to be in good agreement with the values measured in this work for Si(100). However, if such an upper limit exists, it must be substantially higher, as the E=20 keV with Φ_H=1 and $1.5 \times 10^{17}\text{cm}^{-2}$ implantations both blister in our investigation. Further evidence that such upper limits must be higher (if extant) is seen in the E=40 keV implantations at Φ_H=$1.5 \times 10^{17}\text{cm}^{-2}$ and $3 \times 10^{17}\text{cm}^{-2}$, as well as in several other sources [152, 334].

Examining the data from this study as shown in Fig. 4.4, note that at the lowest implantation energy – E=20 keV – the germanium did not blister from the applied anneal. Most similar work [53, 56, 101, 130, 170, 178, 336, 337] suggests that the lower bond energies of Ge-Ge and Ge-H (compared to Si-Si and Si-H) allow for more ready creation of hydrogen molecules and fracture of the Ge crystal, so the absence of this behaviour in the T=400°C/10 minute annealed $6 \times 10^{16}\text{cm}^{-2}$ H-implanted Ge is puzzling. Higher fluences ($>10^{17}\text{cm}^{-2}$) of hydrogen implanted into Ge at lower energies were not investigated after initial tests showed that entire surface delamination and regular destruction of the sample took place – as mentioned earlier and in Section 4.6.2. This limited the capacity to examine blister depths, shapes and roughnesses when the surface no longer remains. It did however agree with previous work [178, 337] showing the lower fluence requirements to induce blistering in Ge. The lack of blistering in the lower fluences implanted is likely due to the anneal's short duration at relatively lower temperature.

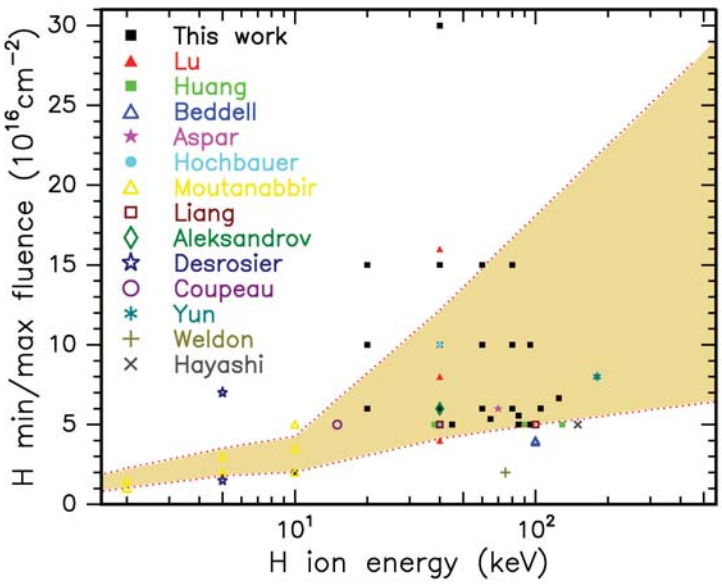

Figure 4.5: H fluences resulting in blistering in ion implanted and annealed Si(100). Data from Aleksandrov *et al.* [335], Aspar *et al.* [17], Beddell & Lanford [21], Coupeau *et al.* [81], Desrosiers *et al.* [334], Hayashi *et al.* [55], Höchbauer *et al.* [24], Huang *et al.* [90], Liang *et al.* [20], Lu *et al.* [152], Moutanabbir *et al.* [61], Weldon *et al.* [106, 113] and Yun *et al.* [104]. Red dotted lines indicate upper and lower boundaries to blistering window, as suggested by Terreault [28].

More striking are the differences between the two (100) oriented wafers and the Si(110) material. For the annealing durations and temperatures studied, it appears a much larger concentration of hydrogen must be present in (110) silicon in order for blistering to occur. As the blisters are expected to form from platelets aligned along {001} and {111} habit planes, these cannot be parallel to the surface in Si(110), making this substrate less prone to blistering [28]. Only at implant energies E$\geqslant$80 keV, when the peak in the hydrogen profile is found at depths of 700 nm, do we see blistering occurring in Si(110) for fluences less than Φ_H=1.5 $\times$ 10^{17}cm^{-2}. For all other samples exposed to T=400°C/10 minutes, no blistering occurred. In general, clearly Si(110) requires higher fluences to induce blistering, which is supported by annealing work performed in Section 4.6, where no blistering was induced in Si(110) for lower fluences independent of annealing duration or temperature. Note that at E=80 keV, the Φ_H=1$\times$10^{17}cm^{-2} implanted Si(110) sample also underwent blistering in the annealing window. It is possible that were a longer duration anneal applied to those Si(110) samples implanted with Φ_H=1$\times$10^{17}cm^{-2} but at lower implantation energies, they too would blister. This suggests a lower limit between 6$\times$10^{16}cm^{-2} and 1$\times$10^{17}cm^{-2} of hydrogen is required to induce blistering in Si(110).

4.5 Blister mechanics

Considerable attention has been focused in the literature in contrasting hydrogen-induced blister size (i.e., diameter) with the implantation energy or depth of the peak in the hydrogen concentration profile [14, 28, 69, 81, 90, 100, 113, 338]. Little work has focused on the blister heights above the wafer surface in relation to implantation parameters. All of these studies are combinations of modelling and experimental work for hydrogen-implanted Si(100); few attempts have been made for Ge(100) [339], and no similar attempts to model Si(110) or Si(111).

4.5.1 Blister modelling

Coupeau *et al.* [81] treats the blisters as spherical shells formed by plastic deformation, using methods laid out by Dion *et al.* [340], the classical Föppl-von Karman (FvK) theory of thin plates. This model develops the following equation for the diameter D of the blisters:

$$D = \sqrt{\frac{16hR_{\mathrm{P}}\sigma_{\gamma}}{P}} \tag{4.1}$$

where h is the height of the blisters above the wafer surface, R_{P} is both the thickness of the blister membrane and the depth of the peak in the hydrogen implantation, P is the hydrogen gas pressure within the blister relative to the ambient outside the substrate ($P = P_{inside} - P_{outside}$), and σ_{γ} is the material's yield or critical buckling stress. All values are MKS SI. When defined with appropriate boundary conditions (i.e., a plate with clamped edges), this term is given by:

$$\sigma_{\gamma} = \frac{\alpha E}{1-\nu^2}\left(\frac{R_{\mathrm{P}}}{r}\right)^2 = \frac{12\alpha}{R_{\mathrm{P}}r^2}\mathscr{D} \tag{4.2}$$

where E is Young's modulus of the material, ν is Poisson's ratio, r is the blister radius, α is a numerical constant depending on the boundary conditions, of order $\sim$1 (Coupeau defines it as between 0.5-0.6, Huang $\sim$1), and $\mathscr{D}$ is described as the bending rigidity. Substituting Eq. 4.2 into Eq. 4.1 leads to an expression of the blister height relative to radius or diameter:

$$\begin{aligned} h &= \frac{r^4 P}{48\alpha\mathscr{D}} \\ &= \frac{r^4 P}{24\mathscr{D}} \qquad \text{if } \alpha = 0.5 \\ &= \frac{D^4 P}{384\mathscr{D}} \\ &= \frac{r^4 P(1-\nu^2)}{2ER_{\mathrm{P}}^3} \end{aligned} \tag{4.3}$$

A different approach is taken by Aleksandrov *et al.* [335] and Huang [90], which rely on the same plate model, but assume a zero change in pressure, and an elastic deformation as described by Mitani *et al.* [341], and Young and Budynas [342]. Starting with the equation of Gibbs Free energy for the blisters forming beneath a thin layer of substrate, the equations for the blister height relative to the surface h with regard to surface diameter D, and fraction of the diameter subsurface, relative to implantation depth R_{P}, are:

$$h = \frac{r^4 P}{64\mathscr{D}} \tag{4.4a}$$

$$= \frac{3r^4 P(1-\nu^2)}{16ER_{\mathrm{P}}^3} \tag{4.4b}$$

$$r = \left(\frac{16ER_{\mathrm{P}}^3\gamma}{9\alpha(1-\nu^2)P^2}\right)^{\frac{1}{4}} \tag{4.4c}$$

$$D = 4\left(\frac{ER_{\mathrm{P}}^3\gamma}{9\alpha(1-\nu^2)P^2}\right)^{\frac{1}{4}} \tag{4.4d}$$

where γ is the interface surface energy of the blister, defined as $\gamma = 1.5 \times 10^{-4}T + 5 \times 10^{-3}\mathrm{Jm}^{-2}$, where T is annealing temperature in kelvin [343] (generally in the range 0.1-0.5 Jm^{-2}).

4.5.2 Blister heights versus diameter

Optical profilometry was used to measure the dimensions of the hydrogen-induced blisters formed during the T=400°C/10 minute anneal in Si(100), Si(110) and Ge(100). The height and diameters of the blisters were profiled relative to the surrounding unblistered surface.

Si(100)

In the case of the Si(100) H-implanted materials, as shown in Fig. 4.6, there is a

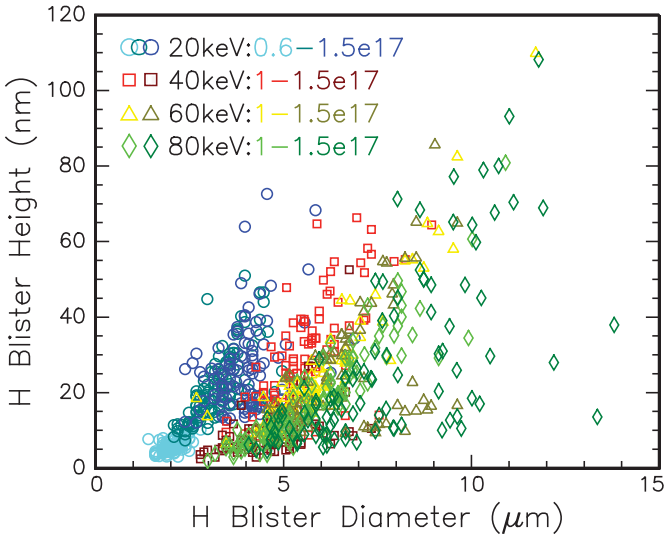

Figure 4.6: Hydrogen blister diameter versus height in Si(100) implanted at E=20 keV, 40 keV, 60 keV and 80 keV, annealed at T=400°C/10 minutes. Fluences of implantation from $6 \times 10^{16} - 1.5 \times 10^{17}\text{cm}^{-2}$ as labelled, and individual graphs for each fluence can be found in Appendix D.5.

correlation between the blister's diameter and maximum height, while the diameter and heights both have a weaker relationship with the implantation fluence.

If we take the particular case of the lowest energy implantation (E=20 keV), as hydrogen fluence increases, there is a distinct broadening of the range of heights for a given diameter of each blister, and an increase in both mean heights and diameter. At $\Phi_H = 6\times10^{16}\text{cm}^{-2}$, blister diameters measure between 1 and 3 μm, and the variation in height was limited to ∼3-12 nm. Then, as $\Phi_H = 1 \times 10^{17}\text{cm}^{-2}$, there is a widening of both the range of blister diameters and heights, and further again at $\Phi_H = 1.5 \times 10^{17}\text{cm}^{-2}$, with diameters $D = 3.97 \pm 0.78$ μm and heights $h = 26.4 \pm 11.6$ nm.

Looking at the distribution of blister heights in each implantation energy and fluence presented in Fig. 4.7(b), there is no strong correlation between blister heights and implant parameters, with inconsistent effects across the data. Such irregularity may be a selection bias effect. However, considering the consistent trend in the blister diameters determined from the same data, this may instead be an indication there is no correlation. For individual figures showing histograms of blister diameter for each implantation in this section, see Appendix D.5.

While Equations 4.1 and 4.4d include no specific term for fluence, the pressure manifest

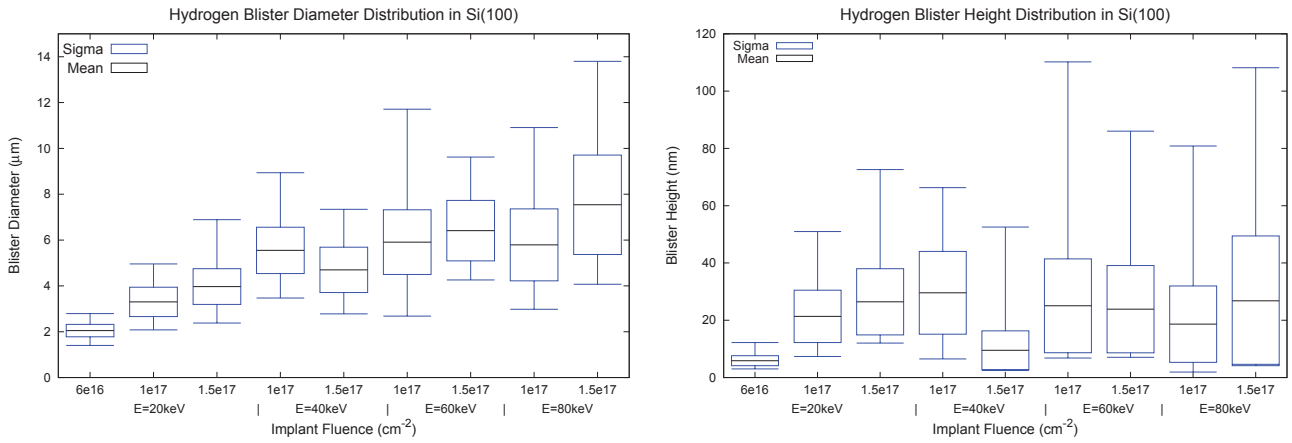

Figure 4.7: Hydrogen blister diameter and height for Si(100), hydrogen implanted with various ion fluences and energies as labelled in graphs, and annealed at T=400° C for 10 minutes. Composite and individual histograms from which this data was derived can be located in Appendix D.5.

in each blister is related to the concentration of hydrogen present. With higher fluences leading to higher relative pressures, both Eq. 4.1 and 4.4d suggest that the diameters of the blisters should decrease with increasing implant fluence, while the height of the blisters should increase. This is contrary to the majority of data measured in this study, which instead suggests a proportional relationship between fluence (via relative pressure) and blister diameter, and very little indication of increase in height for increase in fluence.

Using the theory outlined in Section 4.5.1, for the experimentally measured values of the blister diameter, the predicted height of the hydrogen blisters was contrasted with observations. Table 4.2 lists the blister dimensions for the H-implanted Si(100) samples studied in this section, and contrasts heights predicted for specific values of relative gas pressure. These pressure values were selected to best represent the data, whilst straying least from values listed in the literature [81, 90, 335, 339, 340] (see resultant pressure figures in [339] and [81] particularly). Both models give a reasonable fit to the data for a pressure range from P=10–25 MPa, factoring in depth ranges R_{P} calculated by software package SRIM-2008 [251] and experimental blister diameter values. Such agreement suggests that blisters can be reasonably modelled using expressions derived from Gibbs free energy arguments based around plastic or elastic fixed plate distortion.

A relationship linking implantation energy or ion depth with increases in diameter, and an inverse relationship to blister height is in both Eq. 4.1 and 4.4d. Contrasted with the

Energy	Depth	Fluence	**Experimentally Measured**				**Modelled Heights** (nm)	
			Diameter		Height		Eq. 4.4a	Eq. 4.3
(keV)	R_P (nm)	(cm^{-2})	D (μm)	σ_D (μm)	h (nm)	σ_h (nm)	P=25 MPa	P=10 MPa
20	223.7	6.00E+16	2.05	0.27	5.88	1.75	2.52	2.69
20	223.7	1.00E+17	3.30	0.64	21.36	9.13	16.94	18.06
20	223.7	1.50E+17	3.97	0.78	26.44	11.55	35.47	37.84
40	373.1	1.00E+17	5.55	1.01	29.58	14.44	29.20	31.15
40	373.1	1.50E+17	4.70	0.99	9.52	6.77	15.02	16.02
60	530.7	1.00E+17	5.91	1.41	25.05	16.38	13.05	13.92
60	530.7	1.50E+17	6.41	1.32	23.87	15.24	18.06	19.26
80	689.3	1.00E+17	5.79	1.57	18.64	13.33	5.49	5.85
80	689.3	1.50E+17	7.54	2.17	26.79	22.63	15.78	16.83
40	373.1	6.00E+16	3.97	0.94	9.42	7.14	7.63	8.14
45	416.6	5.00E+16	7.23	1.68	54.63	26.44	60.44	64.47
65	569.4	5.35E+16	9.43	2.80	52.19	38.00	68.45	73.01
85	730.0	5.56E+16	11.94	2.96	55.90	38.39	83.40	88.96

Table 4.2: Blister heights and diameters in Si(100), as measured by optical profilometry, by hydrogen ion implantation at energies and fluences as labelled. Contrasted with Eq. 4.4a and 4.3, modelling blister heights with pressures as labelled, and parameters E=168.9 MPa, ν=0.28, for the experimental diameters and depths.

results in our work, showing a clear increase in blister diameter with implantation energy, and little effect upon blister height, this theory is in good agreement.

No strong relationship exists between hydrogen blister diameters and hydrogen fluences within each sample set. Mean diameter increases with increasing fluence clearly at E=20 keV, while less significantly for E=60 keV and 80 keV, while E=40 keV shows a decrease in diameter, not entirely consistent with modelling. Perhaps fluence does scale blister diameters, but in some composite process also influenced by implantation energy. Increasing implantation energy at a given fluence also increases the mean blister diameter, perhaps more strongly than the influence of the hydrogen fluence, in general agreement with modelling. The variability and some inconsistency in these trends are shown in Fig. 4.7(a) (see also Fig. D.71 in App. D.5).

Si(100) - Variation in both E and Φ

A series of Si(100) samples implanted with variable hydrogen ion energies and fluences above the blistering threshold were annealed at T=550°C for 30 minutes in the Ar ambient of a quartz tube furnace. These samples, produced to study the depth and roughness

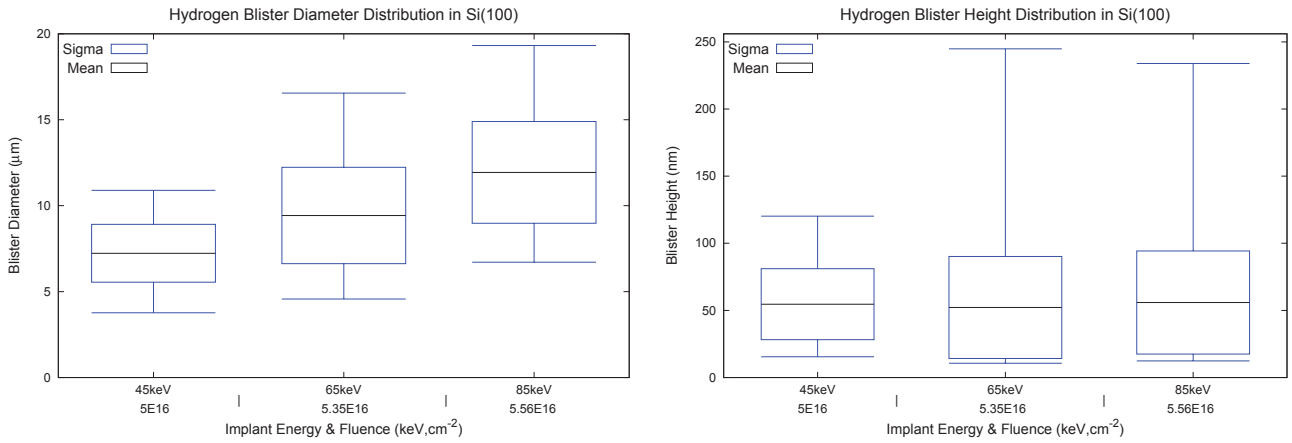

Figure 4.8: Hydrogen blister diameter and height for Si(100), hydrogen implanted with various ion fluences and energies as labelled in graphs, and annealed at T=550°C for 30 minutes. Composite and individual histograms from which this data was derived can be located in Appendix D.5.

of hydrogen crater floors, had their fluences selected complementary to their energies, to ensure that the peak hydrogen concentration (C_P) was the same in all the samples. These specimens will be referred to as the "*common peak hydrogen concentration*" samples. Figure 4.8 shows the spread in blister dimensions of those which remained unburst following the annealing. The relationships between implantation conditions and the blister dimensions are clearer than those in the previous samples, however the links between diameters, heights, energy and fluence are harder to isolate.

Examining the distribution of the diameters of the hydrogen blisters formed on these samples, there is an increase with increasing energy, but as fluence is also increasing at the same time, it is difficult to establish which plays a stronger rôle. The heights of the blisters for all samples show only small variation in the mean and modal values, or range of the height distribution, to within two standard deviations. Both these observations are in reasonable agreement with modelling by Eq. 4.1, 4.3 and 4.4. The quality of these observations – from a single series of samples from a separate study, examined opportunistically in this section – really requires further confirmation via complementary samples using combinations of each ion energy fluence.

The fact that all samples had the same peak concentration may indicate that the hydrogen blister heights are not so much decided by the total concentration of hydrogen distributed in the silicon, as being limited instead by a particular concentration being

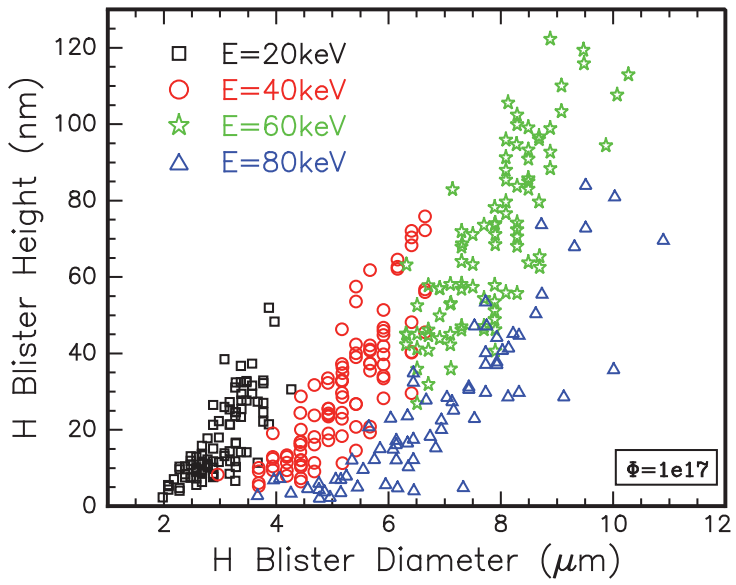

Figure 4.9: Hydrogen blister diameter versus height for Ge(100) implanted with $\Phi_H = 1 \times 10^{17}\text{cm}^{-2}$ at various ion energies, as labelled, annealed at T=400°C/10 minutes.

reached at some point within the sample. This may indicate that for these fluences, sufficient hydrogen is already present around the implantation peak to induce blistering upon annealing, rather than requiring diffusion and accumulation from the rest of the implantation.

Ge(100)

Examining blisters caused by a fixed hydrogen fluence and variable ion energies in Ge(100), shown in Fig. 4.9, a relationship occurs between the blister diameters and heights as was seen for Si(100). Perhaps hydrogen implantations of equal fluences evolve with annealing in a similar manner under the same conditions in similarly structured substrates. The corresponding box-and-whisker plot of the hydrogen-induced blisters' diameters and heights in Ge is shown in Fig. 4.10.

The range in blister diameters increases linearly with implantation energy, however the mean blister diameter is only linear with energy until E=60 keV. It is possible that the higher energy E= 80keV requires a greater critical fluence to produce the same array of blister dimensions, however as this comparison is between common implantation conditions, it is difficult to extrapolate further. For these increasing implantation energies, which are linked to additional depths of implantation and allows for larger blisters, there is good

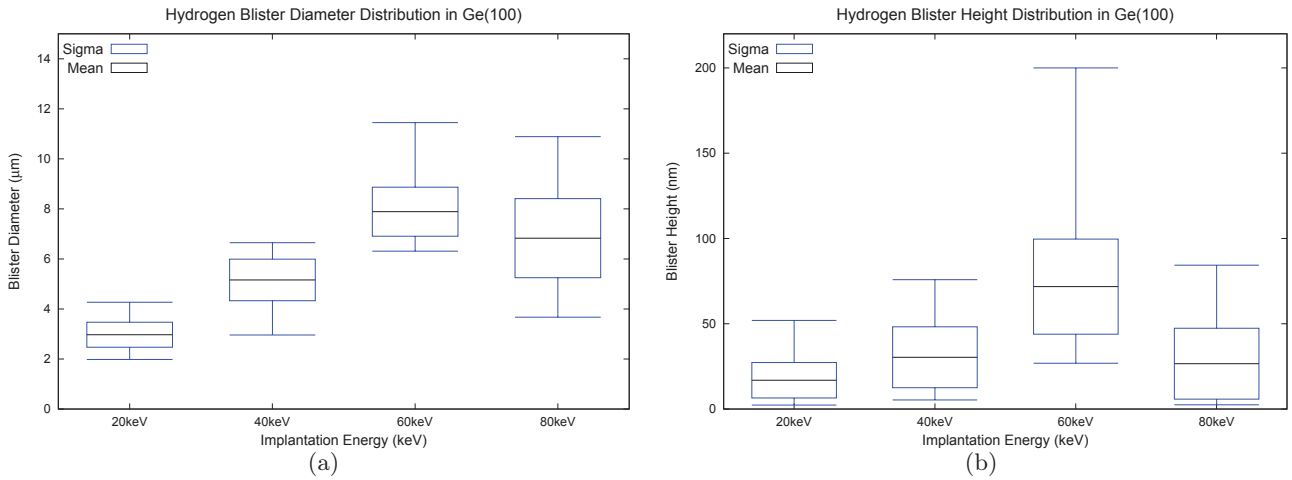

Figure 4.10: Hydrogen blister diameter and height for Ge(100) implanted with $\Phi_H = 1\times10^{17}\text{cm}^{-2}$ at various ion energies, as labelled, annealed at T=400°C/10 min. Composite and individual histograms from which this data was derived can be located in Appendix D.5.

agreement with modelling from Section 4.5.1. A similar divergence and spread of heights as the diameter increases occurs in all samples. The only discrepancy between the model and data is that in the majority of the data, while the maximum height value increases, the mean blister height value is not influenced by implantation energy. While contrary to the $h \propto \frac{1}{R_\text{P}^3}$ relationship in Eq. 4.4a *et al.*, as the equation describes only the final state of the Gibbs free energy expression used to model blister formation dynamics, kinetics may possibly explain the discrepancy. Blister heights may grow beyond observed values for the lower implantation energies if given sufficient annealing duration. Such overall reasonable agreement indicates that any variation between modelled predictions and observations of the relationships of implant depth, mean blister diameter and height, is not significant.

When the distribution of diameter and height values are examined, seen in Fig. 4.10, the range of blister diameter values increases with increasing implantation energy. The mean value of the blister diameter also increases, although the link is weaker. An apparent offset in values in the E=60 keV is observed in both diameter and height data. Alternatively, the E=80 keV implanted material may be the outlier, as it does not fit a possible increasing trend in the blister diameter data from E=20 to 60 keV. While this may seem reasonable for the blister diameter data, the large difference displayed by the E=60 keV sample's height data should give us pause before suggesting such an alternative. Overall, the blister height data is very similar to that seen in Si(100), where there is little shift in either

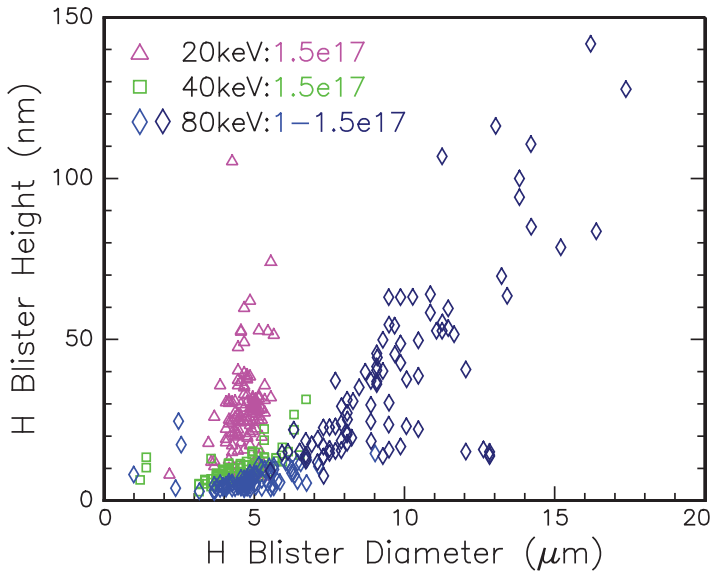

Figure 4.11: Hydrogen blister diameter versus height in H-implanted Si(110), at energies of 20 keV, 40 keV, & 80 keV. Φ_H=1.5×10^{17}cm^{-2} unless otherwise labelled, and annealed at T=400°C for 10 minutes.

range or mean value for all the energies compared at this fluence. Again, there is some discrepancy between the E=60 and 80 keV implantations, as to which presents a more consistent trend. The mean blister height is largely independent of implantation energy, while range of heights increases with energy. The hydrogen fluence is constant across these samples, so its influence cannot be determined for Ge.

Si(110)

Figure 4.11 shows the hydrogen blister sizes via diameter versus height for those measured in Si(110). The overall trend in blister diameters is similar to that described in Si(100) and Ge(100), but there are some noticeable differences. For instance, the E=40 keV implantation has a significantly curtailed range of heights across the range of diameters. There are also some distinctly high aspect ratio blisters with very large heights despite small diameter sizes, in both the E=40 keV and the lower fluence (Φ_H=1×10^{17}cm^{-2}) E=80 keV implantations. Such distinct oddities may be due to an additional anthropic bias different to that for other samples, as a separate operator manually extracted the values from the experimental data. It is difficult to quantify what impact this selection difference may have had on this sample set. We can examine the trends in these samples overall, but compare with other measurements with caution. This is also borne out in the distributions of the

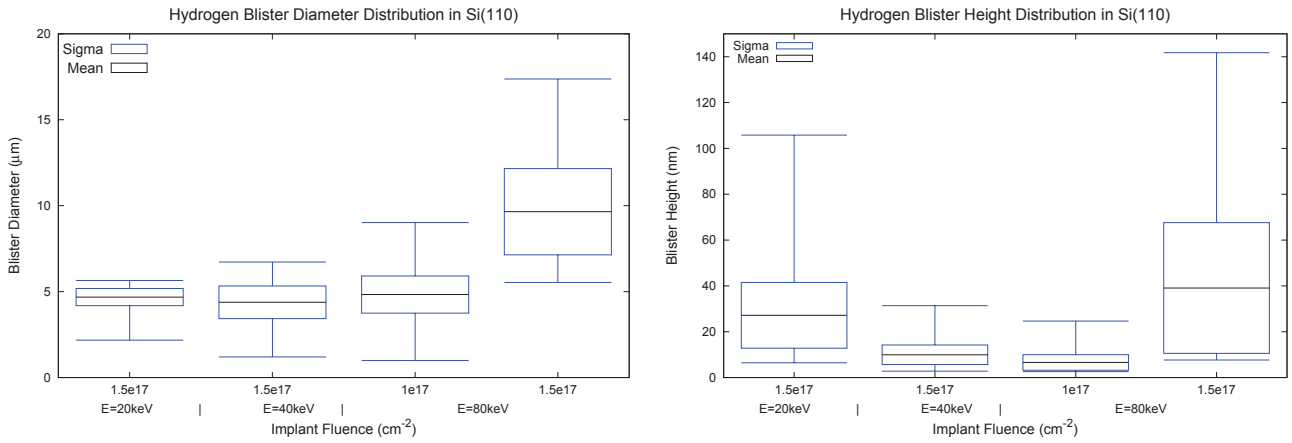

Figure 4.12: Hydrogen blister diameter and height for H-implanted Si(110), at ion energies and fluences as labelled, annealed at T=400°C/10min. Composite and individual histograms from which this data was derived can be located in Appendix D.5.

blister diameters and heights in the Si(110) implantations, shown in box-and-whisker plot Fig. 4.12.

The mean blister diameter is largely unaffected by implantation energy (in contrast to Si(100) and Ge(100), and in disagreement with Eq. 4.1 and 4.4d), although the range of diameters increases. Variation in fluence does not appear to produce regularly larger mean blister diameters, and may actually show the reverse, more consistent with the models. There may be link between fluence and the blister heights' mean, although results are inconclusive.

Conclusion

A higher implantation energy increases both the mean value and range of hydrogen blister diameters in both Si(100) and Ge(100). Higher fluences may also increase the mean diameter size, and have less impact on range of diameter values, although both correlations are inconclusive. In Si(110), increasing implantation energy seems to have less influence on blister diameter than hydrogen fluence. The average blister height slightly increases with increasing fluence but is largely unaffected by implant energy for Si(100) and Ge(100). The peak fluence may be more critical than the total fluence for blister height, as Si(100) samples implanted with variable H fluences and energies with a constant peak fluence manifested the same mean blister height. In Si(110), there was no clear relationship between implantation parameters and blister height. All samples show approximately equal minimum blister

height values, due to the measurement resolution of the OP.

Generally, the larger the blister diameter, the larger range of blister heights it was able to "support". This is not unreasonable, as the energy of maintaining a "membrane" of substrate material would increase with height. If the blisters have a larger circumference, then they have a smaller contact angle with the surrounding material, which decreases the surface tension required and allowing energy to instead be expended on supporting greater heights.

4.5.3 Blister diameters versus implantation conditions

Both the models described above in Section 4.5.1 can be compared to the measured heights and diameters and known hydrogen ion implant depths, with assumptions of constant pressure, energy and α values. Figure 4.13 compares blister diameter D with hydrogen ion implantation energy or depth in Si(100) for data from previous studies [28,49,62,90,113,338] and our work. The relationship between implantation energy and depth was established by SRIM-2008 [251] simulation.

Attempts at fitting the data with Eq. 4.1 quantitatively were problematic, as the equation relies on input of blister height and implantation depth to calculate the blister diameter. Terreault [28] uses a power law fit relating D and R_{P} such that $D \sim (R_{\mathrm{P}})^n$, and assuming P is constant, can model Eq. 4.1 by taking $n = 0.5$. By the same principle, Eq. 4.4d is best fit by $n = 0.75$, although such approximations are not required as it can be used quantitatively with the data available. The previous data shows a value of n substantially smaller than 0.75 (and maybe 0.5), suggesting that the pressure required to blister in those systems was increasing. In contrast, fitting such a power law to the data in our study shows reasonable agreement with n=0.75.

With a relationship of $D \sim R_{\mathrm{P}}^{0.75}$ readily fitting the data, Eq. 4.4 is used to fit the blister diameters with respect to implantation depth (in our work, i.e., ion implantation energy). An array of fluences and annealing times are accounted for in this data, as labelled in Fig. 4.13 and so caution is recommended in drawing specific conclusions. Better agreement exists between the model and our data than any of the previous work. Larger diameter blisters were measured in this study in comparison to previous work, for all energy ranges investigated. For these blisters to have larger diameters for the same implantation depths

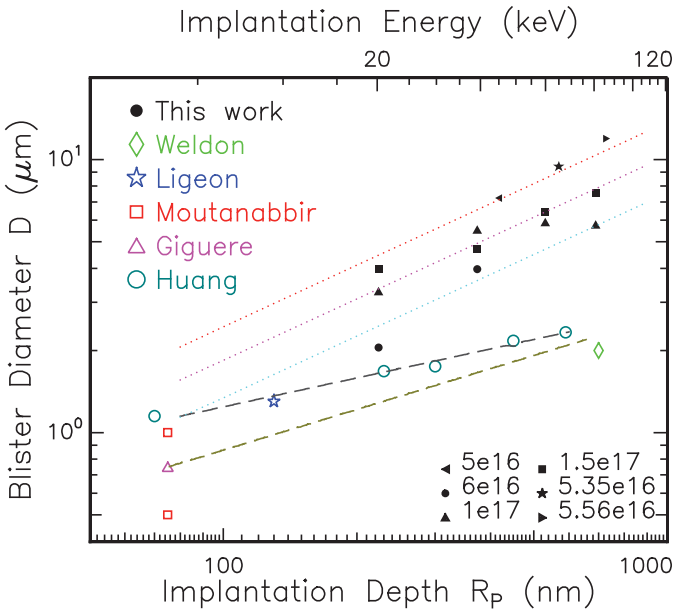

Figure 4.13: Logarithmic plot of mean blister diameter D with respect to hydrogen ion implantation energy E and depth R_P, contrasted with work by previous researchers. Data from Weldon [113], Ligeon [338], Moutanabbir [60,62], Giguere [49] and Huang [90]. Mustard and grey dashed lines shows Terreault [28] fit using power law approximation of Eq. 4.4 ($n = 0.5$ and 0.35); red, magenta and cyan dotted lines show Eq. 4.4 fits for T=550°C & P=5 MPa, T=400°C & P=8 MPa, and T=400°C & P=15 MPa respectively. Other fit parameters: γ=0.11-0.13 Jm^{-2}, E=169 GPa, ν=0.3, α=0.6-1.0.

(with reasonable values of γ, ν, E and α), Eq. 4.4 indicates much lower values of pressure were needed, on the order of $\sim$ 10 MPa. In contrast, Coupeau and Huang both use values of hydrogen gas pressure P=25-80 MPa, which offer reasonable fits to their data.

The three implantations where the H profile peak concentration was the same – H(45keV, 5×10^{16}cm^{-2}), H(65keV,5.35×10^{16}cm^{-2}), and H(85keV,5.56×10^{16}cm^{-2}) – show excellent agreement with Eq. 4.4, indicating that for a constant pressure the peak concentration is perhaps more critical to the relationship between blister diameter and implantation depth than the total fluence.

A similar comparison is shown in Fig. 4.14 for both Ge(100) and Si(110). While there is little data available in the literature, the figure presents a comparison between the experimental data obtained in our study and the model as described by Eq. 4.4d, and a power law to approximate Eq. 4.1. In both cases, values of surface energy, Young's modulus and Poisson ratio were adjusted for the appropriate substrate, and pressure values selected similar to literature for best match of the range of the data.

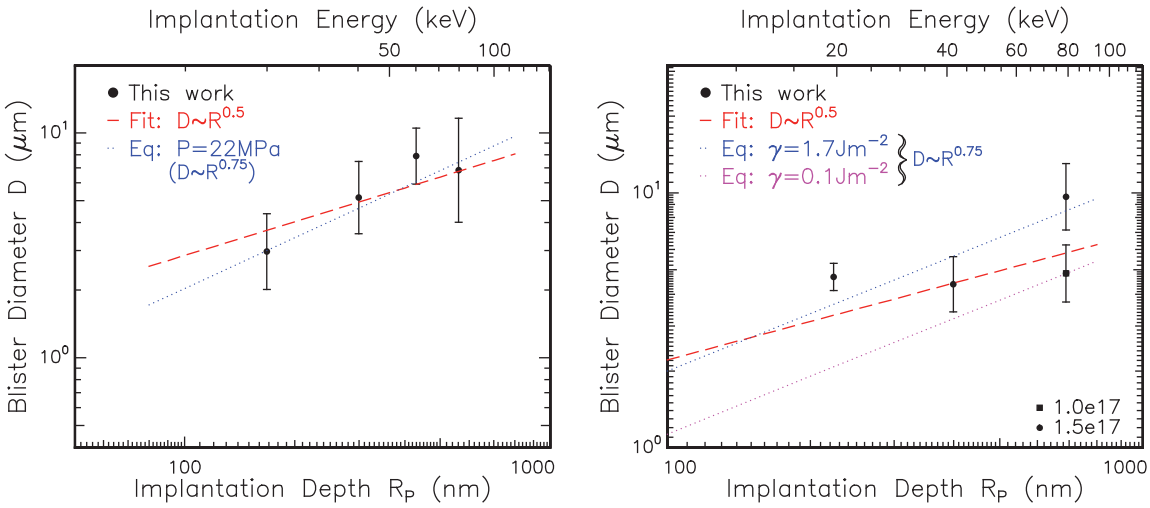

Figure 4.14: Logarithmic plot of optical profiler measured mean blister diameter D with respect to hydrogen ion implantation energy E and depth R_{P} in (a) Ge(100) and (b) Si(110), compared with blister diameters determined by Eq. 4.4. Parameters for (a) γ=1.57 Jm^{-2}, E=102.6 GPa, ν=0.278, α=0.6, P=22 MPa, $\Phi_H = 1 \times 10^{17}$cm^{-2}. Parameters for (b) γ=0.11-0.71 Jm^{-2}, E=187.5 GPa, ν=0.36, α=0.6, P=25 MPa, hydrogen fluences as labelled. Error bars indicate one standard deviation in spread of diameter measurements. Power law approximation of Eq. 4.1 ($n = 0.5$) is given in red dashed line.

Ge(100) shows reasonable agreement with the $n = 0.5$ power series, but also good agreement with Eq. 4.4, suggesting that the plate model within the Gibbs free energy expression can be readily applied. However, while both these materials had wafers in the (001) plane, perhaps alternative crystalline substrate orientations are not so easily accounted for. Si(110), even with amending parameters, is not so well modelled by Eq. 4.4. The greatest variation in the literature for the surface energy γ allows the model to scale the range of blister diameters, but the data is better fit with a lower order power series, such as the $n = 0.5$ example shown here.

Conclusion

The models for blistering dynamics proposed by Dion [340] and Mitani [341] both provide reasonable models describing the blister dimensions in (100) crystalline material. While the equations are governed by $D \sim R_{\mathrm{P}}^{0.75}$, lower order powers such as $n = 0.35 - 0.5$ also show reasonable agreement with experimental data. Such agreement suggests that the pressure may not be a constant within the system, as modelling by Aleksandrov [335] and Huang [90] required. This may indicate loss of hydrogen prior to blister rupture and crater

formation, or other variation in the internal environment of the wafers. Hydrogen blister diameters increase with increasing ion implantation depth for Si(100) and Ge(100), with very little change for Si(110). The near perfect $D \propto R_{\mathrm{P}}^{0.75}$ observed in the implantations with a common peak hydrogen concentration may indicate blistering dimensions are dependent upon a critical local concentration more so than total concentration. If the critical concentration exists following implantation but prior to annealing or diffusion, the system may more ideally obey the dynamics described by the models in Section 4.5.1. The blister heights were the same in all common peak hydrogen concentration samples, independent of hydrogen profile depth. There may be some limit to the heights formed in blistering, if the total concentration influences the process. From these data, local implantation damage influences the blister diameter, but not height of blisters.

4.6 Kinetics of hydrogen-induced blistering

Following on in this behavioural study of the blistering process, the focus turns to the thermal, temporal and environmental effects upon hydrogen evolution and blistering in semiconductors. To simplify the comparisons between materials and wafer thicknesses, a single fluence and energy of hydrogen ions was selected, which are referred to as the "standard conditions". This implantation was Φ_H=6×10^{16}cm^{-2} and E=40 keV, performed at room temperature. The semiconductor materials studied were Ge(100), Si(111), Si(110), and Si(100) with a standard thickness of 375±30 μm, and additionally 50±5 μm Si(100).

To study the thermal evolution of these materials, the implanted wafers were cleaved and attached to a resistively heated hot stage with a vacuum seal, and annealed under standard atmospheric conditions. As described in the Section 3.3.1, during the annealing process, the sample surface was monitored by an 8 megapixel high definition digital video camera, through one of the eyepieces of a stereoscopic microscope. This provided sufficient resolution and magnification ($\geqslant \times 10$) to identify individual craters (and possibly blisters) that formed on the surface of the material. [The recording tended to suggest that the measurement certainly reached the stage of hydrogen-induced craters, or burst blisters, as ejecta from the sample emerged from the sample during the recorded footage. In fact, optical profiler scans of all semiconductor samples included the "lids" from ruptured blisters lying nearby the newly formed crater, as seen for example in Fig. 4.15.]

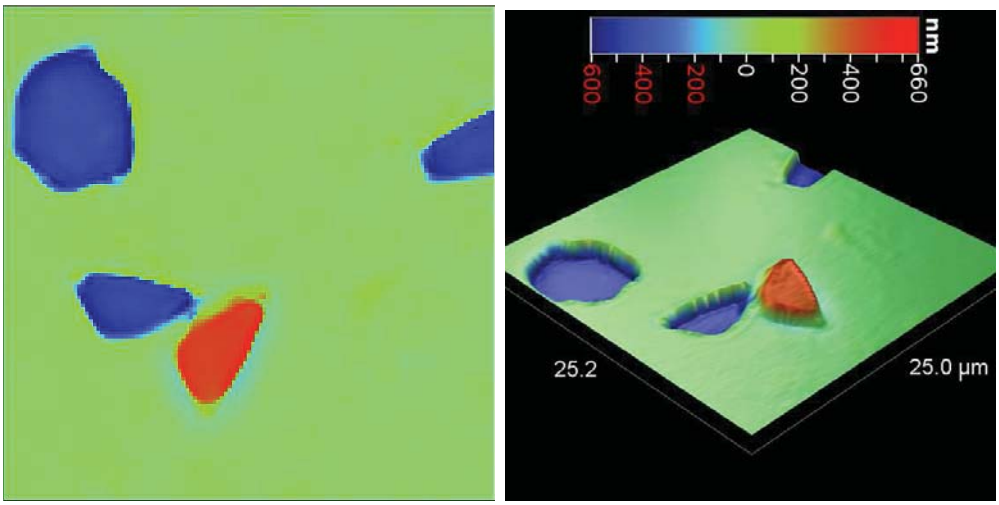

Figure 4.15: Optical profiler measurements of H(40keV,6×10^{16}cm^{-2},RT)-implanted 50μm thick Si(100), annealed at T=450°C for 30 minutes, showing the hydrogen-induced blister "lid" cast off newly formed crater in a (left) two dimensional, (right) three dimensional projection. Measured in VSI mode, ×50 magnification lens, F.o.V. ×1.0, plotted with Wyko Vision32™ [315] software, vertical scale in right hand image, red numeric values indicate relative negative values (depth below surface).

Analytical methods

To establish the kinetics and energy requirements of the blistering process, significant data was extracted from the video recordings made observing the samples during annealing. These video recordings were then separated into photographic slices by extracting the individual frames of the footage, selected for the actual blistering periods. Each slice or frame allowed the statistical measurement of the number of blisters present. For samples annealed at lower temperatures, where the rate of blistering was slower and fewer appeared between each frame of the recording, individual blisters were manually counted from all the extracted images. However, at higher temperatures, the rate with which blisters appeared became so great that the precise number of blisters needed to be measured automatically by software or fit by software approximation. To this end, images taken from frames of the video at set time intervals were calibrated to a threshold level to allow changes such as blisters to be readily identifiable. For example, prior to blister appearance, a frame was used to calibrate a zero count. Each of the initial frames where the number of blisters was still manually countable was subsequently used to define those number of blisters relative to the number of circular regions classified by the software as blisters, producing some small offset with the raw software value.

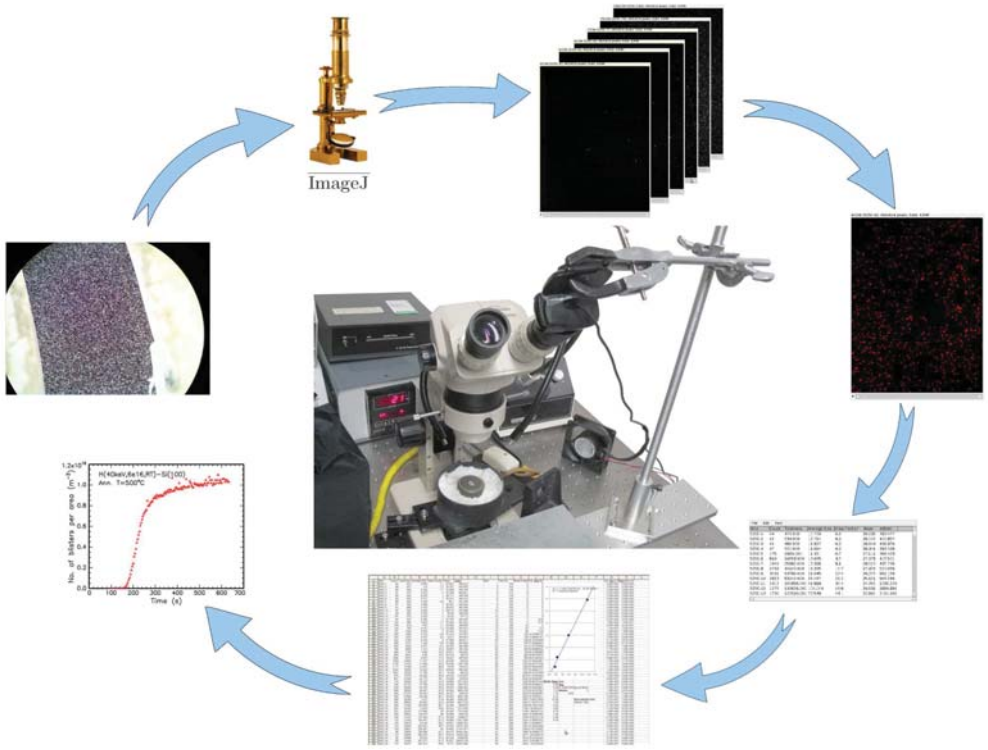

Figure 4.16: Representative schematic flowchart of the method with which video recordings of the samples undergoing annealing were used to measure the number of blisters per area per time, flowing clockwise from upper left.

Software attempts to identify the individual blisters also became difficult however, as the fitting of circular or ellipsoid shapes to a thresholded image often overlapped the shapes and merged regions of similar intensity that lay too close together, masking the true number of blisters present. So in most cases, a fitting approximation of the number of blisters forming was determined from a number of initial measurements made while individual blisters were still distinguishable. This fitting used the value of total area measured by analysis suite imageJ [319, 320]. From the video captured snapshot frames (as described earlier), a baseline was established in the pre-blistered images, and then the relative intensity of the blisters measured. The image frames were converted to grey scale to more clearly distinguish between virgin surface and blister, as the blisters appeared whiter than the black of the silicon surface, allowing relatively easy threshold level discrimination.

A simplified schematic of this processing routine is presented graphically in Fig. 4.16. However, despite the reasonably extrapolated numbers which these fits produced, the slight variations in brightness occurring during the recording of the annealing process led to

changes in the measured intensity sufficient to produce changes in blister numbers in imageJ. Small drops in intensity led to the software concluding the number of blisters had *decreased* from the previous frame. Such irregularities could be absorbed in the errors associated with the approximations of the fit for the total number of blisters at some time t. However it caused more difficulties in extracting instantaneous blistering rates, as the change between the number of blisters measured in each time interval – each frame of the blistering video – could produce *negative* values. To investigate the quality of these fitting approximations, the same process was applied to the low temperature annealing data where every blister was counted manually. Figure 4.17 shows comparisons between models extrapolated from all, partial or very short blister counts with the measured values. This comparison showed that if a reasonable proportion of the data was used to create the approximation, the fit was within 10% of the actual values. In all cases, the early stages of the anneal were generally poorly fit, with predicted and actual values showing discrepancies of up to 900%. However, even in the worst cases, the models provided a reasonably consistent behavioural trend relative to the measured values. Considering such, while the fits provide reasonable comparison of trends and changes, the data from the lower temperature anneals where the individual blisters could be identified manually by an operator were still more reliable.

From the recorded footage, several key characteristics could be determined from each hydrogen-implanted semiconductor. The number of blisters forming per area over time could be established by using software to fit the sizes of the blisters and area, as described in Section 4.6.1. The initial blistering time relative to the applied anneal could be used to determine the activation energy of the hydrogen blistering process for that material, as calculated in Section 4.6.2. The influence of elevated substrate dopant levels could be explored with judicious selection of materials, as shown in Section 4.8.

Preliminary summary

The underlying observation of all these measurements was the event of hydrogen blistering. In all the Si(100), Si(111) and Ge(100) wafers, blistering occurred for the standard condition implantation within the temperature ranges applied, if annealed for sufficient duration. It was not seen in the Si(110) wafers implanted with the standard conditions implant, requiring higher hydrogen concentrations to blister.

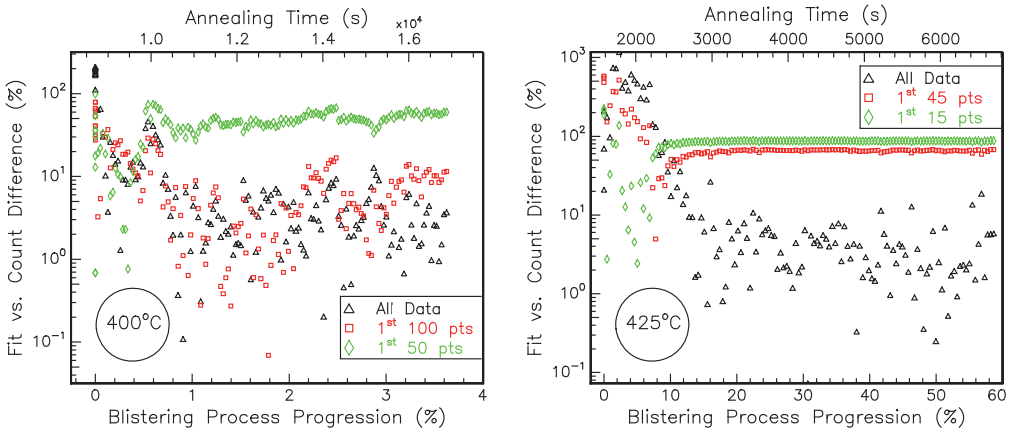

Figure 4.17: Comparison of manual blister count with fitting function extrapolations based on fractions of complete data set, as labelled, for H(40keV,6×10^{16}cm^{-2},RT)-implanted Si, annealed at (left) T=400°C, (right) T=425°C.

It is worth noting that the behaviour at longer exposure of each annealing temperature did add weight to the argument presented in Section 4.4, that perhaps some of the other fluences and energies examined there may also have blistered, if annealed at higher temperature or duration. In particular, Si(100) and Ge(100) with the same standard implantation conditions in the critical fluence for blistering study, when exposed to T=400°C for 10 minutes, showed either no blistering or only inconclusive behaviour (e.g. small surface features, no clear blisters or craters). However, at a large range of temperatures and even larger range of time intervals, these same implantations produced blistering in Si(100) and Ge(100).

4.6.1 Blister formation versus time

Blister areal coverage over time was examined for Si(100), Si(110) and Si(111), as well as Ge(100). Initially, a common implantation of hydrogen ions was applied – E=40 keV, $\Phi=6\times10^{16}$cm^{-2}, room temperature, angled at 7° to the sample normal. However, no blistering was observed for the Si(110) sample at this fluence, and a second implantation was performed in that substrate at $\Phi=1\times10^{17}$cm^{-2}, with all other parameters the same. To contrast the influence of ion fluence and energy in Ge, two additional implantations were performed – H(40keV,3×10^{16}cm^{-2},RT) and H(100keV,6×10^{16}cm^{-2},RT) into Ge(100). Pieces of each of these implanted samples were annealed under atmospheric conditions on a resistively heated stage, while monitored by digital video camera, as described earlier

and in Section 3.3.1.

The areal density was determined by a linear fit made of number of blisters present in each of the frames of the video recording of annealed hydrogen-implanted semiconductors. The initial blistering time was determined when a single surface blister became visible within the region observed.

The accuracy in determining the initial time, Δt_i, is derived from the time between the first and second observed blister/crater. Assumptions underpinning this error value are the possibility of other blistering having occurred elsewhere on the sample surface within that interval, prior to the first observed blister, yet unobserved due to the limited area monitored by the camera.

Silicon

The rate at which the blistering took place at each temperature shows largely consistent logistic function-like behaviour, where the total number of blisters (or craters) dramatically increased before reaching a saturation value, approximately constant. The number of blisters per area over time for each annealing condition in the H(40keV,6×10^{16}cm^{-2},RT)-implanted Si(100) and Si(111) can be seen in Fig. 4.18(a) and (b) respectively. Figure 4.19 shows blisters per area with respect to time for the H(40keV,1×10^{17}cm^{-2},RT)-implanted Si(110).

The instantaneous magnitude of the blistering events, and the rate of change during the anneal vary depending upon the temperature of the anneal. For Si(100), the final number of blisters reached was N_B =8.8±0.9×10^9 craters per square metre. Accounting for errors in scaling from small areas observed to large areas - i.e., regions of square micrometres to square metres - the values of final number of blisters could be approximated as equal for all temperatures. So, while the temperature applied did change the rate at which the blisters formed, and the time at which sufficient energy had accumulated to begin blistering, these do not appear to define the total number of blisters that form if sufficient time and exposure is provided. It would suggest that the implantation fluence and energy is more critical to the number of blisters formed.

The maximum areal density of blisters formed on Si(111) is somewhat higher than in Si(100), at N_B =18.8±0.1×10^9 blisters per metre squared, approximately 2-3 times larger.

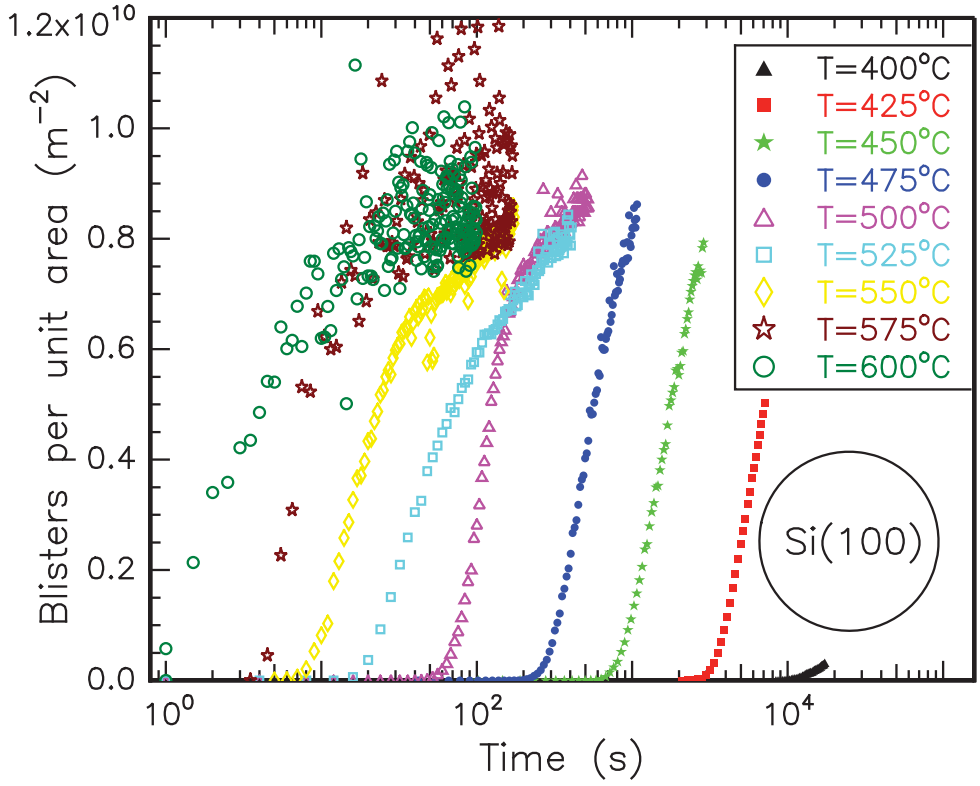

(a)

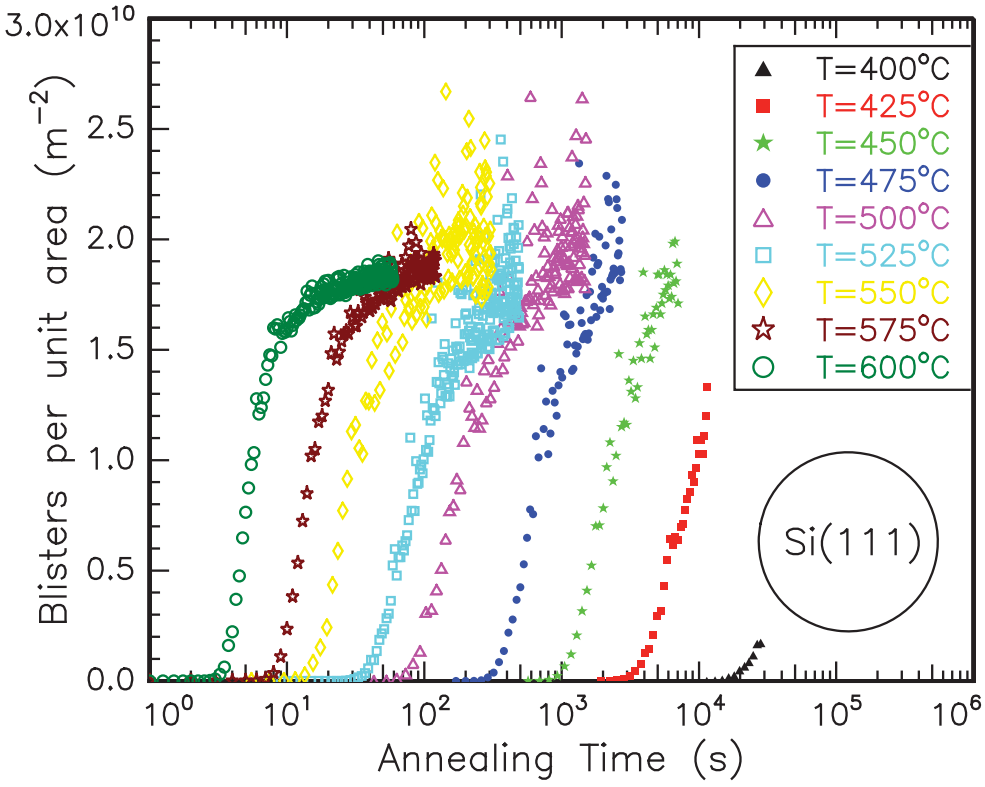

(b)

Figure 4.18: Annealing time dependence of blister formation per area in H(40keV,6×10^{16}cm^{-2},RT) implanted (a) Si(100) and (b) Si(111). Annealing temperatures as labelled.

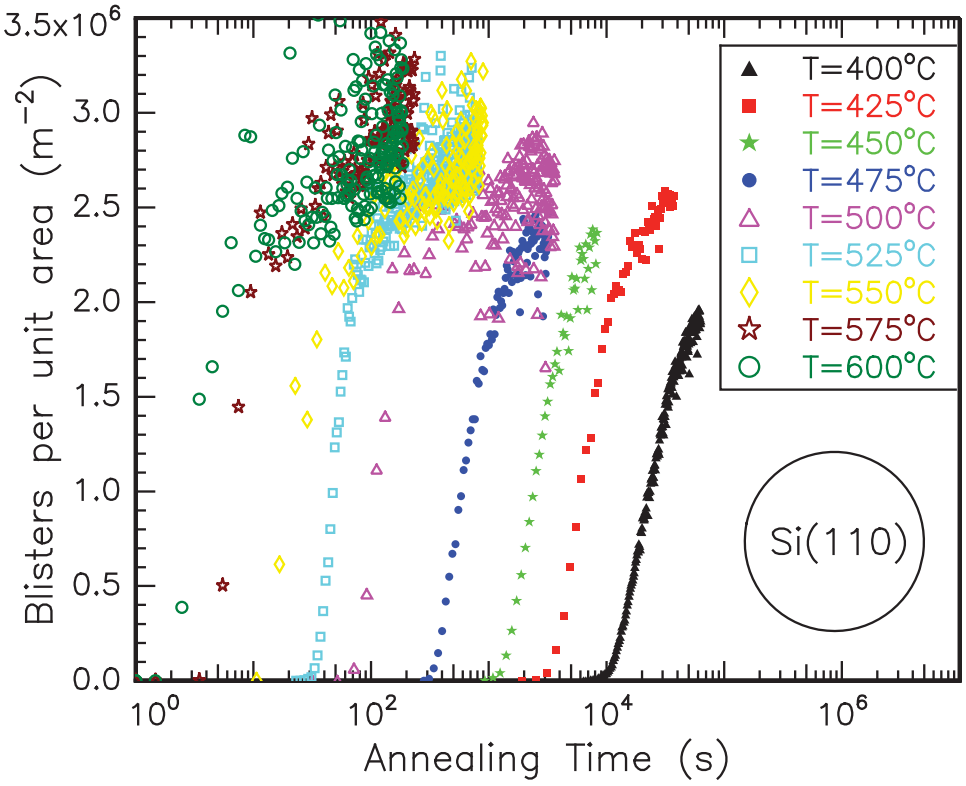

Figure 4.19: Annealing time dependence of blister formation per area in H(40keV,1×10^{17}cm^{-2},RT) implanted Si(110). Annealing temperatures as labelled.

In Si(110), which was implanted at the same energy by higher hydrogen fluences ($1.7\times\Phi_H$), the areal density of blisters was significantly lower, with $2.4\pm0.2\times10^8$ craters per square metre, over 30 times sparser than Si(100). This indicates an orientation dependence on blistering, as the same fluence in two different crystal orientations produced different blister areal densities, while a higher fluence into a third orientation produced a lower blistering density.

The rate at which the hydrogen blisters formed in all substrates in this work appear to follow sigmoidal logistics functions, in particular either the Johnson-Mehl-Avrami-Kolmogorov (JMAK) equation or the Gompertz function. Both models describe changes or growth in material composition within finite systems – JMAK is used to describe changes in phase for solids at a given temperature, while Gompertz describes tumour or population growth. The dominant limitations in both the equations are the available resources or material undergoing transformation, and the remaining volume or environment for the

new state to occupy. JMAK describes the fraction of transformed material Y, following rapid growth at an exponential rate in time t, approaching a given limit value, a simple form of which is given in Eq. 4.5.

$$\begin{aligned} Y &= 1 - exp(-Kt^n) \\ &\text{where} \\ K &= \pi\frac{\dot{N}\dot{G}^3}{3} \\ n &= 1 - 4 \end{aligned} \tag{4.5}$$

Where $\dot{N}$ is the nucleation rate of new particles per unit volume, $\dot{G}$ is the rate of spherical volume particle growth, and there is no clear physical interpretation of n. Gompertz predicts a slower initial growth rate prior to a period of rapid growth, then rapid slowdown as it trends towards a limit. The basic formula for the Gompertz function describing a fraction of transformed material y with respect to time t is given in Eq. 4.6.

$$y(t) = ae^{\left(-be^{-ct}\right)} \tag{4.6}$$

where a describes the asymptote value (i.e., maximum blister areal density), b defines the displacement of the function in time, and c defines the growth rate in time (i.e., gradient of growth region of function).

Blister rates at lower temperature (T$\leqslant$475°C) anneals in Si(100) are fit better by Gompertz, while higher temperatures are better fit by JMAK. The blister formation rate in Si(111) was more consistent across applied temperatures than the Si(100) material, and were better fit by a JMAK function. Si(110) displayed a transition similar to Si(100), with JMAK describing blistering rates for T$\geqslant$475°C. The transition between fits may indicate a shift in the rate of blistering between domination by available volume (Gompertz) to remaining hydrogen concentration (JMAK). Potentially, the rapid growth at higher temperature brings the blisters into close proximity sooner, leading to the available hydrogen concentration playing a more significant role. Modelling of blistering area rates by both Eq. 4.5 and 4.6 for all anneals is shown extensively in Appendix D.3.

Only the early stages of blistering are visible at lower annealing temperatures, but the data are readily fit by Eq. 4.5 and 4.6 with similar constants to the blister saturated

anneals, suggesting a similar ultimate behaviour. The time offset in blister appearance between each annealing temperature is due to lower temperatures requiring greater time to diffuse the hydrogen and transform its state, as similarly reported by Huang *et al.* [90]. As temperature decreases, there is an increase in the time hydrogen platelets take to combine within the material, then open up into cavities with sufficient hydrogen gas pressure to distort the overlying silicon upwards.

In discussing the annealing evolution of sub-surface platelets that form during hydrogen implantation of silicon, Grisola *et al.* [224] reported a dramatic decrease in number, with a proportional increase in spherical and cylindrical defects. The growth rate of spherical defects in particular, likely the precursors to surface blistering, followed a similar JMAK function to the high temperature anneals in this work. Such a similar growth rate suggest the two processes, if not the same, are intrinsically linked.

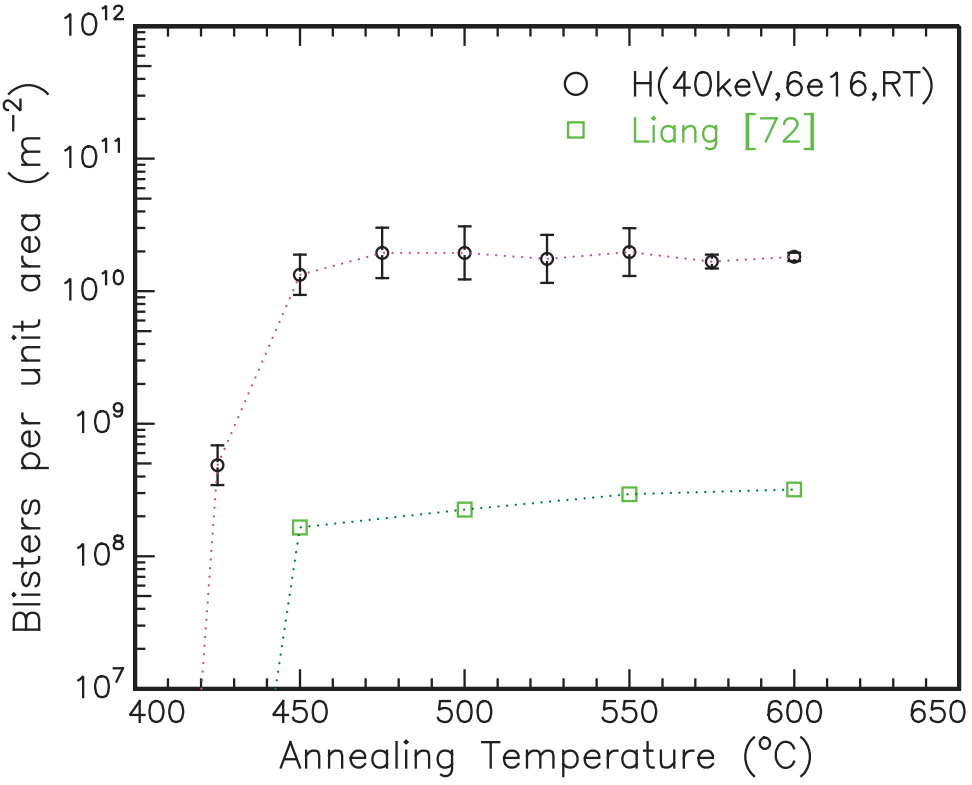

Figure 4.20: Crater numbers formed per unit area following annealing for t=1 hour, as measured in H(40keV,6×10^{16}cm^{-2},RT) implanted Si(111) compared with work by Liang *et al.* [72]. Liang implant conditions: H(40keV,5×10^{16}cm^{-2},RT). Errors show standard deviation in measured data range.

Giguere *et al.* [94] describe a fixed area of the sample surface blistering proportionally

to hydrogen fluence implanted, when studying a range of lower and elevated implantation temperatures; these areal coverages are between 70% and 80%. These blister areal density values are slightly higher than the findings in this project, which showed blister coverages in Si(100) saturating between 50–60%. As may have been apparent from the number of blisters per area data, Si(110) has a very low saturation value (assuming it was reached in the data) of 1–2%. Si(111) shows the very opposite, with 100% saturation of hydrogen craters littering the surface.

Contrast with other work

When the number of blisters per area in Si(111) is contrasted with findings by Liang *et al.* [72], there is a significant difference in magnitude, although the trend is very similar, as shown in Table 4.3. With a very similar set of implantation conditions (E=40 keV, Φ=5×10^{16}cm^{-2}, room temperature, angled at 7°), these data sets are relatively comparable. However, Liang's annealing treatments were under a nitrogen ambient while those in this study occurred under standard temperature and pressure (STP) conditions. Oxidation effects on the Si are likely to be minimal for all temperatures annealing over one hour. The Deal-Grove Model [344] describes SiO_2 formation at T⩽600°C requires significantly greater than one hour. The total duration of annealing applied to samples as described in [72] is 1 hour. While anneals in our study extended in some cases up to ∼28 hours (T=400°C), surface blister areal density values present at 1 hour are used here for comparison. For the single hour duration, blistering completion (i.e., when the cratering of the wafer surface has saturated) has already occurred on the samples annealed above T=475°C in our work.

Annealing Temperature (°C)	Areal Density of Surface Craters		
	Liang [72]	Our Work	
	N_B (m^{-2})	N_B (m^{-2})	σ (%)
400	0.0	6.9×10^7	15
425	-	4.3×10^9	15
450	1.65×10^8	1.8×10^{10}	10.2
475	-	2.0×10^{10}	9.7
500	2.25×10^8	1.9×10^{10}	10.3
525	-	1.8×10^{10}	10.3
550	2.94×10^8	2.0×10^{10}	9.1
575	-	1.7×10^{10}	3.1
600	3.19×10^8	1.8×10^{10}	1.7

Table 4.3: Surface crater areal density upon t=1 hour annealed H(40keV,6×10^{16}cm^{-2},RT)-implanted Si(111) wafers [see Fig. 4.18(b)] contrasted with results by Liang *et al.* [72]. Incl. the standard deviation σ of derived area density values from our work.

Notably there is a significant offset in the total area covered by the craters, but proportionally both samples show similarities. At t=3600 seconds, the sample in our study annealed at T=400°C has yet to blister or crater its surface, in agreement with [72]. In addition to this, the sample annealed at T=425°C is of proportional magnitude to the values presented by Liang *et al.* at the same exposure duration; these data are shown in Fig. 4.20.

The differences in cratering area are likely the effect of the different hydrogen ion implantation fluences. The lower fluence (5×10^{16}cm^{-2} versus 6×10^{16}cm^{-2}) in Liang's work means that there is less hydrogen present to form the complexes necessary to evolve into platelets, then on to blisters and craters. Even foregoing this simplistic explanation, as seen earlier in the case for both Si(100) and Ge(100), variations in fluence can have a significant influence on the initial blistering (and cratering) times, and thus activation energy. It would thus not be unreasonable to assume that the total fluence would also play a significant rôle in the kinetics dominating the activation of the hydrogen-driven blistering process.

Germanium

Figure 4.21 shows the hydrogen-induced blisters per area formed during annealing for the $\Phi=3\times10^{16}$cm^{-2} and 6×10^{16}cm^{-2} implanted Ge(100). As with the silicon, a logistic sigmoidal function is evident in both blister areal density rate for both implantations. The maximum areal blister density measured for both implantations was very similar, despite a 2:1 ratio of hydrogen fluence. As both share a common implantation energy, the surprising suggestion is that the ion energy plays a more critical rôle in the number of blisters that form per unit area and time. This may be unique for Ge(100), and an indication that the blistering process operates differently to previous models in this material.

However, a ready fit of the data is seen by Eq. 4.5 and 4.6, suggesting the same limiting factors govern the blistering process, e.g. hydrogen concentration and available volume. It is possible that there is a critical local concentration of hydrogen required for blistering, with excess hydrogen escaping via diffusion or other mechanisms. The Gompertz and JMAK function fits to the measured blistering data do not necessarily tell us anything about the rôle of hydrogen concentration, as the average maximum blister areal density determined experimentally was used to scale the fits.

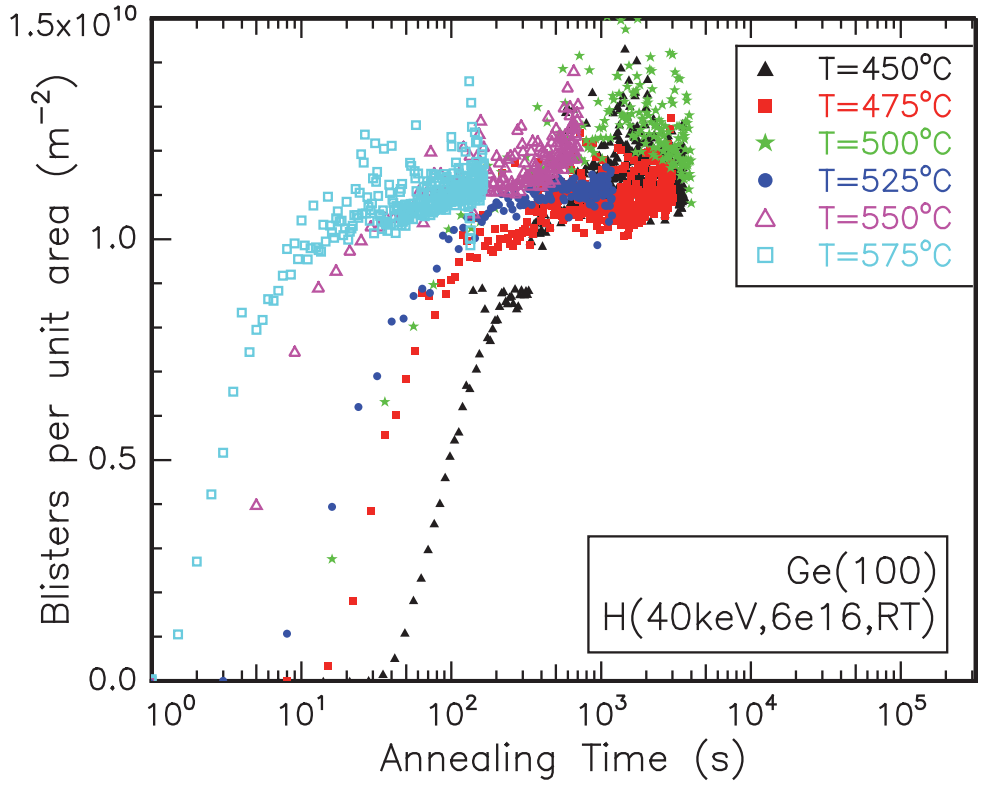

(a)

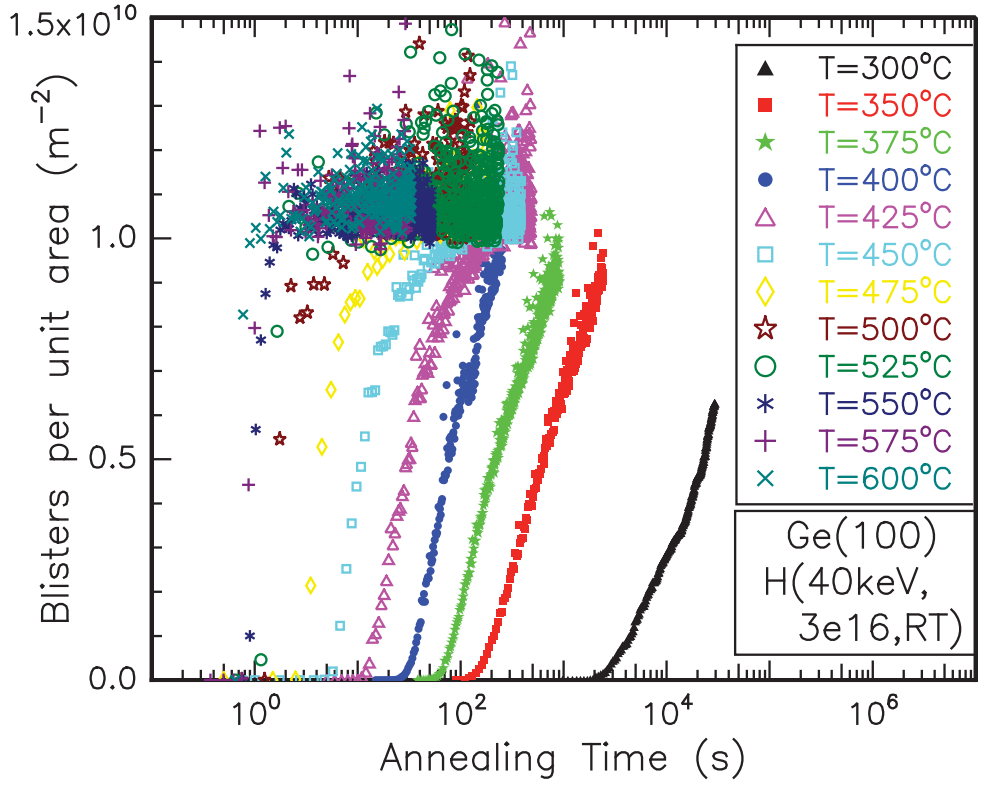

(b)

Figure 4.21: Annealing time dependence of blister formation per area in (a) H(40keV,6×10^{16}cm^{-2},RT) and (b) H(40keV,3×10^{16}cm^{-2},RT) implanted Ge(100). Annealing temperatures as labelled.

Temperature (°C)	Φ=3×10^{16}cm^{-2}		Φ=6×10^{16}cm^{-2}	
	t_{appear} (s)	$t_{saturate}$ (s)	t_{appear} (s)	$t_{saturate}$ (s)
450	4.3	95.3	24	700
475	2.0	31.0	11	360
500	1.5	11.5	6	226
525	0.85	2.7	4	212
550	0.83	2.2	2	63
575	0.68	1.1	1	15

Table 4.4: Comparison of surface blister appearance (t_{appear}) and surface area saturation ($t_{saturate}$) times for H-implanted Ge(100). Implantation conditions: E=40 keV and room temperature, fluences as labelled. Plotted in Fig. D.14

Counterintuitively, the blister appearance time for each temperature is shorter in the 3×10^{16}cm^{-2} H-implanted Ge, as is the time to saturation of the surface with craters, as shown in Table 4.4. The explanation for the lower fluence sample blistering and reaching its surface areal saturation sooner is uncertain.

The size of the remaining craters measured on each implantation was much larger ($\geqslant \times 2$) for the *lower* fluence. The crater diameters measured in the Φ=3×10^{16}cm^{-2} H-implanted Ge increased from 5–6 μm at T=300-350°C, up to 10–12 μm at T=500-600°C. For the 6×10^{16}cm^{-2} H-implanted Ge, the craters were roughly constant at all temperatures, 4–5 μm. Values are listed in Table D.5 in Appendix D.3. One conclusion could be that the size of the blisters is inversely proportional to the implantation fluence, but this seems contrary to work by previous researchers [28]. In Section 4.5.2, we saw that at a constant fluence in Ge(100), blister diameters increased with increasing ion energy (Fig. 4.10(a)), however lack other data on varying the H fluence.

The trend across annealing temperatures for blistering rate per area is the opposite of that seen in silicon. In hydrogen-implanted germanium, the rate of blistering per area is better fit by a JMAK function at low temperatures (T$\leqslant$450–475°C), and a Gompertz function at higher temperatures. The differences between the least squares fit of each equation for the Φ_H=6×10^{16}cm^{-2} implanted sample is slight, and thus any trend is uncertain. However, the 3 × 10^{16}cm^{-2} H-implanted samples show a more definite transition in its blister areal density rate of change, becoming markedly steeper/faster at T$\geqslant$475°C.

While both samples had the same total number of blisters, the surface area above the implantation in the lower fluence sample was 100% filled, and the same area in the higher

fluence sample only reached 20–25% full. Such variation in areal coverage despite same total number of blisters is accounted for by the size of the blisters, i.e., the lower fluence has larger blisters than the higher fluence implanted Ge.

4.6.2 Blister temperature dependence

In this section, the initial blistering times for each of the Si crystal orientations and Ge H-implantations was used to derive the activation energy of the blistering process for each system. Implantation energies and fluences for each semiconductor type and orientation were the same as discussed in Section 4.6.1.

Si(100)

For the Si(100) material studied, both ULTRATHIN® 50 μm and 375 μm wafers were implanted with H(40keV,6×10^{16}cm^{-2},RT). While there was no significant difference between the activation energy of hydrogen blistering, there was a temporal offset between the two thicknesses. As is clear from Fig. 4.22, the thinner wafers began blistering earlier at all temperatures. For the 375 μm Si, the activation energy calculated was E_a=2.27±0.18 eV; for 50 μm Si, E_a=2.30±0.22 eV. The temporal offset, manifest as a factor of two in the pre-exponential factor of the fitting functions ($\frac{1}{\tau}=1\times10^{13}$ s^{-1} for the 375 μm Si versus $\frac{1}{\tau}=2\times10^{13}$ s^{-1} for the ULTRATHIN® Si), is possibly due to mechanical differences within the two wafer types, considering the only difference in the samples is their thickness. While it may be expected that the relative stress produced by the ion implantation would be the same in each wafer, the results in Section 4.3 showed that there was a greater effect upon the thinner of the wafers. A higher stress in the thin wafers may be caused by the lack of the wafer bulk to act as a restoring force on the distorted crystal lattice. Any increase in stress may speed the blistering process, while any reduction in stress may slow it.

Figure 4.23 contrasts this work with previous studies where hydrogen was implanted into Si(100), by Tong *et al.* [108], Beddell and Lanford [21], Zheng *et al.* [107], and Aspar *et al.* [17]. The activation energy determined from our measurements – E_a=2.27±0.18 eV – showed reasonable agreement with the work of Beddell and Lanford [21], but varied from the other reports. While our work showed a constant activation energy for all temperatures, Aspar [17] and Zheng [107] observed two values around some transition temperature. The low temperature splitting energy is related by Aspar [17] to a trapping-detrapping

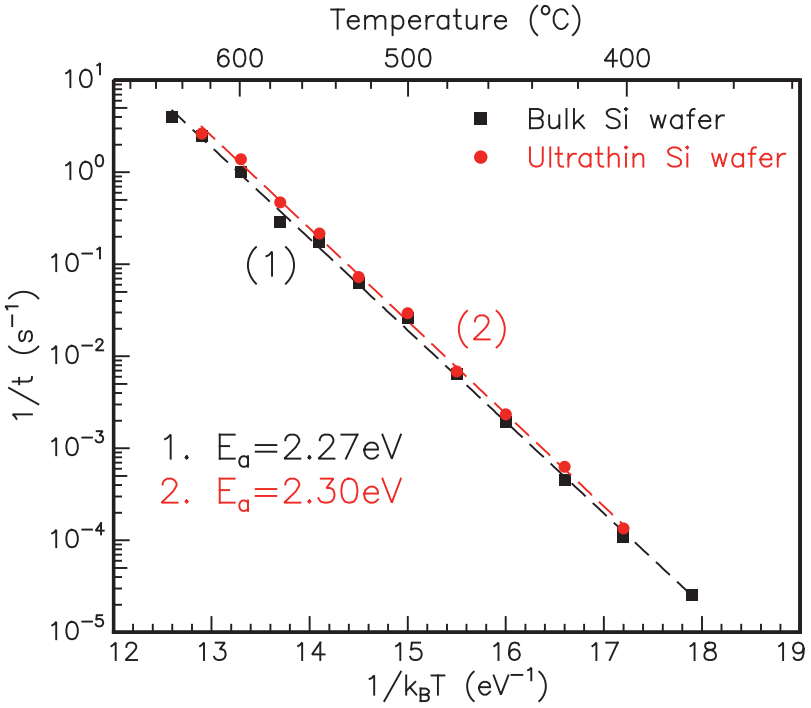

Figure 4.22: Comparison of hydrogen blister appearance time in H(40keV,6×10^{16}cm^{-2},RT) implanted bulk (~375 μm) and ULTRATHIN® (50 μm) silicon wafers. Activation energies of each wafer type as listed.

phenomenon of hydrogen complexes dominating the blister process, with pure atomic hydrogen diffusion defining the lower activation energy occurring at higher temperatures. Zheng offers no explanation as to the factors producing multiple activation energies. The low temperature values given by these authors [17, 107] are roughly consistent with those determined by Beddell and Lanford [21] and in our work. Tong *et al.* [108] show a significantly lower activation energy, despite similar concentrations to our and other works, although using a slightly higher effective ion energy.

Ge(100)

In the case of Ge(100), as well as the "standard conditions" implantation, two additional implantation conditions were examined – H(40keV,3×10^{16}cm^{-2},RT) and H(100keV, 6×10^{16}cm^{-2},RT). For all three of these implantations, from T=250°C to 600°C, blistering's occurrence and rate of egress was measured. The latter implantation shows that blistering still occurs when the required fluence is distributed across a larger integrated volume by the higher implantation energy, while the former implantation shows that some range of lower fluences are capable of inducing blistering if annealed for sufficient duration

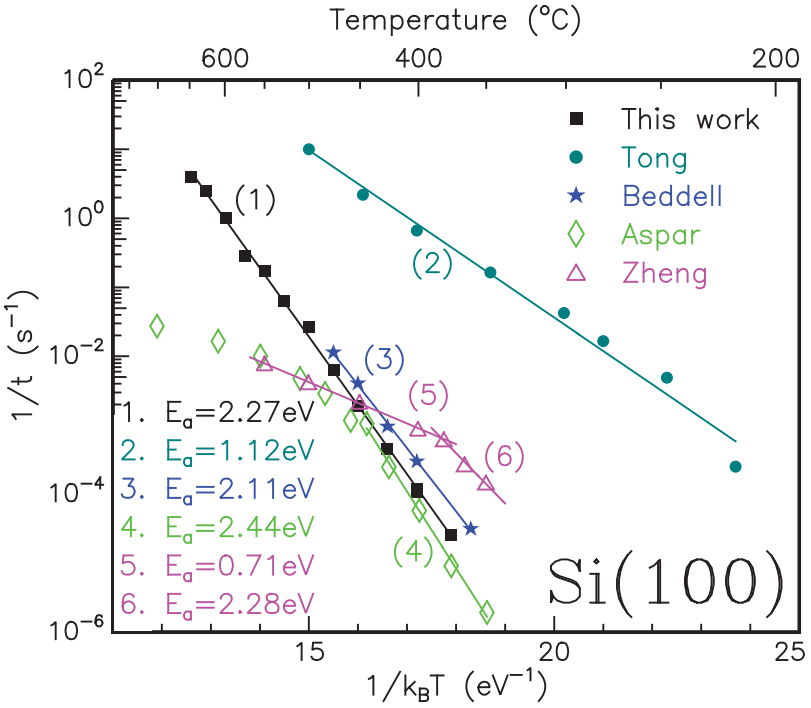

Figure 4.23: Comparison of hydrogen blister appearance time in H(40keV,6×10^{16}cm^{-2},RT) implanted Si(100) with similar results from literature. Implant conditions for literature sources - Beddell *et al.*:H(100keV,6×10^{16}cm^{-2}); Tong *et al.*:H_2(160keV,6×10^{16}cm^{-2}); Aspar *et al.*: H(70keV,6×10^{16}cm^{-2}); Zheng *et al.*: H(50keV,6×10^{16}cm^{-2}). Activation energies as listed.

and with sufficient temperature.

For the largest part of the range of values examined for these materials, there was no temperature for which blistering did not eventually take place. The curious exception was in the case of the E=100 keV implanted Ge(100), where the anneals at T=550°C – 600°C failed to produce any blistering. Rather, an odd surface discolouration took place, which resembled some form of contaminant denaturing on the surface, or possibly sample surface oxidation. This may also have been indicative of rapid changes in the implanted hydrogen profile, as anneals performed at immediately lower temperatures (350°C <T<550°C) produced total lift-off of the surface layer rather than individual blisters, as also reported by Beddell *et al.* [21]. For this second range of temperatures, the blistering was very similar to the lift-off induced in ion-cut, where the entire layer above the implantation is delaminated. Due to the explosive nature of this decomposition, in concert with the cooling fan applied across the surface to remove heated air currents (due to their interference with steady images on the video recording), these layers disappear approximately instantaneously with

the blister point. Clear, individual blistering – where small blisters or craters form over a period of time, allowing measurement of the rate – only began after the anneal temperature dropped below T=350°C.

When contrasting with previous studies where solely hydrogen was implanted into Ge(100), by Tong *et al.* [108], Beddell and Lanford [21], Letertre *et al.* [170], and Yang *et al.* [171] as shown in Fig. 4.24(b), the blistering activation energy measured varied significantly from previous work. Similarly, when the blistering rates monitored in the higher E and lower fluence implantations are noted, it is clear they not only disagree with the other work, they have a different activation energy from the core H(40keV,6×10^{16}cm^{-2},RT) implantation. The variations between each study may be accounted for in the differences in implantation energy and fluence. As illustrated in the data collected over the duration of this project, any differences in implantation energy and fluence can have significant impact on the activation energy of the hydrogen blistering. Similarly, neither were the previous works contrasted here applying exactly the same implantation methods and conditions.

For the H(40keV,6×10^{16}cm^{-2},RT)-implanted Ge(100), the activation energy is determined to be E_a=1.40±0.14 eV, as a constant value for all annealing temperatures. However, both implantations not performed with the "standard conditions" could not be fit with a single activation energy. Shown in Fig. 4.24(a) over the course of the applied thermal anneals, as the temperature decreases, the effective activation energy increases. A similar phenomena was reported in Tong *et al.* [108], where there appeared a critical temperature below which blistering times become significantly longer. In our work, it could be read the same way, as critical temperature transitions.

Germanium is the only material where multiple activation energies were observed in our work – all of the different Si samples show a consistent activation energy for all annealing temperatures. Were we to assume that a single rate limiting process defines the activation energy, then it is unlikely that it would result in multiple values. Continuing on with this assumption, it is then likely that some number of uncontrolled factors are at play in the Ge measurements, unaccountably altering the behaviour to present the illusion of multiple activation energies. Such a situation is not without precedent, as work by Rankin *et al.* [345, 346] on the SPE rate in $SrTiO_3$ and $CaTiO_3$ found that the moisture content of the ambient atmosphere played a significant rôle in crystallisation rates. Analogously,

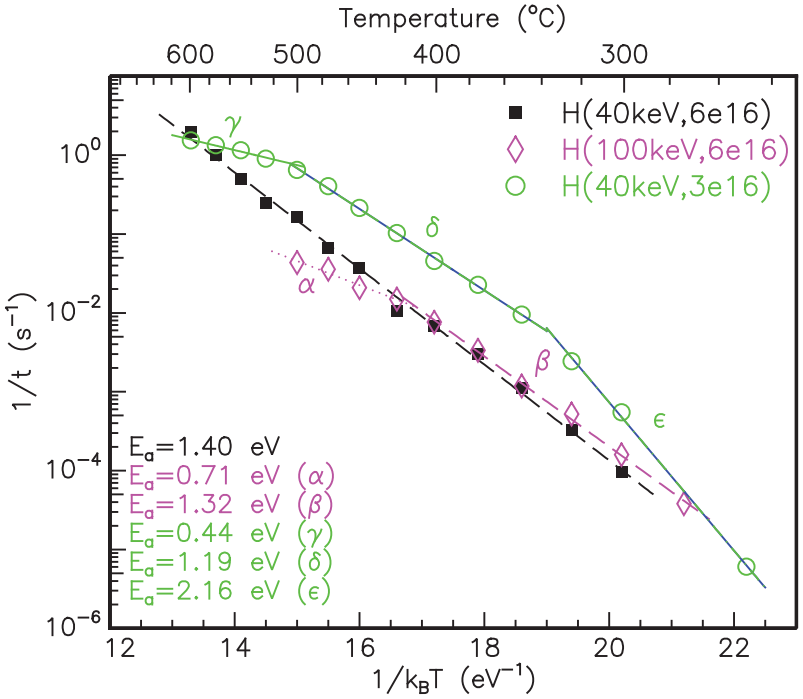

(a)

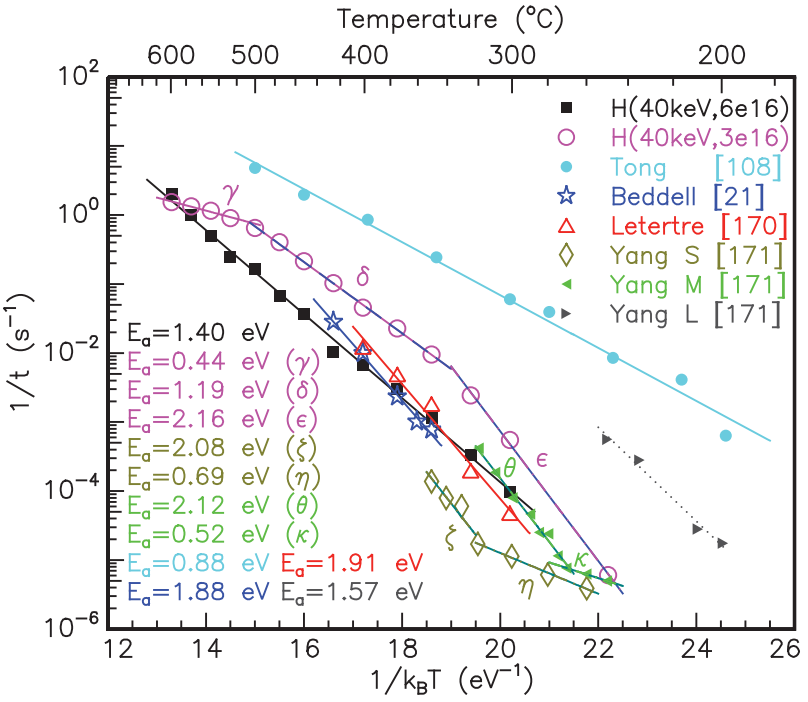

(b)

Figure 4.24: Comparing inverse time for the onset of blistering versus inverse temperature for (a) three different implantations H-implanted Ge(100), and (b) previous literature [21, 108, 170, 171] and two implantations in this work. Sources & activation energies E_a as labelled. All implantations performed at room temperature. Implant conditions for literature sources- Beddell *et al.*:H(100keV,6×10^{16}cm^{-2}); Tong *et al.*:H_2(160keV,6×10^{16}cm^{-2}); Letertre *et al.*: Undef. H(50-100keV,$\sim5\times10^{16}$cm^{-2}); Yang *et al.*: **S**mall H(60keV,3×10^{16}cm^{-2}), **M**edium H(60keV,5×10^{16}cm^{-2}), **L**arge H(60keV,1×10^{17}cm^{-2}).

it is possible some range of factors were in effect upon the Ge during their annealing and blister production. If these were better controlled during annealing, a single activation energy may emerge from the two irregular samples. Future work should endeavour to fit as strict a protocol as possible on the blistering process, in order to eliminate all potential factors of influence. As an alternative, it is possible that there *is no single factor* that governs hydrogen-related blistering in germanium. Instead, maybe a number of different factors are involved, precluding the need for a single activation energy. In either situation, the multiple effective activation energies described in our work still have a use as a type of phenomenological description of the data from these samples. Such values can be used for comparison and may allow any subsequent work to identify similar patterns, either to describe a more appropriate mechanism for hydrogen blistering, or in eliminating sources of interference. To that end, we will discuss these values as "effective activation energies" in the remainder of this text.

There appears to be a transition at approximately T=450°C in the higher energy H-implanted Ge series studied. At T$\leqslant$425°C, the high energy E=100 keV implantation has an effective activation energy of E_a=1.32±0.03 eV, which is very similar to the "standard conditions" sample and the higher fluence implant of Yang *et al.* [171], but transitions to E_a=0.71±0.08 eV at T$\geqslant$450°C.

Two transitions in effective activation energy occur in the Φ=3×10^{16}cm^{-2} H-implanted Ge – at T=335°C (E_a=2.16±0.09 eV to 1.19±0.02 eV) and at T=500°C (E_a=1.19±0.02 eV to 0.44±0.04 eV). The lower fluence Φ_H=3×10^{16}cm^{-2} implantation shows a distinct offset in initial blistering time from most other energies measured or reported, except at T$\leqslant$340°C, where it has reasonable agreement with some of the findings of Yang *et al.* [171] on $\Phi = 3 - 6 \times 10^{16}$cm^{-2} implantations.

As to why the "standard conditions" chosen for this project appear to have a single activation energy when the two selected "either side of it" in terms of less hydrogen fluence or greater ion energy have such variable behaviour is difficult to explain simply. Rather, as prefaced above, the differences are more likely to be rooted in environmental factors than any significant influence by the implantation conditions variation.

Yang *et al.* [171] reports some of the more unusual behaviour, as at lower temperatures the apparent activation energy appears to decrease dramatically, at odds with experimental

findings of our work. In particular, the lower fluence (3×10^{16}cm^{-2},60keV) implantation studied by Yang contrasted with the lower fluence implant of our work (3×10^{16}cm^{-2},40keV) shows not just opposite trends in changes to effective activation energy with temperature, but significantly different blistering times for the same temperatures studied. The times do seem to converge for the 3-6$\times10^{16}$cm^{-2} H implantations studied in both our work and [171] at ∼220-240°C. The relatively higher temperature anneals for each fluence as studied by Yang however give activation energies which are in relatively good agreement with Letertre, Beddell and the higher energy implant of our work, as described before. In fact, while all these previous works differ from the measured splitting time values collated in our project, it is not by more than an order of magnitude. With the amount of variation that a slightly different exponential fit can produce in the activation energy measured, these values are not significantly offset, even in the case of Tong *et al.* The only real discrepancy is in work by Yang *et al.*, where the multiple activation energy trend with respect to annealing temperature seems reverse to other reported findings.

Si(111)

Blistering in Si(111) was largely commensurate with the behaviour in Si(100) and Ge. Little work has reported the onset of blistering behaviour in non-Si(100) substrates, but work by Zheng *et al.* [107] is contrasted with the data from our study, shown in Fig. 4.25.

Zheng reports a two activation energy system with a transition at approximately T=435°C, with higher anneals requiring a lower effective activation energy E_a=0.71 eV to begin the blistering process. However, the lower temperature value of E_a=2.28 eV is in good agreement over the ranges of temperatures described with the value measured in our project. The activation energy we determined for Si(111), E_a=2.18±0.11 eV, is highly consistent over the substantial range of temperatures examined. Confidence is higher in a measured single activation energy if we assume a single rate limiting process governs the blistering step, as suggested in discussion of Ge(100) above.

Work by Qian *et al.* [58] describes hydrogen implanted Si(111) as blistering more readily than either (110) (significantly) or (100) (marginally) oriented Si wafers, in similar implantations to this study. While in our study blisters were not induced in the Si(110) sample with the standard implant, the Si(111) began blistering sooner than Si(100) at the same temperatures, in agreement with Qian.

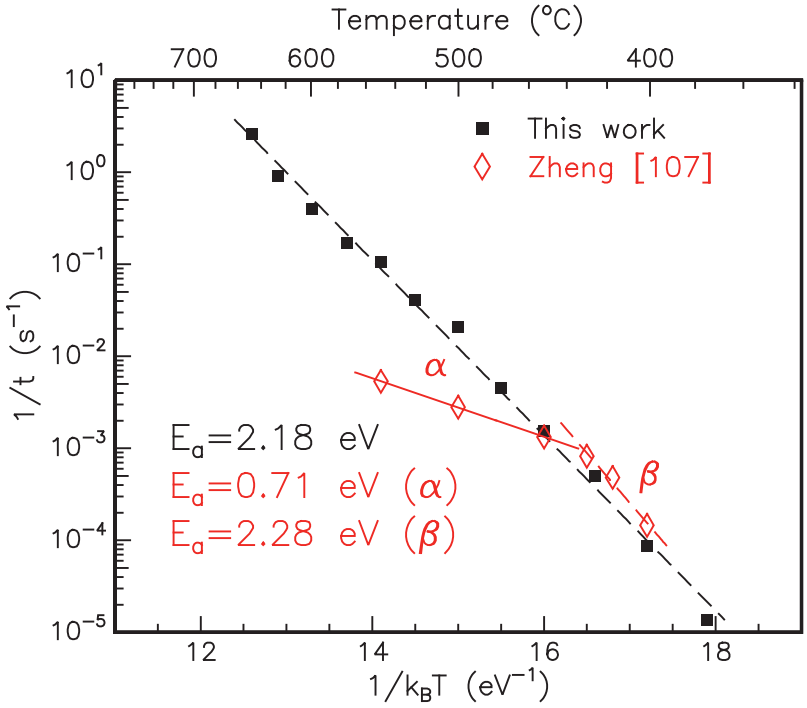

Figure 4.25: Inverse time for the onset of optically detectable blisters versus inverse absolute annealing temperature in hydrogen-implanted Si(111). Errors absent due to small size relative to symbols. Activation energies and implantation conditions as labelled for this work. Implant specifications: H(40keV,6×10^{16}cm^{-2},RT); for Zheng *et al.* [107]: H(6×10^{16}cm^{-2},40-50keV,RT).

While Qian does not describe the on-set of blistering time for any of the three systems, their arguments regarding the mechanism allowing blistering to occur predicts different behaviour than that reported by Zheng *et al.* [107]. Some differences were explained by Qian as due to their operating solely in the high temperature regime, with lower fluences than Zheng. However as our research uses samples and conditions in closer agreement with Zheng, despite the differences seen in Fig. 4.25, hopes that Qian's arguments support our data are low.

Si(110)

Distinctly different to any of the above described behaviours was the case of Si(110). In the Si(110) wafers implanted with H(40keV,6×10^{16}cm^{-2},RT), independent of annealing duration or temperature, no blistering occurred. This confirmed the findings discussed in Section 4.4, where a fluence above Φ_H=6×10^{16}cm^{-2} is required to induce blistering behaviour in Si(110). This behaviour however is in contrast with work by Zheng *et al.* [107],

who report blistering in all three crystallographic orientations of silicon wafers for the same fluence Φ_H=6×10^{16}cm^{-2} as investigated here. According to their work, blistering is seen in Si(110) wafers annealed at T=550°C after approximately 7 minutes (in [107], see Fig. 1). To contrast, exposures were performed at this temperature upon samples with confirmed hydrogen implantation (from RBS-C, ERD and swelling measurements) for 3 hours and also at T=575°C/1h, 580°C/3h, 600°C/1h, 625°C/2$\frac{1}{2}$h and 500°C/5h. For all these temperatures and durations, no blistering or cratering was found on the wafer surface. Given the range of temperature and durations applied, there is sufficient certainty to claim blistering does not occur in this combined range of fluences and temperatures.

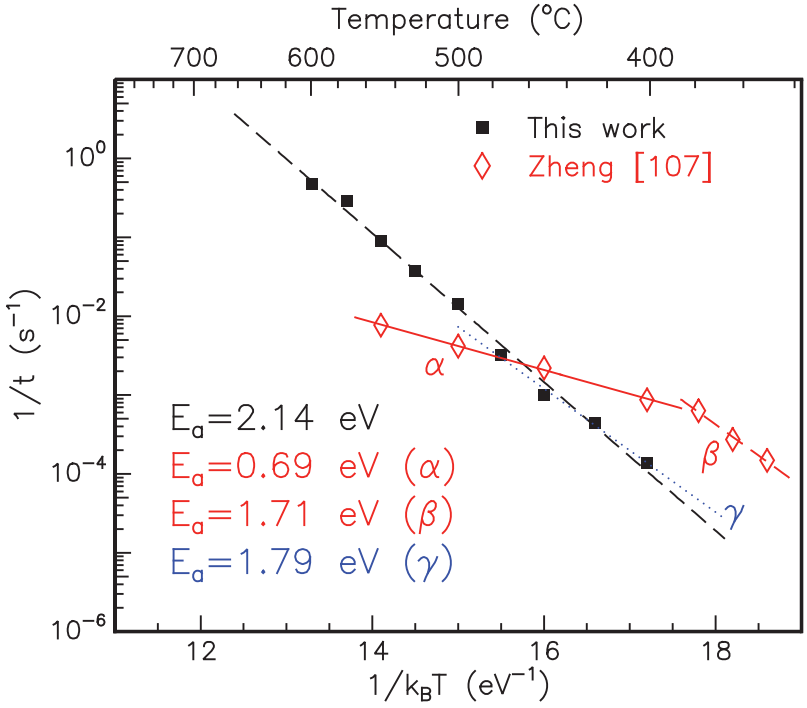

Figure 4.26: Inverse time for the onset of optically detectable blisters versus inverse absolute annealing temperature in hydrogen-implanted Si(110). Errors absent due to small size relative to symbols. Activation energies and implantation conditions as labelled for each series. Implant specifications: H(40keV,1×10^{17}cm^{-2},RT); for Zheng: H(50keV,6×10^{16}cm^{-2},RT).

This confirms that there is a higher minimum concentration or fluence threshold for blistering to occur in Si(110). As seen in the fixed annealing regime, blistering *did* occur at fluences $\Phi_H \geqslant 1.5 \times 10^{17}$cm^{-2}, and at Φ_H=1×10^{17}cm^{-2} when E≥80 keV, so it is reasonable to conclude that a lower hydrogen fluence limitation for blistering in Si(110) exists between 6 and 10 ×10^{16}cm^{-2}.

Previous work [75, 102] describes the natural cleavage planes of silicon as being (110) and (111), and expects that ion-cut occurs in these corresponding directions, with potential for perfectly atomically smooth surfaces produced by (110) cleavage. However, as the present work shows, Si(110) proves less responsive to fluences and energies that readily produce surface-parallel microcracks in Si(100), Si(111), Ge(100) and other similarly crystallographically aligned materials. Work by Qian *et al.* [58, 125] suggests that under certain low energy conditions, blistering is inhibited in hydrogen-implanted Si(110), the given explanation being a combination of two factors. One, that the structure of Si(110) has greater potential for implantation channelling leading to lower density of the required hydrogen and damage defects (also see [347]). Secondly, that the damaged layer produced by the shallow implantation would extend to the surface, allowing H more mobility and ability to escape the wafer prior to reaching critical concentrations for blistering. Addressing the first point, implantation in our project was angled at 7° to the low index crystalline axis, minimising any effects due to channelling. While there is the potential for planar channelling, particularly when the critical angle is larger at low energies, this is addressed by the second point. In our work, higher energies of implantation are used, preventing low energy effects, as reported specifically in [125]. SRIM simulations of hydrogen implantation at E=40 keV show a discrete crystalline layer between the implantation damage and the surface. This leaves the question as to why blistering or cratering was not witnessed in corresponding hydrogen fluence and energies and substrates to previous work unanswered. Hobler *et al.* [348] also show SIMS results indicating that H implanted into Si(110) has a greater straggle than the equivalent into other Si wafer orientations. This may allow for a broader damage region with lower concentration of both hydrogen and defects described as necessary for blistering to occur, following the models proposed by Weldon *et al.* [106] and Di *et al.* [349] for Si(100). Examining results from Section 4.5 however, our findings seem to suggest that the volume over which the defects occur (i.e., E_{ion}, R_{P}) is less important than the total integrated volume (i.e., Φ_H, C_{Defects}). Perhaps a key factor is the orientation of the precursor defects which lead to blistering, hydrogen platelets. These defects are predominantly observed to form along the (100) and (111) family of planes in the crystal structure, providing a more favourable pathway to blistering for wafers similarly orientated. The lack of significant defects along the (110) plane may increase the difficulty of forming hydrogen blisters, explaining the need for greater fluences

(and possibly higher energies and resulting lattice damage/stress).

In order to study blistering in Si(110), another implantation was performed, with a hydrogen fluence of $\Phi_H = 1 \times 10^{17}\text{cm}^{-2}$ at E=40 keV and room temperature. Akin to the previous work described, the sample was thermally annealed under atmospheric conditions at a range of temperatures (400°C <T<600°C) until blistering visibly began and for some duration afterwards. Contrasting the blister appearance time with previous work by Zheng *et al.* [107], the obvious difference is the lack of two-tier activation energy regime in the current data. The consistency of the activation energy is similar to that measured in Si(111) and Si(100), as well as Ge(100) implanted with H(40keV,$6\times10^{16}\text{cm}^{-2}$,RT). Shown in Fig. 4.26, the activation energy measured in our work is constant over the annealing range, with E_a=2.14±0.06 eV. As in previous specimens, for a process defined (presumably) by a single rate limiting attribute, such a consistent activation energy gives greater confidence in the data. The values found by Zheng *et al.* shown on Fig. 4.26 show E_a=1.71 eV from T=350-380°C, then E_a=0.69 eV from T=400-550°C.

It is important to reiterate that the Si(110) studied by Zheng was implanted with a lower hydrogen fluence of $\Phi_H = 6 \times 10^{16}\text{cm}^{-2}$ at E=50 keV. Considering this, and with the variations in behaviour noted for Ge(100) when the energy or fluence are altered, it is not unexpected that differences exist between these two systems. However comparison with samples implanted at similar energy and fluence as used by Zheng proved impossible, as no blistering was observed in such samples in our project. Thus the differences between these sample series are already starkly delineated without accounting for variations in the implantation conditions. If the lower temperature measurements taken in our project, from T=400-475°C, are contrasted with the lower temperature regime of Zheng *et al.*, a similar activation energy is seen (E_a=1.79±0.12 eV) (labelled γ in Fig. 4.26). However, such a trend line alone, or in concert with one fit to the remaining data, would inadequately provide a reasonable fit over the whole data range. In fact, the trend for higher temperatures would be a more rapidly increasing blistering time, the opposite to that reported by Zheng. We conclude from these data that a single activation energy is required for H(40keV,$1\times10^{17}\text{cm}^{-2}$,RT) implanted in Si(110) in order to reach blistering phenomena. Our data also firmly places the hydrogen concentration threshold for blistering in Si(110) between $\Phi_H = 6 \times 10^{16}\text{cm}^{-2}$ and $\Phi_H = 1 \times 10^{17}\text{cm}^{-2}$.

Modelling

Research by Han *et al.* [343] models the blistering process thermodynamically in terms of the implantation fluence, annealing temperature and annealing time. As laid out in their research, the splitting time t (in seconds) for a silicon wafer with a given implanted hydrogen fluence ϕ_0 (in atoms.m^{-2}) at a given temperature T (in kelvin) is expressed by Equation 4.7:

$$t(T) = -\frac{1}{\tau}\exp\left(\frac{E_a + E_d}{k_B T}\right)\log_{\mathrm{e}}\left(1 - \frac{14.8\gamma(T)}{k_B T \phi_0}\right) \tag{4.7}$$

where E_a is the hydrogen complex disassociation activation energy (1.8 eV=2.88×10^{-19} J), E_d is the energy hydrogen requires to diffuse into vacancies (0.48 eV=7.69×10^{-20} J), k_B is Boltzmann's constant, τ is a phenomenological parameter relating to the dissociating X-H bond's stretching or jump frequency ($\sim$10^{12}s) and $\gamma(T)$ is a phenomenological expression of the crack surface tension of silicon due to hydrogen, given as:

$$\gamma(T) = 1.5 \times 10^{-4} T + 5 \times 10^{-3}\mathrm{J.m}^{-2} \tag{4.8}$$

When appropriate values used in our research are entered into this model, the activation energy predictions are in excellent agreement with the values determined from blister appearances measured in this work, as shown in Fig. 4.27.

A similar off-set in initial energy requirements is present to that which occurs in the case of the bulk and ULTRATHIN® Si(100) wafer values (Fig. 4.22). The difference between the pre-exponential factors is 1 to 33, with Han's theory predicting blistering to occur later than the experimental data shows. However, the activation energy extracted from the data fits is in excellent agreement. This offset can be accounted for by modifying the value of the hydrogen complex's jump frequency, τ, or its reciprocal $\nu = \frac{1}{\tau}$, to better align it with calculations by Ma *et al.* [114], Leitch *et al.* [351, 352] and Rice *et al.* [350]. If the pre-exponential value in the model described by Han is modified to ν=2.4×10^{13}s ($\sim \times\frac{1}{4}$), well within the values calculated by Rice, there is excellent agreement with the data. This is shown by the green dashed line in Fig. 4.27. (A fuller justification for this change is given in Appendix D.4.)

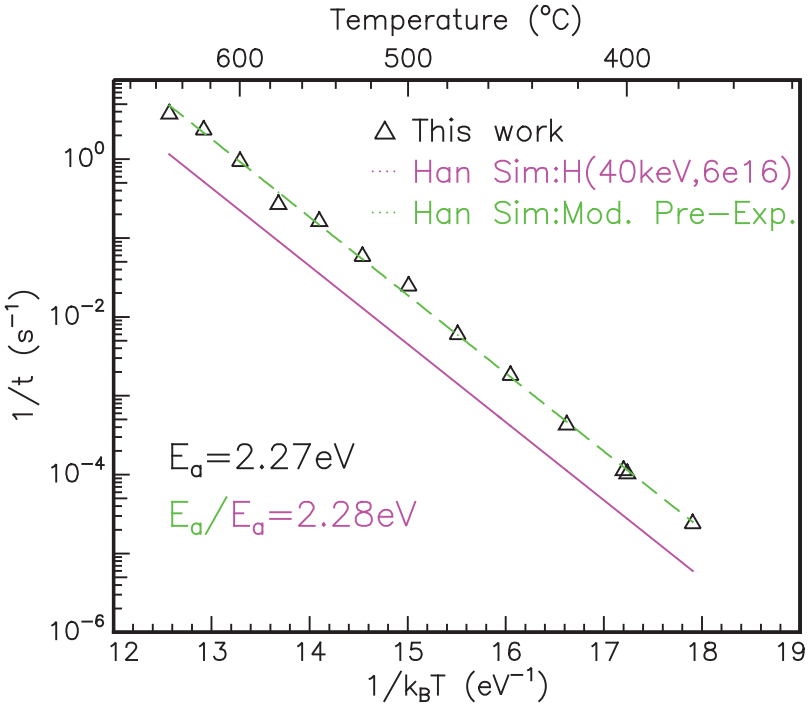

Figure 4.27: Comparing inverse onset time for hydrogen blistering per inverse absolute temperature measured in H(40keV,6×10^{16}cm^{-2},RT) implanted Si(100) with theoretical values calculated by Han *et al.* [343] - original paper value for X-H bond jump frequency in magenta, modified to match values in [114, 350–352] in green. Activation energies as labelled.

What is also telling from [343] is the accuracy with which the underlying theory applied fits the measured Si(100) system, forgiving the variation in the X-H bond dissociation frequency. Effectively, the assumptions made about the physical description of the system, the total free energy of the hydrogen blisters, and the fracture behaviour, are vindicated in the excellence of the simulation's fit to the data.

Attempts to fit this model to the Si(111) data also showed excellent agreement without further modification, and can be seen in Appendix D.3. However, differences arose for the Si(110) and Ge(100) blistering samples.

Fitting the H(40keV,1×10^{17}cm^{-2},RT)-implanted Si(110), the sum of $E_a + E_d$ was amended with E_a=2.14 eV, the activation energy determined from that sample's data. However, the model was a significantly poor match for the experimental findings. By adjusting the X-H jump frequency such that τ=3.95×10^{11} s, still within the bounds of values calculated by Rice [350] or applied by Han [343], the model was found to better replicate

the results, though this showed a rate of blistering slower than results for low temperatures. It is possible that Si(110) features a different crack surface tension energy value than Si(100), with some work suggesting a constant value [69]. If the temperature dependence term is removed, the model is less like the data, requiring an even larger activation energy to predict similar blistering times, making such a situation unlikely. If alternatively the temperature dependence factor were arbitrarily increased by $\times 5$, the model fits the data with the experimentally-derived activation energy. As the values of γ for Si(110) applied in Section 4.5.3 ranged from γ=0.1–1.7 Jm^{-2}, this is also not an unreasonable shift from the range of values calculated by Eq. 4.8 (0.1-0.13 Jm^{-2}). Both fits by decreasing τ and altering $\gamma(T)$ are shown in Fig. D.10 in Appendix D.3.

For the Ge(100) implanted with H(40keV,$6\times10^{16}\mathrm{cm}^{-2}$,RT) – the only Ge sample to exhibit a constant activation energy to allow modelling by Han's theory – the fit also required significant modification. Fitting the equation with the activation energy determined experimentally – E_a=1.40 eV – the predicted blistering times were four orders of magnitude longer than those determined experimentally. As with Si(110), the prime contributing factors which may be different in Ge are the X-H bond stretching frequency τ and the surface crack energy $\gamma(T)$. There are few consistent values for these physical constants in the literature, making it difficult to assess what would be reasonable selections. In order to fit the modelling of Han *et al.* [343] to our work's data, an arbitrary value of $\tau \sim 6 \times 10^7$ s will produce good agreement. Parks Cheney *et al.* [353] give a vibration time of ∼36 ps for the H in Ge, suggesting a lower value for the stretch frequency approximately 10^{10} Hz. But even accounting for this value, the surface crack energy requires a value of $\gamma(T) = 5 \times 10^{-4}T + 3 \times 10^{-2}$ Jm^{-2} in order to reasonably agree with the experimental data, which is close to the upper limit allowed within the logarithm in Eq. 4.7, and places the value of $\gamma(T)$ higher in Ge than in Si. These fits – adjusting τ, or τ and γ – are shown in Fig. D.10. The possibility exists that hydrogen blistering in germanium is governed by a very different bond to the X–H, explaining the different stretching frequency. In light of the relative appearance of agreement between these arbitrary fits and data, it seems more likely that Ge must posses a significantly different τ value than reported in the literature, rather than pursuing large scale modification of the model and underlying theory.

Conclusion

For the standard conditions implantation into Si(100), Si(111) and Ge(100), the blistering process exhibited a constant activation energy with regards to annealing temperature. A higher fluence was required for blistering to occur in Si(110), and a constant activation energy was also seen at each temperature. For higher energy ion or lower fluence hydrogen implantations into Ge(100), multiple effective activation energies were seen, with distinct transitions occurring over the range of anneals 250°C <T<600°C. Thermodynamic analytically derived modelling by Han *et al.* [343] is in excellent agreement with the experimental data for all Si orientations, with suitable adjustments of implant fluence and physical constants. Modelling of Ge with a fixed activation energy was able to match data, but without reasonable explanation for the required values.

4.7 Blister cleavage depth and floor roughness

Optical profilometry (OP) and IBA techniques were used to study the post-annealing ruptured hydrogen blisters or craters in the intrinsic semiconductors analysed in Sections 4.4, 4.5 and 4.6. The depth and roughness of the crater floors were measured from the same Si(100), Si(111) and Ge(100) samples used to determine blistering activation energy and rate, using OP following the annealing procedures as described in Section 3.3.1. Si(100) and Si(111) were implanted with H(40keV,6×10^{16}cm^{-2},RT), while Ge(100) included two implantation conditions at H(100keV,6×10^{16}cm^{-2},RT) and H(40keV,6×10^{16}cm^{-2},RT).

Additionally, a second series of samples in Si(100) with varied ion implantation E and Φ_H, previously introduced in Section 4.5.2 as the *common peak hydrogen concentration* series, were examined. Varying both implant parameters, these samples consisted of hydrogen implantations of (45keV,5×10^{16}cm^{-2},RT), (65keV,5.35×10^{16}cm^{-2},RT), (85keV,5.56×10^{16}cm^{-2},RT), (105keV,6.01×10^{16}cm^{-2},RT) and (125keV,6.65×10^{16}cm^{-2},RT), where the combination of fluence and energy were selected to maintain a constant hydrogen concentration at the R_{P}. The peak hydrogen concentration of $C_H(R_{\mathrm{P}}) = 3.7 \pm 0.3 \times 10^{20}$cm^{-3} selected was above the limit described by Bruel *et al.* [13] required to induce an ion-cut process (i.e., relative $\Phi_H = 5 \times 10^{16}$cm^{-2}). Each sample was annealed under an Ar ambient at T=550°C for 30 minutes prior to examination by OP, and the hydrogen pro-

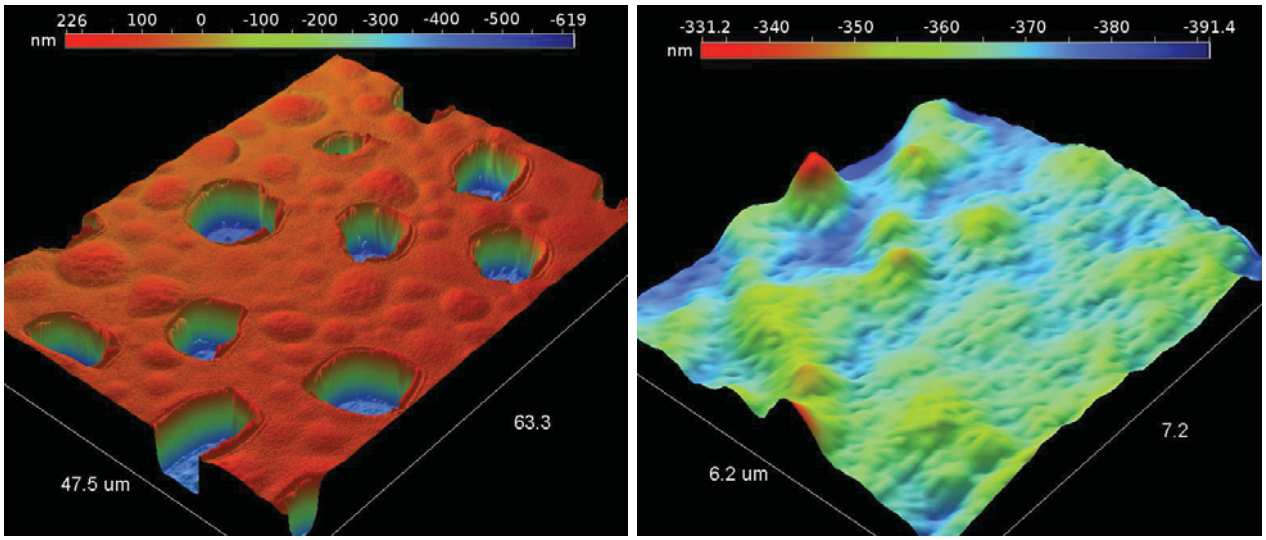

(a) (b)

Figure 4.28: Optical profiler 3D projections of H (45keV,5×10^{16}cm^{-2},RT)-implanted Si(100), annealed at T=550°C/30 minutes, showing (a) hydrogen-induced surface blistering and cratering, and (b) crater floor roughness. All measured in VSI mode, ×100 lens, FoV ×1. Scales as labelled, giving relative height differences.

file and ion implantation damage were measured by ERD and RBS-C respectively before annealing. As mentioned in Section 3.2.3, some subconscious anthropic bias may exist in these series' sampling space. The samples sets are suitably voluminous to minimise any skew to the trends determined from these measurements.

An example of a Si(100) samples with varied hydrogen ion fluence and energy is shown in Fig. 4.28 with a three dimensional projection derived from optical profiler data from the H(45keV,5×10^{16}cm^{-2},RT) implanted Si, showing the surface hydrogen-induced cratering and the roughness of a hydrogen crater's floor.

Si(100)

For H(40keV,6×10^{16}cm^{-2},RT)-implanted Si(100), the variation in the annealing temperature and exposure time does not appear to significantly influence either the depth of the blistered craters (z) or the roughness of the crater floors (Δz). Figure 4.29 shows the relationship between the thermal anneal temperature and the formed hydrogen craters' average depth and floor roughness, as measured using optical profilometry.

There are several key findings that are apparent in this figure. At moderate annealing temperatures (450°C < T < 600°C), the hydrogen bubble-produced craters have a small range of depth and roughness values, between z = 439 and 444 nm, and Δz = 20 and

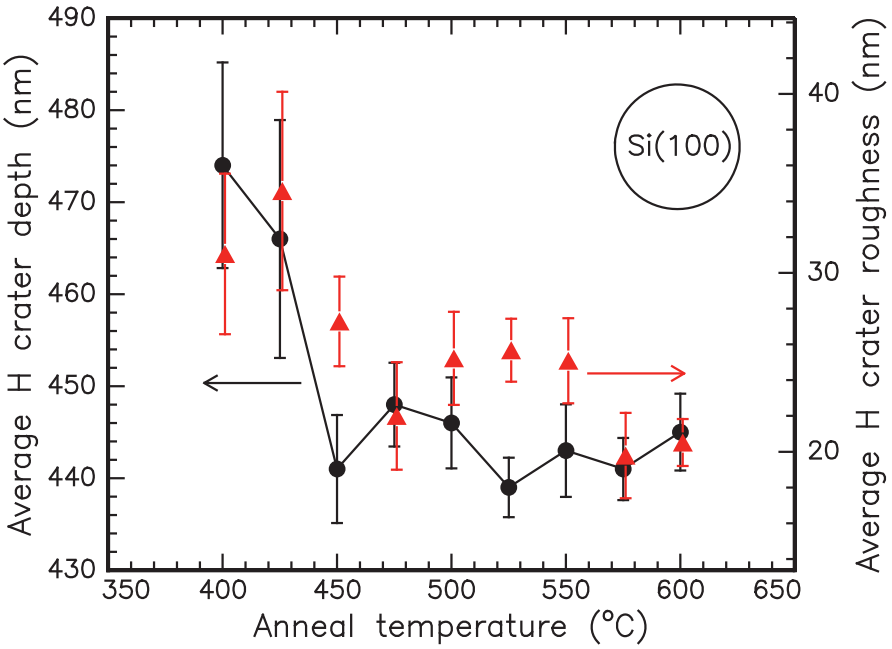

Figure 4.29: Average crater depth and floor roughness in H(40keV,6×10^{16}cm^{-2},RT) implanted blistered Si(100) measured by the optical profiler following cessation of annealing-induced blistering.

28 nm respectively. However, at lower annealing temperatures, the roughness and depth of the craters is noticeably larger. The precise mechanism that leads to lower temperature anneals producing effectively the same blistering behaviour - albeit over longer time scales - but yet emerging with rougher interfaces seems slightly counterintuitive. However, the relative contributions of defect annealing, hydrogen migration, blister and crater formation all vary with temperature. As initially noted, the overall variation in resultant depths and roughnesses is slight. The maximum variation in depth – 35 nm – could be accommodated in variations in straggling within the one sample, due to the statistical nature of ion implantation. The variations can be accommodated within the straggle of the hydrogen ions during implantation and target vacancies that is predicted by Monte Carlo simulator SRIM [251] (64.3 nm and 90.2 nm respectively). Other work by Höchbauer *et al.* [24, 25] describe cratering behaviour that steps between the peak in the strain and the peak in the crystal damage – it is possible that is what is measured here.

Contrasting the areal blister density rate seen in Fig. 4.18, the samples which are still in the rapid growth phase (the steep rise in the logistics function model) are the same as

those with the higher crater floor roughness, while those that have slowed their blistering rate per area as they asymptote to a saturation value all feature the lower floor roughness. This suggests that the roughness of the crater floors changes with annealing duration, and if blister evolution were left to run to completion for the anneals T<475°C, the roughness would be the same as the value measured in samples annealed T>475°C. Moras *et al.* [102] predict atomically smooth cleavage in hydrogen-implanted Si wafers if the entire interface were to lie on the one microcrack or platelet plane, but realistically predicts that steps will exist between each smooth surface. This could allow for the different depths by more of the deeper platelets remaining to form the crater floor at the lower temperatures than at the higher temperature anneals, as well as the roughness in how regularly the planes "transitioned" between microcracks.

Si(100) - Varied implantation E and Φ

With increasing fluences matched to increasing ion energies, maintaining a constant hydrogen concentration at the profile peak for all samples, these Si(100) samples displayed blister depths linearly proportional to ion energy, and a constant roughness. Figure 4.30(a) contrasts crater depths z with the IBA-determined position of their precursors – ion implantation damage in Si from RBS-C, and the hydrogen profile peak from ERD. Histogram distributions of the measured craters' depths are presented in Fig. 4.30(b)-(f).

Figure 4.30(a) shows excellent agreement between the hydrogen crater depth and the depth of the peak in ion implantation damage, measured by the direct scattering peak in RBS-C. At the same time, it also has quite good agreement with the values of the R_{P}(Hydrogen) measured by ERD. In essence, the depth of the hydrogen craters is directly proportional to the implantation energy, whether linked specifically to the implantation damage or hydrogen profile.

Presented in Fig. 4.31, the distribution of the roughness Δz in the crater floors was approximately equal in all samples, independent of implantation energy and fluence, or FWHM of the implantation profile. Equality in range of roughness may be an indication of the particular peak concentration of hydrogen being more crucial to the blistering and ion-cut phenomena than the total concentration within the silicon wafer.

We could infer a small positive increase in roughness with increasing energy, but it is also possible that at the concentrations implanted into these series of samples, a crit-

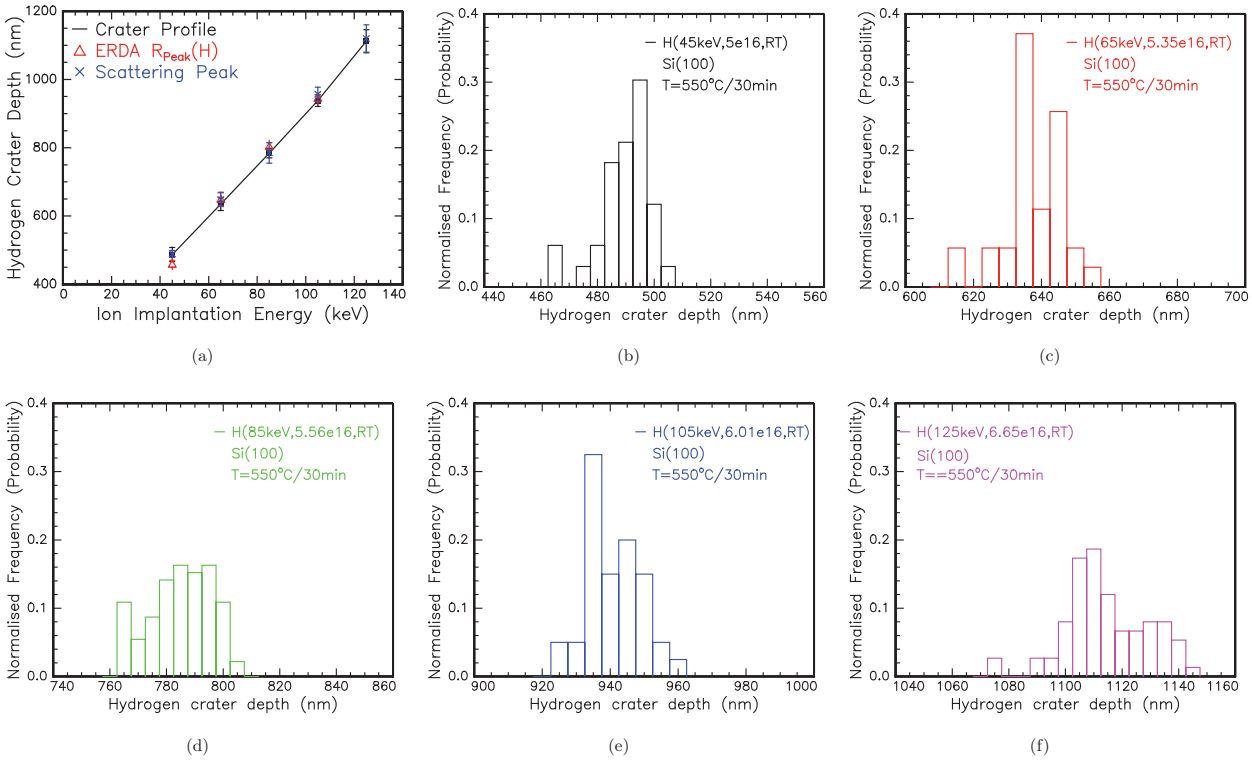

Figure 4.30: Histogram distribution of hydrogen crater depths, measured by the Wyko optical profilometer, from hydrogen-implanted Si(100) annealed at T=550°C/30 minutes in an Ar gas ambient. (a) compares depths measured by profilometry with those derived from RBS-C direct scattering peaks caused by the ion-implantation, ERD measurements of the hydrogen profile, for each implantation energy. (b)-(f) show distribution of crater depths for various energies and fluences of hydrogen, as labelled on each graph. Errors represent range of acceptable fitting values used to extract depths.

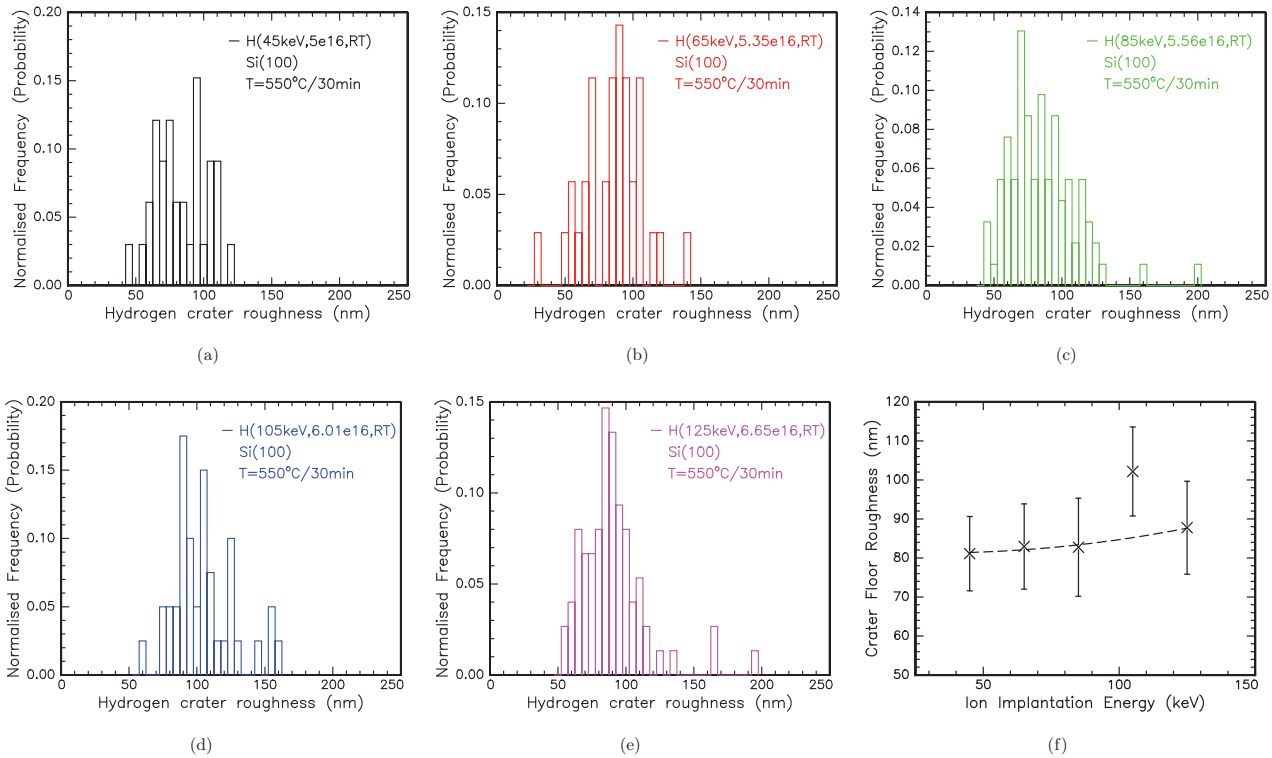

Figure 4.31: Histogram distributions of hydrogen crater floor roughness as measured in (a) E=45 keV, (b) E=65 keV, (c) E=85 keV, (d) E=105 keV, and (e) E=125 keV hydrogen ion implanted Si(100) at room temperature, then annealed in a quartz tube furnace under Ar gas at T=550°C/30 minutes. (f) shows the modal roughness of the crater floors at each implantation energy, errors in roughness is one σ of range of measured values; the dashed line is included only to draw the eye.

ical threshold has been reached, at which the maximal roughness value is produced. If this were the case, we would expect to see samples implanted at the same energies but with higher fluences to have crater floors no rougher than these samples. All of these samples' crater floors are substantially rougher than any of the H(40keV,6×10^{16}cm^{-2},RT) implanted material studied in this section, by a factor of ∼2-3. As these "standard conditions" have a higher peak fluence, this would seem to discount the theory of some critical threshold in the H(45keV-125keV) samples due to fluence. However, it is possible that the higher stresses and gas pressures produced by the greater implantation depth of these common concentration implantations may play a rôle. This could imply the limits upon the roughness may be due to a combination of the implantation energy and fluence. The duration of the annealing process also needs to be considered, as the length of time for exposure changed the roughness in the H(40keV,6×10^{16}cm^{-2},RT) samples in Fig. 4.29. Considering the behaviour of H40keV Si(100) at T=550°C, it is reasonable to assume that all blister (and thus floor roughness) evolution has been completed by t=30 minutes for the H(45–125keV) Si(100). If the combined H:Si state has reached equilibrium from the annealing process, e.g. all blisters formed and/or burst, this may further indicate that above a critical implantation, blisters of the same roughness are produced.

Si(111)

Si(111) exhibited the same behaviour where lower temperature anneals led to rougher crater floors and produced deeper craters, as was present in H(40keV,6×10^{16}cm^{-2},RT)-implanted Si(100), shown in Fig. 4.32. The variation in each value is also still within the standard error of the implantation profile or the damage profile, however the change in roughness at lower temperatures is more step-like than in Si(100), though occurring at the same temperature. It is important to note that both crystal orientations – (100) and (111) – produce similar behaviour at the same temperatures, e.g. crater depth and roughness are approximately constant over anneals at T=500-600°C and higher for T⩽450°C. In addition, as with Si(100), the transition between high and low roughness values coincides with those samples which have reached the second slower growth stage of blisters as predicted by JMAK or Gompertz functions. The shift in the roughness (and to a lesser extent depth) in the craters formed by the hydrogen evolution occurs at similar temperatures to the reported transition in activation energy regimes as reported by Zheng *et al.* [107]

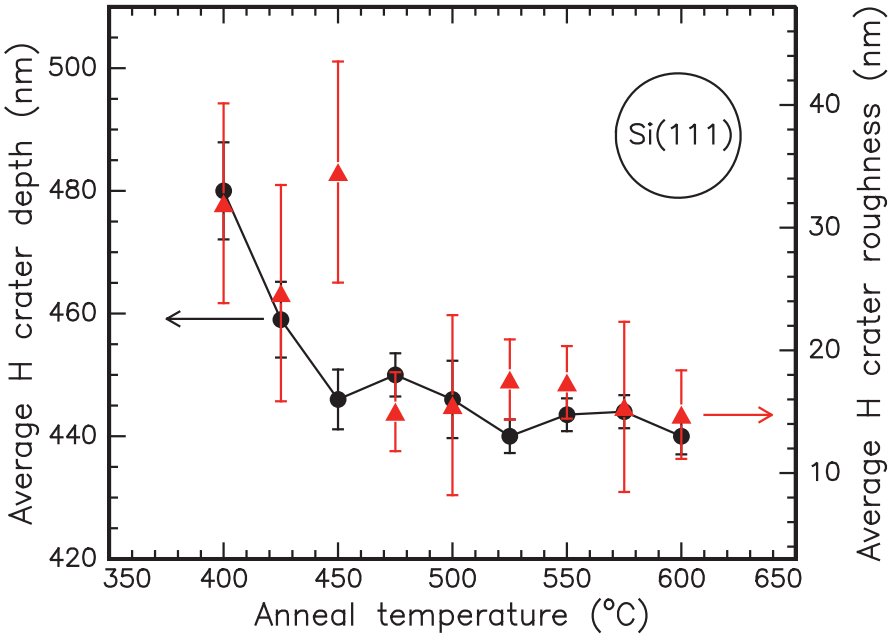

Figure 4.32: Average crater depth and floor roughness in H(40keV,6×10^{16}cm^{-2},RT) implanted blistered Si(111) following cessation of blistering induced by annealing.

As the majority of other work [1, 21, 24, 28, 102] reports that the primary crystallographic axes of platelet formation in Si(100) are along ⟨001⟩ and ⟨111⟩, despite theoretical predictions to contrary [102], it is useful to consider the directions along which hydrogen platelets form within Si(111). Presuming that the hydrogen platelets still preferentially align in the (100) and (111) planes (as the bond energetics in silicon would suggest), and continuing with previous work [27,107] that indicates favourable evolution of platelets into microcracks along the ⟨001⟩ direction over the ⟨111⟩ direction, one could assume that the fracture interface (or crater floor) within a Si(111) wafer to be much rougher. In effect, that much shorter cracks would be propagating along the "flat" (111) plane, and significant lengths of the interface "up and down" jagged {001} planes linking these flat regions [75]. As the range of the average roughness of the crater floor surfaces Δz=19.74 nm is very similar to that seen in Si(100) (Δz=14.79 nm), this does not appreciably seem to be the case. Previous reports by Martsinovich *et al.* [354] suggests that the hydrogen-induced cracks within Si(111) follow the same behaviour as Si(100), in that microcracks propagate along the axis parallel to the surface, although this was reportedly more common in samples which had undergone plasma hydrogenation. Gu *et al.* [105] suggest that extensive

microcracks are prevented from propagating along the ⟨111⟩ direction within a Si(100) crystal due to distortion of the lattice caused by the H implantation itself. It is not unreasonable to suggest that this same distortion produced when hydrogen is implanted into a Si(111) wafer would better facilitate the growth of platelets in the (111) plane and hinder expansion of platelets into microcracks along the ⟨001⟩ direction.

Ge(100)

Additional difficulties existed in attempts to measure precisely the roughness and depth of the hydrogen craters formed in germanium. On the same scale as blisters and craters in Si crystals, and in addition to the scattering of cast-off blister "lids" (see Fig. 4.15), the surface of the germanium wafers also had a high density of unidentified artefacts. These objects, shown in Fig. 4.33, were initially assumed to be void defects as seen by Tracy *et al.* [9]. However, measurements revealed the objects were composed of a Ge_xO_y with a sufficiently different refractive index to prevent easy measurement of their vertical dimensions with OP interferometry. Using SEM, these artefacts were identified as small "hillocks" on the wafer surface, with diameters up to 1 μm, heights ranging up to 80 nm. The artefacts proved to be composed of a germanium oxide which did not decompose during active oxidation annealing [355]. Their origin is uncertain, but most likely were present as a contamination upon production of the wafers, as subsequent tests found them on wafers freshly extracted from the storage compartment. When optical profiling the hydrogen-implanted Ge wafers, these features' different refractive index led them to appear as deep craters with outer circumferences very similar to the hydrogen blisters formed. As identification of the actual hydrogen blisters was confused, several of the measurement series had to be discarded as potentially distorted. This was most apparent in measurements from the E=40 keV, Φ_H=6×10^{16}cm^{-2} implanted Ge, but was also true for the E=100 keV H-implanted Ge.

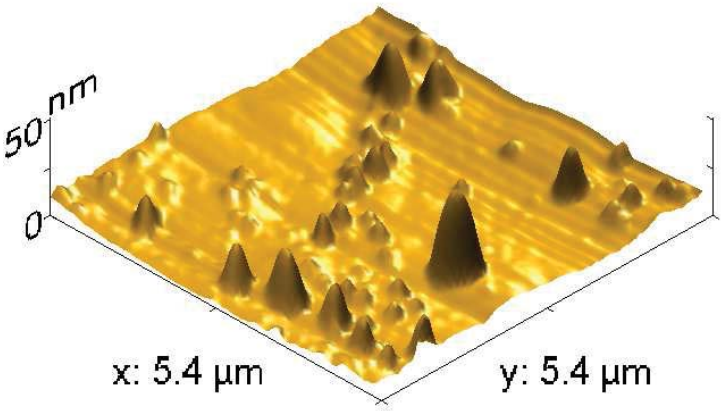

Figure 4.33: AFM 3D projection of GeO artefacts measured upon i-Ge(100) wafers. Scale of scanned region as labelled.

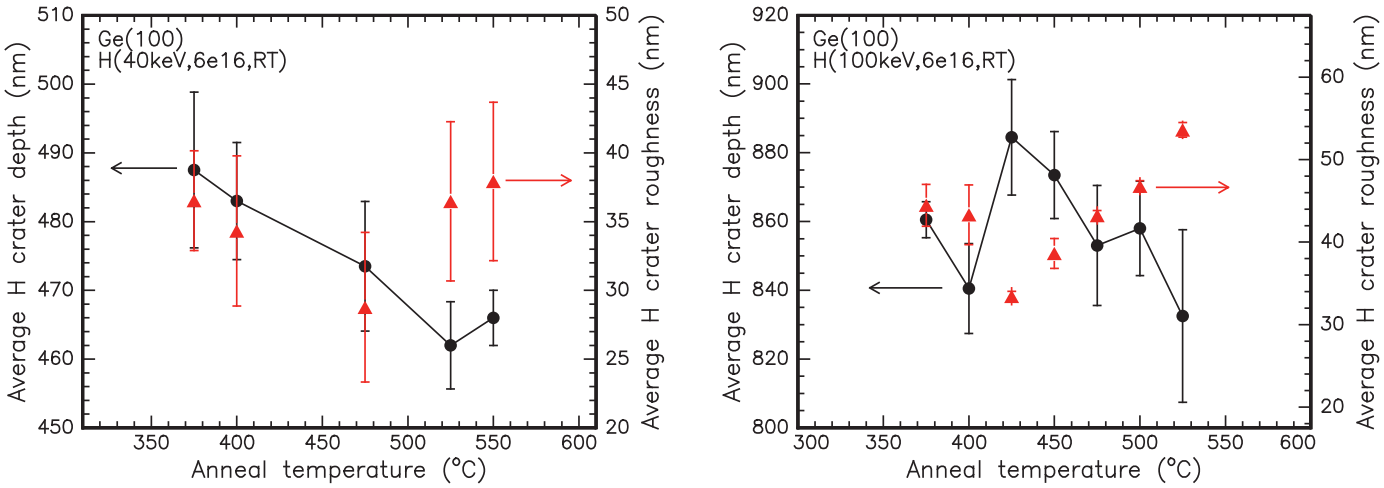

(a) E=40 keV (b) E=100 keV

Figure 4.34: Average crater depth and floor roughness in H-implanted blistered Ge(100) following cessation of blistering during annealing. $\Phi_H = 6 \times 10^{16}\text{cm}^{-2}$, Implant E as labelled, Error shows 1 standard deviation of range of values measured.

Depth and roughness of the craters formed by hydrogen blisters in all the fluence and energy ranges examined presented a much less consistent pattern than that seen in Si(100). In the case of the E=40 keV, Φ_H=6×10^{16}cm^{-2} implanted Ge, the range of average crater depth values was z = 25.5 nm and the range of average crater floor roughnesses was $\Delta z = 9.15$ nm. While it is possible to suggest a decreasing trend wherein the depth of the craters are becoming greater with higher annealing temperature, there is not an obvious trend in the roughness data. The higher energy ion implantation into Ge at E=100 keV showed no clear pattern in the crater depth and floor roughness measurements, with ranges of z_{depth}=52 nm and $\Delta z_{roughness}$=20.18 nm respectively. These data are presented in Fig. 4.34. This lack of trend is perhaps not unexpected following the result measured in Si(100), and following work by David *et al.* [101] suggesting while germanium may blister akin to silicon along platelet/microcrack planes, this can easily proceed along any layer within the implanted region that sufficient hydrogen is present, and can possibly form saw-tooth surfaces between planes by way of ⟨111⟩ platelets.

Comparison with experiment and simulations

The average crater depths measured in Si(100) via OP more closely matched the IBA measurements of implantation damage determined by RUMP [293] than anything simu-

lated by SRIM. This is shown in Fig. 4.35, and appears somewhat at odds with results presented consistently elsewhere [23–28, 76, 356]. Also apparent is the significant offset of both predictions from the actual data.

Similarly, the hydrogen profile peak depth determined by ERD better matches the crater depths for lower temperature anneals (T<450°C), while the resultant crack depth determined by cross-sectional TEM – which has a narrower range of depth values – shows excellent agreement with crater depths measured in all samples which were annealed at T>425°C. These data are in good agreement with the majority of previous works listed earlier, and most other work on the Si:H ion-cut system.

The depth of craters formed on the E=40 keV implanted Ge was higher than the result from the equivalent energy and fluence into Si(100), which disagrees somewhat with predictions by SRIM as to depths of crystalline damage and hydrogen profiles. SRIM predicts a H profile peak at R_P=325.6 nm, and a Ge crystal damage peak at R_P=265.7 nm, while the measurements from the optical profiler vary from depths z=462-487 nm. Similarly, the depth of the craters in the E=100 keV implantation show a dramatic departure from the values predicted by SRIM. Simulations by SRIM predict a H profile with a peak at R_P=734.3 nm, and a Ge damage peak at R_P=686.7 nm, while the profiler measurements of the crater depths varies from z=832.5-884.5 nm.

The most likely explanation for this offset is not that it is an error in measurement or simulation, but rather this is due to different blistering and cratering behaviour in Ge compared to Si. According to SRIM, the end-of-range (EOR) of the hydrogen implanted at E=40 keV into Ge(100) occurs at a depth of z∼472 nm, and for an implantation at E=100 keV, the EOR z∼940 nm. These values are much better aligned with the depth of the craters measured, as can be seen in Table 4.5. The possibility of this deeper location for blistering was discussed in work by Höchbauer *et al.* [24–26], where stress is assumed to shift the ion-cut location deeper into the H profile in Si, beyond the maximum damage range of the ion implantation. Although not explicitly reported in Ge, there are sufficient differences that may explain this behaviour. For example, the differences in how stress can influence Ge compared to Si, due to its lower bond energy and Young's Modulus. Such differences could allow the cavitations caused by the expanding hydrogen blisters to extend further into Ge than Si, acting as a potential mechanism to allow the craters to

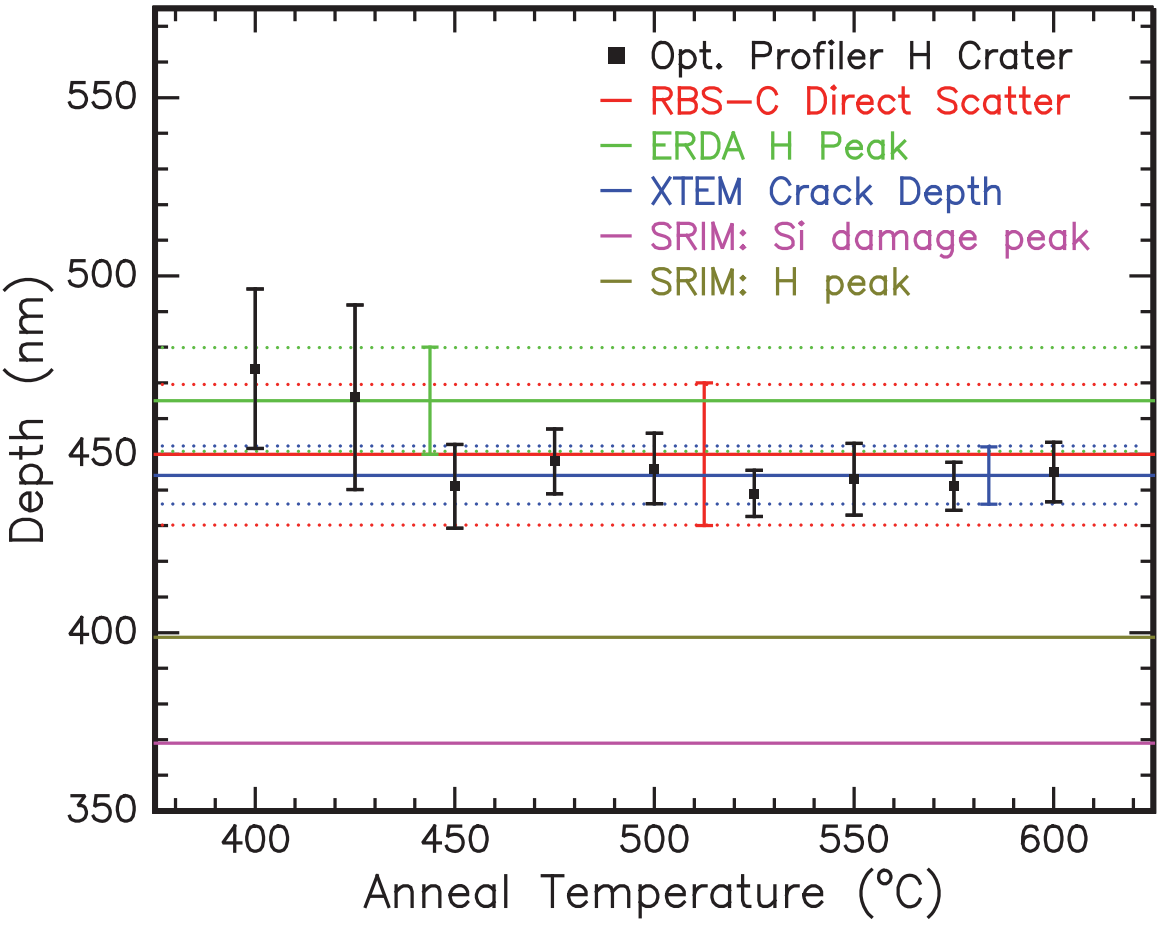

Figure 4.35: Comparing experimentally determined depth measurements of craters in annealed H (40keV,6×10^{16}cm^{-2},RT)-implanted Si(100), as measured by the optical profiler, with the peak maxima in the direct scattering yield from RBS-C, hydrogen profile peak as measured by ERD, hydrogen-induced crack within Si(100) measured by cross-sectional TEM, along with SRIM simulations of H and damage located in implanted Si(100) wafers. Dotted lines and error bars indicate range of values determined by each experimental technique from an archetypal sample.

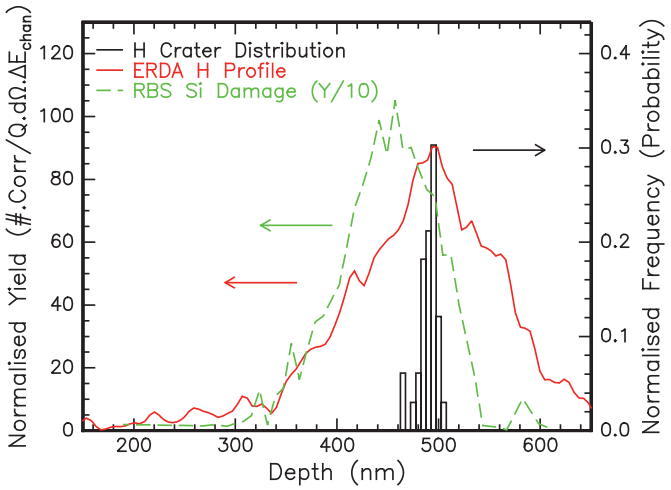

Figure 4.36: Comparison of the hydrogen crater depth distributions after annealing at T=550°C/30 minutes measured by optical profilometry, with ERD measurements of the pre-anneal hydrogen implantation profile and RBS-C measurements of the pre-anneal Si interstitials & vacancies produced in the ion implantation process for H(45keV,5×10^{16}cm^{-2},RT) into Si(100).

reach the EOR. This is also suggested in work by Mazen *et al.* [177], when similar energies and fluences are applied as in our study.

Expanding on the data for the particular case of the H(45keV,5×10^{16}cm^{-2},RT)-Si(100) implantation, seen in earlier Fig. 4.30(a), we can contrast the distribution of crater depths with the hydrogen profile measured by ERD and the Si implant damage profile extracted from the RBS-C yield. Here we see good agreement between the locations of the damage, hydrogen profile and crater depths. Unlike the comparison of the profiler data with the SRIM simulations, it is clear here that the range of the crater distribution is deeper than the damage (direct scattering yield) but is in good agreement with the peak for the hydrogen profile, shown in Fig. 4.36. Unlike examples in other research [25, 27], the distribution of crater depths is not centred in the Si damage peak, but at the peak of the implanted hydrogen profile.

Conclusion

Blister depth in all samples studied was proportional to ion implantation energy. For Si(100) and Si(111), the actual ruptured blister or crater depth appears to lie closer to the peak in hydrogen profile than ion implant damage. For Ge(100), the depth of the craters appears to coincide with the end-of-range of the hydrogen implantation. The roughness of

Substrate & Implantation	Profiler Depth z (nm)	Direct Scattering Peak z (nm)	SRIM Simulation $R_P(Vacancy)$ (nm)	$R_P(HProfile)$ (nm)	E.O.R.$_{(Hydrogen)}$ (nm)
H(40keV,6×10^{16}cm^{-2},RT)-Si(100)	439-474	465	369.0	398.7	514.3
H(40keV,6×10^{16}cm^{-2},RT)-Si(111)	440-480	490	369.0	398.7	514.3
H(40keV,6×10^{16}cm^{-2},RT)-Ge(100)	462-487	335	265.7	325.6	472
H(100keV,6×10^{16}cm^{-2},RT)-Ge(100)	832-884	775	686.7	734.3	940

Table 4.5: Optical profiler measurements of hydrogen crater depths compared with RBS-C determined hydrogen implanted direct scattering peak and SRIM simulations of the same systems. R_P= Peak of the range, E.O.R. = End of Range.

Label	Substrate Wafer	Dopant	Resistivity (Ω cm)	Approx. Concent. (10^{17}cm^{-3})	Hydrogen Implant $\Phi(10^{16}$cm$^{-2})$	E (keV)
csi400	Si(100)	B	$\leqslant$0.05	$<$6.48	6	40
csi500	Si(100)	P	0.0011	652	6	40
csi600	Si(100)	As	0.001-0.005	736-124	6	40

Table 4.6: Doped Si(100) wafers used in extended blistering study in Constant Implantation Regime.

the crater floors seemed to be roughly constant for a fixed ratio of ion energy and fluence in Si(100), suggesting the peak concentration of hydrogen is more critical to the roughness than total concentration, implantation location or annealing temperature. Annealing duration decreases the roughness in Si(100) and Si(111), in addition to producing shallower craters, with the smoother, shallower craters coinciding with the slowing of blister growth rate. In Ge(100) for hydrogen implant energies E=40 keV and 100 keV, the influence of annealing duration was less clear, with a decrease in blister depth but a largely constant crater floor roughness, independent of what stage or rate hydrogen blistering was occurring.

It remains unclear whether there is a saturation level at which roughness of the crater floors remains constant, or particularly what the role of energy or fluence has in conjunction to create specific values. However much longer exposures may also result in "smoother" crater floors, it is hard to imagine how longer exposures could change the depths of the craters as seen in the T=400°C and 425°C anneals in Fig. 4.29 and 4.35 above. Despite such comments, it is reasonable to assume from the data that the temperature too has a rôle in the crater formation dynamics.

4.8 Blister dopant dependence

In addition to the intrinsic Si and Ge wafers examined in Sections 4.5 and 4.6, several series of highly doped Si(100) wafers were examined. These were device-grade Cz-grown (100) silicon wafers available commercially, with enhanced dopant levels of B, As or P, and their specifications and the applied implantation series are described in Table 4.6.

Each highly doped sample was implanted with hydrogen ions at a fluence $\Phi_H = 6 \times 10^{16}$cm^{-2} and E=40 keV, at room temperature. These as-implanted Si wafers were first cut into small samples approximately 3 $\times$ 3 mm in size using a diamond scribe. Following this,

the samples were annealed under atmospheric conditions at a range of preset temperatures (300°C < T < 650°C) upon a resistively heated hot stage. In order to ensure good thermal contact, the samples were held in place by a vacuum chuck threaded through the hot stage. As described in Chapter 3, the samples were monitored with a high definition megapixel digital web camera for the duration of the anneal, recording both initial blistering time, rate of blistering and area of the implanted sample blistered.

Blister activation energy

Contrasting the t_i of blistering/cratering upon the doped samples with intrinsic, low doped (high resistivity, 10-20 Ω cm) hydrogen-implanted Si, we see clear differences in the blistering energy requirements between the sample series. Figure 4.37 shows this comparison of annealing temperature versus initial blistering time.

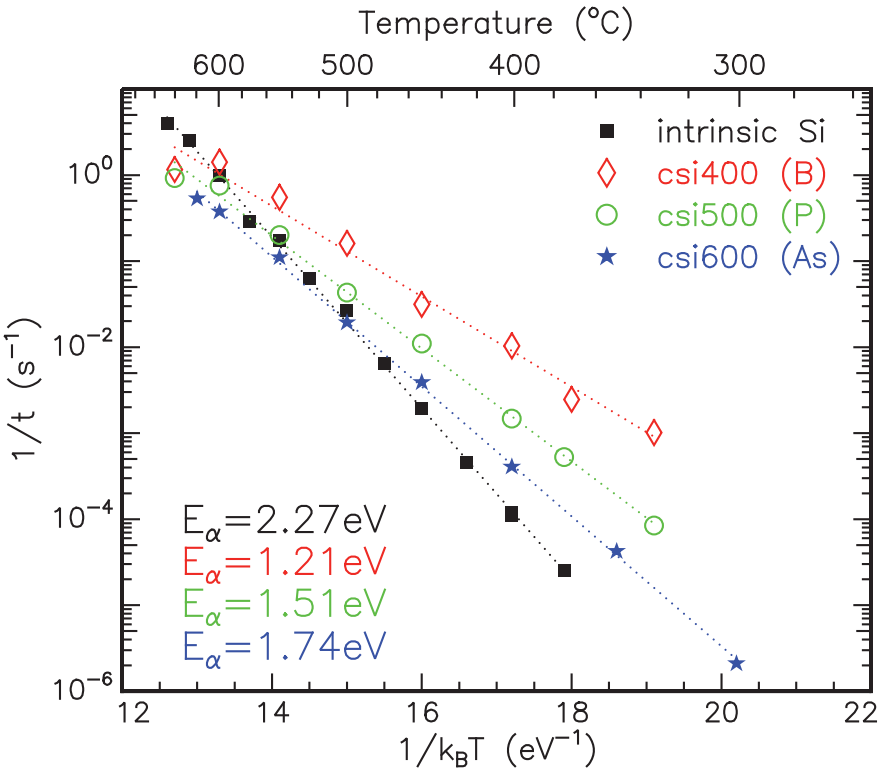

Figure 4.37: Inverse time for the onset of optically detectable blisters versus inverse absolute annealing temperature in intrinsic and doped Si(100). Due to small size relative to symbols, errors not shown. Dopant type and activation energies as labelled for each series.

For each highly doped Si wafer, the activation energy required for blistering to occur decreased from the intrinsic case. This is in contrast to predictions about the influence of

p- or *n*- type dopants by Li [142], which would expect changes in opposite directions for the two dopant types, or Henttinen [85], which would expect no change in the As doped (and presumedly P doped or any p-type) wafers. If solely based upon the concentration of dopants added to the wafer, the trend is at least consistent – higher concentrations of vacancy occupying elements produce relatively smaller changes to the blistering activation energy. However this is hardly a reasonably theory when the electronic and mass differences of the dopants are taken into account.

The p-type material doped with boron has the lowest blistering activation energy at E_a=1.21±0.06 eV, while the two n-type materials, with P or As doping, are higher at E_a=1.51±0.04 eV and 1.74±0.04 eV respectively, contrasted with that measured in hydrogen implanted i-Si, of E_a=2.27±0.18 eV. Relative resistivities do not provide a common trend between the values, while the absolute concentrations of the dopants seems to give some predictability. Were this the case, then as most theories explaining ion-cut rely on the interstitial and vacancy defects within silicon to produce the cleavage, it may be possible that the dopants are occupying vacancies and recombining with free interstitials. By preventing these defects interacting with the implanted hydrogen, the relative dopant concentrations inhibit the ion-cut process. However, all of these dopants lead to lower activation energies than intrinsic silicon. Were it the case that dopants interfere with the blistering process, all activation energies would be expected to be higher than the intrinsic, with the higher concentrations requiring greater energies. Alternatively, were these dopants to passivate those defects detrimental to the formation of hydrogen platelets within the silicon, it would be assumed that the resultant decrease in activation energy would ensure blistering/cratering occurred *sooner* in these doped materials. While the doped materials blister sooner than the intrinsic silicon at low temperature anneals, for T$\geqslant$500°C, each of the doped materials blistered slower than the intrinsic silicon.

The influence on the Fermi energy of the substrate from the dopants as proposed by Johnson *et al.* [143] lends the possibility that the activation energy is tied to this value, or changes in the crystal bond energies when dopants are introduced. While the bond energy between Si-Si is E=1.81 eV [21, 108] and Si-H has been reported between E=1.66 eV and 3.6 eV [20, 357], the bond energy for highly As-, P- or B-doped Si and H has not been clearly defined, and may lie close to the values of energy described in this work. Work by

Nickel *et al.* [103] suggests that the closer to the conduction band the Fermi level is moved, the more blistering occurs within the substrate, and their investigations indicated that the presence of no H platelets in B-doped Si but a greater number in P-doped Si. Moreover, Nickel suggests that platelets (and by extension blisters and craters) are reliant more upon electronic levels within the crystal, and cannot be induced by implantation damage alone (see Fig. 3 in [103]). If this were the case, then no blistering should have been measured in the csi400 series. In contrast, Terreault [28] asserts that n-type doping has no effect on the required fluence or temperature for blistering. If this were the case, then the activation energies of the As- and P-doped Si should be the same as the intrinsic studies. As there were blisters in the c400 and the n-type materials varied from the intrinsic silicon, clearly the system is more complicated, or portions of the previous understanding are incomplete.

Blistering rate

The rate of blister formation per unit area for all three highly doped samples is shown in Fig. 4.38. All show the same characteristic logistic function seen in intrinsic semiconductors, described by either JMAK or Gompertz (Eq. 4.5 and 4.6) functions. Similar to the intrinsic H-implanted Si(100), all show a transition between Gompertz and JMAK functions, with low temperatures better modelled by Gompertz and higher temperature anneals displaying blistering behaviour better described by JMAK. This transition between rates of blister formation occurs at approximately the same point for all samples, between T=400–450°C. Such agreement with the Si(100) sample – to say nothing of Si(110) and (111) – suggests similar governing processes taking place despite the dopants. The saturation value of areal blistering density in all doped material also appears to be limited only by the fluence and energy of the implantation, reaching ρ=2.5×10^{10}m^{-2} for all samples. This saturation value is however higher than seen in any intrinsic Si samples, approximately 2.5 times Si(100). Each comparison of JMAK and Gompertz functions with the csi400, csi500 and csi600 blister areal density per time are shown in Fig. D.11, D.12 and D.13 in Appendix D.3.

The rate of blister formation in the P-doped Si is similar to the velocity of screw and 60° dislocations in similar doped material, as reported by Imai *et al.* [358] (see Fig. 4, Chapter 3.5 in IEEE Knovel Properties of Crystalline Silicon, 2nd Edition, 1999 [359]). The similar relative rates at similar temperatures may indicate the use of particular defects

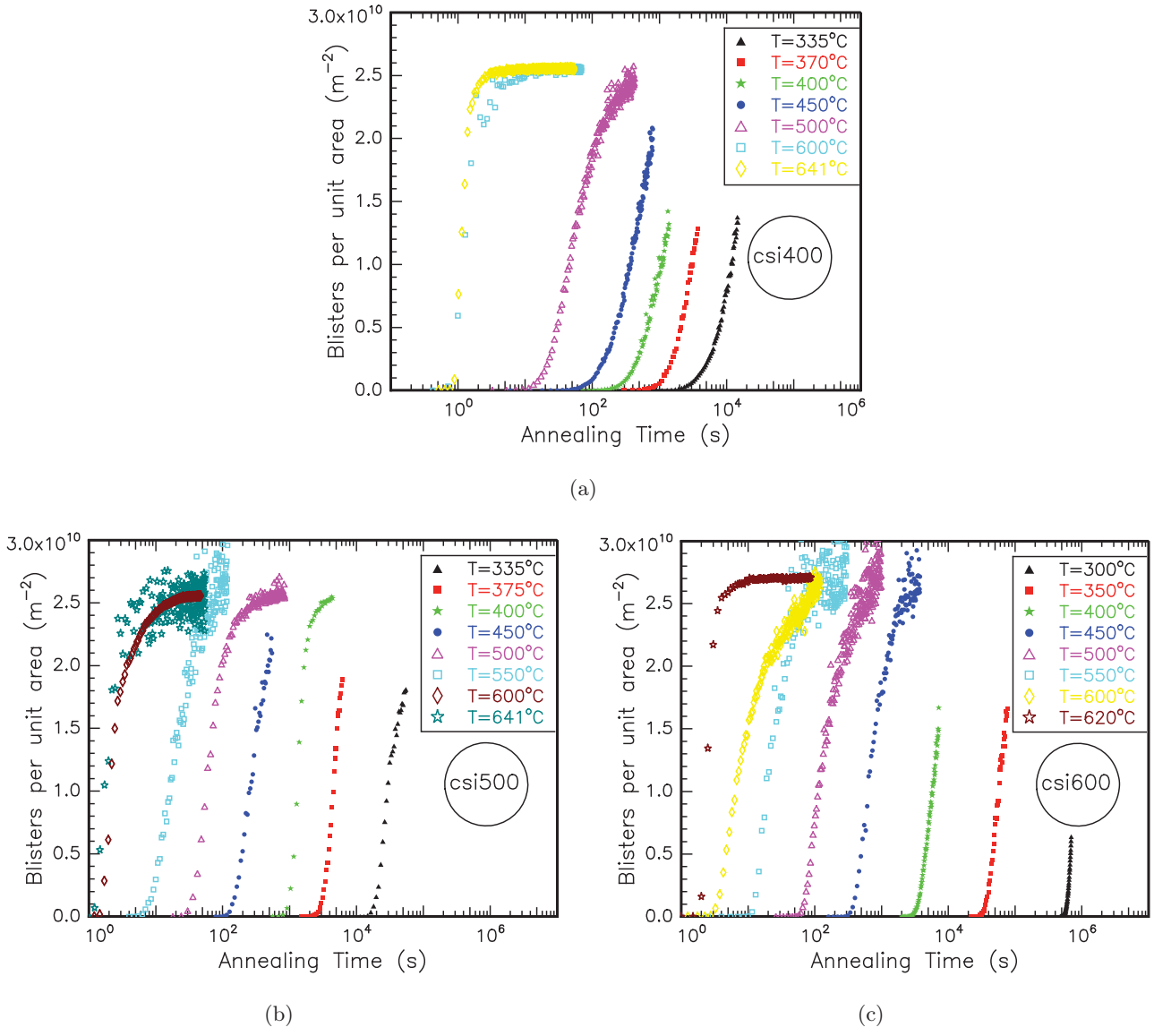

Figure 4.38: Annealing time dependence of blister formation per area in H(40keV,6×10^{16}cm^{-2},RT) implanted (a) highly B-doped, (b) highly P-doped, and (c) highly As-doped Si(100), labelled csi400, csi500 and csi600 respectively. Annealing temperatures as labelled.

to migrate the hydrogen into larger complexes. However, Imai also reports that samples doped with B have a slower dislocation velocity than intrinsic Si – the opposite effect to that measured in our work, making any potential common explanation less likely.

Ruptured blister depth and roughness

The roughness and depth of the craters formed during annealing in these highly doped wafers do not all follow the same trends as those seen in the hydrogen-implanted "intrinsic" Si(100) and Si(111) material. As shown in Fig. 4.39(a), the heavily B-doped csi400 series samples show a potentially greater crater depth when annealed at lower temperatures, as well as a rougher crater floor.

The average roughness of the crater floor appears to reach a constant value at higher anneals of Δz=19.2±0.1 nm. This value is in good agreement with that measured in Si(111) (Δz=19.74 nm) and is of the same order as that in Si(100) (Δz=14.79 nm). Even at the roughest values produced at the lower annealing temperatures, the crater floors are still close to these values at Δz=23–25 nm. At low temperatures (T<500°C), the average crater depth is z ∼458 nm, while at higher temperatures, this decreases to z ∼444 nm. The range of crater depth values is narrower than that seen in either Si(100) or Si(111), suggesting the B may act to confine the range of hydrogen platelets within the material which go on to form blisters and craters.

In the P-doped csi500 sample series, the depth of the craters decrease with increasing annealing temperature, while the roughness of the crater floors is largely constant, as can be seen in Fig. 4.39(b). The roughness of the crater floors is largely confined to the range of Δz=24–26 nm, while the crater depths start at z=477.3 nm for T=330°C annealing and decreases to z=444–449 nm by anneals at T=641°C.

This range in crater depth values (z ∼444–477 nm) is more consistent with that seen in Si(100) (439–474 nm) than csi400 (443–460 nm), suggesting P does not strongly influence the distribution of hydrogen platelets or the intrinsic silicon environment. As most other Si samples studied tend to have either a linearly varying roughness or show a step-like transition between high and low annealing temperature, the consistency of the crater floor roughness in this series is interesting and potentially useful.

Results from the As-doped csi600 sample series also differ from the intrinsic trends.

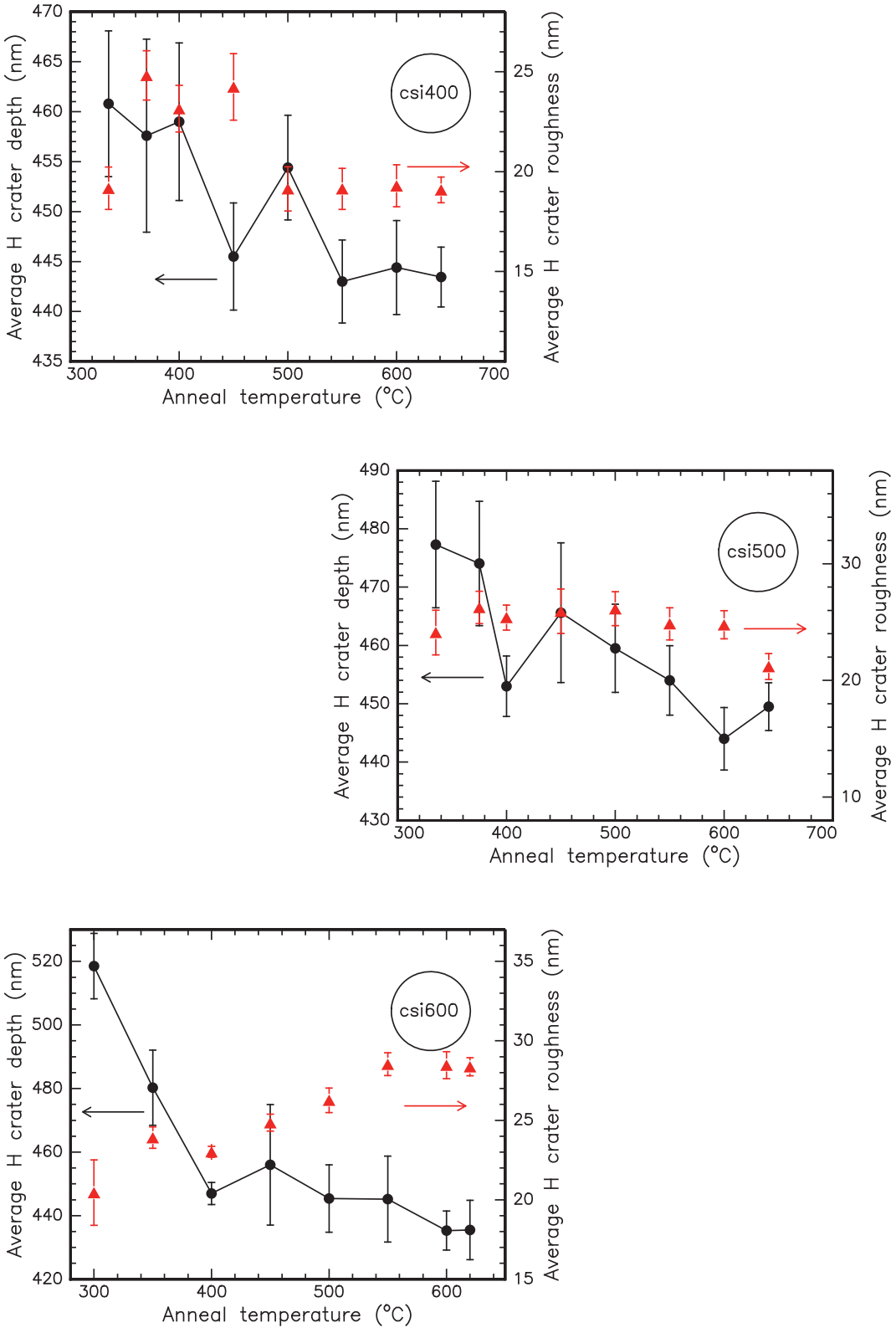

Figure 4.39: Average crater depth and floor roughness in H(40keV,6×10^{16}cm^{-2},RT) implanted blistered (top-to-bottom) B-doped Si(100) (labelled **csi400**), P-doped Si(100) (labelled **csi500**) and As-doped Si(100) (labelled **csi600**) following cessation of blistering during annealing.

While increasing the annealing temperature decreases the depth of the hydrogen craters, a linear increase to the roughness of the crater floors is seen in Fig. 4.39(c). Although the total variation in floor roughness is only ∼8 nm, the small errors in floor roughness values – determined from the standard deviation in the array of measured crater roughnesses – shows this as a clear trend. A reasonable explanation for why the craters should become rougher at higher annealing temperatures was suggested earlier – that by reaching higher temperatures sooner, the blister formation process will begin faster than hydrogen platelets can merge through slower migration of defects. If small enough regions already contain sufficient hydrogen to blister, the process will begin sooner during annealing, rather than first requiring the hydrogen to merge with surrounding platelets. As these small blisters expand and subsequently merge together, the large range of their original platelet depths will form the internal floor of the produced void. The resultant crater produced when such a blister bursts will have on average a rougher floor. This trend is not apparent in any of the other silicon samples studied, however it is possible that the high As dopant concentration uniquely present in these samples allows such dynamics.

IBA implant damage and hydrogen profiling

Figure 4.40 shows the RBS-C spectra from each of these doped Si wafers following hydrogen implantation. For contrast, the channelled and randomly angled spectra from intrinsic Si are shown, as is the spectrum from a hydrogen-implanted intrinsic Si wafer.

Clearly the yield (χ) from the implanted csi400 material is higher than that of the csi500 and csi600 material, and all are lower than the intrinsic Si. Lower RBS direct scattering (DS) yields from p-type doped samples has been reported elsewhere [85, 121, 122], with a concomitant increase in yield in the near-surface dechannelling (DC) yields, which is associated with formation of blister precursors. The data in our study shows the decrease in the DS yield, but no increase in DC yield. The csi400 yield is more in line with the values measured in intrinsic Si(100) implanted with the same ion fluence and energy, and actually has a smaller DC χ component. While inconsistent with predictions, our IBA data is in good agreement with the results revealed by the optical profiler, showing that the crater depths occurred in a similar range for both csi400 and intrinsic silicon. Both csi500 and csi600 show very similar DS and DC yields, with an average yield nearly 50% lower than the H-implanted intrinsic Si, and their peak in the DS yield occurs slightly

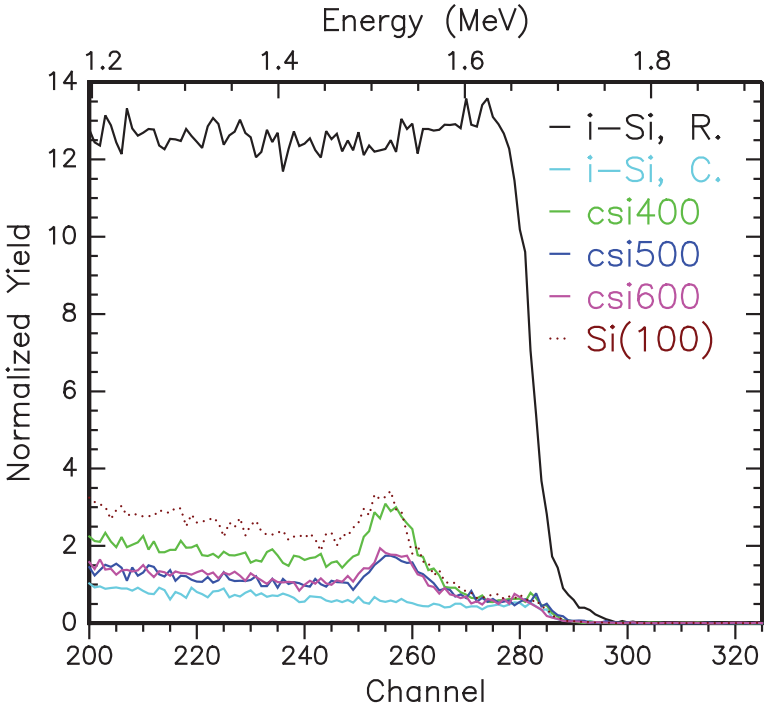

Figure 4.40: 3 MeV $^4He^+$ RBS-C spectra from as-implanted H(40keV,6×10^{16}cm^{-2},RT) in B-, P- and As- doped Si(100). Random angled (**R.**) and channelled (**C.**) yields from intrinsic silicon shown for comparison; also shown spectra from H(40keV,6×10^{16}cm^{-2},RT)-Si(100). Details: IBM Geometry, θ=0°, ϕ=11.68°, Q=20 μC, I=15 nA.

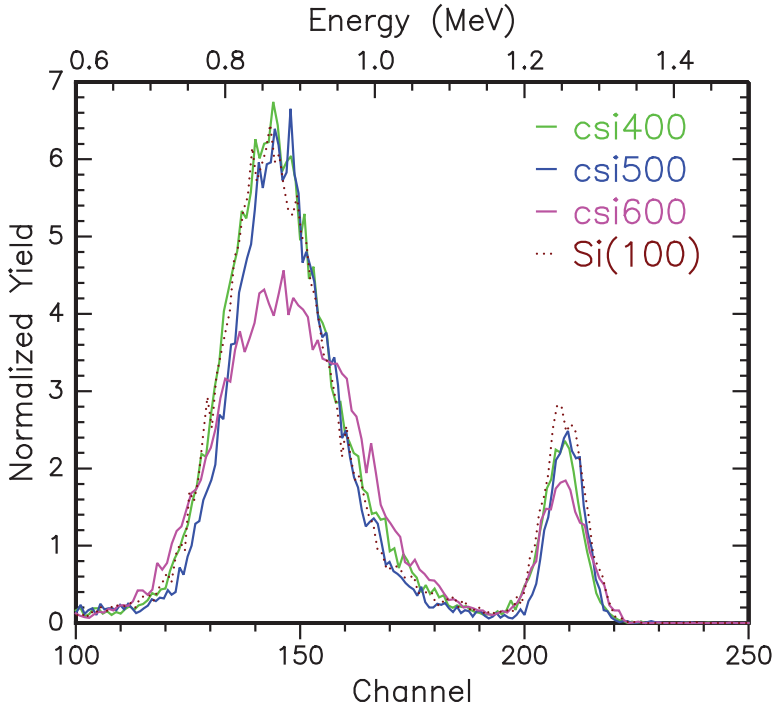

Figure 4.41: 3 MeV $^4He^+$ ERD spectra from as-implanted H(40keV,6×10^{16}cm^{-2},RT) in B-, P- and As- doped Si(100). For comparison, the H(40keV,6×10^{16}cm^{-2},RT)-Si(100) spectra is included. Detector & scattering angles ϕ=25°, sample tilted θ=80° to incident beam, I=23 nA, Q=20 μC.

deeper than the csi400.

The complementary ERD measurements, shown in Fig. 4.41, both confirm and expand upon the trends seen in RBS and optical profiling. The B-doped csi400 samples and H-implanted i-Si both show good agreement in hydrogen concentration and peak location, confirming RBS and OP findings. The As- and P-doped samples have a 10% lower net hydrogen concentration than in the B-doped and intrinsic Si, in agreement with RBS. The FWHM of the hydrogen profile in intrinsic Si, B- and P-doped samples are all approximately equal (∼150 nm), which may explain similar range of crater depths in the OP measurements. Similarly, the width of the csi600 As-doped H-profile was the largest in the samples, similar to the largest range of crater depths seen by the optical profiler. However, the hydrogen profile in As-doped csi600 material is skewed across a shallower depth range than in the other samples, and does not reach the greatest depth of craters measured in it by OP. If we consider the average crater depth measured in csi600 following higher temperature anneals, the ERD profile is in reasonable agreement with the OP measurements. The ion beam damage profiles in the P- and As-doped Si as measured by RBS were very similar, but the hydrogen distributions are quite different in peak location and FWHM.

The data from these two IBA techniques is collated and compared to the values of the optical profiler in Table 4.7. This array details the measured RBS-C DS peak depths and damage concentrations along with the hydrogen profile peak R_P depths derived from ERD measurements. Clearly, there is a significant margin of error around the values for the hydrogen profile depth, due to fitting difficulties and lack of a standard for the ERD technique and analysis tools. Also, the profile concentration itself shows serious variation, such that a 10% deficit of implanted hydrogen is seen in the P- and As-doped series. These data do confirm the lack of a direct link between implantation ranges and the dimensions of the craters. The depths and roughness values of the hydrogen-induced craters as measured by optical profilometry occupy a much smaller depth range than either the FWHM of the RBS-C-measured DS (=ion damage) or ERD-measured hydrogen profiles. This suggests that the necessary conditions for hydrogen platelets and associated defects to interact and form hydrogen blisters (and craters) are restricted to a narrower window than the range of implanted damage or sufficient hydrogen concentrations. Perhaps the requirements for blistering are so high that only the small region around the peaks in either profile provide

Sample &	RBS-C Direct Scatter Yield			ERD H Profile Yield			Crater Optical Profilometry			
Dopant	R_p (nm)	C_{DS} ($\times 10^{21}$cm^{-3})	FWHM (nm)	R_p (nm)	Areal ρ* ($\times 10^{16}$cm^{-2})	FWHM (nm)	Depth z (nm)	z Range (nm)	Roughness Δz (nm)	Δz Range (nm)
csi400 - B	465±25	2.89	155	438±25	6.23	151±5	(443 - 461)	17.8	19.1–24.8	5.74
csi500 - P	450±30	1.92	184	431±20	5.51	148±5	(444 - 477)	33.3	21.2–26.2	5.06
csi600 - As	465±35	1.60	180	419±30	5.45	221±6	(435 - 518)	83.0	20.5–28.5	8.08

Table 4.7: RBS-C determined direct scattering (=ion implantation damage) peak depths, concentrations and FWHM, along with ERD determined H R_p and hydrogen profile FWHM, compared with OP measured crater depth and roughness ranges. *:ERD areal density concentrations calculated assuming Si(100) comparison sample shown in Fig. 4.41 is a reliable standard of Φ=6×10^{16}cm^{-2}.

viable conditions. From the data, it is unclear if the craters are forming closer to the peak depth of the damage or the hydrogen profiles. It appears that the depth lies between the two peaks, tending towards greater depths at lower annealing temperatures. There is possibly a weak relationship between depth of the craters (and marginally between the roughness of the crater floors) and the FWHM of the hydrogen profile.

Conclusion

Dopants play a quantifiable rôle in influencing the hydrogen evolution during the annealing process. The deviation in terms of blistering activation energies is the most notable, as is the shifts in ion implantation scattering centres and hydrogen profiles. Any variation measured however failed to have a significant effect on the eventual hydrogen crater depths and roughnesses. Dopants may thus be used as tools to beneficially modify the ion-cut process in, for example, circumstances where lower thermal annealing budgets are available, expediting the rate of crack formation. Individual influences of the dopants upon other electronic and mechanical properties of the semiconductors to which they are applied would naturally still have to be carefully considered. The rôle these dopants – B, As or P – would play in Ge(100) or composite substrates has yet to be explored, but may prove of interest for future work.

Chapter 5

Stress effects on hydrogen in semiconductors

In this chapter, we explore the rôle external stress influences the behaviour, diffusion and evolution of the hydrogen implanted within semiconductors. Such external influences have two major forms – structural modifications of the substrate wafer, and mechanical stresses applied to the wafer.

The first application of stress was via the structural modification caused during ion implantation and annealing, examined in Section 5.1. This section explores the impact of ion implantation and subsequent annealing upon the curvatures of a series of semiconductor wafers.

The second means of stressing the system, making up the bulk of the chapter from Section 5.2 onward, was achieved via two methods of applied mechanical force. The first of these techniques, featured in Section 5.2, was elevating and depressing sections of the implanted wafer with a series of tantalum clips and wafer stacks during implantation. This was applied to standard, single side polished ∼375 μm thick Si wafer. The use of these wafers was limited to application of tensile stress during implantation or annealing. Application of any significant compression led to cleavage due to propagation of cracks from imperfections in the unpolished side of the wafer.

In order to transition to a study in ULTRATHIN® 50 μm Si(100), a comparison was made between hydrogen behaviour in bulk 375 μm and 50 μm silicon wafers. This com-

parison in Section 5.3 establishes that results determined in either substrate are likely to be equally applicable in both wafer types.

In Section 5.4, the second method of applying mechanical stress was investigated, using a specially designed apparatus where the samples were compressed between two "jaws" by application of a Vernier-driven screw. This mechanical technique was limited to using double side polished, ULTRATHIN® silicon wafers, to allow sufficient distortion of the wafers during implantation and/or annealing without destruction of the sample.

5.1 Implantation induced stress

As described earlier, the heart of this work requires at the least a comparison of the stress induced by ion implantation of the key materials. The magnitude of later applied mechanical stress and its effects will be better understood if we establish some relative gauge of the external and local stresses in the materials produced by ion implantation.

5.1.1 Experimental methods

This preliminary study of the stresses induced was concerned with the ion implantation process and subsequent annealing effects, in contrast to intrinsic stress present. The materials involved were 375 μm and 50 μm Si(100) and Ge(100), each implanted with hydrogen ions at E=45 keV and $\Phi_H = 3 \times 10^{16}$ cm^{-2}. This implantation fluence was selected to lie below the threshold at which hydrogen blistering is expected to occur, in order to study the effects of the stresses without potential release through plastic modification of the surface during blistering, or catastrophic rupture or cratering of the material.

Firstly, samples were cleaved from the source wafers into strips of material approximately 5×18 mm. Three samples were cut in each original wafer, to allow comparison of variations within each substrate medium. Secondly, samples were implanted with the energy and fluence, as listed above, on the low energy implanter. Samples were at room temperature during the implantation, and the beam current was kept at ∼3-5 μA to minimise the potential for any beam heating. During implantation, the strips were held on the implanter block at only one end, to allow any potential distortion induced to be unimpeded. Thirdly, the samples were annealed at T=400°C/10 minutes in an Ar gas ambient

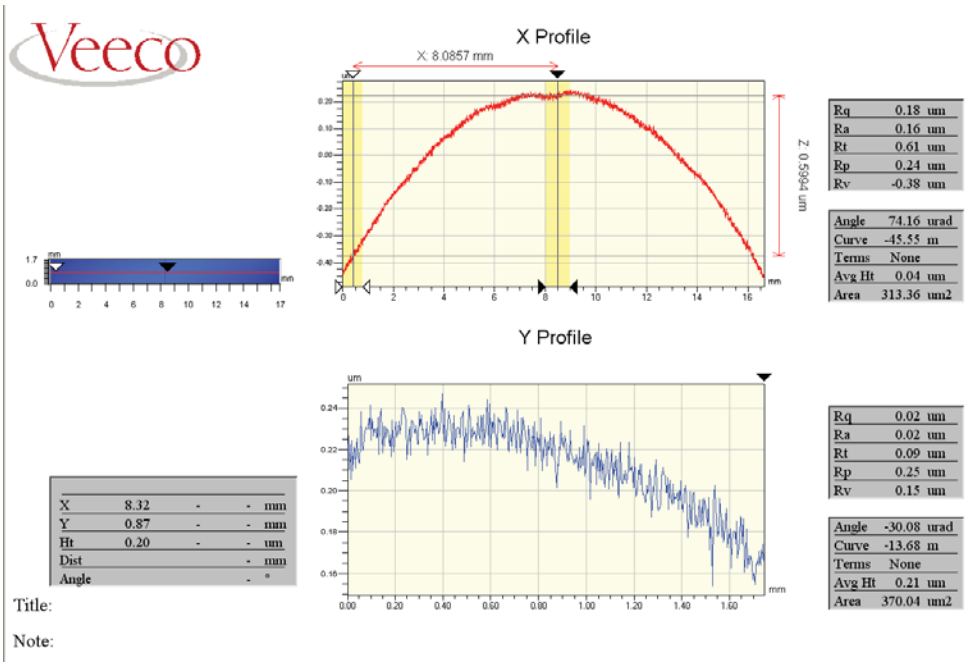

Figure 5.1: Screen capture of Veeco Vision32 software measuring the curvature of a semiconductor wafer (i.e., H(45keV,3×10^{16}cm^{-2},RT)-impl. Si(100) As Implanted) using vertical scanning interferometry mode. Curvature value shown in 2$^{\text{nd}}$ table on right.

within a quartz tube furnace, with gas flow at $\sim$1 cm^{3}s^{-1}. This flow rate was selected to approximate laminar, non-turbulent flow. Each sample underwent the processes of implantation and annealing separately. As such, a greater confidence is given to the observation of any trends apparent in the specimens.

Following each step of cleavage, implantation and annealing, the samples were examined using the Wyko optical surface profiler, using Vertical Scanning Interferometry (VSI) mode, a $\times$5 optical lens and the Field of View (FoV) set at $\times$0.55. Scans were performed over the whole length of the samples using the proprietary Vision32$^{\text{TM}}$ software [315]. With the cursor width set at 1 mm, the radius of curvature of the sample along the major axis of the samples was measured, as depicted in Fig. 5.1. From this value of curvature, the gross stress at points within the wafer could be calculated, using finite element bending equations as determined by Euler-Bernoulli [270] and used by Rudawski *et al.* [268].

Si(100) 375 μm	Initial Conditions		As Implanted				Post Annealing			
Sample Dimensions (mm^2)	r_c (m)	σ (kPa)	r_c (m)	Δr_c (m)	σ (kPa)	$\Delta\sigma$ (kPa)	r_c (m)	Δr_c (m)	σ (kPa)	$\Delta\sigma$ (kPa)
4.1×17.9	160.0	199	45.6	−114.4	669	+470	66.7	+21.1	478	−191
5.5×18.0	-69.5	-459	41.6	+111.1	766	+1225	-143.5	−185.1	-222	−988
4.7×18.0	-39.8	-801	-48.7	−8.9	-655	+146	-32.4	+16.3	-985	−331

Table 5.1: Radius of Curvature (r_c) and stress (σ) present in cleaved 375 μm thick Si(100) strip samples, following ion implantation of H(45keV,$3\times10^{16}cm^{-2}$,RT), and post annealing at T=400°C/30 minutes in Ar ambient quartz tube furnace. Strip sizes as labelled, curvature along major axis, positive stress indicates convex curvature, negative concave. Δ values indicate relative change in sample state from previous measurement.

Si(100) 50 μm	Initial Conditions		As Implanted				Post Annealing			
Sample Dimensions (mm^2)	r_c (m)	σ (kPa)	r_c (m)	Δr_c (m)	σ (kPa)	$\Delta\sigma$ (kPa)	r_c (m)	Δr_c (m)	σ (kPa)	$\Delta\sigma$ (kPa)
5.1×18.5	15.5	274	0.89	−14.6	4775	+4501	1.34	+0.45	3184	−1591
3.8×19.7	16.0	265	1.16	−14.9	3664	+3399	1.67	+0.51	2553	−1111

Table 5.2: Radius of Curvature (r_c) and stress (σ) present in cleaved ULTRATHIN® 50 μm thick Si(100) strip samples, following ion implantation of H(45keV,$3\times10^{16}cm^{-2}$,RT), and post annealing at T=400°C/30 minutes in Ar ambient quartz tube furnace. Strip sizes as labelled, curvature along major axis, positive stress indicates convex curvature, negative concave. Δ values indicate relative change in sample state from previous measurement.

Ge(100)		As Cleaved	As Implanted	As Annealed
Sample 1	$r_{curvature}$ (m)	60.4±6.8	27.2±1.6	30.6±8.1
4.6×18.7mm	**Stress σ (kPa)**	**429±75**	**954±139**	**848±250**
Sample 2	$r_{curvature}$ (m)	610±20	58.4±10.4	43.6±2.4
6.1×18.8mm	**Stress σ (kPa)**	**43±6**	**444±99**	**595±86**
Sample 3	$r_{curvature}$ (m)	155±40	39.5±7.8	37.3±2.8
5.8×19.4mm	**Stress σ (kPa)**	**167±49**	**657±156**	**696±106**

Table 5.3: Curvature and intrinsic stress present in cleaved 375 μm thick Ge(100) strip samples, following an ion implantation of H(45keV,3×10^{16}cm^{-2},RT) and annealing at T=400°C for 30 minutes in the Ar ambient of a quartz tube furnace. Strip pieces as labelled, curvature along major axis, positive stress indicates convex curvature, negative concave. Young's Modulus for Ge: E=138 GPa

5.1.2 Analysis

Tables 5.1, 5.2 and 5.3 show the values of radius of curvature and equivalent stress at each stage for the 375 μm Si(100), 50 μm Si(100) and 375 μm Ge(100) strips respectively. These stress values do not account for potentially large local stresses that may form around point or extended defects within a specimen. The stresses compared in each stage are rather the gross or global value (effectively the median) in the specimen, producing the measured wafer curvature.

After the initial cleaving of the bulk Si(100) wafers, the radius of curvature of the samples was quite large. There were both positively curved (convex) and negatively curved (concave) samples resultant from the same original wafer. There was significant difficulty in achieving reproducible results in this wafer type. The variation in stress was significant, across nearly six orders of magnitude.

Following ion implantation of the samples, the radius of curvature value across each wafer was much more consistent, if not in direction of curvature. This would suggest that the overall effects of the implantation are of sufficient magnitude to overcome any residual stresses caused by the cleaving process.

It is difficult to ascertain exactly what the behaviour of the Si(100) is due to each step in the process – as each different sample respond with different magnitudes and directions at each step. On the local scale, it is very difficult to readily account for the effects of individual point and extended defects produced by ion implantation. Overall, the magnitude of gross stresses induced in the Si was only ever on the order of hundreds of kilopascals. These

stresses are significantly lower than any of the stresses applied mechanically ($\sim$ 100 MPa) explored later in this study.

The Ge(100) wafers, with a thickness of 375 μm, were expected to manifest similar curvatures as those measured in bulk Si(100), due to the common implantation conditions. The initial spread of wafer curvature values in the as-cleaved state was broad, with wafers ostensibly appearing "flat". The ion implantation was the most significant influence on these samples, as all samples shifted to smaller positive (convex) curvatures of similar magnitude, exhibiting tensile stress. The values of stress at each stage are on the same order of magnitude as those determined in bulk Si(100).

In the samples cleaved from the 50 μm thick Si wafer, there was a much more significant and uniform curvature recorded. Both samples were observed to curve or bow upwards with convex curvature relative to the implantation, indicating tensile stress.

Assuming that the same global stress would be present in the samples due to the same implantation conditions and wafer material, it was expected that following implantation a significantly larger curvature would be seen than that measured in the 375 μm samples, due to the greater effect of tension applied to a thinner wafer. The radius of curvature in each sample significantly decreased to approximately 5$-$7% of the intrinsic value. Most notable however, is that the actual stresses experienced by the thin wafer are *an order of magnitude higher* ($\sim$MPa) than those measured in the same implanted bulk silicon wafer. This unusual result suggests that the net stress experienced by these wafers is not solely due to the implantation fluence, ion energy, or material, but that the wafer's dimensions also have some influence. The explanation for this is unclear.

When the samples underwent annealing at T=400°C for 30 minutes, a relaxation of the wafers was observed in both bulk and thin Si, as well as Ge(100). The change, though small, still indicates that the anneal allowed factors causing the tensile stress to be diminished. Despite some relaxation in the samples, significant stress is still present.

Volkert [242] reports that ion implantation-related stresses tend to increase until the amorphisation threshold is reached, requiring temperatures close to the material's melting point to relax, and a number of other studies [208,360–362] all show annealing temperatures in excess of T$\geq$750°C to either reduce or eliminate these defects.

Simulations of our implantation conditions by SRIM [251] suggest our Si(100) samples have a similar magnitude of vacancy-type defects to those reported by Castrillo *et al.* [363], although our lower annealing temperature means simpler defect types and fewer large complexes. It is expected that the T=400°C anneal applied in our study will remove point defects but not larger defect clusters (interstitial or vacancy based), which will continue to have some stress fields associated with them.

Considering these previous studies and our data, it is quite likely that defects are present and producing the stress, while the annealing process has not significantly influenced the stress. The values of stress in these samples is likely primarily to be due to the implantation.

Ultimately it is important to note that the global stress values produced by ion implantation in all sample types – 375 μm and 50 μm Si(100) and Ge(100) – are still at least two orders of magnitude lower than that applied externally in the later mechanical stress study.

5.1.3 Summary

Across all three sample materials studied, the ion implantation played a significant influence on the curvature of the selected samples. While there was some inconsistency in the findings from bulk Si(100), all ULTRATHIN® Si(100) and Ge(100) wafers showed ion implantation increased the positive, convex curvature of the wafer, applying a tensile stress upon the implanted face. Subsequent annealing is clearly shown to relax some of the stress within the ULTRATHIN® Si(100), and this trend was weakly visible in Sample 1 of the Si(100) and Samples 1 and 3 of Ge(100). It was shown that the ion implantation produced global stresses of two or three orders of magnitude higher than that present across the material natively, and annealing produces small, usually relaxation effects upon the tensile stress-induced curvature. However, all the stress values induced macroscopically by either the implantation or annealing are several orders of magnitude lower than those which are applied mechanically in this study, determined in Section A.1. Thus the large scale influence of these stresses is not anticipated to be significant in later applied stress studies.

5.2 Mechanical stress in 375 μm thick Si(100)

5.2.1 Experimental methods

As an initial test of the effects of stress on hydrogen blistering in silicon, a 375 μm bulk Si wafer was implanted with $\phi_H = 3 \times 10^{16}\text{cm}^{-2}$ at E=40 keV while placed under mechanical tension. Tension was achieved by bending the wafer over a pyramidal pivot produced from three small pieces of wafer, and affixing both extremes with Ta mounting clips (see Fig. 5.2). This produced a minimum radius of curvature of r_c=205±19 mm, and a complementary tensile stress of σ=156±17 MPa, calculated with Eq. A.3/5.1. This sample was then examined by RBS-C and cross-sectional transmission electron microscopy, to characterise the hydrogen platelet density and alignment. The data from this sample can be compared with other work to establish if the behaviour of implanted hydrogen has been changed, allowing extrapolation of the overall reproducibility of these effects in other mechanically stressed Si wafers. Further work on similarly fabricated samples would provide greater certainty in the results.

5.2.2 Analysis

RBS-C measurements along the three primary crystal axes – [100], [110] and [111] – are shown in Fig. 5.4. These show a lower yield in the mechanically stressed wafer than in the equivalent unstressed implanted wafer when measured along the [110] crystal axis, as shown in Fig. 5.4(b). However, there are marked increases in the yield from both the [100] and [111] crystal channels, seen in Fig. 5.4(a) and (c) respectively. As this is prior to any annealing, these data solely measure the variation in the lattice (i.e., damage) induced by the implantation itself.

Dechannelling in RBS-C reveals both the fraction of interstitial atoms present within that channel, in addition to the influence upon the analysed channel of distortions in the other complementary crystal planes [364]. Hydrogen cannot be directly measured by RBS using He, as $m_{\text{H}}<m_{\text{He}}$, and only dislodged wafer substrate atoms (in this case, Si) will have any effect. The implanted hydrogen forms platelets aligned with each of the crystal axes, and as the platelets produce a much greater expansion of the lattice out of their plane than along it, this can lead to lattice registry misalignment for complementary channels

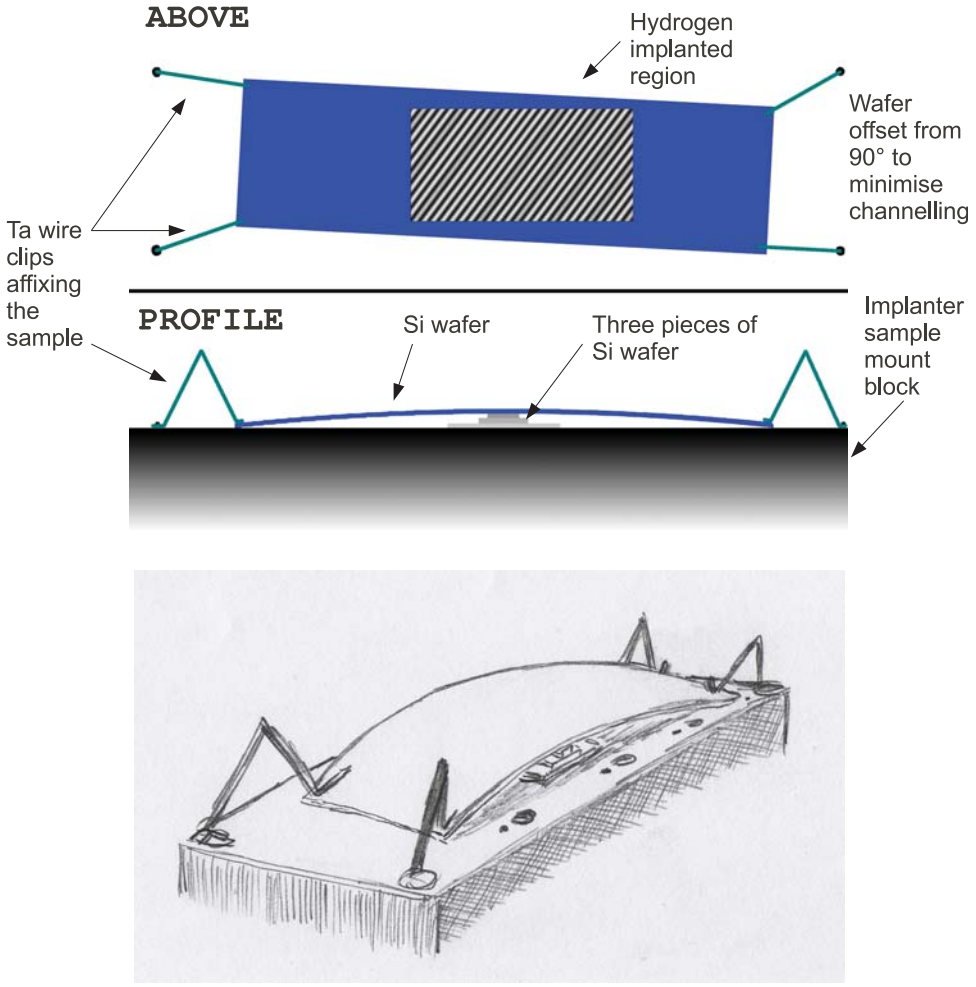

Figure 5.2: Proportional schematic diagram (top) & forced perspective sketch (bottom) of stress application process for intrinsic bulk Si(100) wafer during hydrogen ion implantation of H(40keV,3×10^{16}cm^{-2},RT) as described in the text.

(e.g. {001} platelets distort the [110] and [111] channels – shown for all wafer planes in Appendix E.1).

If the incident beam is orthogonal to the platelets (i.e., if the platelets lie in the plane described by the beam's vector), they will not have significant effect on the beam yield. However, the out-of-plane distortion increases the yield of any beams probing along either complementary axis (e.g. [110] or [111] for {001}-aligned platelets). This effect is illustrated in Fig. 5.3, showing how {001} and {111} platelets in Si(100) affect the dechannelling (DC) and direct scattering (DS) yields from channelled RBS analysing beams.

There may be influence along each channel due to interstitials caused by the implantation, however these will nominally be the same between the stressed and unstressed wafer.

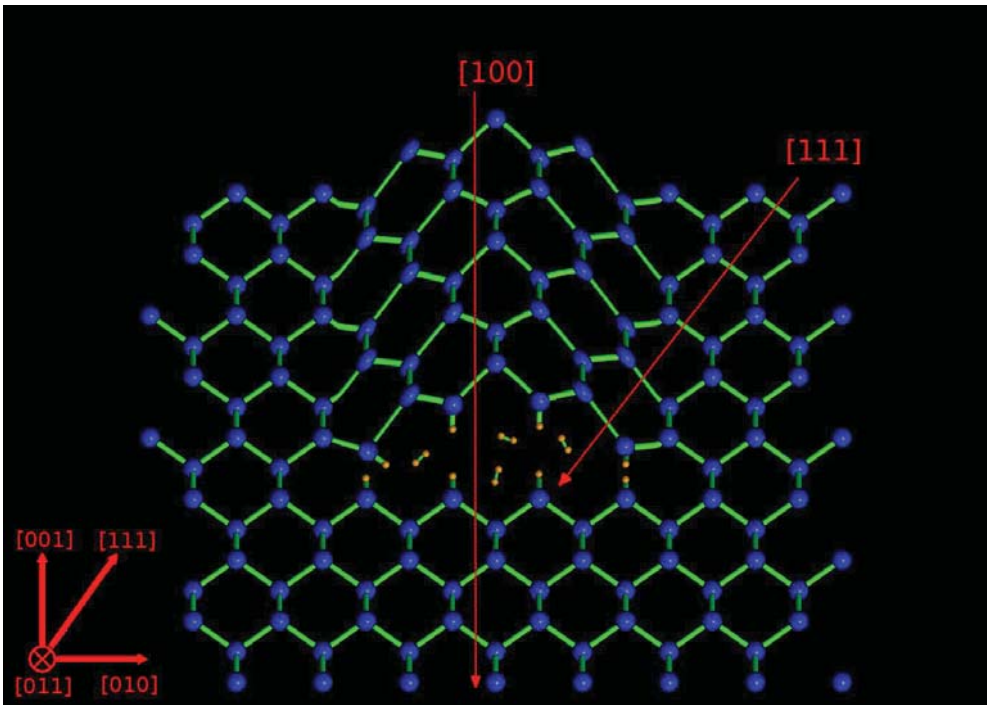

(a) ⟨001⟩ platelet

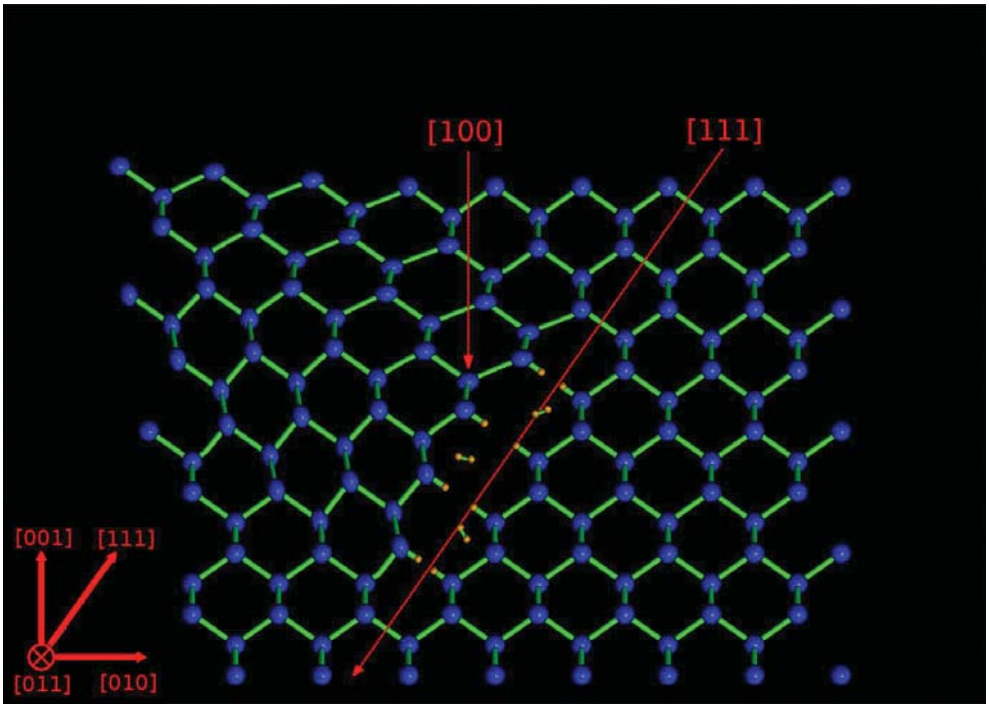

(b) ⟨111⟩ platelet

Figure 5.3: Two-dimensional lattice illustration of hydrogen-stabilised platelet defects in Si(100), with platelets aligned with (a) (100) and (b) (111) planes, probed by channelled analysis beams. Influence of registry shift in crystal lattice on ion beam shown for beams perpendicular and parallel to platelet alignment. Blue and orange spheres represent Si and H atoms.

Channel Orientation	[100]	[110]	[111]
Unstressed $C_{Defects}$ (cm^{-3})	6.39×10^{20}	2.57×10^{21}	5.79×10^{21}
σ=156 MPa $C_{Defects}$ (cm^{-3})	8.49×10^{20}	2.04×10^{21}	1.15×10^{22}

Table 5.4: Comparative hydrogen ion implantation-induced silicon damage density, as determined by RBS-C, for H(40keV,$3\times10^{16}cm^{-2}$,RT) implanted Si(100) in under stressed and unstressed conditions, along three crystallographic axes.

Hence, any difference is due to changes in the hydrogen platelet defects.

With the yield from all three major axes analysed here and assuming the majority of RBS-C yield is due to distortion by platelets in channels other than the one analysed, it seems possible to deduce where the largest concentration of platelets formed.

These defects, assumed to be platelets, show little effect upon [110] channelled beams, but significantly increase the [100] and [111] yields. The lower [110] yield when the sample was under stress, plus the corresponding increased yield observed in the [100] and [111] suggests that most defects are forming along [110] planes.

The variation between channels is also displayed in the integrated yield of the DS peaks, shown in Fig. 5.4(d-f). The $\langle 110\rangle$ channel yield from the stressed implant is lower and also marginally narrower than the unstressed implantation's damage profile. In contrast, the $\langle 100\rangle$ and $\langle 111\rangle$ channel spectra show >10% larger damage peak yields, and commensurate increases in profile depth and range. The integrated yield of the DS peaks, describing the implantation damage in each channel, is shown in Table 5.4. DS yield values are of the same order as those predicted by Monte Carlo simulation program SRIM [251] ($N \sim 1.7\times10^{21}$ cm^{-3}) for the unstressed wafer.

The differences in DC and DS yield allow us to conclude that the applied stress has influenced the number, alignment or both of the defects. Tensile stress appears to increase the number of platelets aligned along $\langle 110\rangle$, and possibly produce a small decrease in platelets aligned along $\langle 100\rangle$ and $\langle 111\rangle$.

XTEM was performed on the stressed sample in the as-implanted state. A 3 mm^2 section of the implantation was excised, glued face-to-face with G1 epoxy, polished down to 10 μm with abrasive SiC paper and Gatan dimple polisher, and ion milled to electron transparency in a Gatan Precision Ion Polishing System (PIPS). The cross-sectional sample

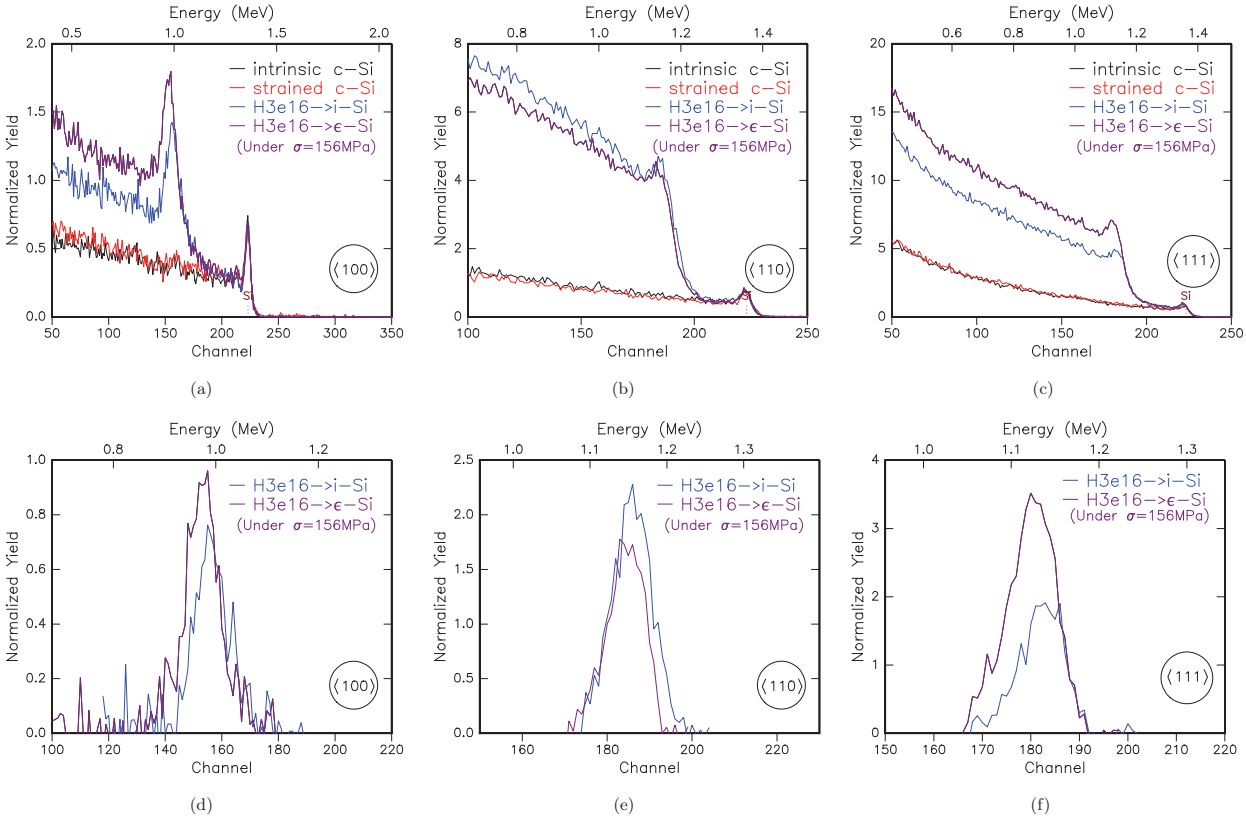

Figure 5.4: 2 MeV $^4He^+$ RBS-C spectra from 2 samples implanted with H (40keV,3×10^{16}cm^{-2},RT), in stressed & unstressed systems, along (a) [100], (b) [110], and (c) [111] channels, measured in glancing geometry where scattering angle ϕ=110°. Also shows yield from i-Si on both wafers. Isolated direct scattering peak yields, extracted from (a-c), shown as measured along (d) [100], (e) [110] and (f) [111] crystal axes.

was examined upon a Philips CM300, at a High Tension voltage of V=300 kV, in bright field (BF) condition, and the sample tilted off Zone Axis (OZA) to maximise contrast between the substrate and defects caused by the hydrogen implantation.

Figure 5.5 shows the cross-section from the surface down past the depth z of the implantation. The surface of the sample is marked by an arrow in the upper left corner. The range spanned by the implantation, marked on the micrograph with a "H", is 124±11 nm ($0.39\pm0.01 < z(\mu\text{m}) < 0.54\pm0.01$).

Contrasting these numbers with values in SRIM and IBA, there is a reasonable match with the simulation and good correlation with the complementary techniques. SRIM predicts a peak in the hydrogen profile at z=397 nm, with accompanying damage distribution peaking at z=374 nm, with end of ranges (EOR) of z=537 nm and z=517 nm respectively. The second half of both predicted distributions (i.e., the section after the profile peak value) coincides with the range of H-related defects seen in the XTEM micrograph. RBS-C revealed (as shown earlier in Fig. 5.4(d-f)) that the depth of the damage ranged from z=390 nm to 560 nm, in excellent agreement with the values taken from the XTEM micrograph. This suggests that the damage may define the location of these hydrogen platelets more so than the original distribution of the implanted hydrogen profile.

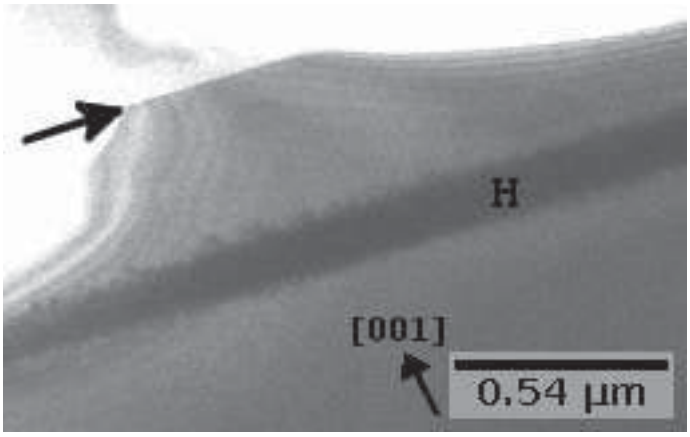

Figure 5.5: XTEM bright-field zone axis micrograph of Si implanted with H (40keV,3×10^{16}cm^{-2},RT), under σ=156±17 MPa stress. Crystal planes labelled, arrow indicating surface, H indicates hydrogen implantation range. In-micrograph scale as labelled.

Compared to previous results [28,105,107,365,366], a noticeable increase in hydrogen platelets in the {111} plane are seen in the XTEM micrograph in Fig. 5.6. While there was still a sizable number of both {001} and {111} platelets, comparisons with previous works indicate a modification of the expected hydrogen platelet distribution found at implantation. This also seems to have some agreement with the RBS-C analysis, suggesting that the increased

DS signal in [100] (and possibly [111]) is due to a larger fraction of platelets lying on the (111) plane, while the large number of {001} platelets accounts for the increase in [111] yield independently. Due to the XTEM sample's plane of cleavage being perpendicular to [110], we cannot easily resolve the fraction of platelets aligned to [110]. However, this does not rule out the possibility that large numbers of defects have formed in alignment with that direction.

Conclusion and next steps

Applying tensile stress influences platelet distributions. Following this assessment of behaviour of hydrogen defects and platelets modified within a bulk silicon environment under moderate gross stresses, the potential to apply more extreme global stresses to thinner silicon wafers presents itself. In order to allow meaningful comparisons with previous work in the literature, first the relative behaviour of hydrogen within bulk thickness and ULTRATHIN® silicon wafers under ion-cut like processes must be compared.

5.3 Silicon substrate thickness comparison

In order to assess the influence of the different substrate thicknesses upon the ion implanted distribution and subsequent hydrogen evolution, a regular 375 μm and an ULTRATHIN® 50 μm Si(100) wafer were simultaneously implanted with the standard conditions of this project – H(40keV,6×10^{16}cm^{-2},RT) – then analysed in both the as-implanted state and following annealing. While neither wafer was expressly under stress during the implantation, only one side of the ULTRATHIN® wafer was pinned down on the sample holder, and the bulk wafer overlapped the end of the 50 μm wafer within the implant region. This slight offset in angle may be insignificant, however the thermal contact of the wafer with the Ta holder may have lead to different behaviour during the implantation. As the implantation energy was E=40 keV, and the beam current of the ions I=2.4 μA, even if the entire beam energy was absorbed by the thick wafer, this would only amount to P=0.1 W, and unlikely to impact on either the implantation or the evolution significantly.

Contrasting the simultaneously performed implantation profiles of hydrogen into a 375 μm thick Si and an ULTRATHIN® 50 μm using ERD, as shown in Fig. 5.7, we see excellent agreement. The total concentration found in both sample spectra, as well as

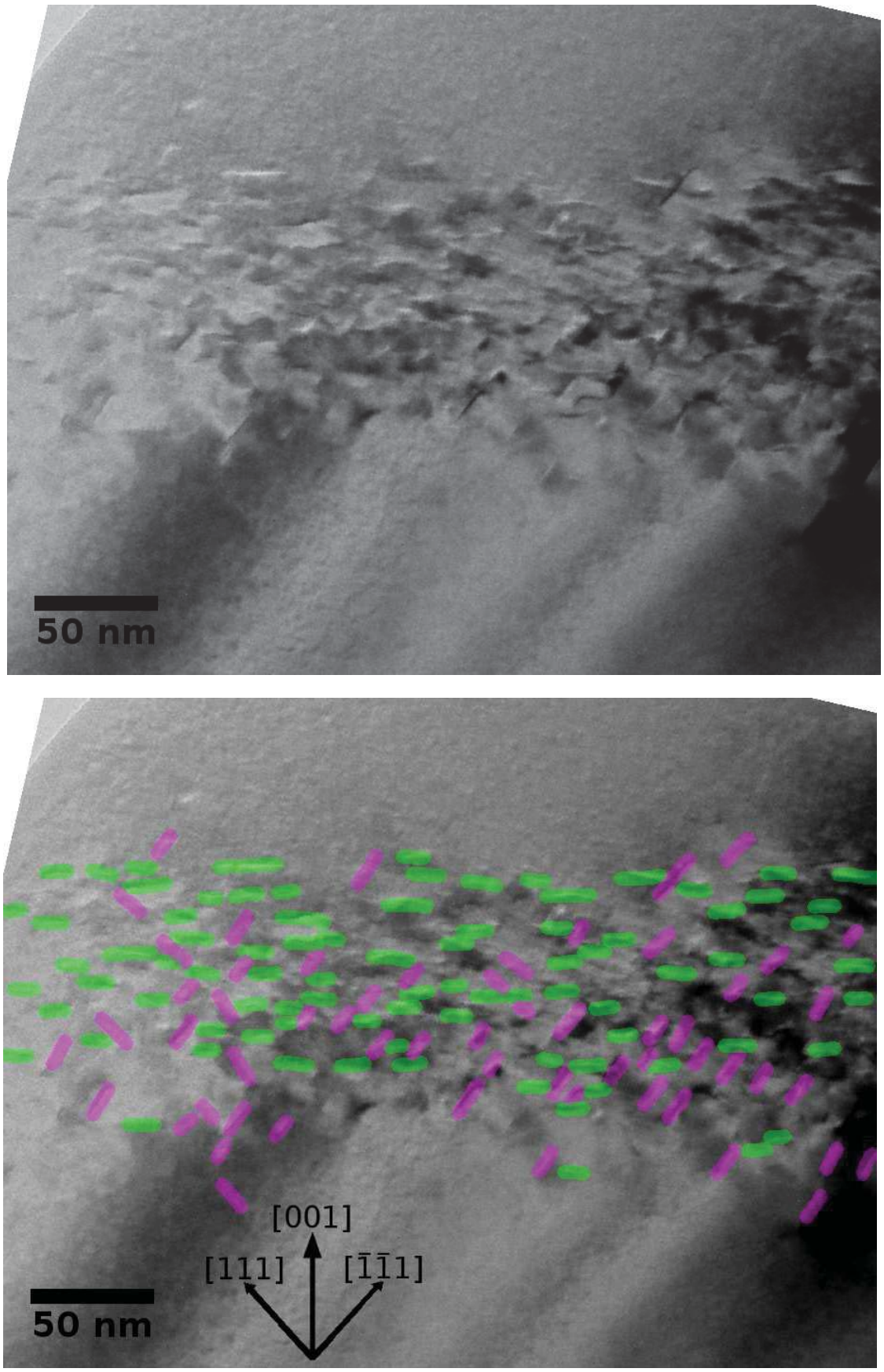

Figure 5.6: XTEM bright-field off-zone axis image from Si implanted with H (40keV,3×10^{16}cm^{-2},RT), under σ=156 MPa stress. Micrograph scales & crystal planes as labelled; right figure highlights hydrogen platelets with overlays of {001} platelets in green and {111} platelets in magenta. Sample surface approximately 325 nm beyond top of the figure(s).

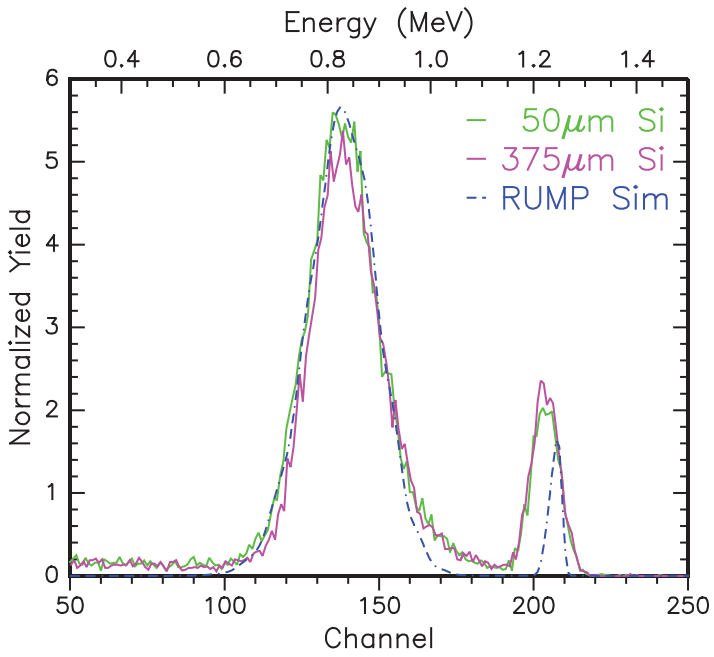

Figure 5.7: 3 MeV He^+ ERD measurement contrasting ULTRATHIN® 50 μm and bulk 375 μm thickness Si(100) wafers implanted with hydrogen at (40keV,6×10^{16}cm^{-2},RT). RUMP simulation of same implantation fluence & energy included for comparison. In IBM geometry, θ=-80°, ϕ=155°; Q=20 μC, I=17 nA; samples as implanted.

in each of the implanted hydrogen profiles and the surface peaks, varied by <10 per cent. These variations in energy are only slightly larger than the FWHM of the detectors used to collect the RBS He yield, given as E=12 keV, and thus within the error in the detectors' energy resolution.

There was also excellent agreement between the RBS-C spectra, seen in Fig. 5.8. The dechannelled yield from the hydrogen-implanted ULTRATHIN® Si wafers was marginally higher than in the bulk Si wafer, and the direct scattering peaks in both substrates from the implantations were very similar. From these data we can conclude that the two wafer thicknesses behave similarly under ion irradiation processes, such as implantation.

With the clear indication that the bulk and ULTRATHIN® wafers behave similarly under ion irradiation, we can read any findings in the 50 μm wafers as applicable to bulk Si wafers. So accepting the variations present between the bulk silicon used for ion-cut on an industrial scale and the ULTRATHIN® wafers studied here, the next step in this project is to study the thin silicon wafers implanted in two different manners. Firstly, the application of various stresses during implantation and/or annealing is contrasted in

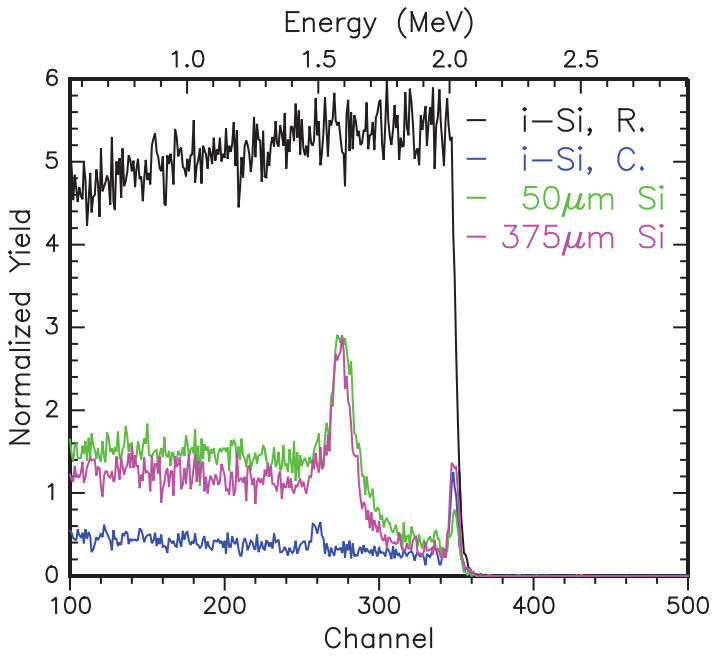

Figure 5.8: 3 MeV He^+ channelled RBS measurements comparing 50 μm and 375 μm thickness Si(100) wafers implanted with hydrogen at (40keV,6×10^{16}cm^{-2},RT). In IBM geometry, θ=0°, ϕ=70°; Q=20 μC, I=17.5 nA. R indicates random angle polar sample rotation of 3° around the channel angle during collection, while C indicates channelled ion beam path. Intrinsic, unimplanted Si(100) shown for comparison. Samples as implanted.

Section 5.4.3. Secondly, a single ULTRATHIN® silicon wafer was ion implanted with hydrogen to explore the influence of extrinsic mechanical stress upon the evolution of implanted hydrogen, when the stress is applied during the thermal annealing, discussed in Section 5.4.4.

5.4 Mechanical stress in ULTRATHIN® Si(100)

5.4.1 Sample production

As described in Section 3.1.1.2 of Chapter 3, this branch of the project involved the ion implantation of commercially-produced undoped ULTRATHIN® Si(100) wafers, with a resistivity of ρ<20 Ω cm and a nominal thickness of 50±5 μm. These were ion implanted with hydrogen at a fixed energy and fluence of E=40 keV and $\Phi_H = 6\times10^{16}$ cm^{-2} respectively. The wafers were cleaved into strips of approximately 20×4 mm, and the implantation was localised to the centre of the Si wafer strips by use of an orthogonally oriented 25 × 5 mm

Ta aperture. Implantation was performed in one of three stress conditions – stress-free, compression or tension; each is described in the appropriate sections.

5.4.2 Experimental methods

Stress was applied to the intrinsic and hydrogen-implanted ULTRATHIN® Si(100) wafers by the mechanical apparatus described in Section 3.3.2. These samples were annealed in the stress apparatus at temperatures T$\leqslant$500°C under an Ar ambient within a quartz tube gas furnace, with a gas flow into the furnace tube of approximately 1 cm^3s^{-1}.

The mechanical "stress boat" apparatus required to maintain the stress upon the wafers prevents the material being as readily exposed to the ambient in the Ar gas furnace, and additionally transfers the energy to the wafer through only two contact points, allowing inhomogeneity to occur in the sample heating. However, as explored in Appendix E.4, the ultimate blistering behaviour may be delayed, but is not significantly influenced.

In order to measure the curvature of stressed samples, they were photographed before and following annealing. This was achieved with a digital still camera with a 10MP 7.6×5.7 mm CCD positioned parallel to the apparatus and sample, with its centre of lens approximately 5 mm above the height of an unstressed wafer resting on the shelves. This offset was to minimise parallax errors in recording images of the samples while under stress. Using the software package DataThief [367], a set of x and y co-ordinates were extracted from the image of the wafer in each photograph. These coordinates were then fit in Genplot [293] with Chebyshev polynomials of order four to determine an analytical function that best represented the curvature of the wafer. A Python script was then used to calculate the radius of curvature for each point along the function, using Eq. A.4. (The radius extracting code can be found in Appendix F.)

Using the symmetric Euler-Bernoulli beam bending equation (Eq. A.3), and the radius of curvature values determined from the analytical functions, the gross stress values at all points along the wafer were determined. The form of that equation is given again here, calculating the stress σ for a (100) Si wafer experiencing uniaxial stress induced by the

bending of the wafer into the (110) direction:

$$\sigma_{11}(x) = \frac{E_{[110]}.c(z)}{r(x)} \tag{5.1}$$

where $c(z)$ is distance from the centre of the wafer (up to half its thickness), E is Young's modulus in the appropriate crystal substrate, orientation and conditions (in this case, Si, [110] and plate bending) [264] and $r(x)$ is the local radius of curvature at the point x on the surface of the wafer. This gives the magnitude of the stress at the distance $c(z)$ from the centre of the wafer, which is assumed to be a neutral surface without stress, with the equal and opposite stress present equidistant from the centre on the opposing face of the wafer. A three dimensional mesh model of the sample, and the stress value at each point could then be plotted in Linux package Gnuplot [368]. A two dimensional colour map, akin to a meteorological heat or rainfall plot, can then display the stress within the wafer. Figure 5.9 shows the sequence of steps and extracted data produced in this whole process, from photograph to (x, y, σ) plot.

Equation 5.1 can be used for all other possible crystallographic orientations, given the appropriate values for Young's Modulus [226, 264]. Fuller explanation of the theory behind these bending behaviour calculations defined by Eq. 5.1 is provided in Appendix A.1.

Following annealing, samples were examined in the un-stressed state by a number of techniques as described in Chapter 3. These included RBS, ERD and XTEM. Concern may exist over potential for plastic deformation of the wafers during the annealing process while under stress. However, as in the work of Rudawski *et al.* [268], in the range of the temperatures to which the wafers are exposed (T=400°C or lower), while this deformation is non-zero, the effect is not significant [369–371]. Further discussion and potential influence is found in Section 5.5.

Two series of hydrogen-implanted ULTRATHIN® 50 μm Si samples were studied in this work. The first series is comprised of a matrix of implantations and anneals performed with or without external stress. Each sample in this series was a unique implantation, and comparison was made assuming consistency in the source material and implantation process. The second series consisted of a single implantation into unstressed silicon, which was divided up to allow application of a range of stresses during subsequent annealing.

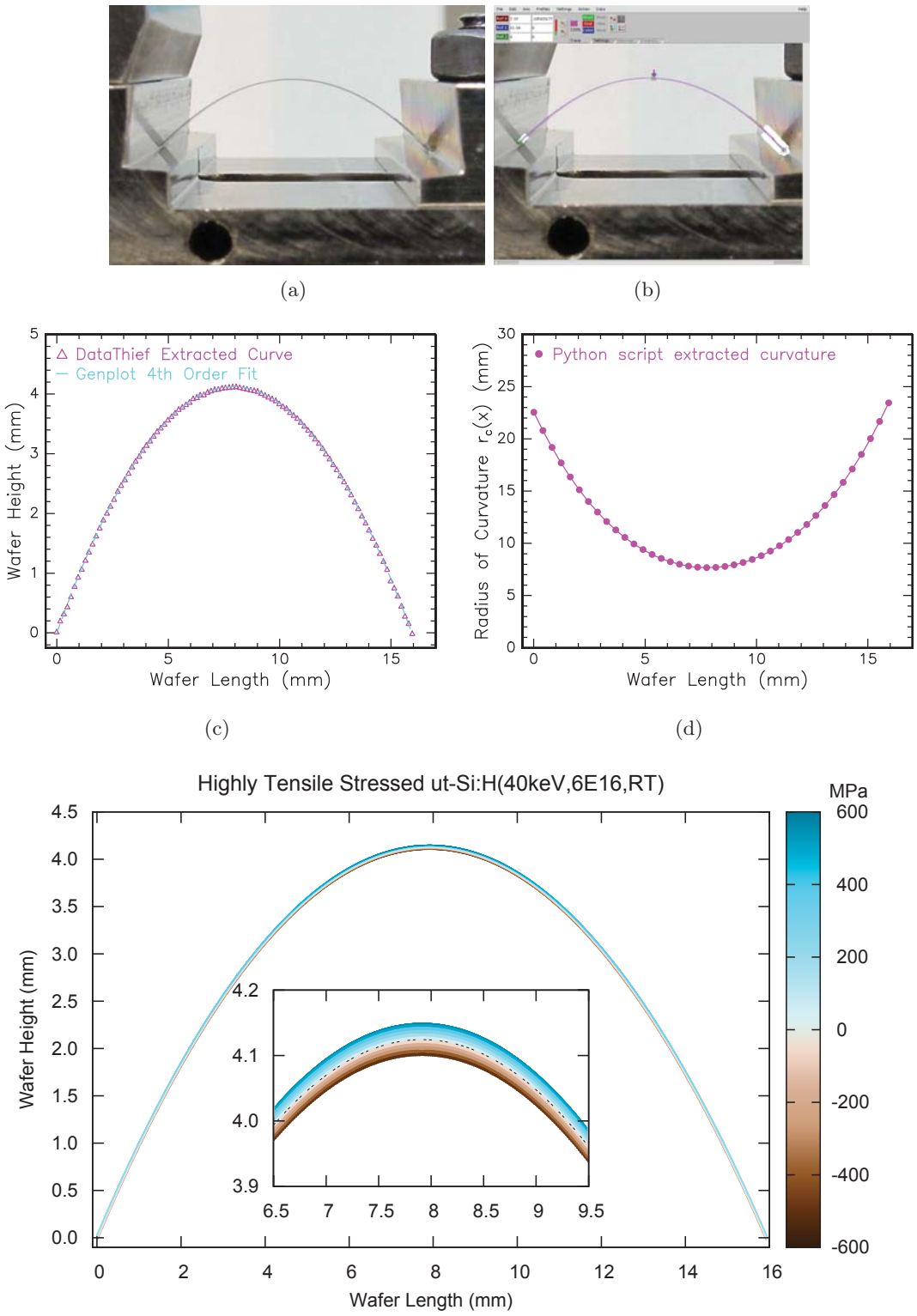

Figure 5.9: Flowchart of steps involved in determining stress in ULTRATHIN® Si wafers used in this project. The sample used in this example is the H(40keV,6×10^{16}cm^{-2},RT)-implanted Si, annealed at T=400°C/30 min under high tensile stress. Step (a) capture image of wafer under stress within apparatus, (b) use DataThief to extract (x, y) co-ordinates of wafer, (c) use Genplot to fit 4th order polynomial analytic function to DataThief-extracted wafer curve data, (d) use Python script to calculate radius of curvature of analytical fitting function of wafer (plotted here in Genplot), (e) plot stress-position colour map of three-dimensional mesh compiled from Eq. 5.1 for a series of complementary wafer curve functions.

Implantation Stress	**Anneal Stress**	$r_c(min)$ (mm)	$\sigma_{11}(max)$ (MPa)
Unstressed	Tension	+15.0±1.0	+283±62
Tension	Unstressed	+28.2±1.3	+151±32
Tension	Tension	+17.4±1.2	+244±53
Unstressed	Compression	-12.0±1.0	-354±80
Compression	Unstressed	-18.7±2.7	-228±58
Compression	Compression	-16.2±1.0	-262±57

Table 5.5: Curvatures and stresses applied during implantation and annealing on ULTRATHIN® Si(100) samples implanted with H(40keV,6×10^{16}cm^{-2},RT) analysed in Section 5.4.3, determined by symmetric Euler-Bernoulli beam bending equation (Eq. 5.1).

The reproducibility of each sample for statistical analysis is made difficult due to their production methods. Each sample had a unique applied stress, due to the exact dimensions of the wafer, its position in the stress apparatus and the force applied, defined by the precise separation of the two "jaws". Replication of specific stresses proved problematic, and thus a broader comparison of similar stress values was pursued. Overarching trends caused by the macroscopic stress values could therefore be compared, but precise identification of quantitative relationships between stress types and hydrogen platelet development is prevented.

5.4.3 Multiple implantations with various stressed conditions

First in our study of the influence of stress, this section deals with a matrix of samples undergoing applied stress during implantation, annealing or both, contrasted with unstressed material undergoing the same processes. Table 5.5 lists the combinations of applied stresses for each sample during production, as well as the measured minimum radius of curvature and maximum global stress values experienced by these samples. The latter stress values were determined by Eq. 5.1, and Figures 5.10 and 5.11 show their stress-position graphs. All anneals in this section were at T=400°C for t=10 minutes duration in the Ar ambient of the quartz tube furnace. Measurements were also performed concurrently on unstressed H-implanted Si, to establish the relative influence of the applied stresses.

External stress only during implantation

We examined wafers subjected to stress during ion-implantation and then annealed in an unstressed state. One wafer was exposed to compressive and the other to tensile stress,

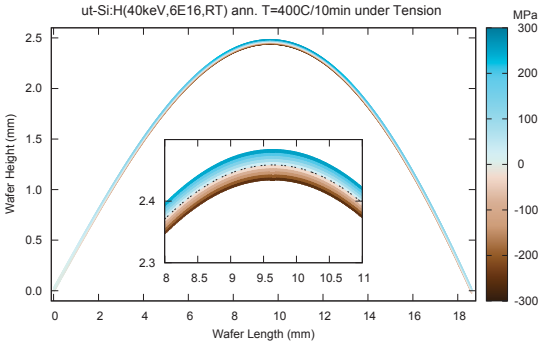

(a) Impl. Unstressed / Ann. Tension

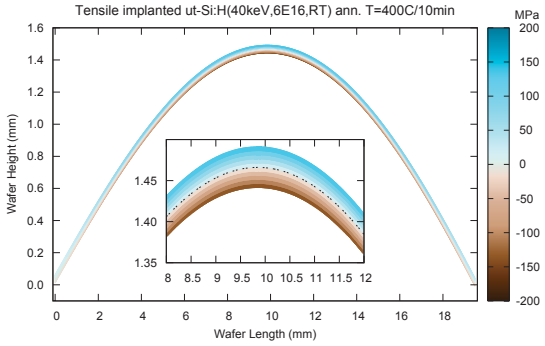

(b) Impl. Tensile / Ann. Unstressed

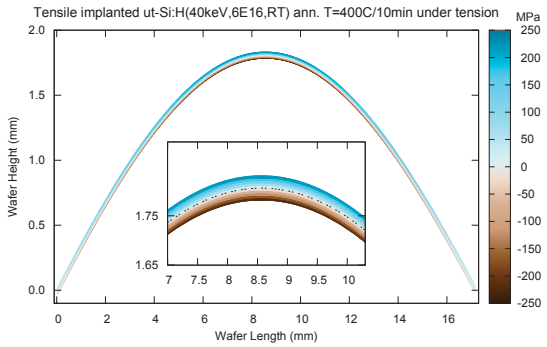

(c) Impl. Tension / Ann. Tension

Figure 5.10: Stress-position colour maps of 50 μm Si(100) implanted with H(40keV,6×10^{16}cm^{-2},RT), then annealed at T=400°C/10 minutes, under tensile stresses as labelled. Blue and (+) indicates tensile stress, brown and (-) indicates compressive stress.

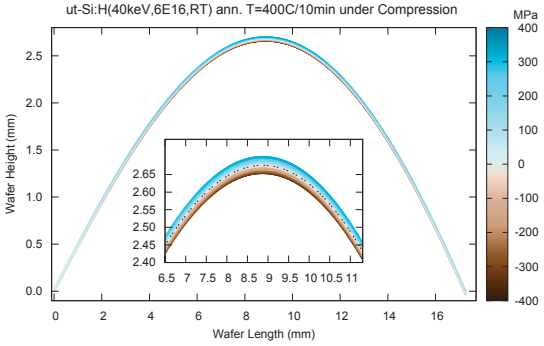

(a) Impl. Unstressed / Ann. Compression

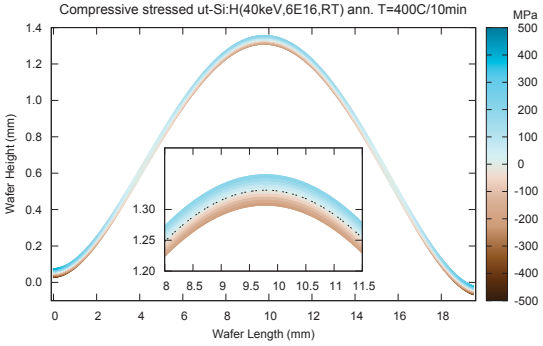

(b) Impl. Compression / Ann. Unstressed

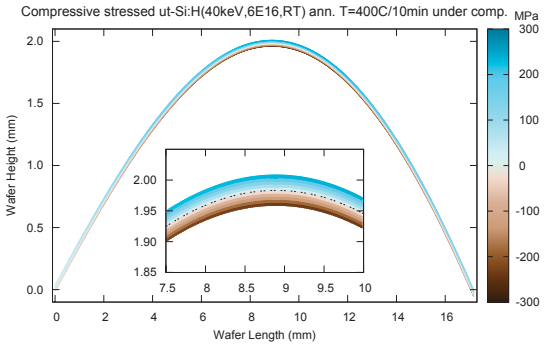

(c) Impl. Compression / Ann. Compression

Figure 5.11: Stress-position colour maps of 50 μm Si(100) implanted with H(40keV,6×10^{16}cm^{-2},RT), then annealed at T=400°C/10 minutes, under compressive stresses as labelled. Blue indicates tensile stress, brown indicates compressive stress.

in addition to an unstressed control sample. Both stressed wafers had opposite radius of curvatures of similar magnitude – $r_{tensile}$(min)=28.2 mm and $r_{compressive}$(min)=18.7 mm. These resulted in maximum global stress values of σ(max)=151 MPa and –228 MPa respectively, shown in Fig. 5.10(b) and 5.11(b). The magnitude of the stress applied to the wafers in the tensile and compressive situations varied over the length of the wafer, but was roughly constant over the length of the hydrogen implantation region ($\sim$5 mm along centre of strip). Considering the magnitude of the peak global stress values in these samples is significantly higher than any median stress induced by ion implantation or annealing, we expected at least moderate changes from any intrinsic hydrogen evolution. However, as noted in Section 5.1, the applied stress values described are global or median values, and do not adequately account for the individual influence of point or extended defect structures. Such defect structures can have significantly high associated local stress values, and could alter the evolution of hydrogen, but are not easily quantified. Therefore we cannot sufficiently account for the influence of specific defects on the hydrogen, so must be cautious in conclusions we draw from the global stress values, considering the situation only on larger, macroscopic scales. This should be considered whenever stress is discussed within this thesis.

Each of these wafers was characterised by RBS and ERD before and after annealing, shown in Fig. 5.12. While it is possible that the RBS-C direct scattering (DS) data shown in Fig. 5.12(a) is consistent with behaviour seen in thick samples (Fig. 5.4), the as-implanted data does not strongly show any change due to the applied stress. This lack of difference between stressed and unstressed samples is also seen following annealing in an argon ambient for 10 minutes at T=400°C. All annealed samples show an increased RBS yield, and the increase in DS yield (10–15%) is smaller than that in dechannelling (DC) yield (16–22%). The depth of the DS peaks in all samples decreased following annealing, moving 10–30 nm. This shift may be an example of reverse annealing, as reported elsewhere [44, 349, 372, 373]. This is not as clear in Fig. 5.12(a) and (c) as in individual graphs of each applied stress condition shown in Appendix E.1.

Relative to the unstressed hydrogen implantation, the ERD-measured hydrogen distributions of the samples implanted under stress both have a decreased peak hydrogen concentration and show a fractional shift in their H profile peak towards the surface, as

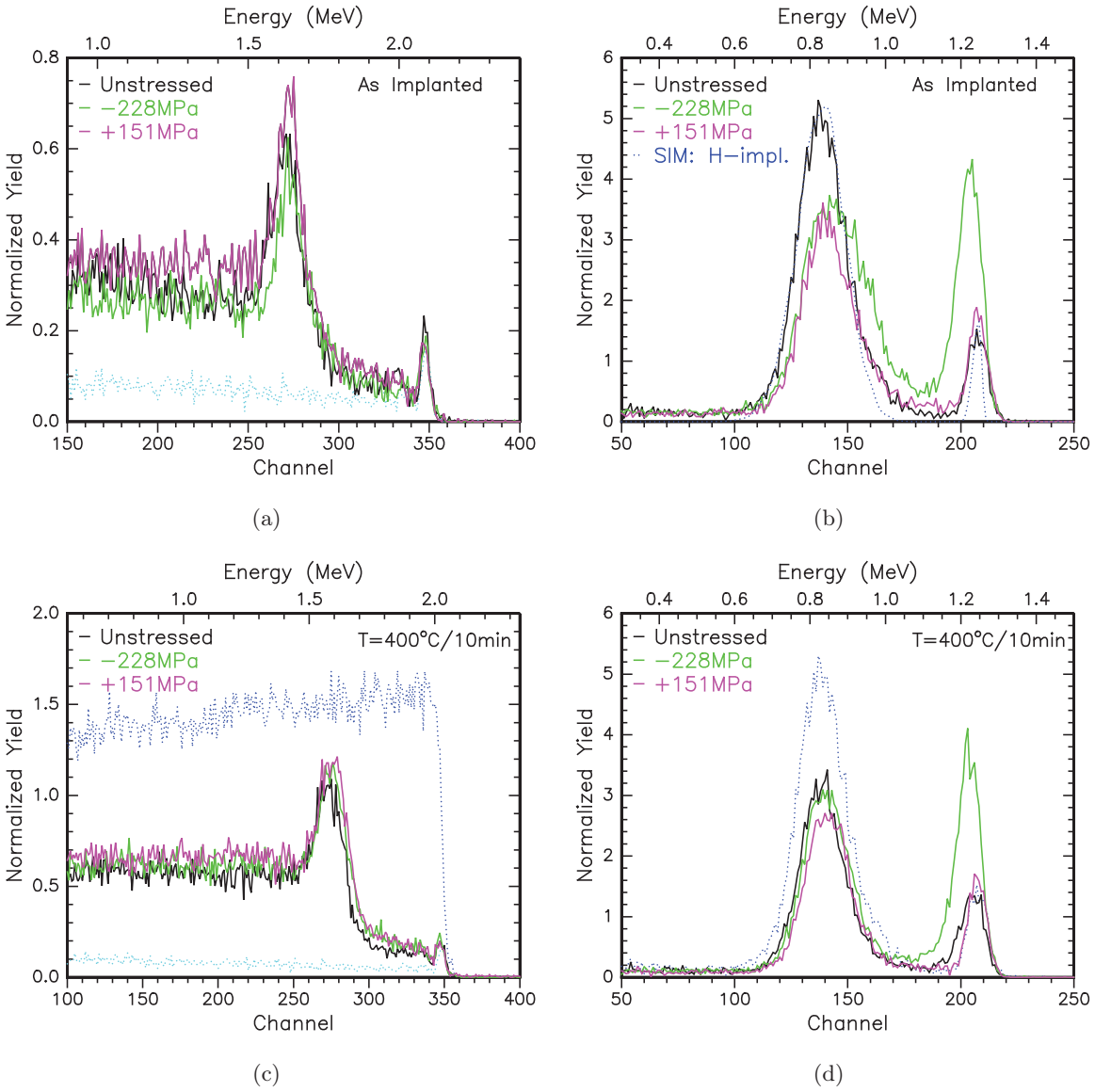

Figure 5.12: 3 MeV $^4He^+$ RBS-C (a,c) and ERD (b,d) spectra of H(40keV,6×10^{16}cm^{-2},RT)-implanted 50 μm Si(100) under stress types as labelled. (a) & (b) show samples as implanted, and (c) & (d) subsequently annealed without stress at T=400°C/10 minutes. Compressive stress $\sigma = -228$ MPa, tensile stress σ=151 MPa. Included for comparison in **(a)** intrinsic Si channelled yield, **(b)** RUMP simulation of H implantation, **(c)** the [100] channelled (cyan) and random angled (blue) yield from an intrinsic Si(100) wafer, **(d)** includes H profile of unstressed, as-impl. Si.

seen in Fig. 5.12(b). However, this difference disappears following annealing, as all samples show a similar H profile distribution in Fig. 5.12(d).

Noted earlier, there is an overall increase in DC yield across the spectra of these samples. Low temperature annealing usually decreases the disorder, as larger hydrogen complexes grow at the expense of point defects. Extended defects have a much larger dechannelling cross-section than simpler defects. As such, increases in DC yield likely reflect thermal evolution of point defects into extended defect complexes.

External stress only during annealing

RBS-C yields of H-implanted samples annealed with or without stress show only small differences, as seen in Fig. 5.13(a). The position of the direct scattering (DS) peaks is not influenced by stress, as very similar depths were determined in both stressed and unstressed annealed samples. Both compressive and tensile stressed samples have lower DS and dechannelling (DC) yields post-annealing, with the tensile sample's DS peak lower than the pre-annealed unstressed sample. However it is unclear if the magnitude of these differences is significant.

A clearer difference occurs in the ERD H profiles, in the case of the material implanted without stress and then annealed under compressive stress of σ(max)=-354 MPa, as shown in Fig. 5.13(b). Post-annealing, the peak concentration of the H profile fell sharply, ending with less than half the yield of the as-implanted and annealed unstressed material. There is a clear increase in hydrogen content in the region between the surface peak and R_{P}, at least double the amount in the sample annealed without stress and nearly three times that in the as-implanted material; however this does not account for the volume of hydrogen lost from the main distribution. In comparison, when annealed under tensile stress of a similar magnitude (σ=283 MPa), ERD shows the hydrogen profile was little changed from the unstressed material.

External stress applied during implantation and annealing - Compression

Broken into two sections, we now examine applied compressive stresses and tensile stresses separately.

Figure 5.14(a) shows the influence of compression upon RBS-C determined damage via the direct scattering (DS) and dechannelling (DC) yields. The total DS yield (∼total im-

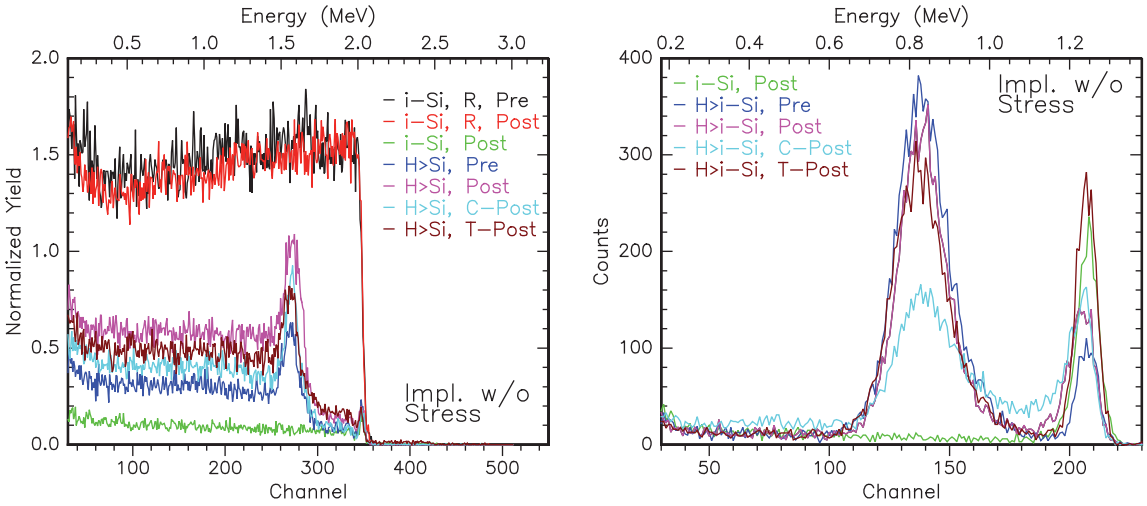

Figure 5.13: 3 MeV He ion beam (a) RBS-C (b) ERD analysis of H(40keV,6×10^{16}cm^{-2},RT)-impl. 50 μm Si(100) under no stress, shown before (**Pre**) and after (**Post**) annealing at T=400°C/10 minutes under various stress values: T=tensile stress, σ=283 MPa; C=compressive stress, σ=-354 MPa. Intrinsic and random yield RBS spectra from i-Si wafer included for comparison in (a), and intrinsic H yield shown in (b). All spectra in (a) channelled unless specified with label "R".

plantation damage present) in the wafer post-annealing is lower when compressive stress is applied both during implantation and annealing. The yield and depth of the DS peaks of the compressively implanted and annealed material are very similar to the compressively implanted material. Both these samples' DS profiles are significantly narrower than the compressively implanted silicon annealed without applied stress. For all applied compressive stress, the DC yield appears to decrease with increasing stress, while DS yields reveal less indication of a trend.

Among the ERD-determined hydrogen distributions shown in Fig. 5.14(b), only the pre-annealed, implanted under compressive stress sample shows significant variation from the other specimens. Following the annealing step, all samples show similar hydrogen distributions. This as-implanted hydrogen profile when performed under compressive stress is broader than unstressed or tensionally stressed implantation. The hydrogen profile narrows following annealing, but this behaviour is common to both stressed and unstressed samples, as is the final distribution. The EOR of the hydrogen profile does not shift following annealing, but the leading edge of the implanted profile migrates ∼55 nm deeper into the silicon (from channel 170 to 160 in Fig. 5.14(b)). A shift occurs too in the profile peak following annealing under any condition, approximately 20 nm deeper than the as-implanted

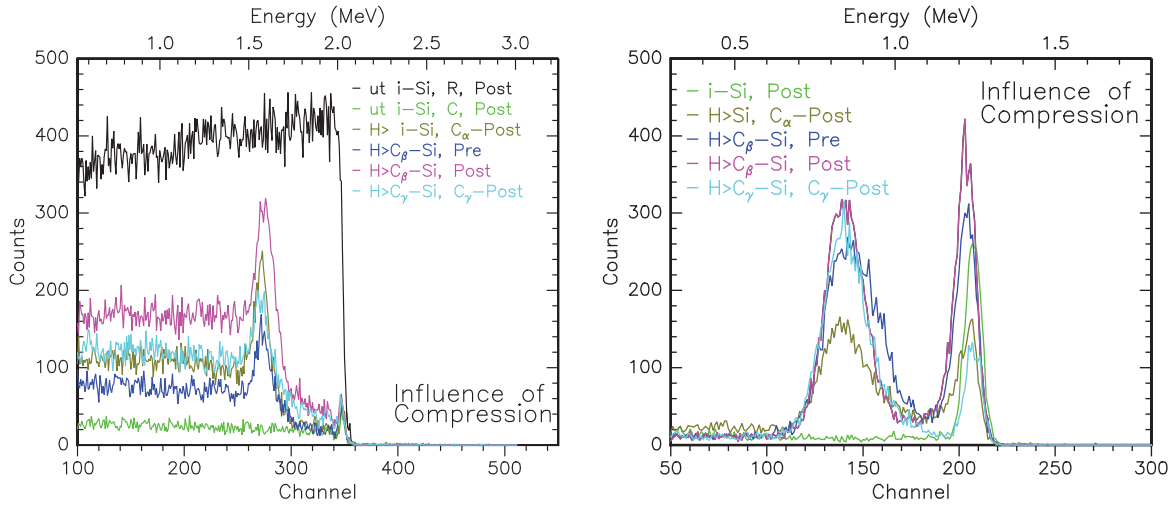

Figure 5.14: 3 MeV He ion beam (a) RBS-C (b) ERD analysis of H(40keV,6×10^{16}cm^{-2},RT)-impl. 50 μm Si(100) under compressive stress, shown before (**Pre**) and after (**Post**) annealing at T=400°C/10min under various stress values: C_α=-354 MPa; C_β=-228 MPa; C_γ = −262 MPa. Intrinsic and random yield RBS spectra from i-Si wafer included for comparison in (a); all spectra channelled unless labelled "R".

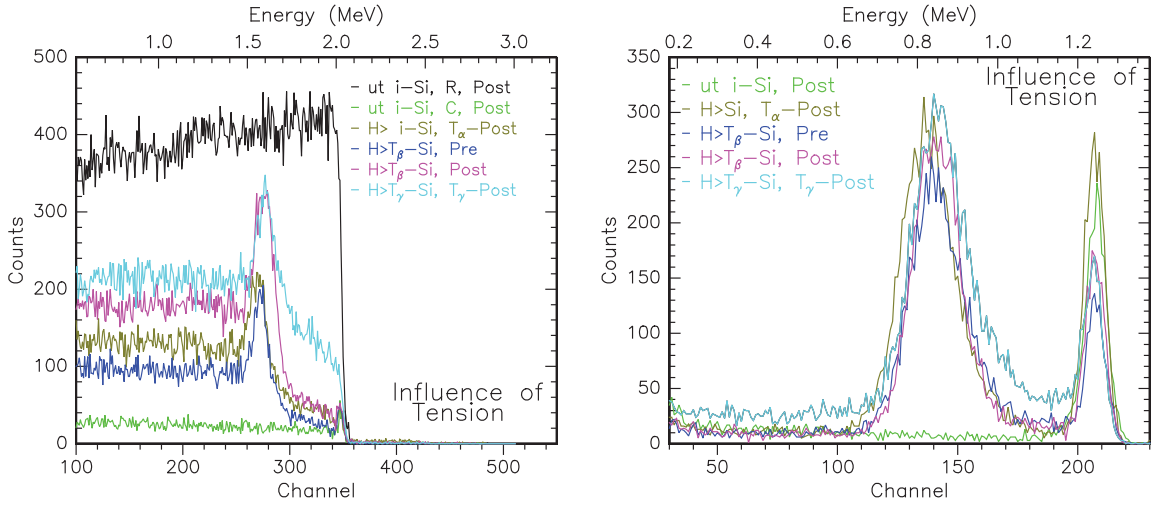

Figure 5.15: 3 MeV He ion beam (a) RBS-C (b) ERD analysis of H(40keV,6×10^{16}cm^{-2},RT)-impl. 50 μm Si(100) under tensile stress, shown before (**Pre**) & after (**Post**) annealing at T=400°C/10 minutes under various stress values: $T_\alpha=\sigma$=283 MPa; $T_\beta=\sigma$=151 MPa; $T_\gamma=\sigma$=244 MPa. Intrinsic & random (R) yield RBS spectra from i-Si wafer included for comparison in (a); intrinsic H yield shown in (b).

case. Following annealing, each of the samples – implanted stress-free then annealed under compression, the sample implanted under compression and then annealed stress-free, and the sample implanted and annealed under compression – all produce roughly equal hydrogen profile yields, positions and widths.

External stress applied during implantation and annealing - Tension

As was the case for the compressively stressed samples, ERD results indicate hydrogen evolution in tensionally stressed material is little changed from the intrinsic, shown in Fig. 5.15(b). However, the RBS-C yields displayed in Fig. 5.15(a) suggest application of tensile stress may alter the evolution of the implantation damage.

All tensile stressed samples show a very similar H profile yield in ERD measurements. Their profiles widen when annealed or implanted and annealed under tensile stress. RBS-C measurements show very similar DS peak positions and yields following annealing, independent of tensile stress regime.

The significant differences emerge in samples where tensile stress was applied during both implantation and subsequent annealing. A significant increase in DC yield is seen, without any major change in DS peak yield or position. The largest increase in DC yield is seen between the peak and the sample surface. It is possible that the hydrogen profile in this sample is slightly broader than other samples, with higher concentration of hydrogen in the region between R_{P} and the surface peak, although its total yield does not increase.

RBS-C DC yield increases between the DS peak and the surface may be an indication of large scale hydrogen defect formation within the material. Although there is no measurable change to the sample surface by eye or optical profiler, it is possible that proto-blisters or large agglomerations of hydrogen platelets are present, stretching from the implanted hydrogen profile through to near-surface depths. This may also account for the slightly increased H yields shown in that region in ERD data.

Analysis and conclusions

The preceding RBS-C and ERD data presented are summarised in Fig. 5.16.

Stress applied during implantation produces lower yield hydrogen profiles, independent of direction. However any influence stress has during implantation of hydrogen diminishes following annealing. Post annealing, the peak depth and yield of the hydrogen profiles

are similar in majority of cases, with some variation in distribution width. Tensile stress during implantation, annealing or both does not show significantly different effects upon the hydrogen profile, or from the intrinsic case. Compressive stress may decrease the hydrogen yield if applied solely during annealing, but otherwise also results in similar profiles post-annealing.

The associated damage produced by the ion implantation (shown in DS) does not show significant differences in yield or position between unstressed, tensile or compressively stressed H-implanted Si. Application of tensile stress both during implantation and annealing may increase the distortion or variation from regularity in the Si crystal (as measured by DC yields), while tensile stress during annealing alone may decrease any changes from intrinsic Si structure. Compressive stress decreases damage yields when applied during annealing, independent of stress state during implantation.

Theoretically, defect formation under external stress alters the number and types of defects that appear, by changing the formation volume [252]. Compression increases the number of interstitials, while tension increases the number of vacancies, as intuitively understood when you bring the lattice closer together or pull it further apart respectively. There is some indirect evidence of compression increasing interstitials in Si in the combined works of Kimmerling and Patel [374] and Lefevre [205]. Pitera *et al.* [256] describes how tensile stress increases the solubility of interstitial molecular hydrogen in silicon, while compressive stress has the opposite effect. Hydrogen tends to getter in tensile regions, allowing a tensile layer to be used to concentrate hydrogen diffused or implanted into a semiconductor. Also, that tensile stress aids the formation of hydrogen-related defects which require dilation or distortion of the lattice, such as platelets [256, 364, 366]. Anatolli *et al.* [253] suggest that vacancies become more abundant in silicon when exposed to *either* compression *or* tension, due to the two potential energy state paths through which vacancies can be formed. Centoni *et al.* [375] calculates that migration of Si vacancies should particularly increase at higher compressive stresses. This ready migration would allow the diffusion of hydrogen through the material but not offer significant trapping options, while providing potential for repair and relaxation of damaged Si bonds and crystal structure. Xuan *et al.* [254] contrarily predicts that tensile stresses will produce a more favourable diffusion environment for hydrogen, and compressive stresses actively decrease

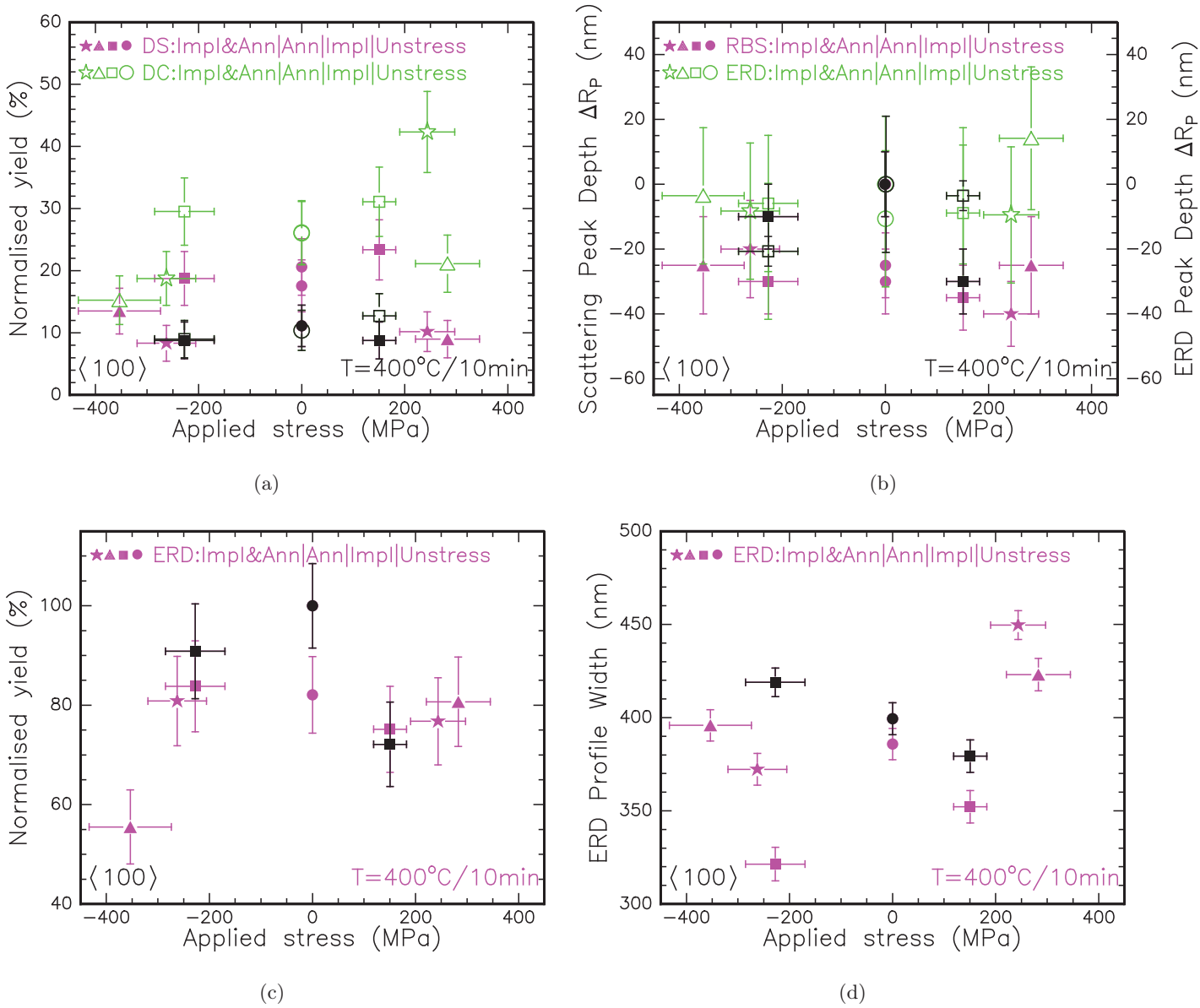

Figure 5.16: IBA measurements of 50 μm Si(100) wafers implanted with hydrogen ions at $\Phi = 6 \times 10^{16}\text{cm}^{-2}$ at E=40 keV, then annealed at T=400°C for 10 minutes. Stress applied during implantation, annealing or both as indicated. Samples measured in the as-implanted state shown in **black**. **(a)** shows RBS-C determined direct scattering **(DS)** and dechannelling **(DC)** yields along the [100] axial channel. **(b)** shows relative change in depth of the direct scattering (∼lattice damage) peaks extracted from [100] RBS-C spectra, in addition to the hydrogen profile peaks R_P from ERD spectra. **(c)** shows ERD yield from evolving hydrogen profiles. **(d)** shows relative change in ERD measured hydrogen profile widths. Beam: 3 MeV $^4\text{He}^+$, angle of back scattering detector θ=11.68°, and forward scattering detector ϕ=25°, Q=5-10 μC, I=10-22 nA.

the solubility of the crystal to hold other dopants or impurities. Xuan's results could also account for smaller changes in hydrogen evolution in compressive environments. We find no strong indication of Xuan's claims that hydrogen is more mobile under tension, but perhaps some signs that compressive stress is decreasing hydrogen's solubility in Si. The consistent picture from the majority of other researchers is that hydrogen should readily move from compressive and trap into tensile regions. While the results we are presenting in this work are not without ambiguity, we find reasonable agreement with the conclusions of Anatolli, Centoni and Pitera *et al.* described above, that tensile stress diminishes and compressive enhances diffusion of hydrogen.

It is important to mention again that our experiments described so far were performed using a number of different ULTRATHIN® Si(100) wafer pieces, with separate wafer and implantation origins. Any differences that may be present between the pieces could thus give rise to difficulties in identifying trends in the hydrogen evolution (such as seen in Fig. 5.14). To avoid such influences caused by sample source variation, subsequent work explores a single sample implantation then exposed to various stressed conditions.

5.4.4 Single implant annealed under various stressed conditions

As prefaced earlier, this section presents the influence of stress applied during annealing to hydrogen implanted ULTRATHIN® Si, looking at hydrogen distribution, blister formation and platelet/micro-crack locations. A 50 μm thick Si sample was implanted with hydrogen at room temperature with $\Phi_H = 6 \times 10^{16}\text{cm}^{-2}$ at E=40 keV before being cleaved up and annealed under a number of stresses. The anneals were performed in a quartz tube furnace under an argon ambient nominally at T=400°C for t=30 minutes, in order to establish blistering behaviour but without the surface damage caused by cratering. Samples were exposed to residual heat from the mechanical stress boat for up to fifteen minutes following their anneal, while their curvature was measured. As noted previously, each sample has a unique applied stress value, despite the original source implanted wafer. Future investigations will be required to extend beyond the broad behavioural analysis discussed here, to specific hydrogen defect dynamics.

Samples annealed without external stress

Prior to examining the impact of applied stress during annealing, the unstressed H-

implanted Si was explored. A comparison of the as-implanted and T=400°C/30 minutes annealed unstressed hydrogen-implanted ULTRATHIN® Si sample by XTEM shows a marked change in the orientation of most hydrogen-related defects. Figures 5.17(a) and (b) show the bright field (BF) off-zone axis (OZA) micrographs of the hydrogen implantation region in each sample, while Fig. 5.17(c) and (d) includes an overlay highlighting the two major hydrogen platelet orientation types, {001} and {111}, as well as indicating the crystal planes relative to the images.

In the as-implanted state, the majority of the hydrogen platelets are aligned along {111} planes, illustrated by the purple overlays in Fig. 5.17(c). The {111} platelets measure between 5 and 30 nm long, spread across a 100 nm depth range. There are also a small number of {001} platelets, shown in the same figure's red overlays. No distinct pattern describes the distribution of either defect, although both are largely confined to the aforementioned 100 nm depth range, with the exception of a few {001} defects, possibly extending just beyond the EOR of the hydrogen ion implantation. (This seems in good agreement with the RBS-C findings shown in Fig. 5.29.)

Following the anneal, a marked shift to {001} platelets occurs, in significantly greater numbers than seen of either type prior to annealing. There is also a corresponding decrease in the number of {111} defects, but as can be seen in Fig. 5.17(d), these are still present, if largely confined to the limits of the implantation damage band. This confinement however may be artificial, caused by the annealing-induced damage distorting the region to prevent easy identification of the defects. The significant damage in this inner band also contains the development of the planar crack used by the ion-cut process. Amalgamation of multiple {001} defects across a broad area within a plane, with {111} defects acting as spars across planes, leads to the formation of this large defect structure, stretching almost unbroken through the examined sample area.

By manifestation of presumedly ion-cut type cracks in these ULTRATHIN® Si(100) wafers, it can be assumed that under the same conditions as those described in the literature [1,13,26,28,78,108,113,123,376], ion-cut could be facilitated in these wafers. By extension, comparisons can be made between our research and other work relating to ion-cut type processes. As this result is established for an unstressed wafer, highlighting the native ion-cut behaviour independent of external stresses, it may confirm several RBS-C conclusions.

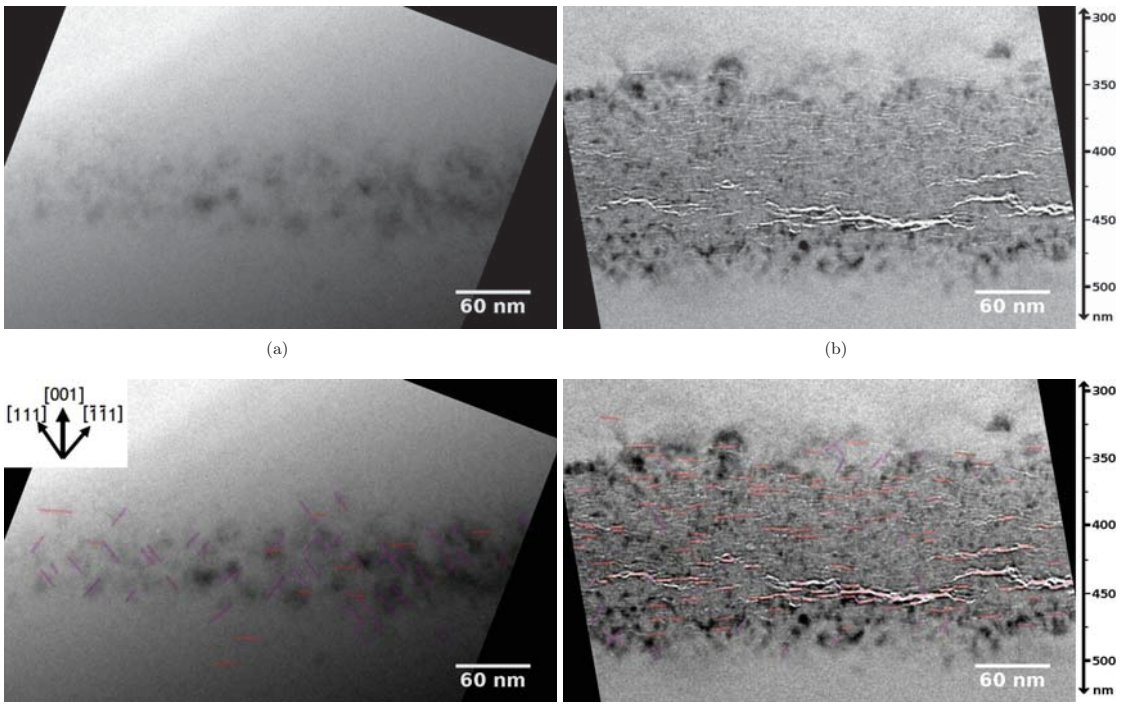

Figure 5.17: XTEM bright field off-zone axis micrograph of ULTRATHIN® Si(100) implanted with H(40keV,6×10^{16}cm^{-2}, RT) (a) as implanted, and (b) annealed at T=400°C/30 minutes. (c) and (d) include overlays of {001} (shown in red) and {111} (shown in purple) hydrogen platelet defects, and indicates relative crystal axes directions. Scales on far right indicate depth from sample surface for (a-b) and (c-d), located beyond top of figures. In-micrograph scales as labelled.

Annealing Stress Type	**Label**	$r_c(min)$ (mm)	$\sigma_{11}(max)$ (MPa)
Lowest Tensile	T0	19.1±0.1	+222±46
Low Tensile	T1	15.8±0.1	+269±56
Median Tensile	T2	12.10±0.04	+351±73
High Tensile	T3	7.67±0.02	+554±116
Low Compressive	C1	17.55±0.04	–242±51
Median Compressive	C2	11.0±0.1	–386±81
High Compressive	C3	7.99±0.03	–532±111

Table 5.6: Minimum $r_c(x)$ and maximum $\sigma_{11}(x)$ annealing condition values for T=400°C/30min anneals of 50 μm H(40keV,6×10^{16}cm^{-2},RT)-implanted Si(100) in Section 5.4.4.

Not only do the defects lead to a distorted silicon lattice preventing channelling of the ion beam, but such distortions may be directionally biased. The defects seen in Fig. 5.17(d) are largely {001}, and are therefore less detectable by a beam channelled along the [100] direction than one along the [110] crystal axis [364]. However, from the RBS-C measurements seen in this study, there is a distinct increase in the yield following annealing. It is possible that a significant number of platelets are forming along the {011} family of planes, having influence on (100) channelled He ions. But these {011} platelets would only appear as point defects in the cross-sectional orientation taken of the sample, which makes it very difficult to identify in this XTEM.

Samples annealed under external stress

Having established the behaviour in unstressed material, the focus shifts to the same material annealed under applied stress. The stress-position graphs of the samples annealed under stress in this section are shown in Fig. 5.18, and the peak magnitude of the stress to which the hydrogen implanted region was exposed is listed in Table 5.6. The photographic stills used to measure these stress values are shown in Appendix E, following the method outlined in Section 5.4.2.

With high density hydrogen cavities formed during the annealing process, the RBS-C yields for each of the samples, independent of stressed condition, are significantly higher than the intrinsic crystalline yield, as seen in Fig. 5.19. At the highest tensile and compressive stresses applied – σ=554 MPa and -532 MPa respectively – the yields decrease from the earlier stresses *and* the unstressed hydrogen-implanted material. These yields suggest a decrease in the disorder in these wafers, contrasted with the wafers annealed with stresses up to $\sigma = \pm270$ MPa. Little variation is seen in the direct scattering (DS)

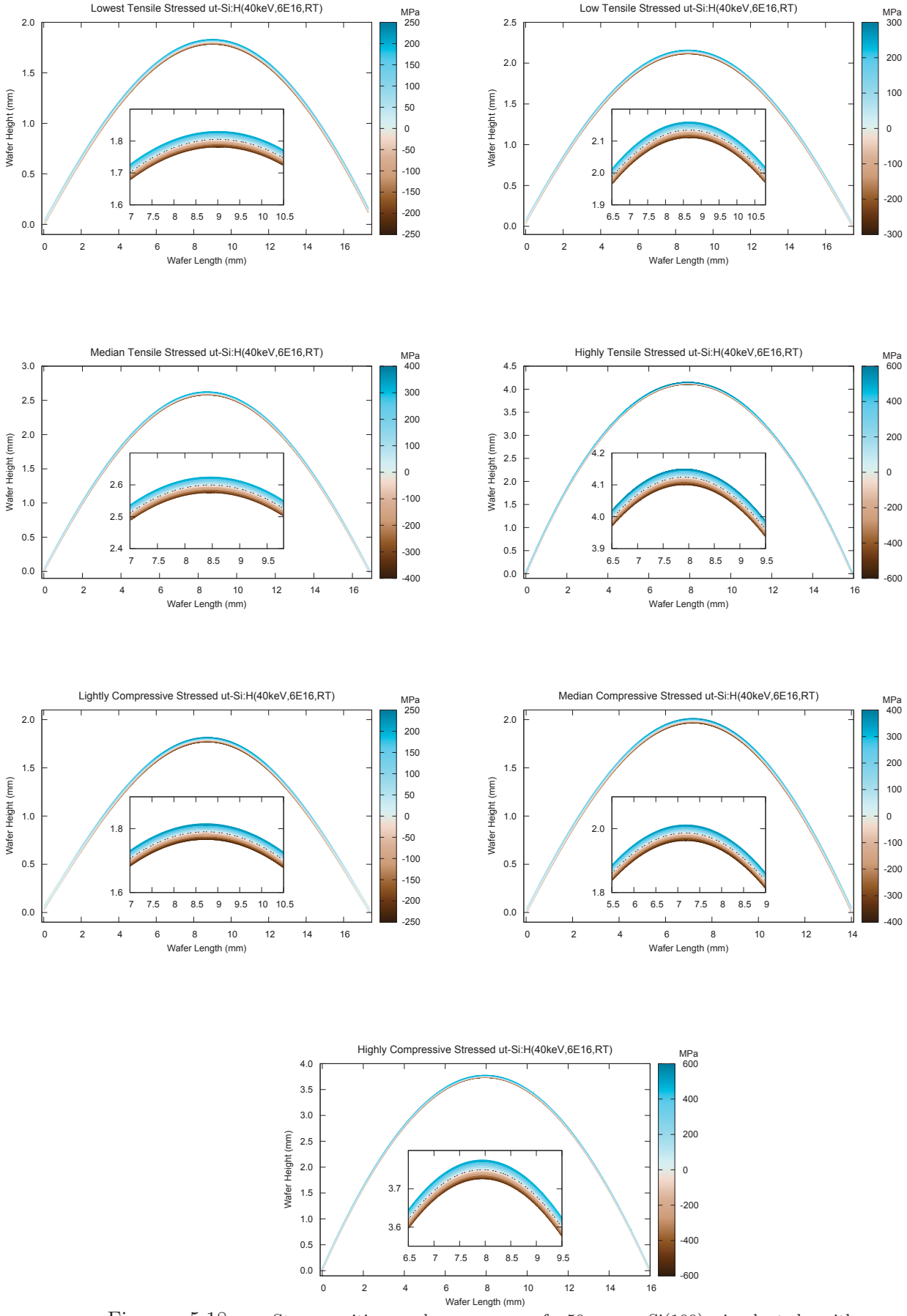

Figure 5.18: Stress-position colour maps of 50 μm Si(100) implanted with H(40keV,6×10^{16}cm^{-2},RT), then annealed at T=400°C/30 minutes under stresses as labelled. Blue and (+) indicates tensile stress, brown and (−) indicates compressive stress. Stress calculated from analytically fit wafer radius of curvature using Eq. 5.1.

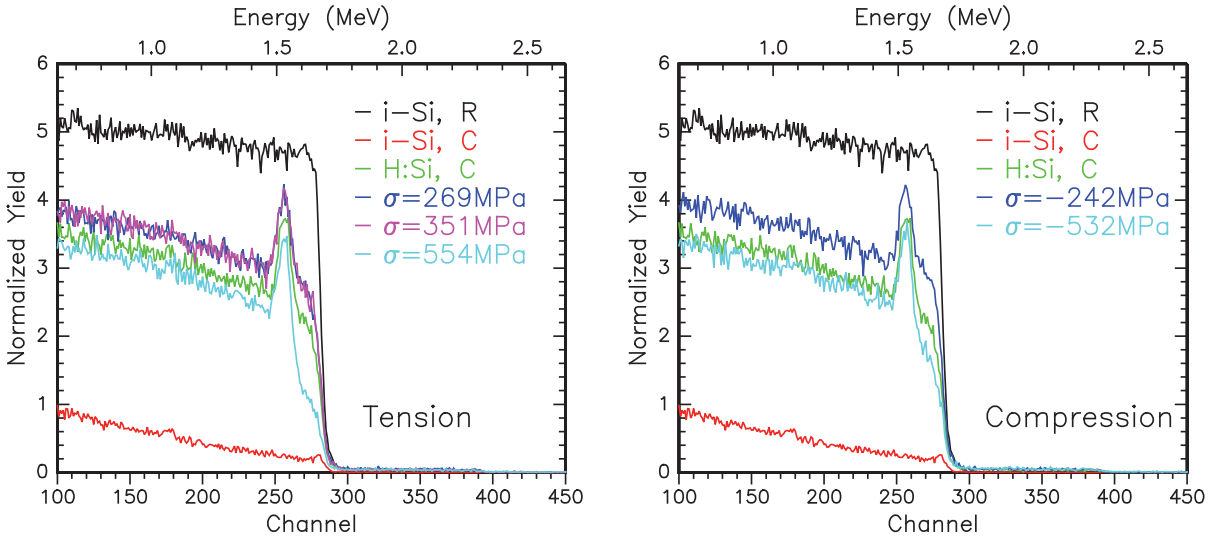

Figure 5.19: 3 MeV $^4He^+$ channelled RBS measurements of ULTRATHIN® Si(100) wafers implanted with H(40keV,6×10^{16}cm^{-2},RT), then annealed at T=400°C/30min under various values of (a) tensile, and (b) compressive stress. C indicates ion beam is channelled, R indicates randomly angled relative to the crystalline lattice. All measurements not marked R are measured along the (100) channel. Scattering angle ϕ=168.2°, Q=20 μC, I=10 nA.

peaks, independent of stress magnitude and direction. A very small increase in DS yield is seen with increasing stress magnitude.

When measured in the backscattering geometry with a scattering angle of ϕ=168°, the yield in each spectrum - even in the direct scattering peak - does not quite reach the level of a random angled spectrum. (Scattering angle ϕ=110° shown in Appendix E.1.) When subtracted from the DC background, the DS peaks in each of the implantations are of similar size and magnitude, seen in Fig. 5.24(a), with the associated tables found in Appendix E.1. In the overall RBS spectra however, the DC yields of the lower and middle stressed anneals were <15% higher than those of the higher stressed and unstressed annealed wafers. The ratio of the peak of the DS yield to the surrounding DC background was approximately 1.4:1 in all samples. As described above, in the region between the surface and the implantation, both the σ=-532 MPa compressed Si and the σ=554 MPa tensioned Si have lower yields than the material annealed without any applied stress, with the compressively stressed sample slightly higher in yield than the tensile stressed Si.

It is worth noting that the changes in RBS-C yields may indicate changes in the distribution of hydrogen damage within the crystal. While the spectra discussed here were

solely collected from a He beam projected along the [100] axis, there may be similar corresponding or complementary changes observed along [110] or [111] axes. This is elaborated on in Section 5.5.

Consider that these samples were annealed for t=30 minutes at T=400°C. In some of the lower stressed samples, this anneal induced high level surface blister formation, but stopped short of cratering, while in the unstressed and highly stressed material, blistering occurred to a lesser degree. Three dimensional projections of each of these samples surfaces as determined by the optical profiler are shown in Fig. 5.20.

For most samples, hydrogen-induced blister heights and distributions are independent of stress direction. The unstressed and stressed samples with $|\sigma|$ <400 MPa all show approximately the same range of blister heights, between 50-60 nm. However, for the two samples annealed at stress values $|\sigma|$ >400 MPa, there is a notable decrease in the range of blister heights. Comparing these two samples, the σ=-532 MPa sample shows less reduction in blister height than the σ=554 MPa. This variation in heights between the samples is comparable to the difference in ion beam yield seen in the RBS-C data from these samples, shown before in Fig. 5.19. This would suggest that the majority of the DC signal measured from these annealed specimens is due to the changes wrought by the hydrogen through surface blistering. The variation in surface regularity itself has been shown previously [301, 377] to cause similar variations in DC yields, though often with additional changes in the relative surface peak channel location. We see in our study not just a relationship between the presence of blisters and changes in RBS-C yield, but specifically the blister heights correspond to the magnitude of the change in backscattered ion beam yield. The distribution of blister heights versus diameter under both tension and compression in Fig. E.22, along with some analysis, is found in Appendix E.3. While the range of blister heights has decreased at the highest stress levels, the density of the surface blistering increases. On the σ=554 MPa, the small decrease in blister diameter and larger change in heights is offset by an increase in blister surface density, covering a larger area of the sample's surface.

The box-and-whisker plot diagrams for both individual hydrogen-induced blister diameters and heights are shown in Fig. 5.21. The comparative histograms showing the distributions of the blister diameters and heights for each stress condition in these figures are

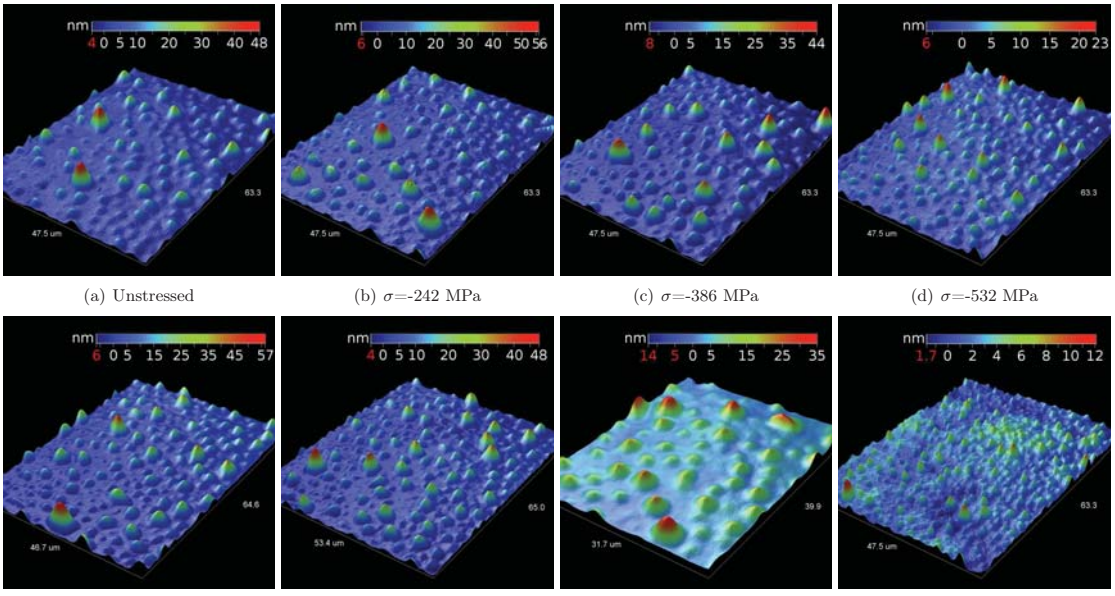

(a) Unstressed (b) σ=-242 MPa (c) σ=-386 MPa (d) σ=-532 MPa

(e) σ=222 MPa (f) σ=269 MPa (g) σ=351 MPa (h) σ=554 MPa

Figure 5.20: Optical profiler measurements of surface blisters on H(40keV,6×10^{16}cm^{-2},RT)-implanted 50 μm-thick Si(100), annealed at T=400°C/30 minutes at stress values as labelled. OP used in PSI mode, using a ×50 lens and F.o.V. set at ×2, using the Wyko Vision32™ [315] software package. Vertical height scales given by the colour bar in each figure, with red numeric values indicating relative depths below the mean sample surface. Scan area of sample σ=351 MPa cropped to avoid ruptured blisters.

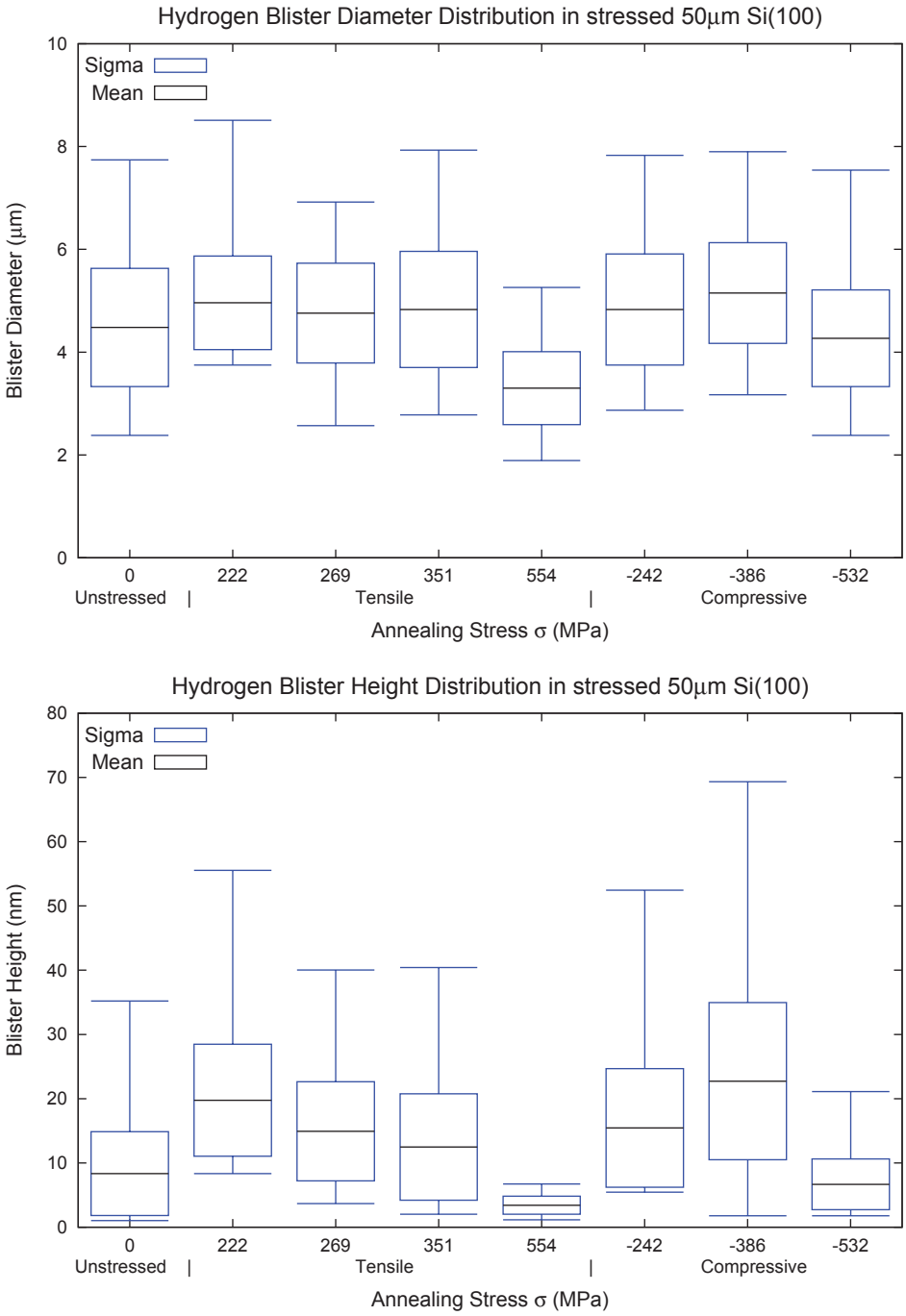

Figure 5.21: Hydrogen blister diameter and height, measured by the Wyko optical profilometer, from H(40keV,6×10^{16}cm^{-2},RT)-implanted 50 μm Si(100), annealed at T=400°C/30 minutes at external stresses as labelled.

shown in Fig. E.23 and Fig. E.24 respectively, Appendix E.3. The distributions in blister diameters shows little variation in range or skew across all the samples studied. Comparatively, the data from the σ=-532 MPa and σ=554 MPa samples seen in Fig. 5.21(b) really highlight the remarkable shift to lower blister heights seen in the samples annealed under higher stresses, with a much sharper positive skew in their distribution. These data support a conclusion that extrinsic applied stress has little influence on the diameters of the hydrogen blisters formed during annealing, and lower scale stresses have little impact on the heights of hydrogen-induced blisters in silicon. However, at $|\sigma|$ >400 MPa, stress serves to significantly decrease the height of the hydrogen blisters formed, as both the range of heights occurring and the maximum value is greatly diminished, and the surface density increases.

These OP and RBS-C data suggest that we would find a greater concentration of hydrogen in the near surface region, filling the annealing-induced blisters. This is not what is seen. As an initial comparison, Fig. 5.22 presents the ERD spectra from the post-annealed hydrogen-implanted silicon under highly compressive, highly tensile or unstressed conditions, in contrast with the unstressed as-implanted Si. Compared to the unstressed sample, approximately 30% more hydrogen is lost for the samples annealed under external stress. The location of the hydrogen profile peak depth (R_P) is similar in both (oppositely) stressed samples, and only slightly shallower than the samples annealed without stress or as-implanted.

In all cases, the surface hydrogen peak is little changed as the peak hydrogen concentration decreases, suggesting no further trapping is possible or occurs at the surface, possibly already saturated prior to implantation. As the earlier RBS-C data confirmed a large degree of disorder in the near-surface region between implant peak and surface (or larger hydrogen complexes of lower disorder), ERD establishes that this is not acting as a sink for the hydrogen diffusing during annealing. Similarly, while optical profiling indicated a high degree of blistering extending from the R_P to the surface, any indication of hydrogen within these blisters is absent. This absence indicates that rather than trapping at defects or decorating blisters and cavities, the hydrogen is escaping the silicon lattice largely unimpeded, possibly assisted by the external stress.

Expanding our examination, we contrast all the tensile or compressively stressed sam-

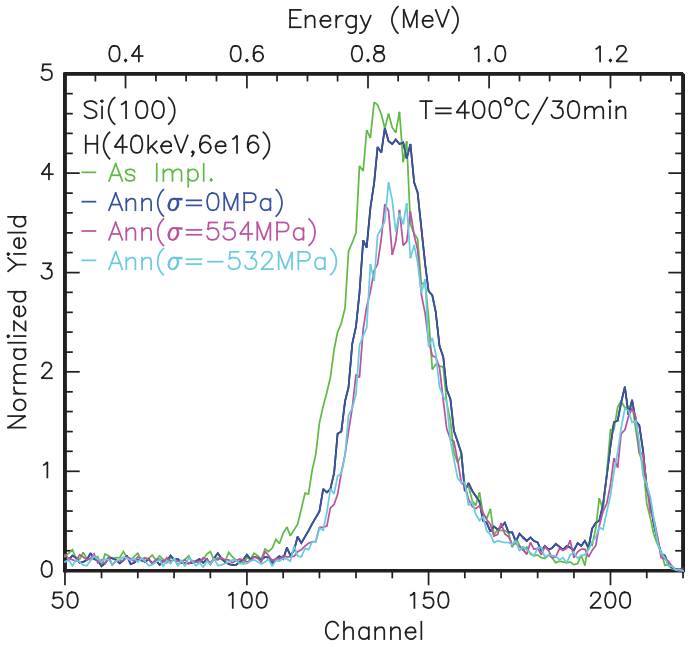

Figure 5.22: 3 MeV $^4He^+$ ERD measurement of H(40keV,6×10^{16}cm^{-2},RT)-implanted 50 μm Si(100), comparing hydrogen distribution following T=400°C/30 minutes annealing under three stress conditions, values as labelled. Detector and scattering angles ϕ=25°, sample tilted θ=80° to incident beam.

ples via ERD, in Fig. 5.23. A shift in the hydrogen profile post-annealing occurs in some of the samples annealed with only tensile applied stress. Fig. 5.23(a) shows a possible broader range of hydrogen trapping, in the σ=269 MPa and σ=351 MPa stressed Si. Such an increased hydrogen yield beyond the original profile into the region between R_P and the surface is not seen in any of the as-implanted or annealed unstressed Si, the compressively stressed material nor even the *most* tensionally stressed Si. At the higher tensile stress levels, the hydrogen profile is restricted to within the H profile (and associated damage profile) range seen in unstressed material. Considering RBS-C and OP measurements, it is possible that the broader H profiles at moderate tensile stress are indicative of blister formation.

Such lack of diffusion under high tensions would agree with previous work and results from OP in this study, suggesting that the higher tensions limit the range of H prior to its development into platelets and void-like defects. Lower concentrations at a given location would likely lead to shorter blisters and less distortion of the silicon lattice. However, the behaviour at low tensile stresses is particularly unexpected, as the increased rate of

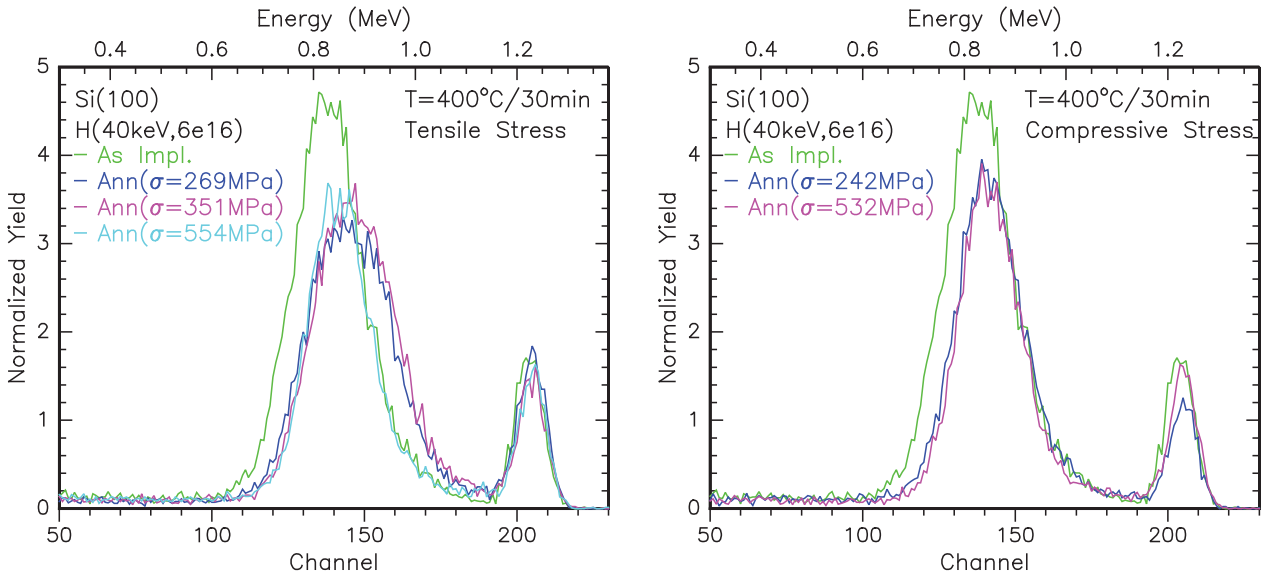

(a) (b)

Figure 5.23: 3 MeV $^4He^+$ ERD measurement of H(40keV,6×10^{16}cm^{-2},RT)-implanted 50 μm Si(100), comparing hydrogen distribution following T=400°C/30 minutes annealing under (a) tensile stress, and (b) compressive stresses, values as labelled. Detector and scattering angles ϕ=25°, sample tilted θ=80° to incident beam.

diffusion and broadening of the hydrogen profiles in the σ=269 MPa and σ=351 MPa samples largely disagrees with previous research, potentially excepting Xuan *et al.* [254].

Seen in Fig. 5.23(b), the hydrogen profile narrows under compressively stressed annealing, decreasing the yield while shifting the profile peak shallower. The surface peak does not significantly change, nor is there any indication of trapping between the implanted profile and the surface. The decrease in integrated yield (=hydrogen concentration) from the samples must thus indicate a loss of hydrogen from the sample, or diffusion throughout the material to sub-ERD detectable levels.

From the ERD data, we see that H is not accumulating far from the as-implanted profile's peak, possibly to the peak in ion implantation damage. The blisters observed by OP and the array of increased dechannelling yields in RBS-C do not harbour increased H concentrations or act as sinks. However we saw in the sample annealed without stress (Fig. 5.17) that ion-cut type defects formed, presumably from the implanted hydrogen. To confirm how the changes in behaviour seen in RBS-C, OP and ERD due to applied stress were linked to changes in micro- and macro-scopic defects, XTEM was performed on samples post-annealing under stress.

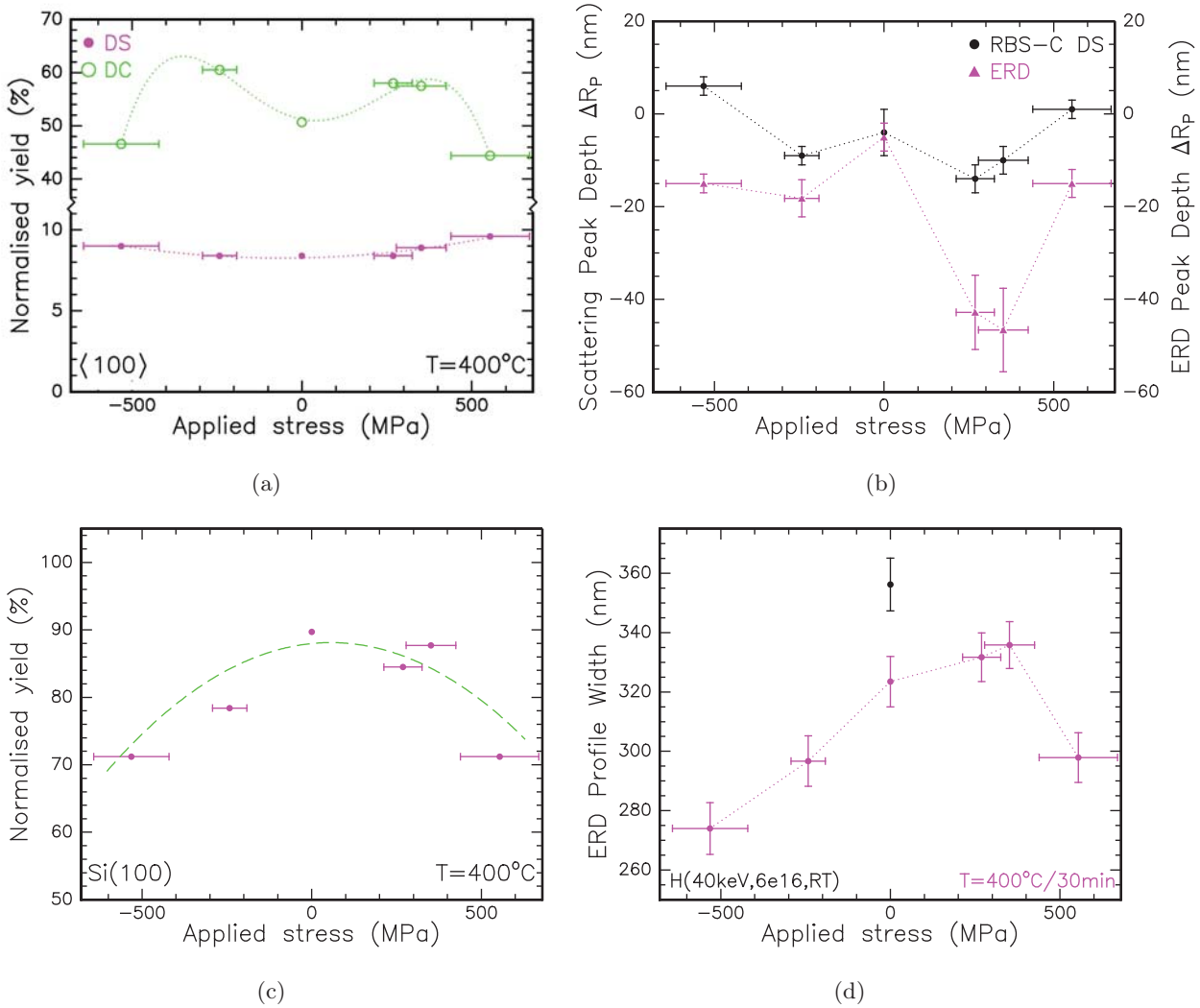

Figure 5.24: IBA measurements of 50 μm Si(100) wafers implanted with hydrogen ions at $\Phi = 6 \times 10^{16}\text{cm}^{-2}$ at E=40 keV, then annealed at T=400°C for 10 minutes, determined from Fig. 5.19. Stress applied during annealing as indicated. **(a)** shows RBS-C determined direct scattering **(DS)** and dechannelling **(DC)** yields along the [100] axial channel. **(b)** shows relative change in depth of the direct scattering (∼lattice damage) peaks extracted from [100] RBS-C spectra, in addition to the hydrogen profile peaks R_P from ERD spectra. **(c)** shows ERD yield from evolving hydrogen profiles. **(d)** shows relative change in ERD measured hydrogen profile widths, with **black** symbol indicating as-implanted unstressed sample. Beam: 3 MeV $^4\text{He}^+$, angle of back scattering detector θ=11.68°, and forward scattering detector ϕ=25°, Q=20 μC, I=7-15 nA. Partial data found in Table E.1.

XTEM micrographs reveal that the ion-cut type "macrocrack" is present under several stressed conditions. Bright Field off Zone Axis (BF OZA) micrographs of the H-implanted Si annealed under several of the applied stress values are shown in Fig. 5.25. In the samples annealed under σ=269 MPa and σ=-242 MPa, there is a common evolution, showing similar planar microcracks amalgamating at approximately the same depth and covering the same range as was seen in the samples annealed without applied extrinsic stress (Fig. 5.17). In addition to this large scale defect, there are also a range of small artefacts, between 5–10 nm in width, which resemble nanovoids [203, 378]. These features became more prominent in the sample annealed under σ=-532 MPa, which shows the formation of approximately spherical void-like defects interrupting the path of the macrocrack, of widths between 10 and 100 nm. The sample annealed under σ=554 MPa shows a less marked macrocrack, and also shows few of the large void-like defects seen in the σ=-532 MPa sample, or the smaller variety seen spotting the implantation region in the σ=269 MPa and σ=-242 MPa samples. The large crack occupies a narrow range in both compressively and tensionally stressed samples, similarly located at a depth close to two-thirds into the defective region, at $z \sim$440$\pm$10 nm.

The greatest extent of the defective band is in the sample annealed under higher tensile stress (σ=554 MPa) seen in Fig. 5.25(c), ranging from depths of z=310-500 nm. Any marginal increase in defect band width observed is though extension towards the surface, as all samples show a sharper rear interface near z=500 nm at the (presumed) EOR of the hydrogen implantation. Across all the samples examined, the number of hydrogen-induced platelets also fluctuates. As observed in the sample annealed without any stress, the {001} platelets appear the most common defect type to develop following the anneal. In addition to the "spars" connecting the smaller platelets in the large crack, {111} defects are also seen clearly in the samples with $|\sigma|$ <400 MPa, but are not as obvious in the more highly stressed samples. In the σ=-532 MPa stressed sample, the {111} platelets are clearest at the fringes of the defect band (Fig. 5.25(d)), and only hints of them can be resolved in the (poorer resolution of the) σ=554 MPa stressed sample (Fig. 5.25(c)).

When tensile or compressive stresses are applied on the samples within the (100) plane by the stress apparatus, there does not seem to be significant changes in the ratio of defects formed in the {001} and {111} orientations, but any influence the stress has in shifting

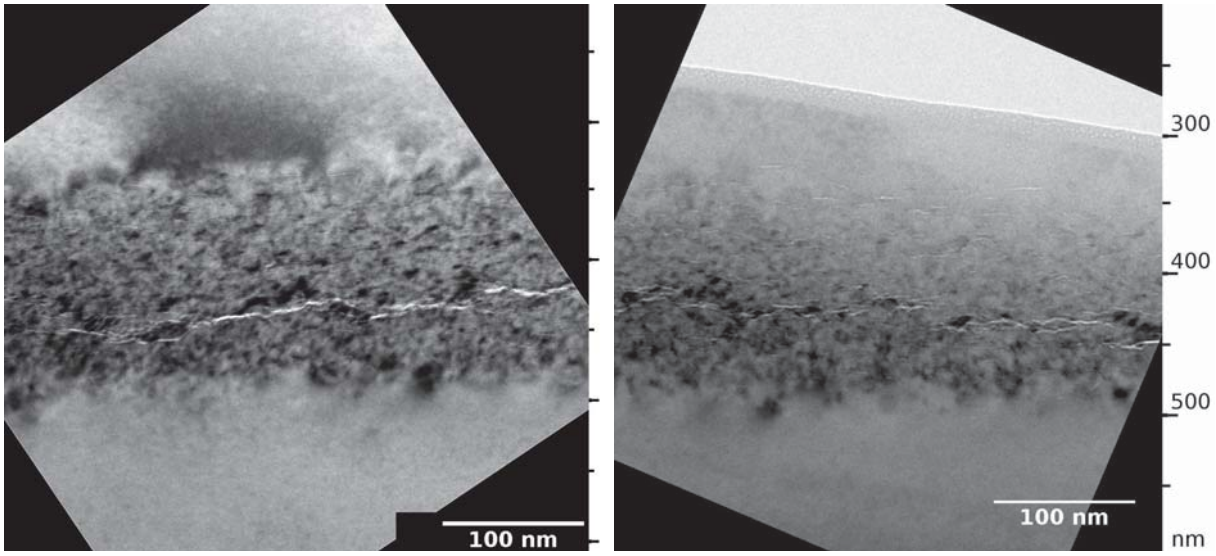

(a) σ=269 MPa (b) σ=-242 MPa

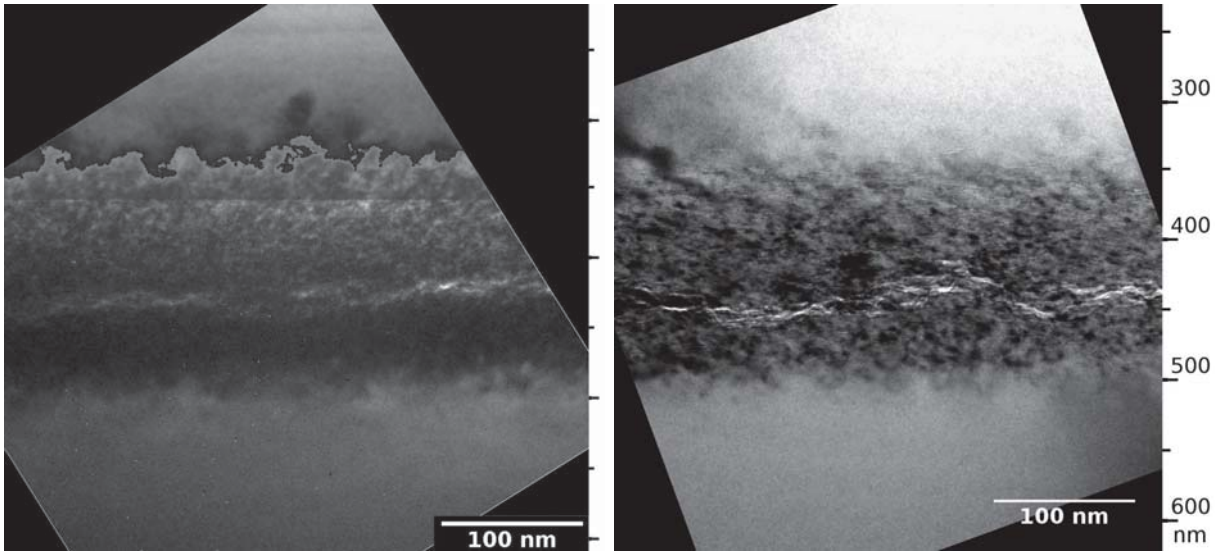

(c) σ=554 MPa (d) σ=-532 MPa

Figure 5.25: XTEM BF OZA micrographs of H(40keV,6×10^{16}cm^{-2},RT)-implanted 50 μm-thick Si(100), annealed at T=400°C/30 minutes under tensile (positive) or compressive (negative) stresses as labelled. Sample surfaces located beyond top of each figure. Depth scales from the surface with values displayed at right hand of micrographs. Note scales are slightly off-set between micrographs.

{011} oriented defects cannot be determined.

The XTEM-determined distribution of defects presented cracks forming most strongly in the lower stressed and unstressed samples, the greater yield in the defects along {001} and {111} planes, and fewer defects seen in both the highly compressively and tensionally stressed samples. These findings show the same consistent trends as were noted for these samples in both the RBS and optical profilometry measurements. Figure 5.26 contrasts the distribution of ion implantation damage as measured by RBS-C and the as-implanted H profile from ERD from the unstressed sample, overlaid on the XTEM micrographs from unstressed as-implanted and annealed samples (N1 and N2), lower compressively (C1) and low tensionally (T1) stressed annealed H-implanted samples.

Looking particularly at the lower tensile stressed sample, the depth at which the ion-cut style crack forms falls close to both the as-implanted peak in the hydrogen profile (z ∼465 nm), and the damage profile (z ∼450 nm). Previous research has indicated that the cracks form at a position between these two peaks, nominally the peak in local stress in a silicon wafer annealed without extrinsic stresses [27]. However this figure shows closer alignment between the direct scattering (DS) damage peak and the cracks in the lower tensile stressed sample. As all three of these positions are quite close, and there is some variation in crack depth, it is difficult to concretely conclude at which of these positions the ion-cut would occur. Between the different applied stresses, Fig. 5.26 shows there is some variation in the location of the macroscopic cracking event. The compressively stressed sample cracks at a depth shallower than the tensile stressed, while the unstressed sample is closest aligned with the DS peak depth.

Summarised in Fig. 5.27, the XTEM-determined average depth and standard deviation of the macroscopic cracking for compressive and tensile stressed anneals, in addition to the unstressed annealed H-implanted Si, are plotted against the depths and ranges of IBA-determined implantation damage and hydrogen distribution. Here the higher compressively and tensionally stressed samples have reversed the trend seen in the lower stressed samples. All macrocrack fractures are clearly shallower than the peak in the hydrogen profile as implanted, but do not necessarily coincide with the DS peak depth. A useful comparison is with Fig. 4.35 – the same fluence implanted into Si(100) and annealed at an array of temperatures without stress, examined in Section 4.7. The relative depths of RBS-C DS

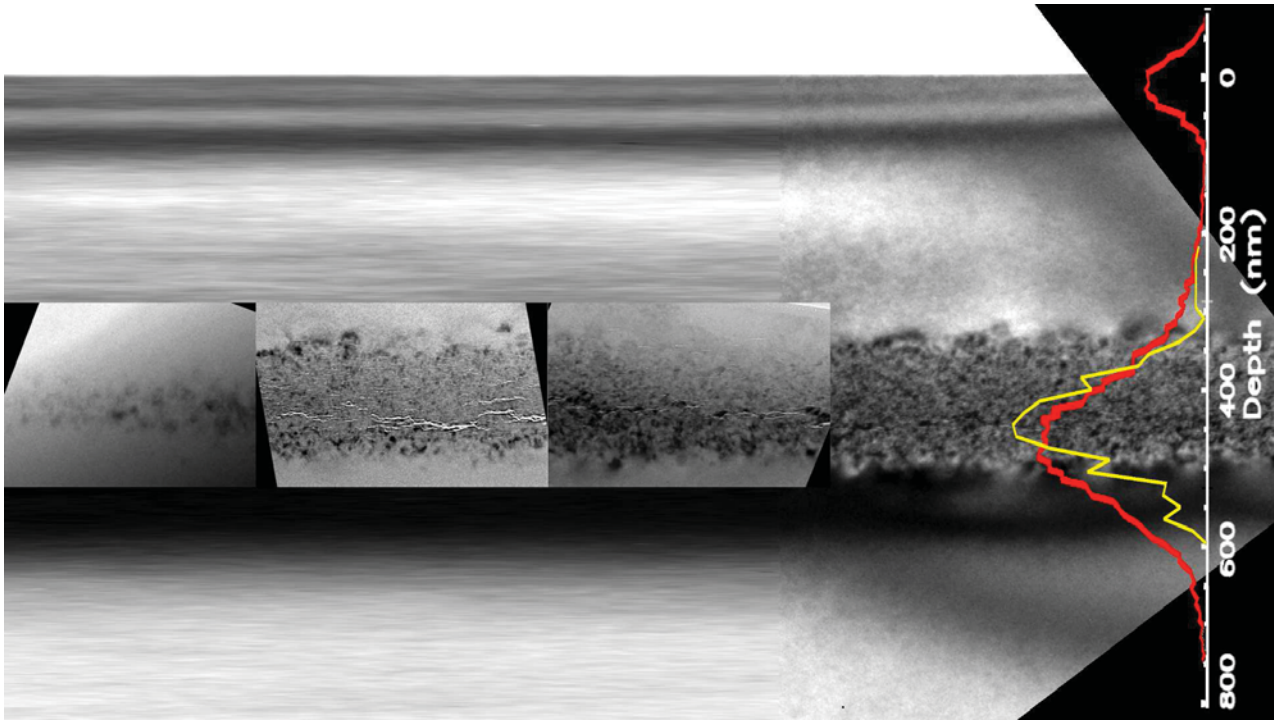

Figure 5.26: XTEM BF OZA micrograph images from hydrogen implanted at E=40 keV and $\Phi_H = 6 \times 10^{16}\text{cm}^{-2}$ at room temperature into 50 μm thick Si(100) wafers, examined (from top to bottom) as implanted; annealed; annealed under compressive stress σ=-242 MPa; annealed under tensile stress σ=269 MPa. Anneals performed at T=400°C for 30 minutes within the Ar ambient of a quartz tube furnace. Contrasted with micrographs are ERD measured H-implantation profile (in red) and RBS-C direct scattering (=damage) profile (in yellow) from the as-implanted unstressed sample. Sample surface indicated on depth scale at bottom of figure.

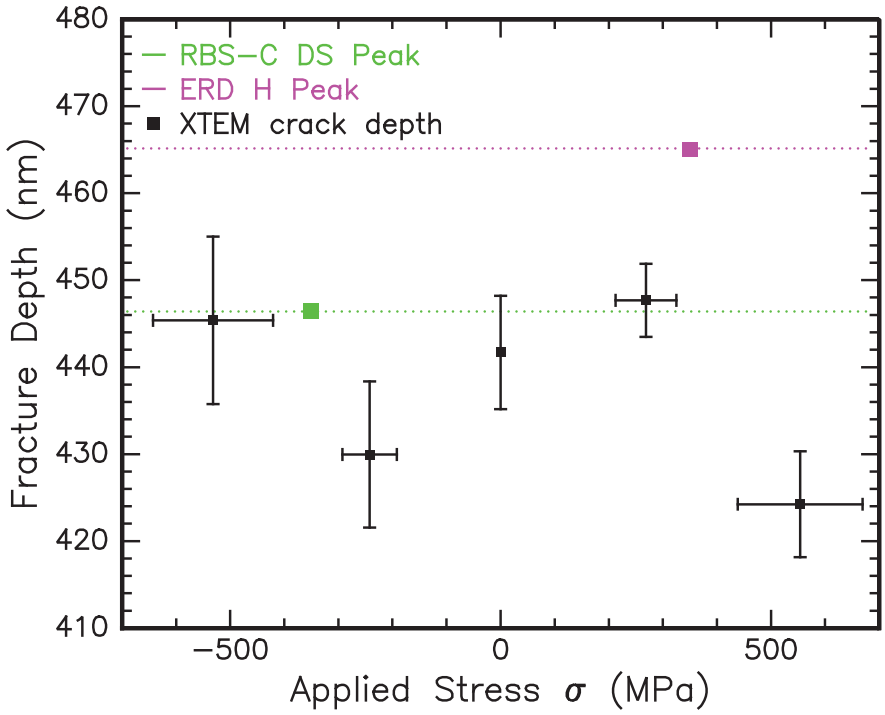

Figure 5.27: Comparison of macroscopic cracking depth determined by XTEM from hydrogen implanted at E=40 keV and $\Phi_H = 6\times10^{16}\text{cm}^{-2}$ at room temperature into 50 μm Si(100) wafers, annealed without stress, under compressive stress and under tensile stress. Anneals performed at T=400°C for 30 minutes within Ar ambient quartz tube furnace. Contrasted with crack depths are the ERD measured H-implantation profile peak (in magenta) and RBS-C direct scattering (=damage) profile peak (in green) from the as-implanted unstressed sample. Data located in Table E.2 in App. E.1.

peaks, ERD H profiles and XTEM crack depths post annealing at T>450°C in that study are in good agreement with the findings here.

However, contrasted with the changes in the depths of the DS peaks and H profile peaks from RBS-C and ERD shown in Fig. 5.24(b) for the particular samples, the behaviour of the XTEM measurements of the changing macrocrack depths differs. Lacking such a correlation between the locations shows that the majority of the remaining hydrogen is not accumulated at the depth of the macroscopic cracking. The possibility that sufficiently large concentrations of hydrogen did exist at these crack locations prior to formation, and presumably escaped from the substrate, is not ruled out. In order to quantify such a possibility would require techniques beyond the scope of this project, such as thermal annealing coupled with ERD, or other *in situ* H measurement methods during annealing.

Analysis and conclusion

The evolution of hydrogen under stress described in Fig. 5.24 shows some agreement with suggestions by Centoni *et al.* [375] discussing how compressive stress allows easier migration of hydrogen and defects within the silicon, while tensile stress actively deters diffusion as suggested by Pitera *et al.* and others [256, 364, 366]. From the data, we see hydrogen yields decrease more rapidly when annealed under compression than tension, leaving narrower profiles, suggesting higher diffusion rates. Moderate tensile stresses show higher post-anneal hydrogen yields and profile widths than the unstressed material, suggestion diffusion has been hindered.

However, there are some differences between previous predictions. For example, the peak in the hydrogen profile shifts further towards the surface in the moderate tensile stressed Si than all other samples. Additionally, the highly tensile stressed sample showed hydrogen loss and profile thinning equivalent to the compressively stressed samples. XTEM results show no consistent trend linking application of stress and depth at which ion-cut occurs. Results suggest the defects form shallower than the peak in the H profile, and possibly even the DS peak, and it is possible the ion-cut depth is decreased by stress.

Trends which do not follow on from any previous prediction are also seen. Moderate stress values increase the DC yield (crystal irregularity) while high stress values lead to lower DC yields and slightly higher DS peaks. A similar trend exists in relative peak shifts for both the DS peaks and ERD hydrogen profiles, where mid-level stress decreases the peak depth, while high level stress moves the peaks relatively deeper (or leaves them unchanged to the unstressed anneal). The lower DC yields also correspond to lower hydrogen-induced blister heights, suggesting less hydrogen is available to form surface defects.

Further work is required to confirm the reproducibility of the results presented in this thesis. A broader continuum of results collated from multiple samples at the same (or as near as can be achieved) stress would give a better sense of the reliability of these data, and the reproducibility of any described trends. Such an assessment does not invalidate our results presented here, it merely limits the confidence in their extrapolations.

From these data, it could be concluded that the application of stress leads to a decrease in hydrogen concentration post-annealing, leading to difficulties in forming defects to produce ion-cut. Compression may speed the diffusion to a "core" profile sooner, although

higher tension ultimately produces a similar result. Hydrogen which allows the formation of platelet-type defects does not remain at their location, nor does any reasonable concentration remain in the cavity of the surface blisters. Applied stress at these levels does not play a significant rôle in the evolution of the hydrogen-silicon system's defects or cracking depth.

When contrasting the influence of tensile and compressive stresses on the hydrogen profiles evolution with annealing, several observations are pertinent. Firstly, a larger fraction of the implanted hydrogen diffuses out of the samples under stress than the unstressed. Secondly, low values of tensile stress slow the diffusion of hydrogen from the implantation location towards the surface, while high level tensile stress and all compressive stresses have less influence over the rate of hydrogen loss. Thirdly, the resultant hydrogen profiles post-annealing are centred shallower, likely around the effective peak in the stress profile generated by the as-implanted hydrogen and the concomitant ion implantation damage. However the location of the resultant ion-cut crack is shallower again than the hydrogen profile peaks. The magnitudes of the stresses applied by the mechanical apparatus do not appear to have significantly influenced the trapping or transport of hydrogen within the semiconductors.

5.5 Problems and Issues

Potential plastic distortion due to annealing under stress

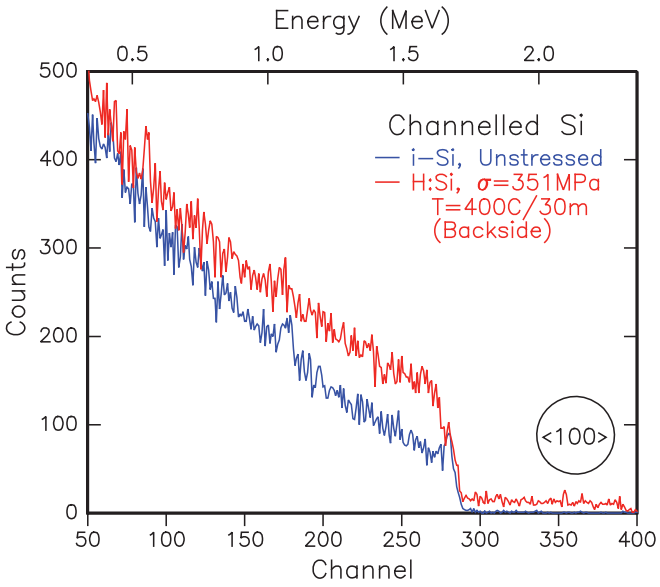

Figure 5.28: 3 MeV He RBS comparison of channelled spectra from intrinsic 50 μm Si, as-produced and annealed under σ=351 MPa.

In Section 5.4.4, for the samples implanted without stress and then annealed under stress, it is possible that the lack of lower channelled yields is due to residual distortion of the wafers, plastically occurring during the anneal process. Some confirmation of this is indicated by the spectra measured from the backside of the σ=351 MPa sample, which is effectively intrinsic silicon for the range of the RBS-C probe. The small sample and relatively large beam spot in this measurement results in a non-zero yield about the surface peak, shown in Fig. 5.28. However as it is clear both surface peaks in these two spectra are of similar yield and position, the subsequent increase in dechannelling (DC) yield is likely due to actual physical differences present in the stressed silicon wafer.

As the direct scattering (DS) peaks in the Si(100) sample implanted then annealed under various stress values (i.e., shown in Fig. 5.19) are all approximately equal, the variation in RBS-C yield must be within DC yields. So any degree of off-set caused by plastic distortion of the wafer will have significant impact on interpretation of the data.

Admittedly, such distortions can not account for the increased DC yield in the *unstressed* but annealed hydrogen-implanted wafer. Considering that this offset occurs in both stressed and unstressed material, it cannot be linked to plastic deformation. This agrees with earlier findings and previous researchers [268,369–371]. Rather, the higher DC offsets are more likely to be due to potential subsurface hydrogen-induced defect formation, induced by the thermal anneal, as discussed in Section 5.4.4.

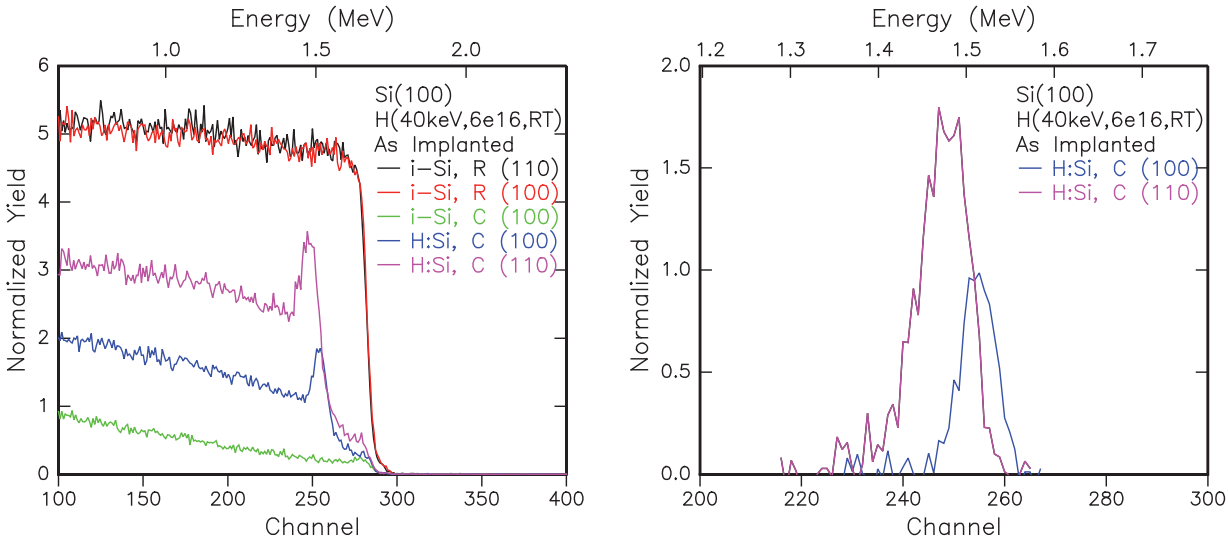

(a) (b)

Figure 5.29: 3 MeV $^4He^+$ RBS channelled (C) measurements of H(40keV,6×10^{16}cm^{-2},RT)-implanted 50 μm Si(100), measured in both [100] and [110] crystallographic axes. (a) includes random spectra (R) when measured around each axes, as well as virgin Si [100] channelled spectra for reference. (b) shows isolated direct scattering peaks induced by hydrogen implantation as measured along both axes. Note that while energy scales are the same for each channel, depth scales are not identical.

RBS channelling angle variations in yield

It is important to note that the change in yields seen in the RBS-C spectra discussed in Section 5.4.4 may be an indication that the hydrogen damage has shifted crystalline location or orientation, as these spectra were solely collected from a He beam projected along the [100] axis. If examined in the [110] or [111] channels, the hydrogen implantation damage yield may differ significantly. It is possible that the annealing process whilst under the application of external mechanical stress (as distinct from the stress produced by the implantation itself) facilitates the hydrogen's evolution along different axes. If platelets predominately formed along {001}, they may be invisible in the [100] channelled spectra, but visible in [110] and [111] spectra. This suggests the possibility of having successfully modified the hydrogen platelet evolution. In an attempt to ascertain some of these differences, Fig. 5.29 shows a comparison of the hydrogen-implanted 50 μm Si wafers as measured by RBS-C along the [100] and [110] crystal axes.

A clearly higher yield is seen in both DS and DC components of the [110] spectra. In the excised DS peaks, the damage yield in the [110] path is nearly twice that measured in

the [100] channel. These data would suggest that most defects present in the as-implanted state do not lie in the {011} family of planes. This may indicate that with three potential core orientations of defects, such hydrogen-induced defects lie primarily in the (100) and (111) planes. As the [110] yield is approximately twice the [100] yield, the population of defects appears equally divided between {001} and {111}, with very little in the way of {011} defects. This may indicate why in the RBS-C DC yields measured along the [100] channel in Fig. 5.19, the yields either decrease or increase. The relative proportion of the defects formed along each crystal orientation may have been altered by the applied stresses. As such, those showing higher than the unstressed implantation yields may have had a greater proportion of {111} and {011} defects, while those with lower yields may have a higher number of {001} oriented defects.

Chapter 6

Discussion and Conclusions

6.1 Overall review

Two major aspects of the interaction of hydrogen within semiconductors were presented in this thesis. The first was a study of hydrogen-induced blisters within crystalline Si and Ge, and the defect structures and physical distortions produced. The second was a study of hydrogen implanted under conditions of stress, and the influence of this stress by compositional or mechanical means on the hydrogen evolution within the semiconductor. Both of these components of the investigation were formulated as part of the over-arching principle of achieving a better understanding of the evolution and transport of hydrogen, in terms of both the ion-cut fabrication technique and the manipulation via stress to improve upon that wafer slicing process.

The first study in Chapter 4 comprised of optical profiling and video recording to ascertain the hydrogen-induced blistering behaviour in Si and Ge, particularly the activation energies and blistering/cratering rates. The nature of the hydrogen defects too were probed via IBA channelling measurements, to establish how the hydrogen was changing within the crystal over thermal annealing. Blistering within a narrow fluence and energy boundary operated with a single activation energy in Si and Ge, with values outside those boundaries presented the appearance of multiple effective activation energies in Ge. Measured along the [100] channels, hydrogen related defects increased with annealing, suggesting changes into (110) and (111) planes.

The second study in Chapter 5, comprising ion beam techniques, transmission electron microscopy and optical profilometry, sought if external mechanically applied stresses could influence the transport of hydrogen within a semiconductor, and to what extent the stress could allow it to be trapped, towards the end of improving the ion-cut technique.

The ultimate conclusion of this thesis, largely guided by the second study, is that modification of the ion-cut process by mechanically or compositionally applying stresses or strains to the hydrogen-implanted semiconductors, at the macroscopic levels which are presented in this project, is unlikely to be successful.

The particular findings from the two components of this thesis are of course still relevant to their respective research fields. These fields, of hydrogen blister formation in semiconductors and the influence of stress on the behaviour of hydrogen in silicon, are key to interests of both the research scientist and microelectronics engineer. The primary insights of these investigations are detailed in Sections 6.2 and 6.3. Like many time-limited projects, there are areas in this study needing further pursuit or improvement. These potential avenues for future expansion are elaborated upon following the study summaries.

6.2 Summary of phenomenology of hydrogen blistering study

Chapter 4 examined the hydrogen implantation influences upon intrinsic crystalline semiconductors. The particular materials which were focused upon were silicon and germanium.

The first section addressed the impact of ion implantation temperature, energy and fluence upon the swelling of the crystal lattice (Section 4.3). Ion implantation induced swelling in crystalline material, proportional to implanted fluence, but largely independent of energy and increasing substrate/ambient temperature. Radiation damage from the ion implantation appeared to correlate to the occurrance of swelling, but subsequent measurements rendered this conclusion uncertain, due to the possibility of defects not measureable by He beam RBS. Larger swelling was observed in material held at liquid nitrogen temperatures (LN2), with samples implanted at T=20°C and T=60°C 10–30% less swollen than the LN2 sample, showing some influence from implantation temperature. Ion implantation energy does not significantly impact surface swelling, and the ultimate magnitude of swelling was relatively small compared to later blistering heights and crater depths.

The second section established that a critical concentration and ion energy was required to induce blistering in a preliminary study of hydrogen's thermal evolution under a fixed temperature and duration anneal for Ge and Si, described in Section 4.4. In a simplistic comparison of 10 minute duration anneals, Si(100) wafers blister more readily than H-implanted Si(110) substrate, and Ge(100) behaves similarly to Si(100) at least until E=500 keV. Any inferred upper limits to fluence or energy requirements in the blistering process do not seem to exist. Lower limits exist to induce blistering – $\sim 8 \times 10^{16}\text{cm}^{-2}$ for Si(110), and $\sim 1 - 2 \times 10^{16}\text{cm}^{-2}$ for both Si(100) and Ge(100).

Substantial focus upon the mechanism behind blister formation was presented in Section 4.5. Broken up into a number of subsections, the blister dimensions (i.e., diameter, height) were investigated, followed by a comparison of blister diameters with implantation conditions (i.e., ion energy and eventual hydrogen depth), for Ge(100), Si(100) and Si(110).

Blister diameter is proportional to hydrogen ion energy (implant depth) and to a lesser extent implanted fluence for Si(100) and Ge(100). In the same specimens, a possible weak link exists between fluence (but not ion energy) and blister height. In Si(110), blister diameter is largely linked to ion fluence not energy, but no clear relationship exists between individual implant conditions and blister heights. Ranges of blister heights were experimentally linked to implant energy or ion depth in all samples. Peak fluence may be more critical to blister dimensions than total hydrogen, as higher fluence implants showed a plateau of values being reached. Relationships described by Eq. 4.1 and 4.4d produce reasonable agreement to data in blister height values when supplemented with experimental blister diameters. Hydrogen blisters in silicon can be acceptably modelled by Gibbs Free Energy arguments using plastic or elastic fixed plate distortion.

Blister dynamic models comparing blister diameters to pressure ($\sim$ hydrogen fluence) proposed by Dion and Mitani require modification of their pressure exponent in order to better fit the experimental data. A critical local hydrogen concentration may be more important in defining blister diameter sizing than total hydrogen, perhaps allowing blisters to form without additional material provided via diffusion or other mechanism. Blister heights seem to plateau at higher hydrogen fluence and energies, giving an upper limit to heights, and suggesting a stronger link between implant damage and diameter than height.

Section 4.6 addressed the kinetics of hydrogen evolution over time, to establish the

conditions that produced blistering, cratering and how these varied between crystal orientations, species and thermal exposures.

Hydrogen-induced blistering and subsequent cratering was observed in Si(100), Si(111) and Ge(100) for the standard condition hydrogen implantation of H(40keV,6×10^{16}cm^{-2},RT). Si(110) required a higher fluence ($\Phi = 1 \times 10^{17}$cm^{-2}) to blister. Two alternative implantations of hydrogen into Ge also blistered.

Total number of blisters (and ultimately craters) formed on the surface of Si(100) reaches an areal density of $N_B = 8.8\pm0.9\times10^{9}$m^{-2} for a H(40keV,$6\times10^{17}$cm^{-2},RT) implantation. The areal density of blisters in Si(111) is N_B =$18.8\pm0.1\times10^{9}$m^{-2}, approximately 2-3 times higher than Si(100) for the same energy and fluence. Surface blistering on Si(110), which required a higher hydrogen fluence, is significantly sparser at N_B =$2.4\pm0.2\times10^{8}$m^{-2}, 30 times less than Si(100). A clear wafer orientational dependence exists in ultimate surface blistering, governing both ion fluence and energy. Resource-limited growth equations such as JMAK and Gompertz functions both produce reasonable fits to the data. Transitions from Gompertz fits at lower annealing temperatures to JMAK at higher temperatures may indicate change in importance during the process from available volume (Gompertz) to hydrogen concentration (JMAK). Relative area of hydrogen blisters at set time intervals gave good agreement with trends shown in previous work, if not the same order of magnitude, which may be accounted for by difference in fluence.

In comparison, the hydrogen-induced blistering areal density measured in Ge(100) seemed better fit by JMAK functions at low temperatures and Gompertz at higher anneals. The critical fluence for reaching particular surface areal densities may be lower in Ge, and lead to an upper limit of blisters for similar implant conditions, as both 3 and 6×10^{16}cm^{-2} implanted hydrogen fluences produced similar density values ($N_B \sim 1.1 \times 10^{10}$m^{-2}).

Examining the temperature dependence of surface blistering (and cratering) in Section 4.6.2 led to measuring rates of blistering, and the energetics of their formation. A constant activation energy was seen for Si(100), Ge(100) and Si(111) implanted with the "standard conditions", as well as higher fluence implanted Si(110), in stark contrast to most previous studies, while variable activation energies were seen in lower fluence and higher energy implanted Ge(100), though not with the same trends as other studies.

Si(100) wafers implanted with H(40keV,6×10^{16}cm^{-2},RT) in both 375 μm and 50 μm

thicknesses demonstrated constant and very similar activation energies for thermally induced hydrogen blistering, with differences due to restoring strain differences from the unimplanted section of the wafer substrate. An activation energy of E_a=2.27±0.18 eV was measured for bulk Si, while an E_a=2.30±0.22 eV was evident in ULTRATHIN® Si.

For Si(111), blistering operated similarly to the Si(100) substrate, with a similar activation energy (E_a(111)=2.18±0.11 eV versus E_a(100)=2.27±0.18 eV). Si(110) was the only series not to blister at all for the standard fluence implantation, independent of temperature or duration of exposure. A threshold fluence of approximately $\Phi = 8 \times 10^{16}\text{cm}^{-2}$ is required for hydrogen-induced blistering in this crystal orientation, suggesting a higher stress level is required to constrict the hydrogen diffusion and aid in production of complexes leading to cavities. Blistering in Si(110) did occur at $\Phi = 1 \times 10^{17}\text{cm}^{-2}$, again with a single activation energy, E_a=2.14±0.06 eV, in contrast to previous studies. It is possible that this value decreased at lower annealing temperatures (E_a=1.79±0.12 eV), however this trend is the opposite to that seen in other materials in this study, or previous studies.

Blistering occurred in H-implanted Ge for three fluence and energy combinations – H(40keV,6×10^{16}cm^{-2},RT), H(40keV,3×10^{16}cm^{-2},RT) and H(100keV,6×10^{16}cm^{-2},RT) – for the majority of annealing temperature and time regimes. For the E=100 keV implantation, anneals from T=550-600°C failed to produce blisters or lift-off, but rather possible oxidation of the surface of the wafer. Between T=350°C and 550°C, the surface layer lifted off in a single instant, while regular individual blistering occurred below T=350°C. The H(40keV,6×10^{16}cm^{-2},RT) implantation in Ge(100) has an activation energy of E_a=1.40±0.14 eV, while the other two fluence and energy combinations presented multiple effective activation energies. For E=100 keV implantation, E_a=1.32±0.03 eV for T$\leqslant$425°C, and E_a=0.71±0.08 eV for T>425°C. For the H(40keV,3×10^{16}cm^{-2},RT) implantation, E_a=2.16±0.09 eV for T$\leqslant$325°C, E_a=1.19±0.02 eV for 325°C < T < 500°C and E_a=0.44±0.04 eV for T$\geqslant$500°C. It is unclear whether the multiple values are a result of uncontrolled factors influencing the blistering process, or indications that blistering in Ge is not governed by a single rate limiting property.

Modelling by Han, confirmed by this study, shows that the factors influencing the blistering and cratering in silicon (100) and (111) are the hydrogen complex dissociation energy (E_a), the hydrogen to vacancy diffusion energy (E_d), the dissociating hydrogen bond

jump frequency (τ), sample temperature (T) and implanted fluence (ϕ). The accuracy with which this model matches the experimental data for Si(100) and Si(111) indicates the assumptions and values used in the model are a good physical description of the hydrogen blistering system. To better fit Si(110), modification must be made to either hydrogen bond jump or stretch frequency and/or surface crack tension values – physically reasonably within previously speculated limits. However for Ge(100), modifications without clear physical meaning were required to match Han's model, suggesting alternative theory or additional research is required for that material.

Following blister formation energetics and dynamics studies, Section 4.7 presented insight into the aftermath of the blisters rupturing. Some results suggest that the peak hydrogen concentration value is proportional to the anneal-induced cratered blister depth and floor roughness, independent of the implant fluence and energy used to achieve that concentration. However, the energy or depth of the peak in the implanted ion profile may influence the roughness of the crater floors.

In Si(100), blister roughness and depth has some temperature dependence, with low temperature anneals (T<450°C) showing rougher and deeper sizes. The lower temperature regime may have a more regular transition between microcracks at either the stress or hydrogen concentration peaks.

Similar to Si(100), the Si(111) substrate showed a trend towards rougher and deeper hydrogen-induced craters for lower temperature anneals (i.e., T$\leqslant$450°C). As both had the same implantation conditions, ion energy and fluence, and the same substrate material (if not crystallographic orientation), this may suggest the same thermal-limiting factor is intrinsic to the material. The order of roughness is also of the same magnitude as seen in Si(100), suggesting cracks propagate parallel to the surface, independent of lattice structure.

Increasing annealing temperature saw craters formed in Ge(100) implanted with the standard conditions decrease their depth and possibly increase roughness. 100 keV H-implanted Ge(100) showed less evident trends, with again a possibly weak decrease in depth and increase in roughness with annealing temperature.

Unlike Si(100) or Si(111), hydrogen-induced blistering in Ge(100) forms via microcracks and defects located at the end-of-range of the ion implantation. It is possibly due to higher

stresses produced by the implantation into Ge, and the sharper interface between implant damaged and intrinsic Ge crystal producing a favourable nucleation site at the interface.

As the bond length over which the hydrogen complexes induced similar fracture differs between (100) and (111) silicon (a_o(100)=5.431 Å, a_o(111)=2.352 Å) [278], and considering that the bond length of Si(100) is similar to Ge(100) (a_o=5.646 Å) which both displayed distinctly different blistering behaviour, it is evident that the structure of the crystal itself is not key to what makes Si(111) and Si(100) blistering roughness (and other) behaviour similar.

High level doping of a silicon substrate was observed in Section 4.8 to change the hydrogen-induced blistering behaviour. Whether positively or negatively doped, the change in the rate of blistering was lower in the doped material, with all exhibiting lower, relatively constant activation energies. Activation energies for B-, P-, and As-doped Si were E_a=1.21±0.06 eV, 1.51±0.04 eV and 1.74±0.04 eV respectively. The pre-exponential constant for each of the doped materials varied from the intrinsic Si, with the doped materials all blistering slower at high temperatures, and faster at lower temperatures (T<500°C for all samples, higher for P- and B- doped material). The particular rates of blistering may be linked to specific defect migrations allowing large hydrogen complexes to form, and dependent upon the complex, some variation will occur sample to sample.

The roughness of the hydrogen-induced craters formed in B- and P- doped samples was largely independent of annealing temperature, unlike the intrinsic silicon, while the depths of the craters decreased with annealing temperature. While the same trend in crater depth was seen in the As-doped Si, the roughness of the crater floors increased with annealing temperature.

All doped samples show a lower implantation damage profile value as measured by RBS-C than the equivalent intrinsic silicon samples. The positively B-doped sample showed a larger peak than the negatively As- or P-doped samples, which are evident to have the same damage profile, confirmed in ERD spectra of hydrogen content and profile distribution for each sample.

6.2.1 Discussion and further work

The simple expansions of several of the prongs of this study would be an obvious first step towards a greater understanding of H in semiconductors. To expand upon the blister appearance study in Section 4.4, a larger array of fluences and implantation energies with a finer gradation would produce a more continuous determination of potential blistering. Perhaps the establishment of a sufficiently long duration anneal, or higher temperature, in order to accurately assess for blister potential.

Beyond this expansion, greater confidence would be provided in the reproducibility of all results by repetition. Multiple samples undergoing the sample processes would confirm most trends and correlations. Considering the volume of the data involved in this study even in one iteration, this would not be a trivial undertaking.

The question of how the Ge implanted with non-"Standard Conditions" hydrogen produced multiple effective activation energies needs close attention. In future annealing-induced blister studies, strict controls should be employed over atmosphere, annealing mechanism and calibration, cleaning and possibly contact contaminants – ideally everything should be performed in a hermetically sealed environment. Additionally, the implantation process needs to be closely monitored to ensure consistency of sample production. Both the array of samples tested within our work, and an expanded sample set should be investigated, to establish if multiple factors are at play for H-related blistering in Ge, or what factors if left uncontrolled produce apparent multiple activation energies.

When comparing the hydrogen implantation evolution along multiple crystalline channels as in Fig. D.3 of Appendix D.1, a third tier of measurements along the [111] axis would be instructive. Also, attempts to examine situations where none of the samples had surface blistering would be more instructive, hence the relegation of this data to the appendices.

For measuring the dimensions of the hydrogen blisters or craters formed on the sample surfaces, some greater degree of automation from a calibrated three-dimensional data array collected by the optical profiler would allow even greater accuracy of statistical spread in the measurements, possibly clarifying some of the more anomalous artefacts. Also, it would remove anthropic bias to the selection process and measurement.

A precise determination of the region monitored during the blistering process through the microscope would also allow better determination of not only the rate of blistering per area per time, but of the number of blisters per the surface area of the wafer formed at any given interval. This would allow comparison with a number of previous studies, such as Qian and Terreault.

A larger array of fluences and energies into each substrate would also allow a more precise picture of how the activation energy evolves in each semiconductor with time, providing a broader continuum of data. Similarly, both cross-sectional and planar TEM could offer the potential to catalogue the array of defects formed within the semiconductors due to the annealing of the hydrogen implantation.

All this data should also be used to attempt more conclusive links between blister areal density models (i.e., Gompertz and JMAK) and activation energy models (i.e., Han [343]) and the underlying physical principles governing hydrogen's behaviour. In particular, blistering in Ge, in light of the effectively changing activation energies, a study of what factors went uncontrolled or unaccounted may allow a single definitive energy to be established, as mentioned above. Blistering in other material substrates needs greater investigation, as well as an extension into III-V and other compound semiconductors. Theoretical underpinnings may then allow a more focused direction for future studies, rather than the catholic approach used here.

6.3 Summary of stress effects on hydrogen study

Chapter 5 described investigations of hydrogen's evolution under modified environments. The chapter was divided into two sections, dealing with the stresses present within ion implanted semiconductors, and the modification via extrinsic mechanical means.

Sample strips from Si and Ge approximately 5×18 mm in surface area were used to examine the intrinsic stresses in semiconductors, and the impact of ion implantation and annealing, in Section 5.1. The radius of curvature decreased following ion implantation into 375 μm and 50 μm Si and Ge, reaching a common value almost independent of their as-produced state. The macroscopic induced stress was largely tensile, and subsequently decreased (with the corresponding increase in radius of curvature) with annealing

at T=400°C for 30 minutes. The influence of either implant or anneal was most evident in the 50 μm thick Si wafers, and in contrast to the silicon, the Ge(100) showed minimal relaxation following annealing. The relaxation of stress with annealing suggests that the migration of defects, dislocations and other crystal irregularities allow the semiconductor substrate to "repair" some of the damage induced in the ion implantation, and hence reduce the induced stress. However the influence of individual defects with potentially highly stressed localised environments was not quantified, leaving this a discussion of macroscopic effects only. These stress values were significantly smaller than values predicted by symmetric Euler-Bernoulli bar bending theory (1 MPa versus $\lesssim$1 GPa), and unlikely to be the dominant factor influencing hydrogen's evolution in an externally stressed system.

The use of mechanical stresses to influence hydrogen was explored in subsequent sections. In this study, Si(100) samples were distorted by extrinsic stresses during hydrogen implantation or subsequent annealing. The H(40keV,6×10^{16}cm^{-2},RT) implantation was sufficient to induce ion-cut, requiring annealing temperatures and exposures being selected to provide diffusion without catastrophic eruption of hydrogen blisters.

Firstly in Section 5.2, during ion implantation a regular 375 μm Si wafer was exposed to tensile stress via a primitive three point bending apparatus. The apparatus consisted of a series of tantalum clips restricting the wafer and a pyramidal stack of Si wafer fragments placed beneath it. RBS-C and ERD profiled the wafer's hydrogen implantation and ion damage, determining lower yields along the [110] channel, and higher yields in both [100] and [111], in contrast to unstressed Si wafers. Indications were that the hydrogen complexes within the silicon were expanding in the (110) plane due to tensile stress. XTEM measurements on the sample following implantation observed an increased concentration of {111} hydrogen platelets than in unstressed H-implanted Si, showing the capacity of stress to influence the hydrogen evolution.

The following majority of this investigation then used ULTRATHIN® (50 μm) Si(100) wafers to investigate hydrogen changes when significant mechanical stresses are applied. In order to qualify the appropriate use of this information in application to regular 350-400 μm thick Si wafers, Section 5.3 indicated RBS-C and ERD comparative measurements observed little difference in implantation damage, hydrogen profile or lattice distortion between the thick and ULTRATHIN® wafers.

An array of implantations into 50 μm Si(100) were performed in combinations of compressively, tensionally and unstressed conditions, and their hydrogen distributions examined with IBA techniques. The stresses were applied by a unique mechanical apparatus devised for this project, as described in Section 3.3. The influence of the apparatus itself on the blistering process was shown to be minimal, allowing comparison with other annealing studies performed in unstressed quartz boats or similar.

Section 5.4.3 featured independent hydrogen implantations into Si under various stresses, or during annealing, or both. All H-implanted Si samples, after an exposure of T=400°C/10 minutes annealing, remain in an unblistered state. The application of either compressive or tensile stress during implantation produces lower hydrogen concentrations in samples relative to the intrinsic, however any significant differences dissipate following any subsequent annealing, with or without stress. Peak depth and yield of the hydrogen profiles following annealing do not show much change, with some variation in profile width, independent of applied stress. It is possible compressive stress applied during annealing may further decrease hydrogen content. Similarly, direct scattering peaks related to implantation damage of the silicon show little variation between samples implanted stressed or unstressed.

When tensile stress was applied during both implantation and annealing, the lattice distortion indicated by dechannelling was significantly higher, possibly leading to the formation of large hydrogen complexes as immediate precursors to blistering. Alternatively, tensile stress applied solely during annealing, or any compressive stress, shows a linear relationship with decreases in lattice distortion.

Section 5.4.4 limited the focus to a single unstressed implantation, which was studied in contrasting annealing stress states, to examine changes in defect formation, hydrogen profile and induced damage. XTEM performed on the unstressed 50 μm Si implanted with H(40keV,6×10^{16}cm^{-2},RT) prior to and post annealing shows a large shift from {111} to {001} orientation for the hydrogen platelets. The wafer cracking used by the ion-cut process formed from amalgamations of {001} platelets into continuous planes, joined by spars or struts composed of {111} platelets. When examining XTEM micrographs of H-implanted Si annealed under stress, there does not appear to be a significant change in the populations of each platelet orientation, though the influence on {011} platelets cannot be easily determined from these cross-sections. General distributions of platelet types and

occurrence of microcracking does agree with results seen in RBS-C and optical profilometry.

Studying stresses applied to samples from this same H(40keV,6×10^{16}cm^{-2},RT) implantation into Si(100) during annealing at T=400°C/0.5h, low-to-moderate compressive or tensile stresses (σ <|400 MPa|) increased the RBS-C dechannelling yield, suggesting higher defect densities, and the surfaces of each of the wafers presented a highly developed field of hydrogen-induced blisters. Higher values of approximately σ >|500 MPa| in either stress type were observed to decrease the RBS-C dechannelling yield, lower than the intrinsic material, indicating that the defect formation readily produced under annealing was being retarded. The RBS-C measured direct scattering yield from all samples was approximately equal, confirming the only factor influencing these peaks height and spread was the implantation process. Optical profiler measurements from each sample showed the highest stressed samples had the surface blisters with the shortest heights, smaller even than the unstressed material, while the low and median stressed samples had taller blisters. Higher stressed samples also showed a higher areal density of surface blistering. Blister diameters do not appear to significantly change, associated more with the implant parameters than stress conditions. The dimensions of these blisters are in general agreement with the dechannelling yields of RBS-C measurements, confirming the link between implantation distortion and blister height, as defect formation was higher in the low and mid-stresses but decreased in the high stresses.

ERD measurements indicate greater loss of hydrogen from samples annealed under any stress, and all implanted profiles move towards the surface akin to reverse annealing. Compressive stress clearly narrows the hydrogen concentration within the original damage profile, while tensile stress is less consistent, initially diffusing into a wider profile at moderate stresses before narrowing at σ>400 MPa to a similar level to the compressive stresses.

RBS-C DC yields appear linked to dimensions of hydrogen-induced surface blisters, as both DC near-surface yields and heights of blisters dramatically decreased with increasing stress σ>400 MPa. Interestingly, the macro-cracks presumed to evolve into the ion-cut defect are clearest at σ<400 MPa, and larger numbers of void-like defects are formed. The formation of the ion-cut defect may preclude or at least minimise the formation of surface blisters. Stress also causes greater loss of hydrogen from the implanted sample

profile during annealing, without any concomitant increase in trapping at defects or cavities determined by ERD. This suggests that the hydrogen which formed the blisters has escaped without catastrophic rupture of the silicon, as indicated by the intact blisters measured by optical profiling.

The XTEM-determined depths of the hydrogen platelets cracking following annealing are similar in unstressed, compressively and tensionally stressed silicon. The observed number and orientation of larger H-related defects also show little influence from stress, with similar ratio of platelets aligned along each crystalline axis in stressed and unstressed Si. The crack location in all samples independent of stress does not appear to coincide directly with the hydrogen profile peak, but shows some agreement with the damage peak (direct scattering). It is possible that the stress application decreases the ion-cut depth further than both these locations.

6.3.1 Discussion and further work

Overall, it appears the the stress does not lead to significant changes in behaviour at these levels, for these materials. Perhaps greater stresses – both on a global macroscopic and localised microscopic level – and different potential substrates should be investigated, to establish how consistent this lack of effect is across materials implanted with hydrogen.

Due to the unique nature of each stressed sample, confidence in correlations or trends is difficult without a significantly increased data set. There was significant difficulty in producing samples with the same (or approximate) applied stress. Greater certainty in reproducibility requires series consisting of more uniform samples. Additionally, widening the sampling window would aid extrapolation of trends – increasing total range while decreasing step size of each stress value would help produce a continuum of results, allowing identification of continuous or step-like effects.

The application of stress by mechanical means used in this project would be unlikely to operate on mass fabrication scales. As such, were mechanical stress to prove useful to device production, alternative means would be needed to externally stress the wafers. One suggestion would be the use of thin films deposited upon the surface of the wafer, which could be etched or polished off once the fabrication was complete. In order to establish that these films themselves would perform this function, and to investigate what other factors

would have to be accounted for, extending the investigation to such deposited materials would be advantageous.

Alternatively, stress could be applied compositionally via buried layers with a different but compatible lattice constant, such as Ge within Si. A novel possibility may be by using SPE to create a "zipper" defect [188, 190] prior to introduction of hydrogen, providing a highly defective band for trapping. The stress provided in these systems may prove beneficial electrically and mechanically, for the ion-cut process and others. Such an extension would also require examining localised stress caused on a microscopic (or smaller) level by point and extended defects. Studying the influence of these defects would have broader application in all stress-related studies of semiconductors.

In fact, the magnitude of the externally applied stress was somewhat limited within this study. If thin films were applied to thick wafers which possess significant restoring forces, much higher levels of in-plane stress could be applied. However, these would not obey the Euler-Bernoulli bar bending formula, but rather Stoney's Equation-type mechanics, so the stress and strain distribution would be somewhat different.

The more precise calibration of the ERD measurements via a set standard would be of untold benefit. Akin to the standards of the RBS or the "Round Robin" measurements performed on other ERD systems, a sample or samples of precisely known concentration, depth range and similar enough density values would allow significantly more confidence in future user determined values. This could be produced by either precision deposition or merely by ion implantation and a series of SIMS measurements to ensure consistency before use.

In studying H platelet and similar defect development using TEM, examining the samples in plane view (PVTEM), or by cross-sectioning them along the alternative orthogonal axis, would allow determination of any objects aligned along the $\langle 011 \rangle$ crystalline axis. Such quantification of platelet orientation and comparison with RBS-C and other data would confirm the level of influence by stress on defect alignment.

For the comparison of defects by RBS-C along each crystal channel as presented in Fig. 5.29, it would be useful to include the [111] axis. Additionally, the change of these defects with time via annealing would also be informative, as well as expanding the comparison to samples under an array of compressive and tensile stresses.

Glossary

BF	Bright field
CCD	Charge-coupled device
Cz	Czochralski
DC	Dechannelling (of RBS yield)
DS	Direct scattering (of RBS yield)
E_a	Activation energy
ERD	Elastic recoil detection
EOR	End of range (of ion implantation)
FET	Field effect transistor
FoV	Field of view
FvK	Föppl-von Karman (Theory)
FWHM	Full-width half-maximum (statistical measurement point)
IBA	Ion beam analysis
JMAK	Johnson-Mehl-Avrami-Kolmogorov (Equation)
LN2	Liquid nitrogen temperature (≈–196°C)
MKS	Metre-kilogram-second (SI unit standard in equations)
MOSFET	Metal oxide semiconductor field effect transistor
OP	Optical profilometry
OZA	Off zone axis
PIPS	Precision ion polishing system
PSI	Phase shifting interferometry
RBS	Rutherford backscattering spectrometry
RBS-C	Rutherford backscattering spectrometry (Channelled)
RF	Radio frequency
R_P	Depth of the peak in the implantation profile
RT	Room temperature (≈20°C)
SEM	Scanning electron microscopy
SI	Le Système international d'unités (International system of units)
SIMS	Secondary ion mass spectrometry
SOI	Silicon on insulator
SPE	Solid phase epitaxy
SRIM	Stopping Range of Ions in Matter (Software package)
TEM	Transmission electron microscopy
t_i	Initial time (of occurrance, appearance)
ULTRATHIN®	Registered trademark of 50 μm-thick Si(100) wafers
VSI	Vertical Scanning Interferometry
XTEM	Cross-sectional transmission electron microscopy

Bibliography

[1] G. K. Celler and S. Cristoloveanu. Frontiers of silicon-on-insulator. *Journal of Applied Physics*, 93(9):4955–4978, 2003.

[2] A. H. Perera, B. Smith, N. Cave, M. Sureddin, S. Chheda, R. Singh, R. Islam, J. Chang, S. C. Song, A. Sultan, S. Crown, V. Kolagunta, S. Shah, M. Celik, D. Wu, K. C. Yu, R. Fox, S. Park, C. Simpson, D. Eades, S. Gonzales, C. Thomas, J. Sturtevant, D. Bonser, N. Benavides, M. Thompson, V. Sheth, J. Fretwell, S. Kim, N. Ramani, K. Green, M. Moosa, P. Besser, Y. Solomentsev, D. Denning, M. Friedemann, B. Baker, R. Chowdhury, S. Ufmani, K. Strozewski, R. Carter, J. Reiss, M. Olivares, B. Ho, T. Lii, T. Sparks, T. Stephens, M. Schaller, C. Goldberg, K. Junker, D. Wristers, J. Alvis, B. Melnick, and S. Venkatesan. *A versatile 0.13 μm CMOS Platform Technology supporting High Performance and Low Power Applications*. International Electron Devices Meeting 2000, Technical Digest. IEEE, New York, 2000.

[3] IBM Corporation. IBM Ships First Microchips for Nintendo's Wii Video Game System, 2006. http://www-03.ibm.com/press/us/en/pressrelease/20213.wss (Accessed 29 November 2011).

[4] C. H. Lin, Y. T. Chiang, C. C. Hsu, C. H. Lee, C. F. Huang, C. H. Lai, T. H. Cheng, and C. W. Liu. Ge-on-glass detectors. *Applied Physics Letters*, 91(4):3, 2007.

[5] Peregrine semiconductor. http://www.psemi.com/index.html, 2011. (Accessed 29 November 2011).

[6] R. Soref. The past, present, and future of silicon photonics. *IEEE Journal of Selected Topics in Quantum Electronics*, 12(6):1678–1687, 2006.

[7] Christophe Maleville and Carlos Mazuré. Smart-Cut® technology: from 300 mm ultrathin SOI production to advanced engineered substrates. *Solid-State Electronics*, 48(6):1055–1063, 2004. 0038-1101 DOI: 10.1016/j.sse.2003.12.029.

[8] S. H. Christiansen, R. Singh, and U. Gosele. Wafer direct bonding: From advance substrate engineering to future applications in micro/nanoelectronics. *Proceedings of the IEEE*, 94(12):2060–2106, 2006.

[9] C. J. Tracy, P. Fejes, N. D. Theodore, P. Maniar, E. Johnson, A. J. Lamm, A. M. Paler, I. J. Malik, and P. Ong. Germanium-on-insulator substrates by wafer bonding. *Journal of Electronic Materials*, 33(8):886–892, 2004.

[10] Carl J. Hepburn. *Britney Spears' Guide to Semiconductor Physics*. Accessed 2011-7-20. University of Essex, Essex, UK, 2008. http://britneyspears.ac/lasers.htm.

[11] K. Izumi, M. Doken, and H. Ariyoshi. Cmos devices fabricated on buried SiO_2 layers formed by oxygen implantation into silicon. *Electronics Letters*, 14(18):593–594, 1978.

[12] J. B. Lasky. Wafer bonding for silicon-on-insulator technologies. *Applied Physics Letters*, 48(1):78–80, 1986.

[13] M. Bruel. Application of hydrogen ion beams to silicon on insulator material technology. *Nuclear Instruments & Methods in Physics Research Section B-Beam Interactions with Materials and Atoms*, 108(3):313–319, 1996.

[14] X. Q. Feng and Y. Huang. Mechanics of Smart-Cut((R)) technology. *International Journal of Solids and Structures*, 41(16-17):4299–4320, 2004.

[15] O. Moutanabbir and U. Gosele. Heterogeneous integration of compound semiconductors. In *Annual Review of Materials Research, Vol 40*, volume 40 of *Annual Review of Materials Research*, pages 469–500. Annual Reviews, Palo Alto, 2010.

[16] C. Maleville, B. Aspar, T. Poumeyrol, H. Moriceau, M. Bruel, A. J. AubertonHerve, and T. Barge. Wafer bonding and H-implantation mechanisms involved in the Smart-cut(R) technology. *Materials Science and Engineering B-Solid State Materials for Advanced Technology*, 46(1-3):14–19, 1997.

[17] B. Aspar, H. Moriceau, E. Jalaguier, C. Lagahe, A. Soubie, B. Biasse, A. M. Papon, A. Claverie, J. Grisolia, G. Benassayag, F. Letertre, O. Rayssac, T. Barge, C. Maleville, and B. Ghyselen. The generic nature of the Smart-Cut((R)) process for thin film transfer. *Journal of Electronic Materials*, 30(7):834–840, 2001.

[18] Lu Xiang, W. Cheung Nathan, D. Strathman Michael, K. Chu Paul, and Doyle Brian. Hydrogen induced silicon surface layer cleavage. *Applied Physics Letters*, 71(13):1804–1806, 1997.

[19] Y. J. Chabal, M. K. Weldon, Y. Caudano, B. B. Stefanov, and K. Raghavachari. Spectroscopic studies of H-decorated interstitials and vacancies in thin-film silicon exfoliation. *Physica B: Condensed Matter*, 273-274:152–163, 1999. TY - JOUR.

[20] J. H. Liang, C. Y. Bai, D. S. Chao, and C. M. Lin. Post-annealing temperature dependence of blistering in high-fluence ion-implanted H in Si <100>. In *18th International Conference on Ion Beam Analysis*, pages 1349–1355. Elsevier Science Bv.

[21] Stephen W. Beddell and William A. Lanford. Investigation of surface blistering of hydrogen implanted crystals. *Journal of Applied Physics*, 90(3):1138–1146, 2001.

[22] J. Weber, T. Fischer, E. Hieckmann, M. Hiller, and E. V. Lavrov. Properties of hydrogen induced voids in silicon. *Journal of Physics-Condensed Matter*, 17(22):S2303–S2314, 2005. Sp. Iss. SI.

[23] T. Höchbauer, A. Misra, R. Verda, Y. Zheng, S. S. Lau, J. W. Mayer, and M. Nastasi. The influence of ion-implantation damage on hydrogen-induced ion-cut. *Nuclear Instruments & Methods in Physics Research Section B-Beam Interactions with Materials and Atoms*, 175:169–175, 2001.

[24] T. Höchbauer, A. Misra, M. Nastasi, and J. W. Mayer. Physical mechanisms behind the ion-cut in hydrogen implanted silicon. *Journal of Applied Physics*, 92(5):2335–2342, 2002.

[25] T. Höchbauer, M. Nastasi, R. D. Verda, A. Misra, K. Henttinen, I. Suni, S. S. Lau, and J. W. Mayer. The use of ion channeling and elastic recoil detection in determining the mechanism of cleavage in the ion-cut process. *Nuclear Instruments & Methods in Physics Research Section B-Beam Interactions with Materials and Atoms*, 190:592–597, 2002.

[26] T. Höchbauer, A. Misra, M. Nastasi, K. Henttinen, T. Suni, I. Suni, S. S. Lau, and W. Ensinger. Comparison of thermally and mechanically induced si layer transfer in hydrogen-implanted si wafers. *Nuclear Instruments & Methods in Physics Research Section B-Beam Interactions with Materials and Atoms*, 216:257–263, 2004.

[27] M. Nastasi, T. Höchbauer, J. K. Lee, A. Misra, J. P. Hirth, M. Ridgway, and T. Lafford. Nucleation and growth of platelets in hydrogen-ion-implanted silicon. *Applied Physics Letters*, 86(15), 2005.

[28] B. Terreault. Hydrogen blistering of silicon: Progress in fundamental understanding. *Physica Status Solidi a-Applications and Materials Science*, 204(7):2129–2184, 2007.

[29] M. Hytch, F. Houdellier, F. Hue, and E. Snoeck. Nanoscale holographic interferometry for strain measurements in electronic devices. *Nature*, 453(7198):1086–U5, 2008.

[30] E. A. Fitzgerald. Dislocations in strained-layer epitaxy - theory, experiment, and applications. *Materials Science Reports*, 7(3):91–142, 1991.

[31] P. J. Goodhew and K. Giannakopoulos. Strain relaxation in III-V semiconductor heterostructures. *Micron*, 30(1):59–64, 1999.

[32] B. A. Joyce and D. D. Vvedensky. Self-organized growth on GaAs surfaces. *Materials Science & Engineering R-Reports*, 46(6):127–176, 2004.

[33] M. Okada, A. Muto, I. Suzumura, H. Ikeda, S. Zaima, and Y. Yasuda. Hydrogen effects on heteroepitaxial growth of Ge films on Si(111) surfaces by solid phase epitaxy. *Japanese Journal of Applied Physics Part 1-Regular Papers Short Notes & Review Papers*, 37(12B):6970–6973, 1998.

[34] G. Wedler, J. Walz, T. Hesjedal, E. Chilla, and R. Koch. Stress and relief of misfit strain of Ge/Si(001). *Physical Review Letters*, 80(11):2382–2385, 1998.

[35] H. Kawanami. Heteroepitaxial technologies of III-V on Si. *Solar Energy Materials and Solar Cells*, 66(1-4):479–486, 2001.

[36] Steven A. Ringel. Hydrogen-extended defect interactions in heteroepitaxial InP materials and devices. *Solid-State Electronics*, 41(3):359–380, 1997. TY - JOUR.

[37] M. L. Lee, E. A. Fitzgerald, M. T. Bulsara, M. T. Currie, and A. Lochtefeld. Strained Si, SiGe, and Ge channels for high-mobility metal-oxide-semiconductor field-effect transistors. *Journal of Applied Physics*, 97(1), 2005.

[38] Newman, John Henry. *The Idea Of A University.* Longmans, Green, and Co., New York, 1907. p103.

[39] E. Toyoda, A. Sakai, H. Isogai, T. Senda, K. Izunome, O. Nakatsuka, M. Ogawa, and S. Zaima. Mechanical properties and chemical reactions at the directly bonded si-si interface. *Japanese Journal of Applied Physics*, 48(1), 2009.

[40] W. K. Chu, R. H. Kastl, R. F. Lever, S. Mader, and B. J. Masters. Distribution of irradiation damage in silicon bombarded with hydrogen. *Physical Review B*, 16(9):3851–3859, 1977.

[41] J. K. G. Panitz, D. J. Sharp, and C. R. Hills. Near-surface microstructural modifications in low-energy hydrogen-ion bombarded silicon. *Journal of Vacuum Science & Technology a-Vacuum Surfaces and Films*, 3(1):1–5, 1985.

[42] J. Keinonen, M. Hautala, E. Rauhala, M. Erola, J. Lahtinen, H. Huomo, A. Vehanen, and P. Hautojarvi. Hydrogen-implantation-induced damage in silicon. *Physical Review B*, 36(2):1344–1347, 1987.

[43] J. Chevallier and M. Aucouturier. Hydrogen in crystalline semiconductors. *Annual Review of Materials Science*, 18:219–256, 1988.

[44] G. F. Cerofolini, L. Meda, R. Balboni, F. Corni, S. Frabboni, G. Ottaviani, R. Tonini, M. Anderle, and R. Canteri. Hydrogen-related complexes as the stressing species in high-fluence, hydrogen-implanted, single-crystal silicon. *Physical Review B*, 46(4):2061–2070, 1992.

[45] G. F. Cerofolini, R. Balboni, D. Bisero, F. Corni, S. Frabboni, G. Ottaviani, R. Tonini, R. S. Brusa, A. Zecca, M. Ceschini, G. Giebel, and L. Pavesi. Hydrogen precipitation in highly oversaturated single-crystalline silicon. *Physica Status Solidi A - Applied Research*, 150(2):539–586, 1995.

[46] B. Terreault, C. Boucher, R. W. Paynter, G. G. Ross, D. Theriault, G. Abel, R. Boivin, R. A. Bolton, J. Castracane, G. Chevalier, P. Couture, R. Decoste, Y. Demers, K. Dimoff, V. Glaude, B. C. Gregory, E. Haddad, C. Janicki, J. Kalnavarns, J. L. Lachambre, H. H. Mai, C. R. Neufeld, H. D. Pacher, G. W. Pacher, N. Richard, R. G. Saint-Jacques, M. Saintonge, C. Simm, B. L. Stansfield, G. Veilleux, D. Whyte, and W. Zuzak. 1st Results on Plasma Surface Interactions in the Tokamak de Varennes. *Journal of Nuclear Materials*, 162:799–803, 1989.

[47] R. G. Saint-Jacques. La formation des cloques. *Nuclear Instruments & Methods in Physics Research*, 209(MAY):333–343, 1983.

[48] J. N. Yu, X. J. Zhao, W. Zhang, W. Yang, and F. M. Chu. Defect production and accumulation under hydrogen and helium ion irradiation. *Journal of Nuclear Materials*, 251:150–156, 1997.

[49] A. Giguere, J. Beerens, and B. Terreault. Creating nanostructures on silicon using ion blistering and electron beam lithography. *Nanotechnology*, 17(2):600–606, 2006.

[50] V. P. Popov, I. E. Tyschenko, L. N. Safronov, O. V. Naumova, I. V. Antonova, A. K. Gutakovsky, and A. B. Talochkin. Properties of silicon oversaturated with implanted hydrogen. *Thin Solid Films*, 403:500–504, 2002.

[51] P. Olivero, S. Rubanov, P. Reichart, B. C. Gibson, S. T. Huntington, J. R. Rabeau, A. D. Greentree, J. Salzman, D. Moore, D. N. Jamieson, and S. Prawer. Characterization of three-dimensional microstructures in single-crystal diamond. *Diamond and Related Materials*, 15(10):1614–1621, 2006.

[52] P. Olivero, S. Rubanov, P. Reichart, B. C. Gibson, S. T. Huntington, J. Rabeau, A. D. Greentree, J. Salzman, D. Moore, D. N. Jamieson, and S. Prawer. Ion-beam-assisted lift-off technique for three-dimensional micromachining of freestanding single-crystal diamond. *Advanced Materials*, 17(20):2427–+, 2005.

[53] I. P. Ferain, K. Y. Byun, C. A. Colinge, S. Brightup, and M. S. Goorsky. Low temperature exfoliation process in hydrogen-implanted germanium layers. *Journal of Applied Physics*, 107(5):5, 2010.

[54] T. W. Simpson, I. V. Mitchell, G. O. Este, and F. R. Shepherd. Ion implantation induced selective area exfoliation of InP and GaAs. *Nuclear Instruments & Methods in Physics Research Section B-Beam Interactions with Materials and Atoms*, 148(1-4):381–385, 1999.

[55] S. Hayashi, D. Bruno, and M. S. Goorsky. Temperature dependence of hydrogen-induced exfoliation of InP. *Applied Physics Letters*, 85(2):236–238, 2004.

[56] X. B. Ma, W. L. Liu, X. F. Du, X. Y. Liu, Z. T. Song, C. L. Lin, and P. K. Chu. Germanium surface hydrophilicity and low-temperature Ge layer transfer by Ge-SiO(2) bonding. *Journal of Vacuum Science & Technology B*, 28(4):769–774, 2010.

[57] M. K. Weldon, V. E. Marsico, Y. J. Chabal, D. R. Hamann, S. B. Christman, and E. E. Chaban. Infrared spectroscopy as a probe of fundamental processes in microelectronics: silicon wafer cleaning and bonding. *Surface Science*, 368(1-3):163–178, 1996.

[58] C. Qian and B. Terreault. Blistering of silicon crystals by low keV hydrogen and helium ions. *Journal of Applied Physics*, 90(10):5152–5158, 2001.

[59] G. Bourque and B. Terreault. Low-energy random and channeled H ion ranges in Si: Measurements, simulation, and interpretation. *Nuclear Instruments & Methods in Physics Research Section B-Beam Interactions with Materials and Atoms*, 140(1-2):13–26, 1998.

[60] O. Moutanabbir, B. Terreault, and G. G. Ross. Isotope and crystal orientation effects in low-energy H/D blistering of Si. *Applied Physics Letters*, 82(26):4675–4677, 2003.

[61] O. Moutanabbir, A. Giguere, and B. Terreault. Narrow fluence window and giant isotope effect in low-energy hydrogen ion blistering of silicon. *Applied Physics Letters*, 84(17):3286–3288, 2004.

[62] O. Moutanabbir, B. Terreault, M. Chicoine, and F. Schiettekatte. The fluence effect in hydrogen-ion cleaving of silicon at the sub-100-nm scale. *Applied Physics a-Materials Science & Processing*, 80(7):1455–1462, 2005.

[63] O. Moutanabbir and B. Terreault. Raman-scattering elucidation of the giant isotope effect in hydrogen-ion blistering of silicon. *Journal of Chemical Physics*, 121(16):7973–7986, 2004.

[64] T. Y. Tan, U. Gosele, and F. F. Morehead. On the nature of point-defects and the effect of oxidation on substitutional dopant diffusion in silicon. *Applied Physics a-Materials Science & Processing*, 31(2):97–108, 1983.

[65] E. P. Neustroev, I. V. Antonova, V. F. Stas, V. P. Popov, and V. I. Obodnikov. Donor center formation in hydrogen implanted silicon. *Physica B*, 270(1-2):1–5, 1999.

[66] I. E. Tyschenko, A. B. Talochkin, B. A. Kolesov, K. S. Zhuravlev, V. I. Obodnikov, and V. P. Popov. Raman and photoluminescence investigations of the H+ ion implanted silicon-on-insulator structure formed by hydrogen ion cut. *Nuclear Instruments & Methods in Physics Research Section B-Beam Interactions with Materials and Atoms*, 186:329–333, 2002.

[67] S. Vincent, J. D. Penot, I. Radu, F. Letertre, and F. Rieutord. Study of the formation, evolution, and dissolution of interfacial defects in silicon wafer bonding. *Journal of Applied Physics*, 107(9):6, 2010.

[68] A. Saad, O. I. Velichko, Y. P. Shaman, A. V. Mazanik, A. K. Fedotov, and V. V. Fedotova. Modeling of hydrogen diffusion in silicon crystals. *Nuclear Instruments & Methods in Physics Research Section B-Beam Interactions with Materials and Atoms*, 253(1-2):118–121, 2006.

[69] J. W. Hong and S. Cheong. A crack model for the onset of blisters using finite surface thicknesses. *Journal of Applied Physics*, 100(9):4, 2006.

[70] J. Weber. *Hydrogen in semiconductors: From basic physics to technology*, volume 5 of *Physica Status Solidi C-Current Topics in Solid State Physics*, pages 535–538. Wiley-V C H Verlag Gmbh, Weinheim, 2008.

[71] F. Pailloux, M. L. David, and L. Pizzagalli. Quantitative HRTEM investigation of nanoplatelets. *Micron*, 41(2):135–142, 2010.

[72] J. H. Liang, C. H. Hu, and C. M. Lin. Silicon orientation effects on surface blistering characteristics due to hydrogen ion implantation. *Surface & Coatings Technology*, 206(5):820–824, 2011.

[73] J. C. H. Spence. Atomistics and mechanical properties of silicon. In *Acta Materialia Workshop on Materials Science and Mechanics of Interfaces*, pages 4153–4159. Pergamon-Elsevier Science Ltd, 1998.

[74] J. G. Swadener, M. I. Baskes, and M. Nastasi. Molecular dynamics simulation of brittle fracture in silicon. *Physical Review Letters*, 89(8), 2002.

[75] R. Perez and P. Gumbsch. Directional anisotropy in the cleavage fracture of silicon. *Physical Review Letters*, 84(23):5347–5350, 2000.

[76] M. Nastasi, T. Höchbauer, R. D. Verda, A. Misra, J. K. Lee, J. W. Mayer, and S. S. Lau. Using ion beam analysis in determining the mechanisms of cleavage in hydrogen ion implanted Si. *Nuclear Instruments & Methods in Physics Research Section B-Beam Interactions with Materials and Atoms*, 219-20:604–610, 2004.

[77] S. Personnic, K. K. Bourdelle, F. Letertre, A. Tauzin, N. Cherkashin, A. Claverie, R. Fortunier, and H. Klocker. Impact of the transient formation of molecular hydrogen on the microcrack nucleation and evolution in H-implanted Si (001). *Journal of Applied Physics*, 103(2):9, 2008.

[78] B. Gu, H. Y. Liu, Y. W. Mai, X. Q. Feng, and S. W. Yu. Fracture mechanics analysis on Smart-Cut(R) technology. Part 1: Effects of stiffening wafer and defect interaction. *Acta Mechanica Sinica*, 25(1):73–81, 2009.

[79] L. Shao, J. K. Lee, T. Höchbauer, M. Nastasi, P. E. Thompson, I. Rusakova, H. W. Seo, Q. Y. Chen, J. R. Liu, and W. K. Chu. Ion-cut of Si facilitated by interfacial defects of Si substrate/epitaxial layer grown by molecular-beam epitaxy. *Nuclear Instruments & Methods in Physics Research Section B-Beam Interactions with Materials and Atoms*, 242(1-2):509–511, 2006.

[80] L. Shao, Z. F. Di, Y. Lin, Q. X. Jia, Y. Q. Wang, M. Nastasi, P. E. Thompson, N. D. Theodore, and P. K. Chu. The role of strain in hydrogenation induced cracking in $Si/Si_{1-x}Ge_x/Si$ structures. *Applied Physics Letters*, 93(4):3, 2008.

[81] C. Coupeau, E. Dion, M. L. David, J. Colin, and J. Grilhe. Effect of pressure and stress on blistering induced by hydrogen implantation in silicon. *Epl*, 92(1):5, 2010.

[82] Q. Y. Tong, R. Scholz, U. Gosele, T. H. Lee, L. J. Huang, Y. L. Chao, and T. Y. Tan. A "smarter-cut" approach to low temperature silicon layer transfer. *Applied Physics Letters*, 72(1):49–51, 1998.

[83] R. W. Bower, L. LeBoeuf, and Y. A. Li. Transposed splitting of silicon implanted with spatially offset distributions of hydrogen and boron. *Nuovo Cimento Della Societa Italiana Di Fisica D-Condensed Matter Atomic Molecular and Chemical Physics Fluids Plasmas Biophysics*, 19(12):1871–1873, 1997.

[84] S. Personnic, K. K. Bourdelle, F. Letertre, A. Tauzin, F. Laugier, R. Fortunier, and H. Klocker. Low temperature diffusion of impurities in hydrogen implanted silicon. *Journal of Applied Physics*, 101(8), 2007.

[85] K. Henttinen, T. Suni, A. Nurmela, I. Suni, S. S. Lau, T. Höchbauer, M. Nastasi, and V. M. Airaksinen. Cold ion-cutting of hydrogen implanted Si. *Nuclear Instruments & Methods in Physics Research Section B-Beam Interactions with Materials and Atoms*, 190:761–766, 2002.

[86] R. D. Verda, M. Nastasi, and R. W. Bower. Boron-induced redistribution of hydrogen implanted at elevated temperature into crystalline silicon. *Nuclear Instruments & Methods in Physics Research Section B-Beam Interactions with Materials and Atoms*, 206:927–931, 2003.

[87] A. Nurmela, K. Henttinen, T. Suni, and I. Suni. Influence of hydrogen dose and boron doping on the ion cutting of Si. *Surface and Interface Analysis*, 35(9):757–759, 2003.

[88] N. Desrosiers, A. Giguere, O. Moutanabbir, and B. Terreault. Ion blistering of boron-doped silicon: The critical role of defect passivation. *Applied Physics Letters*, 87(23):3, 2005.

[89] Miao Zhang, Lianwei Wang, Zuyao Zhou, Zixin Lin, and Chenglu Lin. Annealing Behavior of Crystalline Si Implanted with High Dose of Protons. *Physica Status Solidi (a)*, 165(2):361–365, 1998.

[90] L. J. Huang, Q. Y. Tong, Y. L. Chao, T. H. Lee, T. Martini, and U. Gosele. Onset of blistering in hydrogen-implanted silicon. *Applied Physics Letters*, 74(7):982–984, 1999.

[91] J. K. Lee, M. Nastasi, N. D. Theodore, A. Smalley, T. L. Alford, J. W. Mayer, M. Cai, and S. S. Lau. Effects of hydrogen implantation temperature on ion-cut of silicon. *Journal of Applied Physics*, 96(1):280–288, 2004.

[92] L. Capello, F. Rieutord, A. Tauzin, and F. Mazen. Quantitative study of hydrogen-implantation-induced cavities in silicon by grazing incidence small angle x-ray scattering. *Journal of Applied Physics*, 102(2), 2007.

[93] A. Kinomura, R. Suzuki, T. Ohdaira, M. Muramatsu, C. He, N. Oshima, T. Matsumoto, H. Tanoue, and Y. Horino. Temperature-dependent growth and transient state of hydrogen-induced nanocavities in silicon. *Journal of Applied Physics*, 104(3):6, 2008.

[94] A. Giguere and B. Terreault. Hydrogen blistering of silicon: Effect of implantation temperature, isotope dependence, and key role of dynamic annealing. *Journal of Applied Physics*, 102(10):3, 2007.

[95] Taechung Yi, Lu Li, and Chang-Jin Kim. Microscale material testing of single crystalline silicon: process effects on surface morphology and tensile strength. *Sensors and Actuators A: Physical*, 83(1-3):172–178, 2000.

[96] S. Personnic, A. Tauzin, K. K. Bourdelle, F. Letertre, N. Kernevez, F. Laugier, N. Cherkashin, A. Claverie, and R. Fortunier. Time dependence study of hydrogen-induced defects in silicon during thermal anneals. In K. J. Kirkby, D. Chivers, R. Gwilliam, and A. Smith, editors, *Ion Implantation Technology*, volume 866 of *AIP Conference Proceedings*, pages 65–68. Amer Inst Physics, Melville, 2006.

[97] A. M. Fecioru, S. Senz, R. Scholz, and U. Gosele. Silicon layer transfer by hydrogen implantation combined with wafer bonding in ultrahigh vacuum. *Applied Physics Letters*, 89(19), 2006.

[98] W. Düngen, R. Job, T. Mueller, Y. Ma, W. R. Fahrner, L. O. Keller, J. T. Horstmann, and H. Fiedler. Blistering of implanted crystalline silicon by plasma hydrogenation investigated by raman scattering spectroscopy. *Journal of Applied Physics*, 100(12):5, 2006.

[99] M. Xu and X. Q. Feng. Defect nucleation in soi wafers due to hydrogen ion implantation. *Theoretical and Applied Fracture Mechanics*, 42(3):295–301, 2004.

[100] G. F. Cerofolini, F. Corni, S. Frabboni, C. Nobili, G. Ottaviani, and R. Tonini. Hydrogen and helium bubbles in silicon. *Materials Science & Engineering R-Reports*, 27(1-2):1–52, 2000.

[101] M. L. David, L. Pizzagalli, F. Pailloux, and J. F. Barbot. Atomic scale structure of (001) hydrogen-induced platelets in germanium. *Physical Review Letters*, 102(15):4, 2009.

[102] G. Moras, L. C. Ciacchi, C. Elsasser, P. Gumbsch, and A. De Vita. Atomically smooth stress-corrosion cleavage of a hydrogen-implanted crystal. *Physical Review Letters*, 105(7):4, 2010.

[103] N. H. Nickel, G. B. Anderson, N. M. Johnson, and J. Walker. Nucleation mechanism of hydrogen-induced platelets in single crystal and polycrystalline silicon. *Physica B: Condensed Matter*, 273-274:212–215, 1999.

[104] C. H. Yun, A. B. Wengrow, N. W. Cheung, Y. Zheng, R. J. Welty, Z. F. Guan, K. V. Smith, P. M. Asbeck, E. T. Yu, and S. S. Lau. Transfer of patterned ion-cut silicon layers. *Applied Physics Letters*, 73(19):2772–2774, 1998.

[105] D. F. Gu, H. Baumgart, K. K. Bourdelle, G. K. Celler, and A. A. Elmustafa. Nanomechanical Response of the Si Lattice to Hydrogen Implantation and Annealing for Layer Splitting. *Japanese Journal of Applied Physics*, 48(10):4, 2009.

[106] M. K. Weldon, V. E. Marsico, Y. J. Chabal, A. Agarwal, D. J. Eaglesham, J. Sapjeta, W. L. Brown, D. C. Jacobson, Y. Caudano, S. B. Christman, and E. E. Chaban. On the mechanism of the hydrogen-induced exfoliation of silicon. In *24th Annual Conference on the Physics and Chemistry of Semiconductor Interfaces (PCSI-24)*, pages 1065–1073. Amer Inst Physics, 1997.

[107] Y. Zheng, S. S. Lau, T. Höchbauer, A. Misra, R. Verda, X. M. He, M. Nastasi, and J. W. Mayer. Orientation dependence of blistering in H-implanted Si. *Journal of Applied Physics*, 89(5):2972–2978, 2001.

[108] Q. Y. Tong, K. Gutjahr, S. Hopfe, U. Gosele, and T. H. Lee. Layer splitting process in hydrogen-implanted Si, Ge, SiC, and diamond substrates. *Applied Physics Letters*, 70(11):1390–1392, 1997.

[109] C. Coupeau, G. Parry, J. Colin, M. L. David, J. Labanowski, and J. Grilhe. Kinetic evolution of blistering in hydrogen-implanted silicon. *Applied Physics Letters*, 103(3):031908–1, 2013.

[110] S. Reboh, A. A. de Mattos, J. F. Barbot, A. Declemy, M. F. Beaufort, R. M. Papaleo, C. P. Bergmann, and P. F. P. Fichtner. *Journal of Applied Physics*, 105(9):6, 2009.

[111] S. Reboh, A. A. D. de Mattos, F. Schaurich, P. F. P. Fichtner, M. F. Beaufort, and J. F. Barbot. The mechanisms of surface exfoliation in H and He implanted Si crystals. *Scripta Materialia*, 65(12):1045–1048, 2011.

[112] W. Düngen, R. Job, Y. Ma, Y. L. Huang, W. R. Fahrner, L. O. Keller, and J. T. Horstmann. mu-Raman investigations on hydrogen gettering in hydrogen implanted and hydrogen plasma treated Czochralski silicon. In B. Pichaud, A. Claverie, D. Alquier, H. Richter, and M. Kittler, editors, *Gettering and Defect Engineering in Semiconductor Technology XI*, volume 108-109 of *Solid State Phenomena*, pages 91–96. Trans Tech Publications Ltd, Zurich-Uetikon, 2005.

[113] M.K. Weldon and Chabal Y.J. Hydrogen-induced exfoliation of c-Si. In R. Hull, editor, *Properties of Crystalline Silicon*, chapter 18.6, pages 942–957. Institution of Engineering and Technology, 1998.

[114] Y. Ma, Y. L. Huang, R. Job, and W. R. Fahrner. Dissociation, transformation, and recombination of Si-H bonds in hydrogenated crystalline silicon determined by in situ micro-Raman spectroscopy. *Physical Review B*, 71(4), 2005.

[115] X. Z. Duo, W. L. Liu, M. A. Zhang, L. W. Wang, C. L. Lin, M. Okuyama, M. Noda, W. Y. Cheung, P. K. Chu, P. G. Hu, S. X. Wang, and L. M. Wang. Comparison between the different implantation orders in H(+) and He(+) coimplantation. *Journal of Physics D-Applied Physics*, 34(4):477–482, 2001.

[116] X. H. Duo, W. L. Liu, M. Zhang, L. W. Wang, C. L. Lin, M. Okuyama, M. Noda, W. Y. Cheung, S. P. Wong, P. K. Chu, P. G. Hu, S. X. Wang, and L. M. Wang. Evolution of hydrogen and helium co-implanted single-crystal silicon during annealing. *Journal of Applied Physics*, 90(8):3780–3786, 2001.

[117] R. E. Hurley, S. Suder, and H. S. Gamble. Ion implantation of hydrogen and helium into silicon wafers for layer transfer in devices. *Vacuum*, 78(2-4):167–175, 2005.

[118] R. E. Hurley, H. Wadsworth, J. H. Montgomery, and H. S. Gamble. Surface blistering of low temperature annealed hydrogen and helium co-implanted germanium and its application to splitting of bonded wafer substrates. *Vacuum*, 83:S29–S32, 2009.

[119] C. L. Liu, M. K. Li, Z. Wang, Y. J. Gao, J. Q. Liao, D. C. Zhang, X. L. Zhang, and Y. Y. Shen. Correlation between surface damage and micro-defects in si covered with insulating layer by implantation of he and h ions. *Thin Solid Films*, 519(10):3162–3168, 2011.

[120] S. Reboh, F. Schaurich, A. Declemy, J. F. Barbot, M. F. Beaufort, N. Cherkashin, and P. F. P. Fichtner. On the microstructure of Si coimplanted with H+ and He+ ions at moderate energies. *Journal of Applied Physics*, 108(2):6, 2010.

[121] T. Höchbauer, K. C. Walter, R. B. Schwarz, M. Nastasi, R. W. Bower, and W. Ensinger. The influence of boron ion implantation on hydrogen blister formation in n-type silicon. *Journal of Applied Physics*, 86(8):4176–4183, 1999.

[122] J. K. Lee, T. Höchbauer, R. D. Averitt, and M. Nastasi. Role of boron for defect evolution in hydrogen-implanted silicon. *Applied Physics Letters*, 83(15):3042–3044, 2003.

[123] A. Usenko. Layer-transfer process for silicon-on-insulator with improved manufacturability. *Journal of Electronic Materials*, 32(8):872–876, 2003.

[124] A. Y. Usenko, W. N. Carr, and B. Chen. Transformation of hydrogen trapped onto microbubbles into H platelet layer in Si. *Journal of Materials Science-Materials in Electronics*, 14(5-7):305–309, 2003.

[125] C. Qian, B. Terreault, and S. C. Gujrathi. Layer splitting in Si by H+He ion coimplantation: Channeling effect limitation at low energy. *Nuclear Instruments and Methods in Physics Research Section B: Beam Interactions with Materials and Atoms*, 175-177(0):711–714, 2001.

[126] S. Reboh, J. F. Barbot, M. F. Beaufort, and P. F. P. Fichtner. H-induced subcritical crack propagation and interaction phenomena in (001) Si using He-cracks templates. *Applied Physics Letters*, 96(3):3, 2010.

[127] Z. Wang, C. L. Liu, T. Y. Liu, X. D. Zhang, W. R. Li, W. X. Li, B. Yuan, P. Wu, and M. K. Li. Surface exfoliation and defect structures in Si induced by 160 keV He and 110 keV H ion implantation. *Nuclear Instruments & Methods in Physics Research Section B-Beam Interactions with Materials and Atoms*, 266(2):250–255, 2008.

[128] C. L. Liu, F. Zhu, Z. Wang, M. K. Li, Y. J. Gao, and J. Wang. Surface damage in silicon co-implanted with He and H ions: Effect of H implant energy. *Vacuum*, ((In Press)), 2012.

[129] J. C. McCallum, B. J. Villis, B. C. Johnson, N. Stavrias, J. E. Burgess, S. Charnvanichborikarn, J. Wong-Leung, J. S. Williams, and C. Jagadish. Effect of boron on formation of interstitial-related luminescence centres in ion implanted silicon. *Physica Status Solidi a-Applications and Materials Science*, 208(3):620–623, 2011.

[130] X. B. Ma, X. F. Du, W. L. Liu, C. Chen, Z. T. Song, and C. L. Lin. Enhanced surface blistering of germanium with B(+)/H(+) coimplantation. *Journal of Vacuum Science & Technology B*, 27(3):1063–1067, 2009.

[131] B. C. Johnson, J. C. McCallum, A. J. Atanacio, and K. E. Prince. Intrinsic and boron-enhanced hydrogen diffusion in amorphous silicon formed by ion implantation. *Applied Physics Letters*, 95(10), 2009.

[132] M. H. Gullanar, H. Chen, W. S. Wei, R. Q. Cui, and W. Z. Shen. Roles of hydrogen dilution on the microstructural and optoelectronic properties of B-doped nanocrystalline Si : H thin films. *Journal of Applied Physics*, 95(8):3961–3967, 2004.

[133] S. Charnvanichborikarn, B. J. Villis, B. C. Johnson, J. Wong-Leung, J. C. McCallum, J. S. Williams, and C. Jagadish. Effect of boron on interstitial-related luminescence centers in silicon. *Applied Physics Letters*, 96(5), 2010.

[134] A. Claverie, L. Laanab, C. Bonafos, C. Bergaud, A. Martinez, and D. Mathiot. On the Relation between Dopant Anomalous Diffusion in Si and End-of-Range Defects. In *10th International Conference on Ion Implantation Technology*, pages 202–209. Elsevier Science Bv, 1994.

[135] R. A. Camillo-Castillo, M. E. Law, and K. S. Jones. Impact of dopant profiles on the end of range defects for low energy germanium preamorphized silicon. *Materials Science and Engineering B-Solid State Materials for Advanced Technology*, 114:312–317, 2004.

[136] J. S. Christensen, A. Y. Kuznetsov, A. E. Gunnaes, B. G. Svensson, and H. H. Radamson. Phosphorus diffusion in the presence of threading dislocations in strain relaxed SiGe films. *Materials Science in Semiconductor Processing*, 9(4-5):650–654, 2006.

[137] J. S. Christensen, H. H. Radamson, A. Y. Kuznetsov, and B. G. Svensson. Diffusion of phosphorus in relaxed Si(1-x)Ge(x) films and strained Si/Si1-xGex heterostructures. *Journal of Applied Physics*, 94(10):6533–6540, 2003.

[138] E. Suvar, J. Christensen, A. Kuznetsov, and H. H. Radamson. Influence of doping on thermal stability of $Si/Si_{1-x}Ge_x/Si$ heterostructures. *Materials Science and Engineering B-Solid State Materials for Advanced Technology*, 102(1-3):53–57, 2003.

[139] H. H. Radamson, W. X. Ni, and G. V. Hansson. The role of low temperature growth defects for the stability of strained $Si/Si_{1-x}Ge_x$ heterostructures. *Applied Surface Science*, 102:82–85, 1996.

[140] U. Gosele, D. Conrad, P. Werner, Q. Y. Tong, R. Gafiteanu, and T. Y. Tan. Point defects, diffusion and gettering in silicon. In T. D. de la Rubia, S. Coffa, P. A. Stolk, and C. S. Rafferty, editors, *Defects and Diffusion in Silicon Processing*, volume 469 of *Materials Research Society Symposium Proceedings*, pages 13–24. Materials Research Society, Warrendale, 1997.

[141] M. Seibt, V. Kveder, W. Schroter, and O. Voss. Structural and electrical properties of metal impurities at dislocations in silicon. In *International Workshop on Nitrides Semiconductors (IWN 2004)*, pages 911–920. Wiley-V C H Verlag Gmbh, 2004.

[142] M. H. Li and Q. Wang. Hydrogen ion implantation caused defect structures in heavily doped silicon substrates. In S. Ashok, J. Chevallier, B. L. Sopori, M. Tabe, and P. Kiesel, editors, *Semiconductor Defect Engineering-Materials, Synthetic Structures and Devices*, volume 864 of *Materials Research Society Symposium Proceedings*, pages 521–526. Materials Research Society, Warrendale, 2005.

[143] N. M. Johnson, C. Doland, F. Ponce, J. Walker, and G. Anderson. Hydrogen in crystalline semiconductors - a review of experimental results. *Physica B*, 170(1-4):3–20, 1991.

[144] N. M. Johnson. Mechanism for hydrogen compensation of shallow-acceptor impurities in single-crystal silicon. *Physical Review B*, 31(8):5525–5528, 1985.

[145] N. M. Johnson, C. Herring, and D. J. Chadi. Interstitial hydrogen and neutralization of shallow-donor impurities in single-crystal silicon. *Physical Review Letters*, 56(7):769–772, 1986.

[146] N. M. Johnson, F. A. Ponce, R. A. Street, and R. J. Nemanich. Defects in single-crystal silicon induced by hydrogenation. *Physical Review B*, 35(8):4166–4169, 1987.

[147] A. D. Marwick, G. S. Oehrlein, and N. M. Johnson. Structure of the boron-hydrogen complex in crystalline silicon. *Physical Review B*, 36(8):4539–4542, 1987.

[148] C. G. Van de Walle and J. Neugebauer. Universal alignment of hydrogen levels in semiconductors, insulators and solutions. *Nature*, 423(6940):626–628, 2003.

[149] P. K. Chu and N. W. Cheung. Microcavity engineering by plasma immersion ion implantation. *Materials Chemistry and Physics*, 57(1):1–16, 1998.

[150] P. K. Chu, S. Qin, C. Chan, N. W. Cheung, and P. K. Ko. Instrumental and process considerations for the fabrication of silicon-on-insulators (soi) structures by plasma immersion ion implantation. *IEEE Transactions on Plasma Science*, 26(1):79–84, 1998.

[151] M. I. Current, W. Liu, I. S. Roth, A. J. Lamm, W. G. En, I. J. Malik, L. Feng, M. A. Bryan, S. Qin, F. J. Henley, C. Chan, and N. W. Cheung. A plasma immersion implantation system for materials modification. *Surface & Coatings Technology*, 136(1-3):138–141, 2001.

[152] X. Lu, S. S. K. Iyer, C. M. Hu, N. W. Cheung, J. Min, Z. Fan, and P. K. Chu. Ion-cut silicon-on-insulator fabrication with plasma immersion ion implantation. *Applied Physics Letters*, 71(19):2767–2769, 1997.

[153] L. Shao, Y. Lin, J. K. Lee, Q. X. Jia, Y. Q. Wang, M. Nastasi, P. E. Thompson, N. D. Theodore, P. K. Chu, T. L. Alford, J. W. Mayer, P. Chen, and S. S. Lau. Plasma hydrogenation of strained Si/SiGe/Si heterostructure for layer transfer without ion implantation. *Applied Physics Letters*, 87(9), 2005.

[154] L. W. Wang, R. K. Y. Fu, X. Zeng, P. K. Chu, W. Y. Cheung, and S. P. Wong. Damage in hydrogen plasma implanted silicon. *Journal of Applied Physics*, 90(4):1735–1739, 2001.

[155] R. Singh, S. H. Christiansen, O. Moutanabbir, and U. Gosele. The phenomenology of ion implantation-induced blistering and thin-layer splitting in compound semiconductors. *Journal of Electronic Materials*, 39(10):2177–2189, 2010.

[156] Q. Y. Tong, L. J. Huang, and U. M. Gosele. Transfer of semiconductor and oxide films by wafer bonding and layer cutting. *Journal of Electronic Materials*, 29(7):928–932, 2000.

[157] Q. Y. Tong, T. H. Lee, L. J. Huang, Y. L. Chao, and U. Gosele. Si and SiC layer transfer by high temperature hydrogen implantation and lower temperature layer splitting. *Electronics Letters*, 34(4):407–408, 1998.

[158] T. Signamarcheix, B. Biasse, A. M. Papon, E. Nolot, F. Mazen, J. Leveneur, O. Faynot, L. Clavelier, and B. Ghyselen. Crystallographic orientation engineering in silicon-on-insulator substrates. *Applied Physics Letters*, 96(26), 2010.

[159] K. Senga, T. Kimoto, and J. Suda. Hydrogen implantation and annealing-induced exfoliation process in sic wafers with various crystal orientations. *Japanese Journal of Applied Physics*, 47(7):5352–5354, 2008.

[160] Shao Lin, Y. Q. Wang, J. G. Swadener, M. Nastasi, E. Thompson Phillip, and N. David Theodore. Cracking in hydrogen ion-implanted $Si/Si_0.8Ge_0.2/Si$ heterostructures. *Applied Physics Letters*, 92(6):061904, 2008.

[161] P. Nguyen, K. K. Bourdelle, C. Aulnette, F. Lallement, N. Daix, N. Daval, I. Cayrefourcq, F. Letertre, C. Mazure, Y. Bogumilowicz, A. Tauzin, C. Deguet, N. Cherkashin, and A. Claverie. Splitting kinetics of $Si_{0.8}Ge_{0.2}$ layers implanted with H or sequentially with He and H. *Journal of Applied Physics*, 104(11):5, 2008.

[162] R. Singh, I. Radu, M. Reiche, R. Scholz, D. Webb, U. Gosele, and S. H. Christiansen. Investigation of hydrogen implantation-induced blistering in SiGe. *Materials Science and Engineering B-Solid State Materials for Advanced Technology*, 124:162–165, 2005. Sp. Iss. SI.

[163] Z. Y. Cheng, G. Taraschi, M. T. Currie, C. W. Leitz, M. L. Lee, A. Pitera, T. A. Langdo, J. L. Hoyt, D. A. Antoniadis, and E. A. Fitzgerald. Relaxed silicon-germanium on insulator substrate by layer transfer. *Journal of Electronic Materials*, 30(12):L37–L39, 2001.

[164] S. O. Kucheyev, J. S. Williams, C. Jagadish, J. Zou, and G. Li. Blistering of H-implanted GaN. *Journal of Applied Physics*, 91(6):3928–3930, 2002.

[165] A. Tauzin, J. Dechamp, F. Madeira, F. Mazen, M. Zussy, C. Deguet, L. Clavelier, J. S. Moulet, C. Richtarch, T. Akatsu, M. Yoshimi, and A. Rigny. 3-inch single-crystal LiTaO3 films onto metallic electrode using Smart Cut (TM) technology. *Electronics Letters*, 44(13):822–U59, 2008.

[166] M. Webb, C. Jeynes, R. Gwilliam, A. Royle, and B. Sealy. Characterising ion-cut in GaAs by Rutherford backscattering spectroscopy. *Nuclear Instruments & Methods in Physics Research Section B-Beam Interactions with Materials and Atoms*, 249:429–431, 2006.

[167] C. H. Yun, N. Quitoriano, and N. W. Cheung. Polycrystalline silicon layer transfer by ion-cut. *Applied Physics Letters*, 82(10):1544–1546, 2003.

[168] M. A. Green. Recent developments in photovoltaics. *Solar Energy*, 76(1-3):3–8, 2004. Sp. Iss. SI.

[169] Z. Medunic, D. Gracin, I. B. Radovic, and M. Jaksic. Characterisation of amorphous silicon solar cells by IBA methods. *Nuclear Instruments & Methods in Physics Research Section B-Beam Interactions with Materials and Atoms*, 190:611–614, 2002.

[170] F. Letertre, C. Deguet, C. Richtarch, B. Faure, J. Hartmann, F. Chieu, A. Beaumont, J. Dechamp, C. Morales, F. Allibert, P. Perreau, S. Pocas, S. Personnic, C. Lagahe-Blanchard, B. Ghyselen, Y. M. Le Vaillant, N. Kernevez, and C. Mazure. Germanium-On-Insulator (GeOI) structure realized by the Smart Cut (TM) technology. In M. Caymax, K. Rim, S. Zaima, E. Kasper, and P. F. P. Fichtner, editors, *High-Mobility Group-IV Materials and Devices*, volume 809 of *Materials Research Society Symposium Proceedings*, pages 153–158. Materials Research Society, Warrendale, 2004.

[171] F. Yang, X. X. Zhang, T. C. Ye, and S. L. Zhuang. The Investigation on Surface Blistering of Ge Implanted by Hydrogen under the Low Temperature Annealing. *Journal of the Electrochemical Society*, 158(12):H1233–H1237, 2011.

[172] C. H. Huang, C. C. Ho, S. C. Jeng, and T. H. Lee. Low Stress Silicon Layer Transfer onto Quartz Through Hydrogen Capture within Si (B/Ge) Buried Layer. *Electrochemical and Solid State Letters*, 12(12):H423–H425, 2009.

[173] E. Toyoda, A. Sakai, H. Isogai, T. Senda, K. Izunome, K. Omote, O. Nakatsuka, and S. Zaima. Characterization and analyses of interface structures in directly bonded si(011)/si(001) substrates. *Japanese Journal of Applied Physics*, 48(2), 2009.

[174] S. Acco, D. L. Williamson, P. A. Stolk, F. W. Saris, M. J. vandenBoogaard, W. C. Sinke, W. F. vanderWeg, and S. Roorda. Hydrogen solubility and network stability in amorphous silicon. *Physical Review B*, 53(8):4415–4427, 1996.

[175] S. M. Myers, M. I. Baskes, H. K. Birnbaum, J. W. Corbett, G. G. Deleo, S. K. Estreicher, E. E. Haller, P. Jena, N. M. Johnson, R. Kirchheim, S. J. Pearton, and M. J. Stavola. Hydrogen Interactions with Defects in Crystalline Solids. *Reviews of Modern Physics*, 64(2):559–617, 1992.

[176] J. Weber, M. Hiller, and E. V. Lavrov. Hydrogen in germanium. *Materials Science in Semiconductor Processing*, 9(4-5):564–570, 2006.

[177] F. Mazen, A. Tauzin, L. Sanchez, F. Chieux, C. Deguet, E. Augendre, T. Akatsu, C. Richtarch, and L. Clavelier. Fracture in hydrogen-implanted germanium. In E. G. Seebauer, Y. V. Kondratenko, S. B. Felch, and A. Jain, editors, *Ion Implantation Technology 2008*, volume 1066 of *AIP Conference Proceedings*, pages 217–220. Amer Inst Physics, Melville, 2008.

[178] J. M. Zahler, A. F. I. Morral, M. J. Griggs, H. A. Atwater, and Y. J. Chabal. Role of hydrogen in hydrogen-induced layer exfoliation of germanium. *Physical Review B*, 75(3), 2007.

[179] C. G. Van de Walle and J. Neugebauer. Hydrogen in semiconductors. *Annual Review of Materials Research*, 36:179–198, 2006.

[180] S. J. Pearton. Hydrogen in Crystalline Semiconductors: Part 1 - Silicon. *International Journal of Modern Physics B*, 8(9):1093–1158, 1994.

[181] H. Moriceau, F. Fournel, B. Aspar, B. Bataillou, A. Beaumont, C. Morales, A. M. Cartier, S. Pocas, C. Lagahe, E. Jalaguier, A. Soubie, B. Biasse, N. Sousbie, S. Sartori, J. F. Michaud, F. Letertre, O. Rayssac, I. Cayrefourcq, C. Richtarch, N. Daval, C. Aulnette, T. Akatsu, B. Osternaud, B. Ghyselen, and C. Mazure. New layer transfers obtained by the smartcut process. *Journal of Electronic Materials*, 32(8):829–835, 2003.

[182] S. J. Pearton, J. W. Corbett, and J. T. Borenstein. Hydrogen diffusion in crystalline semiconductors. *Physica B*, 170(1-4):85–97, 1991.

[183] D. Mathiot. Modeling of hydrogen diffusion in n-type and p-type silicon. *Physical Review B*, 40(8):5867–5870, 1989.

[184] M. Stavola. Hydrogen diffusion and solubility in si. In R. Hull, editor, *Properties of Crystalline Silicon*, chapter 9.8, page 1016. INSPEC; Institution of Electrical Engineers, Exeter, 1997.

[185] A. Vanwieringen and N. Warmoltz. On the permeation of hydrogen and helium in single crystal silicon and germanium at elevated temperatures. *Physica*, 22(10):849–865, 1956.

[186] A. R. Khan, Y. Narita, A. Namiki, A. Kato, and M. Suernitsu. Adsorption and abstraction of atomic hydrogen on the Si(110) surfaces. *Surface Science*, 602(11):1979–1986, 2008.

[187] R. C. Newman, J. H. Tucker, A. R. Brown, and S. A. McQuaid. Hydrogen diffusion and the catalysis of enhanced oxygen diffusion in silicon at temperatures below 500-degrees-c. *Journal of Applied Physics*, 70(6):3061–3070, 1991.

[188] G. L. Olson and J.A. Roth. Solid Phase Epitaxy. In D.T.J. Hurle, editor, *Handbook of Crystal Growth 3: Thin Films and Epitaxy - Part A:Basic Techniques*, chapter 7, pages 255–312. Elsevier North-Holland, 1994.

[189] B. C. Johnson, P. Caradonna, D. J. Pyke, J. C. McCallum, and P. Gortmaker. Hydrogen in amorphous Si and Ge during solid phase epitaxy. *Thin Solid Films*, 518(9):2317–2322, 2010.

[190] D. J. Pyke, J. C. McCallum, and B. C. Johnson. Hydrogen refinement during solid phase epitaxy of buried amorphous silicon layers. *Journal of Applied Physics*, 108(4):44091:1–6, 2010.

[191] B. L. Sopori, K. Jones, and X. J. Deng. Observation of enhanced hydrogen diffusion in solar-cell silicon. *Applied Physics Letters*, 61(21):2560–2562, 1992.

[192] S. J. Pearton, J. W. Corbett, and T. S. Shi. Hydrogen in crystalline semiconductors. *Applied Physics a-Materials Science & Processing*, 43(3):153–195, 1987.

[193] K. Nakamura, T. Saishoji, and J. Tomioka. The dissolution behavior of the void defects by hydrogen annealing in czochralski grown silicon crystals. *Applied Physics Letters*, 70(26):3525–3527, 1997.

[194] L. Pavesi and P. Giannozzi. H Passivation of Si Impurities in Gaas. *Physical Review B*, 43(3):2446–2449, 1991.

[195] A. J. Tavendale, D. Alexiev, and A. A. Williams. Field drift of the hydrogen-related, acceptor-neutralizing defect in diodes from hydrogenated silicon. *Applied Physics Letters*, 47(3):316–318, 1985.

[196] A. M. Saad. Raman investigation of hydrogen-implanted and DC hydrogen-plasma-treated Cz Si wafers. *Canadian Journal of Physics*, 87(4):369–375, 2009.

[197] P. K. Giri, G. Galvagno, A. La Ferla, E. Rimini, S. Coffa, and V. Raineri. Formation and annealing of defects during high-temperature processing of ion-implanted epitaxial silicon: the role of dopant implants. In *Symposium F: Process Induced Defects in Semiconductors at the 1999 Spring Meeting of the European-Materials-Research-Society*, pages 186–191. Elsevier Science Sa, 1999.

[198] J. H. Li and K. S. Jones. {311} defects in silicon: The source of the loops. *Applied Physics Letters*, 73(25):3748–3750, 1998.

[199] C. Bonafos, D. Mathiot, and A. Claverie. Ostwald ripening of end-of-range defects in silicon. *Journal of Applied Physics*, 83(6):3008–3017, 1998.

[200] D. Turnbull and J. C. Fisher. Rate of nucleation in condensed systems. *Journal of Chemical Physics*, 17(1):71–73, 1949.

[201] D. Turnbull. Kinetics of heterogeneous nucleation. *Journal of Chemical Physics*, 18(2):198–203, 1950.

[202] J. S. Williams, M. J. Conway, B. C. Williams, and J. Wong-Leung. Direct observation of voids in the vacancy excess region of ion bombarded silicon. *Applied Physics Letters*, 78(19):2867–2869, 2001.

[203] J. S. Williams and J. Wong-Leung. Voids and nanocavities in silicon. In H. Bernas, editor, *Materials Science with Ion Beams*, volume 116 of *Topics in Applied Physics*, pages 113–146. Springer-Verlag Berlin, Berlin, 2010.

[204] P. S. Plekhanov, U. M. Gosele, and T. Y. Tan. Modeling of nucleation and growth of voids in silicon. *Journal of Applied Physics*, 84(2):718–726, 1998.

[205] H. Lefevre. Trap-centers of self-interstitials in silicon. *Applied Physics*, 22(1):15–22, 1980.

[206] L. Laanab, C. Bergaud, C. Bonafos, A. Martinez, and A. Claverie. Variation of end-of-range density with ion-beam energy and the predictions of the excess interstitials model. In *10th International Conference on Ion Implantation Technology*, pages 236–240. Elsevier Science Bv, 1994.

[207] C. S. Nichols, C. G. Vandewalle, and S. T. Pantelides. Mechanisms of dopant impurity diffusion in silicon. *Physical Review B*, 40(8):5484–5496, 1989.

[208] L. F. Giles, M. Omri, B. de Mauduit, A. Claverie, D. Skarlatos, D. Tsoukalas, and A. Nejim. Coarsening of end-of-range defects in ion-implanted silicon annealed in neutral and oxidizing ambients. In *11th International Conference on Ion Beam Modification of Materials (IBMM98)*, pages 273–278. Elsevier Science Bv, 1998.

[209] B. B. Nielsen, L. Hoffmann, and M. Budde. Si-H stretch modes of hydrogen-vacancy defects in silicon. *Materials Science and Engineering B-Solid State Materials for Advanced Technology*, 36(1-3):259–263, 1996.

[210] F. A. Reboredo, M. Ferconi, and S. T. Pantelides. Theory of the nucleation, growth, and structure of hydrogen-induced extended defects in silicon. *Physical Review Letters*, 82(24):4870–4873, 1999.

[211] R. O. Jones, B. W. Clare, and P. J. Jennings. Si-H clusters, defects, and hydrogenated silicon. *Physical Review B*, 64(12), 2001.

[212] B. J. Coomer, P. Leary, M. Budde, B. B. Nielsen, R. Jones, S. Oberg, and P. R. Briddon. Vacancy-hydrogen complexes in germanium. *Materials Science and Engineering B-Solid State Materials for Advanced Technology*, 58(1-2):36–38, 1999.

[213] A. Nurmela, K. Henttinen, T. Suni, A. Tolkki, and I. Suni. Ion beam studies of hydrogen implanted si wafers. *Nuclear Instruments & Methods in Physics Research Section B-Beam Interactions with Materials and Atoms*, 219-20:747–750, 2004.

[214] C. G. Van de Walle and B. R. Tuttle. Microscopic theory of hydrogen in silicon devices. *IEEE Transactions on Electron Devices*, 47(10):1779–1786, 2000.

[215] N. Fukata, S. Sasaki, K. Murakami, K. Ishioka, K. Nakamura, M. Kitajima, S. Fujimura, J. Kikuchi, and H. Haneda. Hydrogen molecules in defective silicon. *Japanese Journal of Applied Physics Part 2-Letters*, 36(11A):L1456–L1459, 1997.

[216] K. Ishioka, K. G. Nakamura, M. Kitajima, N. Fukata, S. Sasaki, K. Murakami, S. Fujimura, J. Kikuchi, and H. Haneda. Raman spectroscopic study on hydrogen molecules in crystalline silicon treated with atomic hydrogen. *Applied Surface Science*, 117:37–41, 1997.

[217] K. Murakami, N. Fukata, S. Sasaki, K. Ishioka, M. Kitajima, S. Fujimura, J. Kikuchi, and H. Haneda. Hydrogen molecules in crystalline silicon treated with atomic hydrogen. *Physical Review Letters*, 77(15):3161–3164, 1996.

[218] M. Kitajima, K. Ishioka, K. Murakami, K. Nakanoya, and T. Mori. Temperature dependence of the formation of hydrogen molecules in n- and p-type silicon. *Physica B-Condensed Matter*, 274:192–195, 1999.

[219] K. Ishioka, N. Umehara, S. Fukuda, T. Mori, S. Hishita, I. Sakaguchi, H. Haneda, M. Kitajima, and K. Murakami. Formation mechanism of interstitial hydrogen molecules in crystalline silicon. *Japanese Journal of Applied Physics Part 1-Regular Papers Short Notes & Review Papers*, 42(9A):5410–5414, 2003.

[220] Jörg Weber, Martin Hiller, and Edward V. Lavrov. Hydrogen molecules in semiconductors. *Physica B: Condensed Matter Proceedings of the 24th International Conference on Defects in Semiconductors*, 401-402:91–96, 2007.

[221] H. J. Stein, S. M. Myers, and D. M. Follstaedt. Infrared-spectroscopy of chemically bonded hydrogen at voids and defects in silicon. *Journal of Applied Physics*, 73(6):2755–2764, 1993.

[222] S. M. Myers, D. M. Follstaedt, G. A. Petersen, C. H. Seager, H. J. Stein, and W. R. Wampler. Chemical and electrical properties of cavities in silicon and germanium. *Nuclear Instruments and Methods in Physics Research Section B Beam Interactions with Materials and Atoms*, 106(1-4):379–385, 1995.

[223] H. Schut, H. van Gog, A. van Veen, M. A. van Huis, and S. W. H. Eijt. A positron beam study of hydrogen confined in nano-cavities in crystalline silicon. *Nuclear Instruments & Methods in Physics Research Section B-Beam Interactions with Materials and Atoms*, 216:251–256, 2004.

[224] J. Grisolia, F. Cristiano, G. Ben Assayag, and A. Claverie. Kinetic aspects of the growth of platelets and voids in H implanted Si. *Nuclear Instruments & Methods in Physics Research Section B-Beam Interactions with Materials and Atoms*, 178:160–164, 2001.

[225] D. J. Dunstan. Strain and strain relaxation in semiconductors. *Journal of Materials Science-Materials in Electronics*, 8(6):337–375, 1997.

[226] G.C.A.M. Janssen, M. M. Abdalla, F. van Keulen, B. R. Pujada, and B. van Venrooy. Celebrating the 100th anniversary of the Stoney equation for film stress: Developments from polycrystalline steel strips to single crystal silicon wafers. *Thin Solid Films*, 517(6):1858–1867, 2009.

[227] J. J. Wortman and R. A. Evans. Young's modulus shear modulus and poissons ratio in silicon and germanium. *Journal of Applied Physics*, 36(1):153–&, 1965.

[228] W. A. Brantley. Calculated elastic-constants for stress problems associated with semiconductor devices. *Journal of Applied Physics*, 44(1):534–535, 1973.

[229] R. G. Elliman. Semiconductor heterostructures. In M.P. Das, editor, *Proceedings of the Tenth Physics Summer School, Physics of Novel Materials*, pages 235–253. World Scientific Publishing, 1997.

[230] I. R. McKerracher, L. Fu, H. H. Tan, and C. Jagadish. Thermal expansion coefficients and composition of sputter-deposited silicon oxynitride thin films. *Journal of Physics D-Applied Physics*, 43(33), 2010.

[231] N. G. Rudawski, K. S. Jones, S. Morarka, M. E. Law, and R. G. Elliman. Stressed multidirectional solid-phase epitaxial growth of Si. *Journal of Applied Physics*, 105(8):20, 2009.

[232] C. Ascheron, H. Bartsch, A. Setzer, A. Schindler, and P. Paufler. The effect of hydrogen implantation induced stress on GaP single crystals. *Nuclear Instruments and Methods in Physics Research Section B: Beam Interactions with Materials and Atoms*, 28(3):350–359, 1987. TY - JOUR.

[233] J. G. Swadener, M. I. Baskes, and M. Nastasi. Stress-induced platelet formation in silicon: A molecular dynamics study. *Physical Review B*, 72(20), 2005.

[234] J. K. Lee, Y. Lin, Q. X. Jia, T. Höchbauer, H. S. Jung, L. Shao, A. Misra, and M. Nastasi. Role of strain in the blistering of hydrogen-implanted silicon. *Applied Physics Letters*, 89(10), 2006.

[235] Peter J. Schultz, C. Jagadish, M. C. Ridgway, R. G. Elliman, and J. S. Williams. Crystalline-to-amorphous transition for Si-ion irradiation of Si(100). *Physical Review B*, 44(16):9118, 1991.

[236] P. X. Zhang, I. V. Mitchell, B. Y. Tong, P. J. Schultz, and D. J. Lockwood. Depth-dependent disordering in α-Si produced by self-ion-implantation. *Physical Review B*, 50(23):17080–17084, 1994.

[237] K. K. Bourdelle, D. J. Eaglesham, D. C. Jacobson, and J. M. Poate. The effect of as-implanted damage on the microstructure of threading dislocations in MeV implanted silicon. *Journal of Applied Physics*, 86(3):1221–1225, 1999.

[238] J. J. Kolata, T. M. Amos, and H. Bichsel. Energy-loss straggling of protons in silicon. *Physical Review*, 1(2):484, 1968.

[239] A. Pesek. Analysis of ion-implanted silicon using high-resolution x-ray-diffraction. *Applied Physics a-Materials Science & Processing*, 58(3):141–147, 1994.

[240] M. Kuribayashi, K. Takumi, A. Inoue, H. Tanaka, H. Tomita, J. C. Jiang, H. Katoh, K. Ishida, K. Aizawa, S. Okayasu, H. Tomimitsu, and Y. Kazumata. X-ray rocking curve study of the strain profile formed by MeV ion implantation into (111) silicon wafers. *Japanese Journal of Applied Physics Part 1-Regular Papers Brief Communications & Review Papers*, 36(12A):7296–7301, 1997.

[241] F. F. Morehead, B. L. Crowder, and R. S. Title. Formation of amorphous silicon by ion-bombardment as a function of ion, temperature, and dose. *Journal of Applied Physics*, 43(3):1112–&, 1972.

[242] C. A. Volkert. Stress and plastic-flow in silicon during amorphization by ion-bombardment. *Journal of Applied Physics*, 70(7):3521–3527, 1991.

[243] C. A. Volkert. Density changes and viscous-flow during structural relaxation of amorphous-silicon. *Journal of Applied Physics*, 74(12):7107–7113, 1993.

[244] A. C. Chami, E. Ligeon, R. Danielou, J. Fontenille, and R. Eymery. Strain in self-implanted silicon. *Journal of Applied Physics*, 61(1):161–165, 1987.

[245] M. Kulik, A. P. Kobzev, A. Misiuk, W. Wierzchowski, K. Wieteska, and J. Bak-Misiuk. Composition and Structure of Czochralski Silicon Implanted with H(2)(+) and Annealed under Enhanced Hydrostatic Pressure. *Acta Physica Polonica A*, 117(2):332–335, 2010.

[246] J. J. Hall. Electronic effects in elastic constants of n-type silicon. *Physical Review*, 161(3):756–&, 1967.

[247] S. Frabboni. Lattice strain and static disorder in hydrogen-implanted and annealed single-crystal silicon as determined by large-angle convergent-beam electron diffraction. *Physical Review B*, 65(16), 2002.

[248] K. Takayama, R. Matsumoto, S. Taketomi, and N. Miyazaki. Hydrogen diffusion analyses of a cracked steel pipe under internal pressure. *International Journal of Hydrogen Energy*, 36(1):1037–1045, 2011.

[249] C Miclaus and M S Goorsky. Strain evolution in hydrogen-implanted silicon. *Journal of Physics D: Applied Physics*, (10A):A177, 2003.

[250] J. Bak-Misiuk, I. V. Antonova, A. Misiuk, J. Domagala, V. P. Popov, V. I. Obodnikov, J. Hartwig, and A. Romano-Rodriguez. Strain in hydrogen and oxygen implanted silicon and soi structures annealed at high pressure. *Journal of Alloys and Compounds*, 328(1-2):181–186, 2001.

[251] J. F. Ziegler, M. D. Ziegler, and J. P. Biersack. SRIM - The stopping and range of ions in matter (2010). *Nuclear Instruments & Methods in Physics Research Section B-Beam Interactions with Materials and Atoms*, 268(11-12):1818–1823, 2010.

[252] Mathieu Bouville. *The Role Of Stress And Diffusion In Structure Formation In Semiconductors*. PhD thesis, The University Of Michigan, 2004.

[253] A. Antonelli, E. Kaxiras, and D. J. Chadi. Vacancy in silicon revisited: Structure and pressure effects. *Physical Review Letters*, 81(10):2088–2091, 1998.

[254] F. Z. Xuan, S. S. Shao, Z. D. Wang, and S. T. Tu. Coupling effects of chemical stresses and external mechanical stresses on diffusion. *Journal of Physics D-Applied Physics*, 42(1), 2009.

[255] Y. Yamashita, Y. Sakamoto, Y. Kamiura, and T. Ishiyama. Characteristic of strained SiGe film preventing hydrogen from penetrating into Si substrate detected by spreading resistance method. *Japanese Journal of Applied Physics Part 1-Regular Papers Brief Communications & Review Papers*, 46(4A):1622–1624, 2007.

[256] A. J. Pitera and E. A. Fitzgerald. Hydrogen gettering and strain-induced platelet nucleation in tensilely strained $Si_{0.4}Ge_{0.6}$/Ge for layer exfoliation applications. *Journal of Applied Physics*, 97(10), 2005. Part 1.

[257] F. Okba, N. Cherkashin, Z. Di, M. Nastasi, F. Rossi, A. Merabet, and A. Claverie. Controlled drive-in and precipitation of hydrogen during plasma hydrogenation of silicon using a thin compressively strained sige layer. *Applied Physics Letters*, 97(3):3, 2010.

[258] D. M. Isaacson, A. J. Pitera, and E. A. Fitzgerald. Relaxed graded sige donor substrates incorporating hydrogen-gettering and buried etch stop layers for strained silicon layer transfer applications. *Journal of Applied Physics*, 101(1), 2007.

[259] J. W. Matthews and A. E. Blakeslee. Defects in epitaxial multilayers .1. misfit dislocations. *Journal of Crystal Growth*, 27(DEC):118–125, 1974.

[260] B. B. Nielsen and H. G. Grimmeiss. Effect of uniaxial-stress on local vibrational-modes of hydrogen in ion-implanted silicon. *Physical Review B*, 40(18):12403–12415, 1989.

[261] S. Reboh, M. F. Beaufort, J. F. Barbot, J. Grilhe, and P. F. P. Fichtner. Orientation of H platelets under local stress in Si. *Applied Physics Letters*, 93(2):3, 2008.

[262] O. Moutanabbir, M. Reiche, N. Zakharov, F. Naumann, and M. Petzold. Observation of free surface-induced bending upon nanopatterning of ultrathin strained silicon layer. *Nanotechnology*, 22(4):5, 2011.

[263] R. G. Elliman, T. D. M. Weijers-Dall, M. G. Spooner, T. H. Kim, and A. R. Wilkinson. Stress and stress relief in dielectric thin films - the role of hydrogen. *Nuclear Instruments & Methods in Physics Research Section B-Beam Interactions with Materials and Atoms*, 249:310–313, 2006.

[264] M. A. Hopcroft, W. D. Nix, and T. W. Kenny. What is the Young's Modulus of Silicon? *Journal of Microelectromechanical Systems*, 19(2):229–238, 2010.

[265] Milton Ohring. *Materials Science of Thin Films - Deposition and Structure*. Academic Press, San Diego, 2002.

[266] C. A. Volkert, E. A. Fitzgerald, R. Hull, Y. H. Xie, and Y. J. Mii. Strain relaxation in $Ge_{0.09}Si_{0.91}$ epitaxial thin-films measured by wafer curvature. *Journal of Electronic Materials*, 20(10):833–837, 1991.

[267] C. R. Olson, E. Kuryliw, B. E. Jones, and K. S. Jones. Effect of stress on the evolution of mask-edge defects in ion-implanted silicon. In *8th International Workshop on Fabrication, Characterization, and Modeling of Ultra-Shallow Doping Profiles in Semiconductors*, pages 446–449. A V S Amer Inst Physics, 2005.

[268] N.G. Rudawski, K.S. Jones, and R. Gwilliam. Stressed solid-phase epitaxial growth of ion-implanted amorphous silicon. *Materials Science and Engineering: R: Reports*, 61(1-6):40–58, 2008.

[269] N. G. Rudawski, K. S. Jones, and R. Gwilliam. Kinetics and morphological instabilities of stressed solid-solid phase transformations. *Physical Review Letters*, 100(16), 2008.

[270] J.W. Gere and S. P. Timoshenkov. *Mechanics of Materials*. PWS Publishing Company, Boston, 4^{th} edition, 1997. p912.

[271] L.N.G. Filon. On An Approximate Solution for the Bending of a Beam of Rectangular Cross-section under any System of Load, with Special Reference to Points of Concentrated or Discontinuous Loading. *Phil. Trans. R. Soc. Lond. A.*, 201:63–155, 1903.

[272] S. P. Timoshenkov. *History of the Strength of Materials: With a Brief Account of the History of Theory of Elasticity and Theory of Structures*, volume 1. Dover Publications, New York, 2nd edition, 1953. p452.

[273] N. G. Rudawski, K. S. Jones, and R. Gwilliam. Solid phase epitaxy in uniaxially stressed (001) Si. *Applied Physics Letters*, 91(17), 2007.

[274] M. Wzorek, A. Czerwinski, J. Ratajczak, A. Misiuk, and J. Katcki. Hydrostatic pressure effect on dislocation evolution in self-implanted Si investigated by electron microscopy methods. In *6th International Conference on Ion Implantation and Other Applications of Ions and Electrons*, pages 1229–1232. Pergamon-Elsevier Science Ltd, 2006.

[275] W. K. Chu, J. W. Mayer, M. A. Nicolet, T. M. Buck, G. Amsel, and F. Eisen. Principles and applications of ion-beam techniques for analysis of solids and thin-films. *Thin Solid Films*, 17(1):1–41, 1973.

[276] W. K. Chu, J.W. Mayer, and M-A. Nicolet. *Backscattering Spectrometry*. Academic Press, New York, 4th edition, 1978.

[277] L. C. Feldman, J. W. Mayer, and S. T. Picraux. *Materials Analysis By Ion Beam Channelling*. Academic Press, New York, 1982.

[278] D. S. Gemmell. Channeling and related effects in motion of charged-particles through crystals. *Reviews of Modern Physics*, 46(1):129–227, 1974.

[279] E. Bøgh. Defect studies in crystals by means of channeling. *Canadian Journal of Physics*, 46(6):653–&, 1968.

[280] H. Erramli and G. Blondiaux. Ion chanelling. *Applied Radiation and Isotopes*, 46(6-7):413–418, 1995.

[281] D. van Vliet. Dechannelling of fast ions at dislocations. *Physica Status Solidi (a)*, 2(3):521–529, 1970. 10.1002/pssa.19700020314.

[282] H. S. Jin and W. M. Gibson. The angular-dependence of energy-loss of channeled 2 MeV Helium-ions along Si(100) axis. *Nuclear Instruments & Methods in Physics Research Section B-Beam Interactions with Materials and Atoms*, 13(1-3):76–80, 1986.

[283] J. S. Williams, M. Conway, J. A. Davies, M. Petravic, H. H. Tan, and J. Wong-Leung. Analysis of semiconductors by ion channelling: Applications and pitfalls. *Nuclear Instruments & Methods in Physics Research Section B-Beam Interactions with Materials and Atoms*, 136:453–459, 1998.

[284] S. T. Picraux and G. J. Thomas. Correlation of ion channeling and electron microscopy results in the evaluation of heteroepitaxial silicon. *Journal of Applied Physics*, 44(2):594–602, 1973.

[285] S. T. Picraux. Ion channeling studies of the crystalline perfection of epitaxial layers. *Journal of Applied Physics*, 44(2):587–593, 1973.

[286] L. Shao, Y. Q. Wang, and M. Nastasi. A new iterative process for accurate analysis of displaced atoms from channeling rutherford backscattering spectrometry. *Nuclear Instruments & Methods in Physics Research Section B-Beam Interactions with Materials and Atoms*, 249:250–252, 2006.

[287] L. Shao, Y. Q. Wang, M. Nastasi, and J. W. Mayer. Measurements of the stopping powers of He ions incident along the different channel axes and channel planes of Si. *Nuclear Instruments & Methods in Physics Research Section B-Beam Interactions with Materials and Atoms*, 249:51–54, 2006.

[288] G. F. Cerofolini, F. Corni, G. Ottaviani, and R. Tonini. A fast technique for the quantitative-analysis of channeling RBS spectra. *Nuclear Instruments & Methods in Physics Research Section B-Beam Interactions with Materials and Atoms*, 71(4):441–444, 1992.

[289] J. R. Tesmer and M.A. Nastasi. *Handbook of Modern Ion Beam Materials Analysis*. Materials Research Society, University of Michigan, 1995.

[290] J.R. Bird and J. S. Williams. *Ion beams for materials analysis*. Academic Press Australia, Marrickville, 1989.

[291] G. Boudreault, C. Jeynes, E. Wendler, A. Nejim, R. P. Webb, and U. Wätjen. Accurate RBS measurement of ion implant doses in silicon. *Surface and Interface Analysis*, 33(6):478–486, 2002.

[292] L. R. Doolittle. Algorithms for the rapid simulation of Rutherford backscattering spectra. *Nuclear Instruments & Methods in Physics Research Section B-Beam Interactions with Materials and Atoms*, 9(3):344–351, 1985.

[293] M. Thompson. *Genplot/RUMP*. Computer Graphic Service Ltd., 9665 Japonica Drive El Paso, TX, USA, 1996. http://www.genplot.com.

[294] N. P. Barradas, K. Arstila, G. Battistig, M. Bianconi, N. Dytlewski, C. Jeynes, E. Kotai, G. Lulli, M. Mayer, E. Rauhala, E. Szilagyi, and M. Thompson. International Atomic Energy Agency intercomparison of ion beam analysis software. *Nuclear Instruments & Methods in Physics Research Section B-Beam Interactions with Materials and Atoms*, 262(2):281–303, 2007.

[295] N. P. Barradas, K. Arstila, G. Battistig, M. Bianconi, N. Dytlewski, C. Jeynes, E. Kotai, G. Lulli, M. Mayer, E. Rauhala, E. Szilagyi, and M. Thompson. Summary of "IAEA intercomparison of IBA software". *Nuclear Instruments & Methods in Physics Research Section B-Beam Interactions with Materials and Atoms*, 266(8):1338–1342, 2008.

[296] E. Szilagyi, F. Paszti, and G. Amsel. Theoretical Approximations for Depth Resolution Calculations in IBA Methods. *Nuclear Instruments & Methods in Physics Research Section B-Beam Interactions with Materials and Atoms*, 100(1):103–121, 1995.

[297] G. Amsel. CUTBA (cleaning up the tower of Babel of acronyms) in IBA. *Nuclear Instruments & Methods in Physics Research Section B-Beam Interactions with Materials and Atoms*, 118(1-4):52–56, 1996.

[298] E. Szilagyi. Energy spread in ion beam analysis. *Nuclear Instruments & Methods in Physics Research Section B-Beam Interactions with Materials and Atoms*, 161:37–47, 2000.

[299] E. Szilagyi and F. Paszti. Theoretical calculation of the depth resolution of iba methods. *Nuclear Instruments & Methods in Physics Research Section B-Beam Interactions with Materials and Atoms*, 85(1-4):616–620, 1994.

[300] E. Szilagyi. Energy and depth resolution in elastic recoil coincidence spectrometry. *Nuclear Instruments & Methods in Physics Research Section B-Beam Interactions with Materials and Atoms*, 268(11-12):1731–1735, 2010.

[301] J. Tirira, Y. Serruys, and P. Trocellier. *Forward Recoil Spectrometry: Applications to Hydrogen Determination in Solids.* Plenum Press, New York, 1996.

[302] E. Bronchalo, L. delPeral, J. Medina, J. Sequeiros, and N. Hasebe. Parametrization of charge and mass resolution for Delta E-E telescopes. *Nuclear Instruments & Methods in Physics Research Section a-Accelerators Spectrometers Detectors and Associated Equipment*, 399(1):65–75, 1997.

[303] Á. Z. Kiss, E. Somorjai, J. Räisänen, and E. Rauhala. Stopping Powers of 1.5-7.2 Mev He-4 Ions in Havar, Nickel, Kapton and Mylar. *Nuclear Instruments & Methods in Physics Research Section B-Beam Interactions with Materials and Atoms*, 39(1-4):15–17, 1989.

[304] D. C. Santry and R. D. Werner. Stopping Power Measurements of C, Al, Si, Ti, Ni, Ag, Au and Mylar Using Radioactive Alpha-Sources. *Nuclear Instruments & Methods in Physics Research Section B-Beam Interactions with Materials and Atoms*, 229(1):13–15, 1984.

[305] D. C. Santry and R. D. Werner. Stopping Power Values of Be, C, Al and Si for He-4 Ions. *Nuclear Instruments & Methods*, 178(2-3):523–530, 1980.

[306] E. Rauhala and J. Raisanen. Energy-loss of 450-2400 KeV prototns in Havar, Kapton and aluminized Mylar foils. *Nuclear Instruments & Methods in Physics Research Section B-Beam Interactions with Materials and Atoms*, 12(3):321–324, 1985.

[307] E. Rauhala and J. Raisanen. Energy-loss of 1.3-2.6 MeV He-4 ions in Havar, Nickel, Kapton and Mylar foils. *Nuclear Instruments & Methods in Physics Research Section B-Beam Interactions with Materials and Atoms*, 24-5:362–365, 1987.

[308] E. Szilagyi, L. S. Wielunski, and F. Paszti. Theoretical approximation of energy distribution of elastically recoiled hydrogen atoms. *Nuclear Instruments & Methods in Physics Research Section B-Beam Interactions with Materials and Atoms*, 137:701–706, 1998.

[309] M. Wielunski, M. Mayer, R. Behrisch, J. Roth, and B. M. U. Scherzer. Simultaneous profiling of hydrogen and deuterium by 2.6 MeV He-4 ERDA using a Delta E-E telescope detector. *Nuclear Instruments & Methods in Physics Research Section B-Beam Interactions with Materials and Atoms*, 122(1):113–120, 1997.

[310] R. D. Verda, C. J. Maggiore, J. R. Tesmer, A. Misra, T. Hoechbauer, M. Nastasi, and R. W. Bower. Depth profiling of hydrogen in crystalline silicon using elastic recoil detection analysis. *Nuclear Instruments and Methods in Physics Research Section B: Beam Interactions with Materials and Atoms*, 183(3-4):401–412, 2001.

[311] R. D. Verda, C. J. Maggiore, J. R. Tesmer, A. Misra, T. Hoechbauer, M. Nastasi, and R. W. Bower. Erratum to "Depth profiling of hydrogen in crystalline silicon using elastic recoil detection analysis" [Nucl. Instr. and Meth. B 183 (2001) 401-412]. *Nuclear Instruments and Methods in Physics Research Section B: Beam Interactions with Materials and Atoms*, 184(4):656–656, 2001. 0168-583X doi: DOI: 10.1016/S0168-583X(01)00975-2.

[312] R. J. Sweeney, V. M. Prozesky, and K. A. Springhorn. The quantitative determination of H in geological materials (silicates) by elastic recoil detection analysis (ERDA). *Nuclear Instruments & Methods in Physics Research Section B-Beam Interactions with Materials and Atoms*, 130(1-4):623–627, 1997.

[313] F. Schiettekatte, M. Chicoine, S. Gujrathi, P. Wei, and K. Oxorn. Allegria: a new interface to the ERD program. *Nuclear Instruments & Methods in Physics Research Section B-Beam Interactions with Materials and Atoms*, 219:125–129, 2004.

[314] G. Boudreault, R. G. Elliman, R. Grotzschel, S. C. Gujrathi, C. Jeynes, W. N. Lennard, E. Rauhala, T. Sajavaara, H. Timmers, Y. Q. Wang, and T. D. M. Weijers. Round Robin: measurement of H implantation distributions in Si by elastic recoil detection. *Nuclear Instruments & Methods in Physics Research Section B-Beam Interactions with Materials and Atoms*, 222(3-4):547–566, 2004.

[315] Carrie Lamb and Mike Zecchino. *WYKO Surface Profilers Technical Reference Manual*, volume 2.2.1. Veeco Metrology Group, 2650 East Elvira Road, Tucson, Arizona 85706, 1999. p149.

[316] E. Ruska and M. Knoll. Die magnetische Sammelspule für schnelle Elektronenstrahlen. *Zeitschrift fur Physik*, 12(389):448, 1931.

[317] E. Ruska. The development of the electron-microscope and of electron-microscopy. *Reviews of Modern Physics*, 59(3):627–638. ISI Document Delivery No.: J9630.

[318] D.B. Williams and C.B. Carter. *Transmission Electron Microscopy - A Textbook for Materials Science*. Plenum Press, New York, 1st edition, 1996.

[319] W. S. Rasband and D. S. Bright. NIH IMAGE - A Public Domain Image-processing Program for the Macintosh. *Microbeam Analysis*, 4(3):137–149, 1995.

[320] M.D. Abramoff, P.J. Magalhaes, and S.J. Ram. Image processing with imagej. *Biophotonics International*, 11(7):36–42, 2004.

[321] N. G. Rudawski, K. S. Jones, and R. Gwilliam. Stressed solid-phase epitaxial growth of (011) Si. *Journal of Materials Research*, 24(2):305–309, 2009.

[322] T. W. Simpson and I. V. Mitchell. Annealing behavior of implanted helium in indium phosphide. *Applied Physics Letters*, 78(2):207–209, 2001.

[323] P. J. Simpson, A. P. Knights, M. Chicoine, K. Dudeck, O. Moutanabbir, S. Ruffell, F. Schiettekatte, and B. Terreault. Thermal evolution of defects produced by implantation of H, D and He in Silicon. *Applied Surface Science*, 255(1):63–67, 2008.

[324] S. Ruffell, P. J. Simpson, and A. P. Knights. The effect of the annealing ramp rate on the formation of voids in silicon. *Journal of Physics-Condensed Matter*, 19(46):462202:1–6, 2007.

[325] David R. Evans. *Microelectronic Device Fabrication I*. Course notes, Lecture 12, Portland State University, Portland, Oregon, Fall 2012. http://web.pdx.edu/ davide/Lecture12.pdf.

[326] P. K. Giri. Studies on the surface swelling of ion-irradiated silicon: Role of defects. *Materials Science and Engineering B-Solid State Materials for Advanced Technology*, 121(3):238–243, 2005.

[327] V. Raineri, S. Coffa, E. Szilagyi, J. Gyulai, and E. Rimini. He-vacancy interactions in Si and their influence on bubble formation and evolution. *Physical Review B*, 61(2):937–945, 2000.

[328] O. W. Holland, J. D. Budai, and C. W. White. Uniaxial Lattice Expansion of Self-Ion-Implanted Si. *Applied Physics Letters*, 57(3):243–245, 1990.

[329] C. L. Liu, M. Orlowski, A. Thean, K. Beardmore, A. Barr, T. White, B. Y. Nguyen, H. Rueda, and X. Y. Liu. Theory and simulation of dopant implantation and diffusion in SiGe. *Physica Status Solidi B-Basic Research*, 239(1):35–43, 2003.

[330] R. Ruther and J. Livingstone. The role of substrate-temperature and in-chamber annealing in H-Si bonding configurations in sputtered α-Si-H. *Thin Solid Films*, 226(1):59–64, 1993.

[331] N. Desrosiers, A. Giguere, B. Terreault, M. Chicoine, and F. Schiettekatte. Implantation effects of low energy H and D ions in germanium at -120 degrees C and room temperature. *Nuclear Instruments & Methods in Physics Research Section B-Beam Interactions with Materials and Atoms*, 266(9):1971–1978, 2008.

[332] M. L. David, F. Pailloux, D. Babonneau, M. Drouet, J. F. Barbot, E. Simoen, and C. Claeys. The effect of the substrate temperature on extended defects created by hydrogen implantation in germanium. *Journal of Applied Physics*, 102(9):3, 2007.

[333] S. Tamulevičius, I. Požėla, and M. Andrulevičius. A simple model of radiation swelling of silicon. *Materials Science and Engineering B-Solid State Materials for Advanced Technology*, 40(2-3):141–146, 1996.

[334] N. Desrosiers and B. Terreault. Ion cutting and transfer of sub-100-nm silicon layers using low-keV H, D, and He ions. *Applied Physics Letters*, 89(15):3, 2006.

[335] P. A. Aleksandrov, E. K. Baranova, I. V. Baranova, V. V. Budaragin, and V. L. Litvinov. Behavior of implanted hydrogen in thermally stimulated blistering in silicon. *Radiation Effects and Defects in Solids*, 158(11-12):771–781, 2003.

[336] C. Deguet, L. Sanchez, I. Akatsu, F. Allibert, J. Dechamp, F. Madeira, F. Mazen, A. Tauzin, V. Loup, C. Richtarch, D. Mercier, T. Signamarcheix, F. Letertre, B. Depuydt, and N. Kernevez. Fabrication and characterisation of 200 mm germanium-on-insulator (GeOI) substrates made from bulk germanium. *Electronics Letters*, 42(7):415–417, 2006.

[337] T. Akatsu, K. K. Bourdelle, C. Richtarch, B. Faure, and F. Letertre. Study of extended-defect formation in Ge and Si after H ion implantation. *Applied Physics Letters*, 86(18):3, 2005.

[338] E. Ligeon and A. Guivarc'h. Hydrogen implantation in silicon between 1.5 and 60 keV. *Radiation Effects and Defects in Solids*, 27(3-4):129–137, 1976.

[339] G. Parry, C. Coupeau, E. Dion, M. L. David, J. Colin, and J. Grilhe. About the internal pressure in cavities derived from implantation-induced blistering in semiconductors. *Journal of Applied Physics*, 110(11):8, 2011.

[340] E. Dion, J. Grilhe, J. Colin, and C. Coupeau. Buckling of stressed and pressurized thin films on substrates. *Journal of Applied Mechanics-Transactions of the ASME*, 77(4):5, 2010.

[341] K. Mitani and U. M. Gosele. Formation of interface bubbles in bonded silicon-wafers - a thermodynamic model. *Applied Physics a-Materials Science & Processing*, 54(6):543–552, 1992.

[342] W. Young and R. Budynas. *Roark's Formulas for Stress and Strain.* McGraw-Hill Companies,Incorporated, New York, 2001. p.488.

[343] W. H. Han and J. Z. Yu. Thermodynamic model of hydrogen-induced silicon surface layer cleavage. *Journal of Applied Physics*, 89(11):6551–6553, 2001.

[344] B. E. Deal and A. S. Grove. General relationship for the thermal oxidation of silicon. *Journal of Applied Physics*, 36(12):3770, 1965.

[345] J. Rankin, J.C. McCallum, and L.A. Boatner. Annealing-environment effects in the epitaxial regrowth of ion-beam-amorphized layers on $CaTiO_3$. *JOURNAL OF APPLIED PHYSICS*, 78(3):1519–1527, AUG 1 1995.

[346] J. Rankin, J.C. McCallum, and L.A. Boatner. The effect of annealing environments on the epitaxial recrystallization of ion-beam-amorphized SrTiO3. *Journal of Materials Research*, 7(03):717–724, 3 1992.

[347] G. Bourque, B. Terreault, G. G. Ross, and D. Theriault. Experiments and simulations on the effect of channeling on the ranges of 1 kev deuterons in silicon. *Nuclear Instruments & Methods in Physics Research Section B-Beam Interactions with Materials and Atoms*, 90(1-4):175–178, 1994.

[348] G. Hobler, K. K. Bourdelle, and T. Akatsu. Random and channeling stopping power of H in Si below 100 keV. *Nuclear Instruments & Methods in Physics Research Section B-Beam Interactions with Materials and Atoms*, 242(1-2):617–619, 2006.

[349] Z. F. Di, Y. Q. Wang, M. Nastasi, and N. D. Theodore. Origin of reverse annealing effect in hydrogen-implanted silicon. *Applied Physics Letters*, 96(15):3, 2010.

[350] B. M. Rice, L. M. Raff, and D. L. Thompson. Diffusion Of H-atoms on a Si(111) surface with partial hydrogen coverage - Monte-Carlo Variational Phase-Space theory with Tunneling Correction. *Journal of Chemical Physics*, 88(11):7221–7231, 1988.

[351] A. W. R. Leitch, V. Alex, and J. Weber. H_2 molecules in c-Si after hydrogen plasma treatment. *Solid State Communications*, 105(4):215–219, 1998.

[352] A. W. R. Leitch, J. Weber, and V. Alex. Formation of hydrogen molecules in crystalline silicon. *Materials Science and Engineering B-Solid State Materials for Advanced Technology*, 58(1-2):6–12, 1999.

[353] C. P. Cheney, M. Budde, G. Lupke, L. C. Feldman, and N. H. Tolk. Vibrational dynamics of isolated hydrogen in germanium. *Physical Review B*, 65(3), 2002.

[354] N. Martsinovich, I. Suarez-Martinez, and M. I. Heggie. First principles modelling of (100) H-induced platelets in silicon. In M. Stutzmann, editor, *Physica Status Solidi C - Conferences and Critical Reviews, Vol 2, No 6*, volume 2 of *Physica Status Solidi C-Current Topics in Solid State Physics*, pages 1771–1780. Wiley-V C H Verlag Gmbh, Weinheim, 2005.

[355] G.H. Collin, A. Shalav, and R.G. Elliman. SiOx/GeOx nanowires grown via the active oxidation of Si/Ge substrates. In *Materials Research Forum*, volume 700, pages 133–136, 2012.

[356] T. Höchbauer, A. Misra, M. Nastasi, J. W. Mayer, and W. Ensinger. Formation of hydrogen complexes in proton implanted silicon and their influence on the crystal damage. *Nuclear Instruments & Methods in Physics Research Section B-Beam Interactions with Materials and Atoms*, 242(1-2):623–626, 2006.

[357] K. G. Cheng, J. Lee, and J. W. Lyding. Experimental evidence of Si-H bond energy variation at SiO(2)-Si interface. *Applied Physics Letters*, 77(21):3388–3390, 2000.

[358] M. Imai and K. Sumino. Insitu x-ray topographic study of the dislocation mobility in high-purity and impurity-doped silicon-crystals. *Philosophical Magazine a-Physics of Condensed Matter Structure Defects and Mechanical Properties*, 47(4):599–621, 1983.

[359] K. Sumino and I. Yonenaga. Hydrogen mobilities in c-Si. In R. Hull, editor, *Properties of Crystalline Silicon*, chapter 3.5, pages 113–121. INSPEC; Institution of Electrical Engineers, Exeter, 1998. http://www.knovel.com/knovel2/Toc.jsp?BookID=1148&VerticalID=0.

[360] L. S. Robertson, K. S. Jones, L. M. Rubin, and J. Jackson. Annealing kinetics of {311} defects and dislocation loops in the end-of-range damage region of ion implanted silicon. *Journal of Applied Physics*, 87(6):2910–2913, 2000.

[361] F. Cristiano, J. Grisolia, B. Colombeau, M. Omri, B. de Mauduit, A. Claverie, L. F. Giles, and N. E. B. Cowern. Formation energies and relative stability of perfect and faulted dislocation loops in silicon. *Journal of Applied Physics*, 87(12):8420–8428, 2000.

[362] R. Raman, M. E. Law, V. Krishnamoorthy, K. S. Jones, and S. B. Herner. Effect of surface proximity on end-of-range loop dissolution in silicon. *Applied Physics Letters*, 74(11):1591–1593, 1999.

[363] P. Castrillo, I. Martin-Bragado, R. Pinacho, M. Jaraiz, J. E. Rubio, K. R. C. Mok, F. J. Miguel-Herrero, and J. Barbolla. Physically based modeling of dislocation loops in ion implantation processing in silicon. In *Symposium on Materials Science and Device Issues for Futrue Si-Based Technologies held at the 2005 EMRS Meeting*, pages 404–408. Elsevier Science Sa, 2005.

[364] Z. F. Di, Y. Q. Wang, M. Nastasi, and N. D. Theodore. Evolution of implantation induced damage under further ion irradiation: Influence of damage type. *Journal of Applied Physics*, 105(7):9, 2009.

[365] Z. F. Di, M. Q. Huang, Y. Q. Wang, and M. Nastasi. Dynamic annealing versus thermal annealing effects on the formation of hydrogen-induced defects in silicon. *Applied Physics Letters*, 97(19):3, 2010.

[366] Z. F. Di, Y. Q. Wang, M. Nastasi, L. Shao, J. K. Lee, and N. D. Theodore. Evidence for ion irradiation induced dissociation and reconstruction of Si-H bonds in hydrogen-implanted silicon. *Applied Physics Letters*, 93(10):3, 2008.

[367] B. Tummers. *DataThief III*. 1.6. 2010. http://www.datathief.org/.

[368] Thomas Williams, Colin Kelley, and many others. Gnuplot 4.2: an interactive plotting program. http://gnuplot.sourceforge.net/, September 2009.

[369] P. N. Keating. Effect of invariance requirements on elastic strain energy of crystals with application to diamond structure. *Physical Review*, 145(2):637–&, 1966.

[370] L. J. Vandeperre, F. Giuliani, S. J. Lloyd, and W. J. Clegg. The hardness of silicon and germanium. *Acta Materialia*, 55(18):6307–6315, 2007.

[371] R. F. Cook. Strength and sharp contact fracture of silicon. *Journal of Materials Science*, 41(3):841–872, 2006.

[372] O. W. Holland. The unique role of ion beam analysis in modeling the thermal evolution of hydrogen in si implanted at doses required for ion cutting. *Nuclear Instruments & Methods in Physics Research Section B-Beam Interactions with Materials and Atoms*, 219:788–791, 2004.

[373] O. Moutanabbir, B. Terreault, M. Chicoine, F. Schiettekatte, and P. J. Simpson. Influence of isotopic substitution and He coimplantation on defect complexes and voids induced by H ions in silicon. *Physical Review B*, 75(7), 2007.

[374] L. C. Kimerling and J. R. Patel. Defect states associated with dislocations in silicon. *Applied Physics Letters*, 34(1):73–75, 1979.

[375] S. A. Centoni, B. Sadigh, G. H. Gilmer, T. J. Lenosky, T. D. de la Rubia, and C. B. Musgrave. First-principles calculation of intrinsic defect formation volumes in silicon. *Physical Review B*, 72(19), 2005.

[376] K. Henttinen, I. Suni, and S. S. Lau. Mechanically induced Si layer transfer in hydrogen-implanted Si wafers. *Applied Physics Letters*, 76(17):2370–2372, 2000.

[377] Kenji Kimura. Rutherford Backscattering Spectroscopy. In R.A. Meyers, editor, *Encyclopedia of Analytical Chemistry*, pages 12809–12823. John Wiley & Sons Ltd., Chichester, 2000.

[378] J. Wong-Leung, J. S. Williams, A. Kinomura, Y. Nakano, Y. Hayashi, and D. J. Eaglesham. Diffusion and transient trapping of metals in silicon. *Physical Review B*, 59(12):7990–7998, 1999.

[379] S.P. Nikanorov, Y. A. Burenkov, and A. V. Stepanov. Elastic properties of silicon. *Soviet Physics Solid State (USSR)*, 13(10):2516–&, 1972.

[380] C. Zener and J. H. Hollomon. Problems in non-elastic deformation of metals. *Journal of Applied Physics*, 17(2):69–82, 1946.

[381] W. Schroter, H. G. Brion, and H. Siethoff. Yield-point and dislocation mobility in silicon and germanium. *Journal of Applied Physics*, 54(4):1816–1820, 1983.

[382] J. W. Mayer and S. S. Lau. *Electronic Material Science: For Integrated Circuits in Si and GaAs*. Macmillan Publishing Company, London, 1990.

[383] K. J. Chang and D. J. Chadi. Hydrogen-bonding and diffusion in crystalline silicon. *Physical Review B*, 40(17):11644–11653, 1989.

[384] A. Hara. Diffusion coefficient of hydrogen in silicon at an intermediate temperature. *Japanese Journal of Applied Physics Part 1-Regular Papers Brief Communications & Review Papers*, 46(3A):962–964, 2007.

[385] V. Gusakov. Diffusion of interstitial hydrogen molecules in crystalline germanium and silicon: Quantumchemical simulation. *Materials Science in Semiconductor Processing*, 9(4-5):531–535, 2006.

[386] S. Bedard and L. J. Lewis. Diffusion of hydrogen in crystalline silicon. *Physical Review B*, 61(15):9895–9898, 2000.

[387] Y. L. Huang, Y. Ma, R. Job, and A. G. Ulyashin. Hydrogen diffusion at moderate temperatures in p-type czochralski silicon. *Journal of Applied Physics*, 96(12):7080–7086, 2004.

[388] P. Leary, R. Jones, and S. Oberg. Interaction of hydrogen with substitutional and interstitial carbon defects in silicon. *Physical Review B*, 57(7):3887–3899, 1998.

[389] B. Sopori, Y. Zhang, and N. M. Ravindra. Silicon device processing in H-ambients: H-diffusion mechanisms and influence on electronic properties. *Journal of Electronic Materials*, 30(12):1616–1627, 2001.

[390] C. Langpape, S. Fabian, C. Klatt, and S. Kalbitzer. Observation of H-1 tunneling diffusion in crystalline Si. *Applied Physics a-Materials Science & Processing*, 64(2):207–210, 1997.

[391] S. Rubin. Surface analysis by charged particle spectroscopy. *Nuclear Instruments & Methods*, 5(3):177–183, 1959.

[392] W. K. Chu and J. R. Liu. Rutherford backscattering spectrometry: Reminiscences and progresses. *Materials Chemistry and Physics*, 46(2-3):183–188, 1996.

[393] F. H. Eisen. Channeling of medium-mass ions through silicon. *Canadian Journal of Physics*, 46(6):561–&, 1968.

[394] J. Bøttiger and F. H. Eisen. Conversion from an energy scale to a depth scale in channeling experiments. *Thin Solid Films*, 19(2):239–246, 1973.

[395] D. I. Porat and K. Ramavataram. Differential Energy Loss and Ranges of Ne, N and He Ions. *Proceedings of the Physical Society of London*, 78(505):1135–&, 1961.

[396] D. Niemann, P. Oberschachtsiek, S. Kalbitzer, and H. P. Zeindl. Energy loss and straggling of MeV 4He ions in a Si/Sb multilayer target. *Nuclear Instruments and Methods in Physics Research Section B: Beam Interactions with Materials and Atoms*, 80-81(Part 1):37–40, 1993. 0168-583X doi: DOI: 10.1016/0168-583X(93)96071-J.

[397] G. Konac, S. Kalbitzer, C. Klatt, D. Niemann, and R. Stoll. Energy loss and straggling of H and He ions of keV energies in Si and C. *Nuclear Instruments & Methods in Physics Research Section B-Beam Interactions with Materials and Atoms*, 136:159–165, 1998.

[398] W. N. Lennard, H. Xia, and J. K. Kim. Revisiting the stopping powers of Si and SiO_2 for ^{4}He ions: 0.5-2.0 MeV. *Nuclear Instruments and Methods in Physics Research Section B: Beam Interactions with Materials and Atoms*, 215(3-4):297–307, 2004.

[399] G. Amsel, D. David, G. Beranger, P. Boisot, B. Degelas, and P. Lacombe. A nuclear method for analysing impurities inserted in metals by their surface state preparations . application to zirconium. *Journal of Nuclear Materials*, 29(2):144, 1969.

[400] G. Amsel and W. A. Lanford. Nuclear-reaction techniques in materials analysis. *Annual Review of Nuclear and Particle Science*, 34:435–460, 1984.

[401] G. Amsel, J. P. Nadai, Dartemar.E, D. David, E. Girard, and J. Moulin. Microanalysis by Direct Observation of Nuclear Reactions Using a 2 Mev Van-De-Graaff. *Nuclear Instruments & Methods*, 92(4):481, 1971.

[402] D. Dieumegard, D. Dubreuil, and G. Amsel. Analysis and Depth Profiling of Deuterium with the D(^{3}He,P)^{4}He Reaction by Detecting the Protons at Backward Angles. *Nuclear Instruments & Methods*, 166(3):431–445, 1979.

[403] W. A. Lanford, H.P. Trautvetter, J.F. Ziegler, and J. Keller. New precision technique for measuring the concentration versus depth of hydrogen in solids. *Applied Physics Letters*, 28(9):566–568, 1976.

[404] B. Maurel, G. Amsel, and J. P. Nadai. Depth profiling with narrow resonances of nuclear-reactions - theory and experimental use. *Nuclear Instruments & Methods in Physics Research*, 197(1):1–13, 1982.

[405] W. Rudolph, C. Bauer, K. Brankoff, D. Grambole, R. Grotzschel, C. Heiser, and F. Herrmann. Plastic foils as primary hydrogen standards for nuclear-reaction analysis. *Nuclear Instruments & Methods in Physics Research Section B-Beam Interactions with Materials and Atoms*, 15(1-6):508–511, 1986.

[406] B. L. Cohen, J. H. Degnan, and C. L. Fink. Nondestructive analysis for trace amounts of hydrogen. *Journal of Applied Physics*, 43(1):19–&, 1972.

[407] B.L. Doyle and P.S. Peercy. Technique for profiling 1H with 2.5-MeV Van de Graaff accelerators. *Applied Physics Letters*, 34(11):811–813, 1979.

[408] B. L. Doyle and D. K. Brice. The analysis of elastic recoil detection data. *Nuclear Instruments & Methods in Physics Research Section B-Beam Interactions with Materials and Atoms*, 35(3-4):301–308, 1988.

[409] W. A. Lanford. Analysis for hydrogen by nuclear-reaction and energy recoil detection. *Nuclear Instruments & Methods in Physics Research Section B-Beam Interactions with Materials and Atoms*, 66(1-2):65–82, 1992.

[410] J. L'Ecuyer, C. Brassard, C. Cardinal, J. Chabbal, L. Deschênes, B. Terreault, J.G. Martel, and R. St.-Jacques. An accurate and sensitive method for the determination of the depth distribution of light elements in heavy materials. *Journal of Applied Physics*, 47(1):381–2, 1975.

[411] J. F. Ziegler, C. P. Wu, P. Williams, C. W. White, B. Terreault, B. M. U. Scherzer, R. L. Schulte, E. J. Schneid, C. W. Magee, E. Ligeon, J. Lecuyer, W. A. Lanford, F. J. Kuehne, E. A. Kamykowski, W. O. Hofer, A. Guivarch, C. H. Filleux, V. R. Deline, C. A. Evans, B. L. Cohen, G. J. Clark, W. K. Chu, C. Brassard, R. S. Blewer, R. Behrisch, B. R. Appleton, and D. D. Allred. Profiling hydrogen in materials using ion-beams. *Nuclear Instruments & Methods*, 149(1-3):19–39, 1978.

[412] R. D. Verda, J. R. Tesmer, C. J. Maggiore, M. Nastasi, and R. W. Bower. Geometric considerations relevant to hydrogen depth profiling by reflection elastic recoil detection analysis. *Nuclear Instruments & Methods in Physics Research Section B-Beam Interactions with Materials and Atoms*, 183(3-4):391–400, 2001.

[413] J. C. Banks, J. F. Browning, W. R. Wampler, B. L. Doyle, C. A. LaDuca, J. R. Tesmer, C. J. Wetteland, and Y. Q. Wang. Round robin analyses of hydrogen isotope thin films standards. *Nuclear Instruments & Methods in Physics Research Section B-Beam Interactions with Materials and Atoms*, 219:444–449, 2004.

[414] R. D. Verda, J. R. Tesmer, M. Nastasia, and R. W. Bower. An energy spread correction for depth profiling by elastic recoil detection analysis. *Nuclear Instruments & Methods in Physics Research Section B-Beam Interactions with Materials and Atoms*, 187(3):383–392, 2002.

[415] R. D. Verda, J. R. Tesmer, M. Nastasi, and R. W. Bower. Accurate hydrogen depth profiling by reflection elastic recoil detection analysis. *Nuclear Instruments & Methods in Physics Research Section B-Beam Interactions with Materials and Atoms*, 190:419–422, 2002.

[416] U. Reinholz, W. Bremser, K. W. Brzezinka, E. Strub, H. P. Weise, and S. Merchel. A thin-layer reference material for hydrogen analysis. *Nuclear Instruments & Methods in Physics Research Section B-Beam Interactions with Materials and Atoms*, 266(10):2418–2423, 2008.

[417] I. R. McKerracher. *Post-growth spectral tuning of InGaAs/GaAs quantum dot infrared photodetectors*. Doctor of Philosophy, Department of Electronic Materials Engineering, Research School of Physics and Engineering, Australian National University, ACT 0200, Australia, 2011.

[418] S. Charnvanichborikarn. Doctor of Philosophy, Department of Electronic Materials Engineering, Research School of Physics and Engineering, Australian National University, ACT 0200, Australia, 2011.

[419] A. Binder and G. Kroupa. Novel technology for handling very-thin wafers. *Solid State Technology*, 46(10):64–+, 2003.

[420] K. S. Jones, K. Moller, J. Chen, M. PugaLambers, M. Law, D. S. Simons, P. Chi, B. Freer, J. Bernstein, L. Rubin, R. Simonton, R. G. Elliman, M. Petravic, and P. Kringhoj. *The effect of end of range loops on transient enhanced diffusion in Si.* Ion Implantation Technology - 96. I E E E, New York, 1997. p618-621.

[421] Scott Pakin. The Comprehensive LaTeX Symbols Guide. http://www.ctan.org/, 2003. ⟨pakin@uiuc.edu⟩.

Appendix A

Theoretical simulations

PREDICTIONS of the types and forms of influence expected in this project were sought for the study in stressed materials, presented in Section 5.4. A brief summary of the simulations produced to predict particulars in behaviour is included here. Section A.1 discusses the stresses mechanically applied to materials, as well as touching on those caused by compositional means. Section A.2 discusses the attempts to predict the evolution of ion implanted hydrogen in the crystalline silicon system.

A.1 Simulations of applied mechanical stress

The stresses to be induced in semiconductors mechanically in this study are best described by a classical beam theory as established by Euler and Bernoulli around 1750 [272]. The Euler-Bernoulli equation is shown in Eq. A.1:

$$\frac{d^2}{dx^2}\left(EI\frac{d^2w}{dx^2}\right) = q \tag{A.1}$$

Where $w(x)$ describes the curve or deflection of the beam, E is the elastic or Young's modulus for the material, I is the second moment of area of the beam's cross-section (= the moment of inertia for a section or area subtended through an angle or polar reference frame), and q is the load applied to the beam, as force per unit length.

Building from this relationship between the deflection of a beam and the applied load

inducing it, Euler-Bernoulli beam theory can be used to describe the stress σ under simple bending [270]. This requires the bending to be symmetric, and linear within the plane formed by the radius of curvature and natural length of the beam, without any shear forces, torsional or axial forces affecting the beam. The bending moment of a beam can be given by the expression:

$$M = -EI\frac{d^2w}{dx^2}$$

If Equation A.1 is integrated across dx by some value $c(z)$, the thickness of the beam from a neutral central surface or axis, the equation now solves for force per unit area, i.e., pressure or stress, given in Eq. A.2.

$$\sigma(x,z) = \frac{Mc}{I} = -c(z)E\frac{d^2w}{dx^2} \tag{A.2}$$

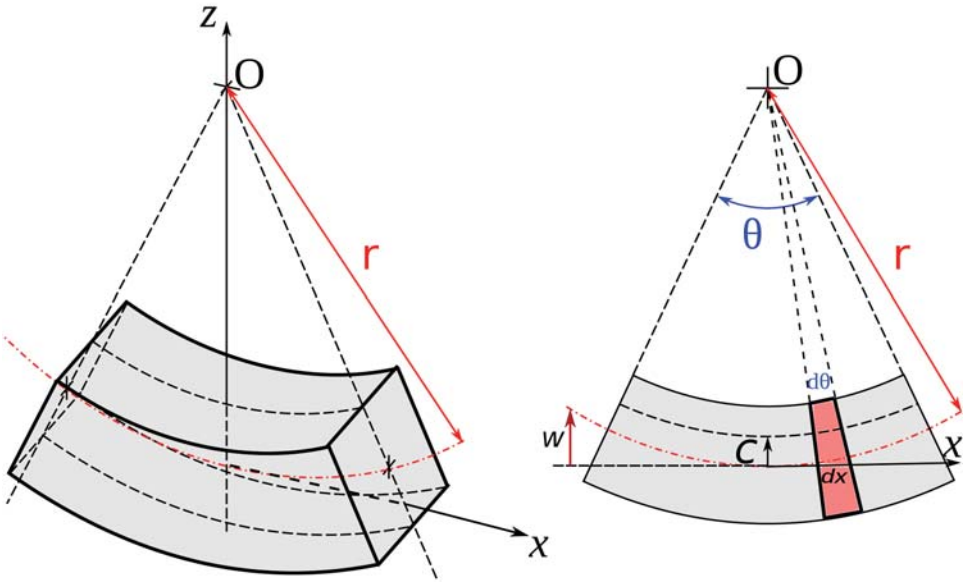

Figure A.1: Three dimensional and cross-sectional representation of a beam undergoing bending. O labels origin of the radius of curvature r along the z axis, red dashed line represents the neutral surface/line through the beam, and c labels the thickness within the beam from the neutral surface.

Equation A.2 describes a situation as shown in Fig. A.1. Here it can be seen that the angle made between the neutral surface and the x axis, θ, can be related to the gradient or slope of the function defining the beam's position, $w(x)$, as $\theta(x) = \frac{dw}{dx}$. From Fig. A.1 one can also define some small element dx in relation to the angle θ and radius of curvature r,

such that $x = r\ d\theta$. Differentiating this, we find:

$$\frac{1}{r} = \frac{d\theta}{dx} = \frac{d^2w}{dx^2} \qquad (= \kappa)$$

This term provides the curvature of the beam, labelled here κ. Inserting it into Eq. A.2, we find:

$$\sigma(x,z) = -Ec(z)\kappa = -\frac{Ec(z)}{r(x)} \tag{A.3}$$

The value of $c(z)$, the distance from the neutral surface, indicates how the maximum value of stress will be experienced at the distance $c(z) = |0.5t_c|$. $(-t_c, t_c)$ is the range of the wafer thickness, with zero stress at the neutral surface halfway between them. The magnitude of the stress experienced compressively and tensionally on opposing sides of the wafer will be equal, though signed opposite.

In addition to finding flexural stress [270] in terms of force per unit area from Eq. A.3, κ and the distance from the neutral surface/axis $c(z)$ give the strain present in the beam, i.e., $\varepsilon = c(z)\kappa = \frac{c(z)}{r(x)}$. Such a relationship can also be reached by the use of Young's Modulus as the ratio between stress and strain, i.e., σ=Eε.

Using modelling software, the symmetric Euler-Bernoulli beam equation (Eq. A.3, also labelled in text as Eq. 5.1) calculations of the compressive and tensile stresses present in equal and opposing amounts in mechanically stressed silicon wafers can be represented graphically.

Figure A.2 shows a simulation of an ULTRATHIN® Si wafer being bent into a parabola. The parabolic shape of the distorted wafer was selected as per the fitting performed by Rudawski *et al.* [268] of similarly stressed silicon wafers. The radius of curvature was determined from the function fit to the curve $y(x)$ with a Python script, using the function:

$$r_c = \frac{\left(1 + \left(\frac{dy}{dx}\right)^2\right)^{\frac{3}{2}}}{|\frac{d^2y}{dx^2}|} \tag{A.4}$$

Using the function fit to the wafer's curvature as its neutral axis or surface, the radius

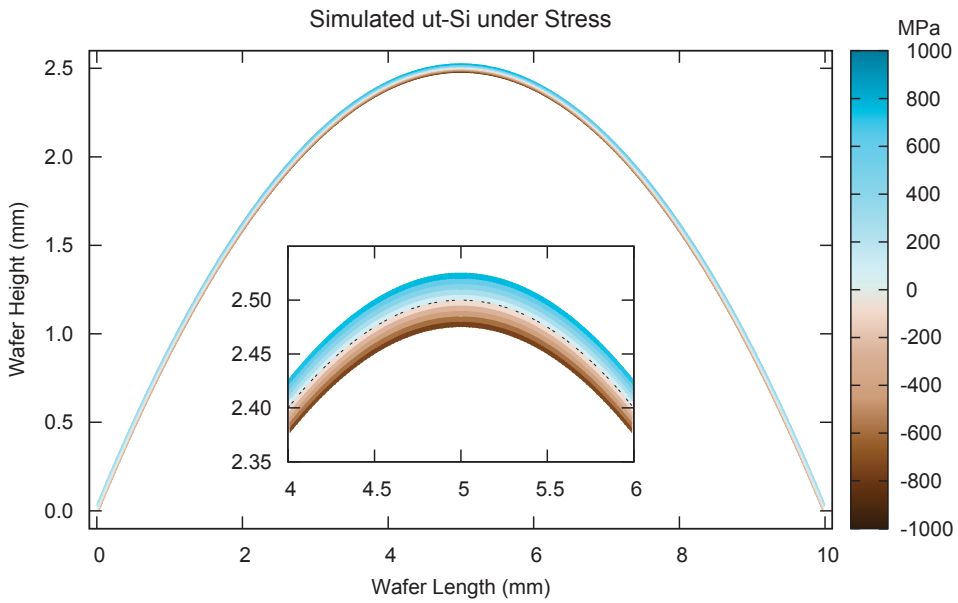

Figure A.2: Colour map of flexural stress within an ULTRATHIN® 50μm Si(100) wafer, modelled with Euler-Bernoulli beam equation (Eq. A.3). Colour represents magnitude of stress, where increasing blue indicates higher tensile stress, and increasing brown indicates higher compressive stress. Neutral surface shown on the inset graphic with a dashed black line.

of curvature for each point around the function can be used to determine the stress at each distance relative to the neutral axis. This method could be applied to either an artificially generated curve representing a bent Si wafer, such as in Fig. A.2, or to fitting functions determined from real samples undergoing stress. This latter application was the method used in this project to determine the stress/strain present in deformed 50 μm-thick Si wafers, discussed in Section 5.4.

In the simulation shown in Fig. A.2, the wafer's parameters were chosen to match the specifications of the ULTRATHIN® Si(100) wafers used in this project, i.e., E=170 GPa [264] and $c(t_c)$=25 μm, while the size was based upon similar wafer bending by Rudawski *et al.* [268,273]. Inset on the figure is a magnification of the region implanted with hydrogen in this study, i.e., a 2–4 mm width across the apogee of the wafer's curvature. The inset allows the gradient of the stress at its highest values to be clearly seen, varying from the dark blue of maximum tensile stress through to the dark brown of the maximum compressive stress. The cross-section of the wafer in the figure shows the neutral surface as an off-white tone, with a dashed black line indicating its location in the smaller inset graphic. The decreasing stress present at the extremes of the wafer (i.e., x = 0 and 10 mm) are shown by softer colours.

From this simulation, we can observe that we ought to achieve stresses on the order of a gigapascal in the vicinity of the hydrogen implantations in this study. However, elastic behaviour, and stresses below the plastic limit, are required for the classical bar bending equation defined by Euler, Bernoulli and (later expanded upon by) Timoshenko [272], to accurately describe the system. The elastic or yield limit of c-Si is given in the literature as 4-9 GPa [371, 379], although some variation is expected with thermal environment, per the work of Zener and Hollomon [380]. Schröter *et al.* [381] report the elastic limit or yield point of silicon lowers at higher temperatures, down to 1 GPa by T=1200°C. Keating [369] shows that distortion is via phase transformations to some temperature, at which it transitions to movement of dislocations, forming permanent distortions of the lattice. Vandeperre *et al.* [370] suggest the hardness of silicon is thermally independent for sufficiently low temperatures, and the influence of temperature only becomes significant at T∼600°C. In the particular case of thin wafers, Cook [371] reports that carefully polished wafers are capable of withstanding higher stresses prior to failure or permanent distortion.

From the magnitude of the stresses experienced in these simulations, it is expected that only elastic behaviour will occur in the bowed silicon wafers. As such, upon release from the stress-inducing apparatus, the wafers are expected to return to their initial curvature. The additional thermal energy via annealing may have a small effect on the structure of the wafers such that upon release from applied stress, the samples do not return to the exact conditions prior to such application and annealing. However, this is not a significant effect at the temperature regime (e.g. T=400°C) applied in our study, and does not invalidate the use of the Euler-Bernoulli formula.

In practicality, the E=40 keV hydrogen implantation in the samples of our study was not at the surface, but buried approximately 450 nm deep. Offset from the surface, the hydrogen profile will not strictly experience the total magnitude of the applied stress calculated above. However, as a total fraction of the distance from the centre of the wafer, the hydrogen profiles lies less than 2% from the surface (and hence maximum stress value). As such, while quantifiable, both the variation over the implantation range and its difference from the maximum calculated value is negligible for our comparative uses.

A.2 Simulations of hydrogen diffusion

If there is an understanding that the distribution with time of hydrogen can be approximated by an error function, the concentration distribution of hydrogen $C_H^{[I]}(x)$ as ion implanted into silicon over depths x can be described by the following equation:

$$C_H^{[I]}(x) = \frac{\Phi_\mathrm{I}}{\sqrt{2\pi}\Delta R_\mathrm{p}} \exp\left(\frac{-(x-R_\mathrm{p})^2}{2(\Delta R_\mathrm{p})^2}\right) \tag{A.5}$$

The resultant distribution described by this equation is a density function with respect to depth x, with units of cm^{-3}, where Φ_I is the implanted fluence in $\mathrm{ions.cm}^{-2}$, R_p is the projected ion range, and ΔR_p is the range straggle, both of the latter in centimetres. The values for R_p and ΔR_p are taken from values determined from experiment by ERD, but could just as well be taken from simulations by program SRIM [251].

Evolution of the distribution in c-Si with time was calculated using [382]:

$$C_H^{[I]}(x) = \frac{\Phi_{\mathrm{I}}}{\sqrt{\pi}(2\Delta R_{\mathrm{p}}^2 + 4\mathscr{D}t)^{1/2}} \left[\exp\left(\frac{-(x+R_{\mathrm{p}})^2}{2(\Delta R_{\mathrm{p}})^2 + 4\mathscr{D}t} \right) + \exp\left(\frac{-(x-R_{\mathrm{p}})^2}{2(\Delta R_{\mathrm{p}})^2 + 4\mathscr{D}t} \right) \right] \tag{A.6}$$

where the density function now includes a time dependence for the implant distribution as well as describing the location with depth x. Also present is the diffusion co-efficient, $\mathscr{D}$, describing the temperature dependence of the hydrogen diffusivity. The form of this equation follows an exponential function:

$$\mathscr{D} = \mathrm{D}_0 \exp\left(\frac{E_a}{k_B T} \right) \tag{A.7}$$

Where T is the temperature in kelvin and $\mathrm{k_B}$ is Boltzmann's constant, E_a is the activation energy of the hydrogen diffusion within crystalline silicon and D_0 is a pre-exponential factor scaling the diffusion by such factors as the entropy of diffusion, and $\mathscr{D}$ has units of $\mathrm{cm}^2.\mathrm{sec}^{-1}$.

The values for D_0 and E_a were first clearly defined by Van Wieringen and Warmholtz (VWW) in 1956 [185], who found D_0=9.4×10^{-3} $\mathrm{cm}^2\mathrm{s}^{-1}$ and E_a=0.48 eV. That particular work was examining the diffusion rates at relatively high thermal anneals (T<1050°C). Numerous investigations subsequently have attempted to confirm the range over which this applies, such as Chang *et al.* [383] examining "moderate temperatures" and Hara [384] at "intermediate" temperatures. While most values are within the same order of magnitude, there still exist significant differences. Hara determines a value for the activation energy close to the VWW original, E_a=0.58 eV, but shows a diffusivity approximately a third smaller, D_0=2.8×10^{-3} $\mathrm{cm}^2\mathrm{s}^{-1}$. Gusakov [385] concurs with Hara's value of diffusivity (D_0=2.6±1.5 × 10^{-3} $\mathrm{cm}^2\mathrm{s}^{-1}$) but shifts the activation energy higher, E_a=0.78±0.05 eV. Other reported values by Chang [383] and Beddard [386] agree in activation energy and diffusivity with one of [185] and/or [385]. In fact, Beddard also determined the value for D_0 and E_a purely as fitting parameters to the host of data from previous research, arriving at D_0=8.9×10^{-3} $\mathrm{cm}^2\mathrm{s}^{-1}$ and E_a=0.58 eV. However, when studying diffusion of hydrogen introduced by plasma and contrasting to data from most other sources, Huang *et al.* [387] arrives at an activation energy E_a=1.27 eV and a diffusivity of D_0=24.85×10^{-3} $\mathrm{cm}^2\mathrm{s}^{-1}$. The overall influence of these values upon the initial conditions of Equation A.6 is zero, as

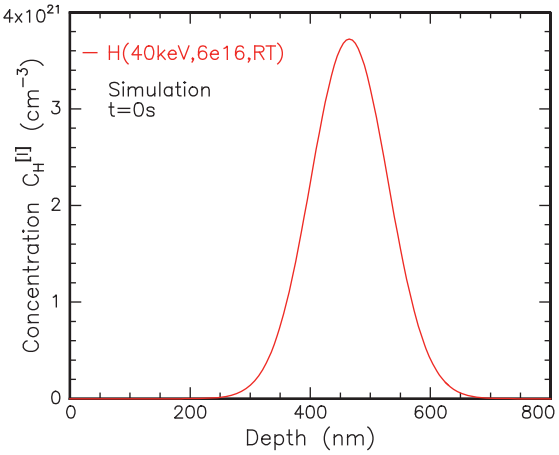

Figure A.3: Simulation using Eq. A.6 of H(40keV,6×10^{16}cm^{-2},RT) implantation into Si(100) at t=0 seconds.

all terms relating to diffusion are multiplied by the time. However, even in the evolving simulation, there is little difference in behaviour seen if *any* of these values are substituted into Eq. A.7.

As described by Mathiot [183], the experimentally observed values of diffusion introduced from plasma hydrogenization show values an order of magnitude lower than that shown in the VWW data. Mathiot instead proposes a different model for lower temperature diffusion processes, relying more on the electronic structure of the silicon, though only for in-diffusion of hydrogen via a plasma source. An excellent broad review and demonstration of these models used to fit H in-diffusion is shown in Pearton [180].

Work by Neustroev *et al.* [65] on the production of donor centres within hydrogen-implanted silicon also explored the diffusion of hydrogen profiles via SIMS. In order to account for the rate of change in hydrogen concentration they measured, Neustroev uses a two-tiered diffusion mechanism. The two components of this model describe the diffusion of vacancies and defects produced by the implantation ($0.5 - 2 \times 10^{-7}$cm^{2}s^{-1}) and the hydrogen diffusion as enhanced by thermal donor production (5×10^{-9}cm^{2}s^{-1}) (apparently sourced from [388]) for anneals at T=450°C. These values are ultimately in agreement with the diffusivity coefficients and activation energies given above.

Figure A.3 shows the simulation produced by Eq. A.6 at t=0 seconds. As all the values defining its depth, peak concentration and FWHM were entered by the operator, unsurprisingly this simulation is in good agreement with the data. The peak and spread in

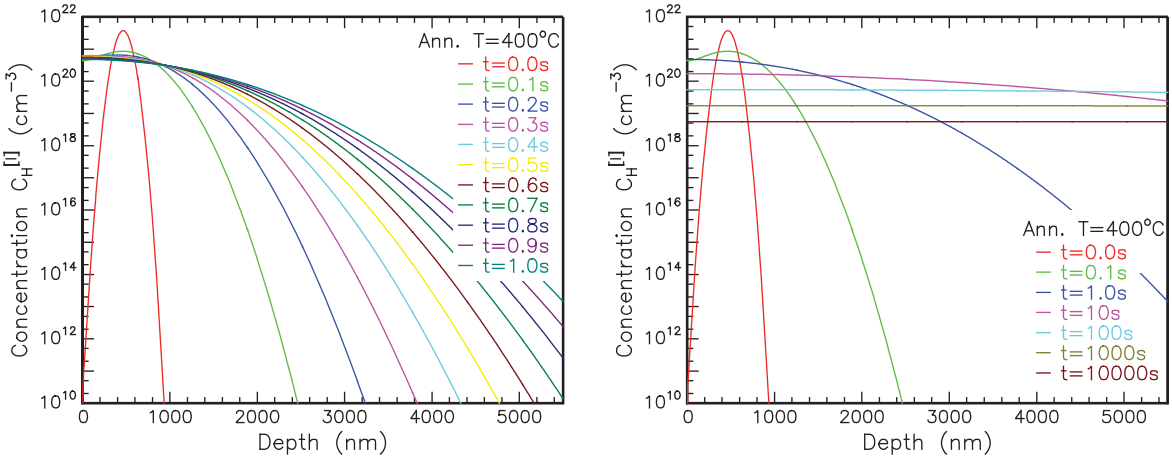

Figure A.4: Simulation using Equation A.6 of H(40keV,6×10^{16}cm^{-2},RT) implantation into Si(100), over the time intervals of (a) t=0 to t=1 seconds, and (b) t=0 to t=10000 seconds. E_a=0.78eV, D_0=2.6×10^{-3}cm^{2}s^{-1}.

the data are somewhat different from the experimental data, insomuch as it represents a pure Gaussian rather than the skewed Gaussian-like profile produced by ion implantation, but this is to be expected.

Figure A.4(a) presents the evolution of this profile over short term, for the time interval of 1 second in 100 millisecond steps. Equation A.6 gives the expected H distribution as a function of time in an infinitely thick c-Si layer distant from any boundaries. Any additional barriers such as surface energy constraints are not considered. Over time, the buried hydrogen profile shows a rapid broadening of the hydrogen available in the silicon, and significant loss from the surface, assumed to be instantaneous upon reaching a depth x=0. This transformation from a Gaussian profile to a constant concentration diffused through the material is seen clearer in Fig. A.4(b). The time interval is presented logarithmically from t=0.1 s to t=10000 s, with the as-implanted (t=0) case for comparison. Again, as with Fig. A.4(a), there is no consideration for trapping at the surface, or preventing loss of hydrogen at that barrier (the equation simply assumes there is a "negative" depth region through which it continues to spread the hydrogen). While in an enclosed system, the total concentration will not change from the implanted hydrogen, this loss relative to the actual sample range produces an increasingly decreasing function, until all the hydrogen has diffused "out" of the silicon.

Experimentally determined data showed very different behaviour, with samples an-

nealed at the same temperature, T=400°C, showing very minor diffusion over a time interval four orders of magnitude greater than these simulations. There are two particular conclusions that can be reached from this inconsistency. Firstly, perhaps the physical situation is sufficiently different that the model's basic assumptions are incorrect. Secondly, if the current model was accepted as correct, that the values of the constants used would be incorrect.

A model better able to recreate and represent our physical model would thus either require construction from the ground up or merely from modifying the values such as E_a and D_0. If the former, the differences in this model and the actual physical system would have to be accounted for. If the later, this would not necessarily rule out that significantly different physics was taking place in the H:Si system.

As the basic theory of the above model assumes an already trap-saturated silicon material with no addition defect sites to capture the diffusing hydrogen [143, 180, 182, 384, 387], this is quite unlikely to represent the reality of the situation. Rather, with the damage from the ion implantation alone, there would be significant defective regions with possibly excess interstitials and vacancy sites modifying the hydrogen's diffusive behaviour. Pearton *et al.* [192] warns against ignoring trapping at defects within the crystal, and the potential for different, slower diffusion behaviour of larger hydrogen molecules which may form. Sopori *et al.* [389] state that the value of hydrogen diffusivity is heavily reliant upon the electronic state of the material, such the location of the Fermi levels, and as such is readily mutable via dopants and structural changes. Johnson *et al.* [143] also report that the different charge states and isotopes of the hydrogen behave differently under the same environmental conditions. This as a whole presents a fraction of the difficulties in modelling the observed behaviour in trap limited diffusion, so while Eq. A.6 and A.7 are useful in ideal crystal models or post trap saturation, they are inadequate for the task required in our work.

While most of the research on the value of the diffusivity present linear fits to cover the entirety of the D versus temperature T relationship, Stavola [184] mentions that Langpape *et al.* [390] showed significantly different values via non-linear fitting. The major value of Langpape's work is that it measured diffusion from an ion-implanted H profile, and is thus more likely to represent the situation in this research project's experiments. Using the

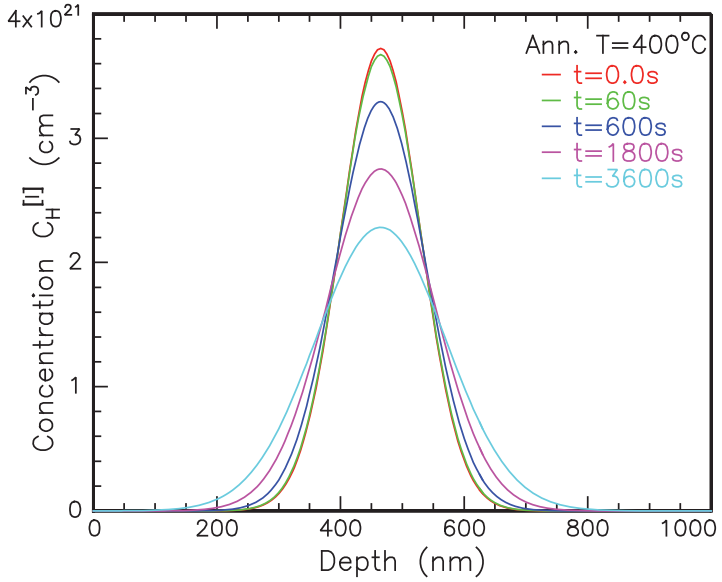

Figure A.5: Simulation using Equation A.6 of H(40keV,6×10^{16}cm^{-2},RT) implantation into Si(100), over the time interval of t=0 to t=3600 seconds. E_a=0.043 eV, D_0=2±1 $\times$ 10^{-14} cm^{2}s^{-1}.

values determined by Langpape *et al.* [390], E_a=0.0043 eV and D_0=2±1 $\times$ 10^{-14}cm^{2}s^{-1}, a remarkable slow down in the diffusion (relative to the VWW values) is predicted, with significant times intervals required to notice any change in the hydrogen profile. Unfortunately there is no clear physically determined basis for the values in [390] (unlike those from the VWW model [185]), rather only that they fit the prescribed data in the paper.

It is possible that the values determined by Langpape [390] represent the behaviour of hydrogen diffusing in a damaged crystal with non-zero/non-saturated trapping sites. While the model itself does not fully accurately represent such a system, the values of the applicable constants may scale the model's output to appropriately match the experimental conditions. Figure A.5 shows the evolution of the hydrogen implantation over a hour as it is annealed at T=400°C with diffusivity defined according to Langpape. Compared to the earlier Fig. A.4(b), the diffusion is significantly lower over similar intervals. The diffusivity equation prefactor, defined here as D_0=2±1 $\times$ 10^{-14} cm^{2}s^{-1}, is the major contributing factor to this difference, as the changing of the activation energy within the exponential by a single order of magnitude fails to change the behaviour significantly. The degree to which this model using Langpape's values fits the data is explored in Section A.2.1.

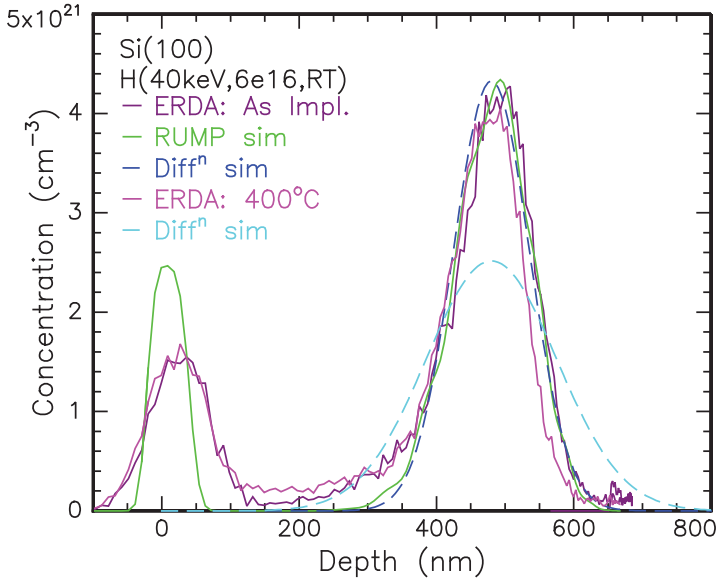

Figure A.6: 3 MeV $^4He^+$ ERD measurement of H(40keV,6×10^{16}cm^{-2},RT)-implanted ULTRATHIN® Si(100), comparing hydrogen distribution as-implanted and following T=400°C/30min annealing under stress-free conditions with simulations performed by RUMP and hydrogen diffusion profiles calculated by Eq. A.6, as labelled. Detector and scattering angles ϕ=25°, sample tilted θ=80° to incident beam. Diffusion simulation values: R_p= 475 nm, ΔR_p= 55.6 nm, diffusivity and activation energy as per Langpape *et al.* [390]. First diffusion simulation t=0 sec, second simulation t=1800 sec, T=0°C.

A.2.1 Contrasting experimental results with diffusion models

To establish the difference between expected and measured influence of annealing on the hydrogen profiles distributions, IBA measurements were contrasted with predictions by the diffusion simulations in Section A.2. Samples both as-implanted and annealed at T=400°C/0.5h from the H(40keV,6×10^{16}cm^{-2},RT) implanted ULTRATHIN® Si were profiled by ERD, and the depths of the hydrogen profiles determined by RUMP simulations. The values of R_p and ΔR_p ($\approx \sigma \sim 0.42466\times$FWHM) determined by RUMP were then entered into Eq. A.6, and the hydrogen distributions determined for t= 0 and 1800 seconds. Figure A.6 shows the comparison of the ERD data and simulation with the distribution calculated by Eq. A.6.

The values of the hydrogen profile depth as determined by the RUMP simulation are in good agreement with concomitant findings in our research project. Yet the hydrogen profile depth and peak concentration value are curiously inconsistent with SRIM simulations, which predicts a R_p= 399 nm for a E=40 keV implantation, and a peak concentration of $C_H = 4.59\times10^{21}$cm^{-3}. In contrast, the IBA and XTEM techniques employed in this

project measure (R_{p}, C_H)=(475±10nm,$4.19 \pm 0.06 \times 10^{21}\mathrm{cm}^{-3}$), and Eq. A.6 predicts a similar peak concentration.

The Gaussian fits produced by the equation do not account for the depth skew in the ion implanted profiles, but never-the-less show a good agreement between the diffusion simulation and the as-implanted ERD data. However it is clear from the figure that while capable of simulating the as-implanted hydrogen profile, Eq. A.6 does not adequately predict the hydrogen distribution at $t > t_i = 0$. Very little change in the hydrogen profile's peak value is observed in the ERD data from the T=400°C/0.5h annealed sample, but a significant decrease and broadening is seen in the accompanying Gaussian simulated profile. In fact, the second simulation presented in Fig. A.6 (in cyan) is not even for an anneal of T=400°C, but rather of T=0°C (=273K). As such, even using the atypical values of diffusivity and activation energies as reported by Langpape *et al.* [390], the function cannot adequately reproduce the distribution of hydrogen with respect to annealing duration. The traps and defect sites which produce the actual diffusion conditions are largely due to the damage caused by the ion implantation [179], and these defects further evolve with thermal annealing.

Appendix B

Experimental method: Additional information

COMPLIMENTING the information provided in Chapter 3, this appendix contains additional background upon the techniques described in the main text. Ion beam techniques such as RBS and ERD are given some historical background, and more details of the operation and sample preparation of XTEM is provided. Calibration data for the annealing stage used in blister video recordings is also shown, in addition to examples of previous stress apparatus constructed by preceding researchers.

B.1 Ion beam techniques

Rutherford Backscattering Spectrometry (RBS)

Rutherford backscattering spectrometry, or RBS, is a non-destructive characterisation technique that allows determination of material composition, impurity concentrations and crystalline structure [275]. Utilising the Coulomb repulsion between a positively charged particle (here, an α) and the atomic nucleus, this technique was largely developed with the advent of high energy particle accelerators in the 1950s and 1960s [391,392]. Excellent comprehensive references on the underlying theory and analysis of this method are Chu, Mayer and Nicolet [276] and Feldman, Mayer and Picraux [277].

Over the course of this project, RBS involved $^4He^+$ ions being scattered off crystalline material at a range of random crystallographically aligned angles. Solid state Ge detectors collected the elastically scattering alpha particles, where their residual energy and yield

was coupled with their angular change to establish the surface and subsurface structure of the material. Essentially, the returning ion's energy is related to the depth of material undergoing irradiation via the measured areal density of atoms per square area. It is important to note that the use of the term "depth" is deceptive, as the measured value is actually the energy loss experienced by the ion as they traverse the solid. Eisen [393] attempted to establish the stopping cross section required to determine energy loss (and hence depth) with an equation of the form:

$$\frac{dE}{dx} = -kE \approx \frac{\Delta E}{\Delta x} = \frac{E_2 - E_1}{\Delta x} \tag{B.1}$$

Equation B.1 is a good approximation if and only if the resultant energy as a composite of the incident and exit beam energies follows $E \geqslant \frac{E_1+E_2}{2}$. This was expanded on by Bøttiger in 1973 [394], who determined the equations at the base of most RBS calculations today, shown in Eq. B.2. Here the stopping energy ε_0 is related to the incident angle θ_1, exit angle θ_2 and the incident and exit stopping powers of the material (where the second or exit term must take into account additional kinetic factors, k).

$$\varepsilon_0 = \frac{k}{cos\theta_1}\left[\varepsilon(E_0)\right] + \frac{1}{cos\theta_2}\left[\varepsilon(kE_0)\right] \tag{B.2}$$

The total change in energy of the yield as measured by RBS can then be related via the stopping energy given in Eq. B.2 and material density N to determine the linear depth x, as shown in Eq. B.3.

$$\Delta E = \varepsilon_0 N x \tag{B.3}$$

Stopping powers have been determined by an array of means from the original irradiation of activated materials (effectively turned into detectors), to passage of the ion beams through thin films composed of the element of interest [395] through to work using multilayer systems for greater accuracy [396]. The stopping powers were further refined by Ziegler *et al.* [251] and later Konac *et al.* [397] in the late 1990s (often referred to as KKK), to more accurately allow simulation of experimental spectra, becoming established as the current standard. The stopping power in Si(100) of He ion measurements as used in RBS in our work, and most other work, was revised by Lennard *et al.* [398] in 2004. In testing the standards used in the original stopping power investigations listed [280, 393, 394], reasonable consistency was maintained for ionic species, but molecular targets showed some variation.

Elastic Recoil Detection (ERD)

ERD is a modification of the RBS principle of ion beam scattering, developed coincidentally with other light ion techniques such as Nuclear Resonant Analysis (NRA) [399–405] and proton-proton scattering [406]. Rather than backscattering or passing a beam completely through the material, ERD relies upon the forward scattering of low mass elements in the near surface region [407–411].

Early development of ERD was hampered by the need for higher energy α particles than were readily available from nuclear decays or could easily be produced by accelerators of the time [314]. As elastic recoil relies on the beam's ion atomic mass to profile lower mass elements within a material, the key subject of this project – hydrogen – requires only a helium beam. This significantly lowers the energy costs associated with operation when attempting to measure high Z elements, and allows retrofitting of existing He beam RBS systems for ERD applications. As mentioned in Section 3.2.1, the influence of geometric factors on resultant ion beam energies in the ERD system need to be carefully accounted for [298]. Szilagyi and Wielunski [308] give the theoretical underpinning for this work.

Verda *et al.* [412] demonstrated that small changes in positioning of the sample on the goniometer or angles of the detectors can have large propagating effects within ERD spectra. As such, analysis of ERD data is often a comparison among non-unique solutions. This difficulty in not just calibration but comparison across multiple accelerators has led to "Round Robin" tests of the same material as a standard at a number of institutions [314,413]. To account for possible inaccuracy, Verda suggested use of a pre-fabricated standard, a hydrogen-rich metal layer buried within a silicon or similar substrate, to accommodate the greater accuracy of backscattering measurements of RBS concomitant to ERD measurement [414, 415]. Reinholz *et al.* [416] similarly lament a standard, and use chemical vapour deposition (CVD) to construct a precision H content α-Si-H:Si calibration sample. Our initial plans to construct standards akin to those of Verda or Reinholz were limited by the accuracy of the fabrication possible within the RSPE, specifically in the concentration of deposited H. An alternative sample production by inducing hydrogen-related cavities within a silicon sample, then decorating them with metals via plasma exposure or ion implantation and drive-in diffusion, allowing identification of the depth in XTEM to be correlated with an RBS measurement, was also proposed but not affected.

ERD Geometric Calibration

As detailed in Section 3.2.2, simulation software suite WDepth [300] was used to determine the optimum parameters for ERD measurement of 400–800 nm deep implanted hydrogen profiles. The exploration of potential incident angles and scattering angles attempted to establish the best possible conditions for a germanium or silicon hydrogen implanted substrate. The final conditions, as described in Section 3.2.2, were derived from the data presented in Fig. B.1 and B.2.

Figures B.1(a-e) show the variation occurring in depth resolution, within the same H-implanted Si simulation, at fixed incident angles α while scattering angle θ is varied. From these figures, there is a clear benefit in maintaining a lower α value, in that each increase of 5° shows the resolution width increase by approximately 20 nm. However, the smallest differences between incident and scattering angle (producing resultant exit angles of only 5°) show a rapid degradation in resolution upon reaching depths between 400–600 nm. This trend is either much smaller or non-existent at α:θ=1:2 (producing a resultant exit angle = α) and higher angle ratios simulated. The geometric contribution confirms this, as the optimal depth range probed becomes foreshortened at very low angles, due to greater path length through the silicon, while higher α and higher θ push this optimal probe depth further and further into the silicon, at the cost of more significant geometric influence in the near-surface region. At much greater incident and exit angles, the maximum magnitude of the geometric influence is quite low, but has much greater variability over the range of interest.

From these simulations, and within the constraints provided by our system, the ideal configuration for measuring H within Si over the depth range of interest would use values of (α, θ) = (10°, 20-30°), or potentially (15°, 25-30°).

Using these values as a guide in narrowing the range of potential values, Fig. B.2 shows the comparison in depth resolution and geometric component to the energy resolution for Ge(100) implanted with the same H(40keV,6×10^{16}cm^{-2},RT) ions. The higher stopping power of Ge leads to shallower limits to the ion beam's probing than in Si. For the beam energies available to our RBS system, these simulations can only use $\theta \leqslant 35°$ before no significant H yield is returned. Over the range of interest, these simulations suggest either using (α, θ) = (10°, 20-30°), provided no measurement at depths x >500 nm was required.

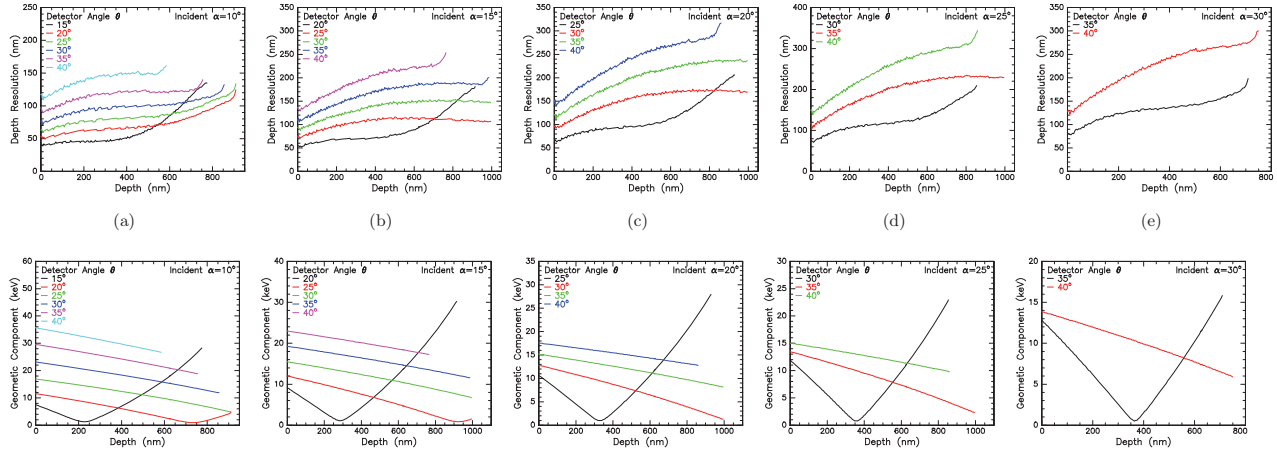

Figure B.1: WDepth [300] predicted resolution at particular geometries for E=3 MeV He ERD measurements of H(40keV,6×10^{16}cm^{-2},RT)-Si(100), for fixed values of incident angle α and variations of scattering angle θ. Subfigures (a)-(e) show depth resolution, (f)-(j) show geometric contributions to energy resolution. Parameters of simulation as follows: Mylar foil 12.6 μm thick, detector FWHM 15 keV, detector aperture 1.5mm × 12 mm, beam aperture 2.5 × 2.5 mm, sample-to-detector distance 145 mm.

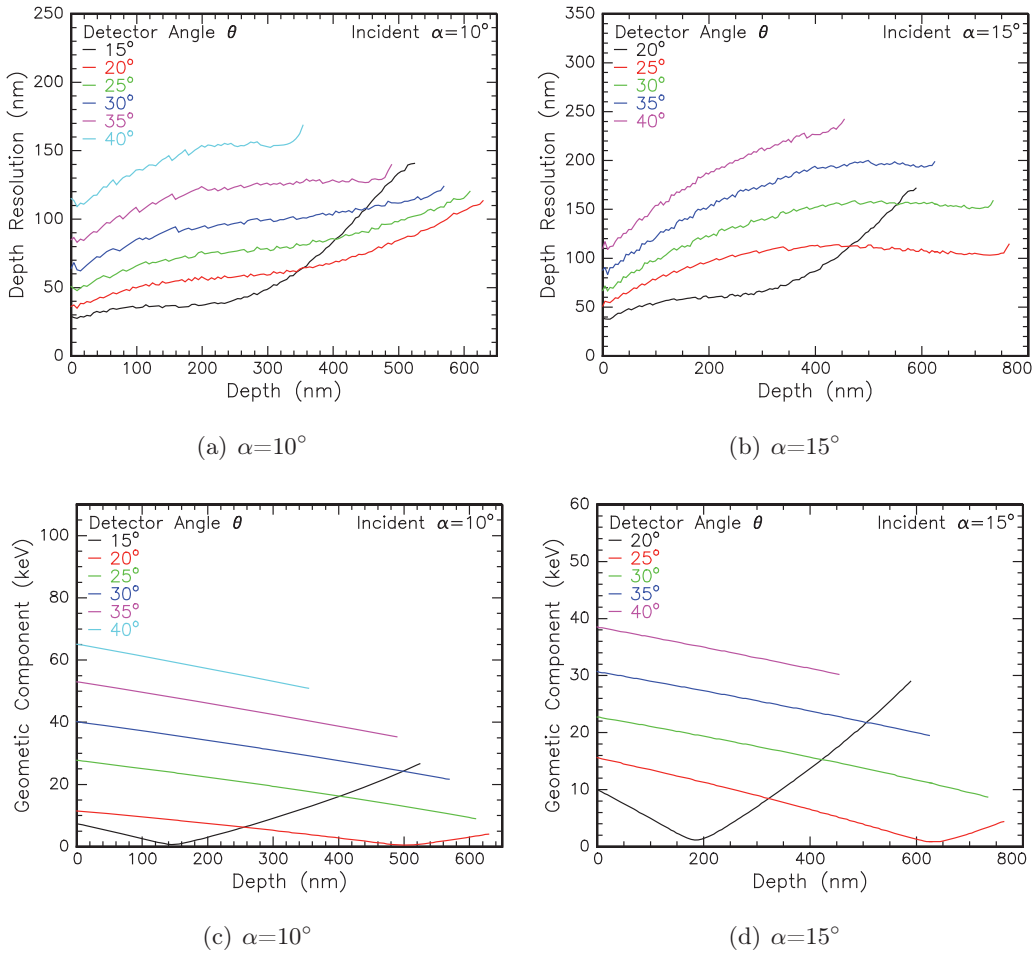

(a) α=10° (b) α=15°

(c) α=10° (d) α=15°

Figure B.2: WDepth [300] predicted resolution at particular geometries for E=3 MeV He ERD measurements of H(40keV,6×10^{16}cm^{-2},RT)-Ge(100), for incident angle α at (a) 10° and (b) 15°, and variations of scattering angle θ, as labelled in graphs. Subfigures (a)-(b) show depth resolution, (c)-(d) show geometric contributions to energy resolution. Parameters of simulation as follows: Mylar foil 12.6 μm thick, detector FWHM 15 keV, detector aperture 1.5 mm × 12 mm, beam aperture 2.5 × 2.5 mm, sample-to-detector distance 145 mm.

More adaptably, (α, θ) = (15°, 25-30°) accommodates measurement of H signal to depths $x \leqslant$750 nm.

In combination, these two simulation sets suggest that the practical positioning of the forward scattering detector should be a compromise, at a scattering angle of θ=25°. This would allow sufficient depth penetration for the Ge system, at reasonable resolutions, when tilting the sample to α=15°, as well as providing acceptable resolution for Si systems when α=10°.

Geometric factors involved in the depth and energy resolutions for ERD are not limited

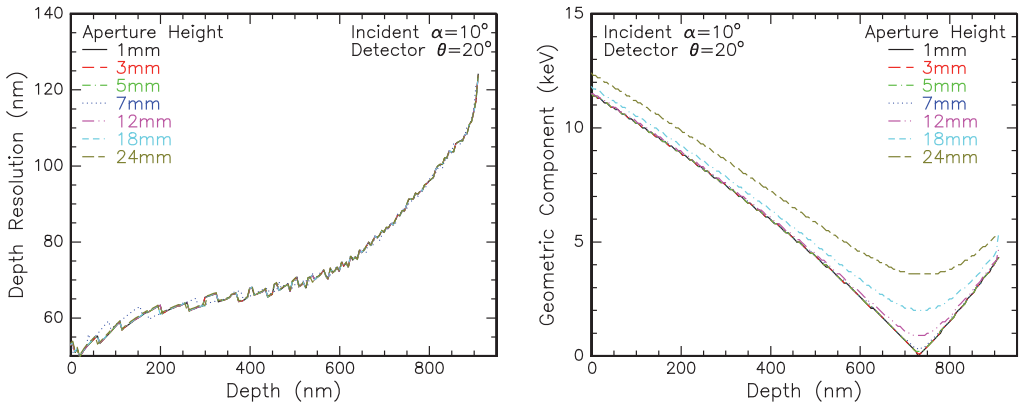

(a) Depth Resolution

(b) Geometric Component

Figure B.3: WDepth simulation predictions of the influence of detector aperture height upon (a) depth resolution and (b) geometric component to energy resolution, for 3 MeV He ERD measurement of H(40keV,6×10^{16}cm^{-2},RT)-implanted Si(100). Parameters of simulation as follows: α=10°, θ=20°. Mylar foil 12.6 μm thick, detector FWHM 15 keV, beam aperture 2.5 × 2.5 mm, sample-to-detector distance 14.5 mm, aperture width 1.5 mm.

to gross angular positions. They also accommodate the angular spread across the face of the detector. The control of this incoming signal is via an aperture formed by a slit incised into a plate, placed between the beam and the detector. WDepth simulations also allow for these values to be altered – in the above simulation sets, the aperture was fixed at a width (in the x plane) of 1.5 mm and a height of 12 mm. Assuming the Si optimised (α, θ) = (10°, 20°) for the same H(40keV,6×10^{16}cm^{-2},RT)-implanted Si(100) sample, WDepth was next used to model variations firstly in height, and then in width of the aperture.

Figure B.3 shows the variation in resolution when the aperture height is varied, from 1 mm to 24 mm. As is clear in predictions of either the depth resolution or the energy resolution's geometric component, there is little change for small aperture height increases. The changes in the energy resolution only appear after the slit reaches 12 mm in height, and only noticeably influence the optimal measurement depth resolution. Once the height reaches 18 mm or greater, the influence of the geometric component increases, though with little impact on the resolution.

In contrast, the influence of the width is much more significant, as can be seen in Fig. B.4. This is to be expected, as the spread of the beam scattered from the sample is in the x-plane which describes width. Even from the smallest changes in the width of the aperture (seen in Fig. B.4(b) from 1 mm to 1.5 mm), a ΔE=2.5 keV increase occurs. As such, the

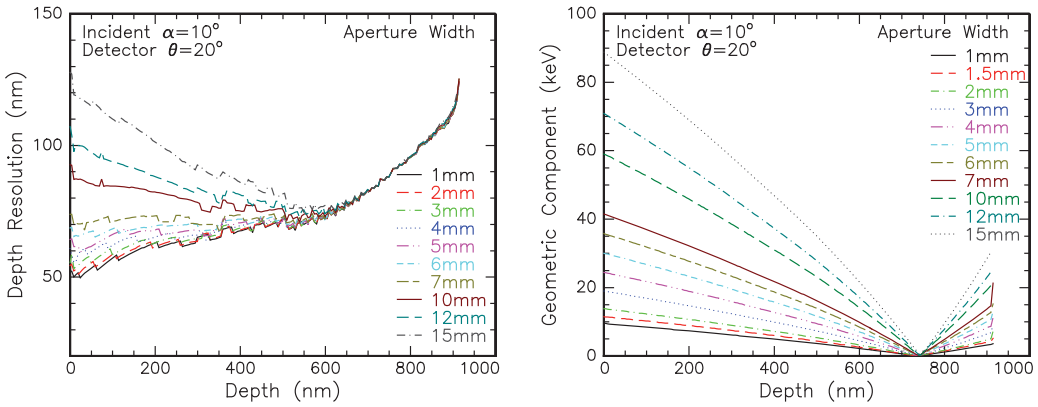

(a) Depth Resolution

(b) Geometric Component

Figure B.4: WDepth simulation predictions of the influence of detector aperture width upon (a) depth resolution and (b) geometric component to energy resolution, for 3 MeV He ERD measurement of H(40keV,6×10^{16}cm^{-2},RT)-implanted Si(100). Parameters of simulation as follows: α=10°, θ=20°, Mylar foil 12.6 μm thick, detector FWHM 15 keV, beam aperture 2.5 × 2.5 mm, sample-to-detector distance 14.5 mm, aperture height 5mm.

simulation predicts a relationship between the energy resolution geometric component and the aperture width of 5 keV.mm^{-1}. However, the depth at which geometric components are minimised does not change as the aperture widens, as this is determined by the ideal path length of the incident beam in the system's gross geometry. There is also little influence of the aperture width on the depth resolution for depths x >650 nm. For depths x <650 nm, the resolution changes at 5 mm per millimetre of width. Rapid influence of the aperture slit suggests trying to keep the physical value to an absolute minimum.

While the utter minimum of resolution degradation should be aimed for, the limits this may place upon signal yield need also be considered. In addition, physical difficulties in producing the aperture for mounting into the ERD goniometer's chamber must be accounted for if following suggestions of sub-millimetre sizes. For example, if the aperture is to be machined from sheet metal, the slit will also have a depth, which would further decrease the allowable beam angles. To that end, it would be the best compromise to select the size of aperture at which resolution degradation has yet to or only just begun to have noticeable effect. From the results of these aperture dimension simulations, the selected size for the physical slit was thus 2×12 mm.

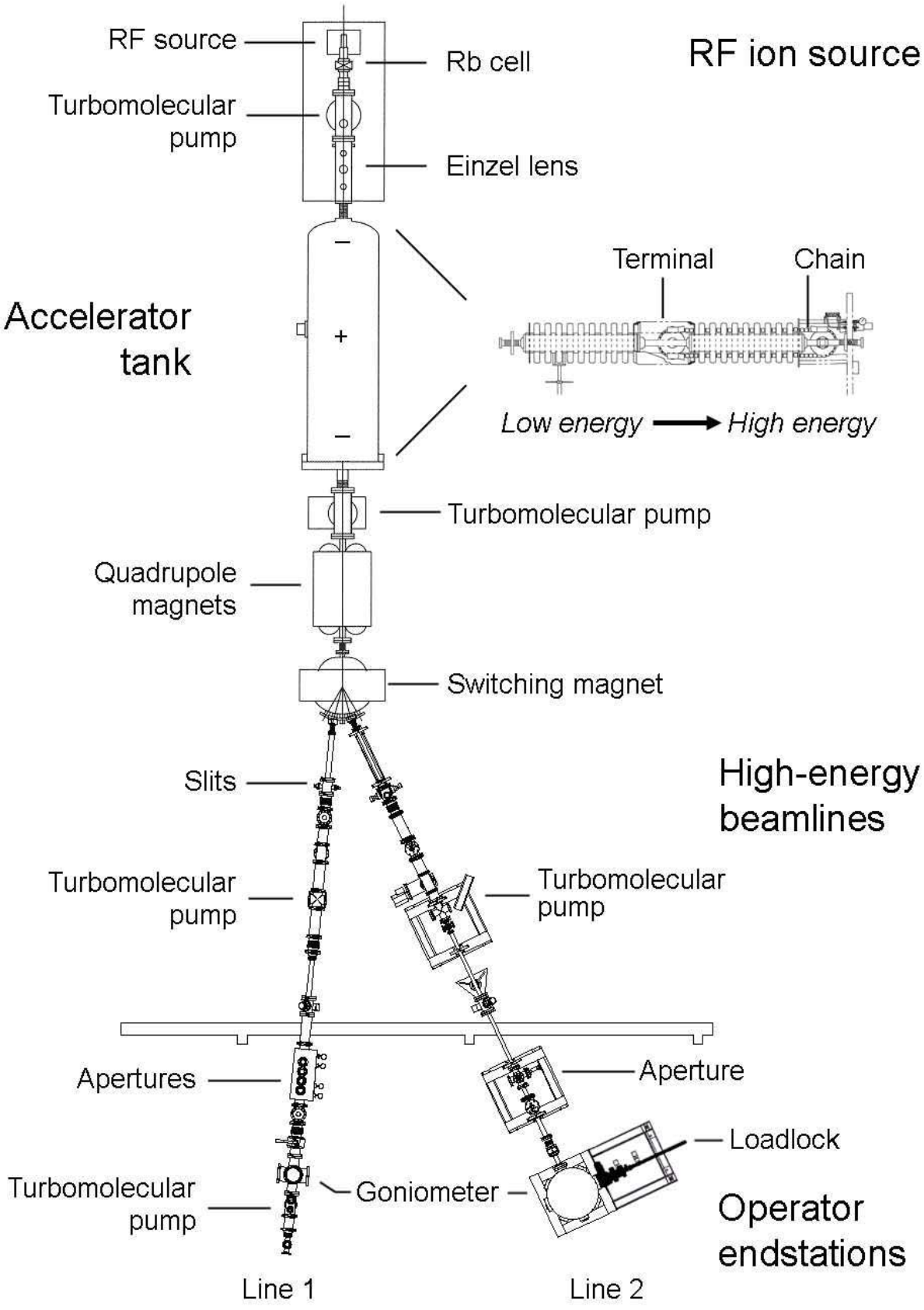

Figure B.5: Annotated schematic diagram of the NEC 5SDH tandem pelletron accelerator used for RBS and ERD, as discussed in Sections 3.2.1 and 3.2.2, derived & amended from [417].

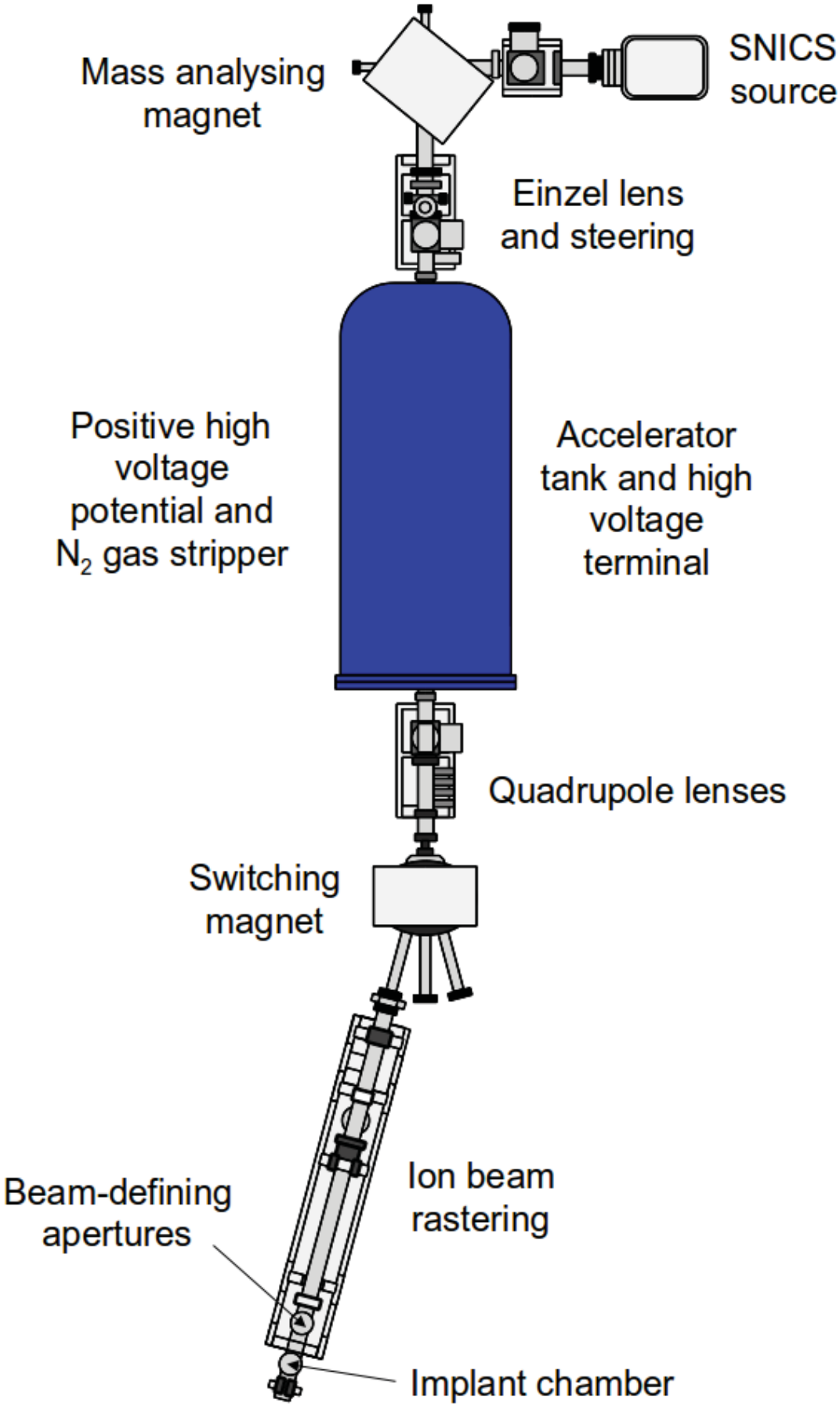

Figure B.6: Schematic diagram of the NEC 5SDH-4 high energy ion accelerator used for implantations at E⩾200 keV, derived and amended from [418].

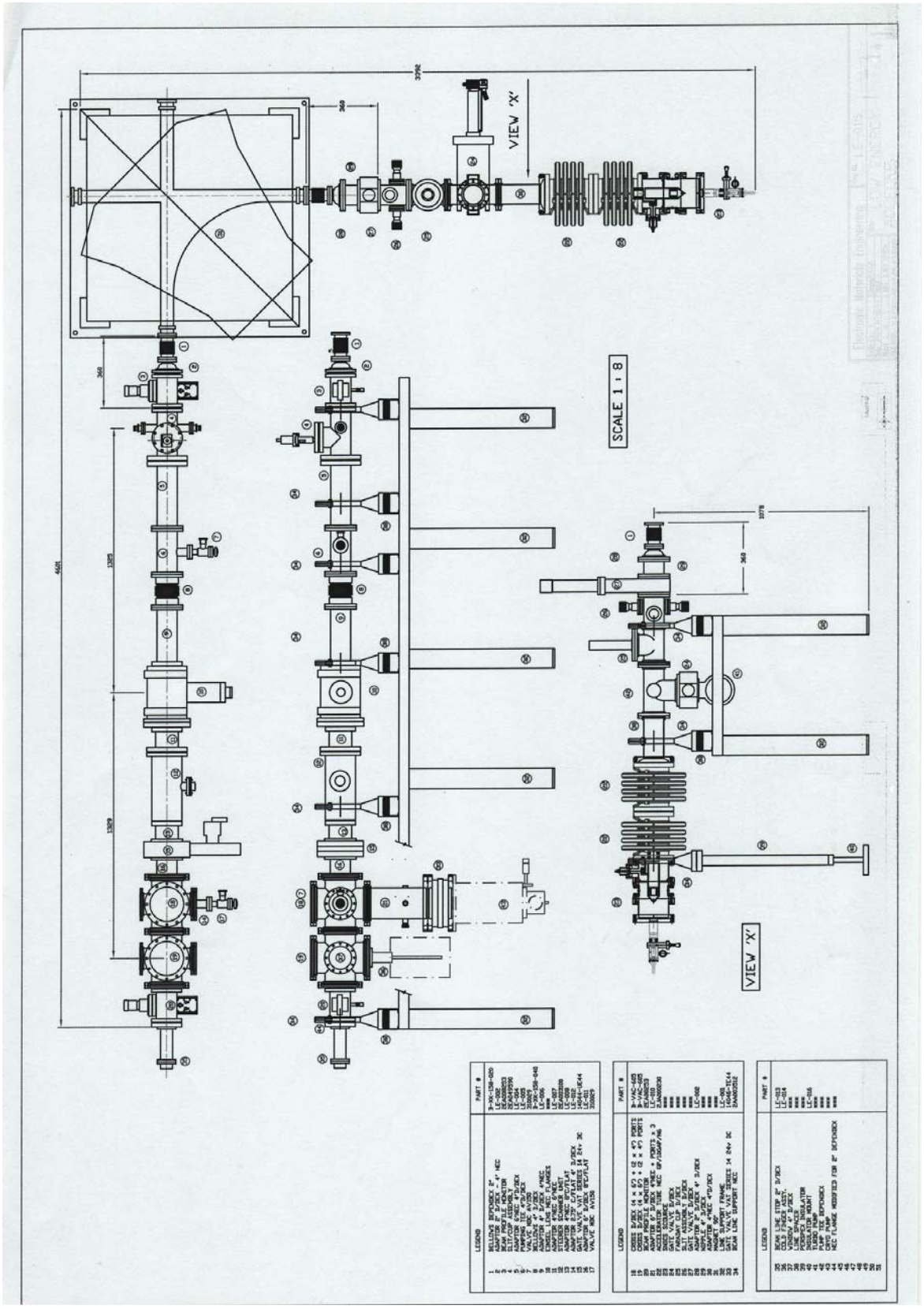

Figure B.7: Schematic diagram of the NEC low energy ion implanter/accelerator used for implantations at E$\leqslant$200 keV.

B.2 Cross-sectional Transmission Electron Microscopy

This appendix contains figures showing a number of features of the TEM sample preparation process, in addition to images of the equipment used to analyse the samples.

In the TEM used in this project, an electric potential source (the filament) produces free electrons by high thermal energies which are accelerated away down the microscope column by a series of anodes. Two magnetic fields are generated by the first and second condensers, focusing the beam. Any remaining highly divergent electrons are then eliminated by use of the condenser aperture, allowing the rest of the beam to fall on the sample area, mounted in the beam path. An objective lens – again formed by electromagnetic fields – forms an image from the transmitted beam, and the objective aperture selects out any highly scattered electrons, increasing the depth of field. The application of a selected area aperture allows the user to isolate particular diffraction patterns from the electron beam. Once selected, the beam passes through several additional lenses prior to being projected onto the phosphor screen. This screen can be lowered to allow the beam to be incident on a CCD array or the emulsion of a film negative. This basic process of obtaining an image from an electron stream is shown in Fig. B.8, contrasting the regions in a cross sectional TEM.

Following the photographs of the TEM in cross-section, Figures B.10 through B.13 show photographs of some of the steps and apparatus involved in producing suitable cross-sectional samples for this study.

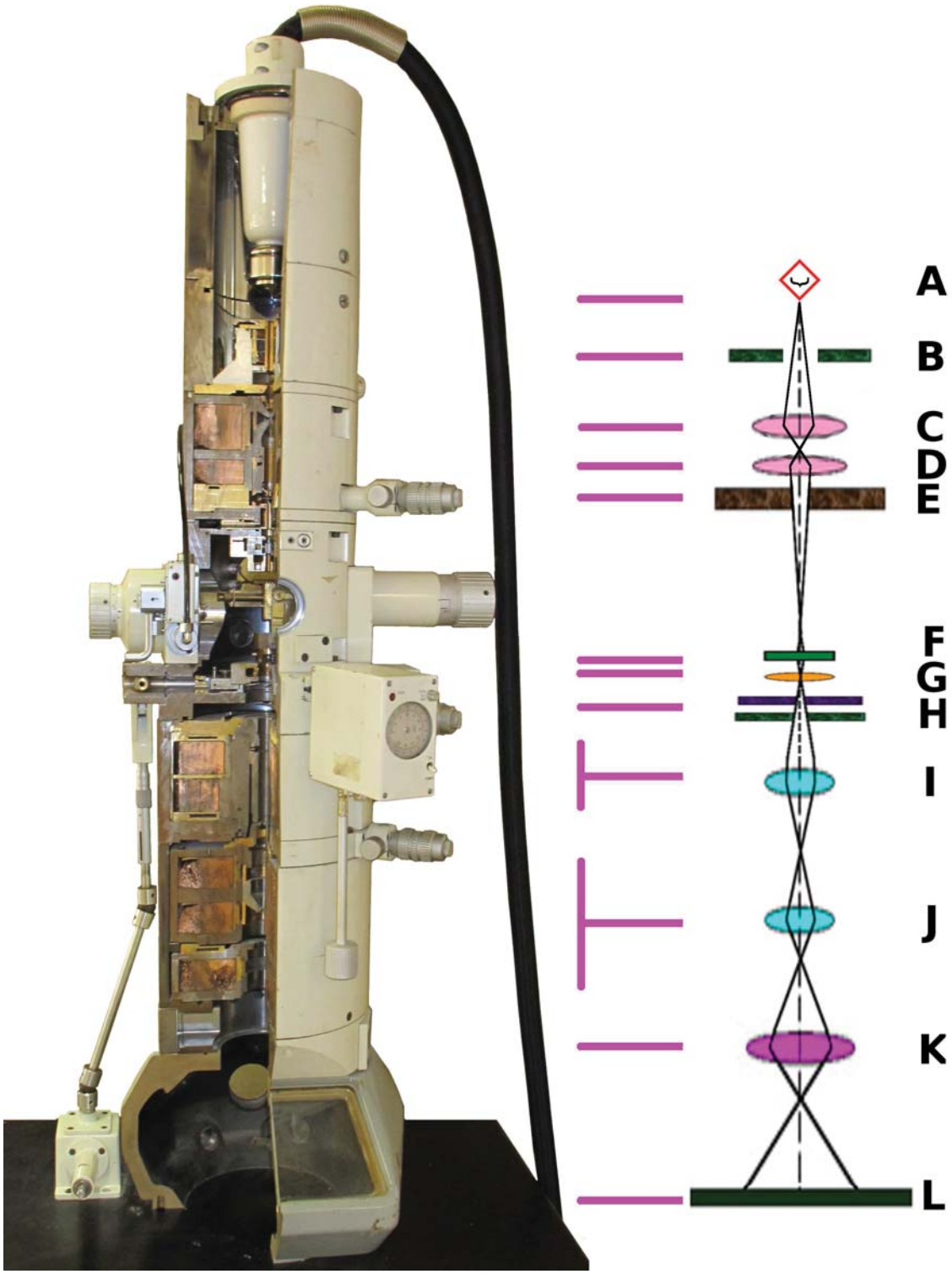

Figure B.8: A Transmission Electron microscope cross-section. Specific model: Jeol 100CX, located in the University of Melbourne Physics Museum. Key to included schematic illustrate components: (A) filament source, (B) accelerating anodes, (C) 1st condenser lens (stigmators), (D) 2nd condenser lens (tilt), (E) condenser aperture, (F) sample position, (G) objective lens, (H) selected area aperture, (I) 1st intermediate lens (objective stigmators), (J) 2nd intermediate lens (objective tilt), (K) projector lens, (L) phosphor screen/CCD array.

Figure B.9: The Philips CM300 transmission electron microscope located in RSES, ANU, used for all TEM analysis in this study.

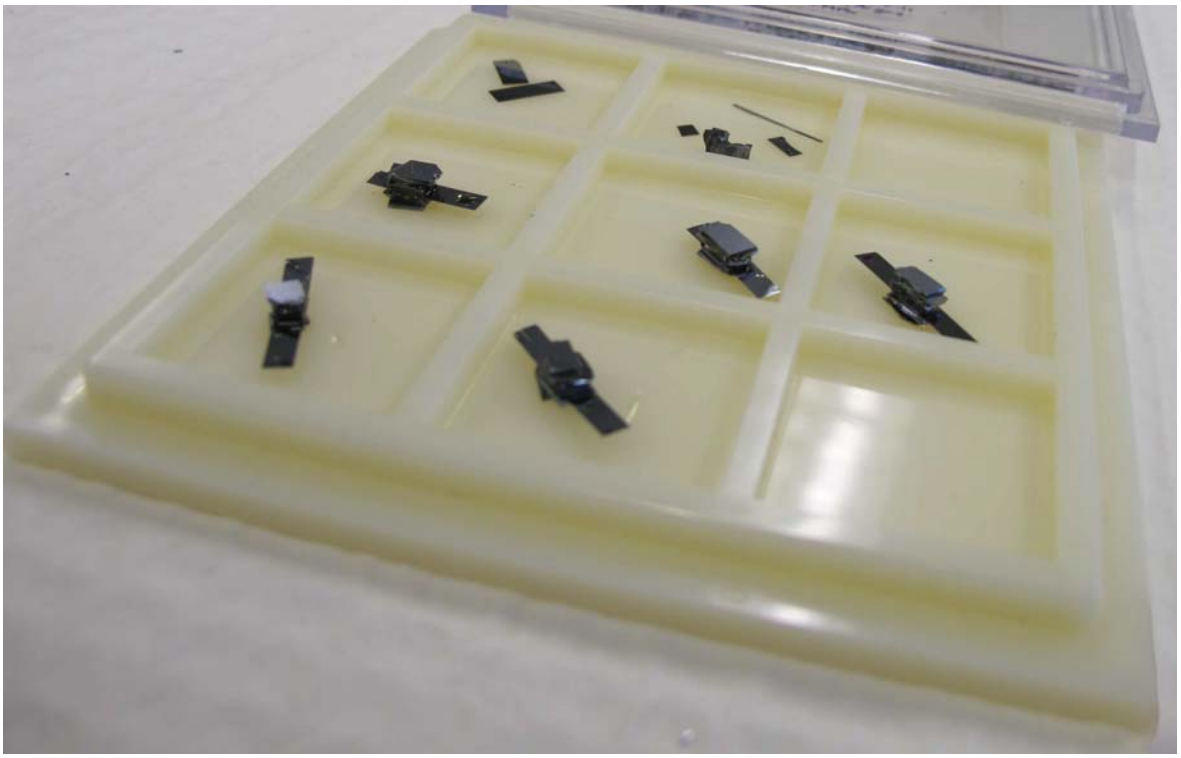

Figure B.10: Cross-sectional TEM samples during preparation. These "stacks" are the 50 μm Si(100) implanted with H(40keV,6×10^{16}cm^{-2},RT) under various external stresses (compressive or tensile), analysed in Section 5.4.4, sandwiched between "dummy" silicon pieces and glued with G1 epoxy.

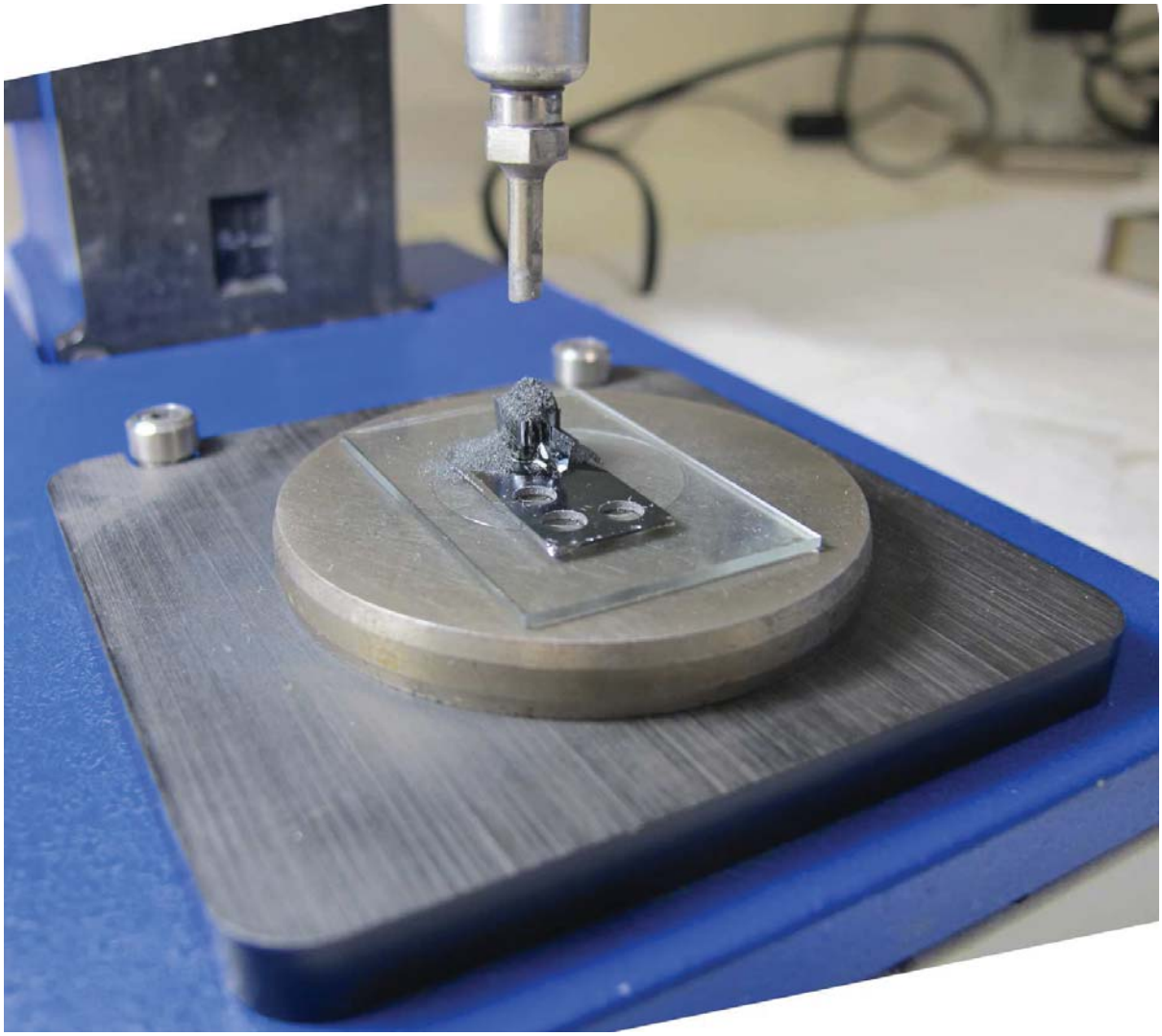

Figure B.11: Gatan Ultrasonic cutter presently cutting a cylinder from a cross-sectional TEM sample stack. The stack is attached via crystal bond to a silicon wafer, which itself is bonded to a glass microscope slide, in turn bonded to the magnetic "puck" which attaches to the metallic base piece of the cutter. The stack here is coated in SiC powder, which will act as the cutting agent as the oscillating head is driven into the silicon.

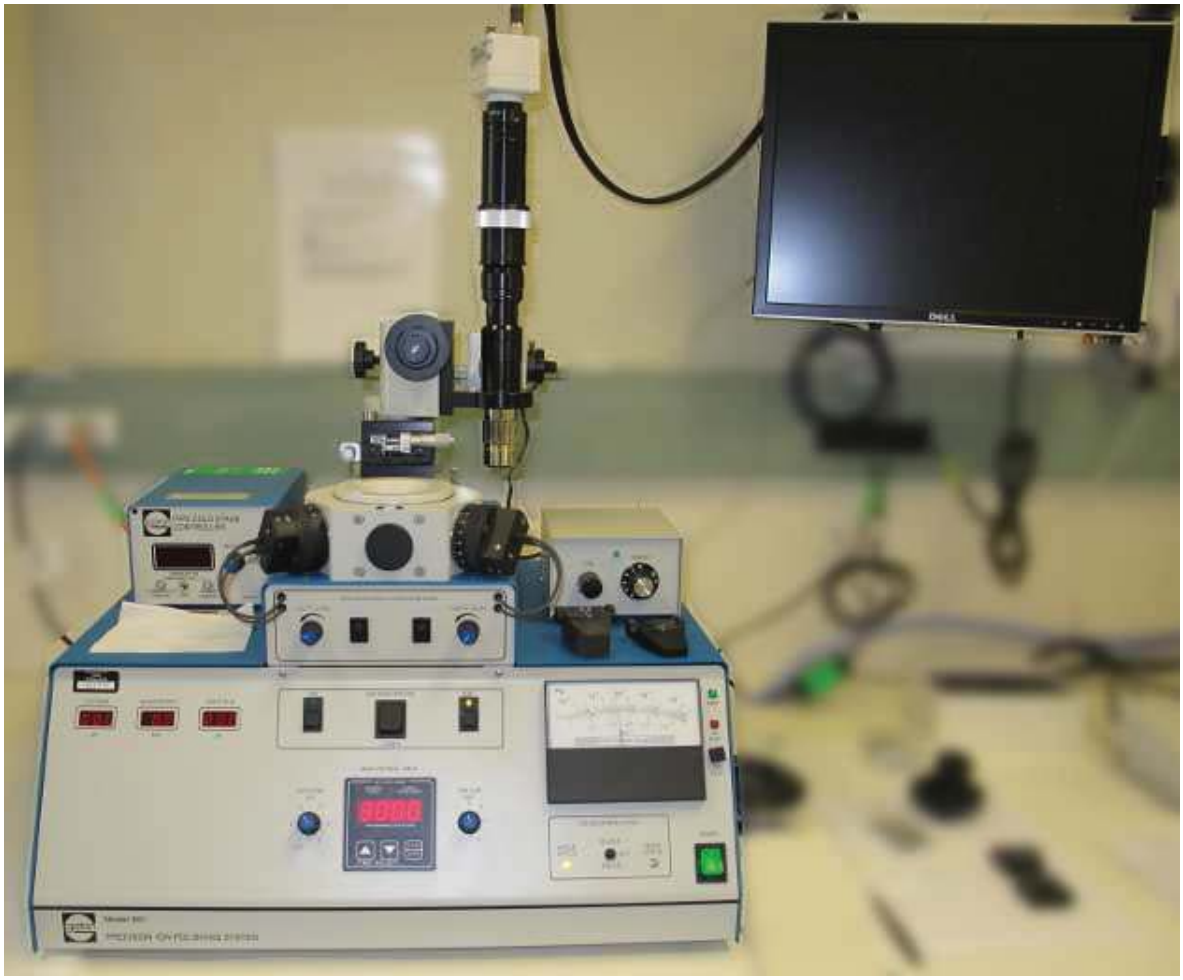

Figure B.12: Gatan Precision Ion Polishing System (PIPS) ion mill. After TEM samples have reached thicknesses of $\sim$5 μm in the region of interest, electron transparency is produced by milling with Ar ions at energies up to 6 keV under vacuum upon a rotating stage.

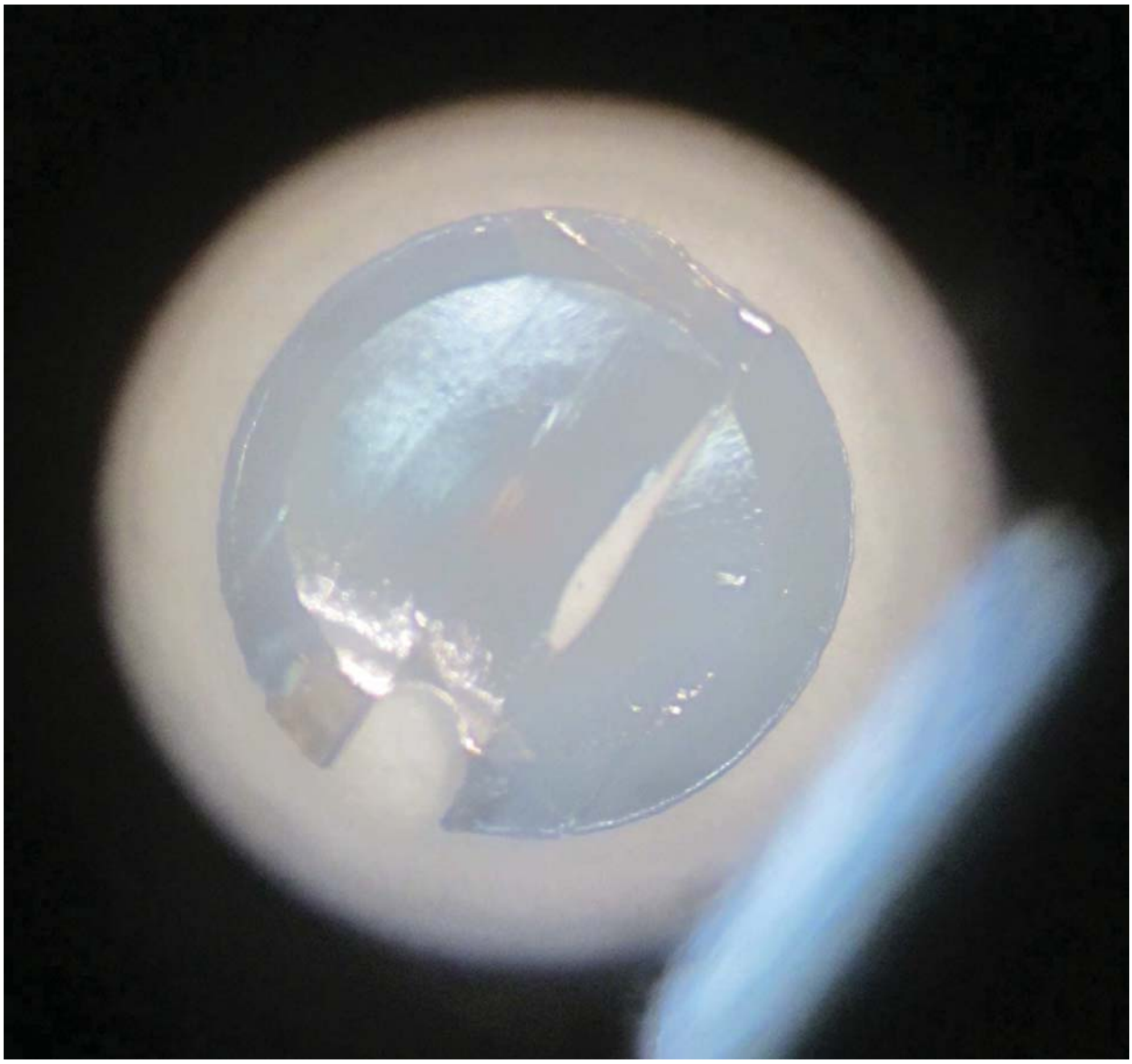

Figure B.13: Cross-sectional TEM sample during preparation, examined through an optical microscope. This sample is the 50 μm Si(100) implanted with H(40keV,6×10^{16}cm^{-2},RT) annealed at T=400°C/30min under no stress (compressive or tensile), analysed in Section 5.4.4. Ion milling has opened a small hole in the sample along the glue line between the 50 μm implanted wafer and the thick Si dummy piece. Conical dimpling of the sample is visible in secondary "ring" inset on sample. Faint red colouration near the centre of the disc indicates sample is thinner than 5 μm.

B.3 Blistering monitoring and recording apparatus

The resistively heated stage with vacuum chuck was used extensively in the annealing of H-implanted semiconductors in Chapter 4. It formed an integral part of the blister monitoring equipment, allowing the samples to be recorded for the duration of their anneal. The accuracy with which the temperature could be set is shown in Fig. B.14 below, which describes an accuracy of better than 2% from the desired set temperature.

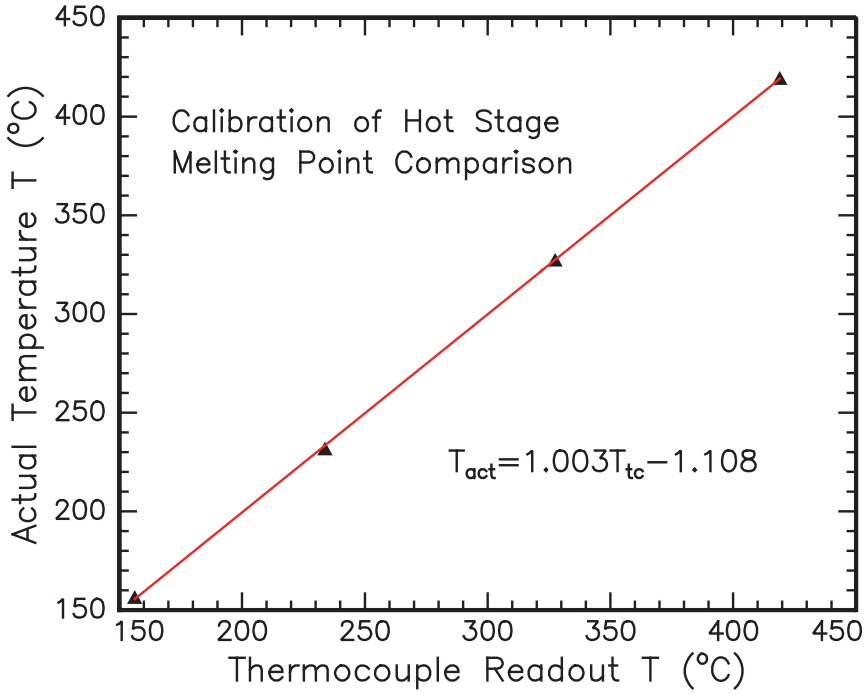

Figure B.14: Calibration of the hot stage used as part of the blister monitoring process, annealing samples while being recorded via webcam, as discussed in Section 3.3.1.

B.4 Stainless steel stress apparatus

This section describes strain apparatus in previous works, which attempts were made to replicate. The special stainless steel apparatus which was designed for our project is also pictured, and its original schematics included.

Previous Stress Boat Designs

In order to produce strain in semiconductor wafers, previous work by Olson *et al.* [267]

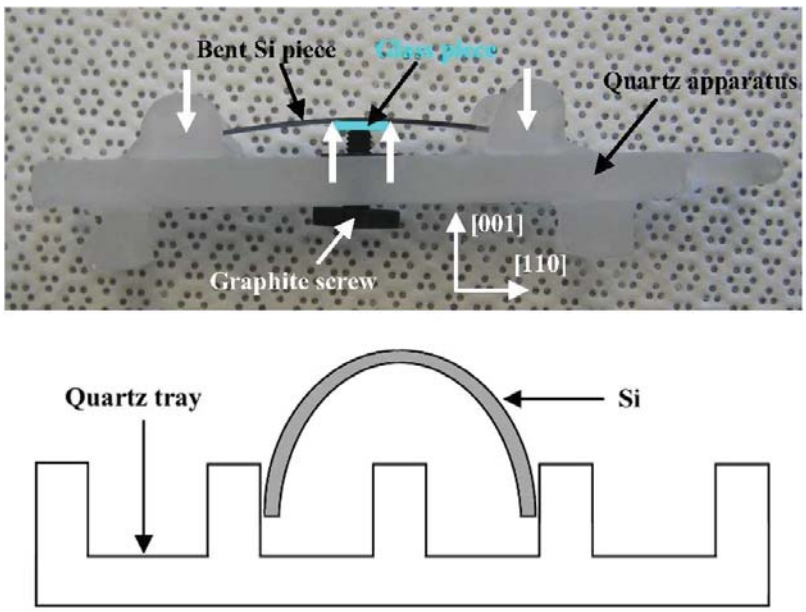

Figure B.15: Mechanical stress-inducing apparatus schematics for work by (upper) Olsen [267] and (lower) Rudawski [268]

and Rudawski *et al.* [231] used a number of modified annealing "boats". These are shown in Fig. B.15. The first of these boats featured a four point bending apparatus, comprising of a screw mechanism applying an upward force on a glass piece beneath the centre of the wafer while a series of cylindrical bollards apply downward forces on the two ends of the wafer. The second, used with double sided polished, 50 μm wafers akin to our study, was a quartz tray that had been incised at right angles to produce regular slots of approximately 1 mm width. The wafers were then bent *by hand* and held under stressed conditions by insertion into appropriately spaced slots, as shown in the aforementioned figure.

Figure B.17 shows photographs of our attempts to replicate these apparatus. While both of these designs proved successful in their original application, attempts in this project to replicate them resulted in several problems for use. The core of the difficulty was the fragility of the ULTRATHIN® Si wafers, an increasing issue in wafer production as thinner and more flexible substrates are sought [419].

For the screw-driven quartz boat, the distribution of the applied force upon the underside of the wafer had a sharp enough interface that led to the subject wafer shattering under most conditions tested. This prevented ready replication and repetition of any measurement and trouble establishing a consistent reference for measurement. In the quartz

Figure B.16: Photograph of stress boat apparatus with the originally designed small shelves mounted, as discussed in Section 3.3.2.

tray design, efforts to bend the wafers and insert them intact into the slots was a virtual impossibility, and despite the finite improbability indicated by the existence of previous work by Rudawski [231, 268, 269, 273, 321], proved beyond this researcher's capacity.

In addition to these stress application difficulties, quartz is unable to be shaped as readily into a design which allows the apparatus to be mounted onto the stages in the ion implanter or RBS/ERD chambers. Due to these difficulties, another option was required to allow significant stresses to be applied to the materials of interest and yet allow their survival for further study.

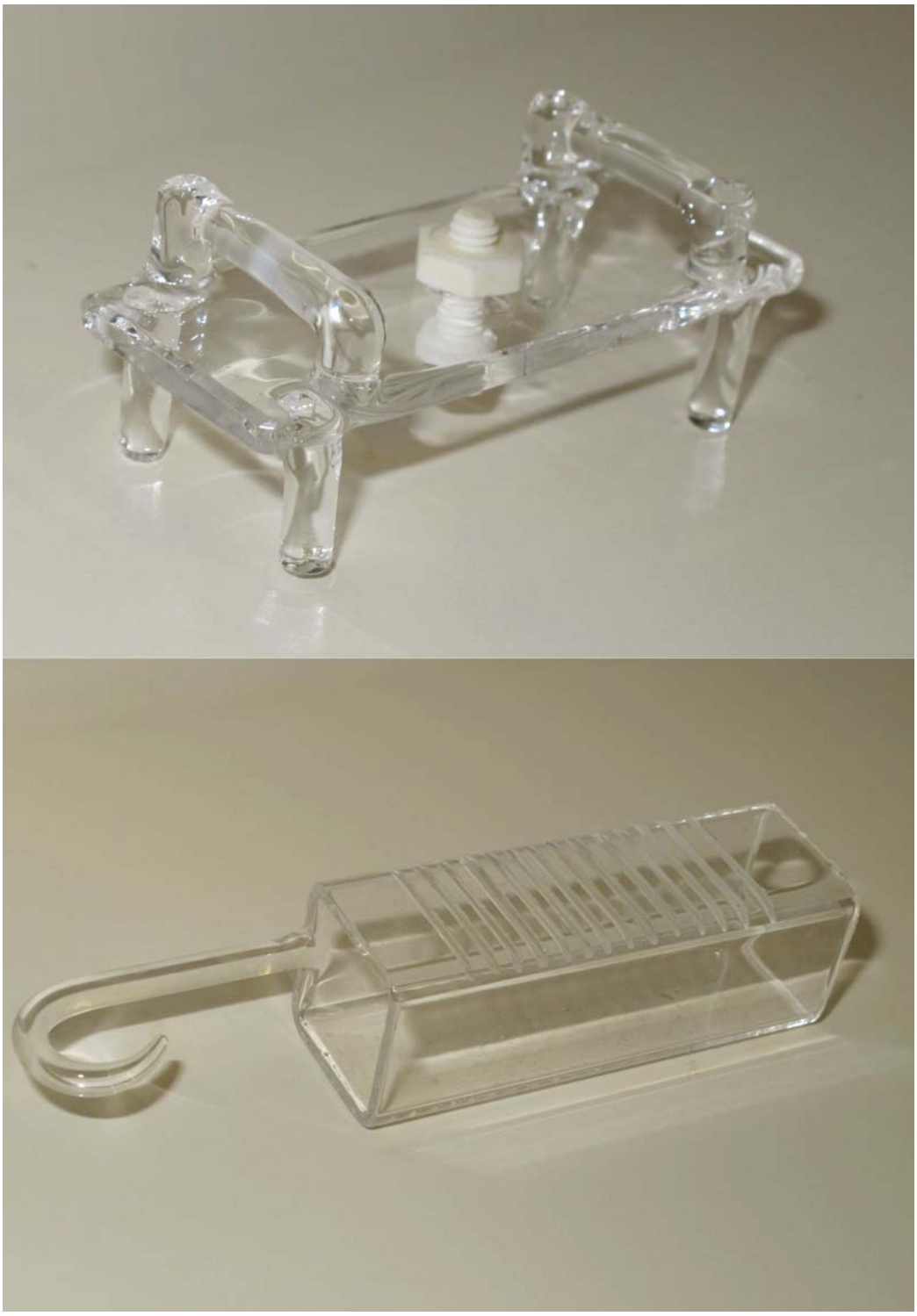

Figure B.17: Reproduced quartz-built apparatus modelled on designs from [267] and [268], manufactured by commercial glass technicians. Note that neither was used for any successful experiments in this project.

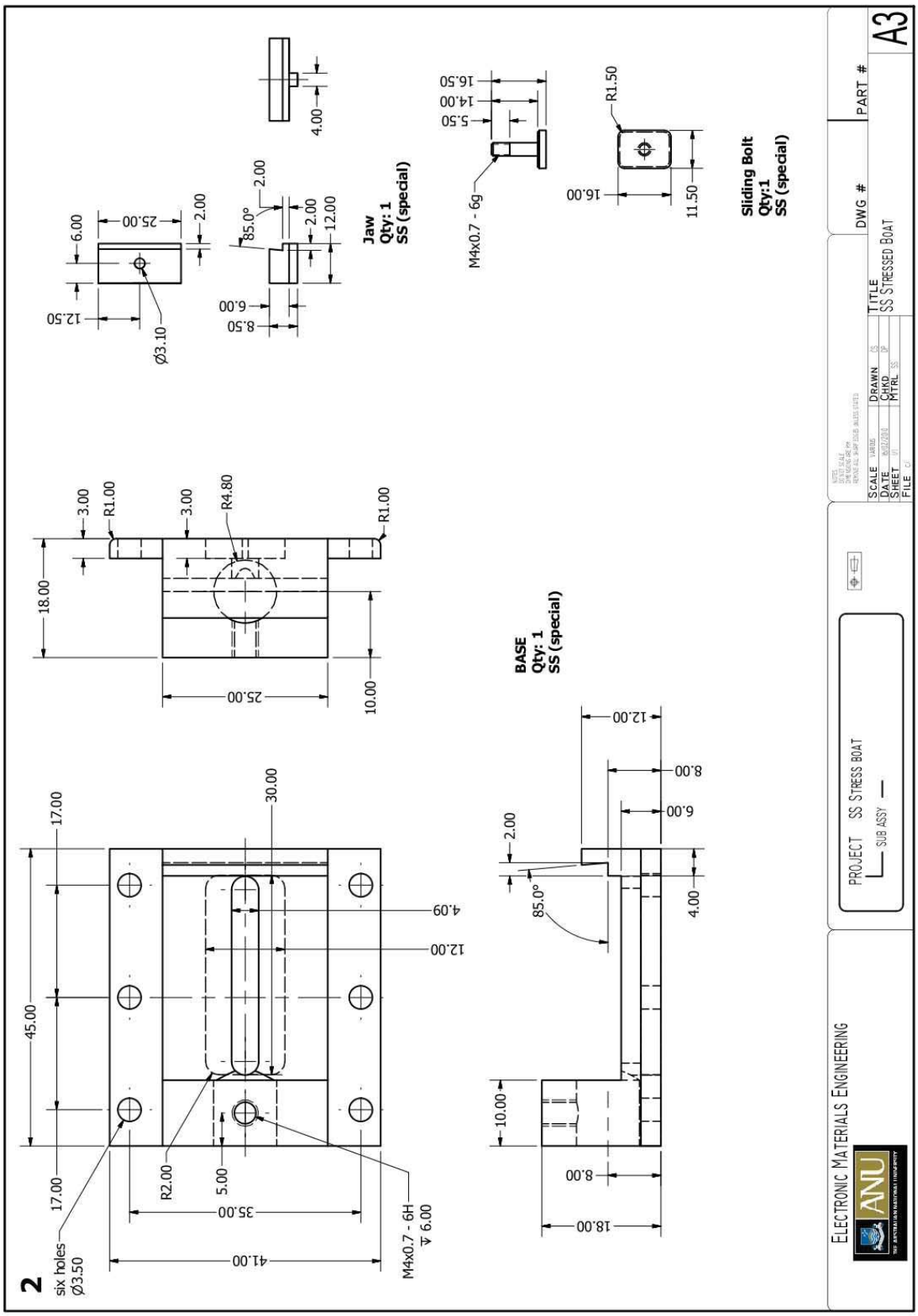

Figure B.18: Schematic of workshop-machined stainless steel stress boat or apparatus, as discussed in Section 3.3.2.

Appendix C

New ERD/RBS beamline operating procedures

This appendix acts as extraordinary operating procedures (EOP) for the new ion beam, under-development at the ANU extending the RBS facilities, prior to the formalisation of a standard operating procedure (SOP). Primarily this EOP is related to the software written in-house to communicate with the hardware, titled "RBSMain". It does not explicitly describe starting the ion source, nor selecting the beam on the NEC 5SDH accelerator. Section C.1 covers the initialisation of the software, leading into Sections C.2 and C.3 giving a detailed description of the primary control panel and secondary (slave or MCA) window of the software. The sub-panels of the main control panel are explained in Section C.4, before Section C.5 describes the operation of the sample changer load-lock mechanism. The configuration of the electronic NIM rack associated with the data collection process is shown in Section C.6.

The specifics of the software and its operation, and position of key elements of the beamline apparatus are unlikely to stay fixed during subsequent development. However, this chapter gives an insight into the early development of this line, one of the more significant tasks occupying this researcher's PhD.

C.1 Starting Up The Control Program

From within the MS Windows operating software, select the RBSMain icon located on the desktop to start up the software. This is a LabView program and thus is the standard LabView project icon, shown in Fig. C.1. Double-clicking on this to open the system, if the PC has been rebooted, will take some time as all the LabView scripts are opened.

Figure C.1: RBS/ERD LabView software main icon, located on the desktop under MS Windows XP™.

The program also uses a third party proprietary software package called Genie2000. This will also open when initially called, and should be noted when attempting to reset the software at any later time, as it must be terminated separately. The hardware that communicates with the software – located in the NIM Rack (shown in Fig. C.25) between the two beam lines in the control room – must be powered up before starting the software, or the system will be unresponsive to software issued commands. Once the first window has opened, the project needs to be "Run" to start its interface with the hardware. This is done by either selecting the arrow icon in the top left of the tool bar, or selecting "Run" from the "Operate" menu.

If for some reason there are errors occurring when you attempt to start the program, these may be either hardware communication failures or bugs in the code. To eliminate the possibility of the former, sometimes if you shut down and restart the NIM rack housing the JTAG box allowing fresh communication (see Fig C.25), and open the software from scratch again, this removes the problem. Do not turn off the encoders to the goniometer, located under the beam line with four red LED displays, unless ALL VALUES ARE ZERO. Otherwise the system will become un-calibrated and require difficult reestablishment of the correct alignment. Sometimes an error occurs in the camera connection, but if the software is allowed to "Continue" this bug sometimes disappears, or has no effect.

The first window that pops up when the software is started is shown in Fig. C.2. This theoretically gives the user the choice of controlling the older RBS line or the new RBS/ERD line. In practice, as of 4th April 2012, this has yet to be connected to the old line, so the first button is effectively redundant. The second button, to select the use of the hardware encoders on the old RBS line is also currently inactive, for the above described reasons.

Note that when a button darkens in this software interface it changes from "on" to "off" – like a push button in the real world. All that you have to do at the moment is click "Ok" and carry on to using the software for the new beamline. Once past this step, the control window changes from an open project (where the code is vulnerable to potential alteration) to an active, fixed program and the MCA slave window appears on the right hand screen. The former of these, the Control window, is described below.

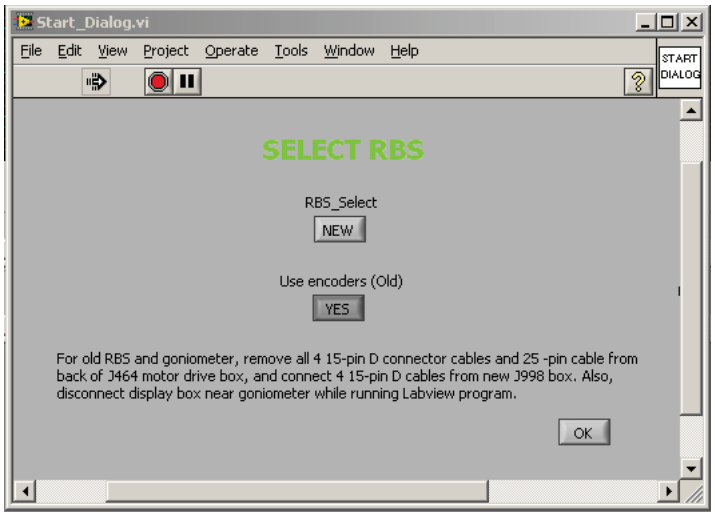

Figure C.2: RBS/ERD LabView software pop-up window, requesting beamline selection.

C.2 RBSMain Primary Control Window

Descriptions for the labels on Fig. C.3 are as follows:

$\boldsymbol{\alpha}$: The quick buttons in the toolbar allowing you to start and stop the project software. This is *NOT* for starting and stopping RBS collections, but killing the entire interface back to the coding stages. Not for regular usage, this control is only when shutting down at the end of the day. These buttons are found on all windows' toolbars, and thus should be treated carefully to prevent accidental shut down.

$\boldsymbol{\beta}$: This green indicator light illuminates to show that the software is operating. In future, there may be a second light alongside it to indicate which line is in use by the software, old or new. Perhaps they will also have more instructive names for people that come after it is all set up and hence all "old". The "Faraday cup in/out" controller beneath it is currently inactive.

$\boldsymbol{\gamma}$: These four readouts display the present location of the goniometer stage in the chamber. Alpha is a rotation in the plane of the floor, Beta is a rotation (labelled as "tilt" throughout the software) in the plane of the walls, while X is translation of the

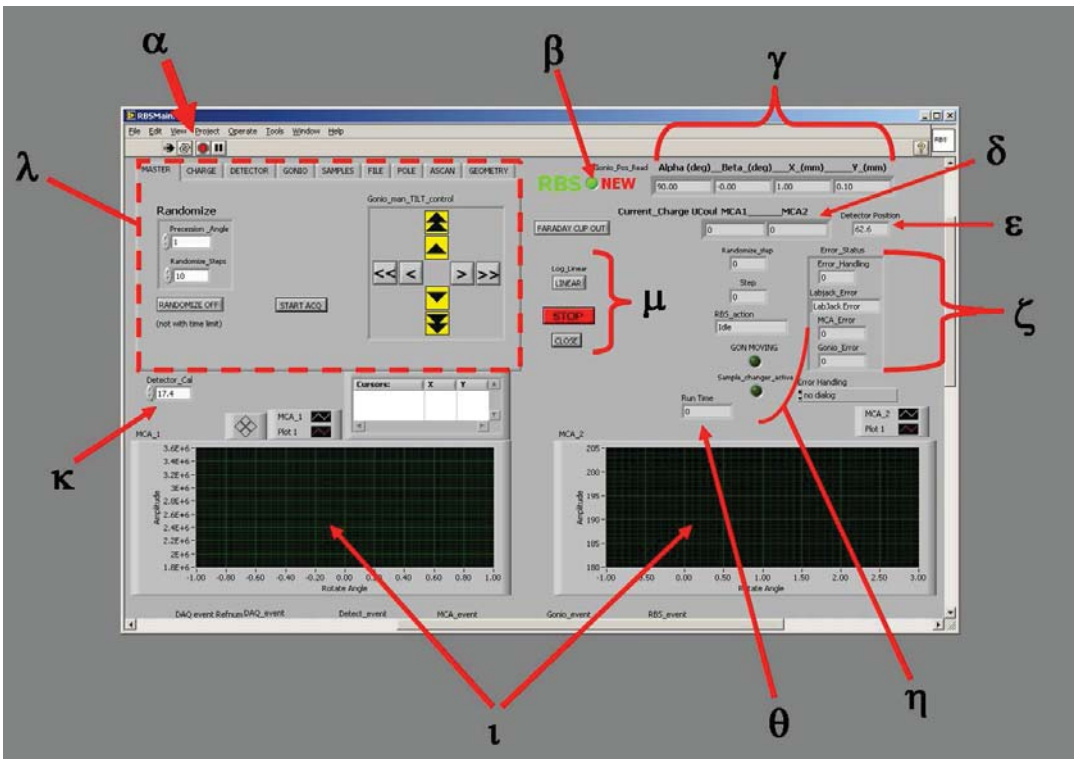

Figure C.3: RBS/ERD LabView primary control window, with labels as described in the text.

stage left and right and Y is translation up and down. These only read out location of the goniometer when stopped, and do not provide real-time feedback when it is in motion, during random angled scans or shifting to a new operating position. To see the live position of the goniometer, the encoder box located under the beamline near the chamber shows the present location in (α,β,x,y), and is shown in the Fig. C.4. Details of this encoder will be mentioned later. Units of each value are given (degrees and millimetres) above each box. These numbers are just the READOUT, not the entry point for manipulating the goniometer. Actual entry will be described in Section C.4.4.

$\boldsymbol{\delta}$: These two boxes display the total integrated charge collected during the RBS run. They are updated, though not exactly live, during the run, giving you an indication of the progress, whether towards any preset limits or otherwise. If these numbers are not updating or changing during a run, ensure that the charge digitiser on the central NIM rack is switched on, to "Operate" on the dial knob (See Fig C.25), and is receiving a BNC cable signal from the chamber.

$\boldsymbol{\varepsilon}$: The position of the moving detector in the chamber. The default home position is

an angle of θ=62.6° from the incident beam. This is NOT where the position is changed; as discussed before for previous features, this is only a readout display. Similar to the goniometer positions, it does not read out live during motion, only once the goniometer has reached its final stopped position.

$\boldsymbol{\zeta}$: These boxes display any errors occurring during the operation of the software. These may include communication errors, bad input errors (e.g. nonsensical values) or software failures. The most common is Labjack error, where signal between the goniometer or moving detector controller comes into conflict with the software, often over reaching limits. As the software does not necessarily have a comprehensive error table list, the exact cause of these errors is often unclear. As such, they're a useful indicator, but insufficient to direct you clearly to a problem's source.

$\boldsymbol{\eta}$: The first two boxes list the total number and present number of steps in a randomised angle scan, the former as defined by the user and the latter wherever the scan is up to during the run. This is not always updated live, but has some delay, however is fairly accurate. (This is ignoring the troubles in getting some randomise scans to start at all.) The third box displays the current action being undertaken by the system and goniometer. It includes "Idle", "Gonio moving", "Collecting", etc.

Figure C.4: Relative encoder and stepping motor operating the new RBS/ERD line's goniometer. Readouts show (clockwise from top left) the rotation α, translation x, translation y and tilt β of the goniometer and hence sample stage. Beneath the readouts are manual operating controls, when the system is not slaved to the software (i.e., software inactive).

The first light indicates when the goniometer is moving, and is live to the action. The second shows whether the goniometer and moving detector are both in appropriate positions and the "Change Sample" option is active. This will be described in more detail later in sub-panel Section C.4.

$\boldsymbol{\theta}$: This box is a time counter, giving an almost accurate readout of the time of each

run instantaneously. It is generated from cycles in the code, and as thus only updates as each cycle completes, more or less close to real time.

ι: These screens are windows for collecting data from defined regions of interest (ROI) (discussed later) over a number of scans to identify crystallographic channelling angles and positions. Data is only collected here when operating ASCAN or POLE collections (described later in Sections C.4.8 and C.4.7).

κ: A "fudge" or offset factor, allowing the definition of the position of the moving detector relative to the system, determined from the software readout value from the fixed encoder. This may later be changed, depending on deliberate or accidental changes to the physical position of the detector, and its relationship relative to the controlling motor and other connection.

λ: This sub panel contains a number of different control interfaces, selected from the nine tabs running along its top edge. Each has specific functions it controls, though occasionally there is some overlap of key functions. The panel displayed is the "root" panel with simple start controls and a live rotation and tilt adjustment paddle. Each of these sub panels will be discussed in detail later in Section C.4.

μ: Log/Linear toggle button changes the scale methods on the y-axes of the two channelling data windows described in ***ι***. The STOP button is the primary means of stopping a data collection run. When pushed, a beep sounds to indicate the signal has been sent to the MDC and TAG collection boxes. This will not usually stop the motion of the goniometer or the moving detector once they are set into motion, unless it is part of a randomise collection command. The CLOSE button shuts the whole Control window, killing the program as effectively as pushing the red stop button on the top tool bar. It is only to be used when shutting down the software at the end of the day, and only after shifting all the goniometer settings to appropriate holding pattern positions.

C.3 RBSMain Secondary (Slave) Control Window

This window contains the multichannel analyser (MCA) data display, as shown in Fig. C.5. This window appears to the right of the primary control window, in the second LCD monitor, when the software is "Run". The key features as labelled in the figure are now

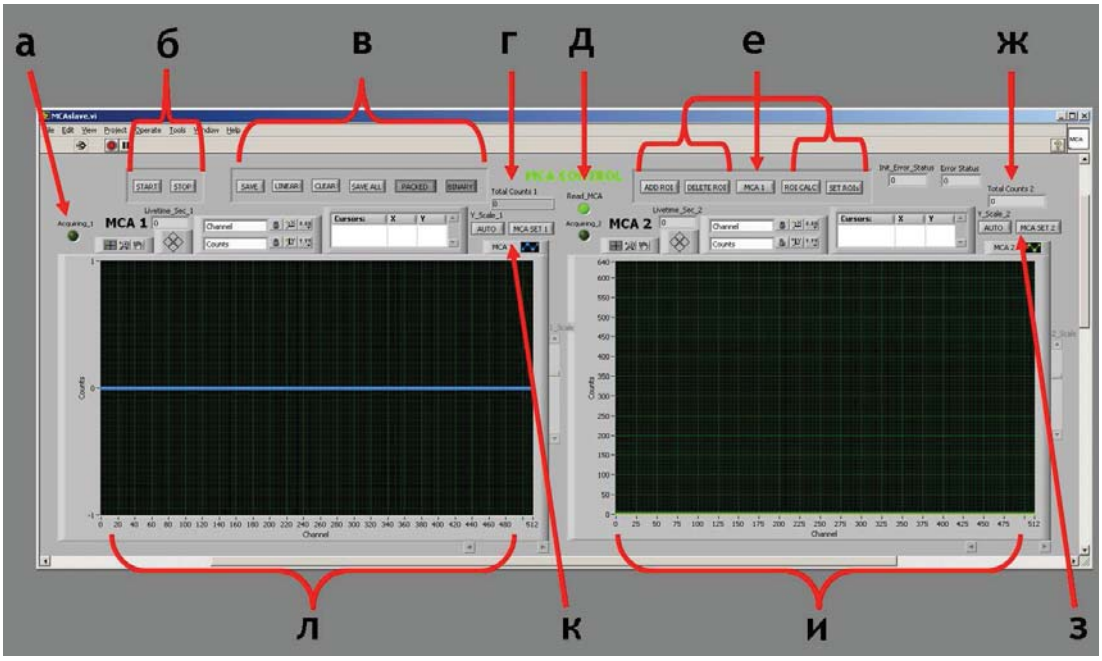

Figure C.5: RBS/ERD LabView secondary control window, displaying input from multichannel analyser (MCA), with labels described in the text.

described.

а: This light, and its counterpart in the centre of the window, indicate when the system is actively acquiring, illuminating and darkening as the collections are started and stopped respectively.

б: These buttons allow the collections of data to be started and stopped without any conditions attached to the run from the Control window. These are not designed to be used in ordinary operation, rather as a redundancy if software faults and similar require them.

в: These buttons are of three types. The first – Save and Clear – record and dismiss the data in the two MCA windows collected below. The second – Save All, Packed, Binary/Text – are toggles to control how the data which is saved is stored. Save All is a command like HCOPY in Genplot, recording all that has come before to ensure no data is lost prior to saving. Binary is to save them data in a format readable by RUMP, Quark, etc., while Text saves the information as a raw ASCII file. Packed (I'm not sure about yet). The third type – Linear/Log – toggles how the data is displayed in the MCA windows below it.

г/ж: These display total counts collected during that particular run, not integrated charge. These are reset on each run.

д: This light continually flashes when software is in communication with the hardware, whether collecting data or not. It is a useful indicator if the software has "frozen", as obviously in such a circumstance so will the light.

е: The arrow indicates a toggle to control settings for each MCA (lighter for MCA 1, darkened for MCA2). The four adjacent icons allow regions of interest (ROI) to be established in the defined MCA. These regions are used for channelling data collection, where the counts are compared in each subsequent collection. This is analogous to the upper and lower window value set manually on the old line. After a ROI has been added, and the two terminals moved via clicked and dragging with the mouse to appropriate sites, the "Set ROIs" button must be clicked to confirm the parameters. More than one ROI can be added, though only one will have data collected from it – addition ROIs in each MCA are effectively useless. (I'm not sure what ROI calc does, but I suspect it gives a count for the region defined post collection.)

з/к: The MCA Set 1/2 button allows the definition of the lower level discriminator (LLD) and upper level discriminator for the MCA's data collection. This is given as a percentage of the channel numbers in the MCA window, in order to remove low energy/frequency noise entering the collection. In some ERD/Hydrogen collections, it can be used to remove the He signal that successfully passes through the Mylar foil shield. Usually set around 5% at E=3 MeV. The window that pops up to allow modification is shown in the adjacent Fig. C.6.

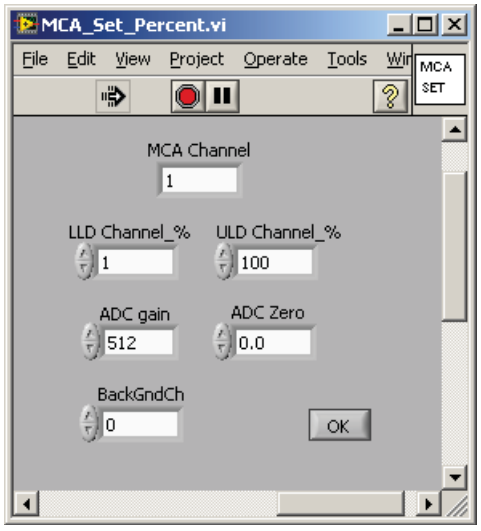

Figure C.6: RBS/ERD LabView software MCA Set pop-up window, activated by either control з or к.

The scale button allows for AUTO and MANUAL operation; in the latter, the scroll bar alongside the MCA windows can be used to adjust the maximum y-axis value. When in AUTO, the window automatically scales to include the highest y-value within the display.

и/л: These are the main displays of the data collected on multichannel analyser (MCA)

1 and 2. They have a predefined maximum of 512 channels, though adjusting the gains on the preamplifiers and amplifiers will change where the data is placed for its respective energy. These receive the signals of two of the detectors connected to the central NIM rack's hardware; all three detectors cannot be measured from simultaneously. Note that upon every new scan initiated by clicking the "Start Acquisition" (or similar) button, the data present in these windows is CLEARED (in marked difference to the older beam line, where new data was simply added to what had already been collected), and lost if the user has not actively saved it at completion of the scan.

C.4 RBSMain Primary Control Window Subpanels

As noted previously in Section C.2, there are nine separate subpanels accessed by the various tabs present on the Main control window (see tag **λ** in Fig. C.3). Each of these has specific functions, and these will be examined now.

C.4.1 Master

This is the "root" control panel in the RBS system. It allows the user to start acquiring data, and establish a simple randomisation routine. The Randomize function on the left has inputs for the precession angle around the present goniometer position (in degrees) and the number of steps to take around that point at the defined angle. This function works most of the time, when the RANDOMIZE ON/OFF button is toggled to the active position. Sometimes it takes a few start stops before the system realises you do want to randomise the angle of collection.

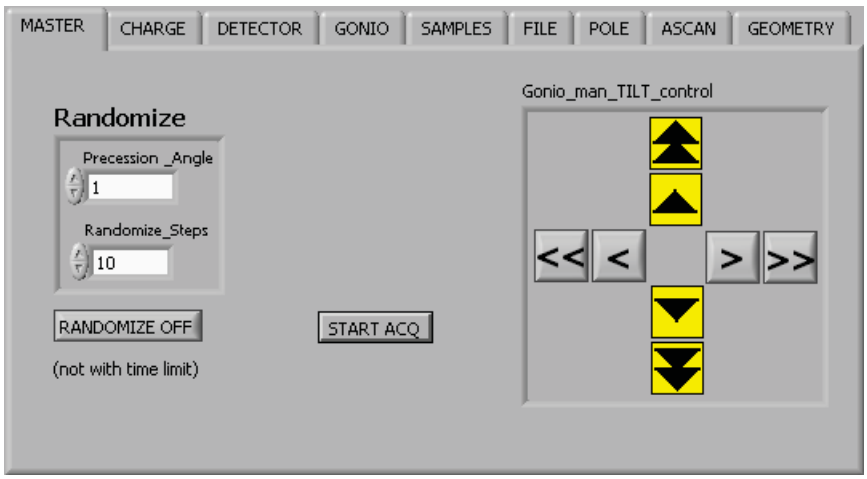

Figure C.7: Layout of the "Master" subpanel on the primary control panel.

The Goniometer manual tilt controller allows the user to adjust the alpha rotation and beta tilt both prior and (critically) during the collection. The small arrows change the angle by 0.01 degrees, the large arrows by 0.1°, with left and right defined relative to the beams perspective of the sample holder overlaid with a Cartesian axis.

Note while START ACQ button is in the subpanel, the button to stop acquisition is located in the main control window, labelled ***μ*** in Section C.2.

C.4.2 Charge

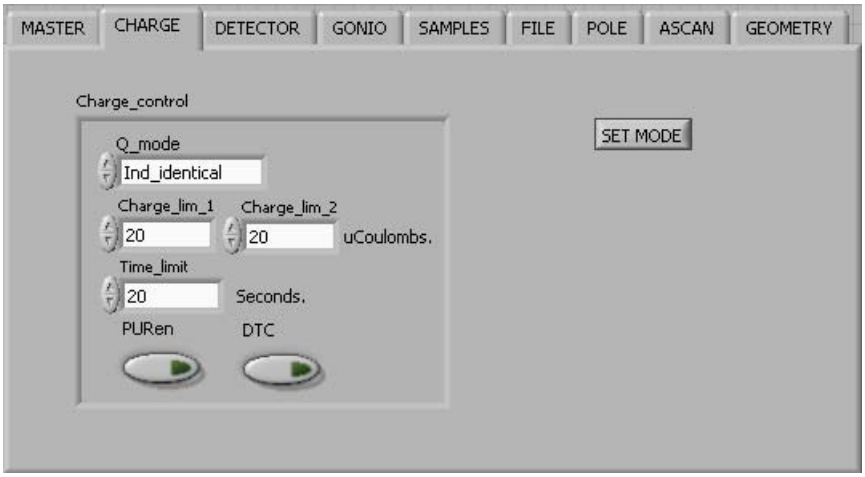

Figure C.8: Layout of the "Charge" subpanel on the primary control panel.

This panel lets the user set the limits of RBS/ERD collections, whether by charge collected or time elapsed. The limits can be set to be individual to each MCA, or identical, as well as choosing whether the stop point should be measured against both MCA or just one (e.g. if MCA 1 reaches 10 μC, to stop both even if MCA 2 is only at 9 μC). The two lower toggles with green highlights when active determine if (PURen) and dead time correction (DTC) are applied to the collection statistics. Once these values are selected to the user's desires, the "SET MODE" button must be clicked to establish these "ground rules" for the software. Note these charge limit values may be overridden by additional conditions applied under other subpanels.

C.4.3 Detector

The user here has control over the moving detector. The position of the detector is relative to the incident beam, hence 0° is a scattering angle of 180°. The "Move Detector" button is clicked after selecting appropriate values. The green light illuminates when the arm is in motion. The Home button returns the detector to the preset home position of θ=62.6°.

The "ARM STOP" button in the lower right is a fail-safe if the user feels the detector is behaving erratically or incorrectly, with risk of damage to the rest of the chamber's equipment; effectively an emergency stop button. Note that I've never tried to actually *use* this button, so uncertainty exists about its effectiveness.

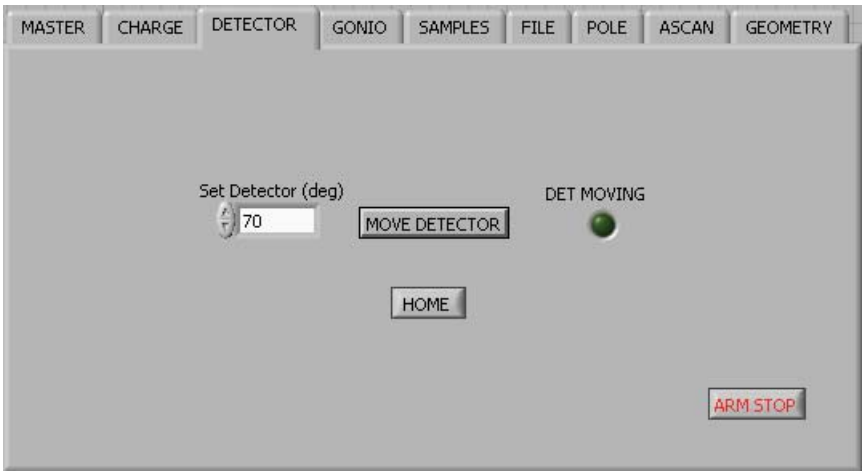

Figure C.9: Layout of the "Detector" subpanel on the primary control panel.

C.4.4 Gonio

The controls for adjusting the position of the goniometer are present in this panel. Alpha, Beta, X and Y are all entered via the left column of boxes – this is best done via keyboard, as the increments of the up and down arrows are a bit erratic, sometimes moving whole integer values! If you only wish to alter a single parameter without filling in every other box, the "Axis" drop down menu allows selection of which parameters will be altered when the "Move Goniometer" button is clicked.

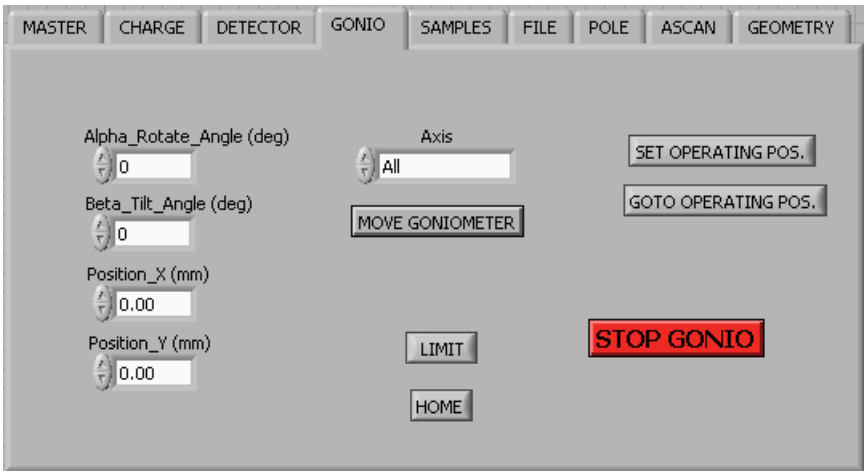

Figure C.10: Layout of the "Gonio" subpanel on the primary control panel.

"Set Operating Pos." allows the user to pick a particularly useful angle, position, tilt, etc. and temporarily set it for easy recall with the "Goto Operating Pos." button below it. I have never used the Limit button. I assume it takes the gonio to one of its limits in each axis, though what purpose one would have for this I am unsure, also which or how it de-

cides such. Alternatively, it may set a "Limit" position, allowing the translation or angular rotation not to pass that point.

The "HOME" button returns the goniometer to its preset home position, set for when the sample puck is to be inserted or removed, at (-2.5, -2.5, 0, 0). "STOP GONIO" is fairly self explanatory, but be warned I have rarely seen it function, in that the goniometer tends to continue on its merry way to whatever its last instructions were, rather than stop dead in its tracks.

C.4.5 Samples

In this panel, there are some as yet implemented buttons that should allow the user to move to a pre-set position based on ID tags. Until active, or more than in testing, it is unnecessary with which to be concerned.

The goniometer and detector can be returned to their home positions by the use of the other two buttons on the right. When the motion has ceased, the light alongside the button with illuminate to indicate that the device has reached the desired position within some tolerance or accuracy. Once both goniometer and moving detector have reached their home positions, the "Sample_changer" option above will cease to be greyed out, and allow the change of state to "Enabled", which allows the user to start the sample changing process. Details of this process are given in Section C.5.

The central "VIEW SAMPLE HOLDER" opens a new window above the MCA Slave interface, showing the chamber's attached digital camera's last collected image. If the software is newly started, this will be a blank screen. Otherwise, you can collect images or video feed, as described in the following subsection.

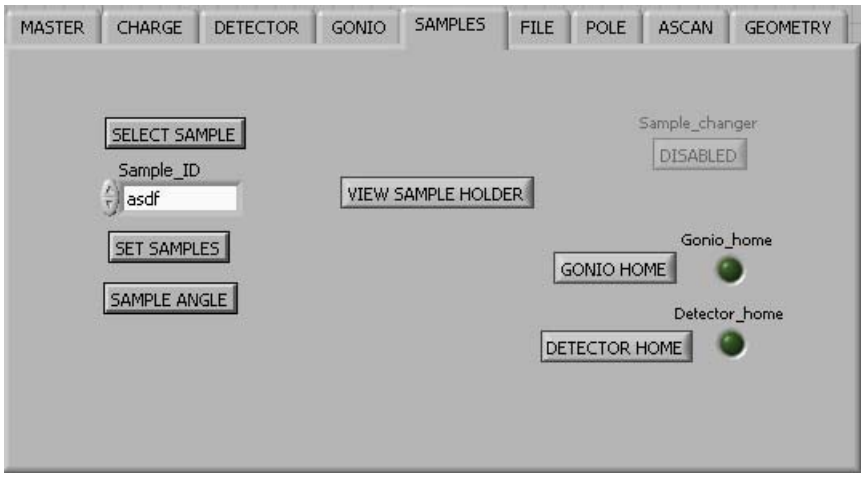

Figure C.11: Layout of the "Samples" subpanel on the primary control panel.

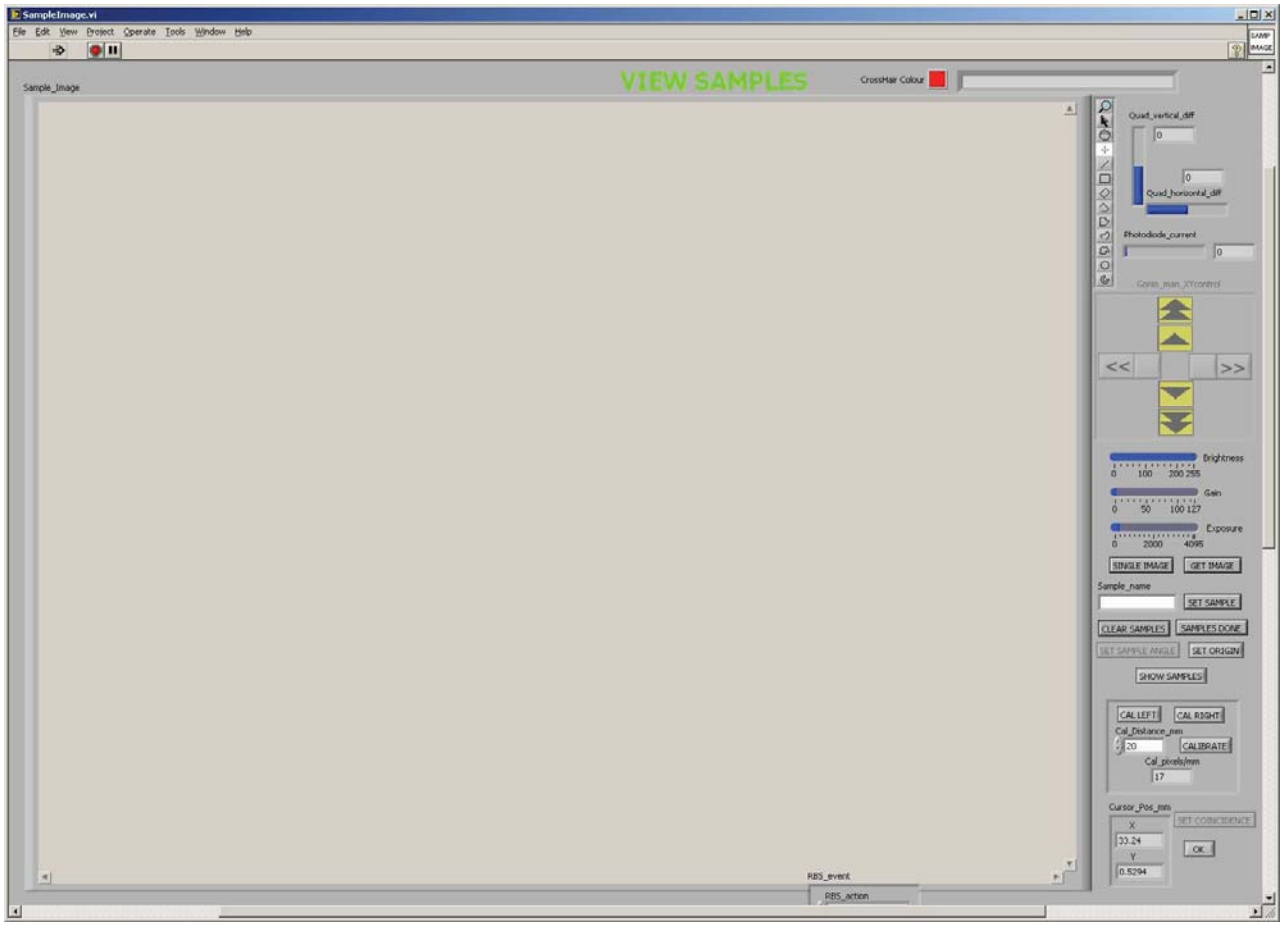

Figure C.12: The control window for the digital camera mounted on the ERD/RBS line, popping up in the right hand LCD monitor, in front of the MCA Slave window.

C.4.5.1 Digital Camera Collection

Figure C.12 shows the overall layout of the "SampleImage" window that opens when you select "View Sample Holder" from the "Samples" tab on the Main Control window. The large grey expanse is generally filled with a still snapshot or video feed of the chamber by the attached Firewire digital camera. Looking at the right hand panel in more detail, as shown in Fig. C.13 and Fig. C.14 it can effectively be broken into two sections.

The upper half allows for the control of the as-yet unimplemented laser alignment system. This will shine a beam on to the target and then measure the signal back in a photodiode, in order to calibrate the exact angle and tilt of the sample puck. The photocurrent bar is indicative, but so too are the control development tools on the left, still present and telling that this function has yet to be effected.

The Gonio control beneath, greyed out, is also for adjustment to match the values collected with the laser alignment on the photodiode with preset or previously recorded values for known positions.

The last options here, the three control bars for Brightness, Gain and Exposure, are operative, and allow you to calibrate the signal collected from the camera dependent on ambient light conditions, lamp sources and contrast to best resolve the details of your samples in the images/feed. These too are rarely altered, but may be more use when a fixed internal light source is fitted to the chamber, rather than the ramshackle lamp which is brought in and out from the nearest porthole to gain the appropriate intensity and contrast. Figure C.26 shows the exposed housing (cover removed) holding the camera by the chamber's porthole, and the desk lamp used as illumination source.

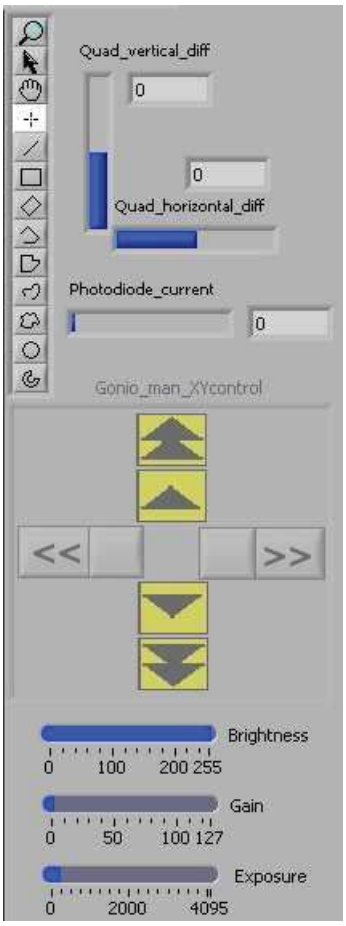

Figure C.13: The upper half of the strip of controls on the window for the digital camera.

In the second half of the strip, we find the controls for the collection of images and calibration of the coordinate system of the image. The "Single Image" button alternates to a darkened "Video" option when clicked, and the "Get Image" button captures the image or starts the video feed. The sample name and "Set Sample" are designed for the labelling of samples during a run to allow ease of movement back and forth to calibrated locations. Also related are the "Clear Samples", "Samples Done" and "Show Samples" options, though as yet to be effectively implemented, and I've yet to use them.

The "Set Origin" button allows the present cursor location – defined by the small green cross hair located over the image – to be 'reset' as (x,y)=(0,0). This is best done after the calibration of the image scale, and set atop the beam spot location when the goniometer reads (0,0) too.

The calibration of the scale of the image is performed with the indented region of the panel. The "Cal_Distance_mm" box is used to enter a distance value the user knows on

the sample puck (e.g. any multiple of 10mm as the screw points are separated by this distance), and then the "Cal Left" and "Cal Right" buttons are clicked after the user has moved the green crosshair cursor to positions separated by the specified distance. Once this has been performed, the "Calibrate" button is clicked to confirm the coordinates. It is then useful to move the green cross hair back to the beam spot location, move the goniometer to (x,y)=(0,0), and click the "Set Origin" button, as described above. Once calibrated, the lower display box will list the number of pixels per millimetre from the user's input – useful if later studying a saved copy of the camera feed. Also, the live position of the mouse cursor over the window is displayed in the final two boxes at the bottom of the control bar. The "Ok" button closes the "SampleImage" window and loses any calibrations the user has performed. My experience is that it is better to minimise the screen for future use.

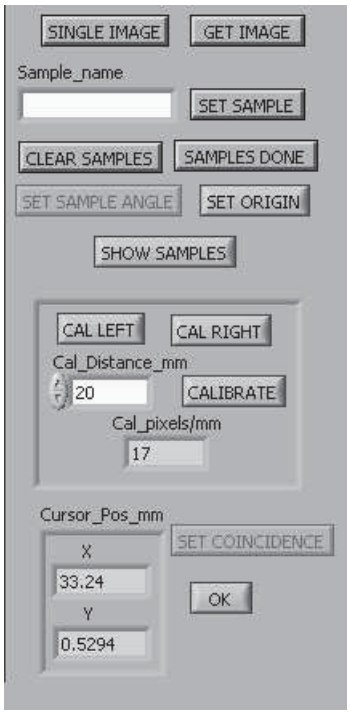

Figure C.14: The lower half of the strip of controls on the window for the digital camera.

The picture in the display can be saved as a .PNG file if the software must be reset, or for future reference, etc. As the detectors cannot withstand the light source – currently the desk lamp alongside the beamline – or any other photon source when they are biased with voltage, the chamber is too dark to collect images when in collection. As such, it's best to capture an image containing all samples in the chamber when the light is on and after the calibration has been performed with the video mode. This can then be referred back to in order to locate samples from the static image, and unless you click "Get image" again or close the SampleImage window, won't change when the chamber is darkened.

C.4.6 File

This panel allows the user to save conditions of this session, and recall the same settings for future operation. As yet, I've yet to use successfully either the Setup or Geometry saving functions, but have no reason to doubt they may function. The "Save MCA" button I am

unsure if I have ever clicked.

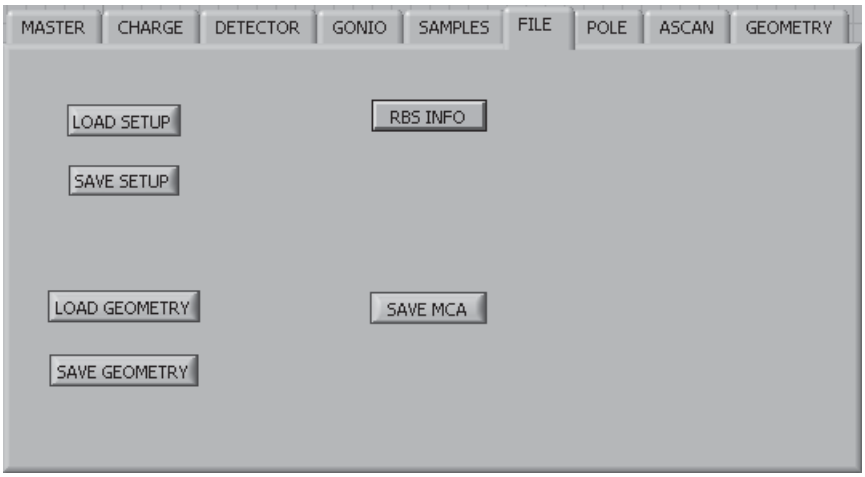

Figure C.15: Layout of the "File" subpanel on the primary control panel.

The "RBS Info" button opens a new window shown in Fig. C.16, allowing the user to enter details about the collections beam energy, beam type and coordinate system, amongst others. This information is entered into the binary header file of your RBS/ERD data files. Some is auto populated, such as the angles of the beam relative to the samples expressed in (θ, ϕ, ψ) in General, IBM or Cornell coordinate systems. However, while this is successful (usually) for the RBS mode, when performing ERD, these numbers are incorrect and need to be manually altered.

In particular, the beam current, which is used for normalisation of the yield with the total integrated charge, is not automatically populated, and requires the user to note the values prior to each run from the accelerator control station. Geometries are automatically set to "General" in RUMP encoding, with any negative value. A value of "0" or "1" will return IBM or Cornell geometry, respectively.

The first five of the entry boxes located in the lower half of the window are largely unimplemented at the moment. To be honest, I'm not sure they'll ever really be useful, except maybe as data stored in ASCII text format.

The sixth box is not useful for regular RBS/ERD scans – it fails to set an "active" directory for saving each user collection – but designates where the many short scans performed in the channelling calibration are saved. If you wished to do a number of scans over many angles, this would be useful, in that as well as saving the small channelling MCA windows labelled **и** in Section C.2, it saves each scan from the two "main" MCA windows, labelled **и/л** in Fig. C.5. However, it will not just accept a directory, but requires a "root" filename which the software will iterate upon, e.g. file001, file002, file003, etc.

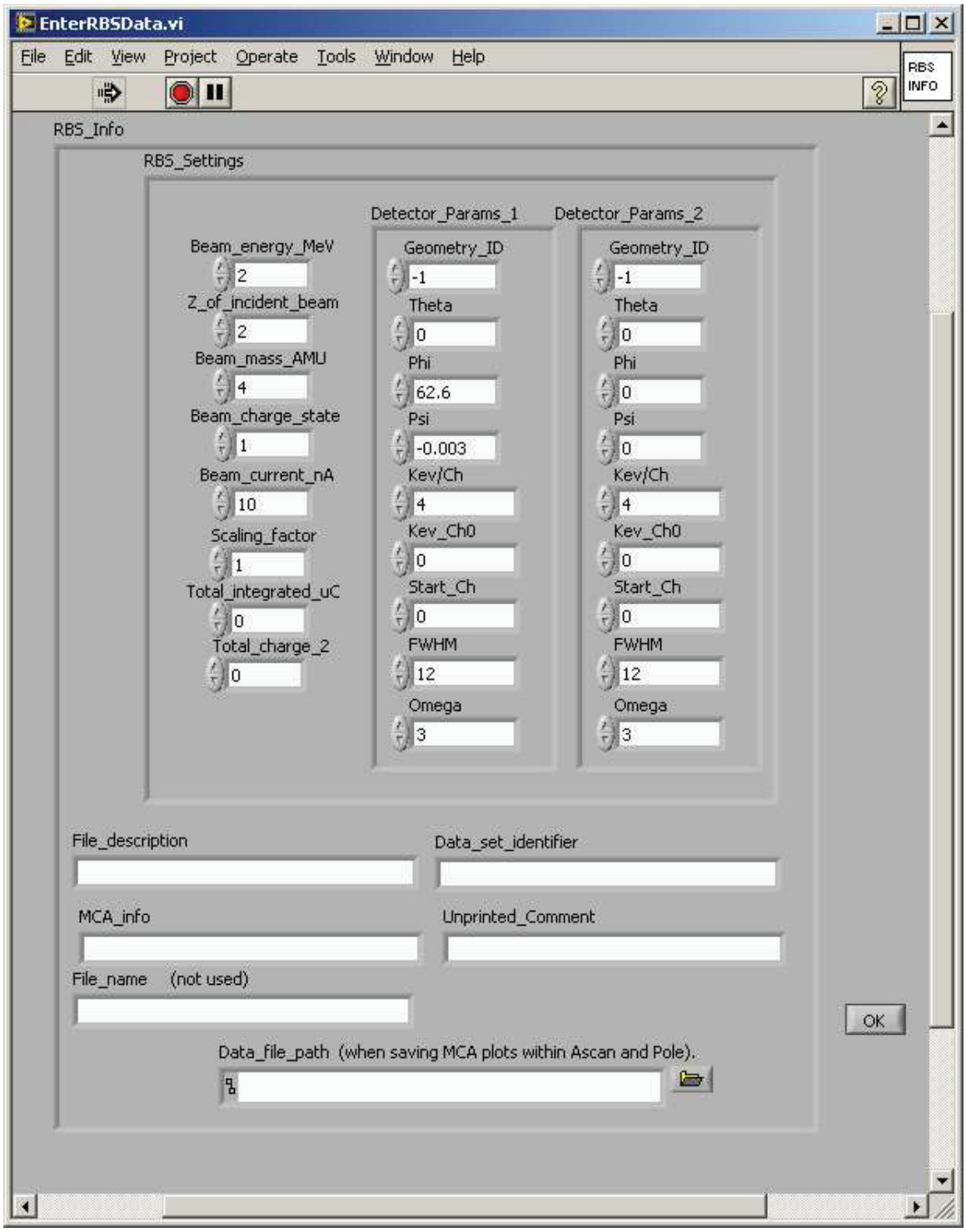

Figure C.16: Pop-up windows from the "File" subpanel, allowing header information reading the collection to be entered.

The software currently appends a "B" to the filenames of data displayed in MCA2. This can be misleading to users of the old system, where B implied backscattering geometry. However, such a "fixed" system cannot be set up for the new line, as changing of the data input on what would traditionally be the backscattered data MCA for the ERD data precludes such easy labelling. Ultimately, such labelled may be applied to the output filenames anyway, depending on user convenience or consensus, orders from above, etc.

C.4.7 Pole

The first of the panels allowing scans that vary the position and angle relative to the sample normal. Pole allows polar scans around a central position at a given angle (declination) in a fixed number of steps. The "Save Data" button here allows the data in the sub MCA windows located on the Master Control panel (see ι in Section C.2) to be saved.

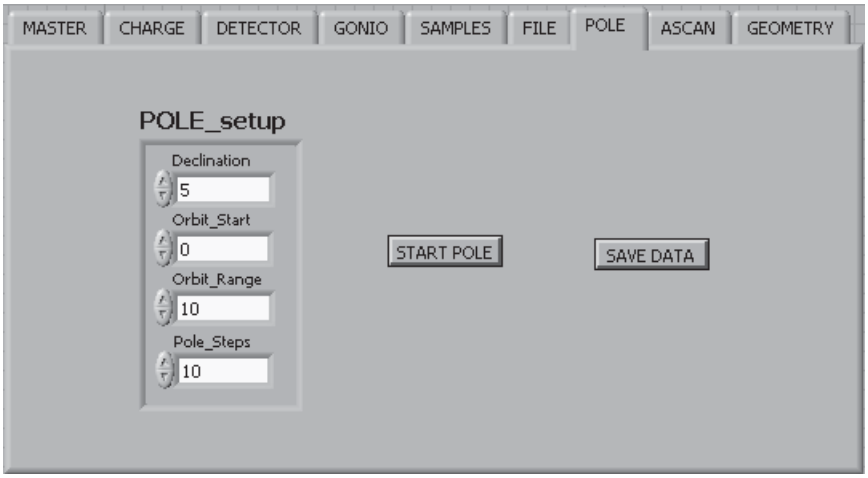

Figure C.17: Layout of the "Pole" subpanel on the primary control panel.

C.4.8 ASCAN

This panel allows collections of samples while the goniometer moves around some preset rotation and tilt values. This can allow for crystallographic channelling measurements, where the channel can be identified from changes in yield. The charge limit specified here will override any set in the second panel described in Section C.4.2, and needs to be remembered if simple collections from the master window are collected after an ASCAN.

Rotation or tilt can be selected for with the enable buttons in the centre, and the number of steps given in the lower half of the inset window. The values of rotation (alpha) and tilt (beta) provided in the initial and final boxes are absolute to the goniometer

reference frame. There is a button in the lower left that allows changing this to a relative number of degrees in each direction, however this has not been implemented yet. The "Save Data" button again allows the small MCA windows on the Control window's lower half to be saved, showing the channelling locations for each scan. There is a minimisation option where the goniometer will move to the lowest yield value collected in the ASCAN run, assuming it to be closest to the crystal channel. This minimisation ONLY moves the goniometer in the plane last scanned, e.g. alpha or beta, and returns the other angle to zero. So if performing a channelling routine in tilt after having minimised the yield in alpha, when it finds the minimum for beta and moves there (if this subroutine is active), it will forget the best alpha value and move to zero.

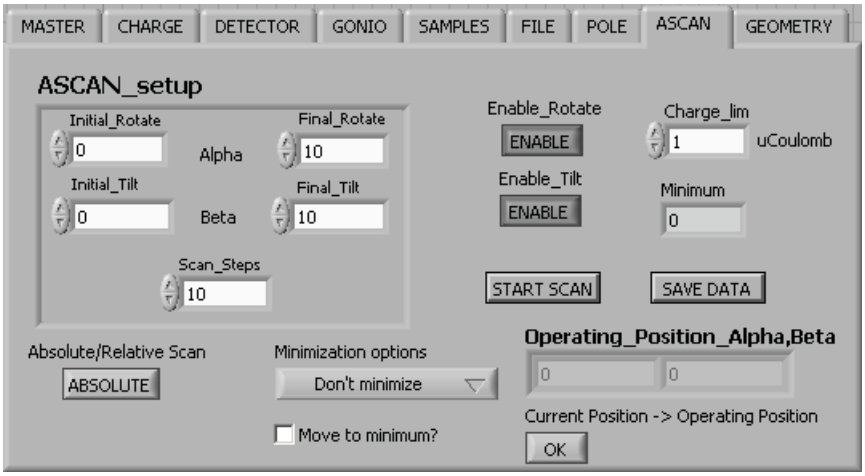

Figure C.18: Layout of the "ASCAN" subpanel on the primary control panel.

The "Ok" button is an odd calibration of the current goniometer position as the home or operating position. This button I have not used, and may be a vestige of earlier programming ideas/plans.

C.4.9 Geometry

The last of the subpanels is designed to calibrate the precise position of both the goniometer (and hence sample) and detectors. This function will operate in conjunction with the laser passed down the beam line by the insertion of a mirror. A

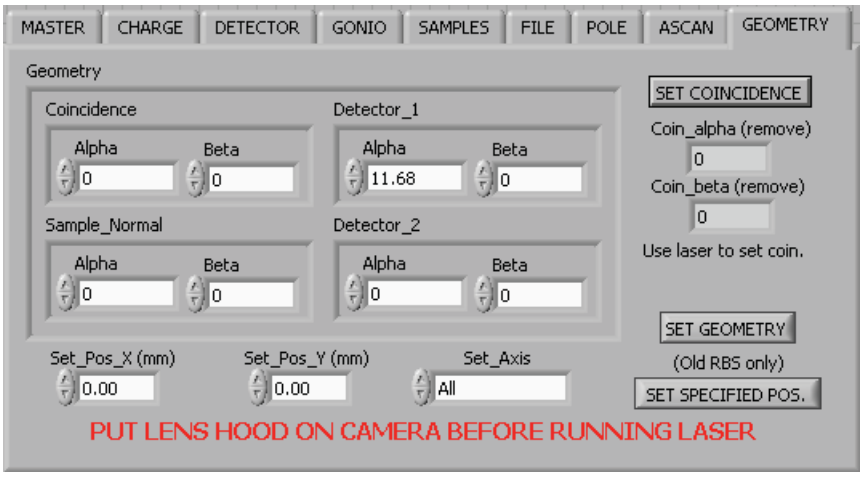

Figure C.19: Layout of the "Geometry" subpanel on the primary control panel.

Figure C.20: Chamber and loadlock mechanism on the new ERD/RBS line, attached to second line of NEC 5SHD accelerator.

control switch to insert the mirror is located on the operating computer bench, to the right and beneath the monitors. With the issues of alignment with the new system until major overhaul work in March-April 2011 (now 2012), this function has yet to be implemented. Effectively it will use coincidence of the laser beam reflected from the sample when positioned normal to the beam path into a known and fixed position detector.

C.5 Using The Load-lock Sample Changer

Unlike the old RBS beam line, the portable roughing pump and liquid nitrogen cooling of a sorption pump are not required. Rather, the system has its own vacuum load lock system, located at right angles to the beam line, for introducing samples to the target/goniometer chamber. Figure C.20 shows both the chamber of the new system and the attached load-lock.

To operate this load lock system, the operating software must be active, and the NIM rack containing the JTAG interface must be switched on. The process relies upon settings controlled in the software, is activated by physical or touch screen switches, and requires monitoring of pressure in each part of the system by the operator.

Within the RBSMain computer program, the goniometer and moving detector must be

moved to their "Home" positions – (α,β,x,y)=(-2.5,-2.5,0,0) and θ=62.6° respectively – on the Sample subwindow (see Section C.4.5). After these have returned a confirmation signal to the software via the JTAG interface, the "Sample_Changer" button can be enabled. Until this button has been pushed (darker, with "Enabled" label), the sample changer will not allow the load lock system to be evacuated.

Figure C.21: Specialised mounting puck designed for the new ERD/RBS line goniometer system.

Samples must be mounted on to the specialised mounting blocks or pucks designed for the system. These pucks, shown in Fig. C.21, have a six-by-five grid of screw points for anchoring clips to hold the samples – as seen in the fourth position in the top row. Samples could alternatively be attached with carbon tape or silver paste.

The range of the goniometer allows the whole region *WITHIN THE RANGE OF SCREW POINTS* to be accessed by the beam. There are only (at present) six screws with the right shaft length for these pucks as, despite having the same radius, the threaded screw points have only two-thirds the depth of the older RBS holders. Please take care not to lose them! The hooks on the edge of the puck are designed to allow attachment to the loading arm, clicking either side of a cross beam with a spring-loaded central aperture to ensure a firm pressure against these arms.

Once the samples have been secured upon the puck, it is attached to the end of the load lock insertion arm, and sealed within the interlock chamber, as shown in Fig. C.22. When the latch has again been secured and the puck enclosed in the chamber, the system will then allow the chamber to be pumped down. To start this, either press the red "PUMP" button on the small control paddle located beneath the load lock, or on the touch panel screen controlling the vacuum interlocks on the control column, both shown in Fig. C.23.

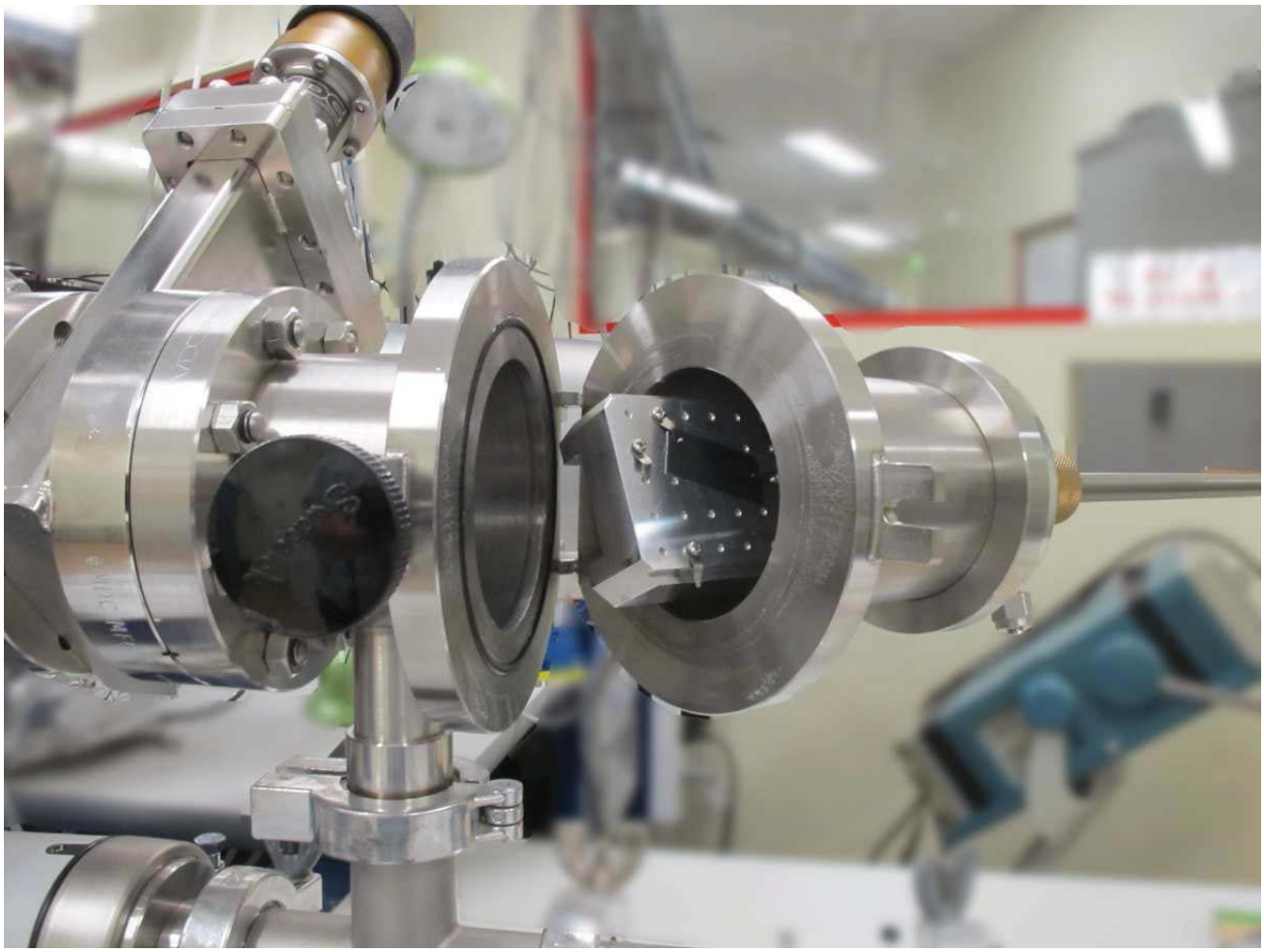

Figure C.22: Attaching the mounting puck to the arm within the load-lock, to allow insertion into the goniometer chamber system.

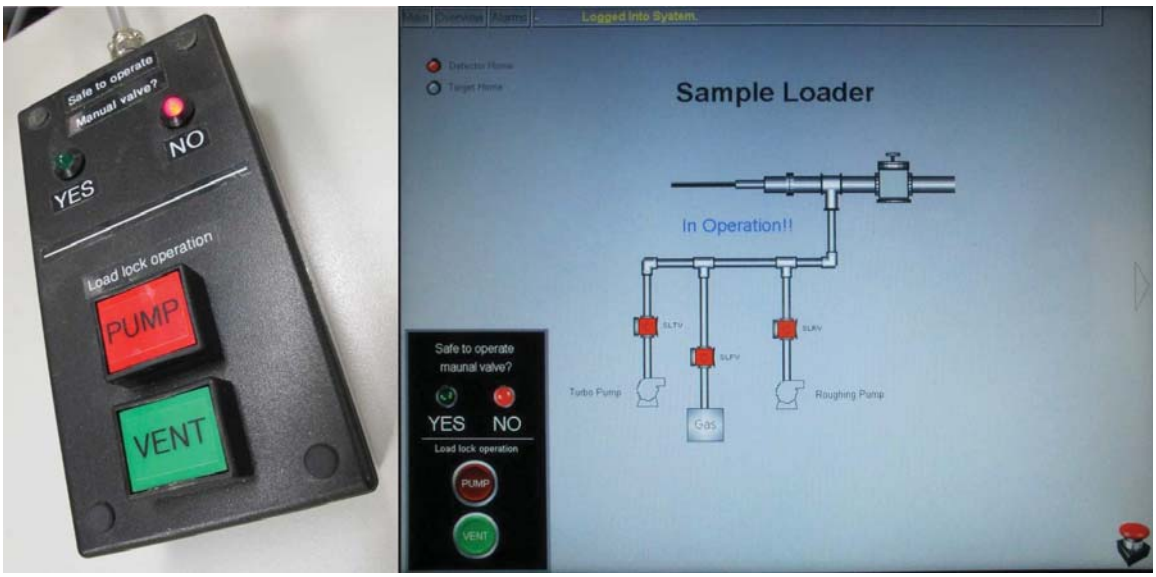

Figure C.23: Controls to evacuate or normalise ERD/RBS chamber via (left) manual push button paddle, or (right) touch panel.

If all is in order, then the system will begin to evacuate the load lock. While this is taking place, the "In Operation!!" label in the Sample Loader window of the touch screen panel will flash off and on. This is notably in the wrong order, as the panel will continuously display "In Operation!!" when the system is *NOT* pumping.

When the pressure in the load lock reaches less than P=10^{-5} mbar, the green LED on the control paddle and on the touch panel will illuminate. At this point, it is safe to manually open the valve separating the load lock from the main chamber. This is the black-and-tan screw knob above the load lock at $\sim 45°$. The red dimple in the centre of the knob will fully retract once the valve is completely open. This process should not be performed too slowly, to prevent pressure losses or leakages, rather a smooth shift to the backing pump on the chamber overriding and taking over from the pumps on the load lock.

At this point, the puck can slowly be entered into the chamber, by gently applying pressure to the load lock insertion arm. Generally, the difference in pressure between the chamber and the atmosphere is enough to draw the puck and arm forward without operator intervention. In this case, a gentle opposite force must be applied to allow a controlled insertion of the puck in to the chamber. The pressure within the chamber should be monitored during this process, to prevent the chamber rising too high and tripping the interlock system between it and its backing pump. Generally, values in the high 10^{-5}

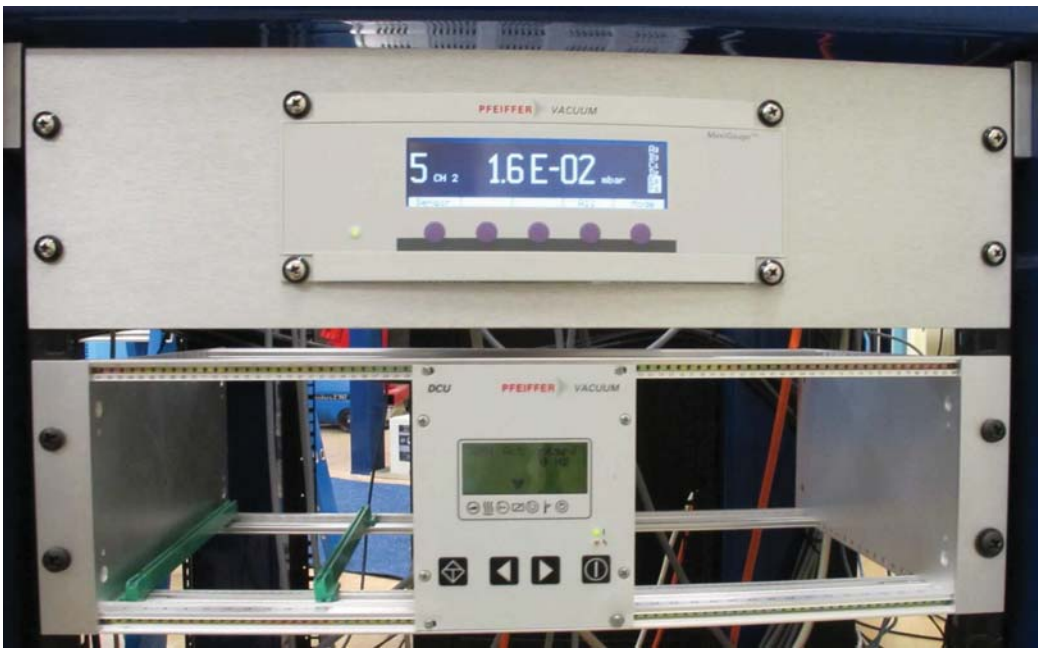

Figure C.24: Pfeiffer Vacuum gauge monitor (above) and vacuum controller (below) for the new ERD/ RBS chamber and beam line, located beneath the incoming line.

mbar are a good upper limit. The pressure can be monitored from the gauge display in the rack/bin beneath the beam line, shown in Fig. C.24.

When the puck passes the vacuum valve between the interlock and the chamber, it can sometimes gently scrape along the lower section of the port. This is not unusual, and the user should merely proceed gently until the puck clears the rough region. It is probably a good reminder that your samples should be attached firmly to prevent them being dislodged by the light vibration that occurs at this time. Once clear, the puck will often be pulled more than pushed, as described above, and the user must be cautious not to overload the interlock switches for the chamber's pressure. At this point, it is also advisable to monitor the progress of the puck towards the goniometer through the portal window to the left of the load lock. This will allow you to carefully align the puck with the slot of the goniometer, and ease the insertion process.

As the puck slides along the goniometer slot, it will reach a pole that acts as the completely mounted position, preventing further movement. To remove the insertion arm from the puck, rotate the handle and push gentle against the mounted puck. This will allow the cross beams to be rotated out from the twin hooks on the puck, and the retraction of the arm. Prior to retracting it from the chamber, use the cross beams to gently push

against the hooks on the puck, to ensure the removal process didn't drag the puck a little back out from the goniometer slot by the effect of friction. After this, retract the arm and close the manual valve. Take care to close it as thoroughly as possible by hand – no need for a spanner – and that the red dimple in the centre has again emerged clear of the knob surface.

Unfortunately, the load lock chamber must now be allowed to return to atmosphere, prior to the software allowing the user to deactivate the "Sample_Changer" button. This can be done by pressing the green button on either the control paddle or touch screen (as shown in Fig. C.23).

Occasionally the software does not allow the user to simply deactivate the sample changer button, and the central red "STOP" button (See label $\boldsymbol{\mu}$ in Fig. C.3) must first be pushed to override the control signal being fed to the software. Following this, you are now free to begin calibrating the sample positions, collecting images of the puck with the attached camera, preparing for collection, etc.

C.6 NIM Rack and External Camera Mount

The front configuration of the NIM rack housing the amplifiers, MCAs, detector bias and analogue to digital converters (ADC) is shown in Fig. C.25. This was the configuration at the end of 2011, and used as such for all RBS and ERD experiments in this thesis.

Figure C.25: NIM rack enclosure for beam line 2. From left to right, rack contains digital charge integrator, JTAG communications interface, pulser, Multiport II MCA, 2 amplifiers and a quad port bias supply. The overriding power switch is located on the far right.

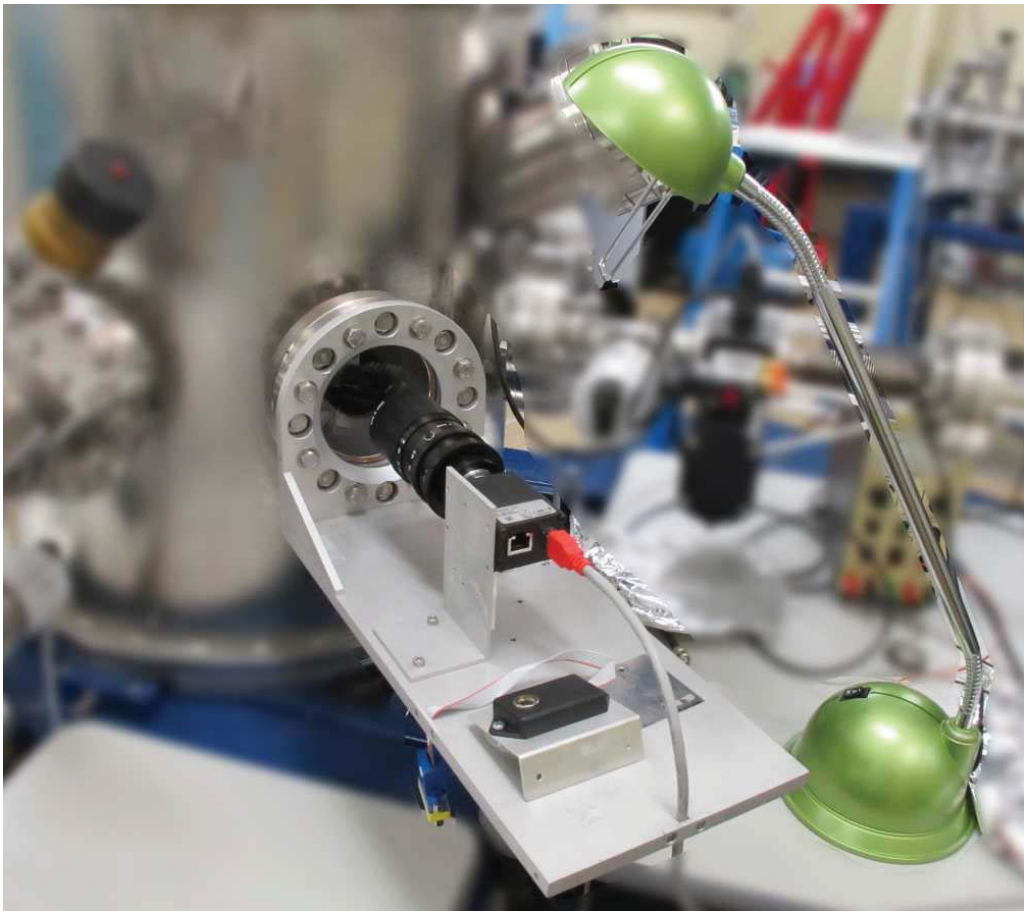

Figure C.26: The external mounting system for the digital camera fitted on the ERD/RBS chamber, including the simple illumination source of a halogen desk lamp.

Appendix D

Phenomenology of hydrogen blistering: Additional details

PRESENTED in this appendix are extra information regarding the study outlined in Chapter 4. Opening this chapter is an in-depth study into hydrogen evolution in Si(100), exploring the effect of fixed duration thermal annealing via IBA techniques. However due to unaccountable blistering occurring in some samples, the data was excised from the thesis' main body. The spectra collected by RBS-C and ERD of the annealing study of the H(5×10^{16}cm^{-2}16)-implanted Si(100), including the isolated direct scattering peaks, are shown, in addition to tables of the data used in the figures of Section D.1. A supplementary comparison of hydrogen blisters per area in Si(111) is shown, following on from Fig. 4.20. Significant focus is also lent to data regarding hydrogen-induced blistering and crater formation. There is an extensive presentation of histograms, displaying hydrogen-induced blisters' width and height, as well as plots contrasting the height and width of blisters on the semiconductors substrates studied.

D.1 Annealing evolution of implanted H:Si(100) system

Prior to investigating the external effects of hydrogen blistering (i.e., gross changes observable on the sample such as craters), we first looked at the behaviour of implanted hydrogen undergoing annealing in silicon. A series of hydrogen implantations were performed at ion energies from E=25–85 keV in 25 keV steps, at a fixed fluence of Φ_H=5×10^{16}cm^{-2} – equal to the usual fluences employed in studies of ion-cut phenomena. These implantations were

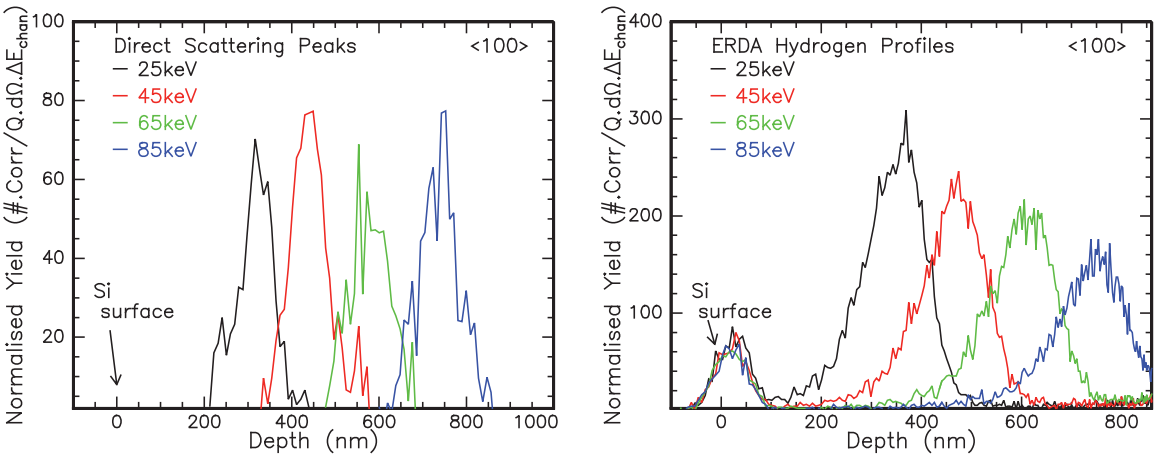

(a) (b)

Figure D.1: Experimentally measured profiles of (a) RBS-C determined DS peaks, and (b) ERD determined hydrogen profiles, for Si(100) implanted with various ion energies (as labelled in graphs) at a fluence of Φ_H=5×10^{16}cm^{-2}, as implanted. Samples channelled along ⟨100⟩ axis for RBS-C measurements, depth scales determined by RUMP package.

performed into a single 375 μm thick Si(100) wafer in four 2.5 cm × 0.5 cm strips, at room temperature with a scanned beam current of I=3 μA.

Each sample was studied using ERD and RBS-C, where the latter examined them along both ⟨100⟩ and ⟨110⟩ axes. The sample wafer was cut between the E=45 keV and 65 keV implantation strips, and the two pieces underwent annealing at T=400°C in a quartz tube furnace under an Ar ambient, for intervals of t=15 minutes, up until t=60 minutes. The as-implanted profiles of these samples' direct scattering (DS) peaks determined by RBS-C and their hydrogen profiles determined by ERD are presented in Fig. D.1.

Previous studies [107, 349] have investigated the influence of hydrogen implantation upon the silicon crystal lattice along each crystallographic plane or axial channel. As Di *et al.* [364, 366] discuss, while channelling along both ⟨100⟩ and ⟨110⟩ axes is equally sensitive to interstitial-vacancy (IV) defects formed in ion implantation, the orientation of extended defects produced by hydrogen are not channel symmetric. Defects such as hydrogen platelets that move the alignment of the lattice planes to either side around the platelet shifts Si atoms into the [110] path, while producing no lattice shift for the perpendicular [100] direction. Within these axial studies, interest has been raised in the so-called *reverse annealing* effect [44,338,349,373]. This term is used to describe situations where the DS peak is seen to migrate closer to the surface after annealing.

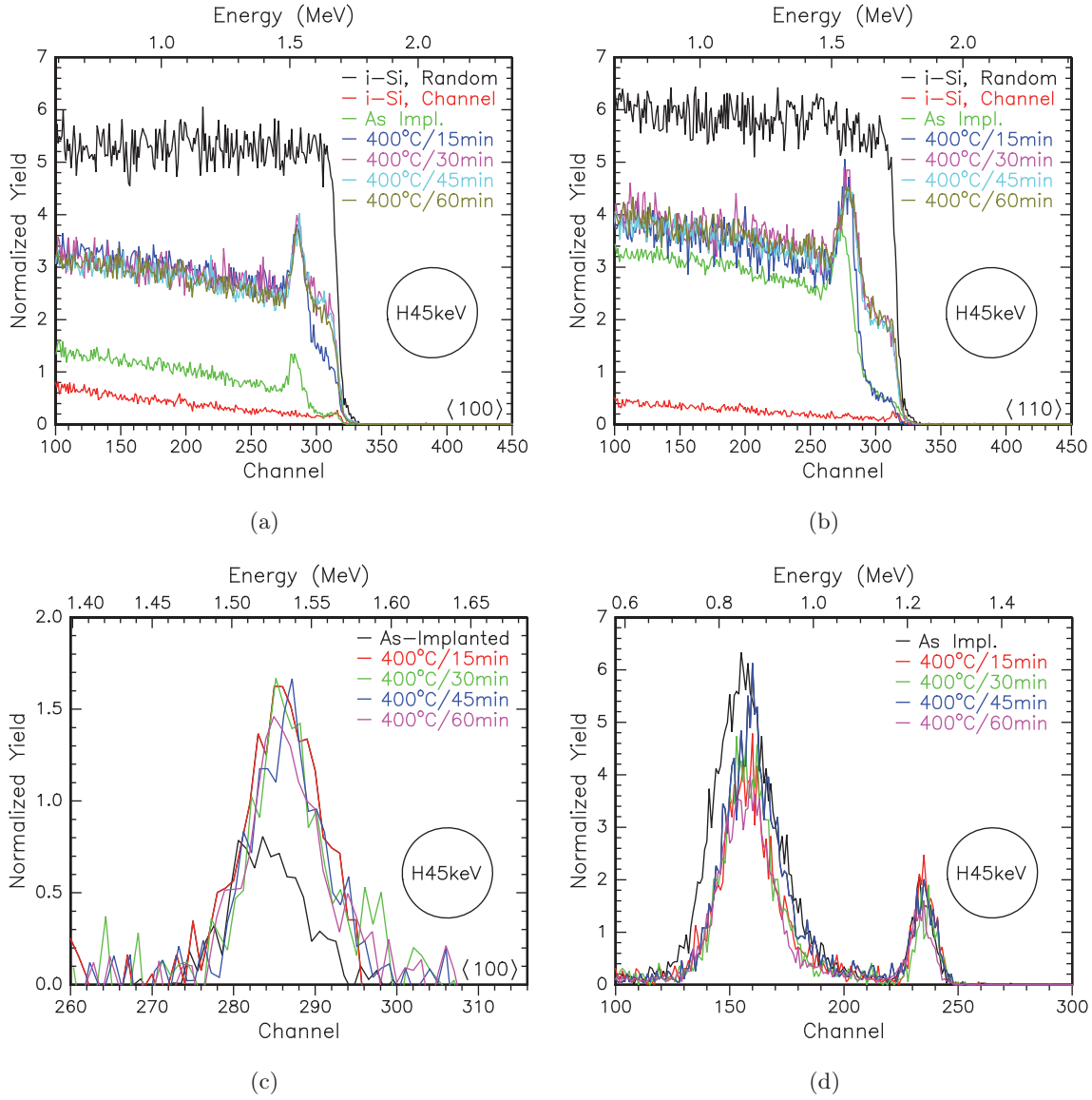

(a) (b) (c) (d)

Figure D.2: IBA measurements of Si(100) wafers implanted with hydrogen ions at $\Phi = 5 \times 10^{16}\text{cm}^{-2}$ at particular energy E=45 keV, then annealed at T=400°C in 15 minute intervals, up until t=60 minutes. **(a)-(b)** show RBS-C measurements performed along the ⟨100⟩ and ⟨110⟩ axial channels. **(c)** shows DS (∼lattice damage) peaks extracted from ⟨100⟩ RBS-C spectra, and **(d)** shows spectra of evolving hydrogen profiles determined by ERD. Beam: 3 MeV $^4\text{He}^+$, angle of back scattering detector θ=11.68°, and forward scattering detector ϕ=25°, Q=5-10 μC, I=10-22 nA.

Figure D.2 shows the RBS-C and ERD measurements in the specific case of the H(45keV, 5×10^{16}cm^{-2},RT) implantation. From each of these spectra for all the implantation energies in this section, the depths, profiles and relative yields of implantation damage and lattice distortion and hydrogen concentration were determined. These data are presented in Fig. D.3, and the extended data from which the figure was derived in Appendix D.2.

In the initially implanted and T=400°C/15 minute annealing state measurements in most of the samples, as shown in Fig. D.3, the behaviour is consistent with that previous reported [338, 349]. Despite most previous studies focusing on changes when increasing the annealing temperature, rather than our changes to the duration of the anneal, both produce equivalent effects. Upon annealing from the as-implanted state, a clear increase in dechannelling (DC) yield occurs for all the energies and along both crystal axes. The change is much less significant in the ⟨110⟩ axis than the ⟨100⟩, as the former shows only a 10-20% change in yield contrasted with a ∼100% yield increase for the latter.

By the reasoning of Di *et al.* [364], the RBS-C data showing little change in yield from the ⟨110⟩ channels ($\chi_{<110>}$), but significant effects occurring into the ⟨100⟩ channel yield ($\chi_{<100>}$), suggests two possibilities. Either there is little in the way of new hydrogen platelet formation with annealing, but an increase in other ⟨100⟩-sensitive extended defects. Alternatively, platelet formation or growth in non-(100) planes is occurring at a higher rate than (100) surface parallel platelets, increasing $\chi_{<100>}$. These non-(100) plane platelets would have to be located largely in the (110)-parallel plane, in order for the lack of influence on $\chi_{<110>}$. Both before and after annealing, the resultant $\chi_{<110>}$ is still higher than the $\chi_{<100>}$, suggesting that (100) hydrogen platelets were present in large numbers upon implantation, and remain common post-annealing. The small post-annealing increases in both $\chi_{<100>}$ and $\chi_{<110>}$ may be indicative of further {001} and {011} platelet growth, or potentially platelet development in the plane orthogonal to the ⟨111⟩ channel.

For the E=25 keV and E=65 keV implanted samples, any duration of annealing produces little change in the DS (=damage/defects) and DC (=distortion/strain) yields. In contrast, the E=45 keV and E=85 keV implanted samples show a clear increase in the near-surface yields of the channelled signals after 15 or 30 minutes annealing, along the ⟨100⟩ or ⟨110⟩ axes respectively. In the measurements for the E=45 keV implanted sample in Fig. D.2(a)-(b), the yield rapidly reaches the same degree of DC as seen after the DS peak. The amount

of damage or distortion present in the near surface layer has reached similar levels to that produced by the implantation itself. This behaviour is very similar to that reported by Ligeon and Guivarc'h [338], who reported an increase in surface DS in hydrogen-implanted silicon following annealing. Their investigation revealed the higher DC yield was due to surface blistering distorting the lattice.

Optical measurements confirmed surface blistering took place on the E=45 and 85 keV implanted samples after annealing for t=30 minutes, following easily notable discolouration of the implanted region. In addition to blisters or hydrogen-filled membranes as reported in Ligeon's work [338], the majority of the blisters appeared to have ruptured to craters. No similar discolouration was seen for either E=25 or 65 keV implanted samples, and no blistering was measured on these samples at any point in the annealing study.

It is notable that the E=25 keV and 65 keV implanted Si samples did not form blisters or surface craters, as their ion implantation energies and fluences lie within the required limits for blistering suggested in previous work [28, 334]. All four implantations were into the one Si wafer, and all were implanted from the same cathode on the one day, nominally at room temperature at a similar ion beam current. Given these details, it is curious to note that the sample implanted at E=65 keV did not blister while both E=45 keV and 85 keV samples did. The reason for the lack of blistering remains a puzzle.

Examining the evolution in the implantation damage via the DS peaks in Fig. D.3(c), there are clear signs of what has been termed *reverse annealing* [28, 44, 349]. In a model proposed by Di *et al.* [349], this peak shift is theorised to be caused by the different local densities of interstitials and vacancies due to the implantation process present on either side of the hydrogen profile. The greater number of such defects *shallower* than the profile allows more H_2 nucleation and mono- and divacancy formation *deeper* than the hydrogen peak. At elevated temperatures however, reached via annealing or other means, the V_nH_m (where $n \geqslant m$) complexes present *shallower* than the hydrogen peak begin to be broken up, facilitating the creation of hydrogen platelets within the silicon.

In all implantations and independent of axial channel probed, following the initial stages of annealing, the DS peak depth shifts towards the surface. As in previous work [349], the rear position of the DS peaks does not change, while the front migrates towards the surface, giving good agreement to the proposed model for *reverse annealing*. The shift in depth

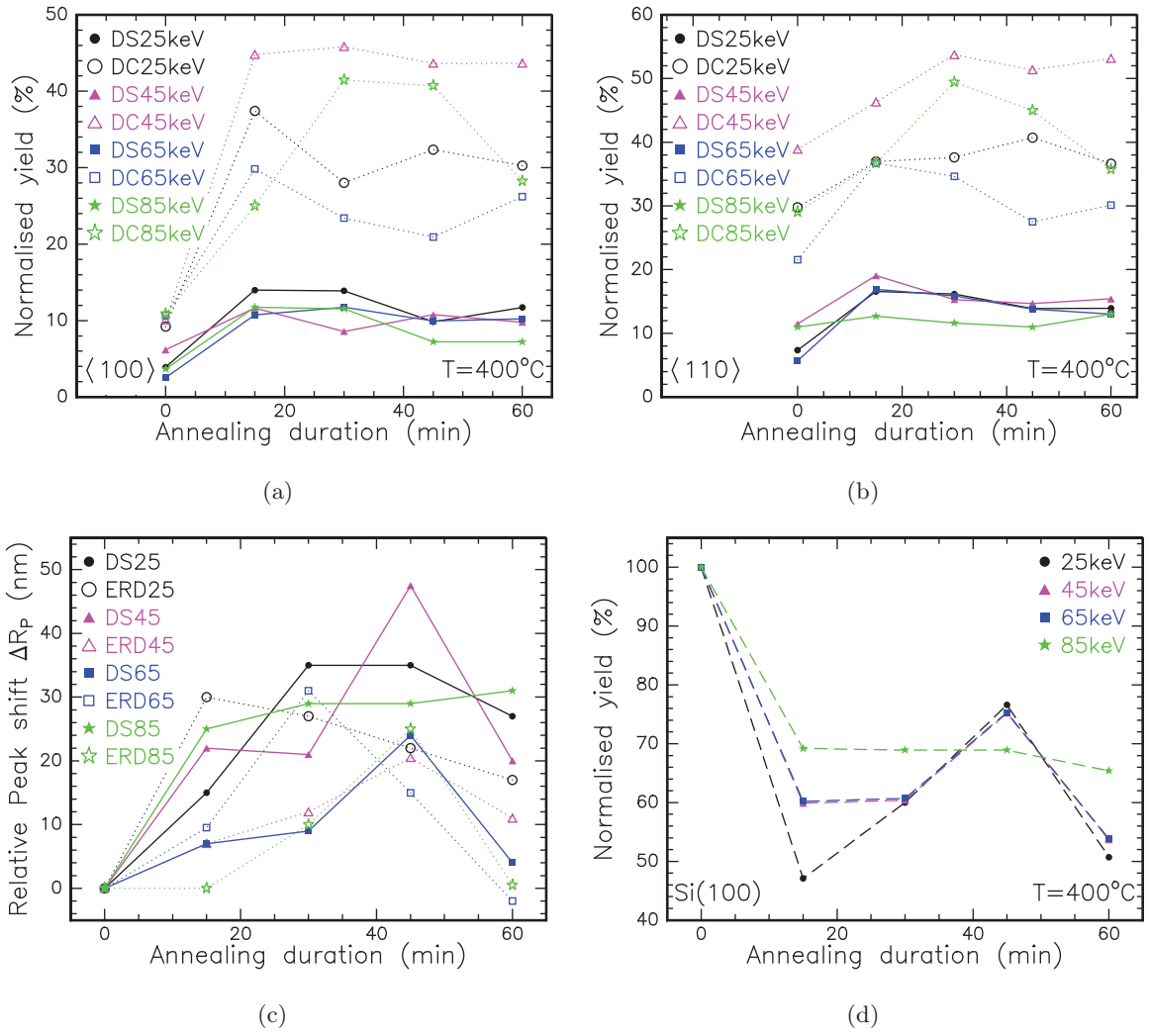

Figure D.3: IBA measurements of Si(100) wafers implanted with hydrogen ions at $\Phi = 5{\times}10^{16}\text{cm}^{-2}$ at energies from E=25-85 keV, then annealed at T=400°C in 15 minute intervals, up until t=60 minutes. **(a)-(b)** show RBS-C determined direct scattering **(DS)** and dechannelling **(DC)** yields along the ⟨100⟩ and ⟨110⟩ axial channels. **(c)** shows change in depth towards the sample surface of the DS (∼lattice damage) peaks extracted from ⟨100⟩ RBS-C spectra, in addition to the hydrogen profile peaks R_P from ERD spectra. **(d)** shows ERD yield from evolving hydrogen profiles. Beam: 3 MeV $^4\text{He}^+$, angle of back scattering detector θ=11.68°, and forward scattering detector ϕ=25°, Q=5-10 μC, I=10-22 nA.

range may be linked to the yield increases in local lattice damage, as DS peak yield increases in the initial annealing stages as the peak depth becomes shallower. However, the yield of the DS peaks remains largely constant after the initial anneal of T=400°C/15 minutes, shown in Fig. D.3(a)-(b). This suggests all annealing-induced evolution in the damage and hydrogen profiles has already occurred by this stage.

If we were to contrast this RBS-C data with the ERD measured normalised yield of hydrogen implanted into the samples, shown in Fig. D.3(d), similar trends are borne out. A significant decrease in hydrogen concentration was measured for all samples following the initial 15 minute anneal, and then the normalised yield χ_H remains largely unchanged. The percentage of initial hydrogen lost from the sample exhibits some inversely proportionality to the implantation depth, with $\chi_H(25\text{keV}, 15\text{min})$ almost a third smaller than $\chi_H(85\text{keV}, 15\text{min})$. Hydrogen loss is of similar magnitude in all samples, and occurs at this rate independently of any surface blistering. This raises questions as to why blistering occurred in some samples and not others, if conditions allow hydrogen to be lost through (possibly) less energetically costly means. As a possible corollary to *reverse annealing*, the depth of the hydrogen profile peak R_P also shifts closer to the surface with longer annealing duration. Unlike the ion damage profile, the end-of-range (EOR) of the hydrogen profiles also shifts toward the surface during annealing.

The consistency in hydrogen yield across samples for t>15 minutes annealing suggests that any processes by which hydrogen is converted to platelets, forms blisters and then escapes as they burst, as observed in the E=45 and 85 keV implanted samples, has already taken place by this time. Considering that over 50% of the implanted hydrogen remains in these samples despite the appearance of blisters, this seems unlikely. Also, as seen in discussions of blistering dynamics and kinetics, the blister production process is unlikely to have completed after only 15 minutes – at T=400°C, H(40keV,6×10^{16}cm^{-2},RT)-implanted Si(100) is observed to take over two hours for surface blisters to *begin* appear! Assuming the process has reached completion, only half of the implanted fluence is released from the silicon, indicating significant concentrations are still present. Such levels of hydrogen doping could prove parasitic or toxic to device fabrication, yet considering SmartCut™'s use in such production, the residual hydrogen concentrations must be lower if the entire layer was lifted off, rather than blistering.

As the RBS-C yields do not change significantly following initial annealing, and only half the implanted hydrogen is being lost from the substrate, this may suggest that the remaining hydrogen is trapped in defects and complexes such as platelets and coating internal cavities, located within the ion implantation damage region. No new platelets or defect features were observed, nor significant change in hydrogen concentration, damage profile or DC yield after initial annealing. Greater duration of annealing, or higher temperatures, may be required to break the bonds preventing them from either diffusing out of the sample, or forming into gas-filled blisters.

Conclusion

RBS-C demonstrated as-implanted DS and DC yields were higher in ⟨110⟩-channelled measurements, indicating most hydrogen was present in defects and complexes within the surface-parallel (100) plane, such as platelets. Following annealing, the greatest yield increase was in ⟨100⟩ measurements, with little change in the ⟨110⟩ yield, indicating defect formation increasingly in the (110) plane. Following initial annealing t>15 minutes, little change was observed in DS, DC or ERD-determined hydrogen yields. Independent of gross behaviour differences – surface blisters forming only for E=45 keV and 85 keV implanted samples – approximately the same amount of hydrogen loss occurred from all samples, proportional to annealing duration. The lack of increase in the RBS-C DS or DC yields after t>15 minutes suggests a cessation of new defect or platelet formation [28,55,133,175, 265,349,420], while the lack of hydrogen loss beyond ∼50% of the implanted concentration suggests hydrogen is strongly trapped in the defects formed in implantation and early stages of annealing. The required energy and kinetics to liberate this hydrogen into blisters or ruptured into craters may allow understanding of the forms into which this hydrogen is tightly bound.

This study leads us to ask the following question: what is required to shift from production of internal hydrogen platelets and defects to external hydrogen blisters and craters? Exploration of this question is found in Section 4.4.

D.2 Ion beam analysis techniques

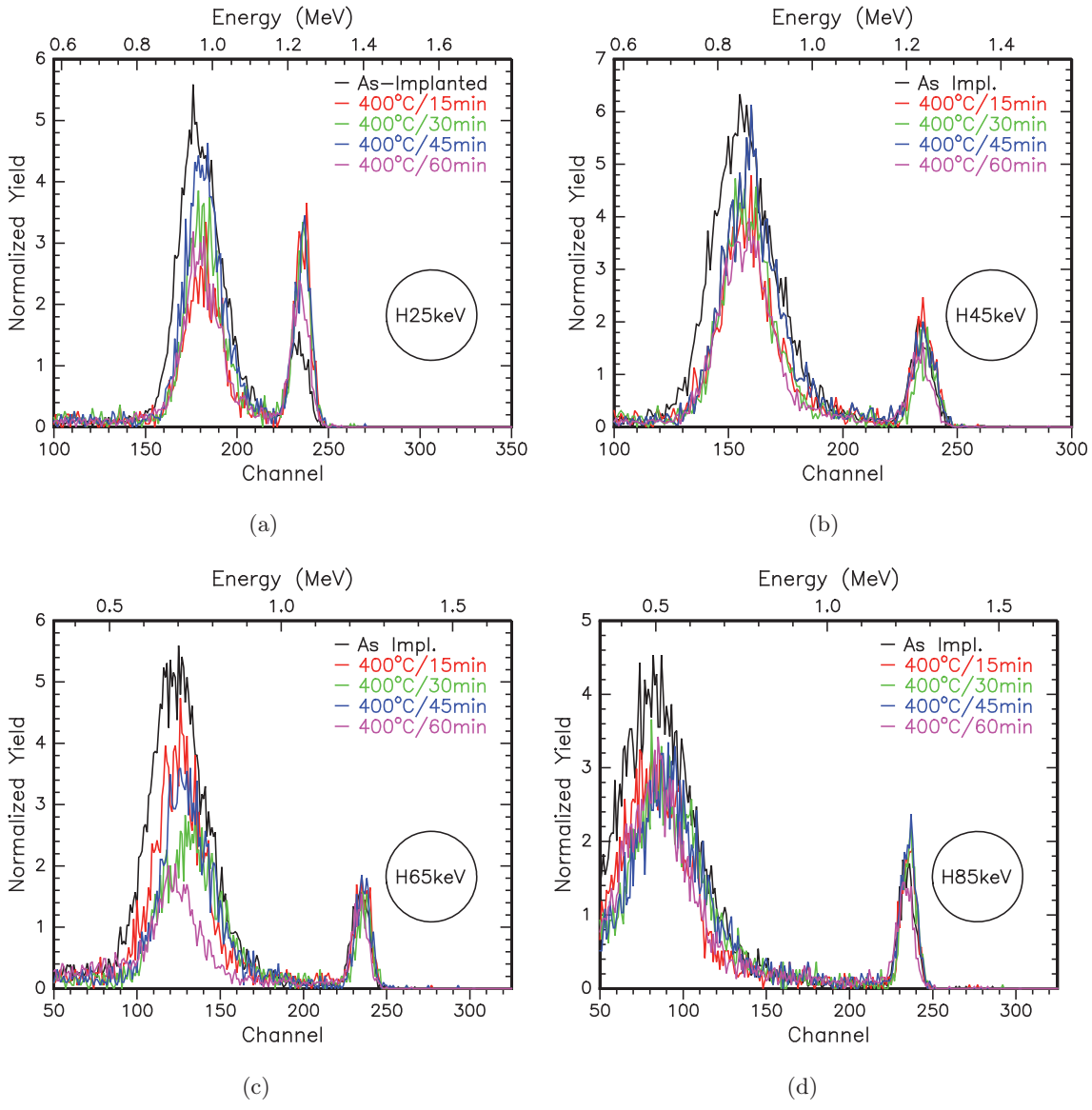

Figure D.4: 3MeV He beam ERD spectra obtained from an annealing series of hydrogen-implanted Si(100), at a fluence $\Phi = 5 \times 10^{16}\text{cm}^{-2}$, at energies ranging from E=25-85 keV as labelled in plots. Anneals performed at T=400°C in 15 minute intervals, in an Ar ambient quartz tube furnace.

Implantation E (keV)	25		45		65		85	
Annealing Conditions	Yield %	ρ ($\times 10^{16}$cm^{-2})	Yield %	ρ ($\times 10^{16}$cm^{-2})	Yield %	ρ ($\times 10^{16}$cm^{-2})	Yield %	ρ ($\times 10^{16}$cm^{-2})
As Implanted	100	5.00	100	5.00	100	5.00	100	5.00
T=400°C/15min	47.1	2.36	59.9	3.00	60.2	3.01	69.2	3.46
T=400°C/30min	60.0	3.00	60.4	3.02	60.7	3.03	68.9	3.45
T=400°C/45min	76.6	3.83	75.2	3.76	75.3	3.77	68.9	3.44
T=400°C/60min	50.7	2.54	53.7	2.68	53.8	2.69	65.4	3.27

Table D.1: Relative hydrogen areal densities measured by ERD in Si(100) implanted at room temperature at a fluence of Φ=5$\times 10^{16}$cm^{-2} and energies as labelled, to three significant figures. Density values calculated assuming standard implantation of 5$\times 10^{16}$cm^{-2} is represented accurately in the as-implanted data shown in Fig. D.4. Data also plotted in Fig. D.3(d).

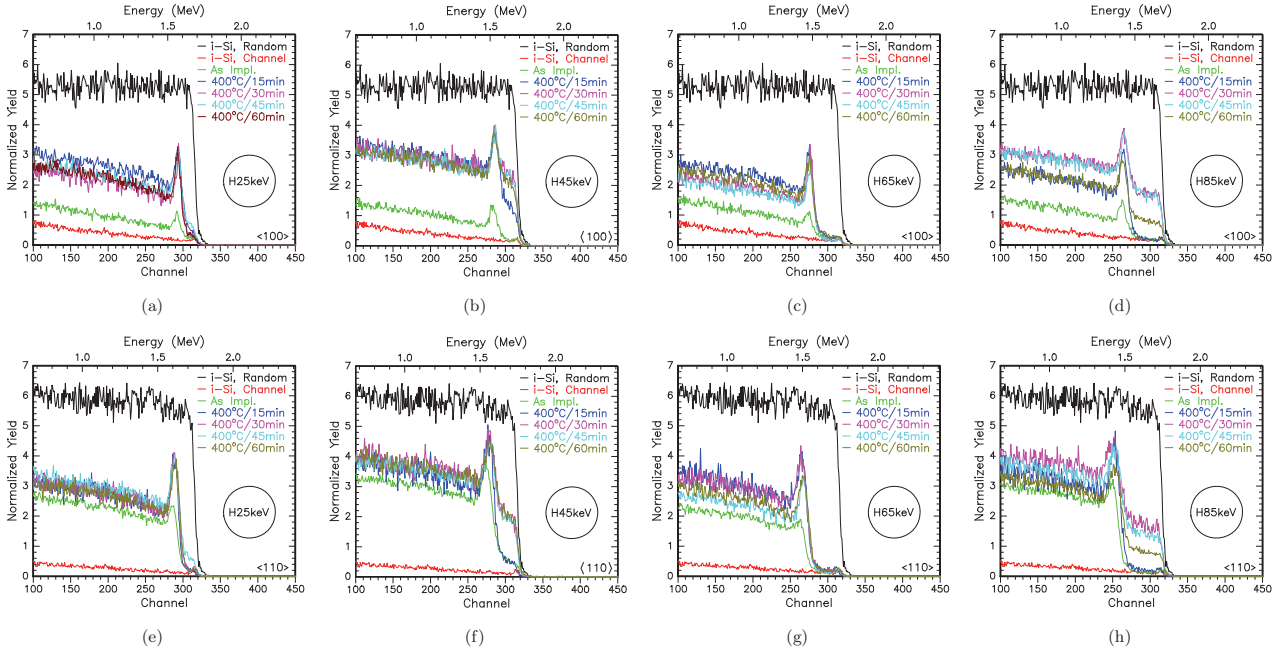

Figure D.5: RBS-C spectra of Si(100) wafers implanted with hydrogen ions at $\Phi = 5 \times 10^{16}\text{cm}^{-2}$ at energies between E=25 keV and E=85 keV in 25 keV steps, then annealed at T=400°C in 15 minute intervals, up until t=60 minutes. (a)-(d) show measurements performed along the ⟨100⟩ crystal axis, while (e)-(h) show those along ⟨110⟩ for the same samples.

Implantation E (keV)	25		45		65		85	
Dechannelling Yield (%)	⟨100⟩	⟨110⟩	⟨100⟩	⟨110⟩	⟨100⟩	⟨110⟩	⟨100⟩	⟨110⟩
As Implanted	9.21	29.8	10.1	38.9	10.7	21.5	10.9	29.1
T=400°C/15min	37.4	36.9	44.8	46.3	29.8	36.7	25.0	36.7
T=400°C/30min	28.0	37.6	45.8	53.7	23.4	34.6	41.5	49.4
T=400°C/45min	32.4	40.7	43.6	51.4	20.9	27.5	40.7	45.0
T=400°C/60min	30.3	36.6	43.7	53.1	26.2	30.1	28.2	35.7

Table D.2: Normalised RBS-C dechannelling yields measured in Si(100) implanted with hydrogen at room temperature to a fluence of Φ=5×10^{16}cm^{-2} and energies as labelled, along ⟨100⟩ and ⟨110⟩. Yield values given to three significant figures. Original spectra shown in Fig. D.5, and plotted in Fig. D.3(a)-(b).

Implantation E (keV)	25		45		65		85	
Direct Scattering Yield (%)	⟨100⟩	⟨110⟩	⟨100⟩	⟨110⟩	⟨100⟩	⟨110⟩	⟨100⟩	⟨110⟩
As Implanted	3.91	7.35	6.18	11.5	2.53	5.70	3.68	11.0
T=400°C/15min	14.0	16.6	11.7	19.1	10.8	16.9	11.7	12.7
T=400°C/30min	13.9	16.2	8.57	15.3	11.7	15.9	11.5	11.6
T=400°C/45min	9.84	13.9	10.8	14.7	9.94	13.8	7.24	11.0
T=400°C/60min	11.7	13.9	9.79	15.4	10.2	13.0	7.23	13.0

Table D.3: Normalised RBS-C direct scattering peak yields measured in Si(100) implanted with hydrogen at room temperature to a fluence of Φ=5×10^{16}cm^{-2} and energies as labelled, along ⟨100⟩ and ⟨110⟩. Yield values given to three significant figures. Original spectra shown in Fig. D.5, and plotted in Fig. D.3(a)-(b).

Implantation E (keV)	25		45		65		85	
Direct Scattering Peak (nm)	R_P	ΔR_P	R_P	ΔR_P	R_P	ΔR_P	R_P	ΔR_P
As Implanted	370±3	0.0	480±10	0.0	592±2	0.0	760±3	0.0
T=400°C/15min	355±2	15	458±5	22	585±5	7.0	735±2	25
T=400°C/30min	335±3	35	459±3	21	583±5	9.0	731±3	29
T=400°C/45min	335±3	35	433±3	47	568±2	24	731±3	29
T=400°C/60min	343±3	27	460±5	20	588±3	4.0	729±4	31

Table D.4: RBS-C direct scattering peak depth and shift measured in Si(100) implanted with hydrogen at room temperature to a fluence of Φ=5×10^{16}cm^{-2} and energies as labelled, along ⟨100⟩. Depth values given to three significant figures, in nanometres. Original spectra shown in Fig. D.6, and these data plotted in Fig. D.3(c).

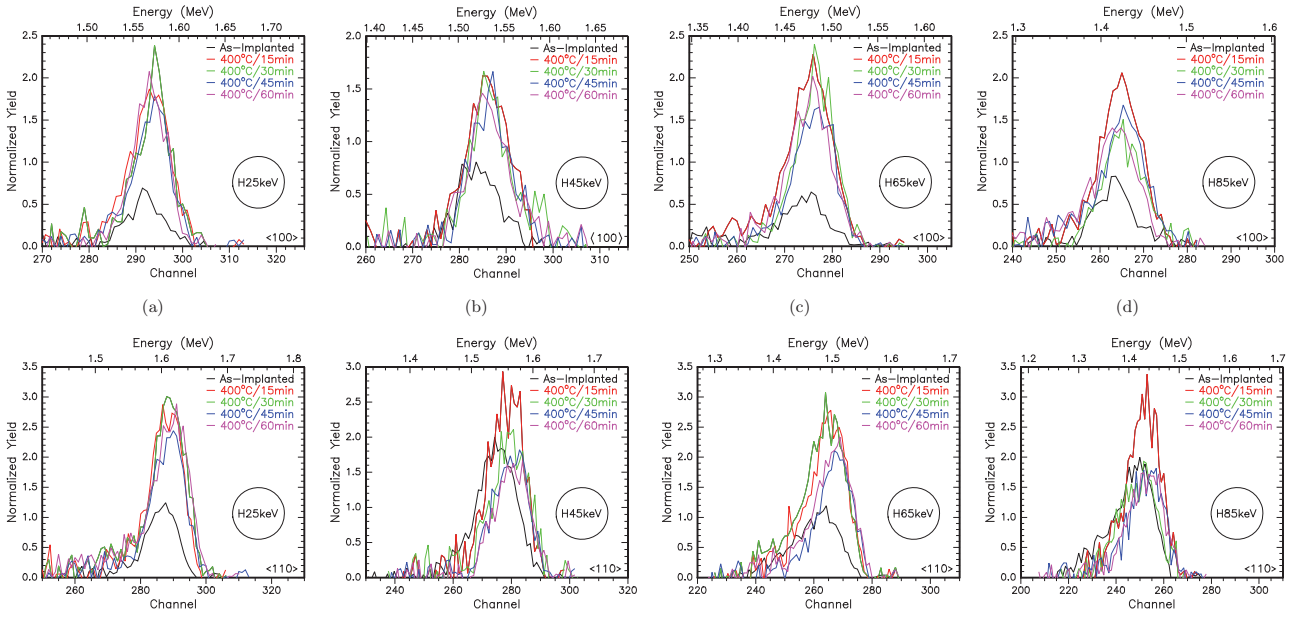

Figure D.6: Direct scattering peaks extracted from RBS-C spectra of Si(100) wafers implanted with hydrogen ions at $\Phi = 5 \times 10^{16}\text{cm}^{-2}$ at energies between E=25 keV and E=85 keV in 25 keV steps, then annealed at T=400°C in 15 minute intervals, up until t=60 minutes. (a)-(d) show measurements performed along the ⟨100⟩ crystal axis, while (e)-(h) show those along the ⟨110⟩ upon the same samples. Silicon surface is found at channel 319; lower channels indicate deeper into material.

D.3 Blister monitoring and recording

As described in Section 4.6.1, attempts were made to fit logistic sigmoidal functions (JMAK and Gompertz) to the blister areal density with respect to time data. The individual figures of these fits for Si(100), Si(110), Si(111) and Ge(100) implanted with H(40keV) at fluences as labelled, are shown.

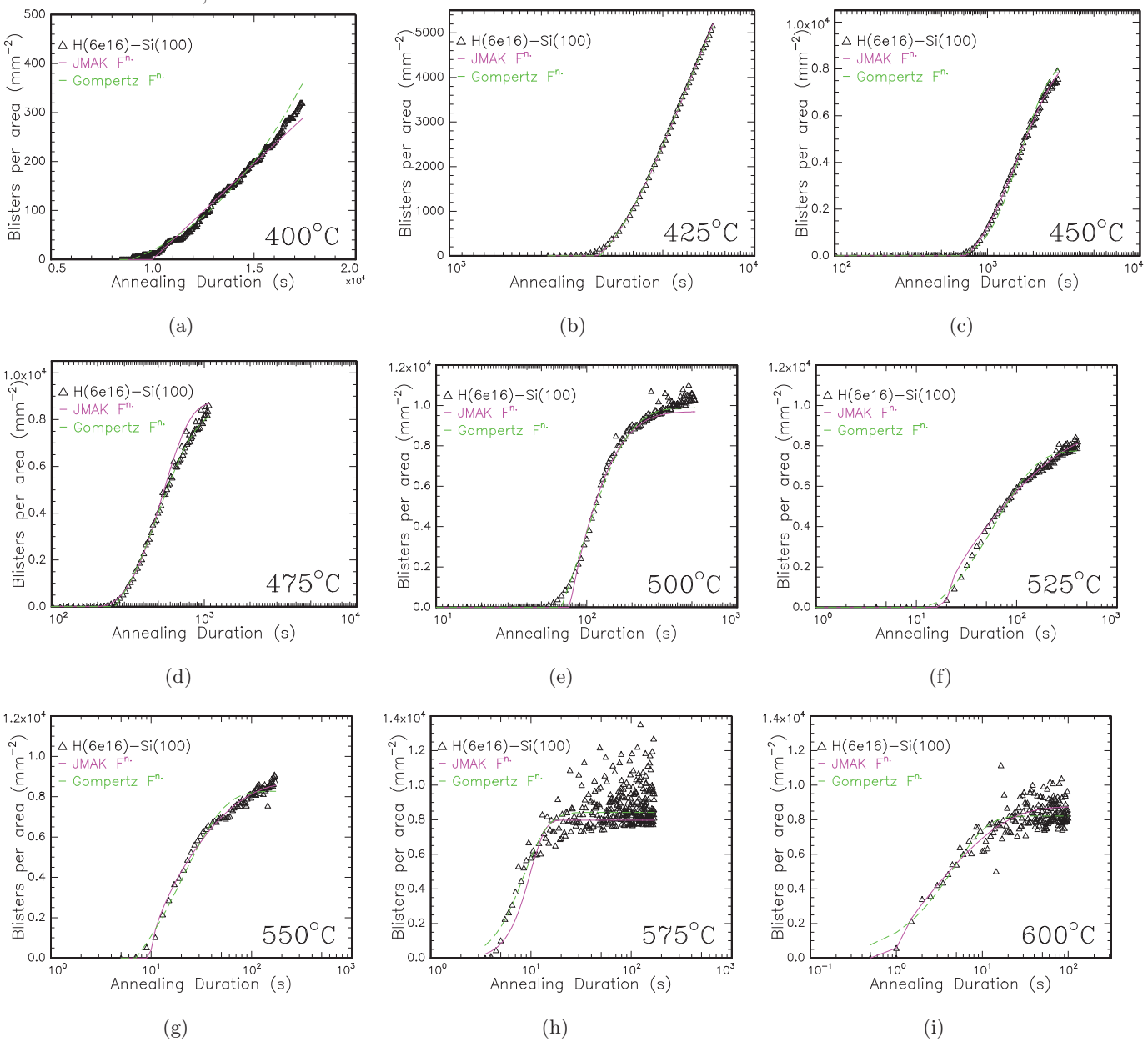

Figure D.7: Comparing rate of blistering per unit area per time in annealed H(40keV,6×10^{16}cm^{-2},RT)-implanted Si(100), with rates predicted by Eq. 4.5 (JMAK) and 4.6 (Gompertz), for temperatures as labelled in plots.

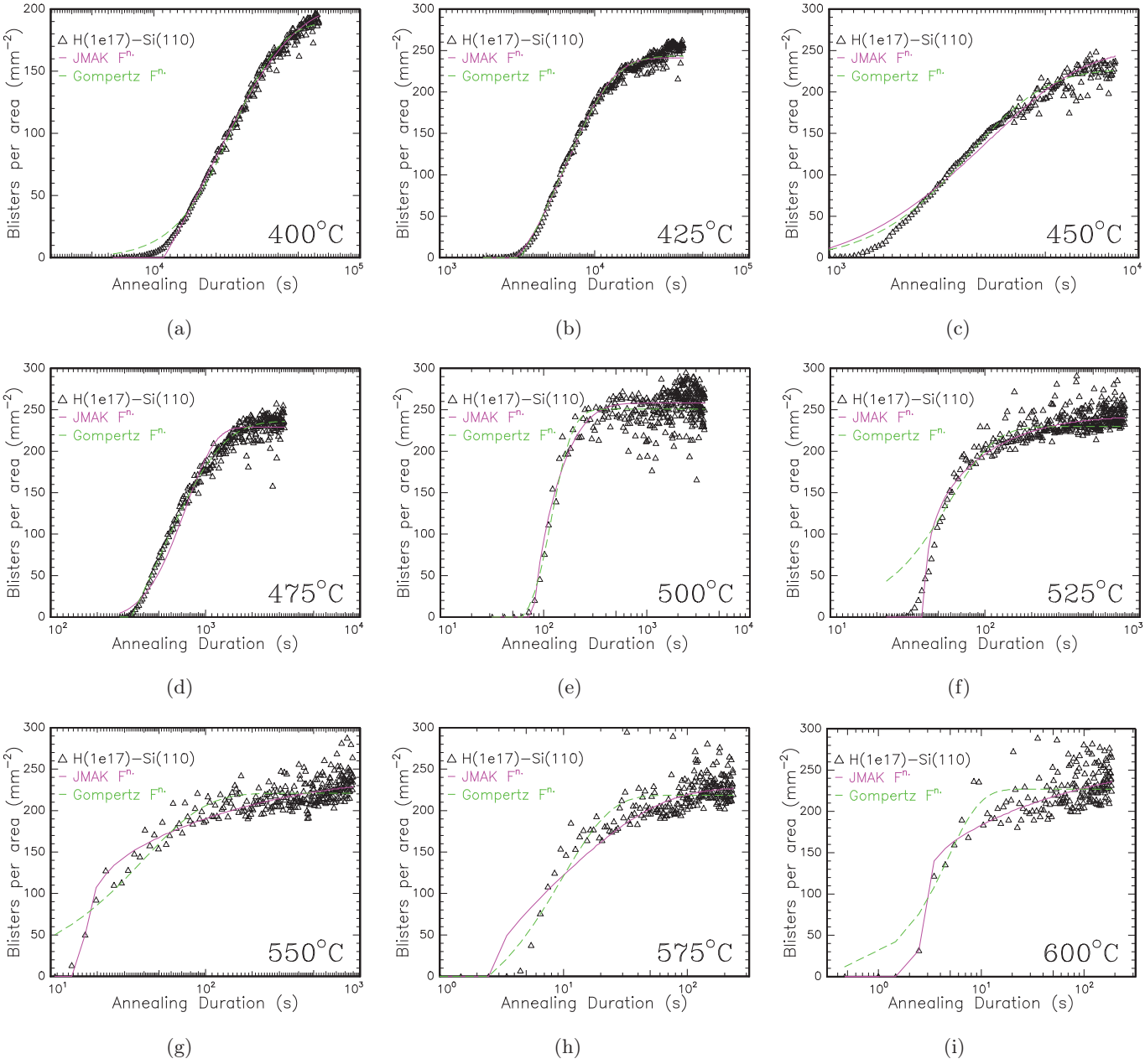

Figure D.8: Comparing rate of blistering per unit area per time in annealed H(40keV,1×10^{17}cm^{-2},RT)-implanted Si(110), with rates predicted by Eq. 4.5 (JMAK) and 4.6 (Gompertz), for temperatures as labelled in plots.

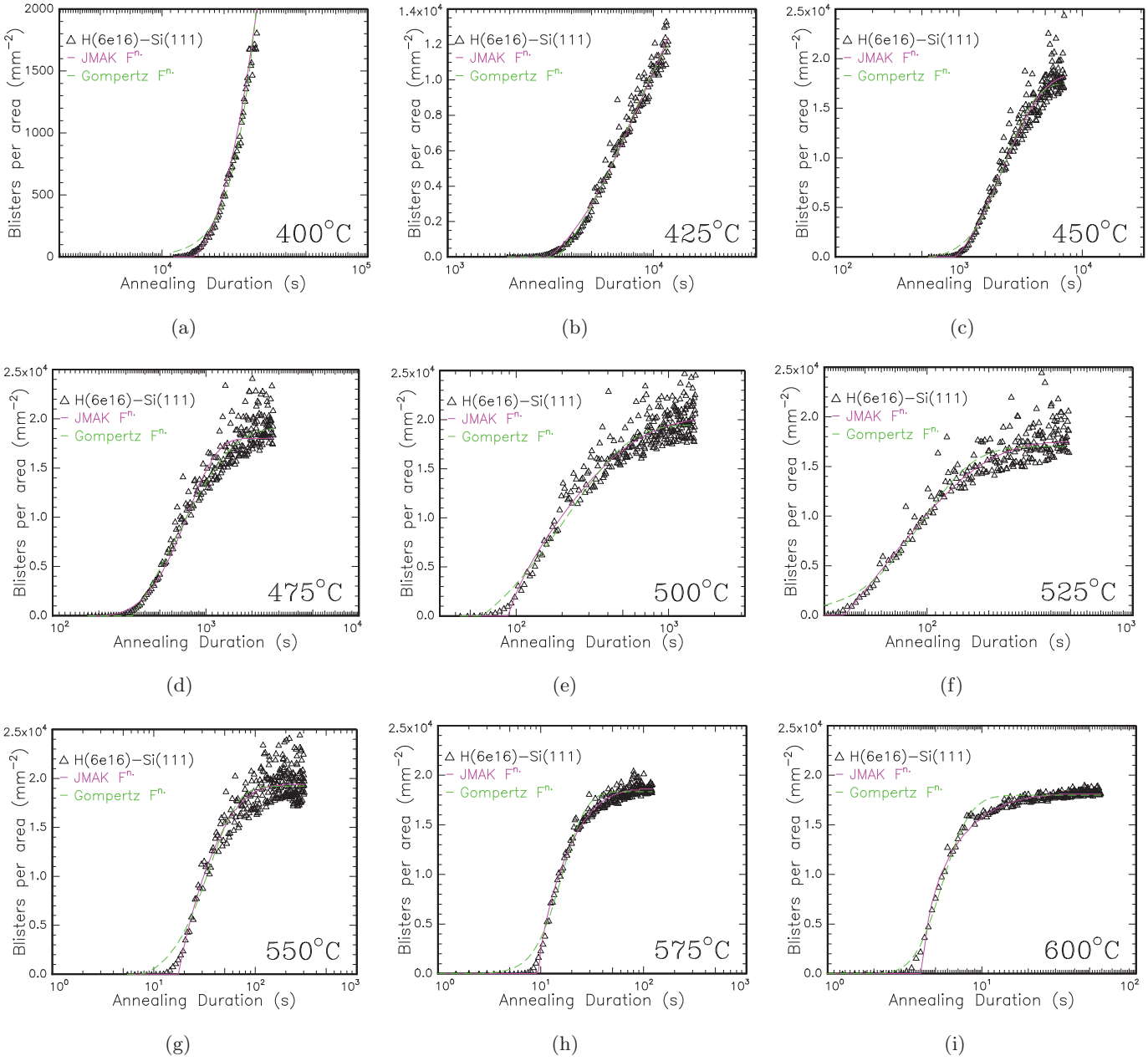

Figure D.9: Comparing rate of blistering per unit area per time in annealed H(40keV,6×10^{16}cm^{-2},RT)-implanted Si(111), with rates predicted by Eq. 4.5 (JMAK) and 4.6 (Gompertz), for temperatures as labelled in plots.

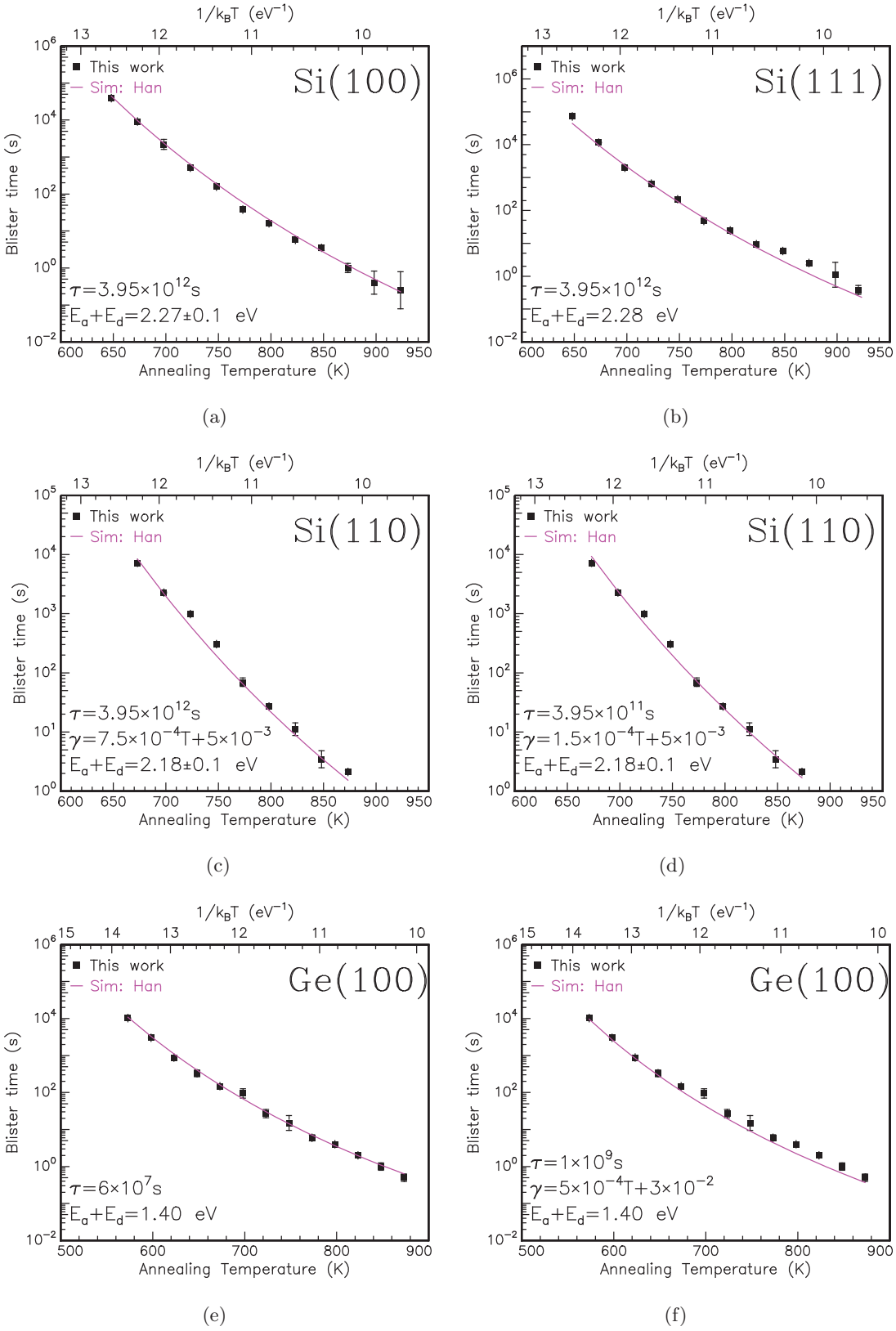

Figure D.10: Comparing inverse onset time for hydrogen blistering per inverse absolute temperature measured in hydrogen-implanted (a) Si(100), (b) Si(111), (c-d) Si(110) and (e-f) Ge(100), with theoretical values calculated by Han *et al.* [343] in magenta. Implant H(40keV,6×10^{16}cm^{-2},RT) for all but Si(110), with H(40keV,1×10^{17}cm^{-2},RT). Labels included activation energies experimentally derived and used in model, modified value for X-H bond jump frequency τ, and surface crack energy $\gamma(T)$.

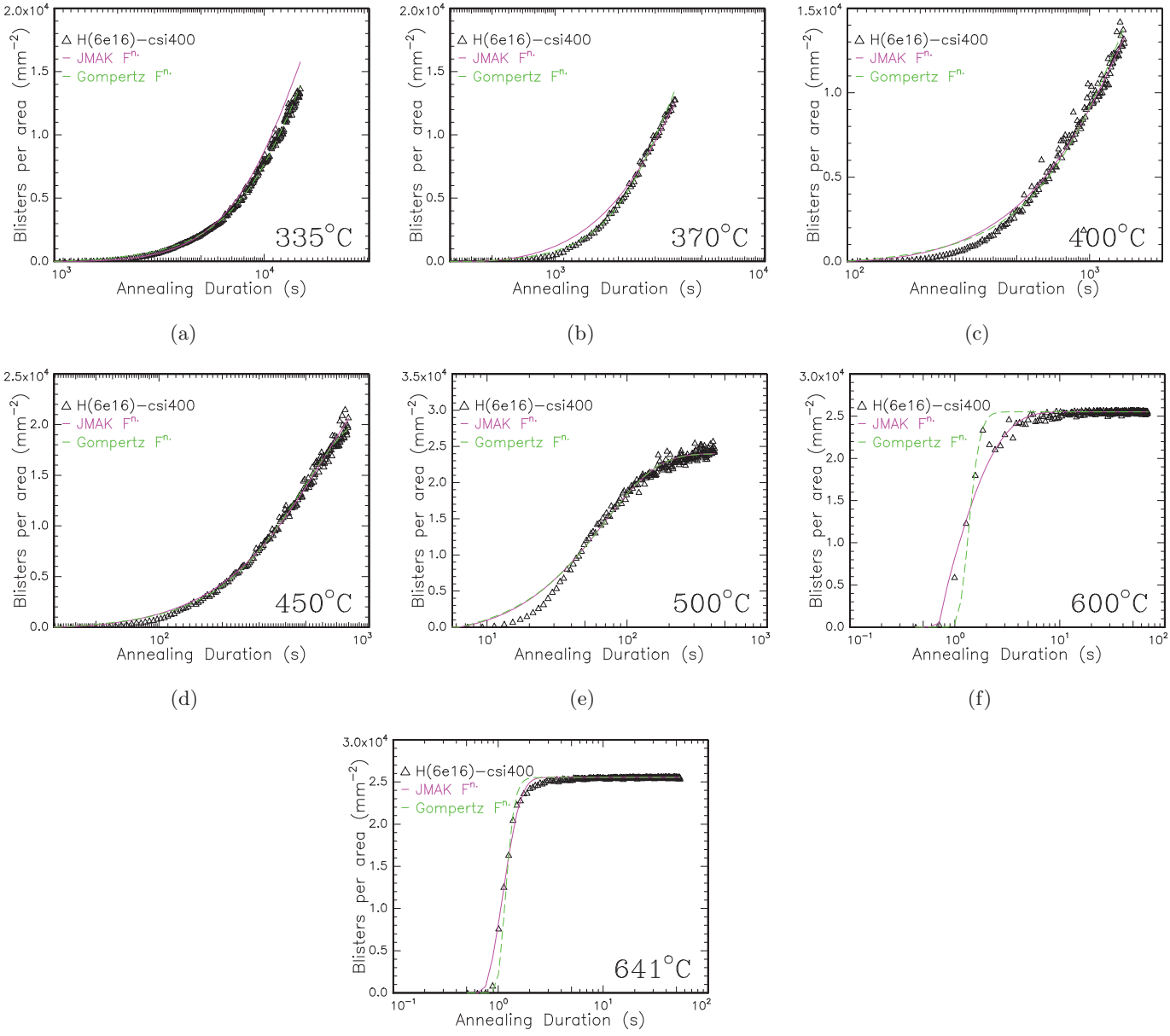

Figure D.11: Comparing rate of blistering per unit area per time in annealed H(40keV,6×10^{16}cm^{-2},RT)-implanted heavily B-doped Si(111), labelled csi400 in text, with rates predicted by Eq. 4.5 (JMAK) and 4.6 (Gompertz), for temperatures as labelled in plots.

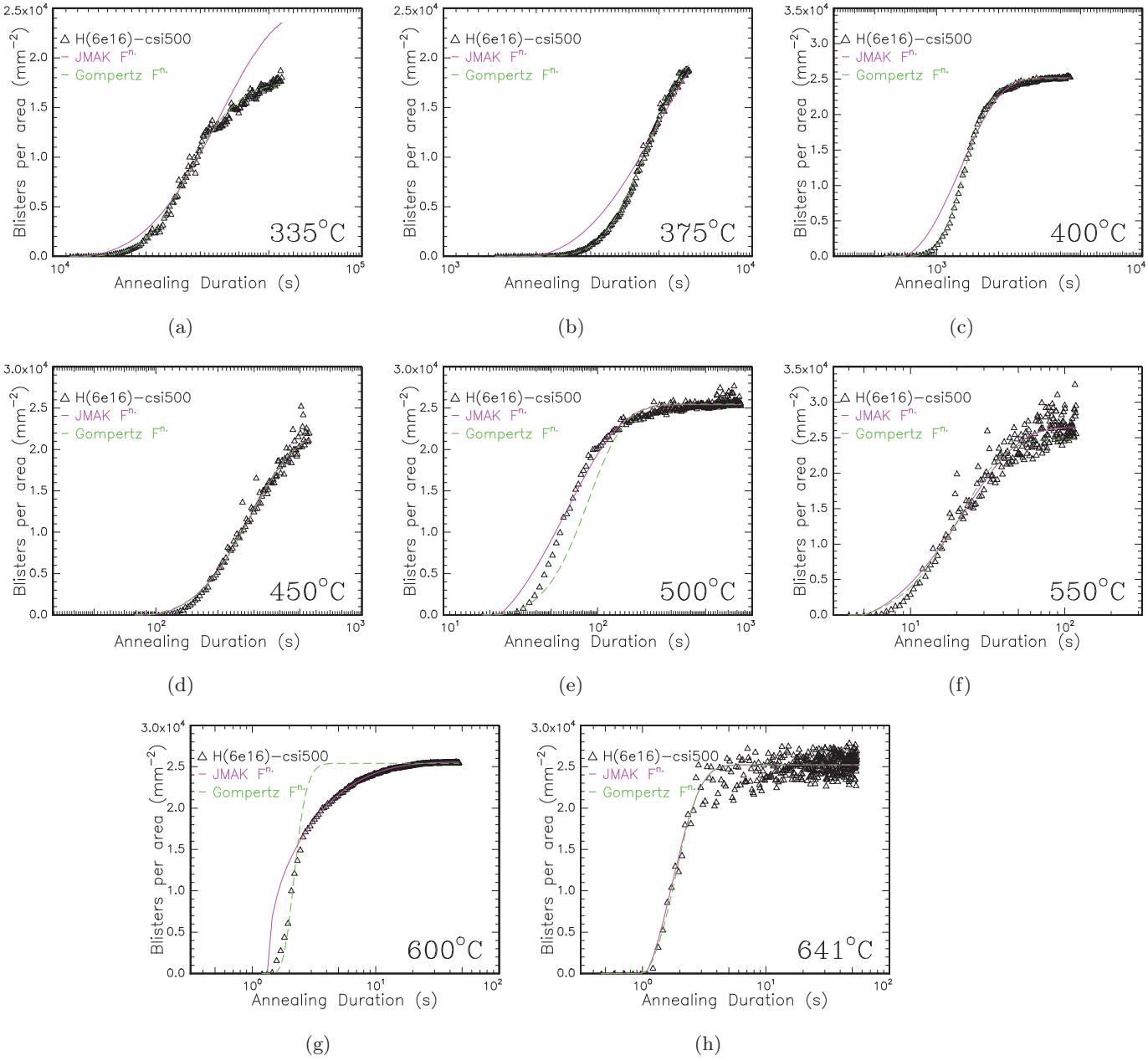

Figure D.12: Comparing rate of blistering per unit area per time in annealed H(40keV,6×10^{16}cm^{-2},RT)-implanted heavily P-doped Si(111), labelled csi500 in text, with rates predicted by Eq. 4.5 (JMAK) and 4.6 (Gompertz), for temperatures as labelled in plots.

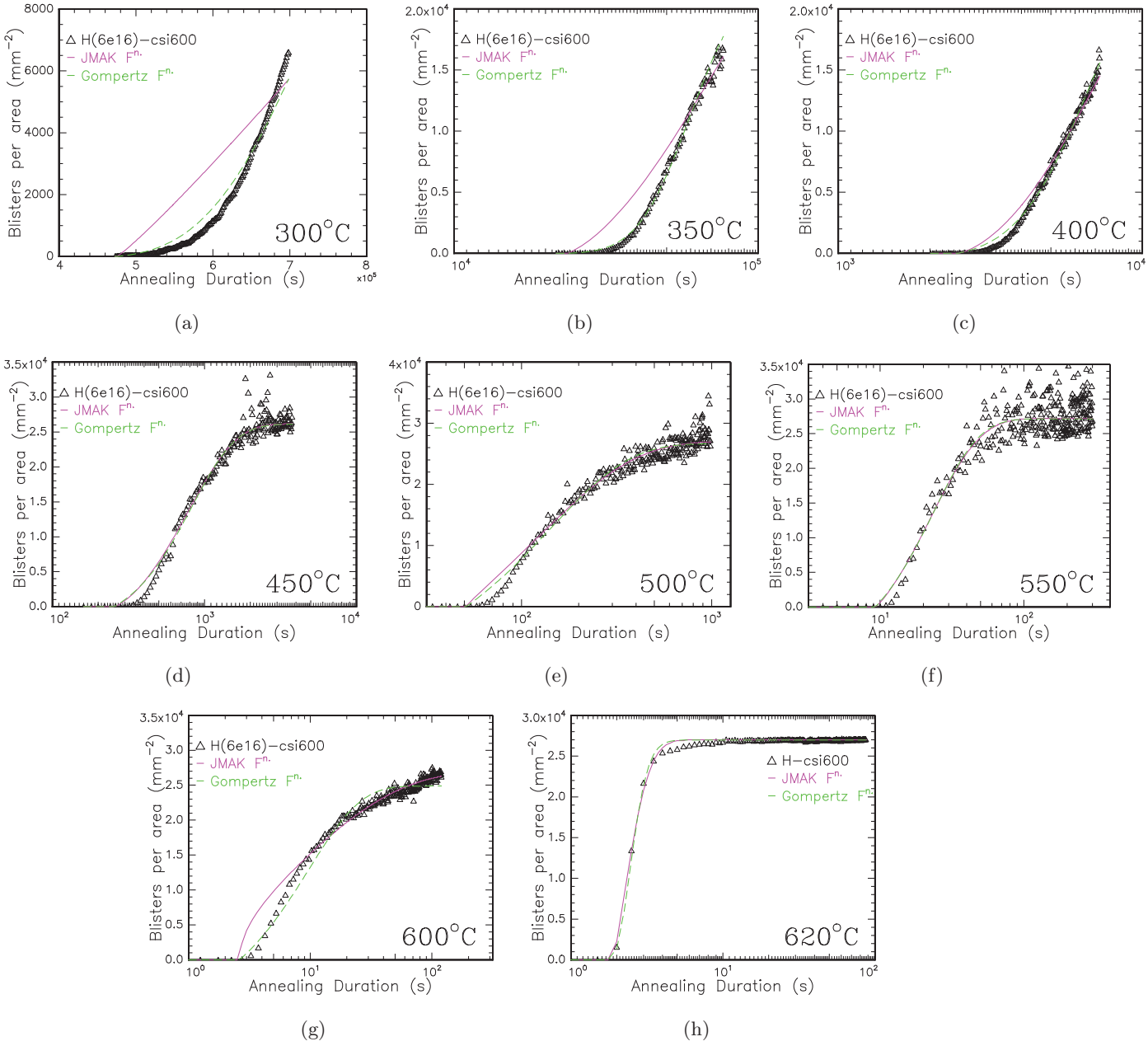

Figure D.13: Comparing rate of blistering per unit area per time in annealed H(40keV,6×10^{16}cm^{-2},RT)-implanted heavily As-doped Si(111), labelled csi600 in text, with rates predicted by Eq. 4.5 (JMAK) and 4.6 (Gompertz), for temperatures as labelled in plots.

Temperature	Silicon		Germanium	
	(100)	(111)	3×10^{16}cm^{-2}	6×10^{16}cm^{-2}
300°C	-	-	6.44	-
350°C	-	-	5.69	-
375°C	-	-	7.96	-
400°C	5.42	5.43	8.86	-
425°C	6.35	5.56	9.51	-
450°C	6.84	6.47	10.50	4.42
475°C	7.63	7.00	11.15	4.88
500°C	8.02	7.53	13.73	4.08
525°C	9.37	8.60	11.43	4.95
550°C	8.83	9.71	12.33	5.56
575°C	8.92	8.99	10.85	4.66
600°C	9.29	10.58	10.03	-

Table D.5: Average ruptured blister (=crater) diameter measured by optical profilometry from post-annealing hydrogen-implanted semiconductors, at temperatures as labelled. Implantation H(40keV,6×10^{16}cm^{-2},RT) and crystal orientation (100) unless indicated otherwise. Measurements in micrometres. Profiler settings: PSI mode, ×50 lens, F.o.V. ×2.0.

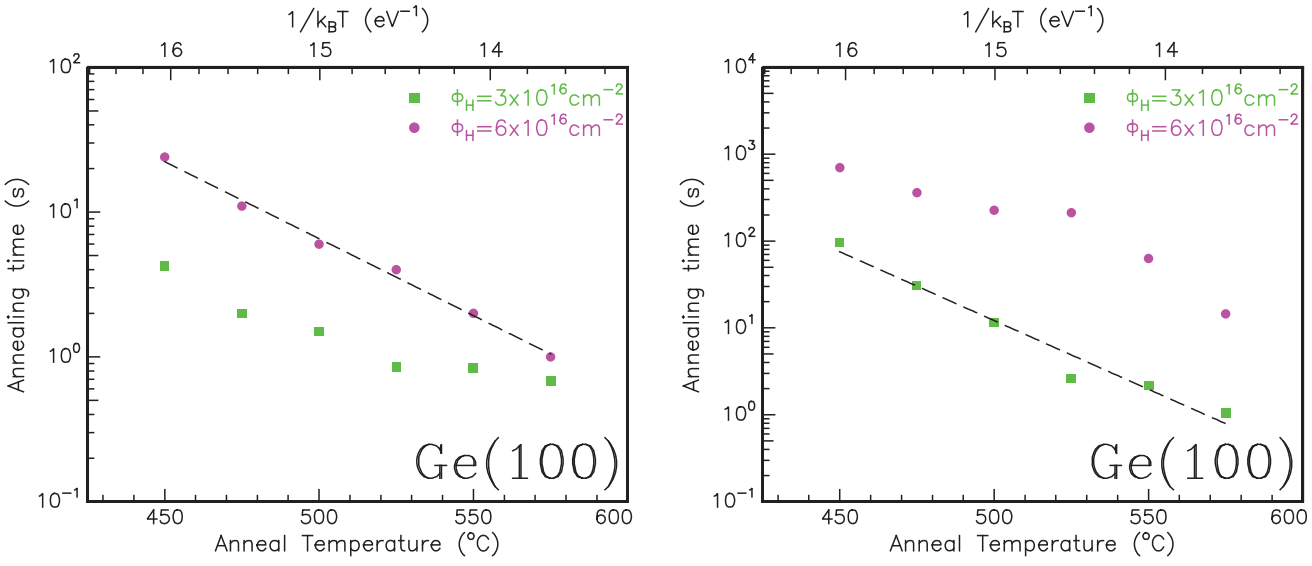

(a) Blister Appearance Time

(b) Blister Areal Saturation Time

Figure D.14: Comparison of (a) surface blister appearance (t_{appear}) and (b) surface area saturation ($t_{saturate}$) times for H-implanted Ge(100) during annealing. Implantation conditions: E=40 keV and room temperature, fluences as labelled. Data presented in Table. 4.4.

D.4 Justifying modifications to Han *et al.*'s Model

When modelling the activation energy and blister occurrence time for H-implanted Si(100) using the model proposed by Han *et al.* [343] and discussed in Section 4.6.2, we get excellent agreement in activation energies, but notice a temporal offset in the starting times. In order to accommodate this difference in data and theory, the model must be adjusted appropriately. The longer justification for that modification is provided here.

Between the data and the model, the difference in the pre-exponential factors is 1:33, with Han's theory predicting blistering to occur later than the experimental data show. However, the activation energy extracted from the data fits are in excellent agreement. Considering this offset, the factors which could account for the difference between the theory and the data are the energies E_a and E_d, the hydrogen fluence ϕ_0, the crack surface tension $\gamma(T)$, or the value relating the hydrogen complex's jump frequency, τ.

Were we to consider the hydrogen fluence as requiring modification, we are confronted with difficulties of accommodating sufficient change or error in the implantation fluence to match the two results. Note that the same temporal offset is largely expected to be regulated by the hydrogen fluence in Han [343] (see Fig. 5 in that paper), as can be seen in Eq. 4.7. When the value of hydrogen fluence is halved in the model, the corresponding predictions of the splitting time increase by a factor of ∼2.5. Similarly, if the fluence is increased to $\Phi = 1.5 \times 10^{17}\text{cm}^{-2}$, then the corresponding splitting times are decreased from the "standard conditions" implantation by a factor of ∼2.75. Given this is the case, in order for the simulation to reach the same times for blistering as measured over the course of this project, the fluence applied would have to be a gargantuan $\Phi = 2.5 \times 10^{17}\text{cm}^{-2}$! This is discounted as a possibility, as while small variations in the implanted fluence may be possible, such a significant change is unlikely to have occurred without gross negligence on numerous occasions.

It does remain possible that external stresses could also account for off-set in the system. Complementary arguments by Weldon *et al.* [106] ascribe the dynamic behaviour of the blisters' sizes to the presence or otherwise of the handle wafer in ion-cut applications. Dynamic influences of varying stress levels present within the wafer generally, and specifically around the hydrogen implantation profile, are key to the evolution of the hydrogen-silicon

system. However, in the model discussed here, Han is clearly modelling a system without a handle wafer or other attachment, which is the same system studied in our project. There is not thus a case for the differences between the systems in terms of stress to account for the differences.

If the values of the crack surface tension $\gamma(T)$ entered into the calculations of Han *et al.* [343] were decreased by an order of magnitude (specifically, multiplying by 0.025), then there is considerable shortening of the duration until the initial splitting time, moving the simulated spectra much closer to that measured experimentally. Such an influence would seem to confirm the stress conditions of the wafer as a critical factor in the hydrogen blistering in silicon. There is of course no specific physical motivation for modifying this value to such a degree, tending to discount such a change as reasonable.

However, if the activation energy for the dissolution of hydrogen complexes were changed from E_a=1.81 eV to that given by Liang *et al.* [20] of E_a=1.66 eV, then the onset of the simulated splitting time is similarly decreased. The lack of a complementary energy describing the diffusion of H into vacancies from [20] (e.g. E_d) makes it difficult to assume this would adequately account for the offset in the simulation from the data. Changes to these energy factors however alters the rate of change of the blistering process, producing an activation energy value that no longer represents the full range of the data. Thus changes to these energies are similarly discounted.

The remaining candidate for modifying the model to fit the data is τ, which describes the stretching or jump frequency of the X-H complex bond as it dissociates. This frequency is described by Han *et al.* [343] to be a phenomenological or experimentally-derived parameter, with a value of "about 10^{12} seconds". In a number of other publications discussing behaviour related to this particular bond frequency, the supposed value varies somewhat from that given by Han. For example, both Ma *et al.* [114] and Leitch *et al.* [351, 352] describe the hydrogen bond jump frequency $\nu = 10^{13}$ seconds. Rice *et al.* [350] used a modified Monte Carlo simulation to model the behaviour of H in Si, and calculated hydrogen bond jump frequencies ranging from $\nu = 1.3\times10^{14}$s – 9.9×10^{13}s. If the pre-exponential value in the model described by Han is modified to ν=2.4×10^{13}s ($\sim \times\frac{1}{4}$), well within the values calculated by Rice, its predictions are in excellent agreement with the data. This is shown by the green dashed line in Fig. 4.27.

D.5 Optical Profilometry

D.5.1 Histograms: Hydrogen blister diameters

The following graphs are the expansion of the data presented in Section 4.4. the individual data sets for the hydrogen-induced blisters' diameters from each implantation energy and fluence for each semiconductor wafer material are shown.

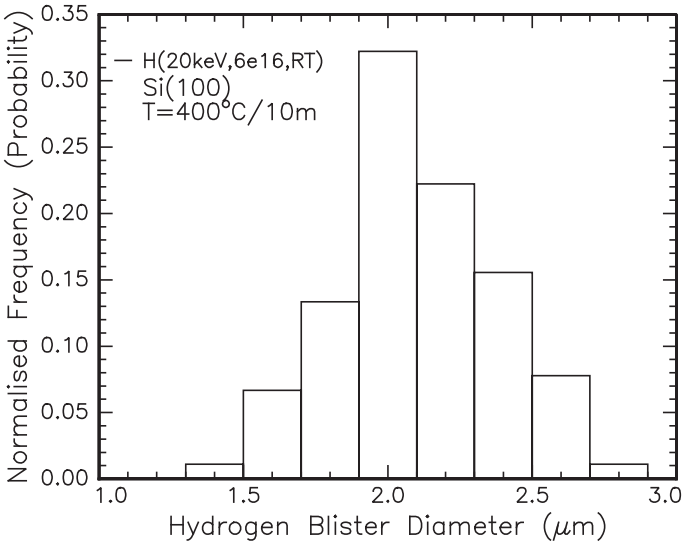

Figure D.15: Hydrogen blister diameter distribution for Si(100) implanted with $\Phi_H = 6\times10^{16}\text{cm}^{-2}$ at E=20 keV, as labelled, annealed at T=400°C/10min.

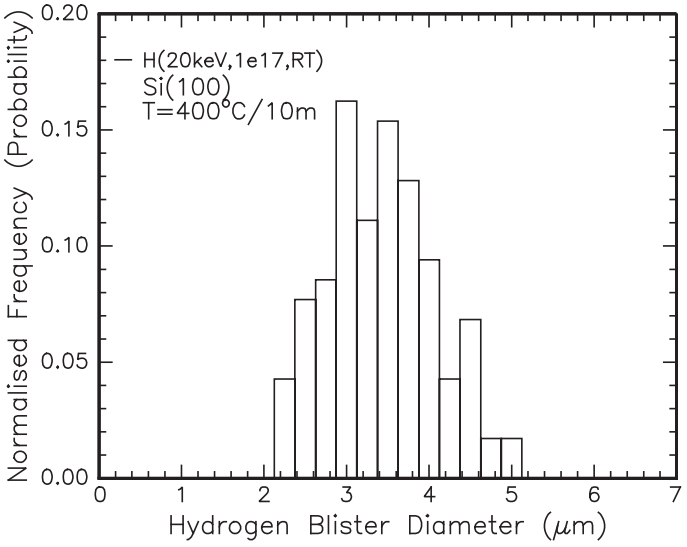

Figure D.16: Hydrogen blister diameter distribution for Si(100) implanted with $\Phi_H = 1\times10^{17}\text{cm}^{-2}$ at E=20 keV, as labelled, annealed at T=400°C/10min.

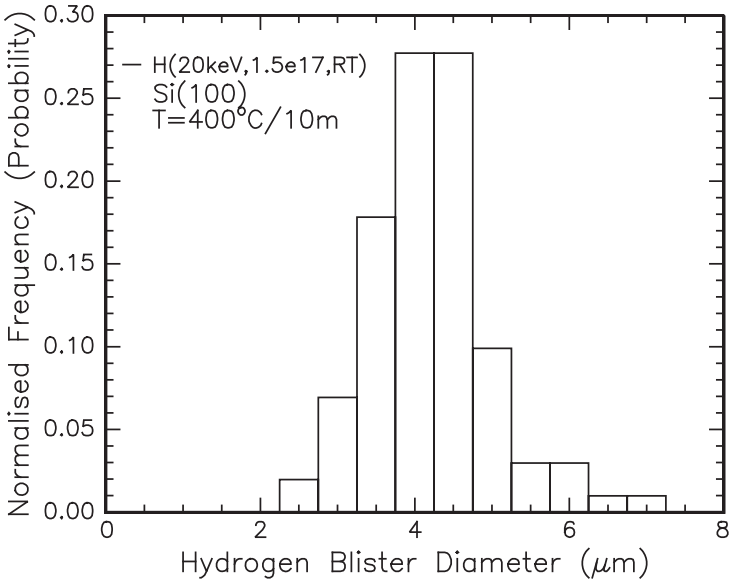

Figure D.17: Hydrogen blister diameter distribution for Si(100) implanted with $\Phi_H = 1.5 \times 10^{17}\text{cm}^{-2}$ at E=20 keV, as labelled, annealed at T=400°C/10min.

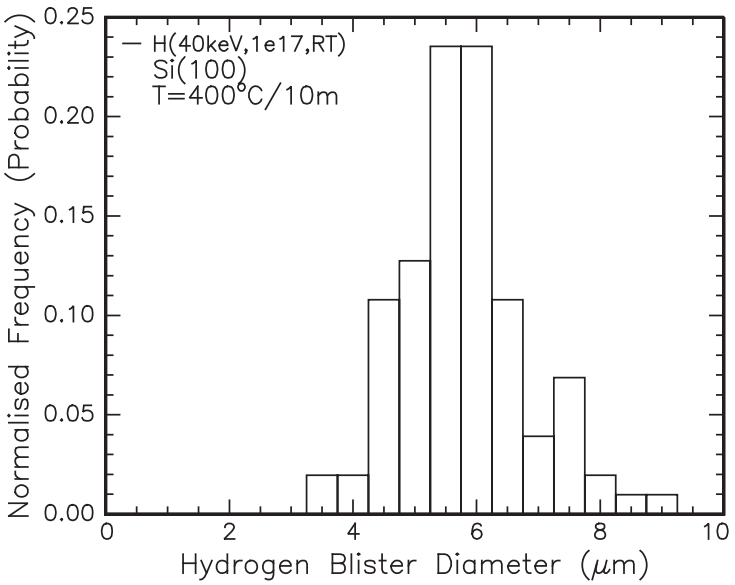

Figure D.18: Hydrogen blister diameter distribution for Si(100) implanted with $\Phi_H = 1{\times}10^{17}\text{cm}^{-2}$ at E=40 keV, as labelled, annealed at T=400°C/10min.

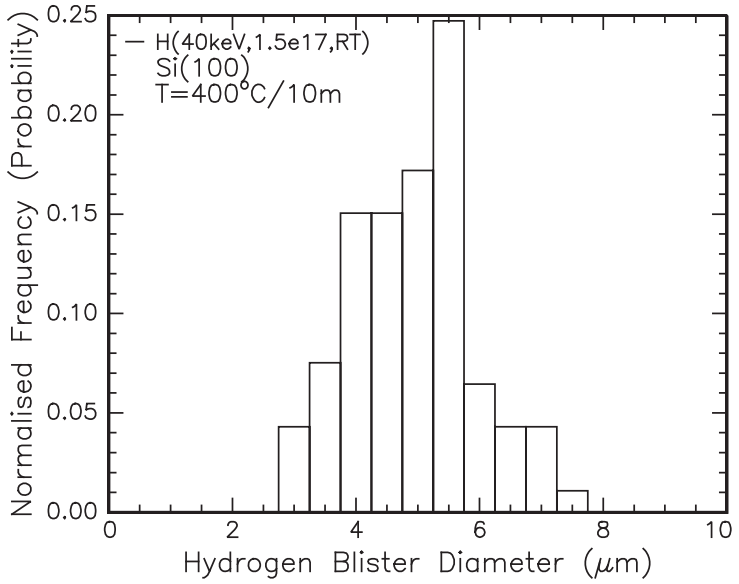

Figure D.19: Hydrogen blister diameter distribution for Si(100) implanted with $\Phi_H = 1.5 \times 10^{17}\text{cm}^{-2}$ at E=40 keV, as labelled, annealed at T=400°C/10min.

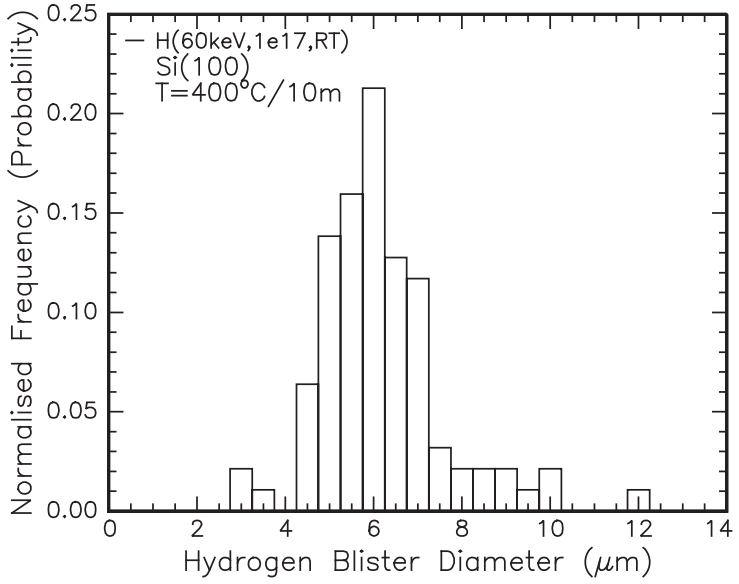

Figure D.20: Hydrogen blister diameter distribution for Si(100) implanted with $\Phi_H = 1 \times 10^{17}\text{cm}^{-2}$ at E=60 keV, as labelled, annealed at T=400°C/10min.

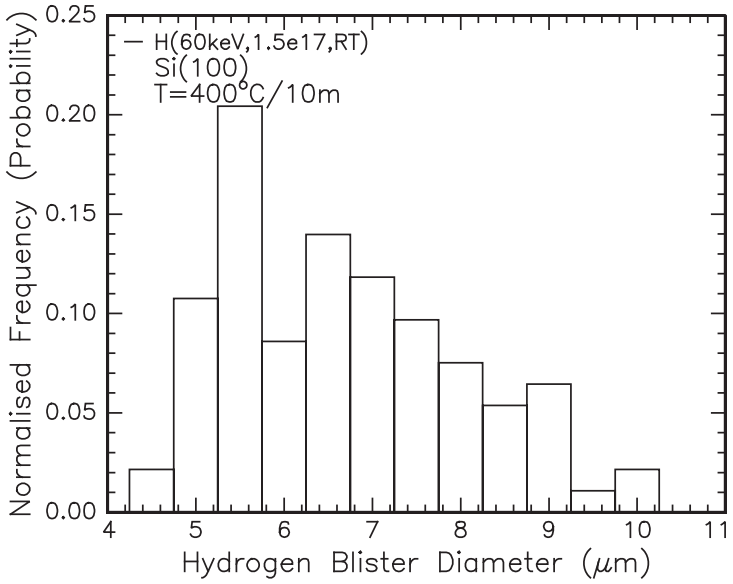

Figure D.21: Hydrogen blister diameter distribution for Si(100) implanted with $\Phi_H = 1.5 \times 10^{17}\text{cm}^{-2}$ at E=60 keV, as labelled, annealed at T=400°C/10min.

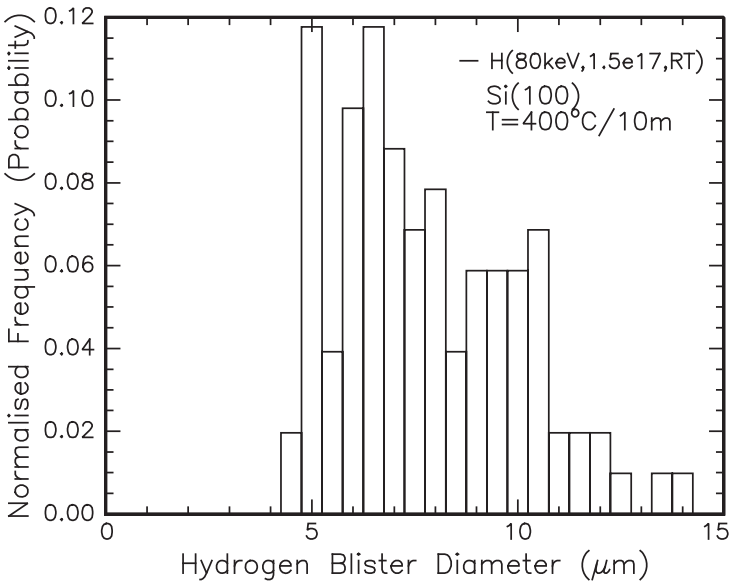

Figure D.22: Hydrogen blister diameter distribution for Si(100) implanted with $\Phi_H = 1{\times}10^{17}\text{cm}^{-2}$ at E= 80 keV, as labelled, annealed at T=400°C/10min.

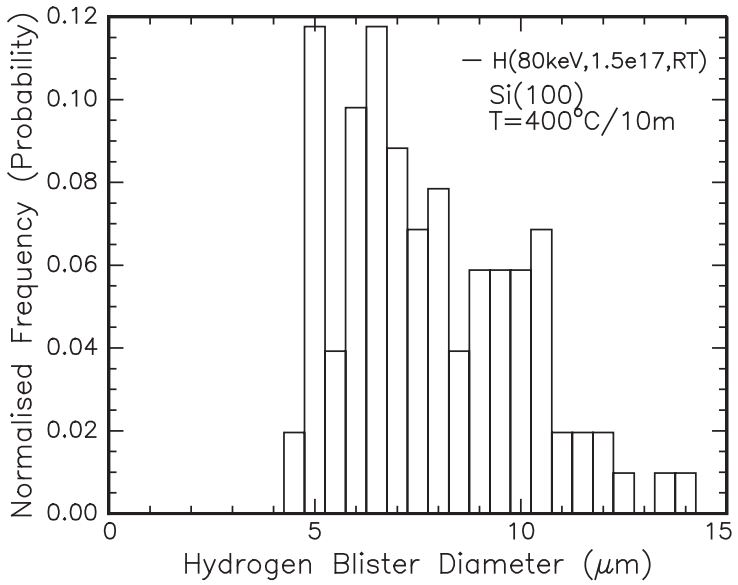

Figure D.23: Hydrogen blister diameter distribution for Si(100) implanted with $\Phi_H = 1\times10^{17}\text{cm}^{-2}$ at E=80 keV, as labelled, annealed at T=400°C/10min.

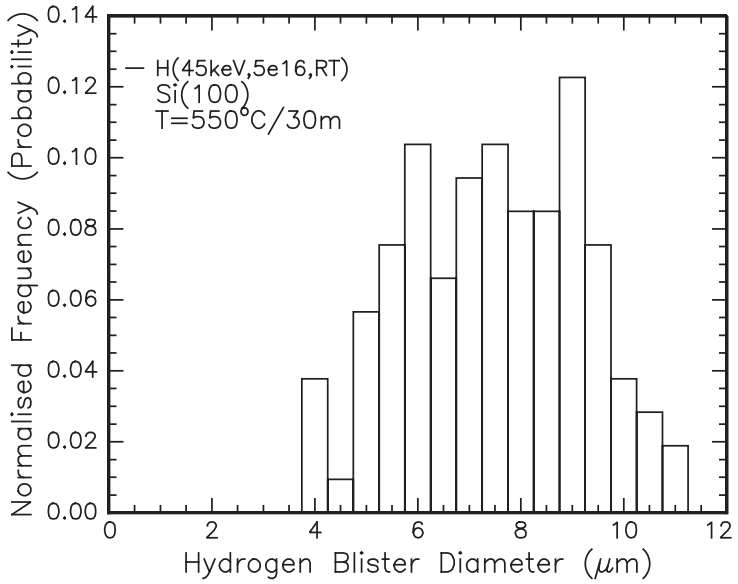

Figure D.24: Hydrogen blister diameter distribution for Si(100) implanted with $\Phi_H = 5\times10^{16}\text{cm}^{-2}$ at E=45 keV, as labelled, annealed at T=550°C/30min.

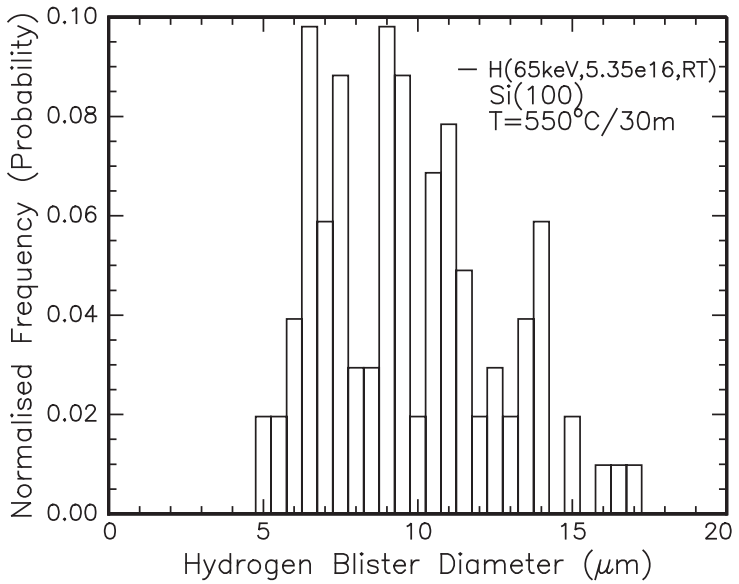

Figure D.25: Hydrogen blister diameter distribution for Si(100) implanted with $\Phi_H = 5.35 \times 10^{16}\text{cm}^{-2}$ at E=65 keV, as labelled, annealed at T=550°C/30min.

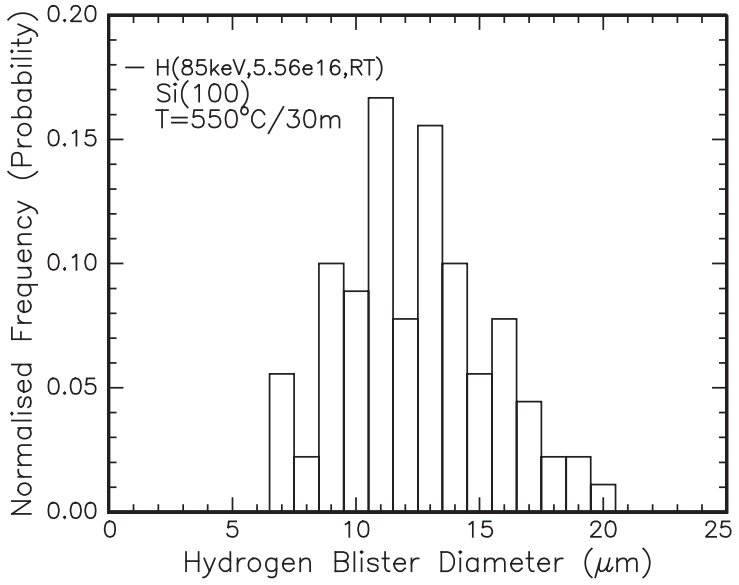

Figure D.26: Hydrogen blister diameter distribution for Si(100) implanted with $\Phi_H = 5.56 \times 10^{16}\text{cm}^{-2}$ at E=85 keV, as labelled, annealed at T=550°C/30min.

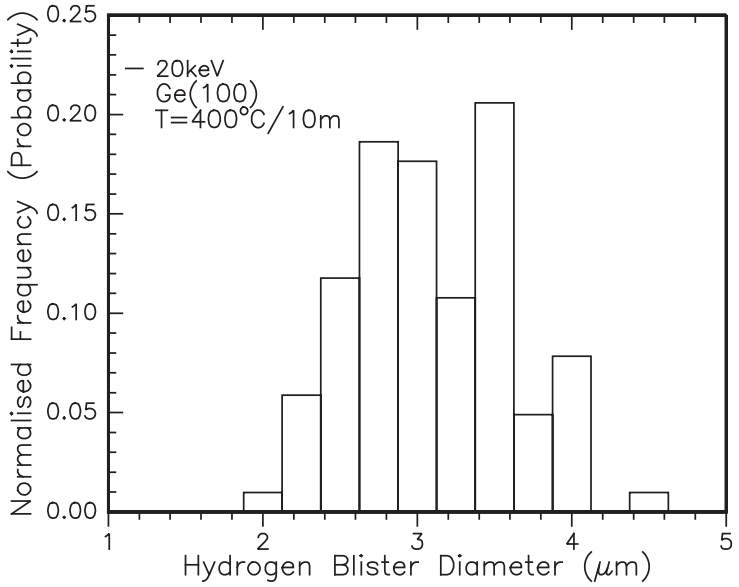

Figure D.27: Hydrogen blister diameter distribution for Ge(100) implanted with $\Phi_H = 1\times10^{17}\mathrm{cm}^{-2}$ at E=20 keV, as labelled, annealed at T=400°C/10min.

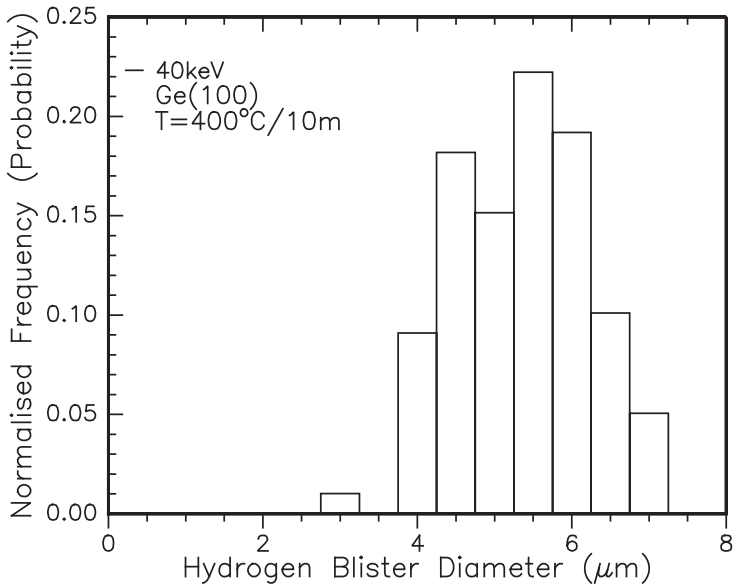

Figure D.28: Hydrogen blister diameter distribution for Ge(100) implanted with $\Phi_H = 1\times10^{17}\mathrm{cm}^{-2}$ at E=40 keV, as labelled, annealed at T=400°C/10min.

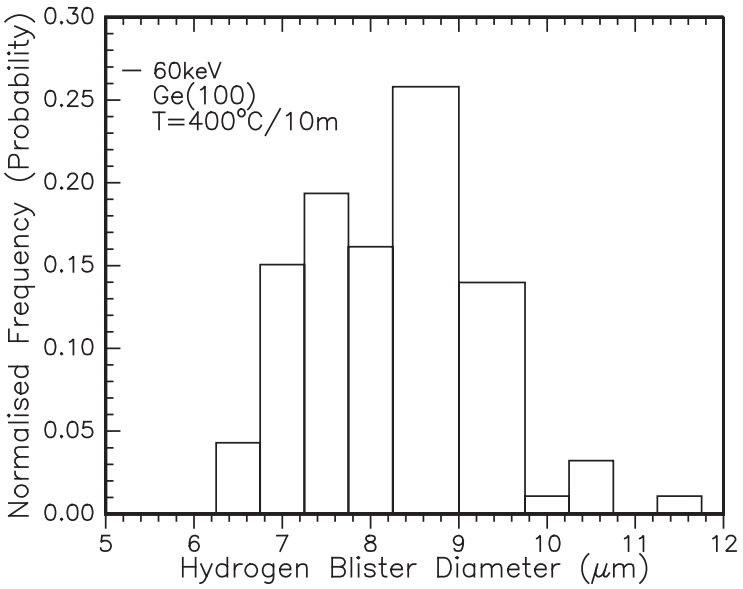

Figure D.29: Hydrogen blister diameter distribution for Ge(100) implanted with $\Phi_H = 1{\times}10^{17}\mathrm{cm}^{-2}$ at E=60 keV, as labelled, annealed at T=400°C/10min.

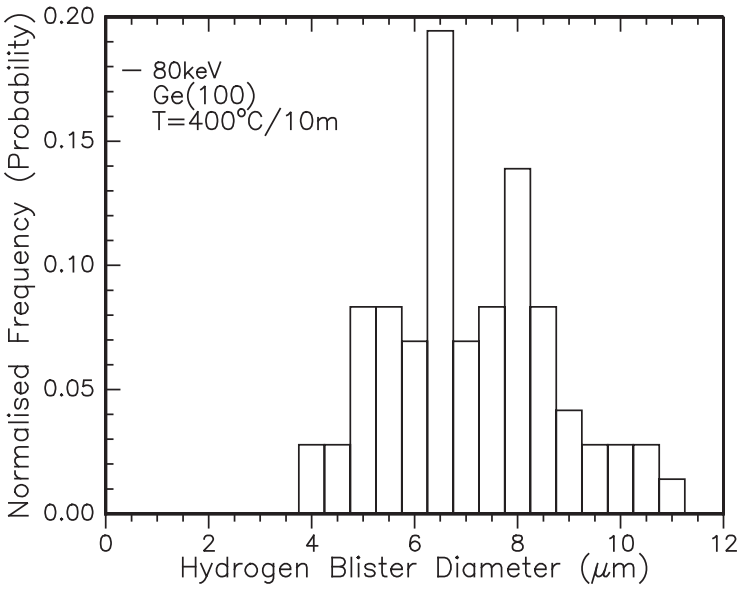

Figure D.30: Hydrogen blister diameter distribution for Ge(100) implanted with $\Phi_H = 1{\times}10^{17}\mathrm{cm}^{-2}$ at E=80 keV, as labelled, annealed at T=400°C/10min.

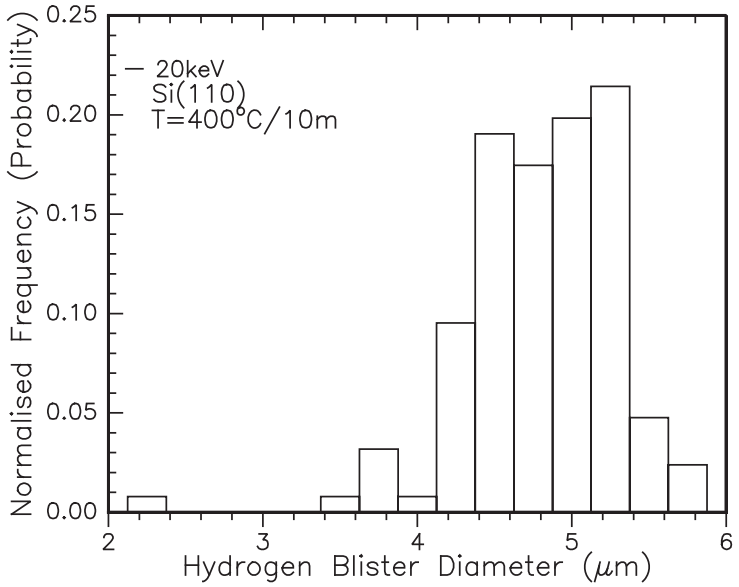

Figure D.31: Hydrogen blister diameter distribution for Si(110) implanted with $\Phi_H = 1.5 \times 10^{17}\text{cm}^{-2}$ at E=20 keV, as labelled, annealed at T=400°C/10min.

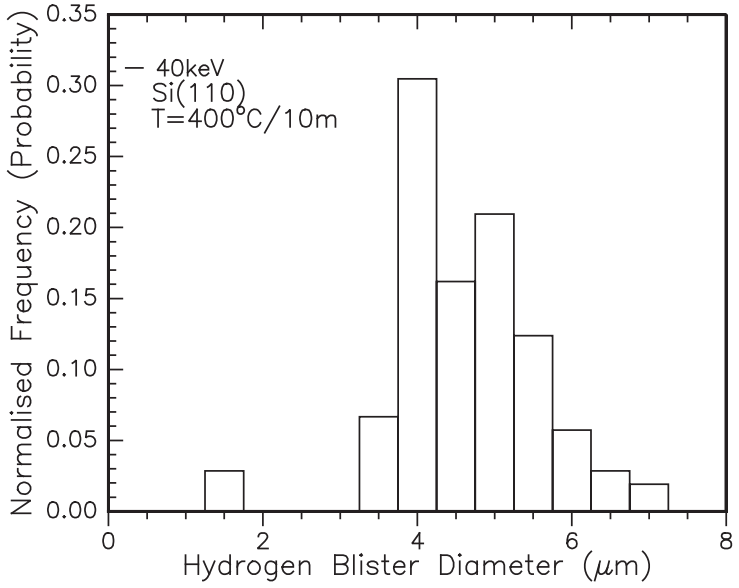

Figure D.32: Hydrogen blister diameter distribution for Si(110) implanted with $\Phi_H = 1.5 \times 10^{17}\text{cm}^{-2}$ at E=40 keV, as labelled, annealed at T=400°C/10min.

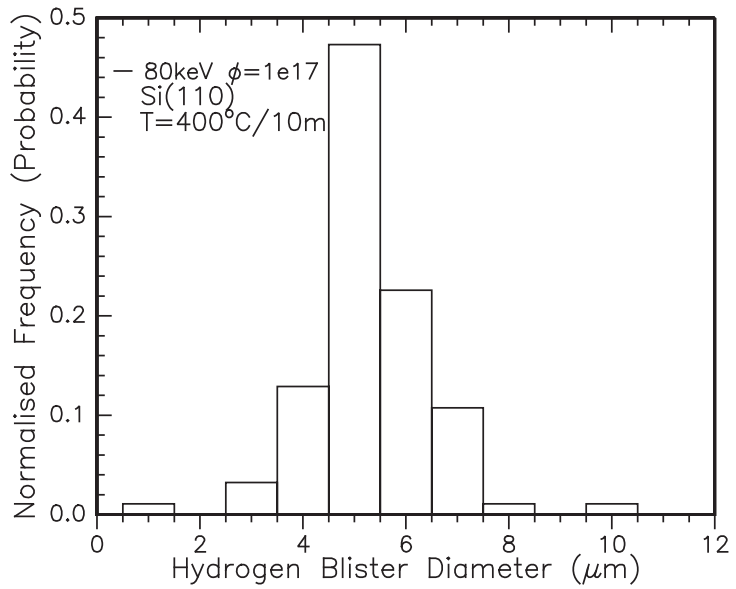

Figure D.33: Hydrogen blister diameter distribution for Si(110) implanted with $\Phi_H = 1{\times}10^{17}\mathrm{cm}^{-2}$ at E=80 keV, as labelled, annealed at T=400°C/10min.

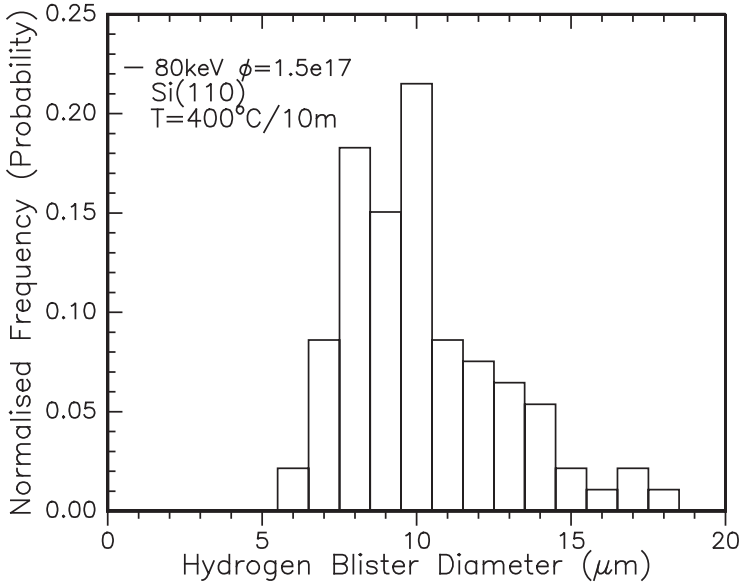

Figure D.34: Hydrogen blister diameter distribution for Si(110) implanted with $\Phi_H = 1.5 \times 10^{17}\mathrm{cm}^{-2}$ at E=80 keV, as labelled, annealed at T=400°C/10min.

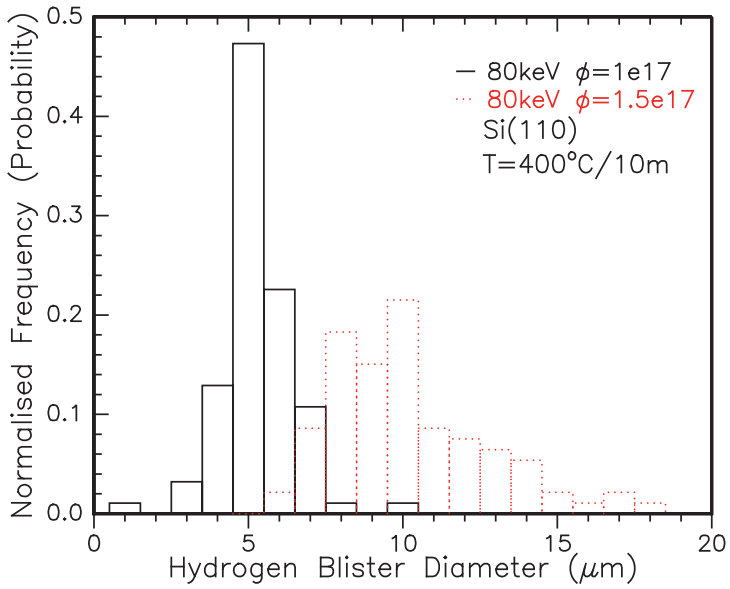

Figure D.35: Hydrogen blister diameter distribution for Si(110) implanted at E=80 keV with different fluences, as labelled, annealed at T=400°C/10min.

D.5.2 Histograms: Hydrogen blister heights

The following graphs are the expansion of the data presented in Section 4.4. Rather than composite figures, the individual data sets for the hydrogen-induced blisters' heights from each implantation energy and fluence for each semiconductor wafer material are shown.

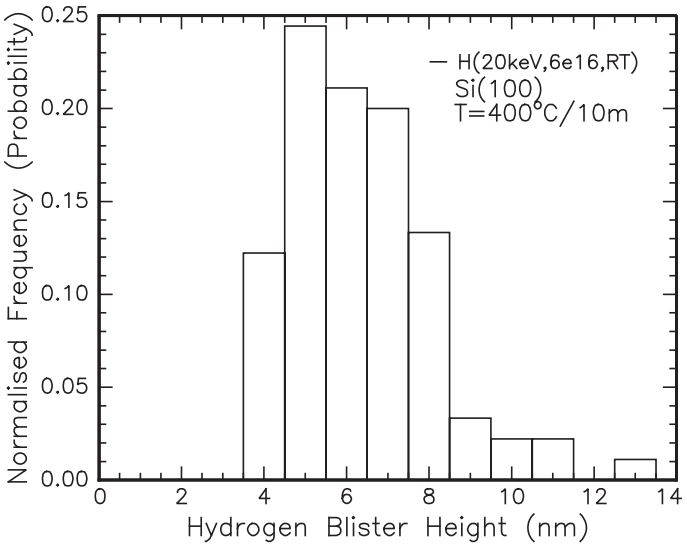

Figure D.36: Hydrogen blister height distribution for Si(100) implanted with $\Phi_H = 6 \times 10^{16}\text{cm}^{-2}$ at E=20 keV, as labelled, annealed at T=400°C/10min.

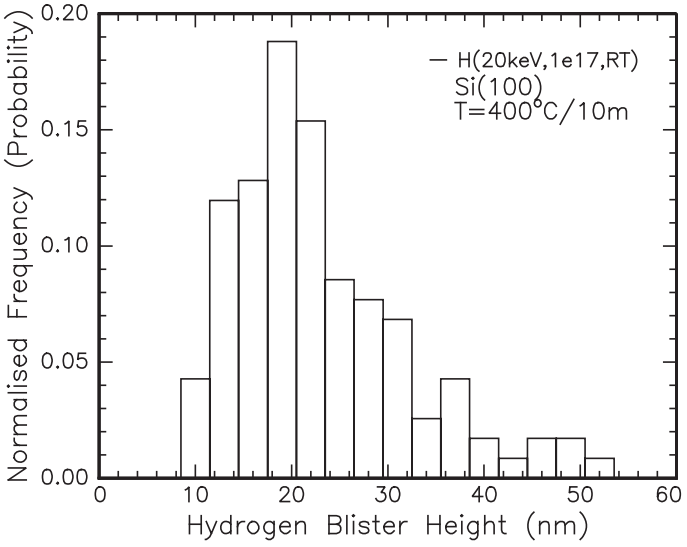

Figure D.37: Hydrogen blister height distribution for Si(100) implanted with $\Phi_H = 1 \times 10^{17}\text{cm}^{-2}$ at E=20 keV, as labelled, annealed at T=400°C/10min.

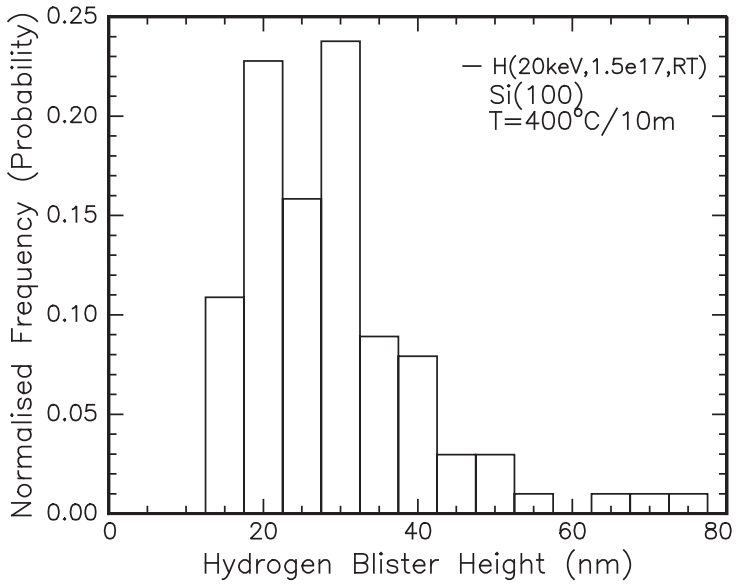

Figure D.38: Hydrogen blister height distribution for Si(100) implanted with $\Phi_H = 1.5 \times 10^{17}\text{cm}^{-2}$ at E=20 keV, as labelled, annealed at T=400°C/10min.

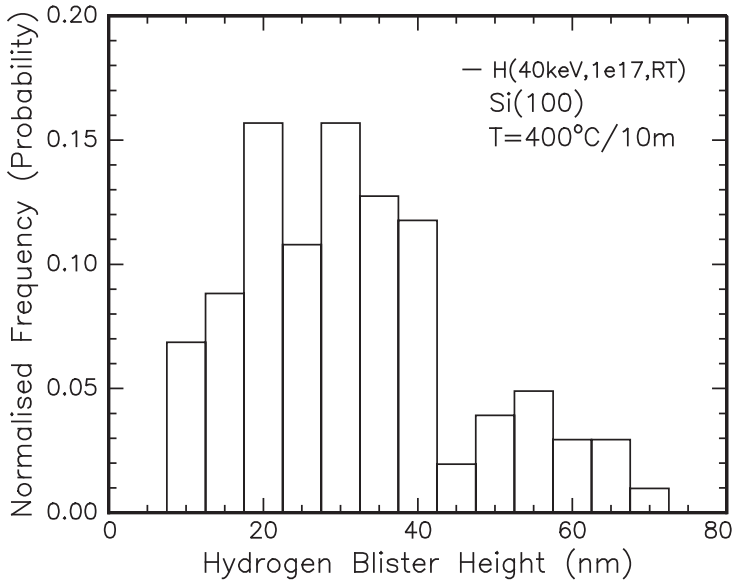

Figure D.39: Hydrogen blister height distribution for Si(100) implanted with $\Phi_H = 1 \times 10^{17}\text{cm}^{-2}$ at E=40 keV, as labelled, annealed at T=400°C/10min.

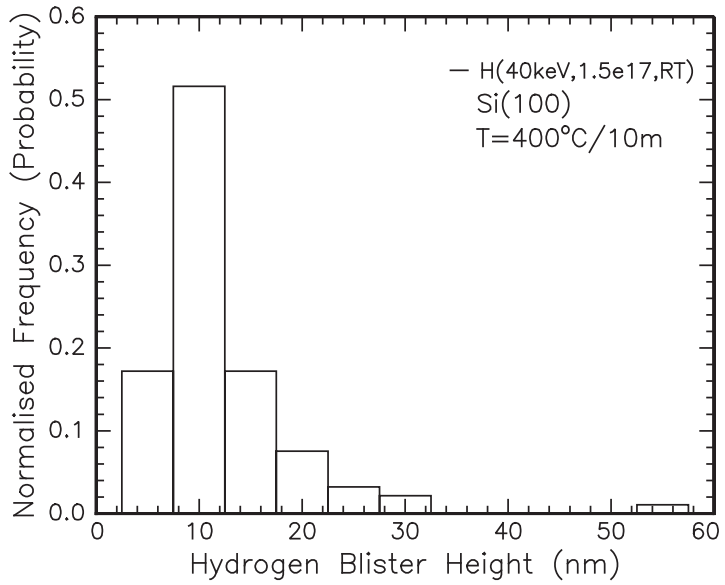

Figure D.40: Hydrogen blister height distribution for Si(100) implanted with $\Phi_H = 1.5 \times 10^{16}\text{cm}^{-2}$ at E=40 keV, as labelled, annealed at T=400°C/10min.

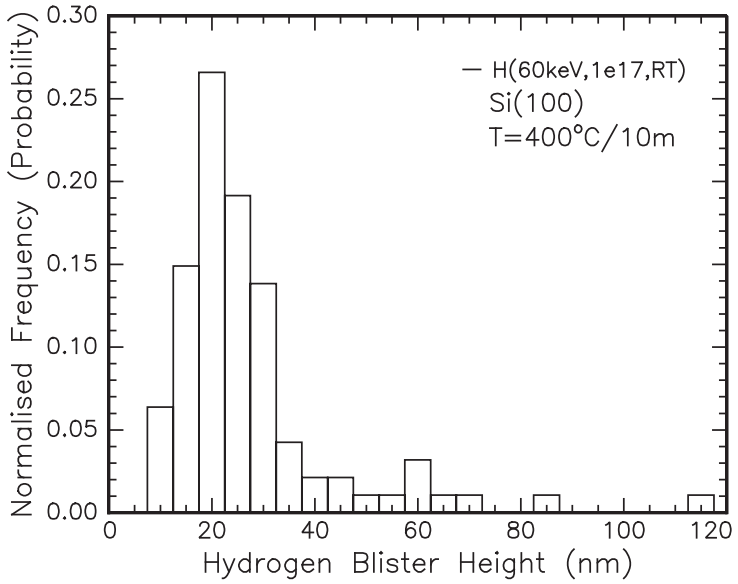

Figure D.41: Hydrogen blister height distribution for Si(100) implanted with $\Phi_H = 1 \times 10^{17}\text{cm}^{-2}$ at E=60 keV, as labelled, annealed at T=400°C/10min.

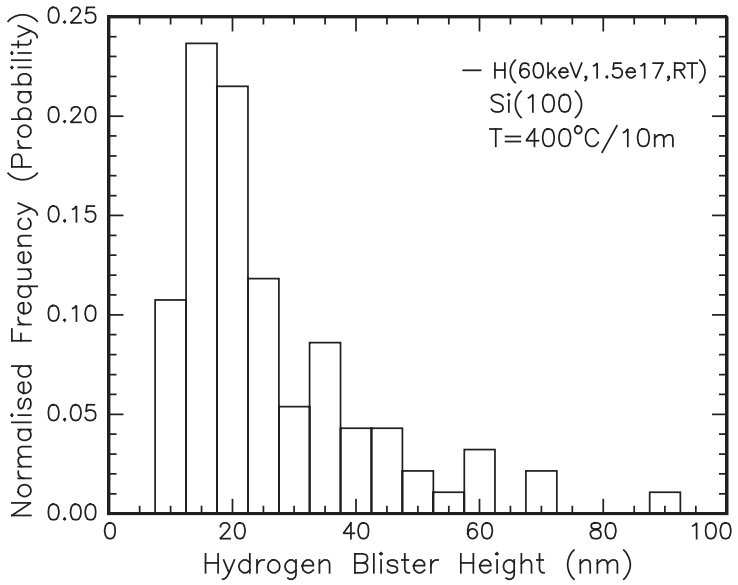

Figure D.42: Hydrogen blister height distribution for Si(100) implanted with $\Phi_H = 1.5 \times 10^{17}\text{cm}^{-2}$ at E=60 keV, as labelled, annealed at T=400°C/10min.

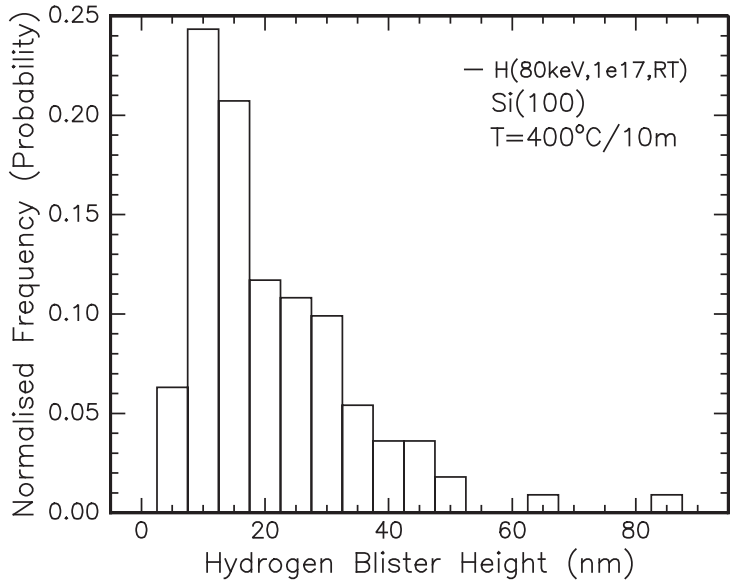

Figure D.43: Hydrogen blister height distribution for Si(100) implanted with $\Phi_H = 1 \times 10^{17}\text{cm}^{-2}$ at E=80 keV, as labelled, annealed at T=400°C/10min.

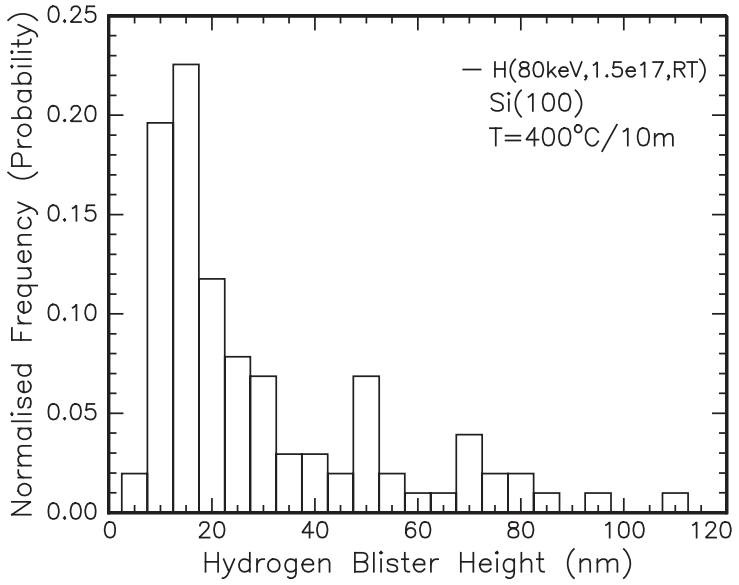

Figure D.44: Hydrogen blister height distribution for Si(100) implanted with $\Phi_H = 1.5 \times 10^{17}\text{cm}^{-2}$ at E=80 keV, as labelled, annealed at T=400°C/10min.

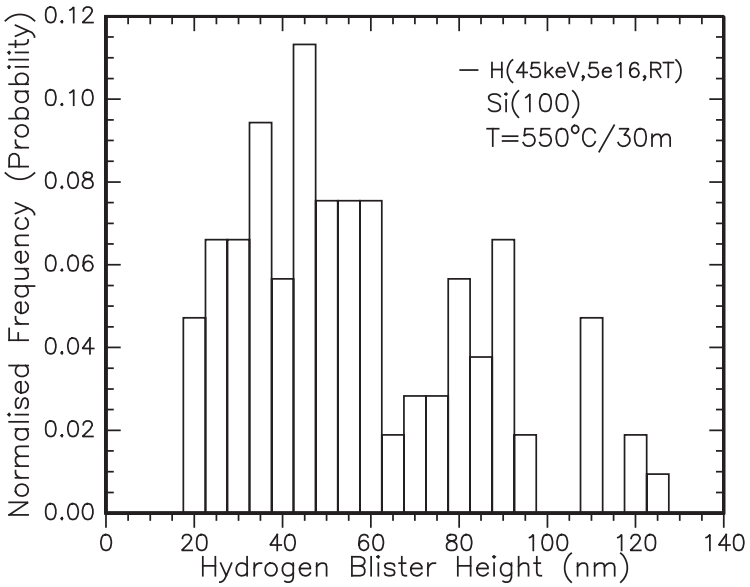

Figure D.45: Hydrogen blister height distribution for Si(100) implanted with $\Phi_H = 5 \times 10^{16}\text{cm}^{-2}$ at E=45 keV, as labelled, annealed at T=550°C/30min.

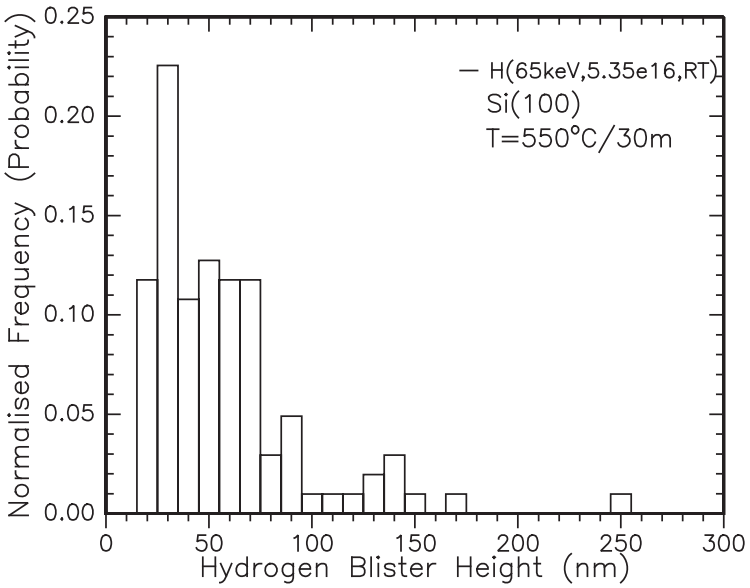

Figure D.46: Hydrogen blister height distribution for Si(100) implanted with $\Phi_H = 5.35 \times 10^{16}\text{cm}^{-2}$ at E=65 keV, as labelled, annealed at T=550°C/30min.

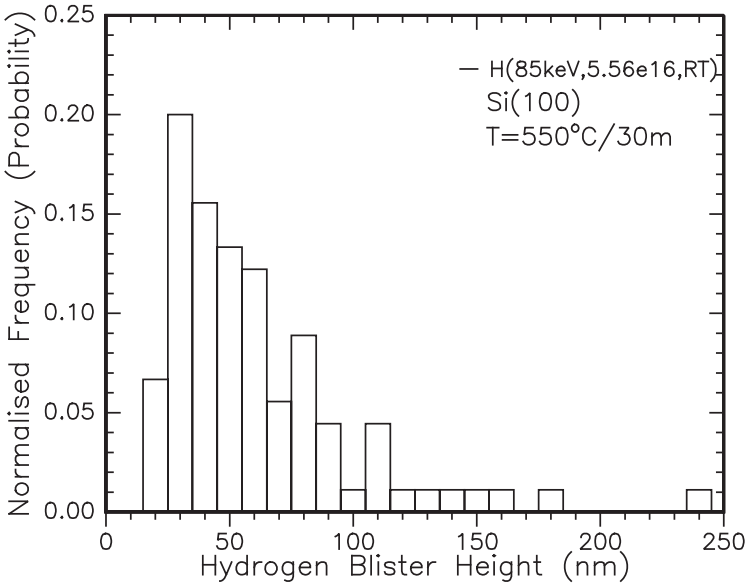

Figure D.47: Hydrogen blister diameter distribution for Si(100) implanted with $\Phi_H = 5.56 \times 10^{16}\text{cm}^{-2}$ at E=85 keV, as labelled, annealed at T=550°C/30min.

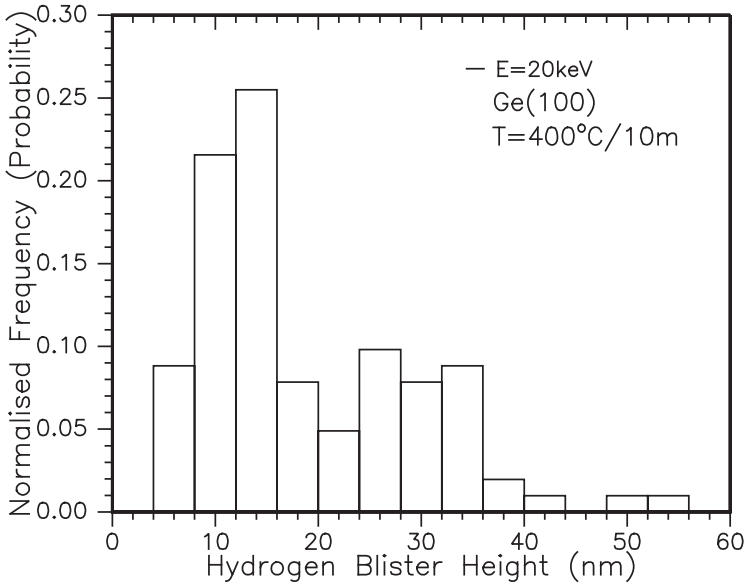

Figure D.48: Hydrogen blister height distribution for Ge(100) implanted with $\Phi_H = 1 \times 10^{17}\text{cm}^{-2}$ at E=20 keV, as labelled, annealed at T=400°C/10min.

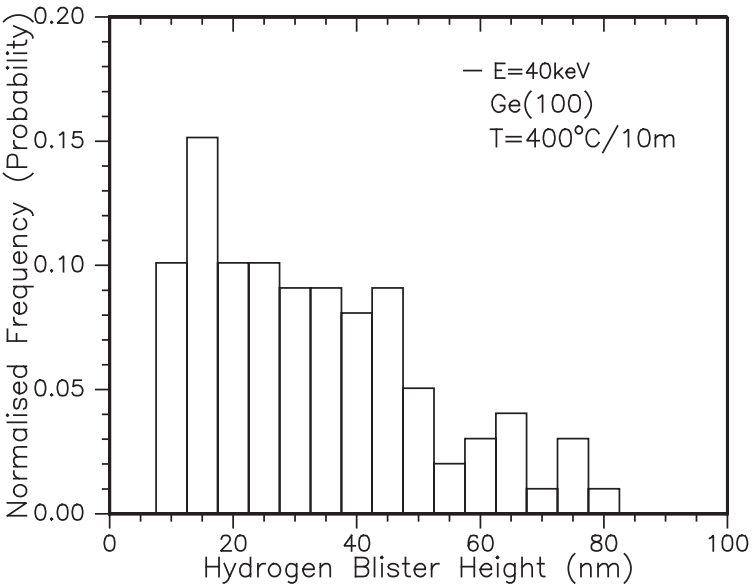

Figure D.49: Hydrogen blister height distribution for Ge(100) implanted with $\Phi_H = 1 \times 10^{17}\text{cm}^{-2}$ at E=40 keV, as labelled, annealed at T=400°C/10min.

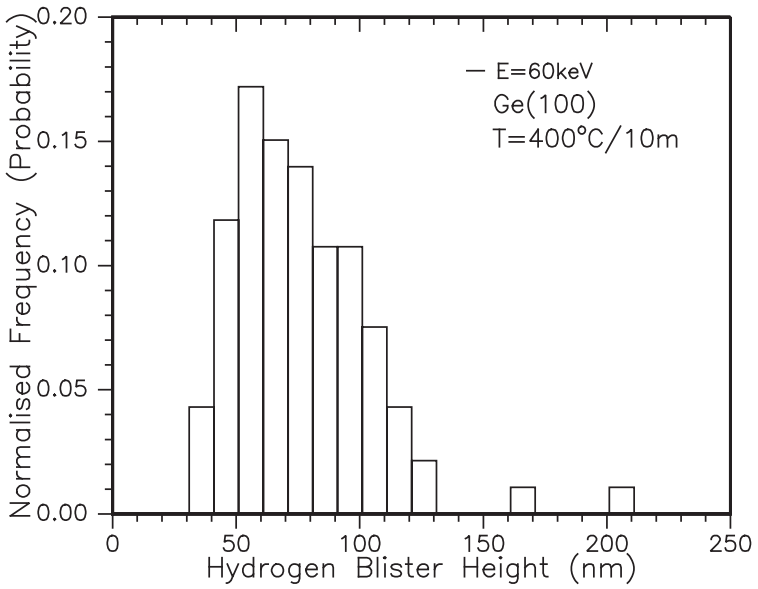

Figure D.50: Hydrogen blister height distribution for Ge(100) implanted with $\Phi_H = 1 \times 10^{17}\text{cm}^{-2}$ at E=60 keV, as labelled, annealed at T=400°C/10min.

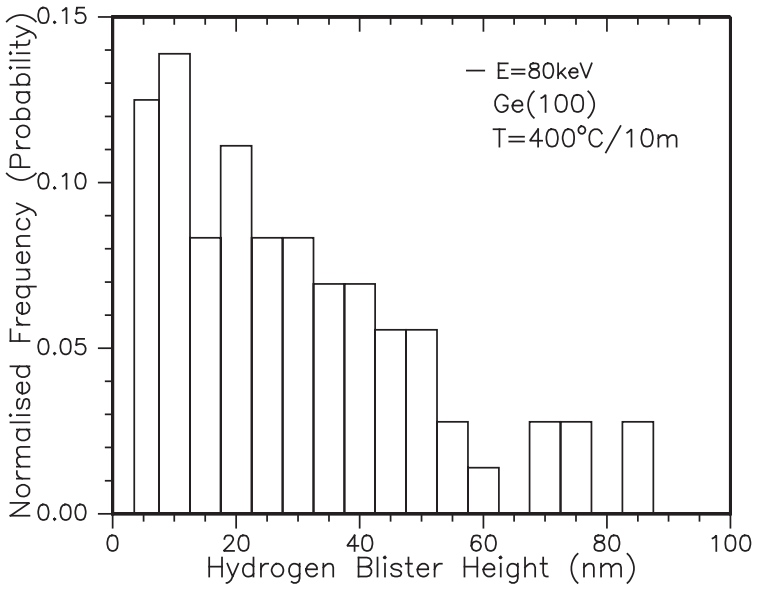

Figure D.51: Hydrogen blister height distribution for Ge(100) implanted with $\Phi_H = 1 \times 10^{17}\text{cm}^{-2}$ at E=80 keV, as labelled, annealed at T=400°C/10min.

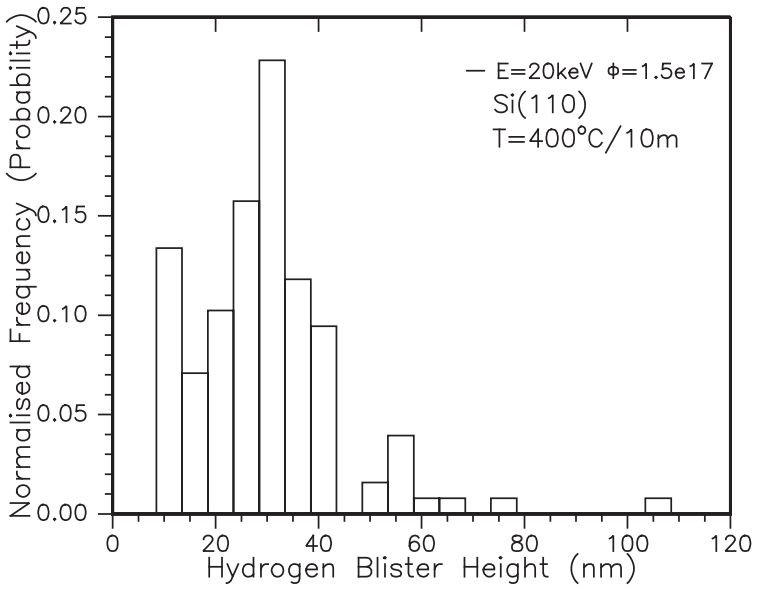

Figure D.52: Hydrogen blister height distribution for Si(110) implanted with $\Phi_H = 1.5 \times 10^{17}\text{cm}^{-2}$ at E=20 keV, as labelled, annealed at T=400°C/10min.

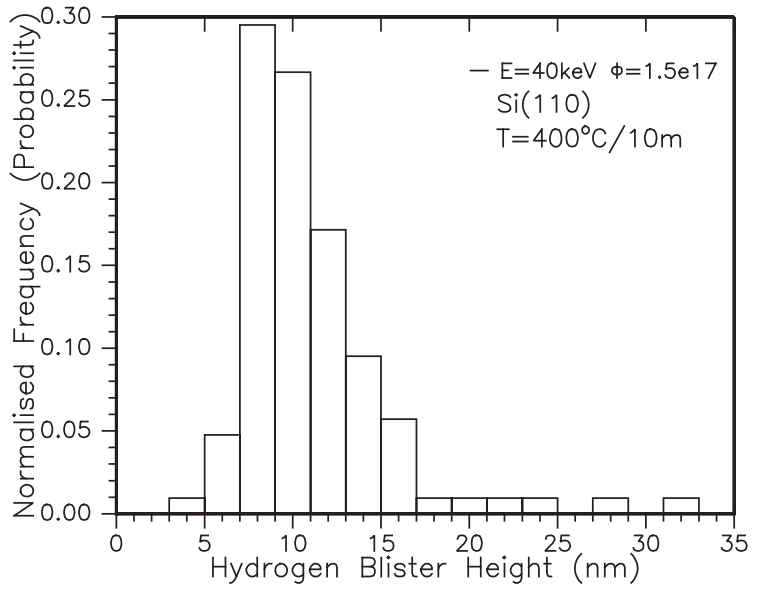

Figure D.53: Hydrogen blister height distribution for Si(110) implanted with $\Phi_H = 1.5 \times 10^{17}\text{cm}^{-2}$ at E=40 keV, as labelled, annealed at T=400°C/10min.

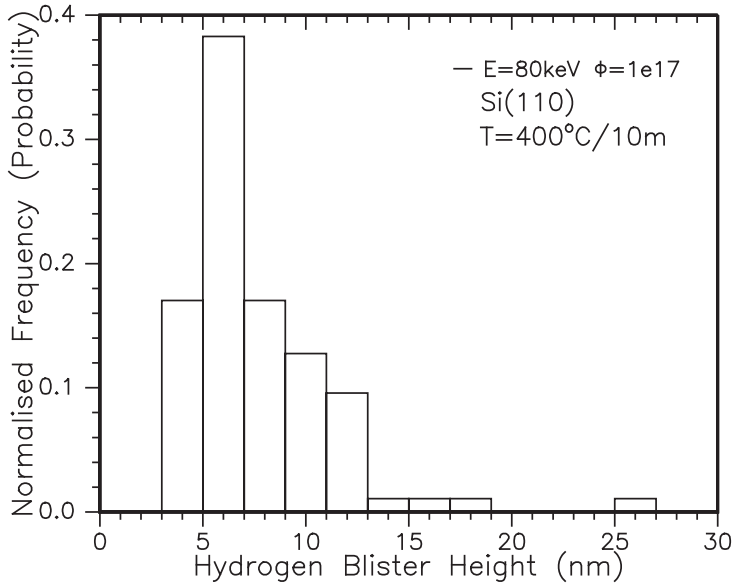

Figure D.54: Hydrogen blister height distribution for Si(110) implanted with $\Phi_H = 1 \times 10^{17}\text{cm}^{-2}$ at E=80 keV, as labelled, annealed at T=400°C/10min.

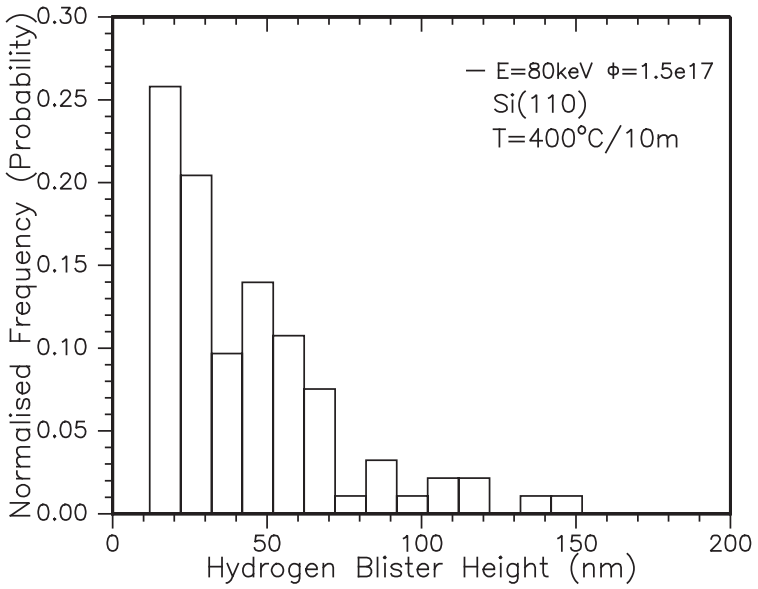

Figure D.55: Hydrogen blister height distribution for Si(110) implanted with $\Phi_H = 1.5 \times 10^{17}\text{cm}^{-2}$ at E=80 keV, as labelled, annealed at T=400°C/10min.

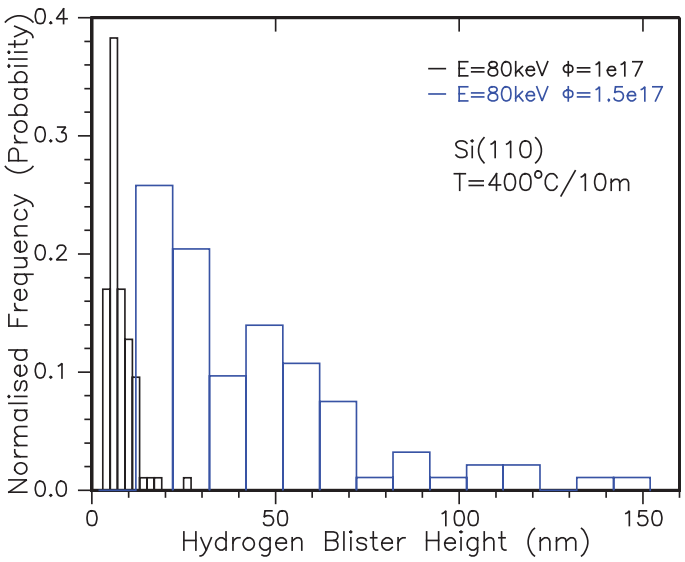

Figure D.56: Hydrogen blister height distribution for Si(110) implanted at E=80 keV with different fluences, as labelled, annealed at T=400°C/10min.

D.5.3 Histograms: Hydrogen crater depths

The following graphs are the expansion of the data presented in Section 4.4. Rather than composite figures, the individual data sets for the hydrogen-induced craters' depths from each implantation energy and fluence for each semiconductor wafer material are shown.

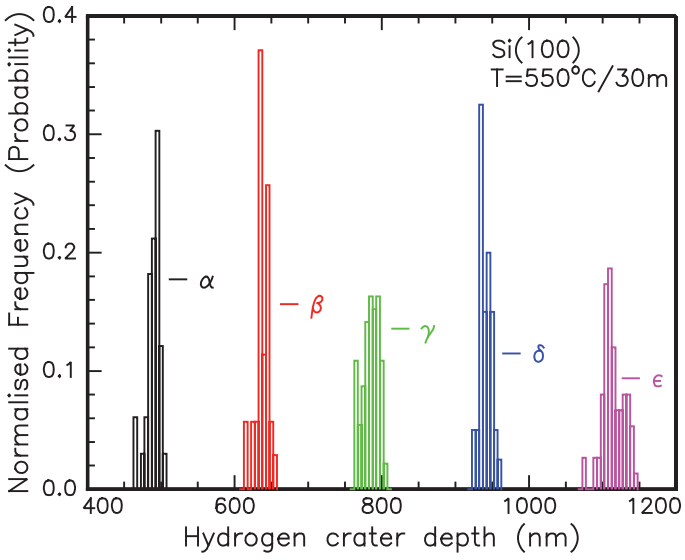

Figure D.57: Hydrogen crater depth distribution for Si(100) implanted at (α) **E=45 keV,** $\Phi = 5 \times 10^{16}\text{cm}^{-2}$, ($\beta$) **E=65 keV,** $\Phi = 5.35 \times 10^{16}\text{cm}^{-2}$, ($\gamma$) **E=85 keV,** $\Phi = 5.56 \times 10^{16}\text{cm}^{-2}$, ($\delta$) **E=105 keV,** $\Phi = 6.01 \times 10^{16}\text{cm}^{-2}$, ($\epsilon$) **E=125 keV,** $\Phi = 6.65 \times 10^{16}\text{cm}^{-2}$, and annealed at T=550°C/30min in a quartz tube furnace under an Ar ambient.

D.5.4 Hydrogen blister dimensions and errata

The data comprising the histograms in the previous sections of this appendix are now combined to contrast relative dimensions. Firstly, plots include hydrogen-induced blister height versus diameter graphs for each implantation energy and fluence. These were combined under each energy in Fig. 4.6 for Si(100), and Fig. 4.9 for Ge(100). Following are a series of composite figures contrasting histogram distributions of blister diameters and heights within each substrate for all implantation energies.

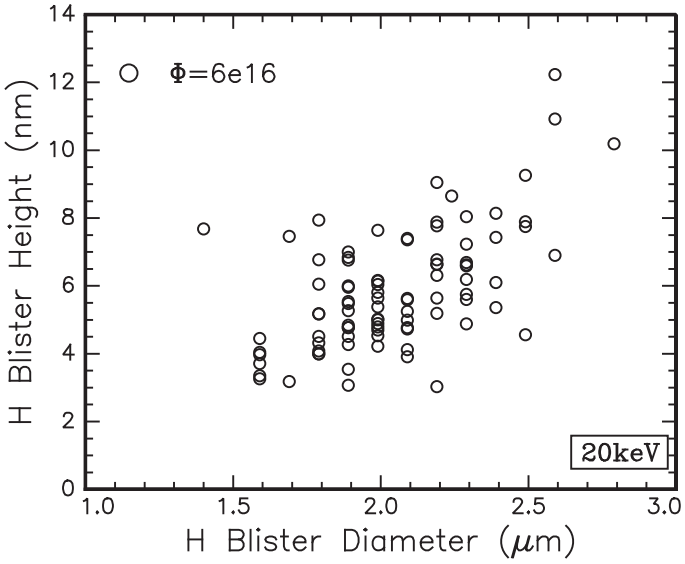

Figure D.58: Hydrogen blister height versus diameter in Si(100) implanted with H(20keV,6×10^{16}cm^{-2},RT) and annealed at T=400°C/10min in Ar gas ambient.

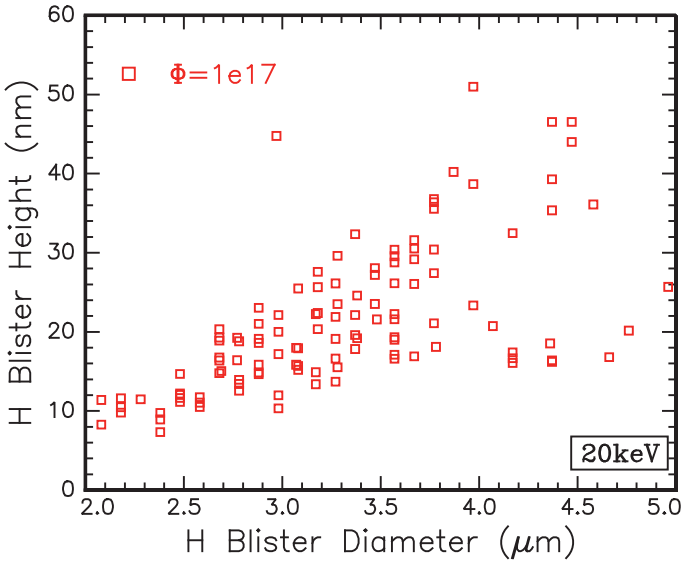

Figure D.59: Hydrogen blister height versus diameter in Si(100) implanted with H(20keV,1×10^{17}cm^{-2},RT) and annealed at T=400°C/10Min in Ar gas ambient.

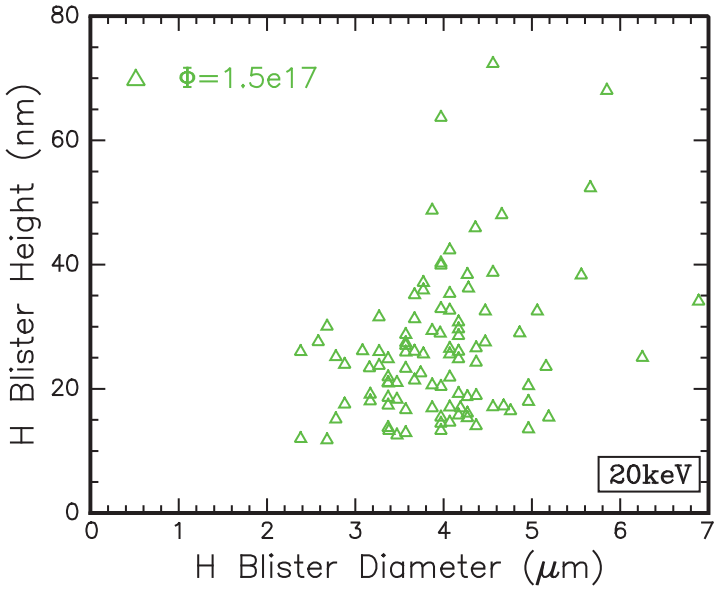

Figure D.60: Hydrogen blister height versus diameter in Si(100) implanted with H(20keV,1.5×10^{17}cm^{-2},RT) and annealed at T=400°C/10Min in Ar gas ambient.

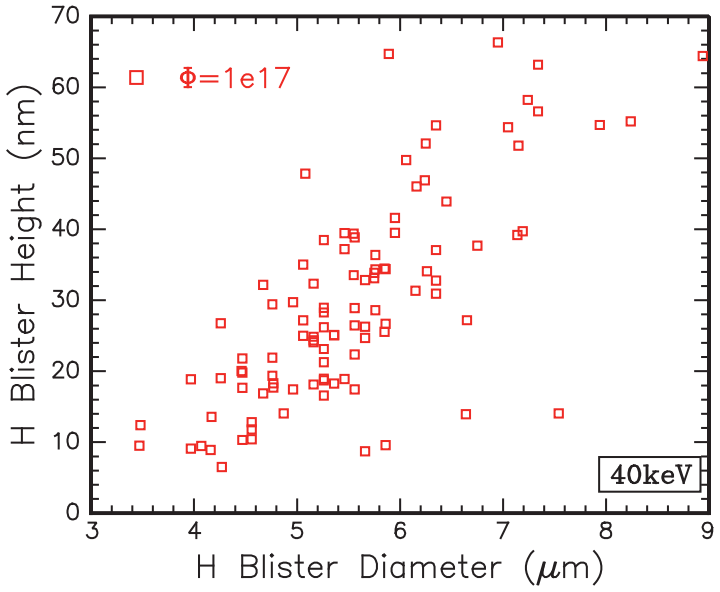

Figure D.61: Hydrogen blister height versus diameter in Si(100) implanted with H(40keV,1×10^{17}cm^{-2},RT) and annealed at T=400°C/10Min in Ar gas ambient.

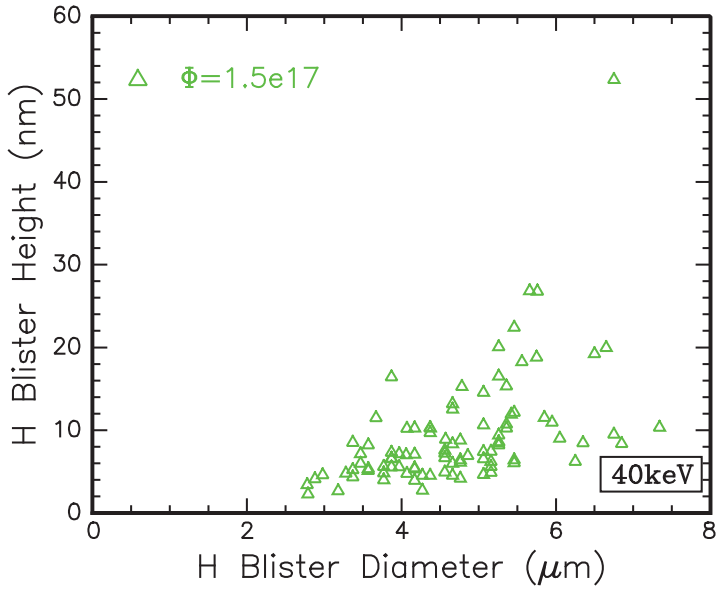

Figure D.62: Hydrogen blister height versus diameter in Si(100) implanted with H(40keV,1.5×10^{17}cm^{-2},RT) and annealed at T=400°C/10Min in Ar gas ambient.

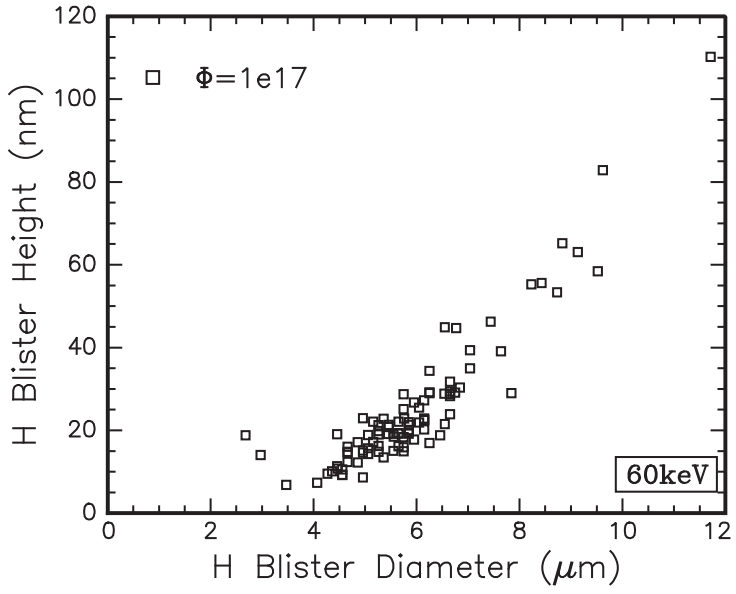

Figure D.63: Hydrogen blister height versus diameter in Si(100) implanted with H(60keV,1×10^{17}cm^{-2},RT) and annealed at T=400°C/10Min in Ar gas ambient.

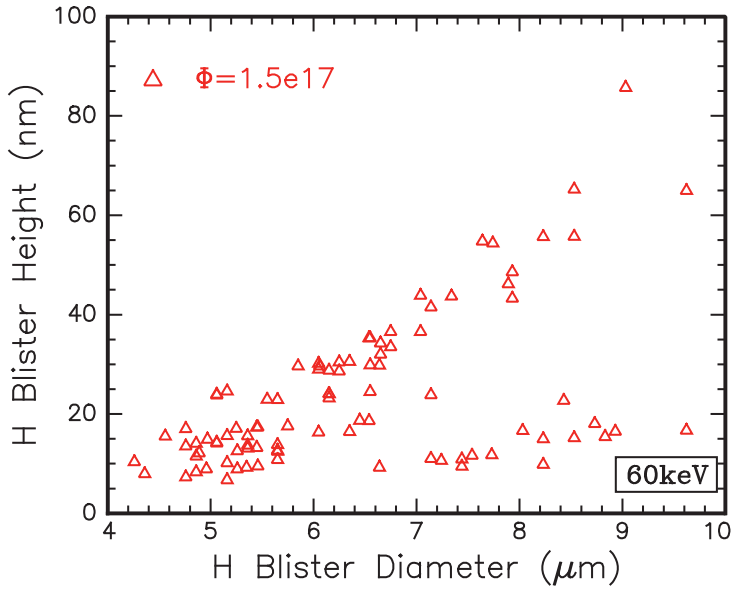

Figure D.64: Hydrogen blister height versus diameter in Si(100) implanted with H(60keV,1.5×10^{17}cm^{-2},RT) and annealed at T=400°C/10Min in Ar gas ambient.

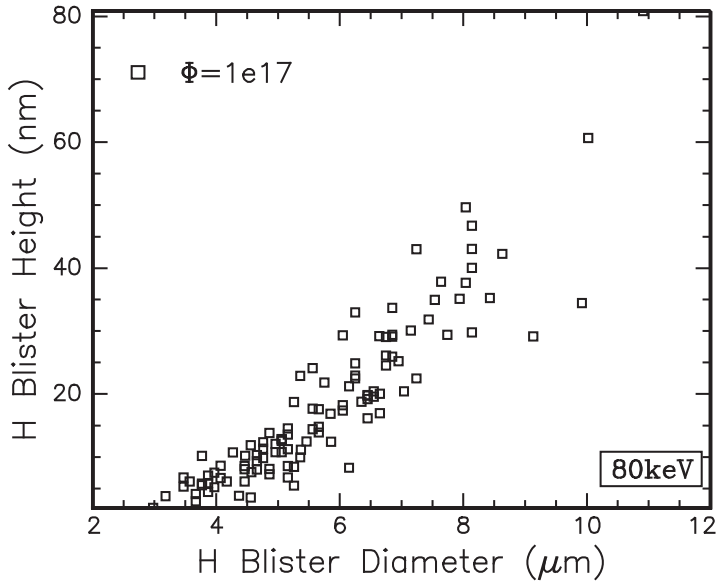

Figure D.65: Hydrogen blister height versus diameter in Si(100) implanted with H(80keV,1×10^{17}cm^{-2},RT) and annealed at T=400°C/10min in Ar gas ambient.

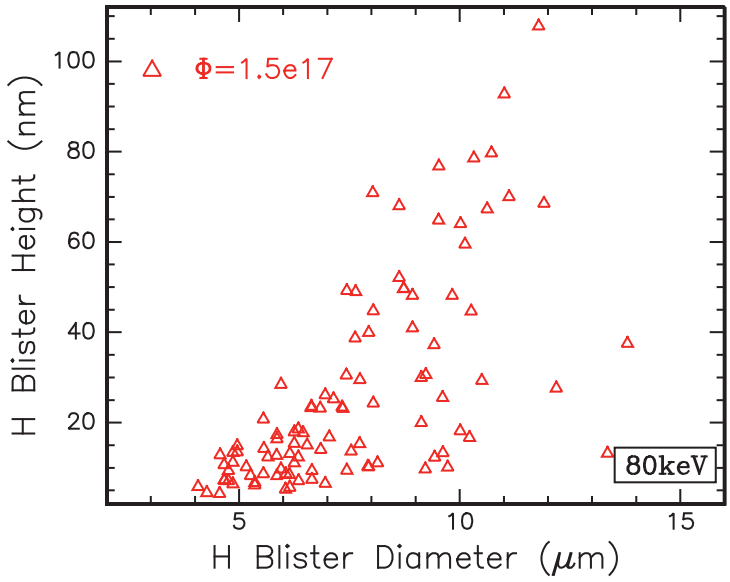

Figure D.66: Hydrogen blister height versus diameter in Si(100) implanted with H(80keV,1.5×10^{17}cm^{-2},RT) and annealed at T=400°C/10min in Ar gas ambient.

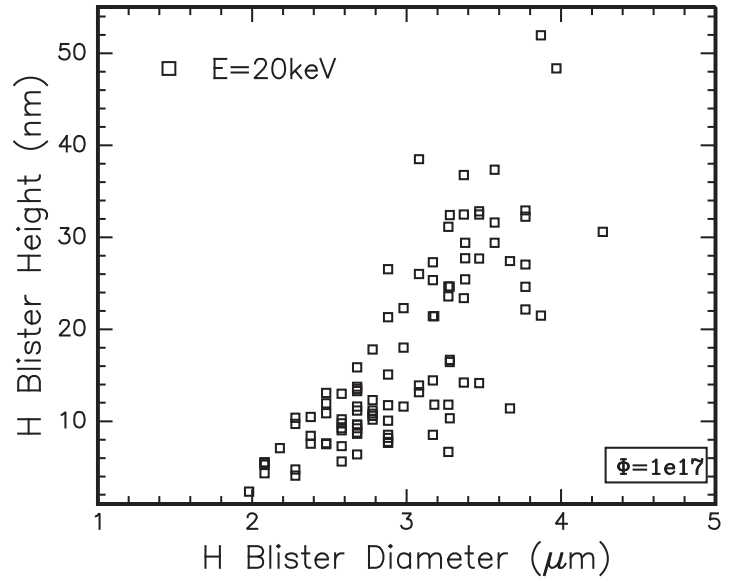

Figure D.67: Hydrogen blister height versus diameter in Ge(100) implanted with H(20keV,1×10^{17}cm^{-2},RT) and annealed at T=400°C/10min in Ar gas ambient.

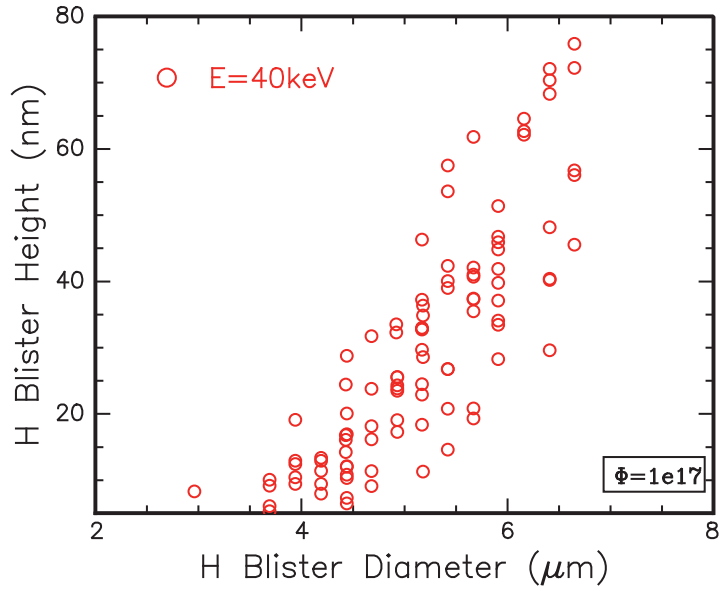

Figure D.68: Hydrogen blister height versus diameter in Ge(100) implanted with H(40keV,1×10^{17}cm^{-2},RT) and annealed at T=400°C/10min in Ar gas ambient.

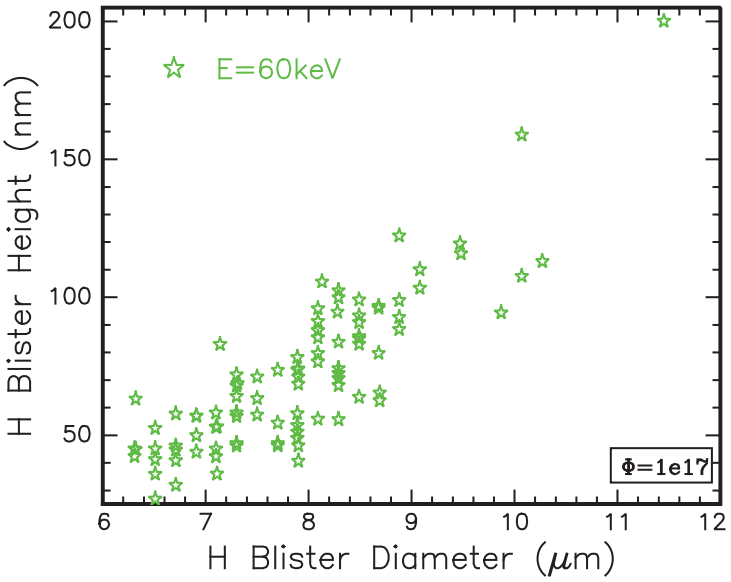

Figure D.69: Hydrogen blister height versus diameter in Ge(100) implanted with H(60keV,1×10^{17}cm^{-2},RT) and annealed at T=400°C/10min in Ar gas ambient.

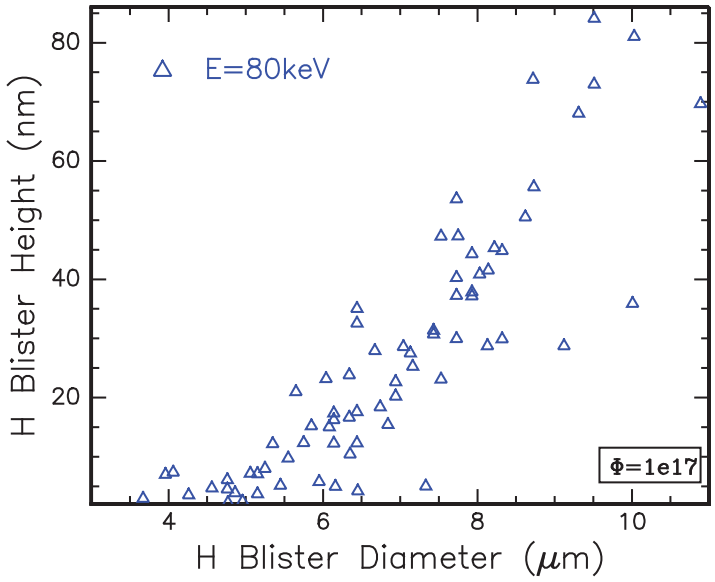

Figure D.70: Hydrogen blister height versus diameter in Ge(100) implanted with H(80keV,1×10^{17}cm^{-2},RT) and annealed at T=400°C/10min in Ar gas ambient.

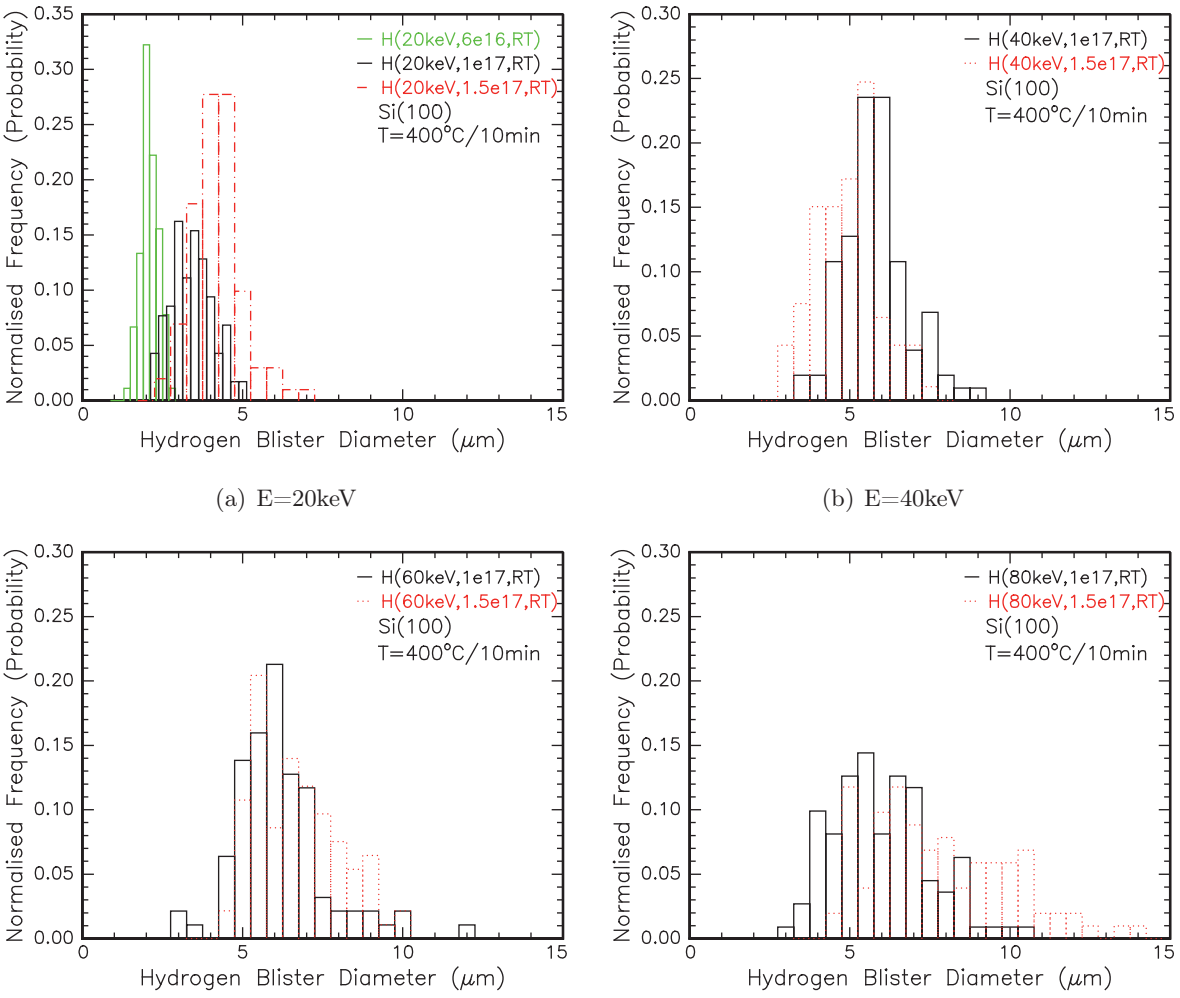

(a) E=20keV

(b) E=40keV

(c) E=60keV

(d) E=80keV

Figure D.71: Distribution of hydrogen blister diameters for Si(100) implanted with various ion energies and hydrogen fluences, as labelled, and annealed at T=400°C/10min.

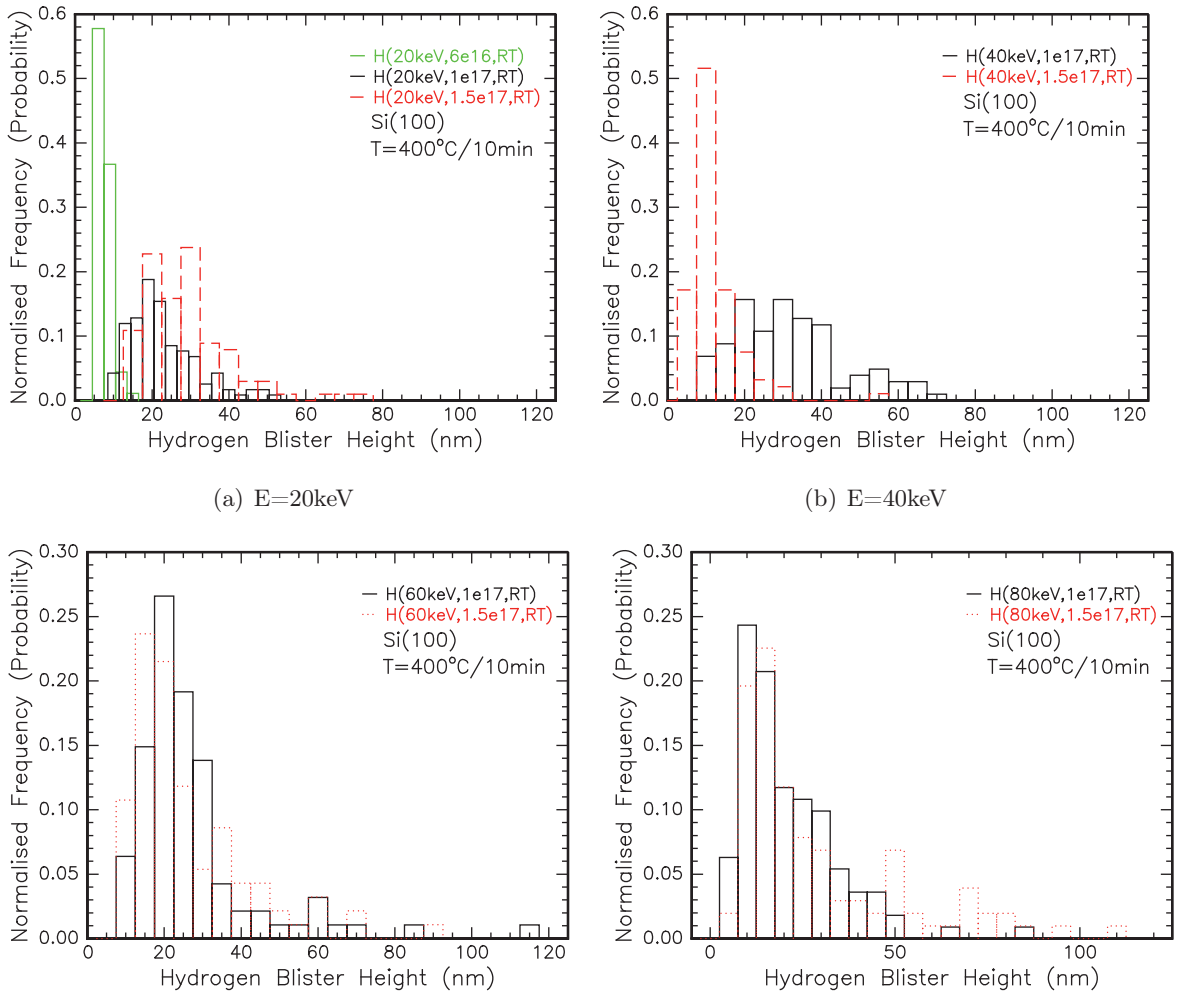

(a) E=20keV

(b) E=40keV

(c) E=60keV

(d) E=80keV

Figure D.72: Distribution of hydrogen blister heights for Si(100) implanted with various ion energies and hydrogen fluences, as labelled, and annealed at T=400°C/10min.

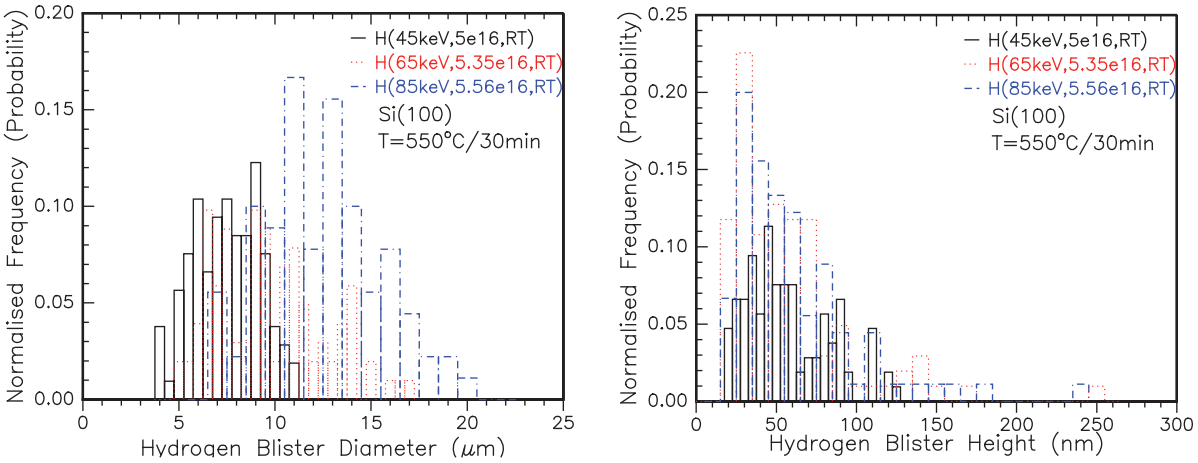

(a) (b)

Figure D.73: Distribution of hydrogen blister (a) diameters, and (b) heights, for Si(100) implanted with various ion fluences and energies, as labelled in graphs, and annealed at T=550°C for 30 minutes.

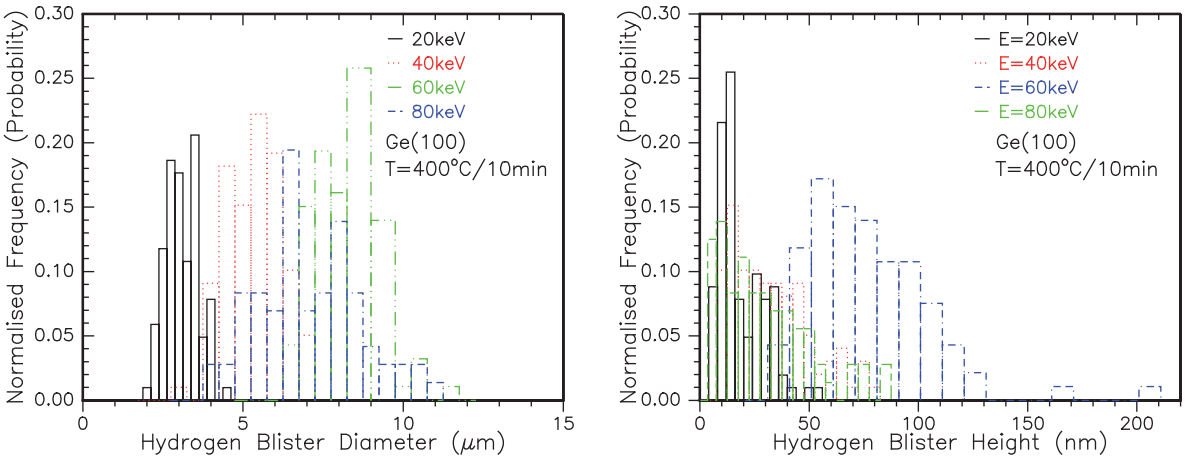

(a) (b)

Figure D.74: Distribution of hydrogen blister (a) diameters, and (b) heights, for Ge(100) implanted with various ion energies (as labelled in graphs) at a fluence of Φ_H=1×10^{17}cm^{-2}, and annealed at T=400°C for 10 minutes.

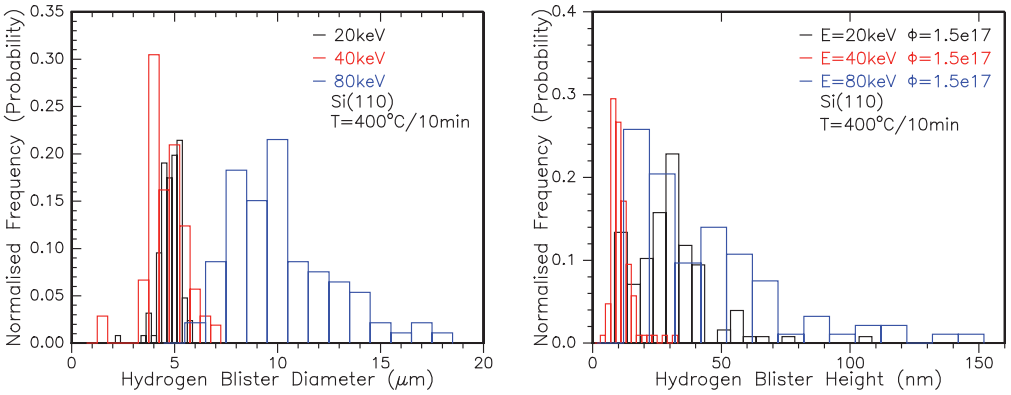

(a) (b)

Figure D.75: Hydrogen blister height distribution in H-implanted Si(110), at ion energies of 20 keV, 40 keV, and 80 keV as labelled. Φ_H=1.5×10^{17}cm^{-2} unless otherwise labelled.

Appendix E

Stress effects on hydrogen in semiconductors: Additional details

A collection of material related to the application of stress to ULTRATHIN® Si wafers comprises the bulk of this appendix. Additional material collected by ion beam techniques such as RBS and ERD are included. Also shown is a colour map, the final product of values of stress which are calculated from an analytical function fit, determined by DataThief from a strained wafer photographs. Following this are the actual photographs used to determine the stress in the silicon wafers, showing both the original and the image overlaid in software package DataThief.

E.1 Ion beam analysis techniques

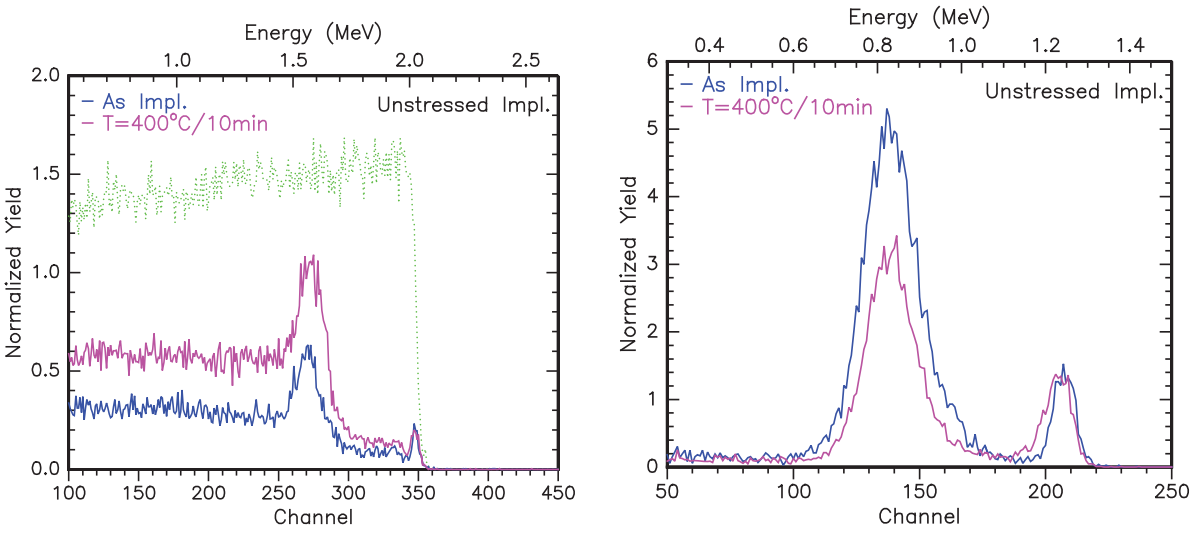

Figure E.1: 3MeV $^4He^+$ RBS-C (left) and ERD (right) spectra of H(40keV,6×10^{16}cm^{-2},RT)-implanted 50 μm Si(100) under no stress as labelled, and subsequently annealed without stress at T=400°C for 10 minutes. Also shown in (a) is the random angled yield from an intrinsic Si(100) wafer.

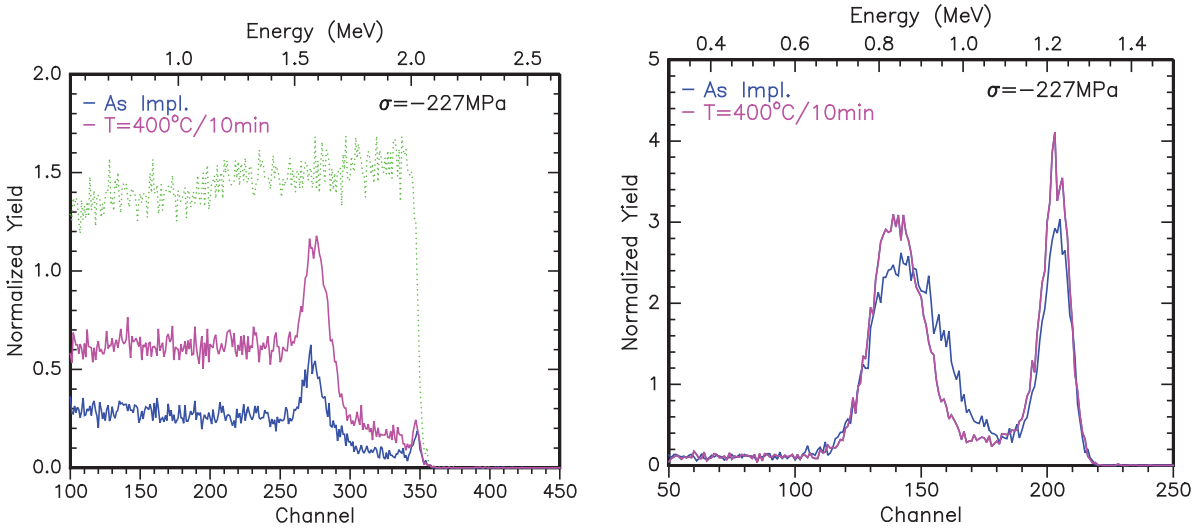

Figure E.2: 3MeV $^4He^+$ RBS-C (left) and ERD (right) spectra of H(40keV,6×10^{16}cm^{-2},RT)-implanted 50 μm Si(100) under compressive stress of σ=-227 MPa as labelled, and subsequently annealed without stress at T=400°C for 10 minutes. Also shown in (a) is the random angled yield from an intrinsic Si(100) wafer.

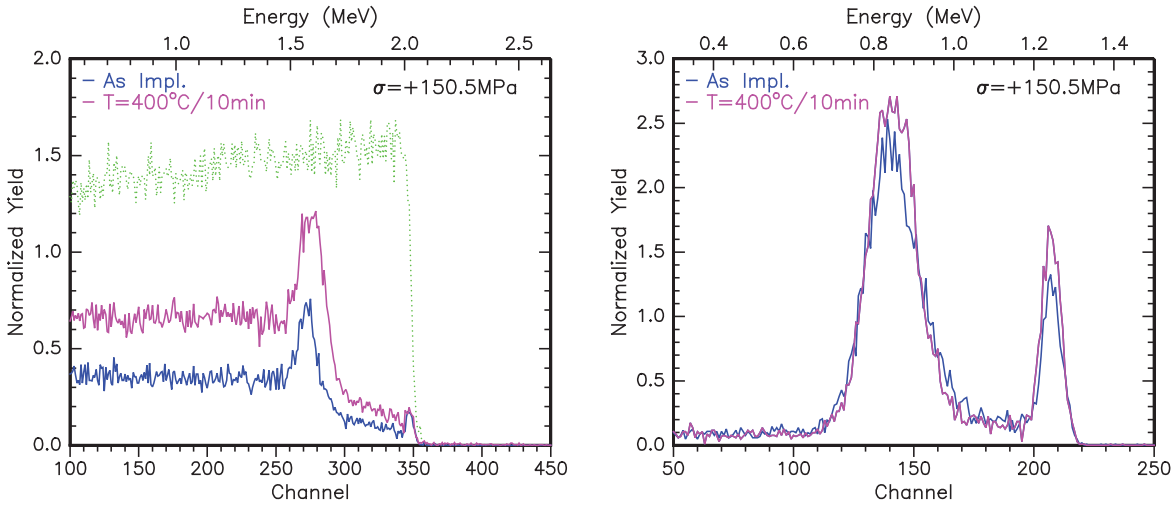

(a) (b)

Figure E.3: 3MeV $^4He^+$ RBS-C (a) and ERD (b) spectra of H(40keV,6×10^{16}cm^{-2},RT)-implanted 50 μm Si(100) under tensile stress of σ=+151 MPa as labelled, and subsequently annealed without stress at T=400°C for 10 minutes. Also shown in (a) is the random angled yield from an intrinsic Si(100) wafer.

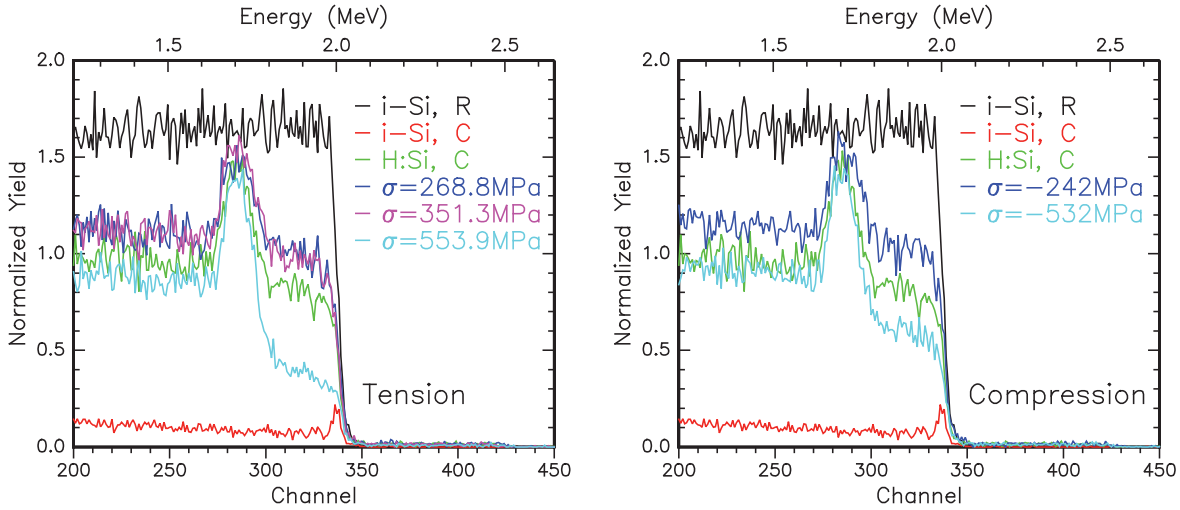

Figure E.4: 3MeV $^4He^+$ channelled RBS measurements of 50 μm Si(100) wafers implanted with H(40keV,6×10^{16}cm^{-2},RT), then annealed at T=400°C/30min under various values of (a) tensile, and (b) compressive stress. C indicates ion beam is channelled, R indicates randomly angled relative to the crystalline lattice. All measurements not marked R are measured along the [100] channel. Scattering angle ϕ=110°, Q=20 μC, I=10 nA.

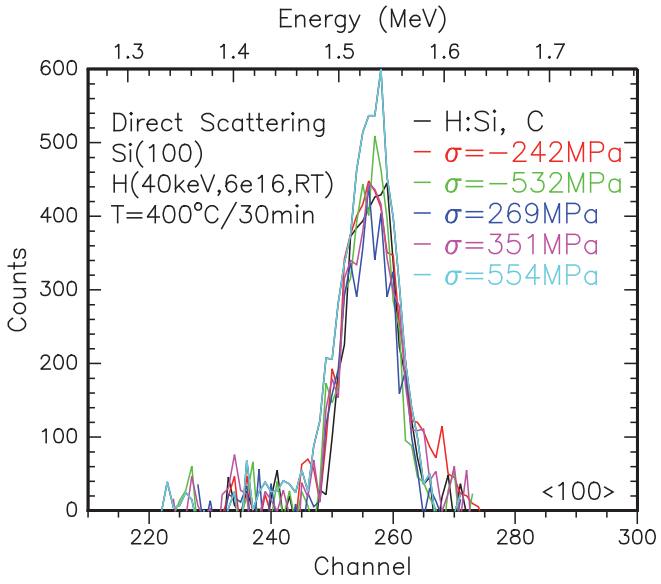

Figure E.5: 3MeV $^4He^+$ channelled RBS measurements of direct scattering peaks in 50 μm Si(100) wafers implanted with H(40keV,6×10^{16}cm^{-2},RT), then annealed at T=400°C/30min under various tensile and compressive stresses, as labelled. All samples measured along the [100] channel. Si surface at channel 283. Scattering angle ϕ=168.2°, Q=20 μC, I=10 nA.

Anneal Stress	Dechannelling		Direct Scattering		
σ **(MPa)**	χ_{DC}/χ_{Random} (%)	ρ (cm^{-3})	χ_{DS}/χ_{Random} (%)	ρ (cm^{-3})	R_P (nm)
As Impl.	18.9	9.4×10^{21}	5.5	2.7×10^{21}	477±4
0	50.7	2.5×10^{22}	8.4	4.2×10^{21}	459±5
–242	60.5	3.0×10^{22}	8.4	4.2×10^{21}	457±2
–532	46.6	2.3×10^{22}	9.0	4.5×10^{21}	457±2
+269	58.0	2.9×10^{22}	8.4	4.2×10^{21}	456±3
+351	57.5	2.9×10^{22}	8.9	4.4×10^{21}	456±3
+554	44.4	2.2×10^{22}	9.6	4.8×10^{21}	453±2

Table E.1: RBS-C ⟨100⟩ dechannelling (**DC**) yield and direct scattering (**DS**) peaks yield and depth measured in 50 μm Si(100) implanted with H(40keV,6×10^{16}cm^{-2},RT), and annealed for T=400°C/30 minutes under applied mechanical stresses as labelled. Experimental RBS-C spectra shown in Fig. 5.19, DS peaks in Fig. E.5, and summarised in Fig. 5.24.

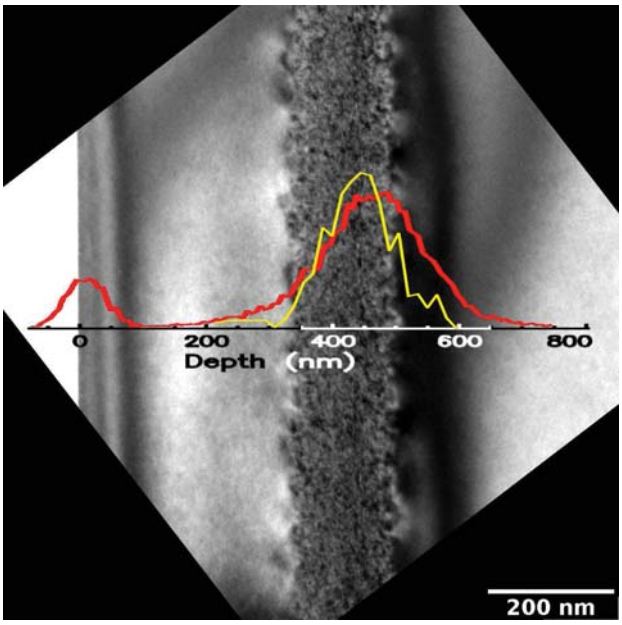

Figure E.6: Comparison of large scale macro-defect formation in H(40keV,6×10^{16}cm^{-2},RT) ion implanted 50 μm Si(100) annealed at T=400°C/30 minutes under σ=269 MPa, with implanted hydrogen profile determined by ERD (red line) and ion implantation damage determined by RBS-C (yellow line). Surface at left of figure, micrograph scale as labelled.

Sample	**Annealed?** ✓/×	**Stress** (MPa)	**XTEM Crack Depth** (nm)	**RBS-C DS Peak** (z_{low}<z(nm)<z_{high})	**ERD H Profile** (z_{low}<z(nm)<z_{high})
N1	×	0.0	n.a.	(308<446<594)	(255.7<465.0<645.6)
N2	✓	0.0	441±7	(290<450<590)	(255.7<460.0<610.2)
C1	✓	-242±51	430±8	(225<455<635)	(255.7<446.8<593.0)
C3	✓	-532±111	443±10	(290<440<590)	(289.2<450.0<593.0)
T1	✓	222±56	448±4	(325<460<580)	(231.9<422.2<593.0)
T3	✓	554±116	426±6	(285<445<615)	(296.9<450.0<594.7)

Table E.2: Depths of macroscopic cracking in hydrogen-implanted 50 μm Si, with stresses as labelled applied during annealing at T=400°C/30 minutes, determined by RBS, ERD and XTEM. Implantation H(40keV,6×10^{16}cm^{-2},RT) and crystal orientation (100).

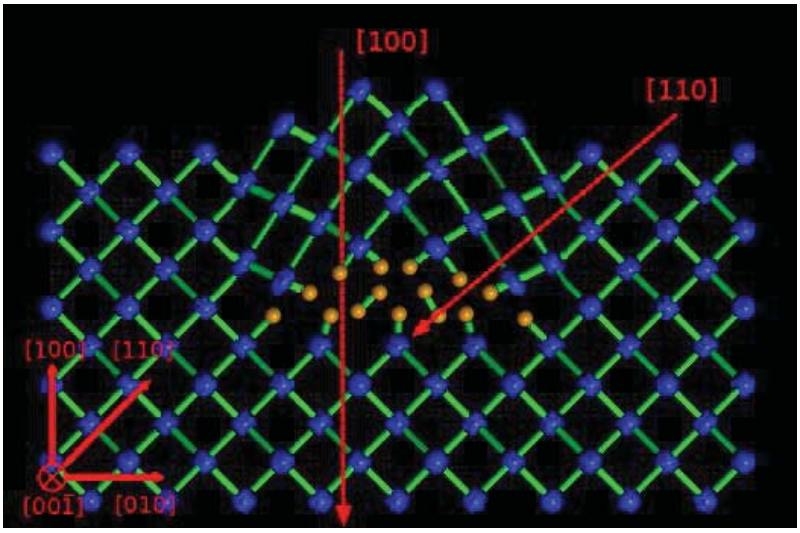

(a) (100) wafer/⟨001⟩ platelet

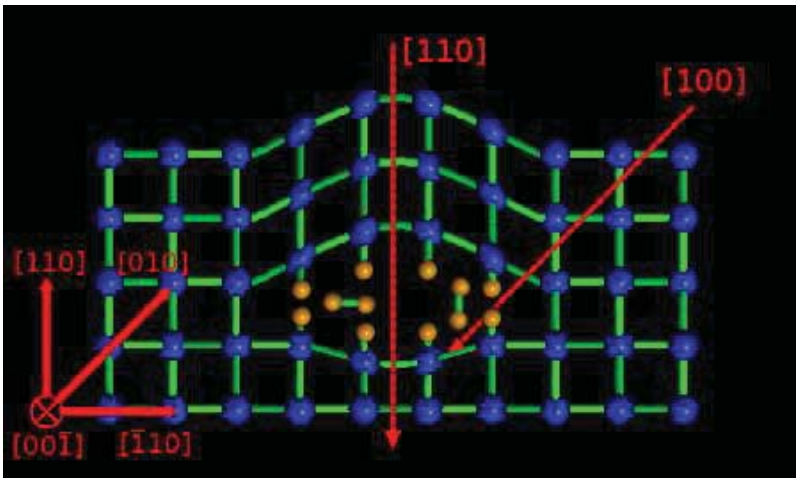

(b) (110) wafer/⟨011⟩ platelet

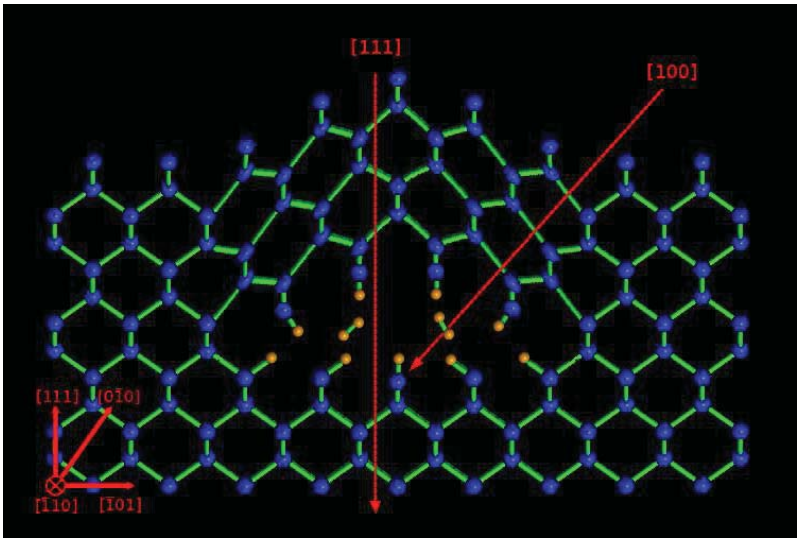

(c) (111) wafer/⟨111⟩ platelet

Figure E.7: Two-dimensional lattice illustration of hydrogen-stabilised platelet defects in (100), (110) and (111) wafers, aligned with plane of wafer, probed by channelled analysis beams. Influence of registry shift in crystal lattice on ion beam shown for perpendicular and off-axis beams. Blue and orange spheres represent Si and H atoms.

E.2 Stress determination photographs

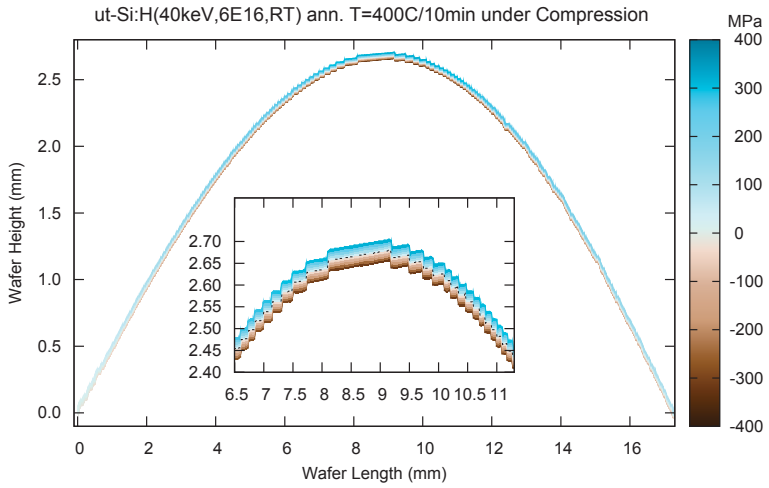

Figure E.8: Stress-position colour map of 50 μm-thick Si(100) implanted with H(40keV,6×10^{16}cm^{-2},RT), then annealed under compressive stress at T=400°C/10 minutes. Tensile stress positive and blue, compressive stress negative and brown. Data extracted from photograph of wafer with DataThief, and radius of curvature calculated numerically at all points to find stress with symmetric Euler-Bernoulli beam equation. Unlike elsewhere in thesis, wafer curve data not fit with polynomial function, as extracted from DataThief.

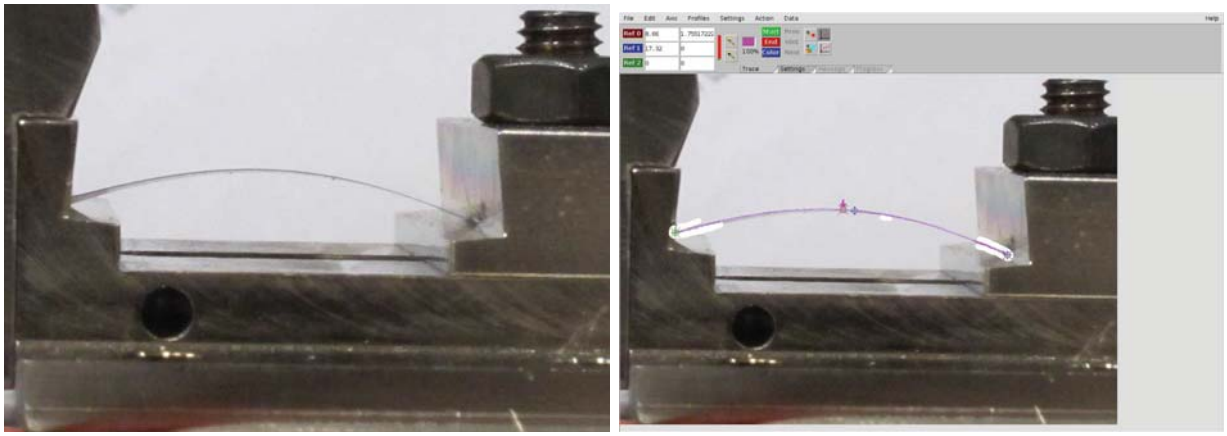

(a) (b)

Figure E.9: Digital still photograph of sample T0 – utSi(100) implanted with H(40keV,6×10^{16}cm^{-2},RT), annealed at T=400°C/30 min under low tensile stress – used to determine stress in wafer. (a) shows the original photograph, while (b) shows the data fit in DataThief [367] to establish a series of (x, y) co-ordinates of a numeric function defining the wafer's curve.

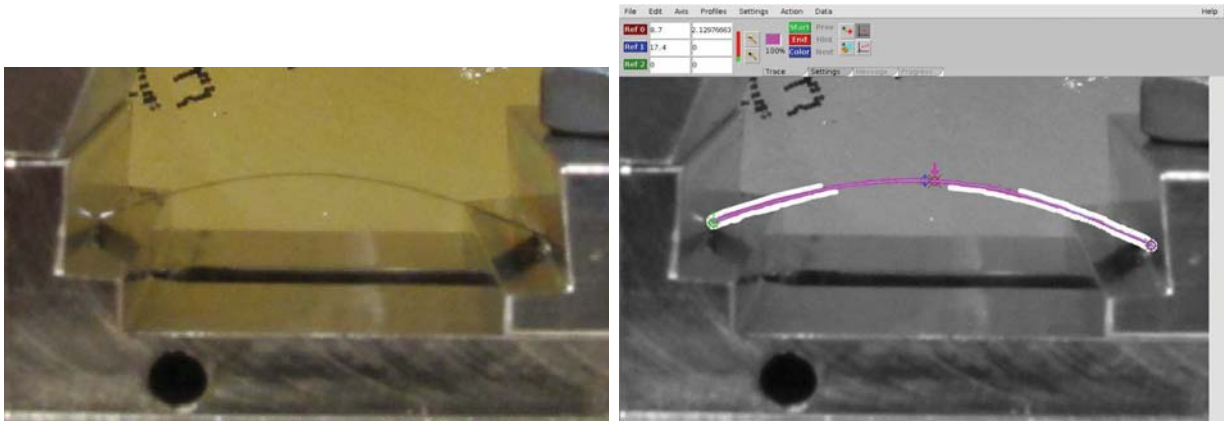

(a) (b)

Figure E.10: Digital still photograph of sample T1 – utSi(100) implanted with H(40keV,6×10^{16}cm^{-2},RT), annealed at T=400°C/30 min under low tensile stress – used to determine stress in wafer. (a) shows the original photograph, while (b) shows the data fit in DataThief [367] to establish a series of (x, y) co-ordinates of a numeric function defining the wafer's curve.

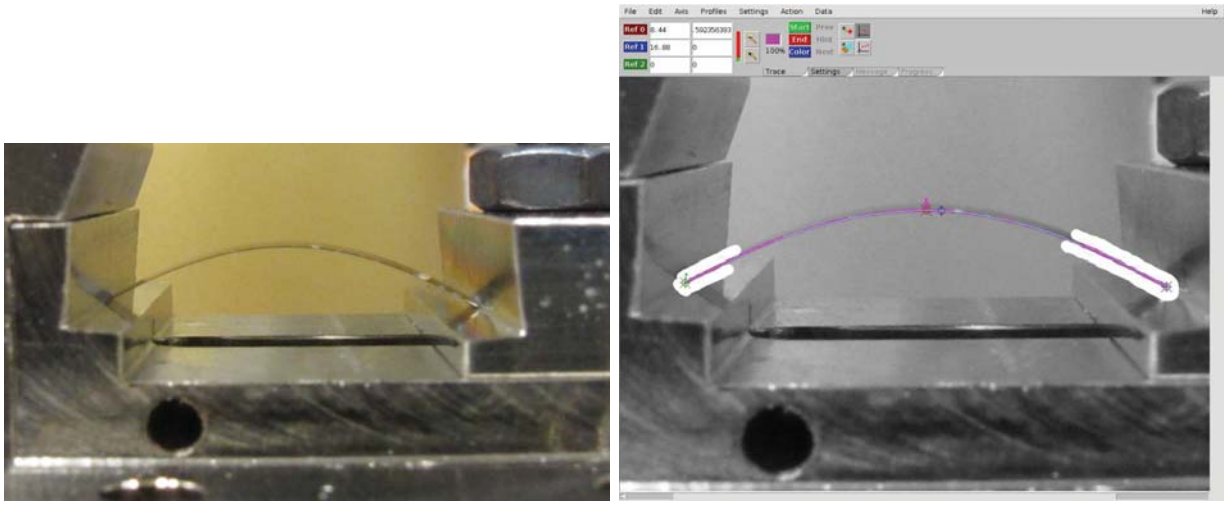

(a) (b)

Figure E.11: Digital still photograph of sample T2 – utSi(100) implanted with H(40keV,6×10^{16}cm^{-2},RT), annealed at T=400°C/30 min under median tensile stress – used to determine stress in wafer. (a) shows the original photograph, while (b) shows the data fit in DataThief [367] to establish a series of (x, y) co-ordinates of a numeric function defining the wafer's curve.

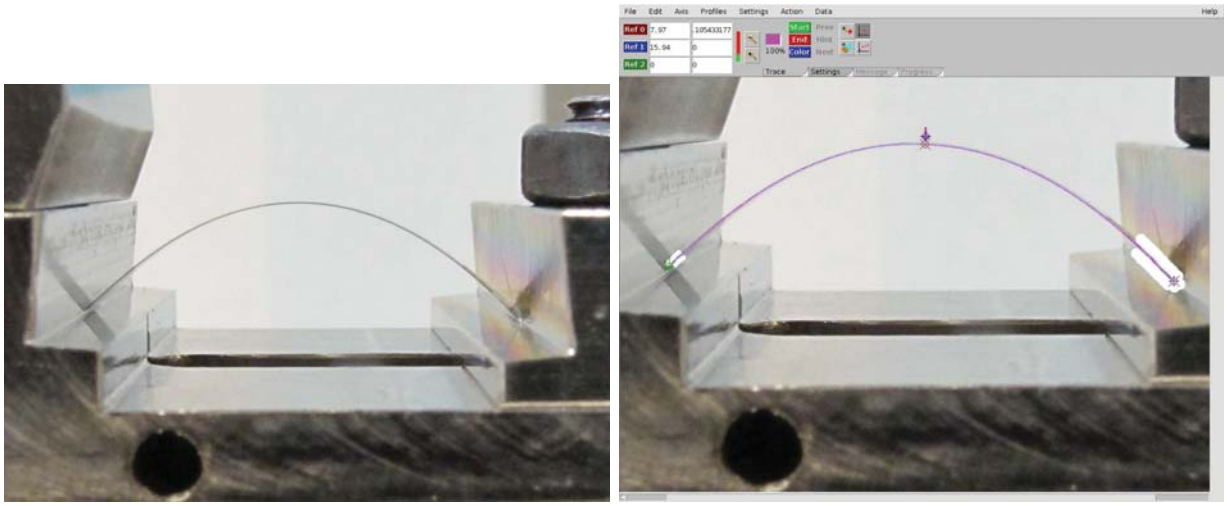

(a) (b)

Figure E.12: Digital still photograph of sample T3 – utSi(100) implanted with H(40keV,6×10^{16}cm^{-2},RT), annealed at T=400°C/30 min under high tensile stress – used to determine stress in wafer. (a) shows the original photograph, while (b) shows the data fit in DataThief [367] to establish a series of (x, y) co-ordinates of a numeric function defining the wafer's curve.

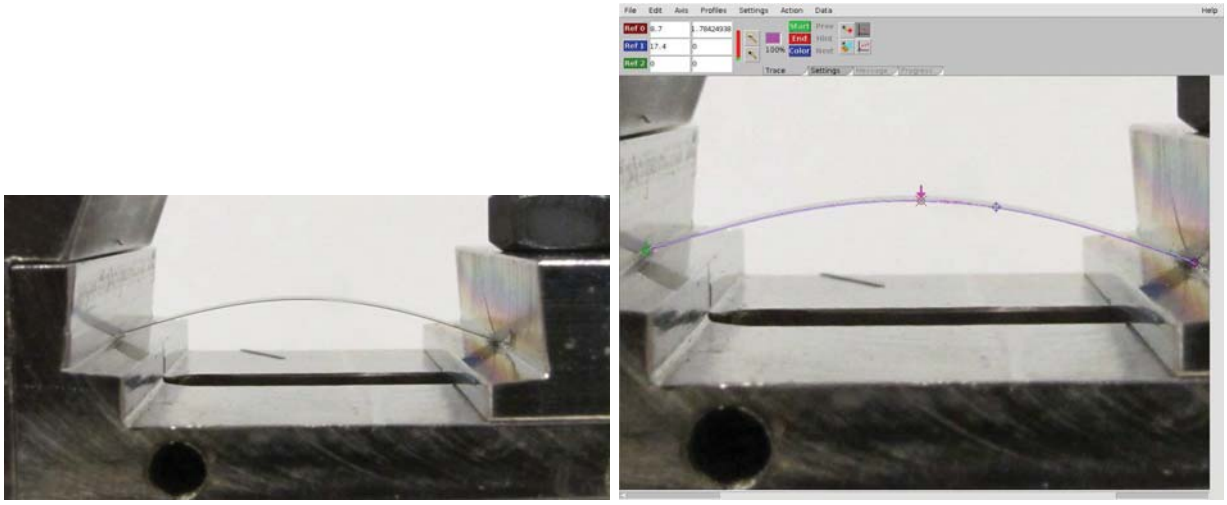

(a) (b)

Figure E.13: Digital still photograph of sample C1 – utSi(100) implanted with H(40keV,6×10^{16}cm^{-2},RT), annealed at T=400°C/30 min under low compressive stress – used to determine stress in wafer. (a) shows the original photograph, while (b) shows the data fit in DataThief [367] to establish a series of (x, y) co-ordinates of a numeric function defining the wafer's curve.

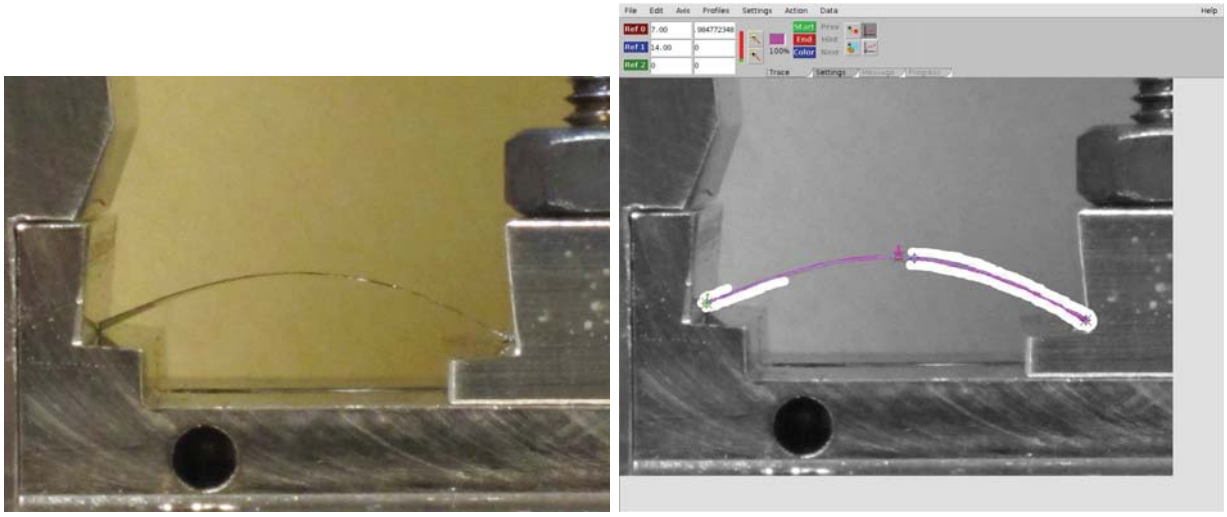

(a) (b)

Figure E.14: Digital still photograph of sample C2 – utSi(100) implanted with H(40keV,6×10^{16}cm^{-2},RT), annealed at T=400°C/30 min under median compressive stress – used to determine stress in wafer. (a) shows the original photograph, while (b) shows the data fit in DataThief [367] to establish a series of (x, y) co-ordinates of a numeric function defining the wafer's curve.

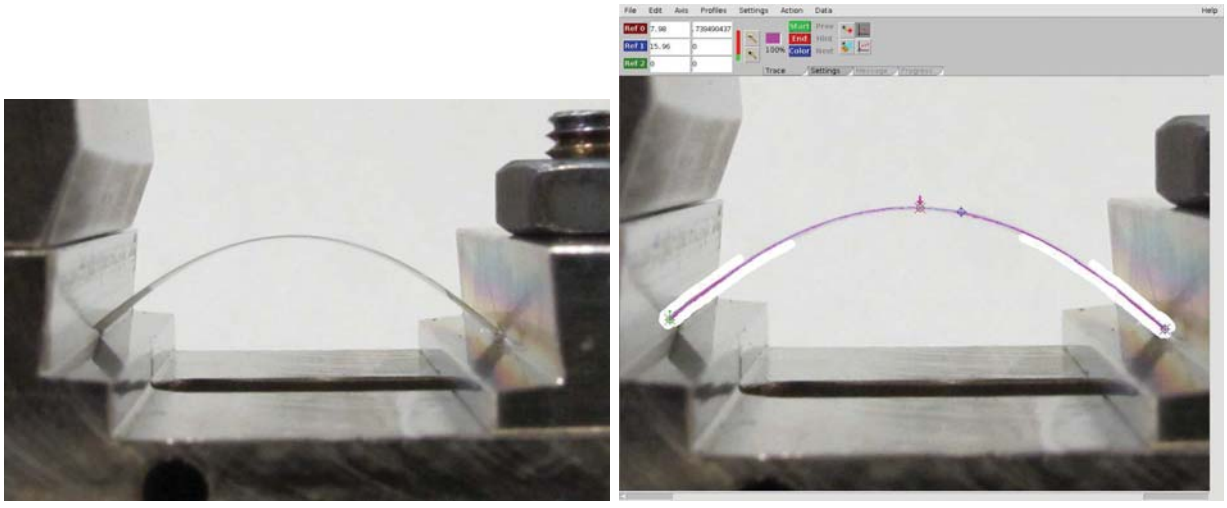

(a) (b)

Figure E.15: Digital still photograph of sample C3 – utSi(100) implanted with H(40keV,6×10^{16}cm^{-2},RT), annealed at T=400°C/30 min under high compressive stress – used to determine stress in wafer. (a) shows the original photograph, while (b) shows the data fit in DataThief [367] to establish a series of (x, y) co-ordinates of a numeric function defining the wafer's curve.

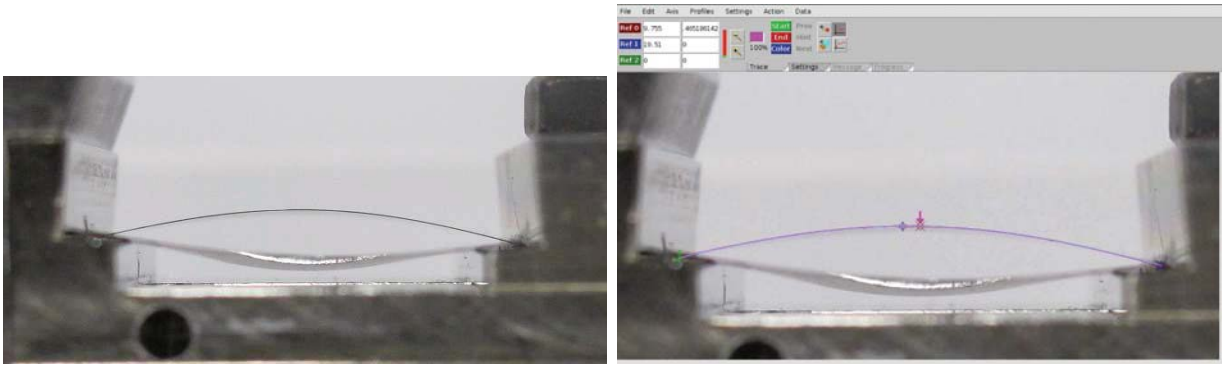

(a) (b)

Figure E.16: Digital still photograph of utSi(100 implanted with H(40keV,6×10^{16}cm^{-2},RT) under tensile stress, then annealed at T=400°C/10 min stress-free, used to determine stress in wafer. (a) shows the original photograph, while (b) shows the data fit in DataThief [367] to establish a series of (x, y) co-ordinates of a numeric function defining the wafer's curve.

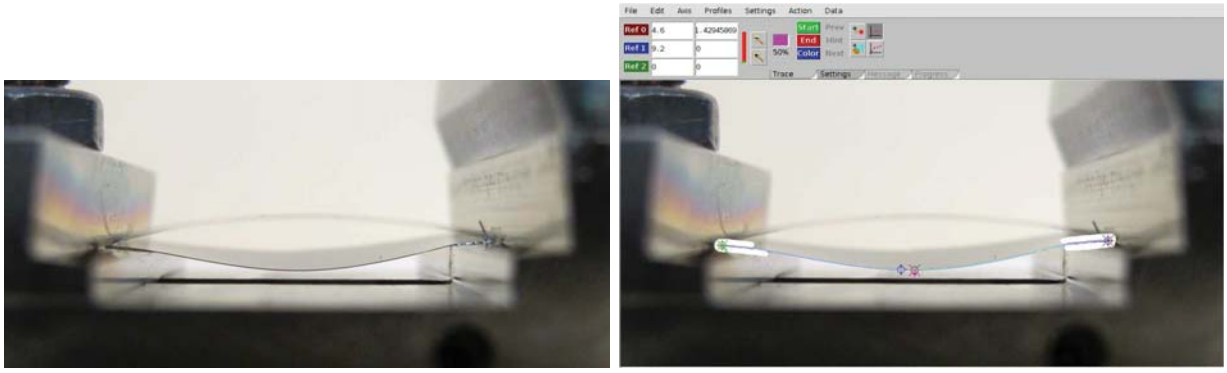

(a) (b)

Figure E.17: Digital still photograph of utSi(100 implanted with H(40keV,6×10^{16}cm^{-2},RT) under compressive stress, then annealed at T=400°C/10 min stress-free, used to determine stress in wafer. (a) shows the original photograph, while (b) shows the data fit in DataThief [367] to establish a series of (x, y) co-ordinates of a numeric function defining the wafer's curve.

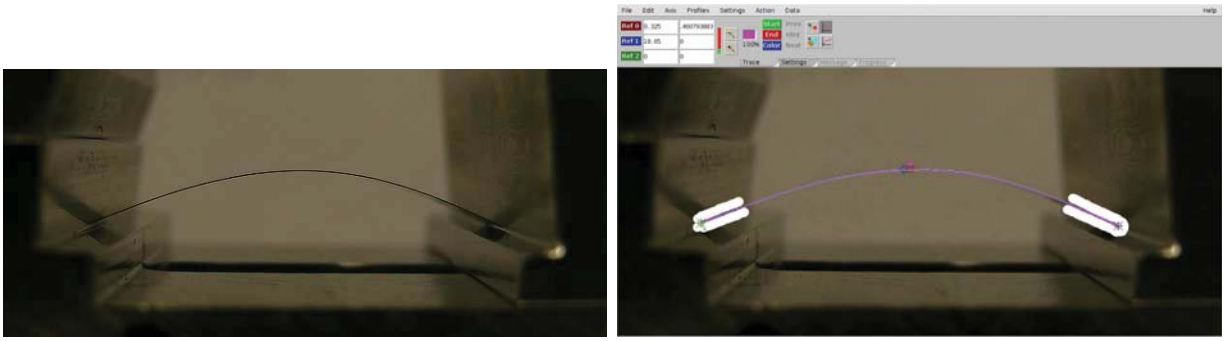

(a) (b)

Figure E.18: Digital still photograph of utSi(100 implanted with H(40keV,6×10^{16}cm^{-2},RT) stress-free, then annealed at T=400°C/10 min under tensile stress, used to determine stress in wafer. (a) shows the original photograph, while (b) shows the data fit in DataThief [367] to establish a series of (x, y) co-ordinates of a numeric function defining the wafer's curve.

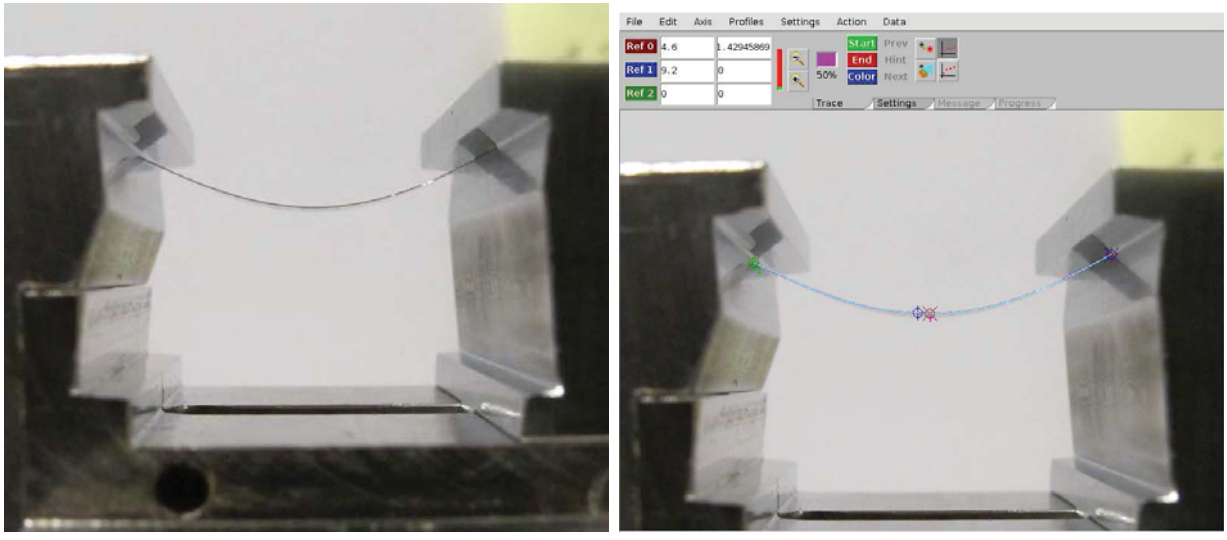

(a) (b)

Figure E.19: Digital still photograph of utSi(100 implanted with H(40keV,6×10^{16}cm^{-2},RT) stress-free, then annealed at T=400°C/10 min under compressive stress, used to determine stress in wafer. (a) shows the original photograph, while (b) shows the data fit in DataThief [367] to establish a series of (x, y) co-ordinates of a numeric function defining the wafer's curve.

(a) (b)

Figure E.20: Digital still photograph of utSi(100 implanted with H(40keV,6×10^{16}cm^{-2},RT) under tensile stress, then annealed at T=400°C/10 min under tensile stress, used to determine stress in wafer. (a) shows the original photograph, while (b) shows the data fit in DataThief [367] to establish a series of (x, y) co-ordinates of a numeric function defining the wafer's curve.

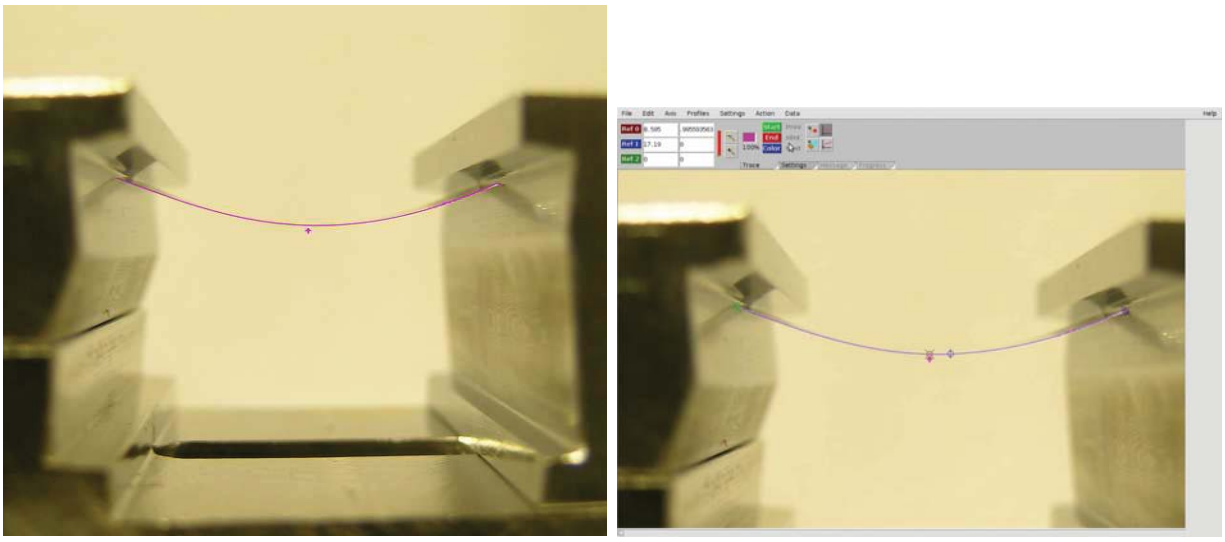

(a) (b)

Figure E.21: Digital still photograph of utSi(100 implanted with H(40keV,6×10^{16}cm^{-2},RT) under compressive stress, then annealed at T=400°C/10 min under compressive stress, used to determine stress in wafer. (a) shows the original photograph, while (b) shows the data fit in DataThief [367] to establish a series of (x, y) co-ordinates of a numeric function defining the wafer's curve.

E.3 Optical Profilometry

Using optical profilometry, the distribution of hydrogen-induced blisters diameters versus heights was characterised for each applied stress. As was apparent from the three dimensional projections of the samples seen in Fig. 5.20, the overall spread in blister heights is approximately the same in all $|\sigma|$ <400 MPa anneals, with smaller ranges in the highest stressed material. A lower limit in blister height increases linearly with blister diameter. This lower height limit suggests not only that larger blisters are capable of supporting higher blister domes, but that a minimum dome height exists for a particular diameter. Such a dimensional limit is possibly due to the energetics of surface tension where the blister meets the silicon surface, making low angles of contact unsustainable. Another possibility is that the relative proportion of pressurised hydrogen gas volume which is required to produce blisters of this diameter is sufficient that the blister will naturally overcome some complementary minimum in the height. Whatever the case, this height minimum stays roughly constant until the blister diameter reaches 4 μm, then increases by approximately 2.5 nm per micron in diameter. Similarly there appears to be an upper boundary on blister heights per diameter seen in the majority of samples, so while there is an increasing open range of possibly height values, blisters are still limited to dimensions lying between these two bounds.

In the case of silicon annealed under compressive stress, the average upper boundary value extends along a curve from a ratio of 2nm:2μm, to 22nm:5μm, through 38nm:6μm, up until 55nm:7μm. In the silicon annealed under tensile stress, the upper values of blister heights is constant for a larger range of low value diameters. The ratio starts at roughly 2nm:1.8μm, but is little changed up to diameters of 3 μm. The increase in blister height per increase in blister diameter follows a slightly flatter curve than in compressively stressed samples, such that while also reaching 22 nm high at 5 μm width, to reach a height of 55 nm requires a diameter of $\sim$8.5 μm.

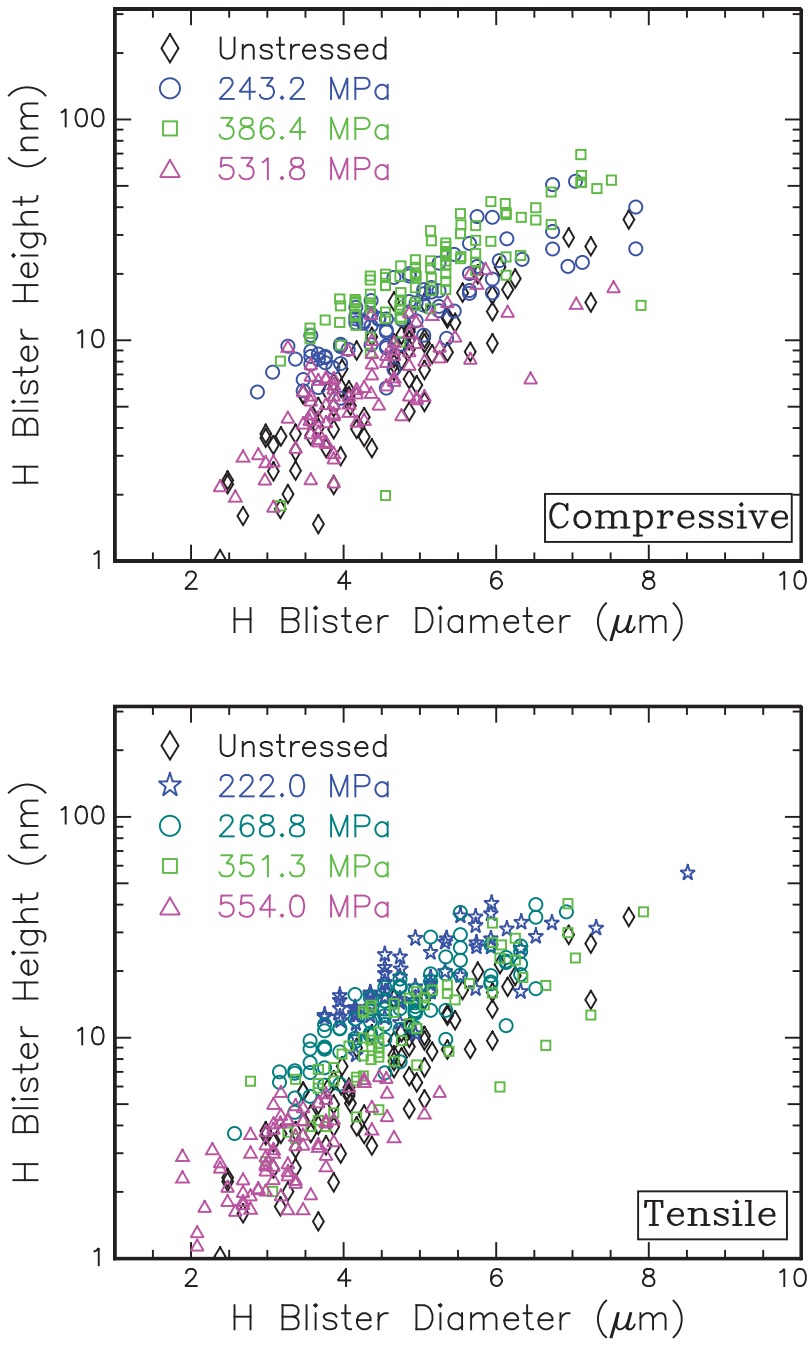

Figure E.22: Hydrogen blister diameter versus height distributions measured by optical profiler from H(40keV,6×10^{16}cm^{-2},RT) implanted 50 μm Si(100) wafers annealed at T=400°C/ 30 minutes under various labelled values of (top) compressive, and (bottom) tensile stress. Profiler in PSI mode, using ×50 lens, FoV ×2.

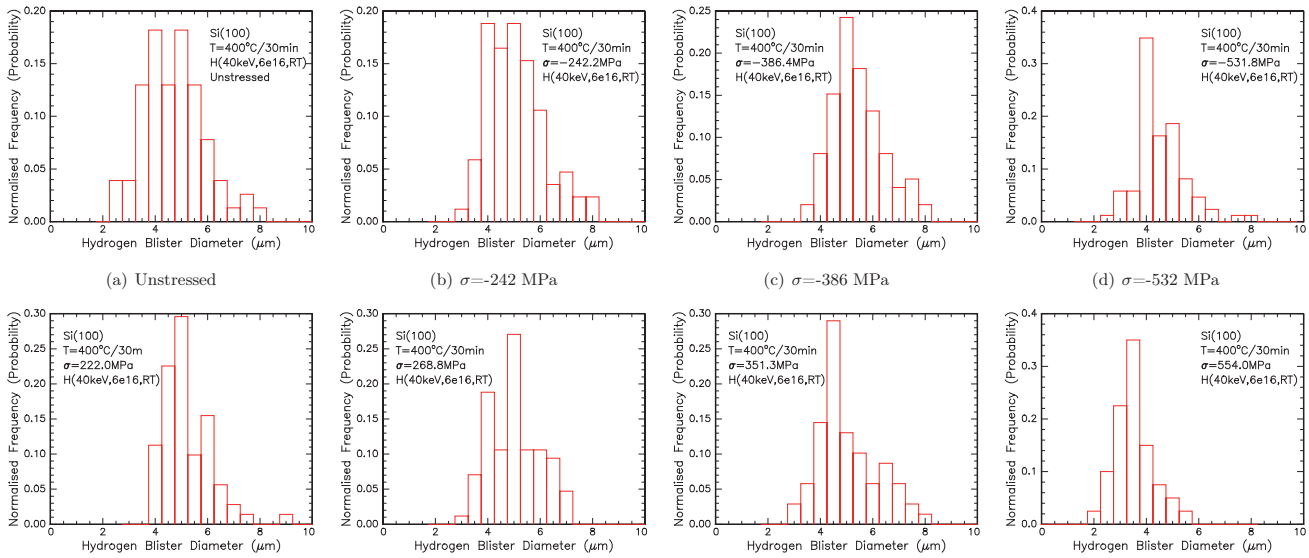

(a) Unstressed (b) σ=-242 MPa (c) σ=-386 MPa (d) σ=-532 MPa

(e) σ=222 MPa (f) σ=269 MPa (g) σ=351 MPa (h) σ=554 MPa

Figure E.23: Histogram distribution of hydrogen blister diameters, measured by the Wyko optical profilometer, from hydrogen-implanted 50 μm thick Si(100) annealed at T=400°C/30 minutes in an Ar gas ambient. (a)-(h) shows distribution of blister diameters for various stresses, as labelled, applied during the annealing process.

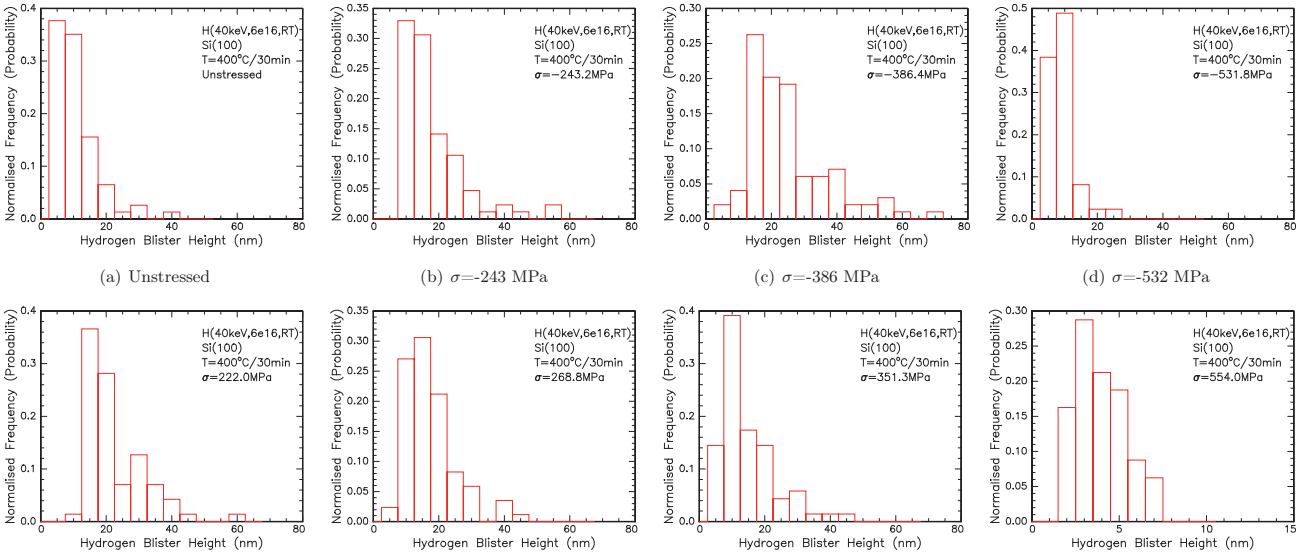

(a) Unstressed (b) σ=-243 MPa (c) σ=-386 MPa (d) σ=-532 MPa

(e) σ=222 MPa (f) σ=269 MPa (g) σ=351 MPa (h) σ=554 MPa

Figure E.24: Histogram distribution of hydrogen blister heights, measured by the Wyko optical profilometer [315], from hydrogen-implanted 50 μm thick Si(100) annealed at T=400°C/30 minutes in an Ar gas ambient. (a)-(h) shows distribution of blister heights for various stresses, as labelled, applied during the annealing process. Note different axis range label for (h).

E.4 Influence of stress apparatus on thermal environment

The mechanical jig (the stress boat apparatus) required to maintain the stress upon the wafers prevents the material being as readily exposed to the ambient in the Ar gas furnace, and additionally transfers the energy to the wafer through only two contact points, allowing inhomogeneity to occur in the sample heating. Under either of these conditions, cratering (and in some instances, blistering) may not occur at previously established times.

In order to observe the environmental rather than stress-induction impact that the apparatus had upon the hydrogen evolution, an implanted 50 μm Si wafer was placed within the stress boat, spanning the apparatus' shelves without external stresses being applied, and allowed to anneal under the same conditions, i.e., T=400°C/30 minutes under an Ar ambient. Contrast between this sample annealed in the stress apparatus with the same material being annealed in a small quartz tray is shown in Fig. E.25. Within the parameters explored in this data, there is little difference between the sample as annealed in the stainless steel stress apparatus and the sample annealed within the quartz tray.

Both the blister diameter and height distributions measured in the two samples reveal near identical behaviour, as does the overall appearance of the samples seen in the three dimensional projections of the optical profiler measurements in Fig. E.25(a) and (e). In the spread of blister heights versus diameter seen in Fig. E.25(d), the range of values measured in either annealing condition are largely in agreement. The sample annealed under the quartz boat does show a slightly increased blister height maxima over the 4–6 μm diameter range, increasing by up to 10 nm higher than upon the stress boat-hosted sample. This may be an indication of the increased exposure to the ambient temperature by the sample within the quartz boat, allowing the implanted hydrogen greater energy to evolve into defect complexes that produce the blistering. However, this could as easily be accommodated by minor changes in local furnace temperature, which has a thermal gradient of approximately 1°C.cm^{-1}. As each anneal could not perforce be performed simultaneously due to the influence being explored, placement within the furnace tube could potentially have been off-set by as much as 5 cm. Therefore, while the data suggests that the stress apparatus modified the dynamics of the hydrogen blistering within the 50 μm Si wafers, it is also shown any such changes to the overall behaviour of the system are not significant.

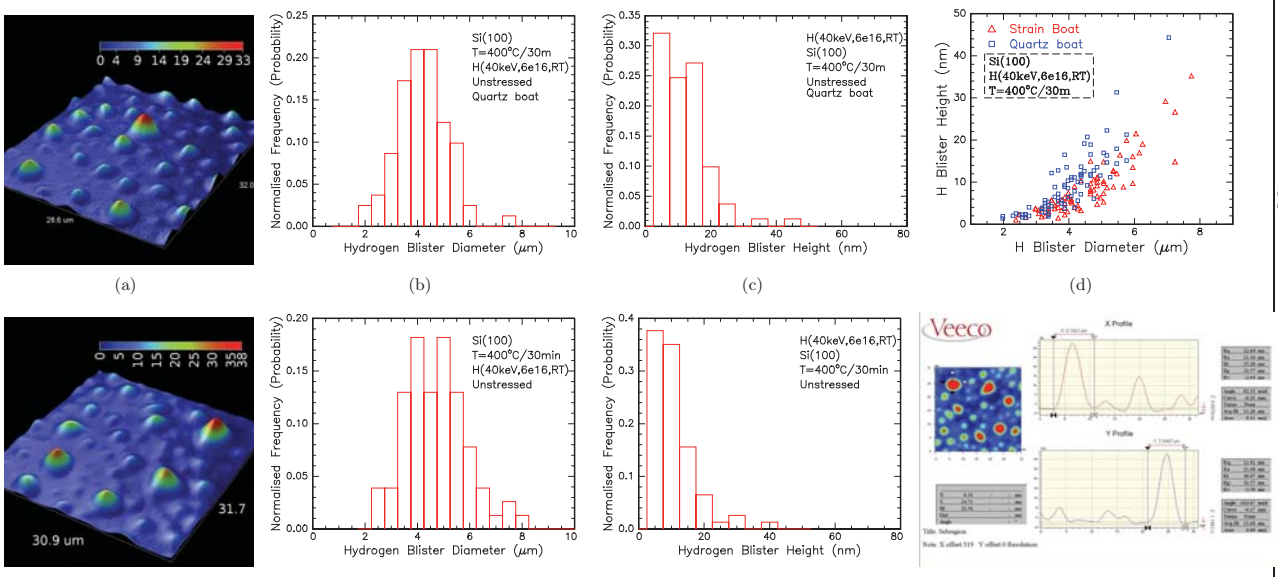

(a) (b) (c) (d)

(e) (f) (g) (h)

Figure E.25: Optical profiler measurements of surface blisters on H(40keV,6×10^{16}cm^{-2},RT)-implanted 50 μm-thick Si(100), annealed at T=400°C/30 minutes in a (a) small quartz tray, (e) stainless steel stress apparatus. Height scale in nanometres. (b) & (f) show the relative histograms of the distribution of measured blister diameters which evolved under the particular annealing conditions, while (c) & (g) show the measured blister heights. (d) shows a direct comparison of the ratio of blister height to diameter produced in the material when implanted either in a quartz or larger stainless steel holder, and (h) shows a screenshot from the Wyko Vision32™ [315] software and how it was used to measure the blisters. OP used in PSI mode, using a ×50 lens and F.o.V. set at ×2.

Appendix F

Radius of curvature extraction Python code

Lastly, the following appendix includes the Python code used in our project to extract the radius of curvature from the DataThief-measured wafer curve function $w(x, y)$. As the code relied upon the first and second derivatives of w, there were minor differences between each script. The example provided here is for the 50 μm Si(100) implanted with H(40keV,6×10^{16}cm^{-2},RT) and then annealed under highly tensile stress at T=400°C/30 minutes. The commenting within the code is perfunctory at best.

The addition of this code into a LaTeX environment required heavy usage of Pakin's "Comprehensive LaTeX Symbol List" [421] (on top of everywhere else in this manuscript, naturally). This script was operated from the Linux terminal prompt, using the command:

```
./find_radius.py --data ⟨filename⟩
```

CODE BEGINS:

```
#!/usr/bin/env python
#       File: find_radius.py
#       Last modified: 2011-09-05T17:30:38+1000

# imports
import sys
import os
import argparse
import string
import re

# A mimic of C-style preprocessor definitions. Not an ideal solution.
REGEX = re.compile("(-*\d+\.*\d*|\d*\.\d+)((e|E)(\+|\-)(\d+))*")
EPSILON = 0.0000001
INFINITY = float('inf')

# definitions
def line_number_scan(f):
        # initialise empty number list
        number_list = []
        # read a line from the file
        line = f.readline()
        # find numbers in line
        numbers = REGEX.findall(line)
        # format numbers and put them in the number list
        for number in numbers:
                number_list.append(eval("%s%s" % (number[0], number[1])))
        # return
        return number_list
def count_line_number(f):
```

```
        f.seek(0)
        for counter, line in enumerate(f):
                pass
return counter + 1

# options
parser = argparse.ArgumentParser()
parser.add_argument("--data", dest="data_fn",
        help="data file name", required=True)
parser.add_argument("--out", dest="out_fn", help="out file name",
        default="output_t3_radius.txt")
args = parser.parse_args()

# check that the data file exists
if os.path.exists(args.data_fn):
        data_f = open(args.data_fn, "r")
else:
        sys.stdout.write("program file %s could not be found\n" % args.data_fn)
        exit(0)

# open the picture file's data (x,y) coordinates.
out_f = open(args.out_fn, "w")

# read data file into list
number_of_lines = count_line_number(data_f)
data_list = [[0, 0] for i in range(number_of_lines-1)]
data_f.seek(0)
# skip first line
line_data = line_number_scan(data_f)
# loop through file
for i in range(number_of_lines-1):
        line_data = line_number_scan(data_f)
```

```
        data_list[i][0] = line_data[0]
        data_list[i][1] = line_data[1]

# debug check
if False:
        sys.stdout.write("number of data lines = %d\n" % (number_of_lines-1))
        for i in range(number_of_lines-1):
                sys.stdout.write("%f %f\n" % (data_list[i][0], data_list[i][1]))

# curvature list
curvature_list = [0 for i in range(number_of_lines-3)]
for i in range(number_of_lines-3):
        x1 = data_list[i][0]
        y1 = data_list[i][1]
        x2 = data_list[i+1][0]
        y2 = data_list[i+1][1]
        x3 = data_list[i+2][0]
        y3 = data_list[i+2][1]
        # the formula for using a polynomial to arc of circle of radius R,
        # to find R itself needs derivatives dy and ddy of the fit to find R:
        # Should note this is a SPECIFIC CASE for T3 data, from Genplot fit.
        a1 = 1.0509
        a2 = -0.067602
        a3 = 9.9935e-5
        a4 = 1.9924e-7
        dy = ( (a4*4*x2**3) + (a3*3*x2**2) + (a2*2*x2) + a1 )
        ddy = ( (a4*12*x2**2) + (a3*6*x2) + a2*2 )

        R = (( 1 + dy**2 )**1.5) / abs(ddy)

        curvature_list[i] = R
```

```
# debug check
if False:
        sys.stdout.write("number of curvature measures = %d\n" % (number_of_lines-3))
        for i in range(number_of_lines-3):
                sys.stdout.write("%f\n" % curvature_list[i])

# write to file
for i in range(number_of_lines-1):
   if (i > 0) and (i < number_of_lines-2):
       out_f.write("%f %f %f\n" % (data_list[i][0], data_list[i][1], curvature_list[i-1]))
   else:
       out_f.write("%f %f nan\n" % (data_list[i][0], data_list[i][1]))

# close files
data_f.close()
out_f.close()
```

CODE ENDS

Lost In Translation

For I think there is no occasion accomplished that is more pleasant
than when festivity holds sway among all the populace,
and the feasters up and down the houses are sitting in order
and listening to the singer, and beside them the tables are loaded
with bread and meats, and from the mixing bowl the wine steward
draws the wine and carries it about and fills the cups. This
seems to my own mind to be the best of occasions.
But now your wish was inclined to ask me about my mournful
sufferings, so that I must mourn and grieve even more. What then
shall I recite to you first of all, what leave till later?
Many are the sorrows the gods of the sky have given me.

But come, I will tell you of my voyage home with its many
troubles, which Zeus inflicted on me as I came from Troy.

- Homer, *Odyssey*, Book IX.5-15,37-38
(Translated by Richmond Lattimore, 1965)